LARGE-SCALE REMOTELY INTERROGATED ARRAYS OF FIBRE-OPTIC INTERFEROMETRIC SENSORS AND FIBRE LASERS

by

Geoffrey Alan Cranch

A thesis submitted for the degree of Doctor of Philosophy on completion of research in the Dept. of Physics,
Heriot-Watt University.

September 2001

Heriot-Watt University

Abstract

LARGE-SCALE REMOTELY INTERROGATED ARRAYS OF FIBRE-OPTIC INTERFEROMETRIC SENSORS AND FIBRE LASERS

by G.A.Cranch

The development of fibre-optic interferometric sensor arrays for application in underwater acoustics has been an area of active research since the late 1970's. The technology has reached a level whereby prototype arrays have been successfully demonstrated in sea-trials. However, the recent development of several new technologies may significantly increase the size and performance of these arrays. We demonstrate the potential increase in multiplexed array sizes using architectures based on combining dense wavelength division multiplexing and time division multiplexing. These architectures also include erbium doped fibre amplifiers for post, pre, inline and remote amplification in order to increase the standoff distance between the array and electronics unit. We also theoretical investigate the limitations imposed on the number of sensors that can be multiplexed, due to nonlinear transmission effects in the link fibre in the presence of high optical powers and multiple wavelengths. We also demonstrate novel DFB erbium doped fibre lasers as optical sources. These sources exhibit linewidths significantly narrower than semiconductor DFB lasers, which are currently used in many sensor arrays, and thus may provide a significant improvement in sensor resolution. We investigate the intensity and frequency noise properties of these lasers, their modulation properties and successfully develop intensity noise and frequency noise reduction techniques. We also investigate the potential of fibre-optic acoustic vector sensors and demonstrate fibre-optic flexural disk accelerometers. Finally, we demonstrate polymer coated in-fibre Bragg gratings as pressure and temperature sensors and investigate polymer coatings as a means to increase the acoustic responsivity of fibre laser acoustic sensors.

TABLE OF CONTENTS

PART II: SENSOR DESIGN

PART III: SENSOR MULTIPLEXING

PART IV: LASER SOURCES FOR SENSOR ARRAYS

LIST OF FIGURES

LIST OF TABLES

Page

ACKNOWLEDGMENTS

The main topics of this thesis arose from an international collaborative project between the Defence Evaluation and Research Agency, Winfrith, UK (now QinetiQ) and the Naval Research Laboratory, Washington DC, USA and a number of people in both organisations have my deepest gratitude for their assistance and helpful advice.

Firstly, I would like to thank my supervisor, Prof. Julian D.C. Jones in the Dept. of Physics, Heriot-Watt University, for his essential advice and careful guidance throughout and his thorough reading and assessment of all the chapters contained herein. Without his experience and advice, maintaining a coherent and cohesive pattern of work would have been less straightforward. I would also like to especially thank my supervisor at DERA, Dr. D.J.Hardie and P.J.Nash for their support and encouragement and for reading and commenting on some of the chapters.

The work described in chapters 3,4, and 5 was carried out while the author was based at DERA. I would particularly like to thank D.J.Hill for his excellent contribution to the fabrication and characterisation of the coated in-fibre Bragg grating sensors described in chapter 4 and for providing fig. 2.5. I would also like to thank R.Wilson and S.Way for their assistance in fabricating sensors and the experimental arrays described in chapters 3 and 5, M.Stone for designing fig. 1.2, A.Kerr and A.Beard for their advice on electronics and signal processing, S.Tanner and B.Hannon for advice on vector sensors and sensor design and J.Payne.

The work described in chapters 6 and 7 was carried out while the author was posted as an MOD exchange scientist to the NRL and the analysis presented in chapter 8 was carried out while the author was employed by SFA Inc., based at the NRL. The opportunity to carry out part of the research at the NRL was particularly exciting for me and I would like to thank G.Cogdell and Dr. A.Dandridge for their assistance in setting up this posting. Also, I would like to thank A.B.Tveten and C.Kirkendall for their useful advice and support and S.Motley for her assistance in some of the experimental work described in chapter 7.

The characterisation of the fibre lasers described in chapter 8 was carried out as part of a collaboration between DERA and the Defence Science and Technology Organisation (DSTO), Australia in 2000. This provided the opportunity for M.Englund to be temporarily posted to the NRL to carry out the characterisation experiments and resulted in the opportunity for two distant defence organisations to work closely together. I would like to especially thank M.Englund for his excellent contribution to this work and skill at writing and characterising the fibre lasers and doped fibre described in chapter 8 and the interesting and illuminating discussions that followed, without which chapter 8 would not have been possible. This period also proved to be a very prosperous time in the history of fibre-optic communications in the USA and Europe!

Finally, I would like to thank the UK Ministry of Defence for their permission to publish the work described in chapters 2,3,4,5,6 and 7 and the NRL for its permission to publish chapter 8. The work carried out during my time with DERA (chapters 2,3,4,5,6,7) was funded from the MOD Corporate Research Programme, Technology Group 1.

-x-

GLOSSARY

Acronyms

ADC	Analogue-to-digital converter
AOM	Acousto-optic modulator
AOTA	All-optical towed array
ASE	Amplified spontaneous emission
BBS	Broad band source
BER	Bit error rate
BPF	Band-pass filter
CNR	Carrier-to-noise ratio
DBR	Distributed Bragg reflector
DFB	Distributed feedback
DSF	Dispersion shifted fibre
DSS0	Deep sea state zero
DWDM	Dense wavelength division multiplexing
EDFA	Erbium doped fibre amplifier
EMI	Electro-magnetic interference
ESA	Excited state absorption
FDM	Frequency division multiplexing
FP	Fabry-Pérot
FRM	Faraday rotation mirrors
FWHM	Full-width half-maximum
FWM	Four wave mixing
GVD	Group velocity dispersion
IFBG	In-fibre Bragg grating
IFL	In-fibre laser
IL	Insertion loss
ITU	International telecommunications union
LD	Semiconductor laserdiode
LIA	Lock-in amplifier
LWPA	Lightweight planar array
MOPA	Master-oscillator power-amplifier
MZI	Mach-Zehnder interferometer
NF	Noise figure
OADM	Optical add/drop multiplexer
OPD	Optical path difference
OSNR	Optical signal-to-noise ratio
PDR	Polarisation diversity receiver
PGC	Phase-generated carrier
PID	Proportional- integral-differential
PNR	Phase noise reduction
PRA	Pulsed reflectometric architecture
PZT	Lead zirconate titanate

QCE	Quantum conversion efficiency
RF	Radio frequency
RIN	Relative intensity noise
RPEDFA	Remotely pumped EDFA
SBS	Stimulated Brillouin scattering
SHB	Spatial hole burning
SMF	Single-mode fibre
SNR	Single-to-noise ratio
SONAR	Sound navigation and ranging
SOP	State of polarisation
SPL	Sound pressure level
SPM	Self-phase modulation
SRS	Stimulated Raman scattering
TDM	Time division multiplexing
WDMUX	Wavelength demultiplexer
XPM	Cross-phase modulation

Chapter 1

INTRODUCTION AND HISTORICAL BACKGROUND

1.1 Historical Background

During the last century, the development of underwater acoustic measurement instrumentation has followed from the continuing development of component and system analysis technology for communication; the situation is no different in the present day. Some of the first underwater acoustic measurement devices emerged after the sinking of the Steamship TITANTIC in 1912. These were based on echo-ranging techniques, using the time of flight of a sound pulse to detect nearby objects, such as icebergs or other ships. This technology was further developed by both the United Kingdom and the US during and after the First World War as active sonar (sound navigation and ranging) systems for anti-submarine warfare [1.1]. The first electronic underwater acoustic sensing arrays emerged towards the end of the First World War, when the need for covert underwater acoustic detection of enemy submarines was identified. Although these early systems consisted of only a few hydrophones deployed on or from a surface ship, they demonstrated all the basic concepts of modern passive sonar arrays. One such demonstration, in the US in 1918 (known as the U-3), consisted of two towed line arrays, each with twelve carbon button microphone based hydrophones, towed approximately one hundred meters behind a surface ship [1.2]. The hydrophones were deployed remotely from the ship in order to reduce the impact of the deployment ship's own acoustic signature on the detection sensitivity. The presence of two towed arrays allowed the problem of left-right signal location ambiguity associated with one dimensional line arrays, to be overcome. The signals were brought on board through conventional copper cable where

time delays were added to the individual hydrophone signals before combining to allow the array signals to be formed into a beam.

Since these early demonstrations, acoustic sensing instrumentation development has focused on increasing array aperture and resolution (i.e. both physical size and number of hydrophones) to allow operation at low frequency, increasing reliability and advanced signal processing systems. Modern passive sonar systems, comprise both 'on platform' arrays (i.e. arrays located on the ship or submarine) and 'off platform' arrays (i.e. arrays located remote from the surface ship or submarine). Shown in fig. 1.1 are the locations of the passive arrays typically found on a submarine.

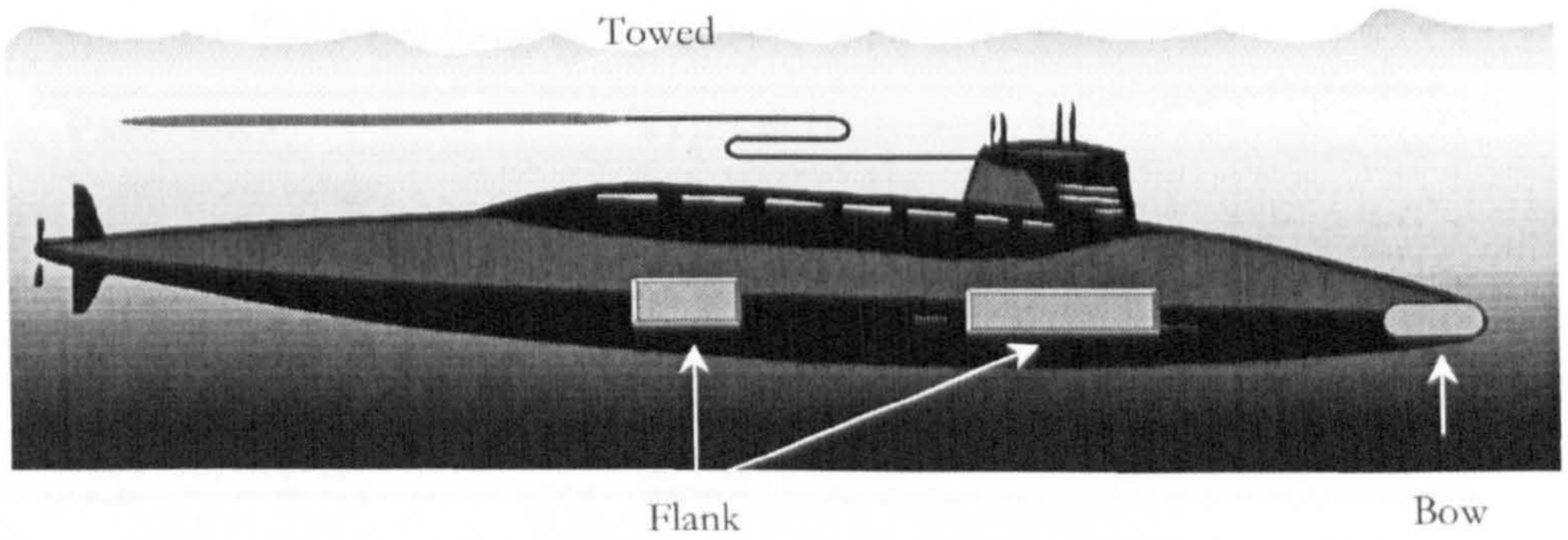

Figure 1.1: Submarine sonar arrays

The advancements made in component technology for communication systems allowed the reliability of the electronic portions of the sonar arrays to be significantly improved. Although much work before and after the Second World War was focused on active sonar systems (which use ranging techniques in the ultrasonic region to localise targets), the need for longer detection ranges and covert operation generated the need for fully passive systems operating in the sub 10 kHz acoustic frequency region, where absorption in the ocean is low. Operation at these frequencies generally requires a large array aperture with a large numbers of sensors in order to achieve an adequate spatial resolution.

As improved platform design brought about reductions in acoustic signature levels, the sensor self-noise limited resolutions were correspondingly improved. By the 1970's, acoustic sensing systems had reached near ideal performance, with sensor self-noise some way below the noise levels due to ambient acoustic noise in the ocean in the quietist of sea conditions. At this time, hydrophones were based on piezo-ceramic materials such at Lead Zirconate Titanate (PZT);

the ceramic nature of these materials means that they can be moulded into the required shape. These materials are still used in most of today's sonar arrays. Fully digital signal processing was also incorporated, in the late 1960's, to handle the huge amounts of data generated in the larger systems. The reliability of both the array (wet end) and signal processing (dry end) portion of these systems had become reasonably good. However, the failure of hydrophones due to water ingress can be a problem even in some modern systems. Repair of platform mounted systems, in particular, usually requires the vessel to return to dry dock and as a result is generally a costly and time consuming exercise.

The exact specification of an individual system is dependent on the application, but the range of the basic specification for many passive sonar systems is shown in table 1.1.

Table 1.1: Range of requirements of a passive sonar array

Parameter	Typical Requirement
Frequency range	5 to 10 000 Hz
System noise floor	Equivalent to 'deep sea state zero'
Dynamic range	up to 10^6
Number of hydrophones	100 to 10 000
Operating depth	down to 500m
Survival depth	down to 1000m

The frequency range of interest for most passive sonar systems is below 10 kHz with a pressure resolution equivalent to the background environmental acoustic noise. This has been empirically quantified by 'sea state' curves, which are discussed more in the next chapter. The dynamic range required is around six orders of magnitude, measured relative to the noise floor. Operational arrays may contain up to 10 000 sensors, but more typically contain between 500 and 1000 sensors. They are usually expected to operate at depths of down to 500m.

The use of a fibre optic interferometer as an acoustic sensor was first demonstrated in the late 1970's [1.3-5] and what started as a research interest developed into a significant military effort into the development of all aspects of interferometric fibre optic sensor arrays. Indeed, this early research effort represented the first major application of single-mode fibre optics; at this time, all optical fibre communication systems were based on multi-mode fibre optics [1.6]. The main perceived advantages of the fibre optic hydrophone array over the conventional piezo-ceramic sensor array are: (i) an electrically passive array, (ii) a multiplexing capability using fused fibre devices resulting in reduced complexity of the wet-end array, (iii) immunity to electro-

magnetic interference and (iv) the potential for lightweight, low volume arrays. It is interesting to note that no significant performance advantage was expected from a fibre optic array, since the conventional array had already demonstrated near ideal performance, but the main advantages lay in reduced size, weight and improved reliability. One of the main challenges in the early development of fibre-optic systems was to demonstrate comparable performance with the piezo-ceramic based array technology.

During the 1980's a number of the key performance requirements from the fibre-optic hydrophones were demonstrated. Much of the work focused on developing passive interrogation techniques for fibre interferometers (thus removing the requirement of active components in the interferometer arms), sensor multiplexing, methods to overcome polarisation induced signal fading and characterising the fundamental noise mechanisms arising in interferometric sensors. Perhaps some of the notable milestones in the development of optical fibre hydrophone technology were: (i) achievement of sub-microradian phase resolution in a Mach-Zehnder interferometer [1.7-8], (ii) demonstration of a polarisation diversity technique for overcoming polarisation induced signal fading [1.9], (iii) successful at-sea deployment of a multiplexed hydrophone array [1.10], (v) demonstration of a high responsivity air-backed compliant mandrel hydrophone [1.11], and (vi) deployment of ultra-low noise hydrophones in the Arctic which achieved pressure resolutions up to 30 dB below deep sea state zero [1.12]. Since these developments, a number of military programmes were initiated, mainly in the US, to alow a transition of the technology into service. During the 1980's and early 1990's an all fibre optic towed array (AOTA) and a lightweight planar array (LWPA) (submarine mounted Flank array) were demonstrated [1.13-14].

At the end of the Cold War, the main focus of underwater acoustic surveillance systems changed and military interest refocused on shallow water operations and the associated shallow water surveillance systems. Applications of fibre-optic hydrophone arrays were then identified as remotely interrogated arrays. A typical configuration is shown in fig. 1.2.

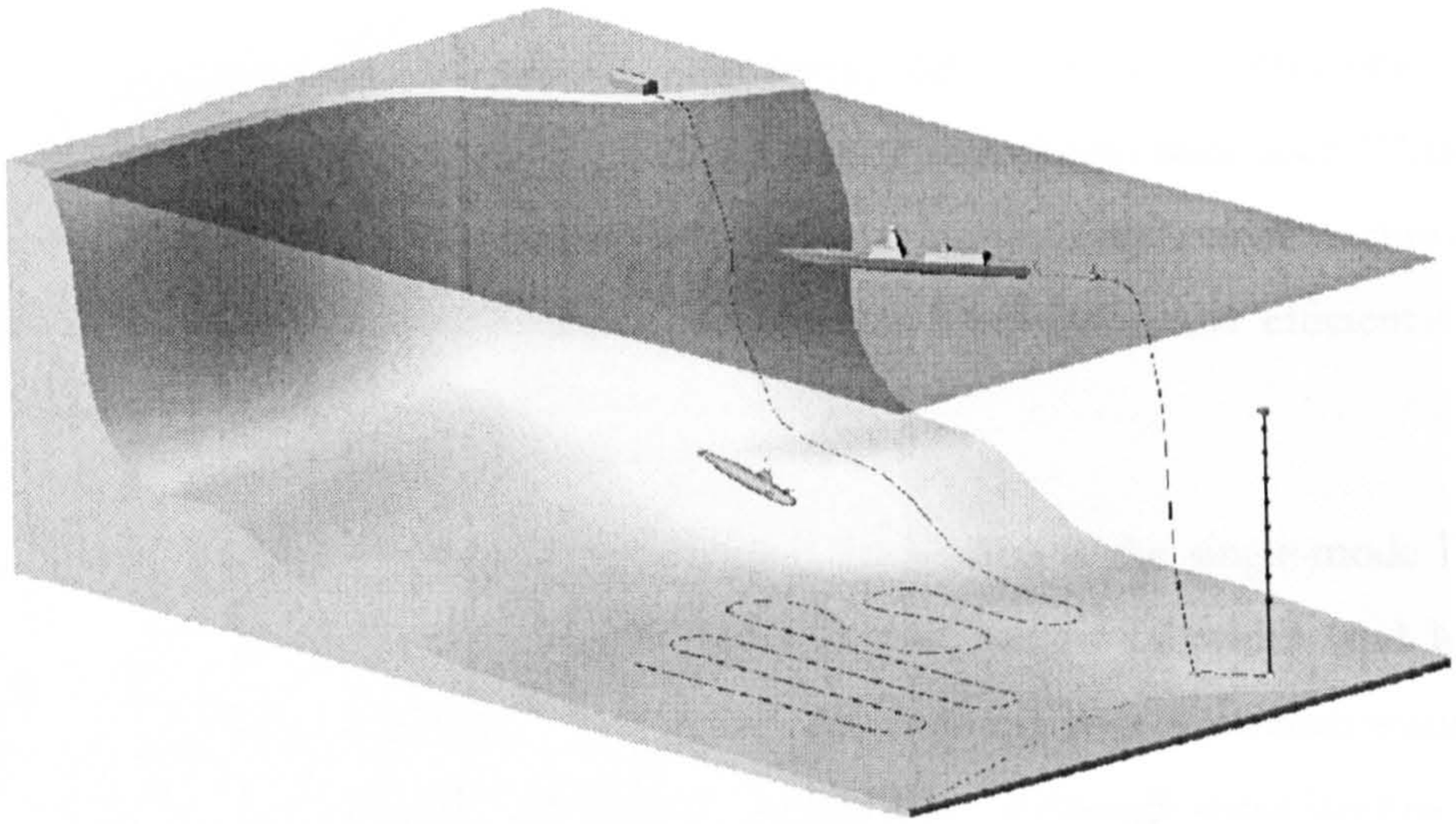

Figure 1.2: Remotely deployed surveillance arrays

The array may be mounted either vertically or horizontally on the sea-bed and be tethered either to a surface ship or shore monitoring station. One of the first demonstrations of a remotely interrogated surveillance array was reported in the US [1.15] which comprised a 64 hydrophone array, with the potential for expansion to 256, using four DFB semiconductor laser sources. A similar system, with 32 hydrophones, was also demonstrated in the UK [1.16]. At this stage, the systems had demonstrated reliability and performance and included most of the components necessary for a full-scale system such as digital demodulation, polarisation control and optical amplifier technology. However, scope for improvement still existed in areas such as multiplexing architecture, laser source technology and remotely pumped amplifier technology and these form the main theme of this thesis. Since the mid-1980's when the erbium doped fibre amplifier (EDFA) was first demonstrated [1.17], this technology has found widespread use in fibre-optic communication systems. Although the concept of wavelength division multiplexing has existed for some time, the use of dense wavelength division multiplexing in communications systems (where the spacing between adjacent wavelengths is typically less than about 2 nm) has generated intense research efforts in both academic and industrial organisations to develop component and system technology. This has been driven by the demand for low cost upgrade of existing fibre-optic communications networks and significantly increased bandwidths of newly installed systems [1.18-19]. Both of these technologies can be incorporated in the optical hydrophone system, to provide an increase in the number of

hydrophones and the link lengths between the array and interrogation electronics. Another technology that has developed from the EDFA is the erbium doped fibre laser. These devices emerged at roughly the same time and developments in component technology and improvement in doped fibre design have assisted the development of efficient fibre laser devices.

Of particular interest to the interferometric sensor application is the single-mode DFB fibre laser: a device with the potential to exhibit an extremely narrow linewidth (and hence high coherence length), moderately high output power, compatibility with the transmission medium and low sensitivity of the emission frequency to temperature. Although these devices have been demonstrated as potential sources for communication systems and sensor applications, surprisingly little work has been presented on optimising their performance for the interferometric sensor application. Incorporation of these technologies into the optical hydrophone system will permit larger arrays interrogated though a small number of fibres (2-3), though longer link lengths possibly with improved sensor resolution than that achieved with current systems using semi-conductor DFB lasers.

1.2 Thesis Objectives

At present, for single-wavelength optical hydrophone systems using time division multiplexing only, the maximum number of interferometric sensors that can be interrogated through two fibres (one launch and one return fibre) is between 32 and 64. This is limited by the requirements of interrogation rate and launch power restrictions. The maximum distance between the array and interrogation electronics (referred to later as the link length) is between 40 and 50 km, dependent on the fibre attenuation. By incorporating dense wavelength division multiplexing and remotely pumped amplifier technology, we aim to demonstrate experimentally a novel architecture and theoretically predict the performance of sensors and, in particular, determine the dependence of the sensor phase resolution on the total number of sensors and link length. We also aim to characterise fully a new laser source technology, based on DFB erbium fibre lasers, incorporating novel noise reduction techniques. The narrow emission linewidth exhibited by these lasers, compared with the semi-conductor DFB may result in improved sensor resolution in systems with unbalanced interferometers. We shall show how an inertial mass based device can be configured as an acoustic sensor and illustrate the potential

advantages of such a sensor, when combined into a large array, in terms of the ability to locate the source of acoustic emission. Therefore, we shall demonstrate a fibre-optic vector sensor based on a flexural disk-based accelerometer and derive an accurate model that will allow the design of the sensor to be fully optimised for performance. Also, we shall present a technique to enhance the response to pressure and temperature of an in-fibre Bragg grating using compliant coatings. We also show how this may be used to develop a high performance acoustic sensor using an in-fibre laser.

1.3 Thesis Outline

The thesis is split into four parts. Each chapter forms a self-contained piece of work and can be read independently. However, some background material on which later chapters build is contained in the review chapter. Chapters 2,3,4,5 and 7 contain re-edited transcripts of published work and chapter 6 builds on the model derived in chapter 5.

In the first part (chapter 2) we review acoustic propagation, all aspects of fibre-optic interferometric sensors and multiplexing, noise properties of the EDFA and include a brief discussion on the in-fibre Bragg grating (which we use as a sensor in chapter 4). We also review the basics of the piezo-ceramic sensor based sonar arrays and phased array techniques. The second part (chapters 3 and 4) is devoted to sensor design. In chapter 3 we shall present a fibre-optic flexural disk-based accelerometer and describe a detailed model that allows the sensor design to be optimised for performance. We show in chapter 2 how these can be used as an acoustic vector sensor by sensing the particle displacement associated with an acoustic wave. In chapter 4 we shall present an in-fibre Bragg grating based temperature and pressure sensor using compliant coatings to enhance the axial strain induced in the fibre. The third part (chapters 5 and 6) is devoted to sensor multiplexing. In chapter 5 we present novel multiplexing architectures based on time and dense wavelength division multiplexing. We also present results from an experiment to demonstrate the concept and derive a noise model to determine the sensor resolution and dynamic range. In chapter 6 we determine the restrictions imposed on the launch powers in wavelength division multiplexed systems due to nonlinear effects in the launch fibre. We derive models to predict the phase resolution achieved in systems with different configurations of optical amplifiers and finally determine the relationship between the number of sensors and link length for these types of system. The fourth part (chapters 7 and 8) is devoted to the development of the DFB fibre laser source. In chapter 7 we characterise the

DFB erbium fibre laser for the interferometric sensor application and present techniques based on active electronic feedback to suppress excess intensity and frequency noise in these devices. In chapter 8 we present experimental data demonstrating the dependence of the laser relaxation oscillation frequency on the doped fibre and grating design and determine the mechanisms that give rise to the observed levels of intensity noise. Finally, in chapter 9 we summarise the main achievements and indicate areas of possible future research.

References

[1.1] E.Kline, 1968 "Underwater sound and Naval acoustical research and applications before 1939" *J.Acoust. Soc. Am.* 43 (5) 931-947

[1.2] W.S.Burdic, 1984 *Underwater acoustic system analysis* Prentice-Hall Chapter 1

[1.3] J.H.Cole, R.L.Johnson, P.B.Bhuta, 1977 "Fibre optic detection of sound" *J. Acoust. Soc. Am.* 62 1136-1138

[1.4] B.Culshaw, D.E.N.Davies, S.A.Kingsley, 1977 "Acoustic sensitivity of optical-fibre waveguides" *Elec. Lett.* 13 (25) 760-761

[1.5] J.A.Bucaro, H.D.Dardy, E.Carome, 1977 "Fibre optic hydrophone" *J. Acoust. Soc. Am.* 62 1302-1304

[1.6] J.Hecht, 1999 *City of light: The story of fiber optics* Oxford University Press

[1.7] D.A.Jackson, R.Priest, A.Dandridge, A.B.Tveten, 1980 "Elimination of drift in a single-mode optical fiber interferometer using a piezoelectrically streched coiled fiber" *Applied Optics* 19 (17)

[1.8] A.Dandridge, A.B.Tveten, T.G.Giallorenzi, 1982 "Homodyne demodulation scheme for fiber optic sensors using phase generated carrier" *IEEE J Quant Elec.* 18 (10) 1647-1653

[1.9] N.J.Frigo, A.Dandridge, A.B.Tveten, 1984 "Technique for elimination of polarisation fading in fibre interferometers" *Elec. Lett.* 20 (8) 319-320

[1.10] M.L.Henning, C.Lamb, 1988 "At-sea deployment of a multiplexed fiber optic hydrophone array" *Proc. of the Optical Fibre Sensors Conf.* Opt. Soc. America Washington D.C. USA xiv+516 I/84-91

[1.11] J.A.Bucaro, B.Houston, E.Williams, 1991 "Fibre-optic air backed hydrophone transduction mechanisms" *J. Acoust. Soc. Am.* 89 451-453

[1.12] A.M.Yurek, A.B.Tveten, A.Dandridge, 1990 "High performance fiber optic hydrophones in the arctic environment" *Proc. of the 7th Conf. on Optical Fiber Sensors Conf.* 321-324

[1.13] A.Dandridge, 1994 "The development of fiber optic sensor systems" *Proc. of the 10th Int. Conf. on Optical Fiber Sensors SPIE 2360* 154-61

[1.14] A.Dandridge, G.B.Cogdell, 1991 "Fiber optic sensors for Navy applications" *IEEE LCS* 81-89

[1.15] A.R.Davis, C.K.Kirkendall, A.Dandridge, A.D.Kersey, 1997 "64 channel all optical deployable acoustic array" *Proc. of the Optical Fiber Sensors Conf. 12* Opt. Soc. America Washington DC xxii+678 616-619

[1.16] P.J.Nash, G.A.Cranch, L.Cheng, D.de Bruijn, I.Crowe, 1998 "32 element TDM optical hydrophone array" *Proc. European Workshop on Optical Fibre Sensors SPIE* 3483 238-242

[1.17] R.J.Mears, L.Reekie, I.M.Jauncey, D.N.Payne, 1987 "Low-noise erbium-doped fibre amplifier operating at 1.54 μm" *Elec. Lett.* 23 (19) 1026-1027

[1.18] C.A.Brackett, 1990 "Dense wavelength division multiplexing networks: principles and applications" *J. Light. Tech.* 8 (6) 948-964

[1.19] G.E.Keiser, 1999 "A review of WDM technology and applications" *Optical Fiber Technology* 5 3-39

Part I
Review

Chapter 2

REVIEW OF SUB-SEA HYDROPHONE ARRAYS AND INTERFEROMETRIC FIBRE-OPTIC SENSOR TECHNOLOGY†

Abstract – In this chapter we review the various aspects of fibre-optic interferometric acoustic sensor systems. We also include a discussion on the fundamental principles and noise properties of the erbium doped fibre amplifier and on the in-fibre Bragg grating.

2.1 Introduction

In this chapter, we shall provide a review of material relevant to the interferometric fibre-optic acoustic sensor and the in-fibre Bragg grating sensor. For historical interest it is worth noting that some of the earliest work on fibre optic acoustic sensing investigated techniques other than interferometric, for sensing acoustic fields using fibre optics. Techniques based on modulation of polarisation (i.e. birefringence) [2.1,2.2] and intensity [2.3] were investigated as well as using fibre devices such as evanescent wave couplers [2.4] and single fibre interferometers [2.5]. Some of these techniques appear promising; for example, by modulating the polarisation or intensity of an optical signal, only one fibre is required for the sensor. When incoherent detection is used, as in the case of the intensity modulated sensor, effects such as polarisation induced signal fading are not observed. However, for a high performance application such as the optical hydrophone, the fibre interferometric sensor is the most promising candidate to achieve the requirements of high resolution, high dynamic range and an efficient multiplexing capability. Predictions of the acoustic pressure resolution of an interferometric sensor made in early work on the subject were based on shot noise limited detection [2.6]. Although shot noise limited detection is achievable in carefully designed single sensor systems at frequencies above a few tens of kilohertz, to date it has not been demonstrated in multiplexed systems at frequencies below a kilohertz. However, the

†This chapter contains excerpts from the book section "Optical fibre hydrophones" to be published in the "Handbook of Laser Technology" IOP Publishing, 2002, chap. D2.5

development of transducers with high mechanical amplification has permitted the pressure resolution required in sonar systems to be achieved.

We first provide a summary of the fundamentals of acoustic propagation in gases and liquids and sound at interfaces and then discuss the origin and spectra of ambient noise in the open ocean. This is followed by a discussion on the basic concepts of conventional acoustic sensor technology based on piezo-ceramic materials. In section 2.6 we derive the basic low frequency responsivity equations for fibre-optic acoustic transduction in water and air and then discuss some of the fibre-optic hydrophone designs that have been demonstrated to provide mechanical amplification of the pressure induced strain in the fibre. This is followed by a discussion on fibre-optic acoustic vector sensor designs. In section 2.7 we present a basic analysis of the fibre-optic Mach-Zehnder interferometer and discuss alternative interferometer configurations in section 2.8. In section 2.9 we discuss the various active and passive techniques developed to overcome the signal fading problem, and then describe the noise sources that can degrade the phase resolution. In section 2.10 we describe the most established multiplexing techniques based on frequency, time and wavelength division multiplexing. This is followed by a discussion on dynamic range and digital demodulation in multiplexed systems. In section 2.11 we describe the phenomenon of polarisation induced signal fading and discuss techniques to overcome this type of fading. In section 2.12, we provide a general discussion on obtaining low noise performance from multiplexed systems. Moving away from the subject of the interferometric sensor in section 2.13, we describe the noise properties of erbium doped fibre amplifiers and finally in section 2.14 we describe the basics of the in-fibre Bragg grating which we shall use as a sensor in chapter 4.

2.2 Acoustic Wave Propagation in Gases and Liquids

Acoustic waves arise from pressure disturbances that can propagate in a compressible medium. The acoustic wave generates adjacent regions of compression and rarefaction, which causes increases and decreases in the localised pressure relative to the ambient pressure. In an inviscid fluid (i.e. zero viscosity), the molecules move in the direction of propagation of the acoustic wave and the restoring force responsible for the propagating waves is simply the force generated when the medium is compressed or expanded. Acoustic wave propagation in gases and liquids is governed by the linearised acoustic wave equation [2.7],

$$\nabla^2 P = \frac{1}{c^2}\frac{\partial^2 P}{\partial t^2} \tag{2.1}$$

where ∇^2 is the Laplacian operator equal to $\partial^2/\partial x^2 + \partial^2/\partial y^2 + \partial^2/\partial z^2$, c is the sound speed in the medium, and P is the pressure (the pressure can be divided into a static part, P_o, and a harmonic part, P. We drop the static part from here onwards). (2.1) is derived by combining: (i) the equation of state, which relates the internal restoring forces of the molecules in the medium to the corresponding deformation; (ii) the equation of continuity, which is determined by the requirement that the net rate at which mass flows into a volume is equal to the increase in mass within the volume; and (iii) the linearised Euler equation, which applies Newton's second law to a volume element. In determining these equations, one assumes that the density changes are small such that if ρ_o is the constant equilibrium density of the medium and ρ is the instantaneous density, then $(\rho_o - \rho)/\rho_o \ll 1$ and that acoustic processes are nearly adiabatic, in that there is insignificant exchange of thermal energy between one molecule and another. Thus, no energy is lost due to thermal conduction from the regions of pressure change. The linearised Euler equation (or linear inviscid force equation) provides the relationship between the pressure and particle velocity, $\underline{u}$,

$$\rho_o \frac{\partial \underline{u}}{\partial t} = -\underline{\nabla} P \tag{2.2}$$

where Del, $\underline{\nabla}$, is the vector operator equal to $\partial/\partial x\hat{\underline{i}} + \partial/\partial y\hat{\underline{j}} + \partial/\partial z\hat{\underline{k}}$. Considering the simplest case of a one dimensional acoustic plane wave propagating in the x direction then from (2.1),

$$\frac{\partial^2 P}{\partial x} = \frac{1}{c^2}\frac{\partial^2 P}{\partial t^2} \tag{2.3}$$

which for a sinusoidal disturbance has a general solution given by,

$$P(x,t) = P_1 \exp\big(i(\omega t - kx)\big) + P_2 \exp\big(i(\omega t + kx)\big) \tag{2.4}$$

where $k(=\omega/c)$ is the wavenumber and P_1, P_2 represent the forward and backward propagating waves; in an unbounded medium P_2=0. From (2.2), the one dimensional form of the linear inviscid force equation is given by,

$$\rho_o \frac{\partial \underline{u}}{\partial t} = -\frac{\partial P}{\partial x} \tag{2.5}$$

Using (2.2) and (2.4), the particle velocity is given by,

$$\underline{u} = \left[\frac{P_1}{\rho_o c} \exp(i(\omega t - kx)) - \frac{P_2}{\rho_o c} \exp(i(\omega t + kx)) \right] \hat{\underline{x}} \tag{2.6}$$

which exists only in the direction of propagation. The relationship between the pressure and particle velocity is then given by (2.4) and (2.6) such that,

$$\frac{P}{u} = \rho_o c = Z_o \tag{2.7}$$

which is known as the characteristic impedance, Z_o, of the medium for a plane wave. We can conclude from this simple analysis that detection of an acoustic wave can be achieved either by measuring the pressure or the particle displacement, velocity or acceleration.

Knowledge of both the pressure and particle velocity allows one to determine the acoustic intensity of a sound wave, which is defined as the average rate of flow of energy through a unit area normal to the direction of propagation. Since the instantaneous rate at which work is done by an element of fluid on an adjacent fluid element is the product of pressure and particle velocity, the acoustic intensity is thus the time average of this quantity such that,

$$I = \langle Pu \rangle \tag{2.8}$$

where $\langle\ \rangle$ denotes the time average over a period longer than the acoustic wave period. For a plane wave travelling in the positive x direction, the acoustic intensity is therefore,

$$I^{+} = \frac{1}{2}\frac{P^2}{\rho_o c} \tag{2.9}$$

It is also instructive to investigate what happens to the pressure and particle displacement in an acoustic field near a boundary; it is common to mount sensors on some form of support, which itself will perturb the acoustic field surrounding the sensor (such that free field conditions will no longer apply). Consider the boundary shown in fig. 2.1, where the incident, reflected and transmitted waves are denoted p_i, p_r and p_t respectively. The amplitude reflection and transmission coefficients are defined as $R = p_r / p_i$ and $T = p_t / p_i$ respectively. If we define the boundary as being at $x = 0$ then, the boundary conditions are derived from the requirement of continuity of pressure and particle velocity at the boundary such that,

$$p_i + p_r = p_t \tag{2.10}$$

and

$$u_i + u_r = u_t \quad \text{at} \quad x = 0 \tag{2.11}$$

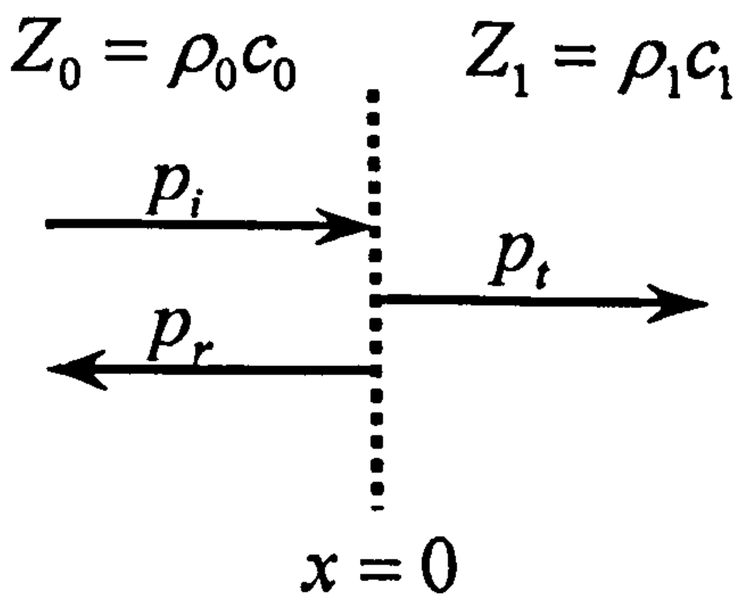

Figure 2.1: Acoustic wave at a boundary

Using (2.4) yields the reflection coefficient at normal incidence in terms of the impedance of each region,

$$R = \frac{Z_0 - Z_1}{Z_0 + Z_1} \tag{2.12}$$

When the impedance of region 1 is much greater than that of region 0, such that $Z_1 \gg Z_0$ then $R \simeq 1$ and using (2.4), the pressure at the boundary is thus twice the incident pressure. It follows

from (2.6) that the particle velocity at the boundary is zero and for this reason this type of boundary is referred to as *rigid*. Conversely, when $Z_1 \ll Z_0$ then $R \approx -1$ and the reflected wave is inverted in phase by π such that the pressure at the boundary is now zero, and the particle velocity is double the incident particle velocity. This type of boundary is known as *pressure-release* or *soft*.

2.3 The Phased Array Concept: Beamforming

The aim of a passive sonar array is to extract acoustic signals, originating from any direction, within a background of ambient noise. An ideal point source hydrophone will exhibit a response independent of direction (i.e. omni-directional), however a hydrophone with a finite size will exhibit some degree of directionality. A hydrophone with dimensions much smaller than the wavelength of the acoustic signal will generally exhibit a response nearly independent of direction and can be considered to be omni-directional. It is thus necessary to apply some form of signal processing in order to discriminate between the signal and the noise. Usually, this process must be carried out without prior knowledge of the form of the signal to be detected (i.e. tonal or broadband, pulsed or cw). One technique, known as beamforming, is based on spatial filtering using an array of sensors and allows both the direction of the signal to be determined and a level of gain to be applied only to the signal of interest, thus providing an improvement in signal-to-noise ratio [2.8]. The concept is best illustrated by an example. An ideal line array of length l and zero width, is shown in fig. 2.2(a),

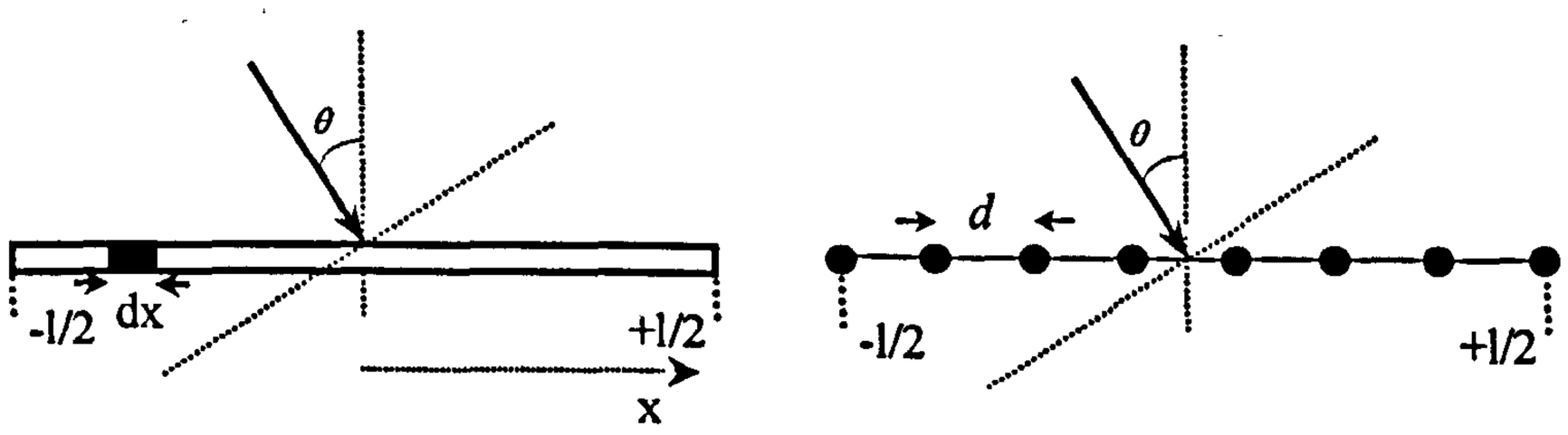

Figure 2.2: (a) Ideal continuous line array and (b) Discrete line array

where the responsivity of the line array as a function of position, x, is given by $T(x)$. Assuming the incident pressure field is composed of plane waves, the phase of an incident acoustic wave on the array as a function of angle of incidence is Kx where $K = 2\pi / \Lambda \cdot \sin\theta$ and Λ is the acoustic wavelength. The response of the line array, $D(K)$, is thus given by

integrating the product of the instantaneous incident pressure and sensitivity of a small element of length dx, over the length of the array such that,

$$D(K) = \int_{-l/2}^{+l/2} T(x)\cos(\omega_a t - Kx)dx \qquad (2.13)$$

If the sensitivity of a length element is $T(x) = 1/l$, then (2.13) becomes,

$$D(K) = \frac{1}{l}\int_{-l/2}^{+l/2} \cos(Kx)dx = \mathrm{sinc}(Kl/2) \qquad (2.14)$$

where we have dropped the time dependence. The resulting pattern is a sinc function, shown in fig. 2.3(a), with a 3dB 'beamwidth'[1] approximately equal to $1/l$.

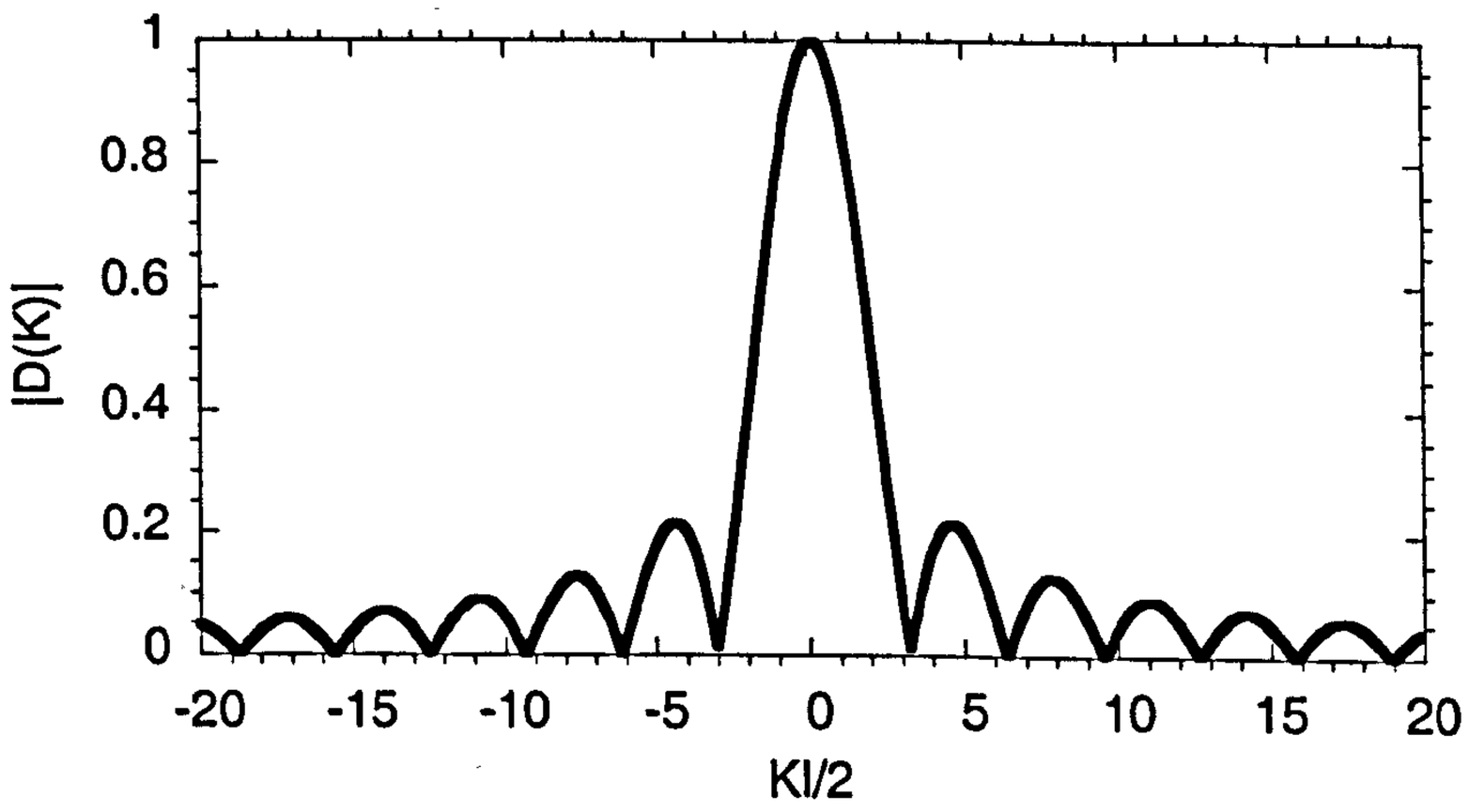

Figure 2.3: Directivity of (a) continuous array

[1] 'Beamwidth' is defined as the angular width in radians of the main lobe in fig. 2.4 measured at the half-power points, i.e. when $D(\theta) \approx 0.707$.

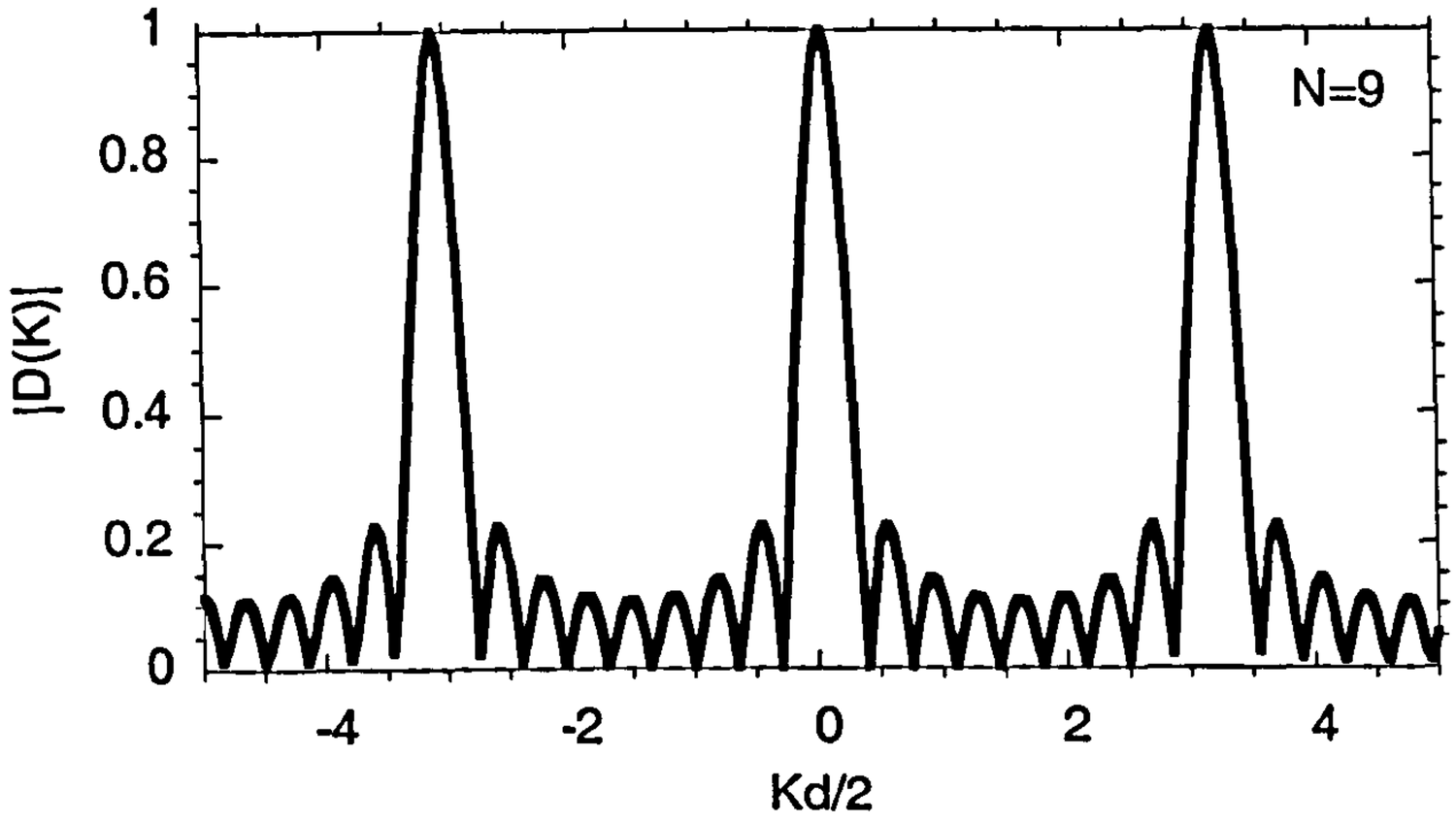

Figure 2.3 (cont): (b) discrete array

For an array operating at low frequency, it is impractical to have a continuous array (due to the large number of sensors required) and in this case the array would consist of discrete sensors, as shown in fig. 2.2(b). In this case the directivity is determined by replacing the integral in (2.14), with a summation of the response of each sensor. Thus, if there are N sensors, such that $N = 2m+1$ where m is either even, odd or zero, each with sensitivity $1/N$ then,

$$D(K) = \frac{1}{N}\sum_{a=-m}^{a=+m}\cos(Kad) = \frac{\sin(NKd/2)}{N\cdot\sin(Kd/2)} \qquad (2.15)$$

where a identifies each sensor element. This is plotted in fig. 2.3(b) in terms of $Kd/2$, for the case when $N=9$. A series of principal maxima (and potential directional ambiguities) now occur in the directivity pattern; however providing the Nyquist sampling condition is met, such that $d \le \Lambda/2$, where Λ is the acoustic wavelength, these principal maxima occur outside the range of real values of θ (i.e. when $Kd/2\pi > 1$). As the element spacing approaches the acoustic wavelength, then these maxima occur within the range of real incident angles and thus introduce an ambiguity in the directivity pattern; a result of aliasing of the incident acoustic signal. Shown in fig. 2.4(a) and (b) are the directivity patterns of the discrete sensor line array in polar form for the cases when $N=9$ and $d=\Lambda/2$ and $d=\Lambda$ respectively.

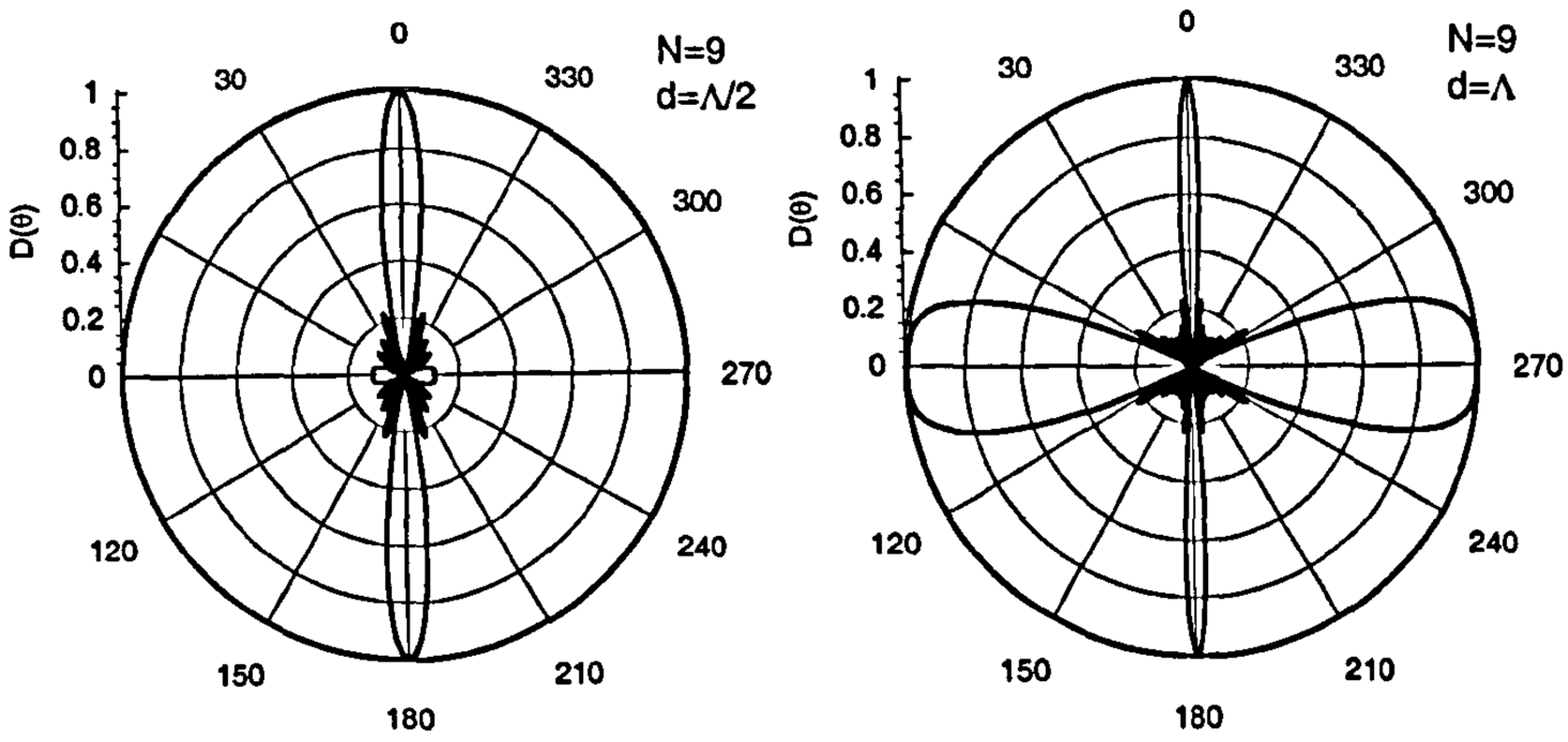

Figure 2.4: Directivity vs. angle of incidence

When the Nyquist condition is met, the directivity response has only a single ambiguity, due to the cylindrical symmetry of the line array, i.e. the sound source may lie anywhere in the region swept out by the directivity pattern as it is rotated about the x-axis of the line array. However, when $d = \Lambda$ principal maxima also occur at $\theta = \pm 90^0$ and unless the range of the incident angle of the acoustic wave is known to be $-45^0 < \theta < 45^0$, then the Nyquist condition must be met to avoid direction ambiguity.

We can now determine the relationship between the signal-to-noise ratio (SNR) from the array compared with that returned from a single sensor. Assuming that the sensor noise is dominated by ambient acoustic noise and this noise is isotropic and incoherent over distances less than the sensor spacing then the signal power is proportional to,

$$\left(\sum_{a=1}^{N} T_a\right)^2 \tag{2.16}$$

where T_a is the sensitivity of sensor a. The noise power is given by the incoherent addition of the noise from each sensor and is thus proportional to

$$\sum_{a=1}^{N} T_a^2 \tag{2.17}$$

Thus, the improvement in SNR due to the beamforming process is proportional to N and is known as the *array gain*. However, this is only the case if the noise is isotropic and incoherent. If

a component of the sensor self-noise (i.e. that is non-ambient acoustic in origin) is coherent over the time scales associated with the interrogation rate of a multiplexed sensor array, then the improvement in SNR calculated above may not be achieved. This can seriously degrade the performance of acoustic arrays when beamforming is used. Some noise components in the fibre-optic interferometric sensor array are generally coherent (such as laser frequency noise). Careful attention must be paid to reducing sufficiently this noise source to avoid severe degradation of the array gain achieved by the beamforming process.

2.4 Environmental Acoustic Noise in the Ocean

The detection sensitivity of underwater acoustic arrays is dependent on the ambient acoustic noise level in the ocean. In general, the ocean is a continually changing environment, and the ambient noise level is dependent on a number of factors such as ocean depth, the acoustic properties of the seabed, the weather conditions, shipping levels and seismic activity. For specifying the sensor performance, one is generally interested in characterising the lowest ambient noise levels to ensure that the sensor noise is designed to be some way (usually 10 dB) below this. For this reason a number of measurements were taken around 1960, to characterise the ambient acoustic noise observed in the deep ocean for different levels of shipping traffic and different weather conditions [2.9]. The causes of the noise observed generally contribute over different frequency ranges and these are indicated at the bottom of fig. 2.5.

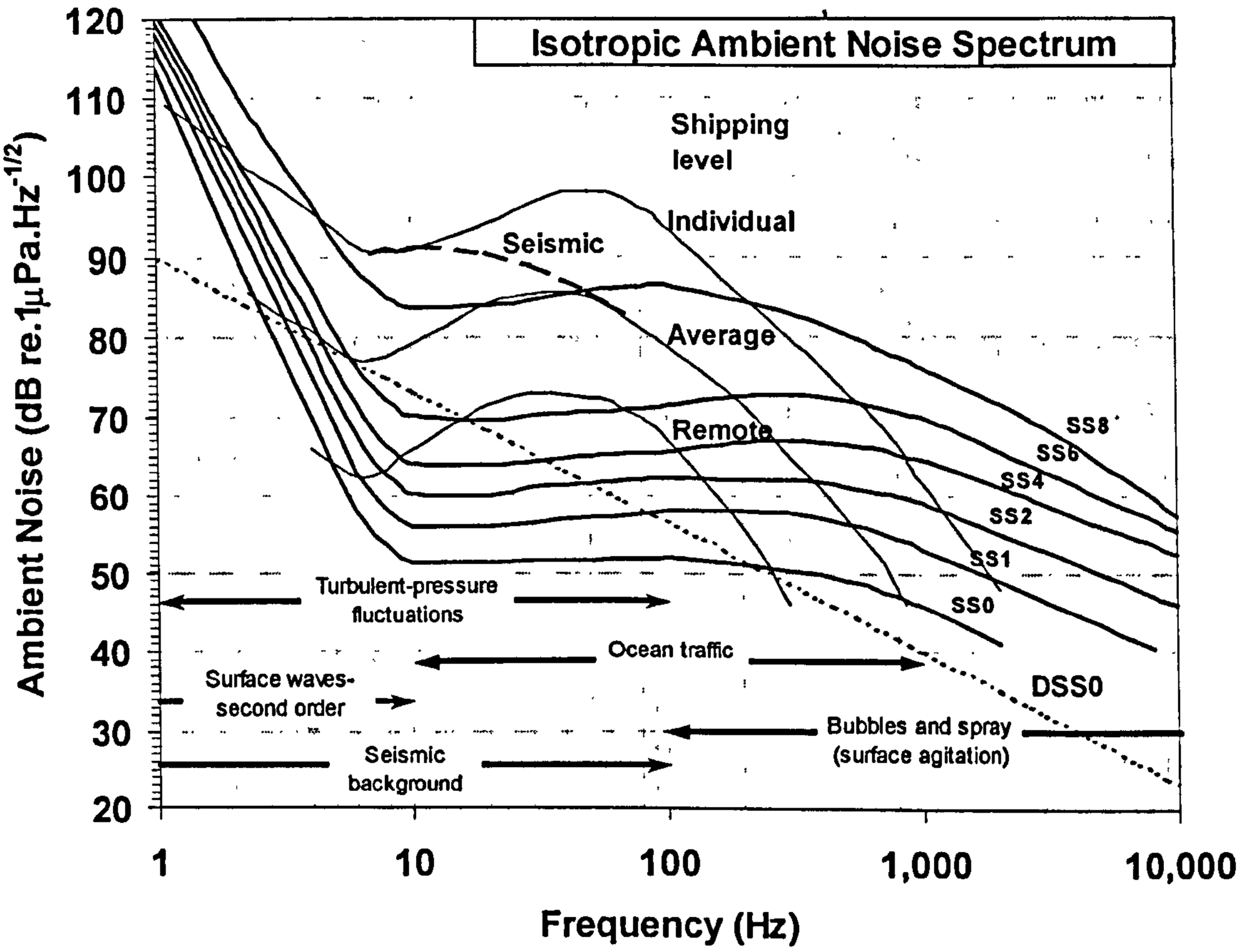

Figure 2.5: Spectra of open ocean ambient noise

This data led to the empirically determined sea state curves. Deep sea state zero (DSS0) is expressed as a sound pressure level spectral density $(SPL)^2$ in dB re 1 $\mu Pa.Hz^{-1/2}$ as,

$$DSS0 = 90 - 16.65 \log f \qquad (2.18)$$

where the unit $Hz^{-1/2}$ specifies a power measurement bandwidth of 1 Hz. We shall use this curve to characterise the dynamic range of sensors in chapter 5.

2.5 Conventional Sensor Technology

2.5.1 Acoustic sensors: scalar and vector

A transducer, by definition, converts energy from one form to another; and a device that converts underwater sound into an electrical signal is called a hydrophone. Materials that have found practical use in underwater acoustic sensors are piezoelectric, magnetostrictive and

---

[2] Recall that sound pressure level, $SPL = 20 \log(\Delta P / 1\mu Pa)$, where by convention the standard sound reference level is 1 μPa.

electrostrictive. A strain applied across a piezoelectric material causes a surface charge to be generated, which is linear with the applied strain providing the strain is within the elastic limit of the material. This provides a means of converting an applied pressure into an electric voltage. When a strain is applied across an electrostrictive or magnetostrictive material, the charge generated is proportional to the square of the applied strain. Transducers based on these devices thus require a polarising field to be applied across the material in order to obtain a linear response for small signals [2.10]. For this reason, most underwater acoustic sensor arrays use piezo-electric materials as the sensor elements. In a piezo-ceramic hydrophone, either the charge, Q, or voltage, v, can be measured; the two quantities are related though the equation, $Q = Cv$, where C is the capacitance. In a hydrophone array, it is necessary to amplify the sensor signal prior to transmitting to the processing electronics and this is usually done with an amplifier placed near to the transducer.

Measurement of pressure due to an acoustic signal requires the transducer to be designed with the required selectivity to distinguish between the pressure and particle displacement components. Most pressure measuring hydrophones rely on the high inertia of the device to ensure that motion of the sensor, in the presence of the acoustic field, is minimal. Also the device may be designed to exhibit low response to external vibration. Conversely, a device to measure the particle velocity must be designed with neutral buoyancy and a low response to external pressure changes.

Devices that measure mechanical vibration are based on the simple harmonic oscillator and can be modelled as a mass-spring resonator [2.11]. The inertial force and hence the responsivity of such a device is governed by the inertial mass and spring stiffness; and the bandwidth is determined by the fundamental resonance of the oscillator. Measurement of the relative displacement between the case and the inertial mass yields the acceleration at frequencies below the fundamental resonance and displacement of the case at frequencies above the fundamental resonance. The relationship between displacement, velocity and acceleration is given by the simple harmonic motion relations for a sinusoidal excitation of frequency ω,

$$\zeta = \Psi \cos(\omega t) \tag{2.19}$$

$$u = -\Psi \omega \sin(\omega t) \tag{2.20}$$

$$A = -\Psi \omega^2 \cos(\omega t) \qquad (2.21)$$

where ζ is the displacement and A is the acceleration. Devices operating above their fundamental resonance are called seismometers or geophones and typically measure the relative motion of the case using a magnet as the seismic mass and measuring the voltage generated in a coil fixed to the case, as shown in fig. 2.4(a). The voltage generated is proportional to the rate at which the magnetic flux lines are cut, and is thus proportional to the velocity of the case. The relationship between the spring stiffness and the mass is set such that the fundamental resonance is low, typically less than about 50 Hz. Devices operating below their fundamental resonance are called accelerometers and typically measure the voltage generated by a mass loaded piezoelectric material as shown in fig. 2.6(b).

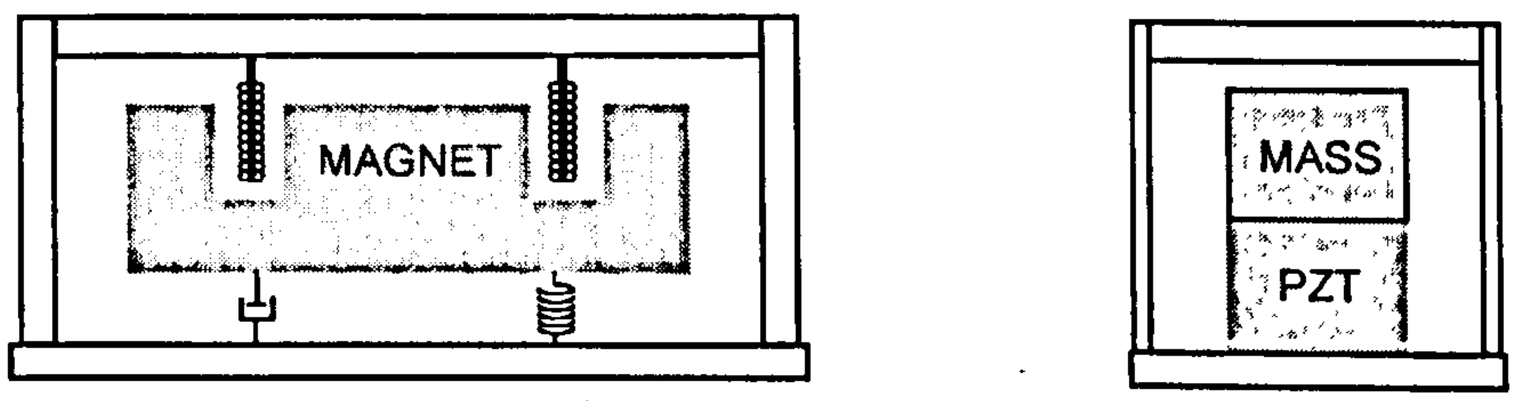

Figure 2.6: (a) Moving coil seismometer and (b) Piezoelectric accelerometer

The stiffness of the piezoelectric material results in a high fundamental resonance; up to 50 kHz in some devices.

Hull mounted sensors (such as the Flank and Bow array in fig. 1.1) are mounted on a structure known as a baffle. For measurement of acoustic pressure a rigid baffle is used; at the surface of which, the pressure associated with the acoustic signal is double the incident pressure and the particle velocity is zero. For some applications, it is desirable to mount the sensor on a pressure-release baffle. In this case the particle velocity must be measured, as described in section 2.2. The sensor must be neutrally buoyant and small compared with the wavelength of the acoustic signal to be measured. Acoustic particle velocity sensors is currently an area of active research and the reader is referred to the most recent review on related work for further discussion [2.12].

2.6 Fibre-Optic Acoustic Transduction

When a single-mode optical fibre is located within an acoustic field, the pressure and temperature fluctuations associated with the wave propagation generate strain within the optical fibre. The total phase of an optical beam propagating through the fibre will thus be modulated in proportion to the magnitude of the pressure and temperature fluctuations.

By considering a length of fibre, l, the total phase of the optical signal propagating through the fibre, ϕ, is given by,

$$\phi = nkl \tag{2.22}$$

where n is the effective refractive index of the fibre mode (which can be roughly approximated to the refractive index of the fibre core) and k is the free space propagation constant equal to $2\pi/\lambda_0$ and λ_0 is the optical wavelength in a vacuum. Differentiation of (2.22) and rearranging yields [2.6],

$$\Delta\phi = nk\Delta l + l\Delta(nk) = nk\Delta l + l\left(k\Delta n + \frac{\partial(nk)}{\partial a}\Delta a\right) \tag{2.23}$$

where a is the core diameter. It was shown in [2.13] that the 'waveguide dispersion' (last) term in (2.23) is negligible and thus (2.23) can be expressed as,

$$\frac{\Delta\phi}{\phi} \simeq \frac{\Delta l}{l} + \frac{\Delta n}{n} \tag{2.24}$$

Thus, the phase of the optical signal is affected by a physical length change of the fibre, Δl, and a change in refractive index of the fibre, Δn, due to the stress-optic effect. If we assume that the sensor fibre occupies a region with a maximum dimension of, Ω, then to determine the acoustic sensitivity of optical fibre it is appropriate to define three separate frequency regimes: (i) low frequency where the acoustic wavelength, Λ, is much greater than Ω; (ii) intermediate frequency where $\Lambda \sim \Omega$; and (iii) ultrasonic where Λ is less than the fibre diameter, d. We shall concentrate our discussion here on the low frequency region, which is most relevant to the sonar application and consider the case of detection of acoustics in water. When $\Lambda \gg \Omega$, the effect of the mismatch in impedance between the fibre and the water is negligible (the acoustic

2.6 Fibre-Optic Acoustic Transduction

When a single-mode optical fibre is located within an acoustic field, the pressure and temperature fluctuations associated with the wave propagation generate strain within the optical fibre. The total phase of an optical beam propagating through the fibre will thus be modulated in proportion to the magnitude of the pressure and temperature fluctuations.

By considering a length of fibre, l, the total phase of the optical signal propagating through the fibre, ϕ, is given by,

$$\phi = nkl \tag{2.22}$$

where n is the effective refractive index of the fibre mode (which can be roughly approximated to the refractive index of the fibre core) and k is the free space propagation constant equal to $2\pi/\lambda_0$ and λ_0 is the optical wavelength in a vacuum. Differentiation of (2.22) and rearranging yields [2.6],

$$\Delta\phi = nk\Delta l + l\Delta(nk) = nk\Delta l + l\left(k\Delta n + \frac{\partial(nk)}{\partial a}\Delta a\right) \tag{2.23}$$

where a is the core diameter. It was shown in [2.13] that the 'waveguide dispersion' (last) term in (2.23) is negligible and thus (2.23) can be expressed as,

$$\frac{\Delta\phi}{\phi} \simeq \frac{\Delta l}{l} + \frac{\Delta n}{n} \tag{2.24}$$

Thus, the phase of the optical signal is affected by a physical length change of the fibre, Δl, and a change in refractive index of the fibre, Δn, due to the stress-optic effect. If we assume that the sensor fibre occupies a region with a maximum dimension of, Ω, then to determine the acoustic sensitivity of optical fibre it is appropriate to define three separate frequency regimes: (i) low frequency where the acoustic wavelength, Λ, is much greater than Ω; (ii) intermediate frequency where $\Lambda \sim \Omega$; and (iii) ultrasonic where Λ is less than the fibre diameter, d. We shall concentrate our discussion here on the low frequency region, which is most relevant to the sonar application and consider the case of detection of acoustics in water. When $\Lambda \gg \Omega$, the effect of the mismatch in impedance between the fibre and the water is negligible (the acoustic

field is effectively unperturbed by the presence of the transducer) and the fibre is effectively subjected to a hydrostatic variation in ambient pressure. This is straightforward to realise in practice if we note that in water the sound speed, $c \approx 1500 \text{m.s}^{-1}$ and $\Lambda = 1.5\text{m}$ at 1 kHz and $\Lambda = 15\text{m}$ at 100Hz. In air, the sound speed, $c \approx 334\ \text{ms}^{-1}$ and the wavelength at 1kHz and 100Hz is 0.33m and 3.3m respectively. A typical transducer maximum dimension is less than 0.1m. The sensor thus responds to the variation in ambient pressure of the surrounding medium. In this case the second term in (2.24) is determined by the optical indicatrix,

$$\Delta(1/n^2) = \sum_{k,l} p_{ijkl}\varepsilon_{kl} \tag{2.25}$$

where p_{ijkl} are the Pockels coefficients and ε_{kl} are the strain components. For the case when $\Lambda \gg \Omega$, there are no shear strains generated in the fibre, thus using cylindrical co-ordinates and contracted notation (2.24) becomes,

$$\frac{\Delta\phi}{\phi} = \varepsilon_z - \frac{n^2}{2}\left[(p_{11}+p_{12})\varepsilon_r + p_{12}\varepsilon_z\right] \tag{2.26}$$

Note that the effect of the refractive index contribution to the total phase-shift is to reduce it slightly. We shall show in section 4.2 that for a bare fibre under hydrostatic boundary conditions, the induced strains are isotropic and $\varepsilon_r = \varepsilon_z = -(\Delta P_o / E)(1-2\nu)$, where ΔP_o is the pressure change, E and ν are the Young's modulus and Poisson ratio of the fibre respectively. Thus (2.26) reduces to,

$$\frac{\Delta\phi}{\phi\Delta P_o} = -\frac{(2\nu-1)}{E}\left[1-\frac{n^2}{2}(p_{11}+2p_{12})\right] \tag{2.27}$$

and the reduction in responsivity due to the refractive index contribution is approximately 70%, using the data in table 2.1. For a fibre under axial strain only (2.27) becomes,

$$\frac{\Delta\phi}{\phi\Delta\varepsilon_z} = \left(1-\frac{n^2}{2}\left[(1-\nu)p_{12}+\nu p_{11}\right]\right) \tag{2.28}$$

and the reduction in responsivity due to the refractive index contribution is approximately 21% [2.13]. The pressure change associated with an acoustic wave is also accompanied with a temperature change due to the adiabatic expansion and contraction process. When a fibre is used as a sensor in air, this temperature change dominates the sensitivity at low frequency and must be included in the responsivity equation. At sufficiently low acoustic frequency, the temperature change at the fibre core can keep up with the temperature change at the fibre surface and the temperature induced phase-shift will dominate the sensitivity. This temperature change is related to the pressure change by [2.6],

$$\Delta T_P = \left[\frac{(\gamma_s - 1)}{\gamma_s}\frac{\Delta P}{K_i \beta_v}\right] \tag{2.29}$$

where γ_s is the ratio of specific heats, K_i is the isothermal Bulk modulus of the medium and β_v is the volume expansion coefficient of the medium. The temperature sensitivity of a bare fibre is given by [2.6],

$$\frac{\Delta\phi}{\phi\Delta T} = \frac{1}{n}\frac{\partial n}{\partial T}\bigg|_\rho + \frac{1}{\Delta T}\left[\varepsilon_z^T - \frac{n^2}{2}\left[(p_{11}+p_{12})\varepsilon_r^T + p_{12}\varepsilon_z^T\right]\right] \tag{2.30}$$

where the subscript ρ in the first term specifies constant density. For a bare fibre and assuming the mechanical properties of the core and cladding materials are the same, then the thermally induced strains are, $\varepsilon_r^T = \varepsilon_z^T = \varepsilon + \alpha\Delta T$. Thus (2.30) reduces to,

$$\frac{\Delta\phi}{\phi\Delta T} = \frac{1}{n}\frac{\partial n}{\partial T}\bigg|_\rho + \alpha\left[1 - \frac{n^2}{2}(p_{11}+2p_{12})\right] \tag{2.31}$$

For standard telecom fibre, the first terms dominates the temperature responsivity thus,

$$\frac{\Delta\phi}{\phi\Delta T} \approx \frac{1}{n}\frac{\partial n}{\partial T}\bigg|_\rho \tag{2.32}$$

For quasi-dc acoustic signals, the fibre responsivity is therefore given by substituting (2.29) into (2.32) such that,

$$\left(\frac{\Delta\phi}{\phi\Delta P}\right)_{DC} \simeq \frac{1}{n}\frac{\partial n}{\partial T}\bigg|_{\rho}\frac{\gamma_s - 1}{\gamma_s}\frac{1}{K_i\beta_v} \tag{2.33}$$

A range of values have been used in the open literature for the material parameters of fibre and we summarise the most commonly used values in table 2.1.

Table 2.1: Material parameters

Parameter	Symbol	Value	Reference
Fibre			
Young's modulus	E	72 GPa	[2.6]
Poisson ratio	ν	0.17	[2.6]
Temperature coefficient	$\frac{1}{n}\frac{\partial n}{\partial T}\Big\vert_{\rho}$	0.68×10^{-5} K^{-1}	[2.14]
	$\frac{1}{n}\frac{\partial n}{\partial T}\Big\vert_{\rho}$	0.93×10^{-5} K^{-1}	[7.40]
Thermo-optic coefficient	$\frac{1}{n}\frac{\partial n}{\partial T}\Big\vert_{\rho}+\alpha$	0.52×10^{-5} K^{-1}	[2.15]
Linear thermal expansion coefficient	α	10.2×10^{-7} K^{-1}	[2.14]
Refractive index of core	n	1.465	[2.6]
Pockels coefficient	p_{11}	0.121	
	p_{12}	0.27	
Thermal diffusivity	ξ	0.82×10^{-6} m^{2}s^{-1}	[2.53]
Thermal conductivity	κ_c	1.37 W.(mK)$^{-1}$	[2.53]
Water			
Ratio of specific heats in water	γ_s	1.001	[2.6]
Air			
Isothermal bulk modulus	K_i	10^5 Pa	[2.6]
Ratio of specific heats in air	γ_s	1.4	[2.6]
Volume thermal expansion coefficient	β_v	$1/T$	

This allows us to determine the responsivity of a bare fibre in water and in air. In water, the ratio of specific heats, $\gamma_s \sim 1$ and the temperature induced phase-shift is small compared with the pressure induced phase-shift; the acoustic responsivity is therefore given by (2.27). Using the data in table 2.1, $\left(\Delta\phi/\phi\Delta P\right)_{water} = -2.8\times10^{-12}$ Pa^{-1}. In air, the ratio of specific heats, $\gamma_s \sim 1.4$, $K_i = P_o$, $T = 300$K and from (2.29) $\Delta T/\Delta P \approx 0.9$ mK.Pa^{-1}. Thus at low frequencies the

responsivity to pressure is given by (2.33), such that $\left(\Delta\phi/\phi\Delta P\right)_{air}$ =5.8×10^{-9} Pa^{-1}. As the frequency increases, the finite thermal transfer time of the glass will cause the responsivity to fall, until it reaches the value given by (2.27). Also, if a compliant coating is applied to the fibre, the temperature induced phase-shift becomes negligible, due to the low thermal conductivity of most polymer coating materials; the coating effectively acts as a low pass filter to heat flux. However, the mechanical properties of these coatings will enhance the axial strain induced in the fibre under pressure and this forms the subject of chapter 4.

2.6.2 Acoustic sensors: scalar

The responsivity of the optical fibre sensor can be significantly enhanced if the fibre is incorporated into a structure that provides mechanical amplification of the measurand. In the case of the optical hydrophone, the transducer is designed to enhance the strain induced in the fibre by the external pressure. The responsivity of these devices is expressed in units of optical phase-shift per unit applied pressure, $\Delta\phi/\Delta P$ measured in rads.Pa^{-1}. To allow comparison between different designs this can be normalised to the total phase, $\Delta\phi/\phi\Delta P$; however, this quantity must be used carefully since the overall stiffness and hence responsivity is also dependent on the fibre length. For the lengths of fibres used in most hydrophones, this effect is fairly small.

Many hydrophone configurations have been proposed based on flexural disks [2.16-2.18], embedded mandrel [2.19-2.20], air-backed mandrel [2.21-2.24], planar [2.25] and ellipsoidal designs [2.26-2.27], which have all demonstrated significant amplification in the pressure responsivity. However, the maximum amplification is dependent on the maximum operating depth requirement of the hydrophone. The strain imposed on the fibre must not exceed the elastic limit of glass (~1% for fused silica) when the hydrophone is at its maximum operating depth. One design of optical hydrophone that has found application in prototype arrays is the air backed mandrel type, an example of which is shown in fig. 2.7.

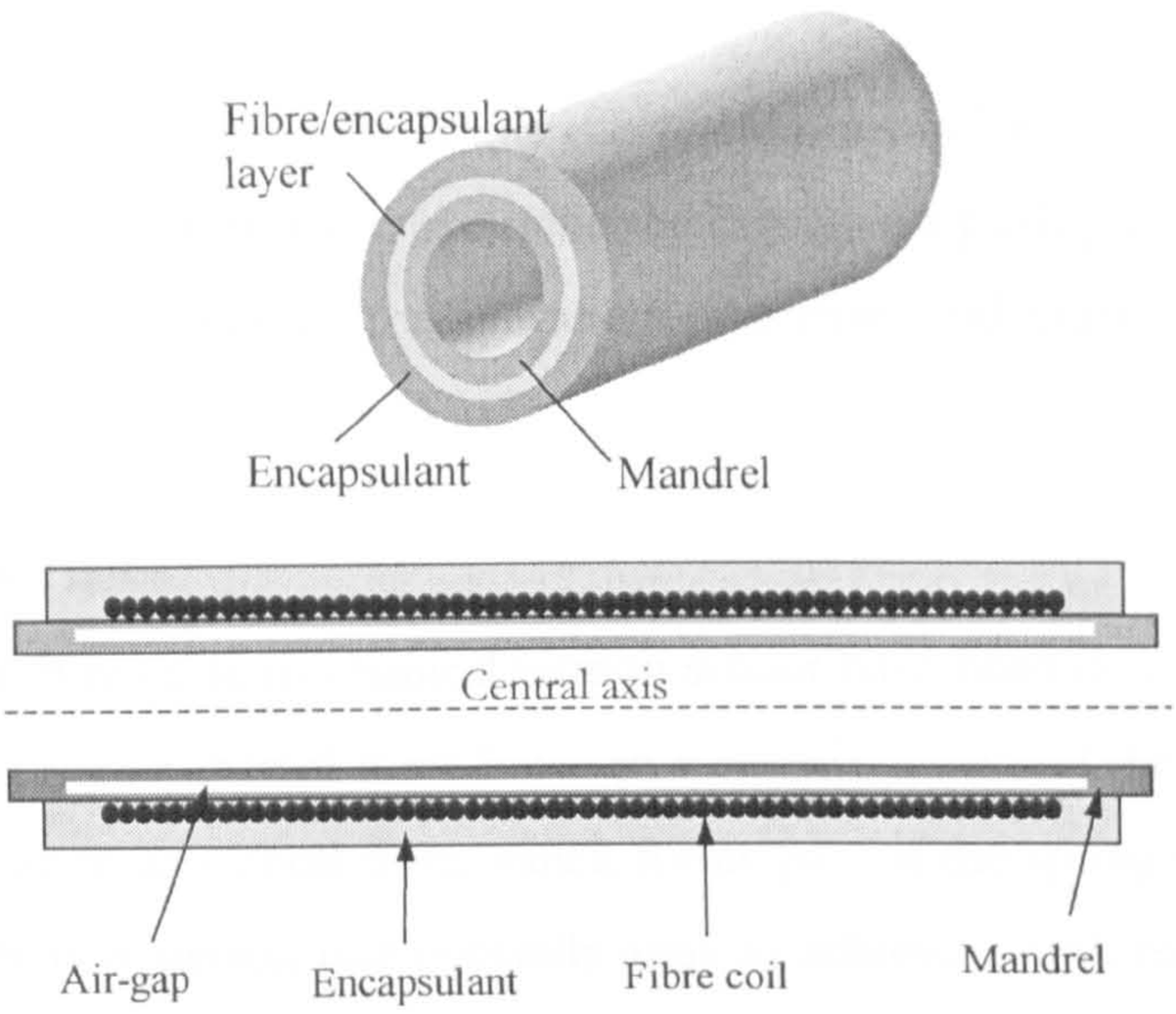

Figure 2.7: (a) Air-backed mandrel hydrophone and (b) Cross-section though hydrophone

In this configuration, the fibre is wound on a thin plastic cylindrical membrane that is supported at each end by a rigid mandrel. A small watertight cavity between the rigid mandrel and plastic membrane provides an air backing. The fibre and membrane are protected with a coating of compliant polymer such as polyurethane or epoxy resin. The presence of the air backing thus results in a highly compliant structure. An external pressure will cause the radius and circumference of the fibre coil to contract generating axial strain in the fibre. In general, the enhancement in axial strain induced in the fibre dominates over the refractive index component and practical devices have been demonstrated to provide around 50 dB of amplification compared with a bare fibre coil [2.24]. The exact responsivity of the optical hydrophone is generally a complicated function of the elastic properties and dimensions of the mandrel and fibre and both analytical and finite element models have been developed to predict the responsivity with accuracies within 2 dB [2.20,2.28]. For a hydrophone in a Michelson interferometer with 100 m of optical fibre wound onto a 20 mm diameter mandrel, one can achieve responsivities typically within the range of 0.5 to 1 rad.Pa^{-1} at 1550 nm corresponding to $\left|\Delta\phi / \phi\Delta P\right|$ between 4.2×10^{-10} Pa^{-1} and 8.4×10^{-10} Pa^{-1}. Another aspect of the design, which is important for certain applications, is to reduce the response of the sensor to other physical perturbations not associated with the signal, such as vibration. A response from other effects will introduce an unwanted signal in the sensor output indistinguishable from noise, which will cause a degradation of the SNR. Reduced acceleration response optical hydrophones based on both the flexural disk [2.16] and the mandrel design [2.28] have been demonstrated. These are generally based on either designing the sensor such that the induced strain in the fibre due to

the unwanted signal averages to zero across the whole sensor fibre [2.28], or alternatively using both arms of the interferometer and operating the sensor in a push-pull arrangement such that common-mode rejection reduces the unwanted sensitivity and enhances the signal induced strain [2.16].

2.6.3 Acoustic sensors: vector

Several designs of fibre-optic mechanical motion sensor have been demonstrated based on the principle of generating an inertial force between a seismic mass and the casing and converting this force into strain in an optical fibre, which forms part of the spring mechanism supporting the mass. In a practical device, one generally aims to achieve a high responsivity over a large bandwidth, thus the design of these sensors involves optimising the size of the inertial mass and stiffness of the supporting springs. The responsivity of these devices is expressed as an optical phase-shift per unit acceleration, $\Delta\phi / \Delta A$ in units of rads.g^{-1} where g is approximately 9.8 m.s^{-2}.

Some of the earliest devices demonstrated the principle using a mass suspended between two fibres as the arms of a fibre interferometer [2.29] or using a mass loaded compliant cylinder around which the fibre was wound [2.30]. Another device used the deformation induced in a liquid filled compliant cylinder around which fibre is wound, when exposed to the mechanical motion [2.31]. Some of the highest responsivity devices were reported in [2.32], which were based also on the mass loaded compliant mandrel design. These devices were demonstrated as both an accelerometer operating below the fundamental resonance frequency and as a displacement sensor operating above the fundamental resonance frequency. Responsivities of the order of 10^4 rad.g^{-1} with a bandwidth of 100 Hz for the accelerometer and 3500 rad.μm^{-1} for the displacement sensor with a seismic mass of around 500 grammes were reported. For application in underwater acoustics, the sensor must be made neutrally buoyant, thus a sensor more compact and lightweight is required. Such a sensor is based on the flexural disk and was first reported in [2.33]. In this device, the fibre is wound onto the surface of a flexible disk, which is either supported at the centre or edge. In the presence of mechanical vibration, the disk flexes imposing strain on the fibre. In this case, the inertial mass and spring stiffness is determined by the mass and elastic properties of the disk respectively. The fundamental resonance frequency is dependent on the elastic properties, dimensions and mounting conditions of the disk. This early device was demonstrated with a responsivity of 50 rad.g^{-1} and

a fundamental resonance frequency of 2.45 kHz. It is these types of sensor that we shall investigate in chapter 3 as potential fibre-optic acoustic vector sensors.

2.7 The Interferometric Fibre-Optic Sensor

To illustrate how a phase change can be measured interferometrically, we now analyse the fibre Mach-Zehnder interferometer, shown in fig 2.8(a), which forms the simplest interferometric sensor arrangement.

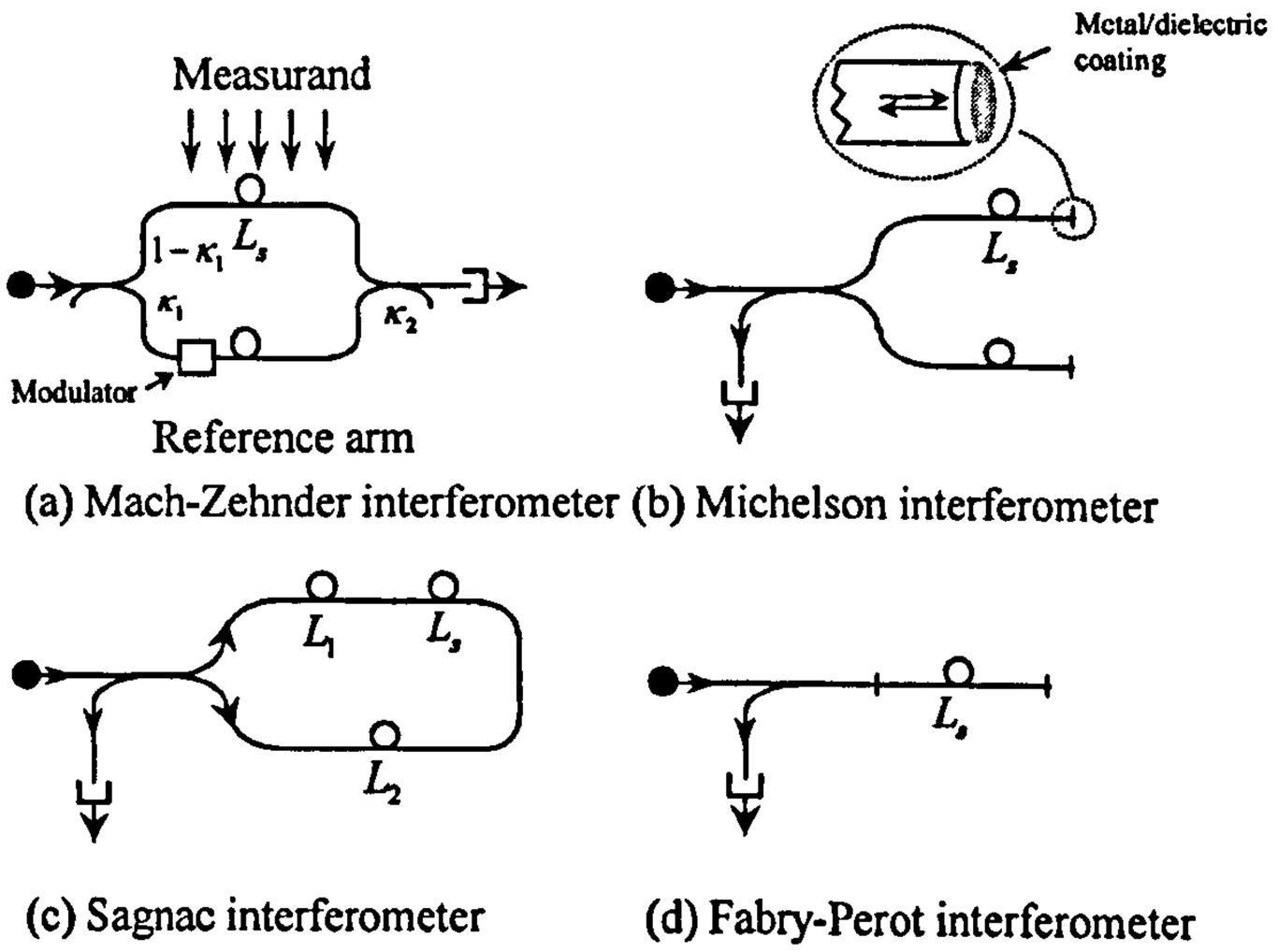

(a) Mach-Zehnder interferometer (b) Michelson interferometer

(c) Sagnac interferometer (d) Fabry-Perot interferometer

Figure 2.8: Fibre interferometer configurations

The sensor arrangement comprises a laser, a twin-arm interferometer, and a photodetector (usually a photodiode). The optical circuit is assembled using single mode fibre to prevent modal interference. The light from the source is split into the two arms of the interferometer using a fibre directional coupler (a fibre analogue of the free-space beamsplitter), and recombined using a second coupler. The hydrophone consists of a length of optical fibre forming one arm of the interferometer that is exposed to the acoustic field to be measured, while the reference arm is shielded from the acoustic field. Path matching the signal and reference arms suppresses noise due to source frequency jitter; however in many practical sensors a small path imbalance may exist. For the hydrophone to exhibit an omni-directional response it is assumed that the acoustic signal has no spatial dependence. Thus, in general the hydrophone dimensions are much smaller than the acoustic wavelength. To analyse the interferometer we make some simplifying assumptions. We assume that the fibre exhibits zero birefringence, such that the fundamental LP_{01} mode is degenerate, and the electric fields can be

treated as scalars. In practical fibres, a small amount of birefringence is present, which lifts the degeneracy of the fundamental mode, giving rise to two copropagating orthogonal polarisation modes. Random variations in the birefringence will cause power to be coupled between the two polarisation modes, hence the state of polarisation (SOP) exhibits a spatial dependence, which leads to polarisation induced signal fading. We also assume that the source is purely monochromatic (i.e. infinite temporal coherence). We shall discuss the implications of polarisation induced signal fading and finite source coherence later. If the launched power is $2P$ then the optical fields incident on the photodiode can be expressed as,

$$E_s = \sqrt{2P\alpha_s\kappa_1\kappa_2}\cdot\exp(i(\omega_s t+\phi_s)) \tag{2.34}$$

$$E_r = \sqrt{2P\alpha_r(1-\kappa_1)(1-\kappa_2)}\cdot\exp(i(\omega_r t+\phi_r)) \tag{2.35}$$

where α_s and α_r represent optical loss associated with the signal and reference arms respectively, κ_1 and κ_2 are the power coupling coefficents of the directional couplers, ϕ_s and ϕ_r are the total phase of the signals from the signal and reference arms respectively and ω_s and ω_r are the optical angular frequencies. To allow us to treat the general case, we have allowed for an optical frequency shift in the reference arm, which can be generated by an acousto-optic modulator as shown in fig. 2.8(a). The total optical field is thus $E_{tot} = E_s + E_r$ and the photocurrent is given by,

$$i_{ph} = r\left\langle E_{tot}\cdot E_{tot}^{*}\right\rangle \tag{2.36}$$

where * denotes the complex conjugate and $\langle\ \rangle$ indicates a time average over the detector time constant. r is the photodiode responsivity in AW^{-1} and $r = e\eta/h\nu$ where e is the electron charge, η is the photodiode quantum efficiency (ratio of the number of electron-hole pairs generated for one photon absorption), h is Planck's constant and ν is now the optical frequency. Evaluating (2.36) yields,

$$i_{ph} = 2\Pr\left[\alpha_s\kappa_1\kappa_2+\alpha_r(1-\kappa_1)(1-\kappa_2)+2\sqrt{\alpha_s\alpha_r\kappa_1\kappa_2(1-\kappa_1)(1-\kappa_2)}\cos(\Delta\omega t+\phi_s-\phi_r)\right] \tag{2.37}$$

Thus, the amplitude of the interference term is dependent on the optical losses in the interferometer and the coupler split ratios. It will also be dependent on the coherence properties of the laser and the birefringence properties of the interferometer arms. For this analysis we shall include these effects by introducing a fringe visibility factor, V, where $0 \leq V \leq 1$ and we shall return to the cause of these effects later. In practice it is possible to reduce the optical losses to near zero, hence $\alpha_s \simeq \alpha_r \simeq 1$ and the interference term is maximised by setting $\kappa_1 = \kappa_2 = 1/2$, thus (2.37) reduces to,

$$i_{ph} = rP\left[1 \pm V\cos(\Delta\omega t + \phi_s - \phi_r)\right] \tag{2.38}$$

where $\Delta\omega = \omega_s - \omega_r$. When $\omega_s = \omega_r$ (i.e. $\Delta\omega = 0$) the detection regime is referred to as *homodyne.* However, if the optical frequencies were shifted relative to one another such that $\Delta\omega > 0$, the detection regime is referred to as *heterodyne.* In this case the phase signal is mixed onto an intermediate frequency (IF), $\Delta\omega$. This can be used as a means of remotely interrogating multiplexed interferometers and the techniques available to achieve this frequency shift will be discussed later.

For the case when $\Delta\omega = 0$, the output of the fibre interferometer will be proportional to the cosine of the phase difference between the received signals. Environmental effects on the interferometer arms due to changes in ambient temperature and pressure will cause a slowly varying phase drift that will prevent a higher frequency signal phase term from being linearly recovered. This is known as the fading problem in fibre interferometers and a passive signal recovery technique is thus required to extract the phase signal of interest. It is also shown in (2.37) that an ambiguity in the signal phase occurs when the phase-shift corresponding to a signal is over 2π radians. Some form of fringe counting technique is therefore required to measure large phase-shifts.

Finally, we note a useful property of the Mach-Zehnder interferometer, which arises due to the availability of two outputs from the second coupler. By consideration of conservation of energy, it is straightforward to see that the two outputs are complimentary (i.e. phase-shifted by π), which is shown in (2.38) by the sign of the cosine term. Thus assuming $\Delta\omega = 0$, then after detection the difference between the two outputs can be taken to remove the DC term. This

also results in the rejection of common mode noise such as laser intensity noise. In this configuration, the receiver is referred to as 'balanced'.

2.8 Interferometer Configurations

The Mach-Zehnder interferometer was the basis for many of the early hydrophone systems and is still used in some present designs. However, a number of other interferometer configurations offer various advantages for practical systems and are often used in more recent systems. Three other interferometers that have been used to implement the optical hydrophone are shown in fig. 2.8(b), (c) and (d). These are the Michelson, Sagnac and Fabry-Pérot interferometers. It is instructive to compare interferometers by determining the frequency response of each. For this, we shall use the approach presented in [2.34] and [2.35] and apply this to the Michelson and Sagnac interferometer. We shall treat the Fabry-Pérot separately and shown that in a certain configuration, the response of the Fabry-Pérot interferometer is similar to the Michelson interferometer.

If a harmonically varying acoustic signal with no spatial dependence is incident on an optical fibre of length, L_s, this will cause a perturbation of the propagation constant, β, of the optical signal travelling in the fibre. This is due to the effects illustrated in (2.24) (i.e. the length and refractive index change). The propagation constant can thus be expressed as,

$$\beta(x,t) = \beta_0 + \delta\beta \exp(i\omega_a t) \tag{2.39}$$

where β_0 $(=nk)$ is the unperturbed propagation constant, $\delta\beta$ is the amplitude of the propagation constant modulation, ω_a is the acoustic frequency and x is the axial coordinate along the fibre. The total phase of the optical signal, $\phi_s(t)$, is then given by integration of the propagation constant over the sensor fibre length, L_s,

$$\phi_s(t) = \int_0^{L_s} \beta\left(x, t - \frac{xn}{c}\right) dx \tag{2.40}$$

where c is the light velocity in a vacuum. We shall assume in the following analysis that only the sensor fibre is exposed to the acoustic signal and maintain the assumption that the acoustic

wave has no spatial dependence (i.e. at a particular instant, the sensing fibre sees the same pressure).

Mach-Zehnder: The frequency response of the Mach-Zehnder interferometer, shown in fig. 2.8(a), can be determined by substituting (2.39) into (2.40) such that,

$$\Delta\phi_{MZ} = \delta\beta \int_0^{L_s} \exp(i\omega_a x n / c)dx \tag{2.41}$$

to obtain the responsivity,

$$|\Delta\phi_{MZ}| = \delta\beta L_s \left|\mathrm{sinc}\left(\frac{\omega_a n}{2c} L_s\right)\right| = \frac{2c\delta\beta}{\omega_a n}\left|\sin\left(\frac{\omega_a n}{2c} L_s\right)\right| \tag{2.42}$$

which at all practical acoustic frequencies can be approximated to,

$$|\Delta\phi_{MZ}| \approx \delta\beta L_s \tag{2.43}$$

Michelson: The Michelson interferometer is shown in fig. 2.8(b). Light from a laser source is split into two fibres by a directional coupler. At the end of each fibre arm, a mirror coating is applied to the end of the cleaved fibre. To achieve high reflectance, the fibres must be accurately cleaved before a metal or dielectric coating is applied, which can be achieved by chemical or vacuum deposition; however, thermal and electron beam evaporation have also been used [2.102]. Alternatively, 'fibre loop reflectors' can be used [2.101] which have the advantage of achieving close to 100% reflectance. The light is thus reflected back along the same path to exit through the remaining port of the directional coupler. Care must be taken to avoid optical feedback into the laser cavity, by use of an optical isolator on the input port of the directional coupler. It should be noted that the fringe visibility obtained from the Michelson interferometer is independent of the coupler ratio.

The frequency response for the Michelson interferometer is determined in a similar way to that shown above and the phase responsivity is given by,

$$|\Delta\phi_M| = 2\delta\beta L_s \left|\mathrm{sinc}\left(\frac{\omega_a n}{2c} L_s\right)\cos\left(\frac{\omega_a n}{2c} L_s\right)\right| = \frac{2c\delta\beta}{\omega_a n}\left|\sin\left(\frac{\omega_a n}{c} L_s\right)\right| \quad (2.44)$$

which can be approximated to,

$$|\Delta\phi_M| \approx 2\delta\beta L_s \quad (2.45)$$

Sagnac: The use of the Sagnac interferometer as a hydrophone was first reported in [2.36] and the basic interferometer is shown in fig. 2.8(c). Here, the light is split into two paths by a directional coupler that travel in opposite directions through the same closed loop. The loop contains two delay coils of length L_1 and L_2 and a sensor coil of length L_s. A static perturbation acting on the complete loop will have no net effect on the phase delay between the two beams, because both beams will be affected equally. However, a dynamic signal acting on the sensor, but not on the delay coils, (i.e. non-symmetrically about the loop) will introduce a phase difference between the two counter-propagating beams due to the fact that one beam is in a different part of the loop when the other beam is passing through the sensor. Analysis of the Sagnac interferometer requires separate integration of each beam and has been carried out in [2.34] where it was shown that,

$$|\Delta\phi_S| = 2\delta\beta L_S \left|\mathrm{sinc}\left(\frac{\omega_a n}{2c} L_s\right)\sin\left(\frac{\omega_a n}{2c} L_d\right)\right| \quad (2.46)$$

where $L_d = L_2 - L_1$. For the case when $\omega_a \ll \pi c / nL_d$ (i.e. below the first null in the phase responsivity), the responsivity of the Sagnac interferometer is reduced to,

$$|\Delta\phi_S| \approx 2\delta\beta \frac{\omega_a n}{2c} L_s L_d \quad (2.47)$$

It is now possible to compare the frequency response of the three interferometers. The normalised responsivity, $|\Delta\phi|/(\delta\beta L_s)$, of each interferometer is plotted in fig. 2.9 as a function of normalised frequency, $\omega_a n L_s / 2c$.

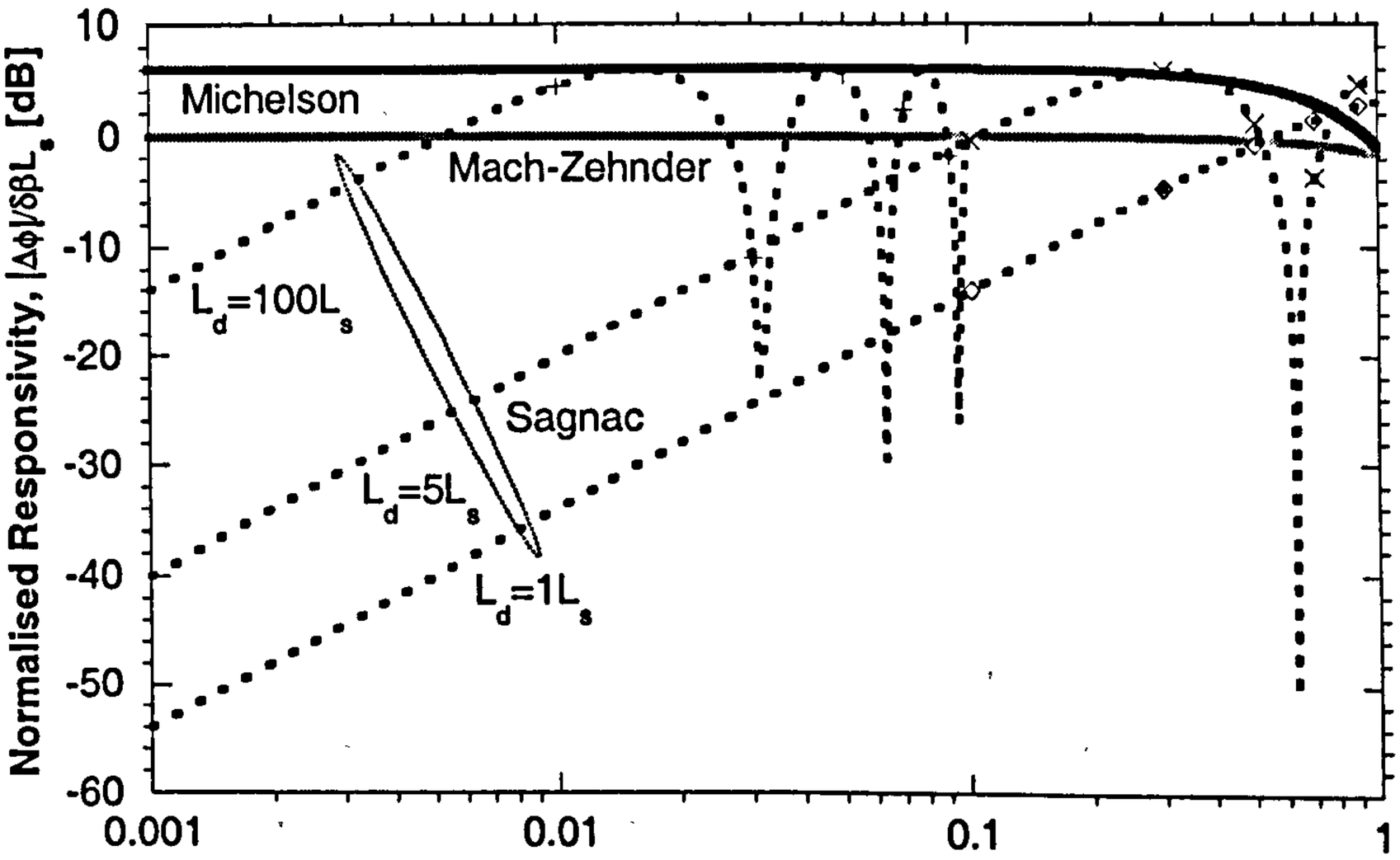

Figure 2.9: (i) Normalised responsivity versus normalised frequency for the Mach-Zehnder, Michelson and Sagnac interferometers

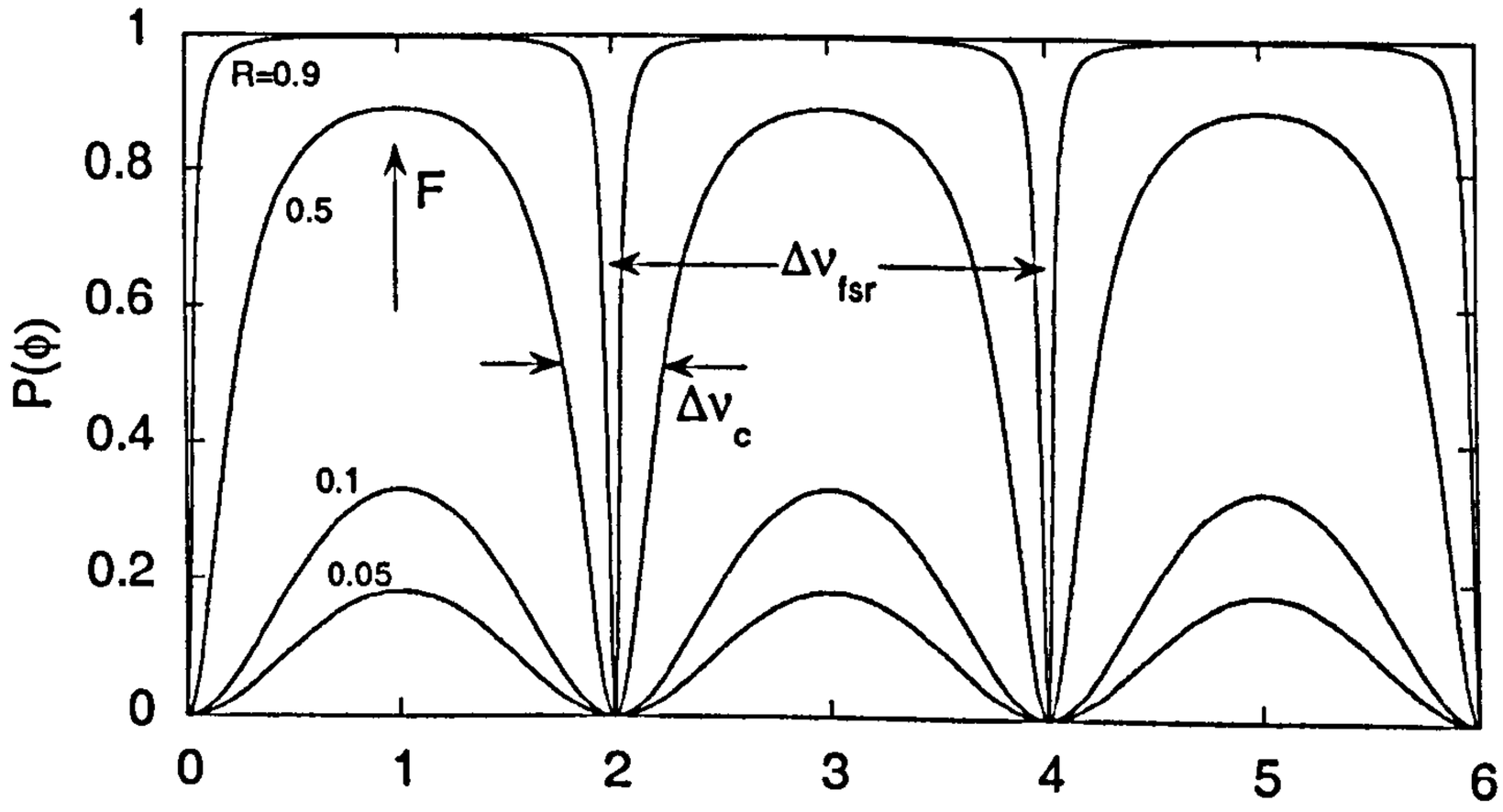

Figure 2.9: (ii) Response in reflection of FFP to a monochromatic light source

The responsivity of the Michelson interferometer is twice (6 dB) the responsivity of the Mach-Zehnder interferometer due to the dual pass of the optical signal through the sensor coil. The responsivity of the Sagnac interferometer is proportional to the frequency for $\omega_a \ll \pi c / nL_d$. This property of the interferometer has been used to increase the available dynamic range in an optical hydrophone since the frequency dependence of the responsivity compensates for the background acoustic noise spectrum (which exhibits an $f^{-0.83}$ dependence on frequency), such that the resulting sensor noise floor is roughly flat [2.37]. However, in general for the hydrophone application, the delay coil length required is very large. For example, for a practical hydrophone with L_s=100 m, the interferometer responsivity must be approximately equal to its Michelson equivalent at f_a~10 kHz. This requires a delay coil length, $L_d = 100L_s$ or 10 km, as shown in 2.9, to give the required responsivity. Packaging of this length of fibre in an acoustic array may be problematical.

Fibre Fabry-Pérot (FFP): The FFP interferometer, shown in fig.2.8(d) is a multiple beam interferometer. Its performance as a sensor has been investigated by a number of groups [2.103-4]. An interference signal is generated by the reflection from opposite ends of a length of fibre. If we assume that the interferometer is illuminated by a monochromatic source and there is no birefringence or attenuation in the sensor fibre, then in reflection the FFP produces Fizeau fringes and the power response is given by [2.105],

$$P(\phi) = P_{inc}\left[1 - \frac{(1-R_1)(1-R_2)}{1+R_1R_2 - 2\sqrt{R_1R_2}\cos(\phi)}\right] \qquad (2.48)$$

where R_1, R_2, are the mirror reflectivities, P_{inc} is the incident power and $\phi = 4\pi nL_s/\lambda$. This transfer function is plotted in fig. 2.9(ii) for a range of R, where we have assumed $R_1 = R_2 = R$. It is useful to define three parameters for the FFP. The free-spectral range, $\Delta\nu_{fsr}$, specifies the frequency spacing of adjacent minima in fig. 2.9(ii) and is given by,

$$\Delta\nu_{fsr} = \frac{c}{2nL_s} \qquad (2.49)$$

The coefficient of finesse, F, is defined as,

$$F = \left(\frac{2\sqrt{R}}{1-R}\right)^2 \tag{2.50}$$

and allows us to reformulate (2.48) in terms of F such that,

$$P(\phi) = P_{inc}\left[\frac{F\sin^2(\phi/2)}{1+F\sin^2(\phi/2)}\right] \equiv P_{inc}\left(1-\mathrm{A}(\phi)\right) \tag{2.51}$$

where $\mathrm{A}(\phi) = \left(1+F\sin^2(\phi/2)\right)^{-1}$ is the Airy function and represents the transmitted flux density. Finally, the finesse, $\mathbb{F}$, defines the relative width of each minima,

$$\mathbb{F} = \frac{\Delta\nu_{fsr}}{\Delta\nu_c} = \frac{\pi\sqrt{R}}{1-R} \tag{2.52}$$

Two interesting configurations are considered. Operating a high finesse FFP at the point of steepest gradient yields a high responsivity. By differentiating (2.51) twice it can be shown that the response has a maximum when $\phi^2 = 4/3F$ and $\Delta P/\Delta\phi \simeq 0.32P_{inc}\sqrt{F}$. However, this doesn't necessarily yield an equivalent increase in SNR compared with a Mach-Zehnder interferometer with the same fibre length, if laser frequency noise limits the phase resolution (the noise is also multiplied by the responsivity factor). Conversely, a low finesse FFP ($R \ll 1$) allows us to use the approximate relation $(1+R)^n \approx 1+nR$ and show that (2.48) reduces to,

$$\begin{aligned} P &\approx 2RP_{inc}\left(1-\cos(\phi)+2R\cos(\phi)(1-\cos(\phi))\right) \\ &\approx 2RP_{inc}\left(1-\cos(\phi)\right) \end{aligned} \tag{2.53}$$

and resembles the response of the two beam interferometer ((2.38)). Note that the last term in (2.53) generates a small distortion in the response if R is not sufficiently low. Finally, it should also be noted that these interferometers have been implemented using in-fibre Bragg gratings as the reflective elements [2.63]

2.9 Interferometric Sensor Signal Processing

To obtain a linear response from the fibre interferometer in the presence of environmental perturbations, an interrogation scheme must be used to overcome the fading problem (not to be confused with polarisation induced signal fading described later). We divide techniques into two groups referred to as: (i) *active* where feedback must be applied to an individual sensor and an electronic modulator (such as a phase or frequency modulator) may be incorporated into one arm of the interferometer; and (ii) *passive* where no direct feedback is required and the differential phase or frequency between the interferometer beams may be controlled by either direct or external source modulation. The relative merits of each technique can be compared in terms of the phase resolution achieved and the ease of implementation. For application to sensor arrays, the technique must also be combined with a multiplexing technique. Reviews on various active and passive techniques developed can be found in [2.43-44]. Here we shall describe the active technique which we use as a frequency discriminator in chapter 7 and follow this with a discussion on two passive techniques referred to as heterodyne and homodyne 'phase-generated-carrier', which have been widely used in prototype hydrophone systems. A noise analysis will also be presented that will allow calculation of the phase resolution achievable with such interrogation schemes followed by a discussion on dynamic range.

2.9.1 Active interrogation schemes

When an interferometer is exposed to the environment, changes in ambient temperature and pressure will cause the phase of the output signal to drift. Then for the case when $\Delta\omega = 0$, the photocurrent is given by (2.38),

$$i_{ph} = rP\left(1 \pm V\cos(\phi_s(t) + \phi_d(t))\right) \tag{2.54}$$

where $\phi_s(t)$ is the signal phase of interest and $\phi_d(t)$ is the environmentally induced phase drift. The sign of the cosine term depends on which output fibre is used. Thus, the output from a balanced receiver is,

$$v_{bal} = r_b PV\cos(\phi_s(t) + \phi_d(t)) \tag{2.55}$$

where we now define r_b as the responsivity of the balanced receiver in $V.W^{-1}$. If the drift term in (2.55) is $\phi_d(t) = (2m+1)\pi/2$ where m is an integer (i.e. quadrature) and $\phi_s \ll 1$ then,

$$v_{bal} = r_b P V \phi_s(t) \tag{2.56}$$

and the balanced receiver voltage is proportional to the signal phase. The rate of the drift is dependent on the rate of the temperature fluctuations and the spacing and length of fibre in the interferometer arms. We also note that in an interferometer with a fibre path-imbalance of d, the phase is dependent on drift of the source frequency, $\Delta\nu$, through the relationship $\phi = 2\pi n d \Delta\nu / c$. In general, the frequency of the environmentally induced phase-shift is much lower than the signal frequency of interest; thus we can use this slow phase drift to generate a feedback signal using an integrator, to maintain the interferometer in quadrature [2.45,2.46]. A suitable set-up is shown in fig. 2.10.

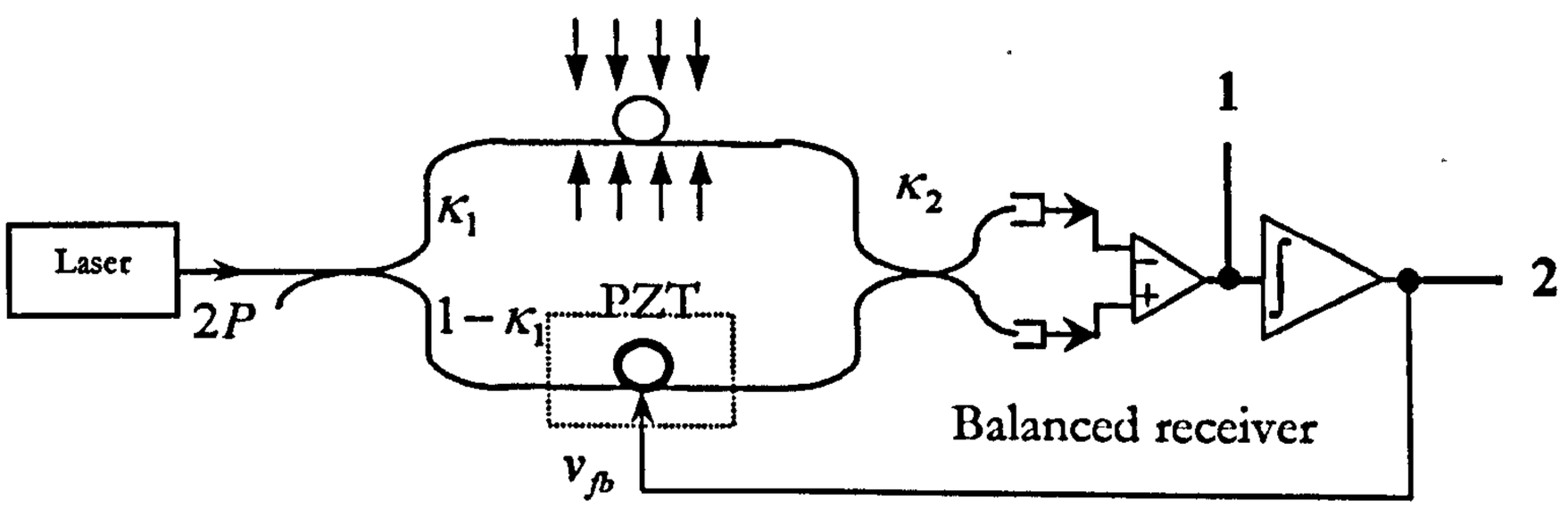

Figure 2.10: Active homodyne interferometric sensor arrangement

The feedback is then applied to a phase modulator located in one of the interferometer arms to close the loop (a popular phase modulator is that based on a loop of fibre wound under tension around a cylindrical piezo-electric tube. Applying a voltage across the wall of the tube generates a radial strain and hence an axial strain in the fibre). The signal phase is taken from output 1. This is known as the low gain-bandwidth product configuration and although a high frequency response can be obtained (limited by the frequency response of the photodetector), it has the disadvantage that variations in the fringe visibility and input power will affect the output phase scale factor. Also, the dynamic range is limited due to the small angle approximation used to derive (2.56). An alternative technique, known as the high gain-bandwidth product configuration involves measuring the feedback voltage applied to the phase modulator (at

output 2). With the loop open, v_{bal} drifts between values of $\pm r_b PV$, crossing zero at the quadrature condition. By applying sufficient gain to the feedback voltage, v_{fb}, and closing the loop, v_{bal} is forced to zero and the total phase in (2.55) is equal to $(2m+1)\pi/2$, which can be expressed as $\phi_d + \phi_s + \phi_c = (2m+1)\pi/2$ where ϕ_c is the phase applied by the phase modulator (at output 2). A loop equation can be derived by consideration of the quadrature condition such that,

$$\frac{dv_{fb}}{dt} + \gamma r_b VPhv_{fb} = r_b VP(\phi_d + \phi_c - \pi/2) \qquad (2.57)$$

where h is the scale factor of the phase modulator in rad.V^{-1}, γ is a gain factor associated with the integrator and we have taken the phase modulo 2π. The feedback voltage is therefore linearly related to the signal phase through the quadrature relation, $hv_{fb} = (\phi_d + \phi_s - \pi/2)$ providing the frequency of the quantity $\phi_d + \phi_s$ falls within the gain-bandwidth product of the feedback loop, which is given by the quantity, $\gamma r_b VPh$. Thus, the signal phase is now independent of fluctuations of the input power and visibility, which only affect the gain-bandwidth product. Since no small angle approximation is made the dynamic range is also significantly increased, limited by the integrator.

Another useful technique to achieve quadrature is to use the feedback voltage to modulate the frequency of the laser. In this case a path-imbalance must be incorporated into the interferometer and the scale factor, h, is now determined by the equation, $h = 2\pi ndj/c$, where j is the scale factor of the laser modulation, measured in Hz.V^{-1}. Environmentally induced drift of the interferometer phase is thus compensated by modulation of the laser frequency. This technique has the disadvantage that an imbalance is required in the interferometer, which may generate excess frequency induced phase noise.

2.9.2 Passive interrogation schemes

Shown in fig. 2.11 is the basic Mach-Zehnder interferometer, where we have placed components in the arms of the interferometer in positions labelled 1 and 2 that can either modulate the phase of the light (using a piezoelectric fibre stretcher) or impose a frequency

shift (using an acousto-optic modulator) on the light. In the following analysis we assume, as before, that the optical losses in the signal and reference arms are zero and the coupler power transmission ratios are ½, hence $\alpha_s = \alpha_r = 1$ and $\kappa_1 = \kappa_2 = 1/2$.

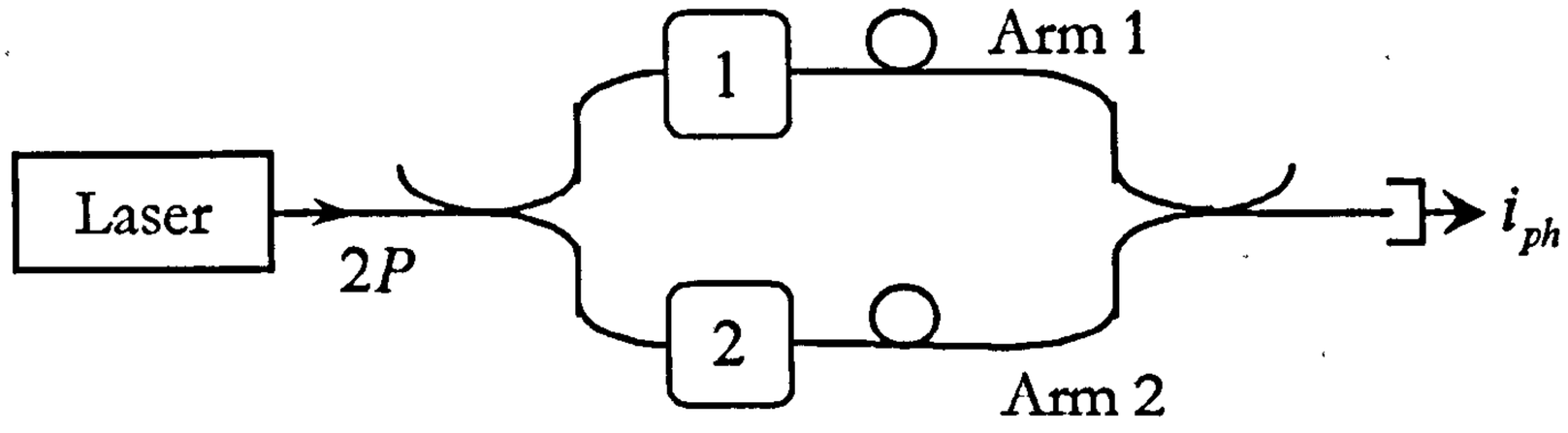

Figure 2.11: Basic Mach-Zehnder interferometric sensor arrangement

Heterodyne: Perhaps one of the simplest techniques is known as heterodyne interrogation where the frequency of the optical signal propagating in one arm of the interferometer is shifted relative to the other using an acousto-optic modulator (AOM). By placing an AOM in position 1 in fig. 2.11 and applying an RF signal to the AOM, a frequency shift equal to the frequency of the RF drive signal will be imposed on the diffracted beam. The photocurrent is then given by (2.38) where $\Delta\omega$ is equal to the RF drive signal of the AOM. By placing a second AOM in position 2 in fig. 2.11, $\Delta\omega$ can be set to any value by varying the frequency of the RF signals driving each AOM. This technique yields a signal that contains only a single carrier frequency component at $\Delta\omega$. Extraction of the signal phase of interest, $\phi(t)$, can be achieved either with an electronic frequency discriminator and integrator or by mixing the photodiode signal with in-phase and quadrature versions of the unmodulated carrier frequency and low pass filtering, as shown in fig. 2.12(a). This yields,

$$0.5 \cdot rPV \cos\phi(t) \tag{2.58}$$

$$-0.5 \cdot rPV \sin\phi(t) \tag{2.59}$$

which are the sine and cosine of the signal phase. Extraction of $\phi(t)$ can be achieved by taking the arctangent of (2.59)/(2.58).

An alternative method uses a technique known as differentiate and cross-multiply and is shown schematically in fig. 2.12(c). If the differentials of (2.58) and (2.59) are taken and multiplied by

the undifferentiated version of the other signal then the difference between the two resulting signals yields,

$$0.25(rPV)^2\dot{\phi}(t) \tag{2.60}$$

Integration of this signal followed by normalisation to remove the unwanted amplitude term yields the signal phase of interest, $\phi(t)$. It is worth noting that this technique allows the phase to be directly obtained with no ambiguity about 2π. Use of the arctangent method requires a fringe counting technique that monitors phase crossing at integer multiples of 2π in order to track phase excursions greater than 2π. It will be shown latter how the heterodyne technique can be used remotely to interrogate multiplexed fibre interferometers.

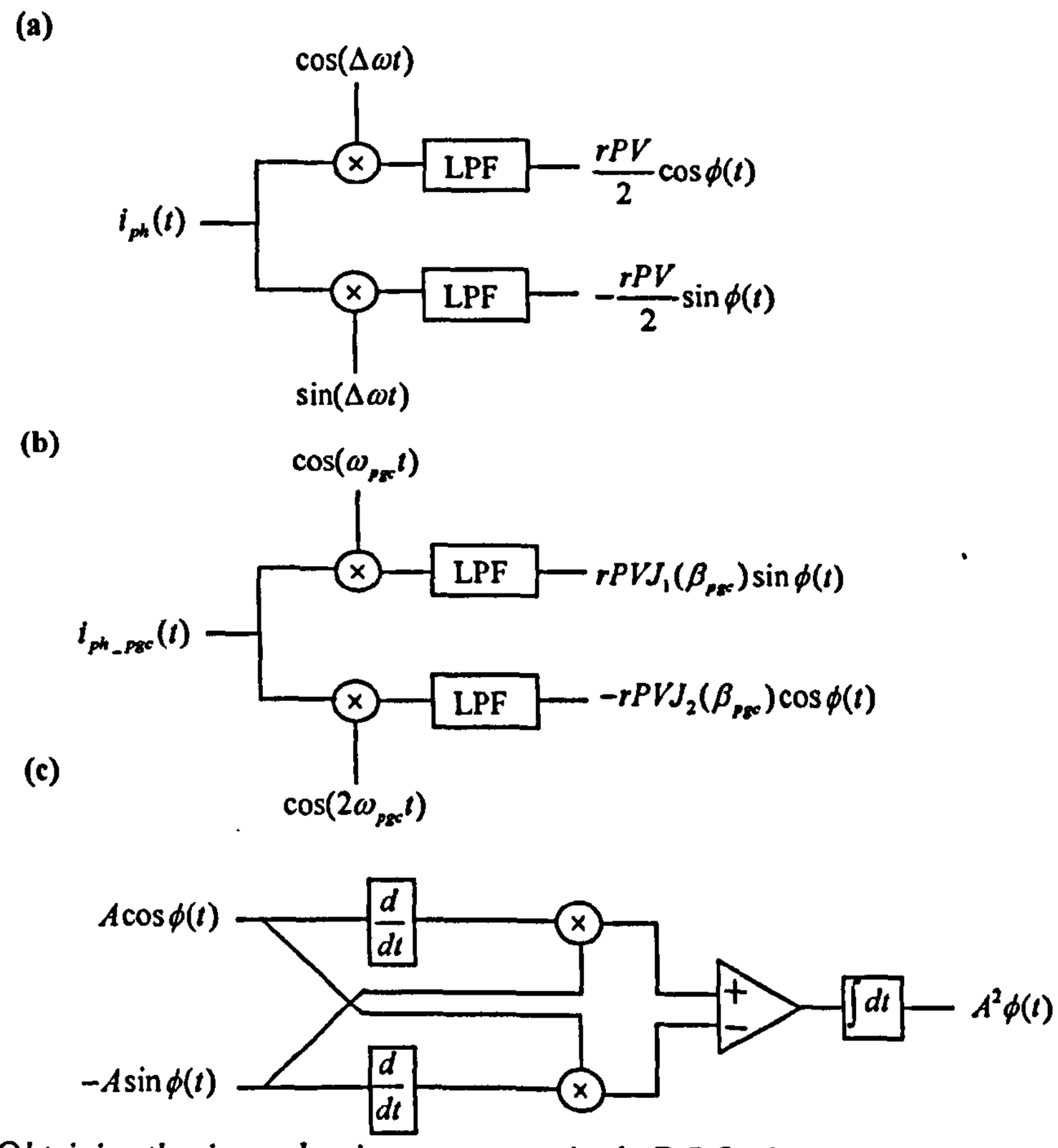

Figure 2.12: (a) Obtaining the sine and cosine components in the PGC scheme, (b) Obtaining the sine and cosine components in the heterodyne scheme, (c) The differentiate and cross-multiply demodulator [2.42]

Another technique that has been demonstrated is called pseudo-heterodyne interrogation [2.39] where a serrodyne ramp is applied to the laser frequency. Incorporating a path-imbalance into the interferometer causes a carrier frequency to be generated; the frequency of which depends on the peak laser frequency excursion and the path imbalance. A similar technique, reported in [2.39], used periodic switching of the laser frequency and sampling of the interferometer output. By switching the laser frequency and incorporating an appropriate path-imbalance in the interferometer, the necessary sine and cosine components of the phase are directly obtained in the sampled output. An interesting technique based on phase diversity was reported in [2.107,2.40] and was based on the 3×3 coupler. It was shown in [2.108] that by incorporating a 3×3 coupler as the output coupler of the interferometer, the sine and cosine components of the phase are contained in the outputs. Early technical problems associated with this technique concerned with polarisation dependence of the 3×3 coupler power split ratio have since been alleviated with improvements in the coupler manufacture process. This technique is attractive as a fully passive method of interrogation of fibre interferometers without the need for source modulation or a path-imbalance [2.109].

Homodyne phase-generated-carrier (PGC): This scheme involves generation of a carrier frequency through high frequency modulation of the optical phase and can be implemented in two ways [2.42]; (i) incorporating a phase modulator in position 1 in fig. 2.11, allows a high frequency phase modulation to be imposed on the optical signal in arm 1 of the interferometer or (ii) modulating the optical frequency of the laser output and incorporating a small path imbalance in the interferometer as shown in fig. 2.13 allows generation of a carrier through frequency discrimination. This latter technique allows remote interrogation of the interferometer without the need for active components in the interferometer and its implementation with semiconductor laser diodes is now discussed.

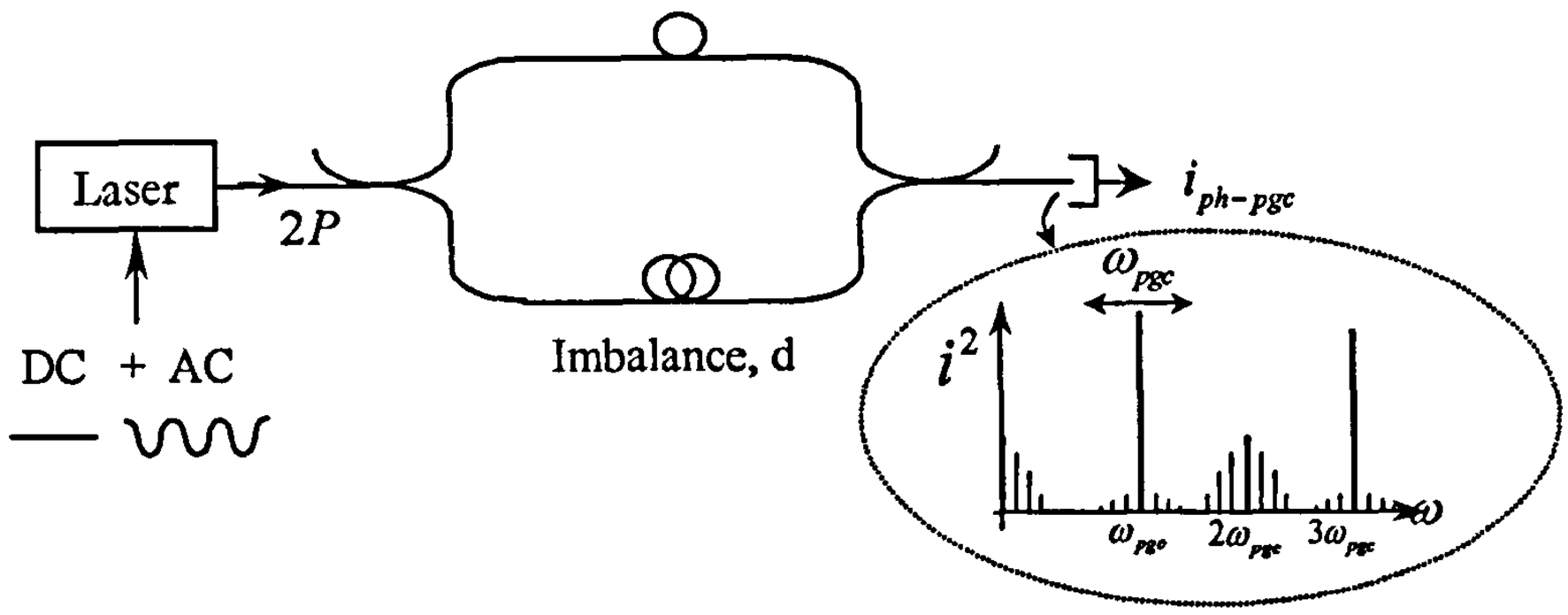

Figure 2.13: Laser frequency modulation implementation of homodyne PGC

The PGC interrogation scheme can be implemented by incorporating a small optical path imbalance in the interferometer and applying a modulation to the semiconductor laser diode (LD) [2.47]. If a sinusoidal current modulation of angular frequency ω_{pgc} is added to the laser diode drive current, as shown in fig. 2.13, then the photocurrent in (2.38) becomes,

$$i_{ph-pgc} = rP + rPV\cos\left[\phi_{pgc}\cos\omega_{pgc}t + \phi_s(t) + \phi_d(t)\right] \qquad (2.61)$$

where $\phi_{pgc} = 2\pi nd\Delta\nu/c$, d is the path imbalance, c is the speed of light in a vacuum, $\Delta\nu$ is the peak frequency excursion of the laser output (determined by the amplitude of the current modulation) and we have replaced the signal and reference arm phase with a time varying signal phase and a slowly varying drift phase, $\phi_d(t)$, due to environmental effects. Expanding (2.61) in terms of its Bessel function components using the following relationships,

$$\begin{aligned}\cos\left(\phi_0\sin(\omega_s t)\right) &= J_0(\phi_0) + 2\sum_{k=1}^{\infty} J_{2k}(\phi_0)\cos(2k\omega_s t)\\ \sin\left(\phi_0\sin(\omega_s t)\right) &= 2\sum_{k=0}^{\infty} J_{2k+1}(\phi_0)\sin\left((2k+1)\omega_s t\right)\end{aligned} \qquad (2.62)$$

and setting, $\phi(t) = \phi_d + \phi_s$, yields,

$$i_{ph-pgc} = rP + rPV\left[\left[J_0(\phi_{pgc}) + 2\sum_{k=1}^{\infty}(-1)^k J_{2k}(\phi_{pgc})\cos 2k\omega_{pgc}t\right]\cos\phi(t) - \left[2\sum_{k=0}^{\infty}(-1)^k J_{2k+1}(\phi_{pgc})\cos(2k+1)\omega_{pgc}t\right]\sin\phi(t)\right] \qquad (2.63)$$

This shows that the photocurrent consists of a fundamental frequency component at ω_{pgc} (referred to as the carrier frequency) plus a series of harmonic components of the carrier

frequency about which the signal of interest, $\phi(t)$, $(=\phi_s(t)+\phi_d(t))$ appears as phase modulation sidebands (shown in the inset of fig. 2.13). The amplitude of each harmonic is thus given by the respective Bessel function amplitude. This signal is then processed (or demodulated) to yield the sine and cosine of $\phi(t)$ by synchronous detection of the PGC components ω_{pgc} and $2\omega_{pgc}$, as shown in fig. 2.12(b). By low pass filtering the resulting signals, the familiar sine and cosine of the signal phase are obtained,

$$rPVJ_1(\phi_{pgc})\sin\phi(t) \tag{2.64}$$

$$-rPVJ_2(\phi_{pgc})\cos\phi(t) \tag{2.65}$$

$\phi(t)$ can then be obtained directly by setting the LD modulation current such that $J_1(\phi_{pgc})=J_2(\phi_{pgc})$ (i.e. $\phi_{pgc}=$ 2.6 or 6.1 as shown in fig. 2.14) and taking the arctangent of (2.64)/(2.65) or using the differentiate and cross-multiply technique described above.

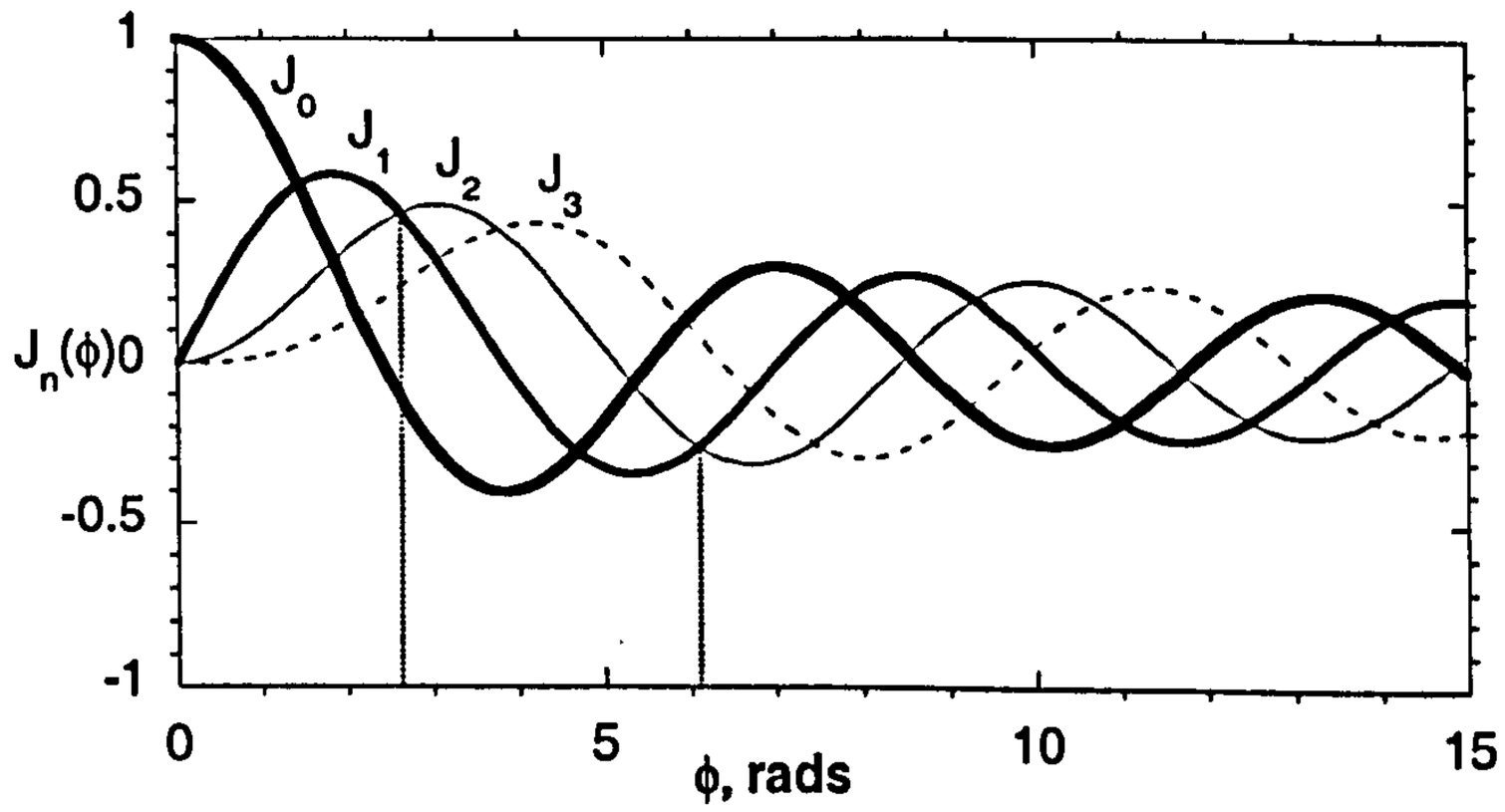

Figure 2.14: Bessel function amplitudes

A similar technique reported in [2.41] was called synthetic heterodyne detection. The optical arrangement is the same as the homodyne-PGC; however, in this scheme, the photodiode output is separately band pass-filtered at ω_{pgc} and $2\omega_{pgc}$ and each signal multiplied by a reference tone at $2\omega_{pgc}$ and ω_{pgc} respectively. The result is two carriers at $3\omega_{pgc}$ with the signal present as a phase modulation sideband on each carrier. Although, each carrier would fade, their orthogonality would prevent them fading simultaneously. Thus, the output is obtained by summing the carriers and extracting the phase signal with a frequency

discriminator. This technique has not been demonstrated to achieve phase resolution comparable to the homodyne-PGC [2.43].

2.9.3 Noise sources and phase resolution

Having derived the form of the received optical signal, the various sources of noise in the interferometric system can be included to calculate the carrier-to-noise ratio (CNR)[3]. This is then related to the minimum detectable phase or phase resolution by using narrow band phase modulation theory [2.48]. The following analysis is based on a heterodyne system although it can also be applied, with some minor modification, to a phase generated carrier scheme.

Taking the ac part of the photocurrent in the case of a heterodyne system gives,

$$i_{ph-het} = rPV\cos(\Delta\omega t + \phi_s(t) + \phi_d(t)) \tag{2.66}$$

Ignoring environmentally induced phase perturbations and assuming a sinusoidal signal excitation, $\phi_s(t)$ equal to $\phi_o \sin\omega_s t$ (2.66) can be expressed as,

$$i_{ph-het} = rPV\left[\cos(\Delta\omega t)\cos(\phi_0 \sin(\omega_s t)) - \sin(\Delta\omega t)\sin(\phi_0 \sin(\omega_s t))\right] \tag{2.67}$$

Using (2.62) and the small angle approximations $J_0(\phi_o) \approx 1$ and $J_1(\phi_o) \approx \phi_o/2$ for $\phi_o \ll 1$, (2.66) can thus be expressed as,

$$i_{ph-het} \approx rPV\left(\cos\Delta\omega t - \frac{\phi_o}{2}[\cos((\Delta\omega - \omega_s)t) - \cos((\Delta\omega + \omega_s)t)]\right) \tag{2.68}$$

where ϕ_0 is the peak phase deviation. The power ratio between the carrier and first modulation sideband is therefore given by,

$$CNR \approx \left(\frac{2}{\phi_o}\right)^2 \tag{2.69}$$

---

[3] In fact, we shall calculate the carrier-to-signal ratio; however, since the minimum detectable signal is limited by noise, we refer to it as the carrier-to-noise ratio.

Thus, to achieve a phase resolution of 1 μrad.Hz$^{-1/2}$, a CNR of 126 dB re Hz$^{-1/2}$ is required (assuming a signal to noise ratio of 1.0 is required to resolve the phase). Using (2.67) and (2.68) the following expression can be derived that relates the sensor rms phase resolution, $\delta\phi$ ($=\phi_0/\sqrt{2}$), to the total noise current, $\overline{i_n^2}$,

$$\frac{0.5(rPV)^2}{\overline{i_n^2}} \approx \left(\frac{\sqrt{2}}{\delta\phi}\right)^2 \tag{2.70}$$

where the factor of 0.5 converts peak to mean-square carrier power.

It now remains to determine, $\overline{i_n^2}$. Fundamentally, $\overline{i_n^2}$ is limited by shot noise, however, in practice other sources of noise will be present. These are: (i) the detector amplifier thermal noise, (ii) intrinsic thermal noise in the fibre waveguide, (iii) RF oscillator noise, (iv) laser intensity noise, (v) laser frequency or phase noise and (vi) spontaneous emission noise from an optical pre-amplifier if present.

Shot noise and photodiode thermal noise: Expressions for the mean-square noise current due to shot noise and amplifier thermal noise are given by,

$$\overline{i_{sh}^2} = 2e^2\eta P\Delta f / h\nu \tag{2.71}$$

$$\overline{i_{th}^2} = 4k_B T_e \Delta f / R_L \tag{2.72}$$

where e is the electron charge, k_B is Boltzman constant, $T_e = T + T_a$, T is the ambient temperature and T_a is the effective noise temperature of the amplifier [2.49], R_L is the photodiode load resistance and Δf is the electrical bandwidth. If it is assumed that the carrier frequency is sufficiently high such that the photodiode generation-recombination[4] noise is

[4] Generation-recombination noise arises from fluctuations in the carrier density and in this way is related to photon shot noise. However, unlike shot noise, it results from secondary carrier density fluctuations due to random electron-hole recombinations. It has a characteristic lifetime to τ_0 and generally exhibits a flat spectral density up to $1/\tau_0$. Its equivalent noise power generation is given by [2.50],

$$\overline{i_{g-r}^2} = \left(4\overline{i^2}\tau_0/\tau_d\right)\cdot\left(1+4\pi^2 f^2\tau_0^2\right)^{-1}$$

where τ_d is the charge lifetime (i.e. time taken for charge carriers to exit junction).

negligible [2.50] then, in principle, the optical power can be increased such that $\overline{i_{sh}^2} \gg \overline{i_{th}^2}$ and shot noise limited detection is achieved.

Waveguide thermal noise: It has recently been shown that, in practice, it will be difficult to achieve resolutions approaching the shot noise limit due to the intrinsic thermal noise in the optical waveguide, which can be significant even for relatively short fibre lengths [2.51,2.52]. Thermal diffusion of heat across the mode field of the optical signal propagating in the core of the optical fibre causes small perturbations to the phase of the signal and has been investigated in [2.53]. We shall return to discuss this source of noise in more detail in chapter 7, and here we shall simply present the defining equation and investigate the effect on the phase resolution in the fibre interferometer. It was shown that the thermally induced phase noise assuming an insulating boundary condition at the fibre cladding-air interface is given by,

$$\delta\phi_{fibre-th} = \left(\left.\frac{\partial n}{\partial T}\right|_{\rho} + n\alpha\right)\left\{\frac{2\pi k_B T^2 L}{\kappa_c \lambda^2}\ln\left[\frac{\left(\left(\frac{2}{w}\right)^2+\left(\frac{2\pi f}{c/n}\right)^2\right)^2+\left(\frac{2\pi f}{\xi}\right)^2}{\left(\left(\frac{2.405}{r_2}\right)^2+\left(\frac{2\pi f}{c/n}\right)^2\right)^2+\left(\frac{2\pi f}{\xi}\right)^2}\right]\right\}^{1/2} \qquad (2.73)$$

where L is the fibre length, κ_c is the fibre thermal conductivity, ξ is the fibre thermal diffusivity, w is the mode field radius, c is the velocity of light in a vacuum, n is the effective refractive index of the fibre and r_2 is the radius of the cladding. For our calculations we use T =300K, κ=1.37W.(m.K)$^{-1}$, ξ=0.82×10^{-6}m^{2}s^{-1}, w=2.3μm, n=1.465, λ=1550nm, $\left.\frac{1}{n}\frac{\partial n}{\partial T}\right|_{\rho}$=0.68×10^{-5} K^{-1} and α=10.2×10^{-7} K^{-1} where we have taken the values of the thermal conductivity and diffusivity and the thermo-optic coefficients from [2.53]. The phase noise is plotted in fig. 2.15 for fibre lengths of 1m, 10m and 100m in a Mach-Zehnder interferometer and for fibre cladding radii, r_2, of 67.5 μm and ∞.

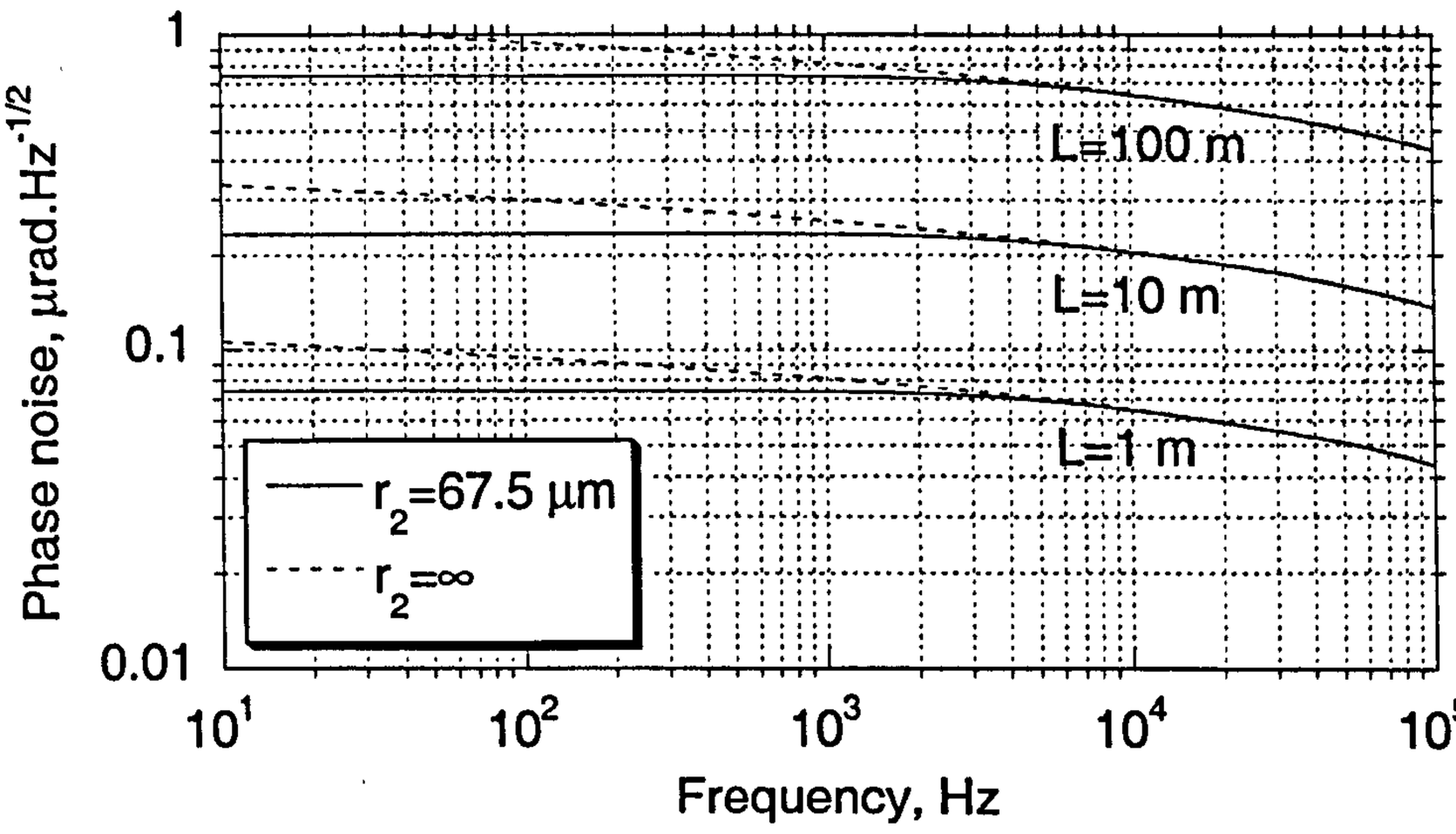

Figure 2.15: Waveguide thermal noise induced phase noise in a Mach-Zehnder interferometer

Thus, we can calculate the received optical power for which the shot noise equals the thermal noise, $P_{sh=th}$ using (2.70) and (2.71). We choose an appropriate frequency of 1 kHz and take Δf =1 Hz, V =1. The thermal noise limited optical power for a range of interferometer fibre lengths is shown in table 2.2.

Table 2.2: Thermal noise limited optical power

Fibre length	$\delta\phi_{th}$	$P_{sh=th}$
	μrad.Hz$^{-1/2}$	μW
1m	0.074	120
10m	0.23	12
100m	0.73	1.2

For a fibre length of 100m, increasing the optical power above 1.2 μW will not generate an increase in the CNR, whereas reducing the fibre length to 1m increases this power limit to 117 μW. We note that partial suppression of this effect is possible with some interferometer configurations using Faraday rotation mirrors [2.51].

Oscillator noise: In the heterodyne system, the acousto-optic modulators (AOM) must be driven by an RF signal, typically a few tens of MHz. This signal must be derived from a stable oscillator to ensure excess noise is not imposed by the AOM. For example, the RF oscillators must be chosen such that their relative noise power spectral density is less than -120 dB.Hz$^{-1/2}$ about the oscillator frequency if μrad.Hz$^{-1/2}$ resolution is required.

Laser intensity noise: Intensity noise from the laser induces amplitude modulation of the optical signal, causing the RIN spectrum to appear as modulation sidebands around the carrier. If the spectrum of the intensity fluctuation is given by $\delta P(\omega)$ then the photocurrent becomes,

$$i_{ph} = r(P+\delta P)+rV(P+\delta P)\cos(\Delta\omega t) \tag{2.74}$$

where $\Delta\omega$ is the heterodyne frequency. Assuming the power fluctuation to have a flat spectral density, such that $\delta P(\omega)=\Delta P\cos(\omega t)$, then (2.74) can be expressed as,

$$i_{ph} = r\left[P+\Delta P\cos(\omega t)\right]+rV\left[P+\Delta P\cos(\omega t)\right]\cos(\Delta\omega t) \tag{2.75}$$

thus,

$$\begin{aligned} i_{ph} = {} & rP+rP\frac{\Delta P}{P}\cos(\omega t)+rVP\cos(\Delta\omega t)+..... \\ & rV\frac{\Delta P}{2}\left(\cos((\Delta\omega-\omega)t)+\cos((\Delta\omega+\omega)t)\right) \end{aligned} \tag{2.76}$$

For the case when the bandwidth of the RIN is much less than $\Delta\omega$ then the RIN induced phase noise is due to the component mixed onto the carrier (i.e. the fourth term in (2.76)) thus using (2.69), the phase noise spectral density contribution due to RIN can be expressed as,

$$\delta\phi'_{laser-RIN} = \sqrt{RIN(f)} \tag{2.77}$$

When the bandwidth of the RIN exceeds $\Delta\omega$, the RIN induced phase noise must include the additional baseband component (second term in (2.76)) thus,

$$\delta\phi''_{laser-RIN} \approx \frac{2}{V}\sqrt{RIN(f)} \tag{2.78}$$

Here we have used the definition of RIN given by (7.7).

Laser frequency noise: Laser frequency noise will generate phase noise in an unbalanced interferometer and a detailed discussion of the origins of this noise source can be found in chapter 7. It is possible to suppress laser frequency induced phase noise using a reference

interferometer, as demonstrated in [2.54,2.55]. The technique involves measuring the phase noise with a reference interferometer and subtracting this signal from the sensor interferometer and has been shown to suppress the laser phase noise by up to 30 dB at 50 Hz [2.55].

2.9.4 Dynamic range

The dynamic range specifies the difference in maximum and minimum signal amplitude that can be measured by the hydrophone. By assuming an ideal demodulator (i.e. one that will not impose any limitation to the dynamic range or add any excess noise to the signal), the dynamic range can be deduced by consideration of the maximum bandwidth available for the phase modulated signal to occupy. Carson's rule [2.56] states that for sinusoidal angular modulation, the bandwidth occupied by the modulation signal is equal to twice the sum of the peak frequency deviation, f_{pk}, and the signal frequency, f_s,

$$\Delta B = 2(f_{pk} + f_s) \tag{2.79}$$

Since $\phi(t) = \phi_o \sin(2\pi f_s t)$ and $\omega_{pk} = \left|\frac{d\phi(t)}{dt}\right|$ then $\left|f_{pk}\right| = \phi_o f_s$ and,

$$\Delta B = 2f_s(\phi_o + 1) \tag{2.80}$$

Thus, for a given signal frequency, the maximum modulation depth (and hence signal amplitude) can be determined from knowledge of the available bandwidth. This is then combined with the interferometric phase resolution to determine the dynamic range. It therefore remains to determine the available bandwidth for each interrogation scheme. In the heterodyne scheme, the available bandwidth is simply $2 \cdot \Delta\omega / 2\pi$ (i.e. twice the carrier frequency). In the PGC scheme, the available bandwidth is given by $\omega_{pgc} / 2\pi$, as illustrated in the inset of fig. 2.13. By comparing (2.63) and (2.67) it is apparent that the PGC signal occupies more bandwidth than the heterodyne signal. Hence, the PGC scheme requires more bandwidth than the heterodyne scheme to achieve a given dynamic range. We determine, in sec. 2.10.3, the dynamic range one would expect from a multiplexed sensor.

2.10 Interferometric Sensor Multiplexing

During the 1980's, a large number of multiplexing schemes for interferometric sensors were proposed; reviews of which can be found in [2.57,2.58]. Here we present some of the basic multiplexing schemes that have found application in practical systems. The first technique to be discussed is known as frequency domain multiplexing (FDM) with homodyne phase generated carrier (PGC) (note the terminology that in frequency division multiplexing, the frequency spacing between adjacent sensor signals is typically a few 10's of kHz and is implemented by direct source modulation, whereas in wavelength division multiplexing, adjacent signal spacing is of the order of a few THz and the signals usually originate from different laser sources). Attention will then be focused on time division multiplexed (TDM) architectures followed by a discussion of recent work on large scale multiplexing architectures.

2.10.1 The frequency domain multiplexing technique

This technique uses frequency multiplexing of carrier frequencies and in practice has demonstrated the potential to multiplex up to sixty-four sensors onto sixteen fibres using eight semiconductor laser diode (LD) sources. This approach was implemented with the homodyne PGC interrogation scheme in a matrix type architecture [2.59]. The array is interrogated by a series of LDs, each modulated at a different frequency. The square matrix is composed of n×n sensors, n photodetectors and n sources, as shown in fig. 2.16(a) for the case of a 2×2 matrix. Each source interrogates n sensors and the outputs from the sensors are combined so that the received signal produces n carrier frequencies on the photodiode, each corresponding to a single sensor. This scheme has been shown to achieve laser phase noise limited detection sensitivity and sensor to sensor crosstalk of less than -60 dB and has the advantage of interrogating all the sensors continuously. However, the large number of telemetry fibres required renders this technique less appealing than the TDM methods described below, for many applications.

2.10.2 Time division multiplexed architectures

The time division multiplexing scheme has been demonstrated to multiplex many sensors onto a single fibre and achieve most of the requirements described above [2.60,2.61]. Schemes using either heterodyne or phase generated carrier interrogation have been demonstrated to multiplex up to sixty-four hydrophones on two fibres [2.62,2.63]. Two architectures based on this scheme are now discussed.

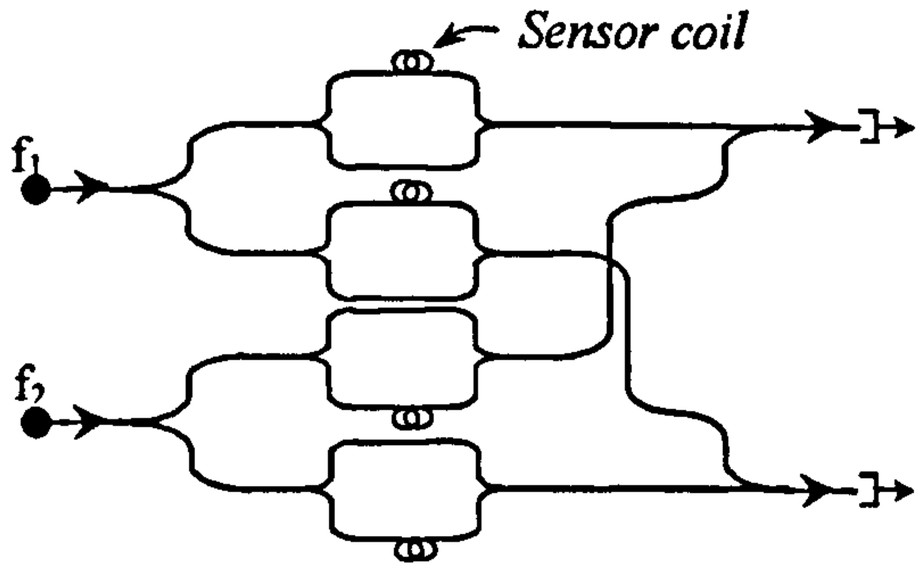

(a) PGC FDM n×n matrix [2.59]

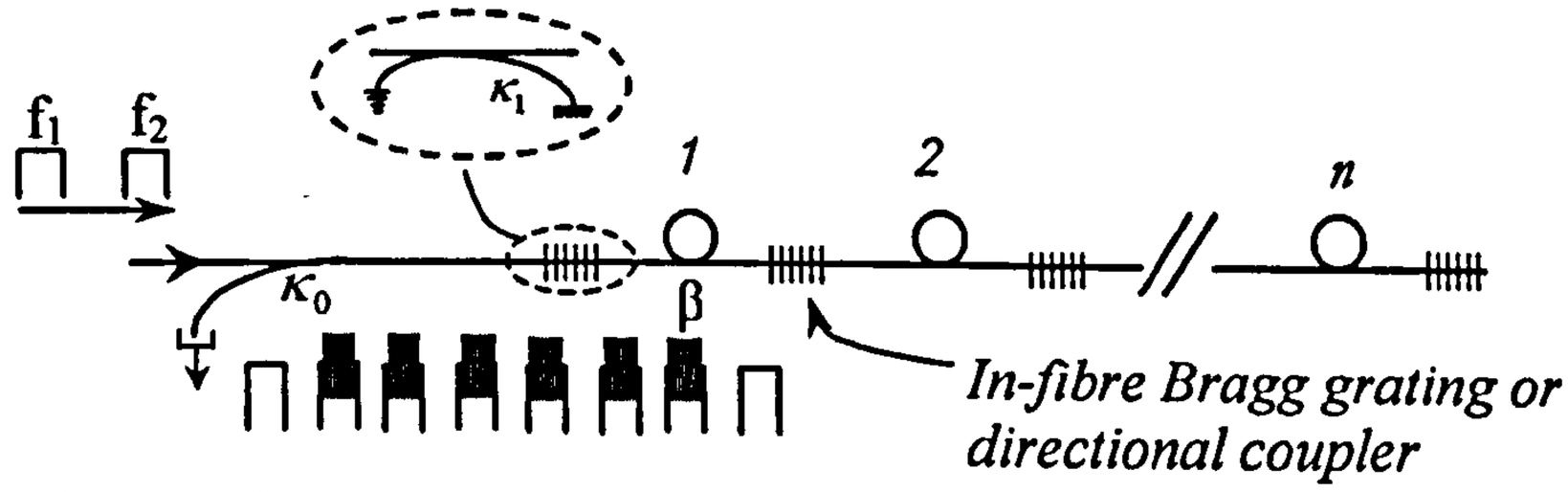

(b) TDM reflectometric [2.61]

Figure 2.16: Multiplexing architectures

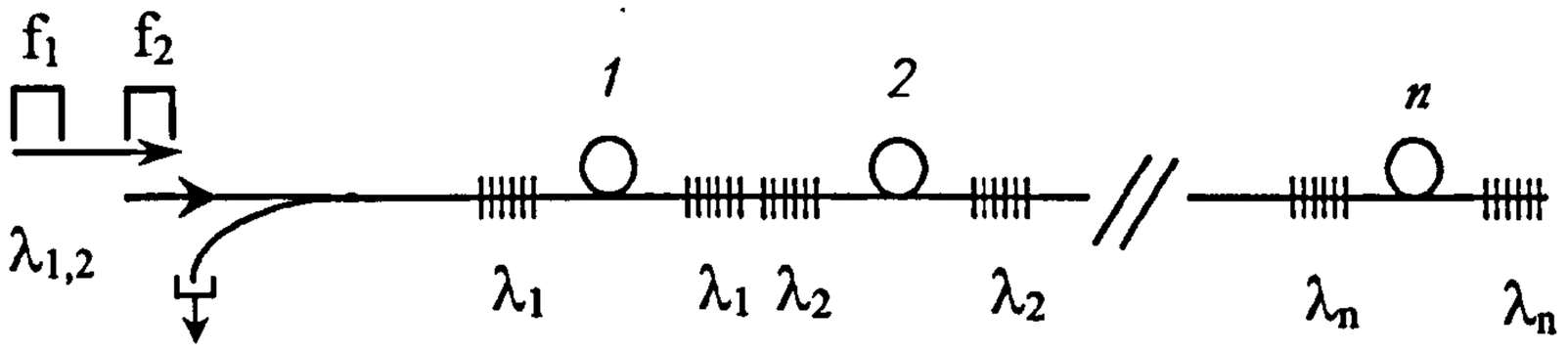

(c) TDM/WDM reflectometric [2.63]

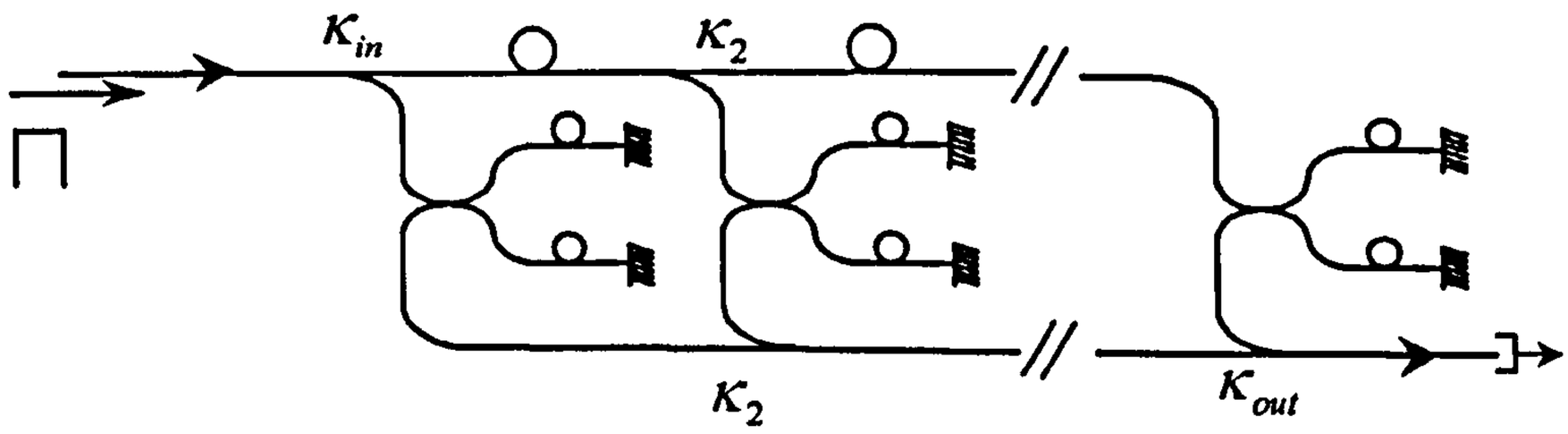

(d) TDM progressive ladder, Michelson

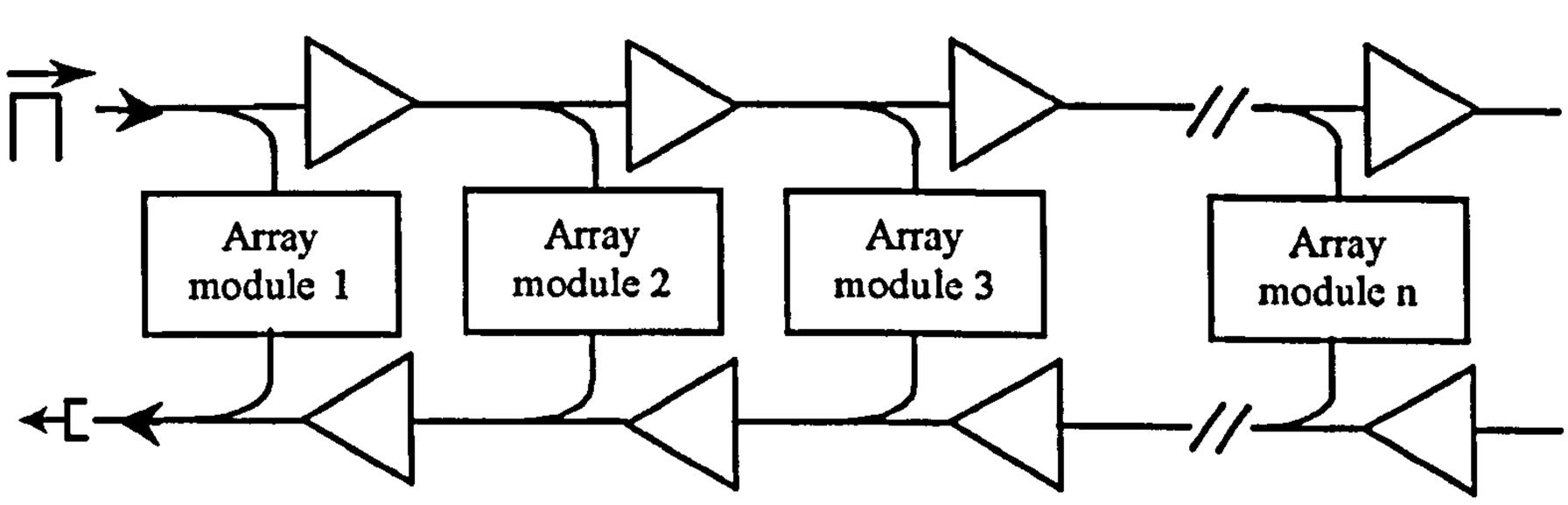

(e) TDM ladder architecture with EDFA telemetry [2.64]

Figure 2.16(cont) :Multiplexing architectures

The pulsed reflectometric architecture (PRA): This architecture, shown in fig. 2.16(b), consists of serially multiplexed Fabry-Pérot interferometers, with low reflectance mirrors (i.e. low Finesse) that can be interrogated by two frequency shifted pulses separated in time by an amount equal to twice the transit time in the interferometer arm, 2τ. The received signal

consists of a series of pulses generated from reflections of the first interrogating pulse overlapped in time but delayed by 2τ with the pulse train generated from the reflections of the second interrogating pulse. Where overlapping of pulses occurs, an interference signal or heterodyne signal is generated. Each sensor, therefore, generates its own heterodyne signal upon which the modulating signal of interest will appear [2.61]. Early development of this architecture used semi-reflecting splices to produce the reflections; however, multi-path interference induced severe crosstalk that limited the number of sensors that can be multiplexed onto a fibre [2.62]. To overcome this problem, an asymmetric reflector was developed using a directional coupler that has a reflective mirror formed on one of the output ports. By index-matching the unused input port, the device will produce a reflection only in one direction as shown in the inset of fig. 2.16(b). In this configuration, the architecture is known as an in-line Michelson. To improve further the optical power budget of this type of network, the power coupling coefficients of the couplers are designed such that equal power is returned from each sensor at the photodiode.

If the individual losses (coupler excess loss, two splices, fibre attenuation) are lumped into a single element, β, the mirror loss is α, the total number of sensors is N and κ_0 is the coupling coefficient of the telemetry coupler (usually 50%), then the power returned from the first mirror for a single injected pulse of power, P_{inc}, is,

$$P_1 = \kappa_0^2 \kappa_1^2 \alpha^2 P_{inc} \tag{2.81}$$

where κ_j is the coupling coefficient of mirror j. Thus, the power returned from the j^{th} mirror is,

$$P_j = \kappa_0^2 \alpha^2 \prod_{i=1}^{j-1} (1-\kappa_i)^2 \beta^2 P_{inc} \tag{2.82}$$

From the condition that $P_j = P_{j+1}$,

$$\kappa_j = \frac{\beta \kappa_{j+1}}{(1+\beta \kappa_{j+1})} \tag{2.83}$$

and a closed-form expression for κ_j can be determined using the condition, $\kappa_{N+1}=1$,

$$\kappa_j = \frac{1-\beta}{\beta^{j-N-1}-\beta} \tag{2.84}$$

For a loss-less system (β =1), (2.84) simplifies to,

$$\kappa_j = \frac{1}{N-j+2} \tag{2.85}$$

The insertion loss of the network is defined as the ratio of the peak pulse power returned from any sensor, P_n, to the injected peak pulse power, P_{inc}, and assuming κ_0 =0.5 is,

$$IL_{PRA} = \frac{P_n}{P_{inc}} = \frac{1}{4(N+1)^2} \tag{2.86}$$

This architecture is shown in chapter 5 to achieve average sensor-sensor crosstalk levels of less than -47 dB, limited by the finite extinction ratio of the drive signal for the acousto-optic modulator (AOM) generating the optical pulses.

A variant of this architecture using in-fibre Bragg gratings (IFBG) as reflective elements and including wavelength division multiplexing (WDM) to overcome the crosstalk problem described above, has also been demonstrated. An array consisting of four serially multiplexed sensor coils each with a pair of IFBG reflectors where every other sensor operates at the same wavelength was demonstrated, as shown in figure 2.16(c). By incorporating a wavelength filter at the array output, crosstalk between sensors operating at the same wavelength was shown to be less than –30 dB and between sensors operating at different wavelengths was less than -60dB [2.63].

The progressive ladder architecture (PLA): This architecture, shown in fig. 2.16(d) incorporating Michelson interferometers, comprises separate fibres for the launch and return pulses. Each sensor forms an individual Michelson interferometer with a small path imbalance that allows interrogation with the homodyne-PGC technique. The inclusion of reference coils for each interferometer confines the sensitive region of the sensor to within the interferometer

(i.e. the leads connecting the sensors are not part of the interferometer arms). Another advantage of the PLA is that the couplers that occupy a symmetric location with the network have the same coupling coefficient. Closed form expressions for the coupling coefficients for a loss-less network have been derived in [2.109] and we quote the results here. The coupling coefficient for the input and output couplers is given by,

$$K_{in} = K_{out} = \frac{K^2}{K^2 - K + 1} \tag{2.87}$$

and the optimum value of coupling coefficient for the couplers positioned symmetrically within the network ($i = 2,3..N-1$) is given by,

$$K_i = \frac{1}{3} - \frac{0.84(N+3)}{A(N-3)^{1/2}} + \frac{0.26A}{(N-3)^{1/2}} \tag{2.88}$$

$$A = \left[39(N-3)^{1/2} - 7N(N-3)^{1/2} + 3^{3/2}\left(3N^3 - 15N^2 + 149N - 137\right)^{1/2}\right]^{1/3} \tag{2.89}$$

For a loss-less networks, optimum coupling coefficients are $K_{in} = K_{out} = 0.5$ and $K_i = 0.2$. Closed form expressions for the lossy network are not trivial to derive and a numerical analysis is presented in [2.109]. This showed that assuming typical losses, the required coupling coefficients deviate only slightly from that predicted by (2.88). It can also be shown that the insertion loss, assuming a loss-less network is well approximated by,

$$IL_{PLA} \approx \frac{1}{N^2} \tag{2.90}$$

Thus, the power returned for a sensor in the PLT is a factor of ~4 higher than in the PRA. Characterisation of sensor-sensor crosstalk in this network has not been published; however, a similar architecture has been shown to achieve a sensor-sensor crosstalk of less than -50 dB [2.64,2.65].

For both of the architectures described above, the number of sensors that can be multiplexed onto a fibre is limited by the required interrogation rate for each sensor (determined by the

dynamic range requirements discussed below) and the optical power. For example, the maximum interrogation rate, f_{rep}, can be deduced from the transit time of the optical pulse through the array, which in the case of the PRA is $1/2\tau(N+1)$ Hz. Assuming the pulse width is set to 2τ, the optical duty cycle, D, is $1/(N+1)$.

Since full size arrays may contain over a thousand sensors, efficient methods of combining more sensors onto one fibre have been investigated. A technique based on incorporating Er^{3+} doped fibre amplifiers in the rungs of a ladder architecture to overcome the power splitting losses has been investigated by two groups [2.66-2.69] and an example of such an architecture is shown in fig. 2.16(e). An experimental system has been set-up with a ten rung ladder and twenty Er:Yb doped fibre amplifiers. By considering the effective noise figure of such an array compared to that of a standard ladder architecture, a system capable of driving up to 300 sensors whilst maintaining an interferometric phase resolution of around 5 $\mu rad.Hz^{-1/2}$ was demonstrated [2.69].

2.10.3 Dynamic range in multiplexed systems

The dynamic range of a sensor in the TDM architecture can be deduced by considering the frequency spectrum of a single heterodyne pulse and determining the available bandwidth. We consider the case for $f_{rep} \gg f_c$. The frequency spectrum in this case is shown in fig. 2.17. To maximise the available bandwidth, the condition $f_c = f_{rep}/4$ should be met so that the spacing of adjacent carrier components is maximised. In this case $\Delta B = 2f_c$ where $f_c = \Delta\omega/2\pi$. Using the example given above and taking the length of fibre in a hydrophone, L_s =100m and using the relation $\tau = nL_s/c$, gives f_{rep} =111 kHz. Thus, f_c =28kHz, ΔB =56kHz and using (2.80) gives ϕ_o =19 rads (rms). Taking the phase resolution as 10 $\mu rad.Hz^{-1/2}$, the dynamic range is 126 dB re $Hz^{-1/2}$. In a hydrophone array this dynamic range would be reduced slightly due to the increase in noise from ambient acoustic noise in the ocean and a more detailed analysis of these systems can be found in chapter 5.

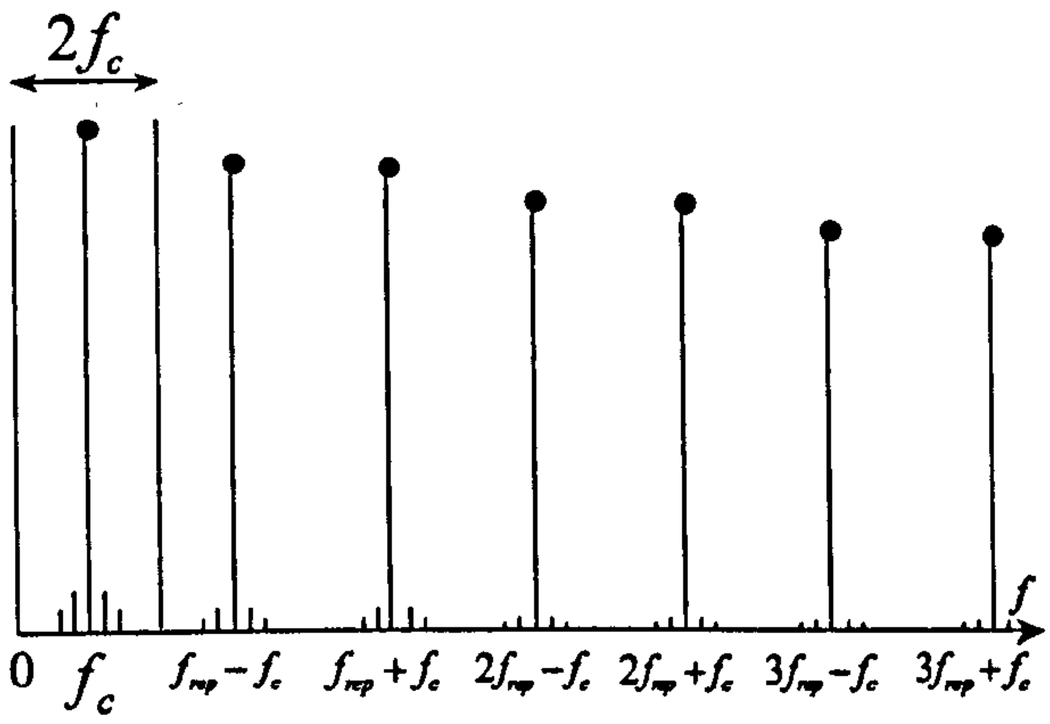

Figure 2.17: Spectral content of heterodyne pulse for case when $f_{rep} \gg f_c$ (DC term removed)

2.10.4 The digital demodulator

Early hydrophone systems used demodulators based on the analogue differentiate and cross multiply technique for the homodyne PGC scheme and frequency discriminators or phase-locked loops for the heterodyne scheme. In these cases, the dynamic range of the sensor was often limited by the dynamic range of the analogue components used in these demodulators rather than due to bandwidth limitations. Recent advances in digital data capture and signal processing has led to the development of the digital demodulator. This involves sampling of the photodiode signal and extraction of the phase signal of interest by applying one of the techniques described above in a processing algorithm. The digital demodulator provides two major advantages over the analogue demodulator: (i) by setting the sampling rate sufficiently high (usually twice the maximum frequency component of the photocurrent signal in order to satisfy Nyquist's sampling theorem), the modulated signal can be captured without experiencing any distortion. Thus, in-principle the bandwidth limited dynamic range described above can be obtained; and (ii) taking a discrete sample during each pulse in a TDM signal returned from a multiplexed sensor array allows simultaneous demodulation of many sensor signals using a single analogue to digital converter. This greatly reduces the cost and complexity of the demodulation electronics for large multiplexed systems.

The digital demodulator also provides considerable flexibility during the process of extracting the phase modulating signal. The lowest signal frequency of operation of the demodulator is specified in the algorithm, which makes possible phase tracking to DC. Once digitised, the signal can be extracted numerically using an algorithm based on the differentiate and cross

multiply or arctangent technique. It is also straightforward to implement a fringe counter allowing unambiguous measurement of phase greater than 2π.

2.11 Techniques to Eliminate Polarisation Induced Signal Fading

When two coherent beams from an interferometer interfere, the fringe visibility, V, is dependent on the relative states of polarisation (SOP) of the two beams. Maximum visibility occurs when the SOPs are aligned and no interference occurs when the SOPs are orthogonal. It is well known that standard telecom grade optical fibre exhibits a small birefringence that causes the SOP of the propagating beams to change randomly as it travels along the waveguide. Also, external effects such as asymmetric stresses (due to changes in pressure or temperature) or twist will affect the birefringence of the fibre [2.70]. These environmental factors result in an effect known as polarisation induced signal fading in interferometric sensors, where the carrier-to-noise ratio (CNR) varies with time due to a time varying fringe visibility. In some circumstances, a finite degradation in the CNR can be tolerated; however, some form of polarisation control scheme is needed to avoid complete extinction of the interference signal. An elegant method to achieve maximum fringe visibility from Michelson interferometers or a reflectometric array uses a type of ortho-conjugate mirror known as an orthogonal mirror [2.71]. This device makes use of the Faraday effect to produce a reflected beam that has a SOP orthogonal to that of the incident beam. If used in place of the standard mirrors in a Michelson interferometer, the light received from each arm will always be in a polarisation state orthogonal to that of the launched light, regardless of the birefringence properties of the fibre interferometer. The non-reciprocity of the fibre birefringence for counter-propagating beams effectively untwists the effect on the SOP of the birefringence on the journey to the mirror during its return journey. These devices have been used in interferometric sensors and have shown that maximum visibility can be maintained from multiplexed sensors [2.72]. However, although these devices are electrically passive, their high cost usually precludes their use in large arrays of sensors. The use of high birefringence fibre throughout the array has also been attempted, but imperfections in the components results in some residual fading. Also component costs and array construction complexity tends to render this approach unviable.

The polarisation and birefringence properties of fibre interferometers have been studied extensively and several schemes have been proposed that rely on either control of the input light SOP or SOP selection of the received light. These are now described.

Techniques based on input light polarisation control: Analysis of the polarisation properties of fibre interferometers revealed that the fringe visibility was dependent on both the input SOP of the light to the interferometer and the birefringence properties of the two fibre arms. It was shown that there exist unique SOPs or eigenmodes of the net birefringence vector for which optimum visibility was obtained and this formed the basis of a technique that used active feedback to maintain optimum visibility [2.73]. Another technique that used pseudo-depolarisation of the input light to the interferometer to overcome fading due to birefringence effects of the input lead has also been demonstrated [2.74]. These techniques cannot fully overcome polarisation induced signal fading for multiplexed arrays. However, more recently a technique based on switching of the polarisation state of the input light into an array of sensors has been demonstrated [2.75]. The principle is shown in fig. 2.18 for a reflectometric array. An electro-optic polarisation modulator is placed between the laser source and AOM that allows the linear SOP of the laser output to be rotated by 90^0 and the SOP of the second pulse in alternate pulse pairs to be rotated by 90^0 relative to the others. When the fringe visibility from one set of pulses falls to zero, the fringe visibility of the second set of interrogating pulses will be approaching maximum. A selection circuit is then employed to choose the interference signal with the larger visibility. Successful operation of this technique relies on the fact that orthogonally polarised light launched into a fibre will remain orthogonal in polarisation regardless of the birefringence properties of the fibre assuming that there is no polarisation dependent loss [2.76].

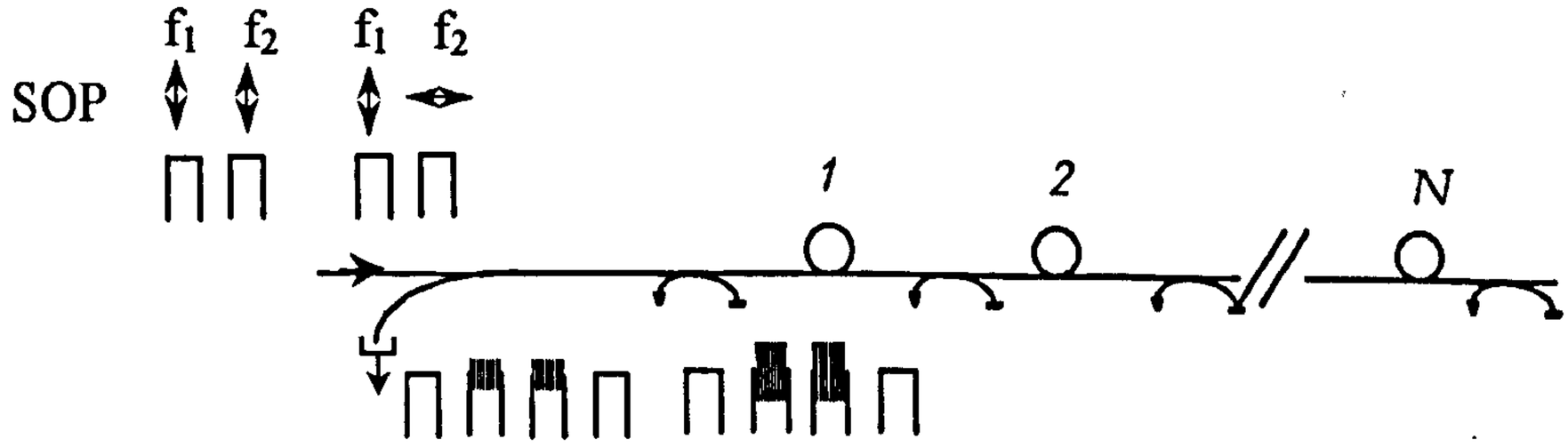

Figure 2.18: Polarisation switching technique with the PRA architecture after [2.75]

Techniques based on received light SOP selection: If the SOP of the two beams from the arms of an interferometer become orthogonal, then direct detection will produce no interference. However, by passing the light through a linear polariser, prior to detection, that is

orientated such that there exists a projection of both polarisation states onto the axis of the polariser, the transmitted light will produce an interference signal since both SOPs are now aligned with the polariser axis. This breaking of the orthogonality between the SOP of the light beams forms the basis of a technique known as polarisation diversity detection and has been demonstrated using a mask formed from three linear polarisers with their axes aligned 60^0 to each other. The light from the interferometer output fibre is expanded and passed through the mask and the output of each polariser is detected separately. It was shown that for all input SOPs there exists an output that exhibits a finite fringe visibility. For slow variations in fringe visibility, selection of the signal with the highest fringe visibility allows for continuous operation of the sensor [2.77,2.78].

2.12 Obtaining Optimum Noise Performance and Dynamic Range in Multiplexed Systems

Self-noise in fibre-optic interferometric sensors is usually generated by the laser source or receiving electronics, rather than in the transducer itself. Only a few exceptions exist such as transducers with very long lengths of fibre generating thermal noise or very high responsivity accelerometers where thermal noise in the mass-spring transducer mechanism can be significant [2.32]. In order to achieve low noise performance in a fibre optic sensor system, the same principle must be applied to the system design as for any other multi-element system. That is, every component must be viewed as a potential noise source and therefore every component should be characterised individually. A single poorly performing component could severely degrade the entire system performance, affecting both the sensor resolution and dynamic range. For example, a poorly chosen oscillator used for the acousto-optic modulator drive signal may significantly reduce the phase resolution of every sensor. The reduction in phase resolution is also accompanied with an equal reduction in dynamic range. In fibre-optic hydrophone arrays that operate in relatively benign environments (such as sea-bed arrays), laboratory demonstrated performance can generally be achieved in field-test systems. However, the performance of systems operating in more extreme environments is more difficult to characterise without rigorous field-testing. High vibration environments may induce both excess frequency noise in the laser and excess phase noise in the path balance optics. Systems with long stand-off fibre links may also be susceptible to polarisation induced phase noise caused by birefringence modulation in the link fibre being converted to phase-shift in the interferometer [2.79]. For

systems of these types, careful attention to aspects such as sensor and fibre packaging become essential in obtaining acceptable performance. Active control of device performance, when exposed to extreme conditions, using feedback techniques may also be required to ensure the required performance is maintained.

Another useful design principle is to reduce stray photons. In systems with optical amplifiers and long fibre links, use of bandpass optical filters and isolators to reduce amplified spontaneous emission (ASE) power residing away from the signal wavelength and backscattered power due to Rayleigh scattering [2.80] safeguards against degrading amplifier performance and removes unwanted noise sources. Unwanted reflections from poor splices and connectors can also generate parasitic optical cavities. Uncontrolled interferometers of this type can be a major source of noise, particularly when high coherence lasers are used, since on detection, the noise fields add coherently [2.81]. This problem can be exacerrbated if the extinction ratio of the launch pulses is not sufficiently high in TDM systems.

Finally, another unexpected noise source can arise from aliasing and cannot generally be removed by spectral filtering. In systems where many carrier frequencies and harmonics are present, such as phase generated carrier [2.82] and multiplexed systems, noise sources that appear as sidebands onto these carriers can generate excess noise at frequencies corresponding to adjacent carrier frequencies. This effect is generally significant if the spectral density of the aliased noise increases with frequency, which is the case for the frequency noise of some lasers [2.83] and intensity noise. Ensuring that the spectral density of all noise sources is either constant or falls with frequency reduces the impact of aliased noise.

2.13 The Erbium Doped Fibre Amplifier

The erbium doped fibre amplifier (EDFA) has become an important component of large-scale hydrophone arrays and we now discuss the basic properties of the erbium gain medium and the noise properties of the EDFA.

In this section we shall outline the properties of the EDFA relevant to the interferometric sensor application. We shall first discuss the basic properties of the EDFA in terms of the gain, saturation power, emission spectrum and noise figure. We then derive simple expressions for the noise generated on detection due to the presence of amplified spontaneous emission in the

received signal. This is followed by a description of the effects of noise accumulation in concatenated chains of EDFA's. Finally, we describe some practical aspects of amplifier designs. It is intended that the expressions developed here to characterise the amplifier performance shall be used in the modelling of sensor arrays incorporating EDFA's presented in chapters 5 and 6.

The EDFA provides amplification to signals that occupy the spectral region corresponding to the emission spectrum of erbium (approximately 1525 nm to 1560 nm for an Al-Ge-Si host glass and a full inversion). By doping the core of an optical waveguide with Er^{3+}, an amplifier can be realised when a short wavelength pump is injected into the guide, which causes the ground state electrons of the Er^{3+} ion to be raised to an excited state. Injection of a second signal beam at a wavelength corresponding to the emission spectrum of the erbium-glass medium causes stimulated emission at the signal wavelengths and hence amplification of the signal beam. Amplifiers of this type were first demonstrated in [2.84,2.110], which instigated considerable research effort into all aspects of the design of the EDFA. This has generated a wealth of literature which we can draw on to describe the operation of the EDFA [2.85-2.87].

The invention of the EDFA paved the way for the development of high bandwidth, long distance optical communication links with all-optical signal regeneration, operating in the low loss wavelength region in silica fibre. This removed the need for the electro-optic signal converter and regenerators in use in the early 1980's. In parallel with this was the development of reliable, low cost, high power pump lasers. For the interferometric sensor application, incorporation of the EDFA permits significant increases in the array size and fibre link length between the array and interrogation electronics; it can also be used to overcome the passive losses associated with fibre telemetry in multiplexed systems.

The long lifetime (τ_2 ~10 ms) of the excited state of the Er^{3+} ion, corresponding to the 1.5μm transition, (the upper laser state) leads to the relatively broad gain bandwidth of the EDFA, undistorted amplification of high bandwidth (i.e. high modulation rate) optical signals and the potential for multi-wavelength amplification. The ability to achieve near unity inversion with low signal and pump excited state absorption and high erbium concentration without significant erbium-erbium ion interaction has resulted in amplifiers with high gain (> 30dB) and low noise figure (~3 dB). The compatibility of the doped silica fibre with the silica based transmission medium also results in low coupling loss between fibres. The gain of the EDFA

has also been shown to exhibit low dependence on signal polarisation. All of these attributes make the EDFA ideal as an amplifier for high bandwidth, multi-channel signal amplification.

The Er^{3+} ion in a silica host has absorption bands around 520nm, 650nm, 800nm, 980nm and 1500nm, which are around 10-20nm in width [2.87]. Highest efficiency is achieved by pumping at 980nm or 1480nm due to the low excited state absorption (ESA) compared with the other absorption bands (pump ESA can still be present when pumping at 980 nm and is observed by the emission of a green fluorescence). When pumped at 980nm the gain medium is a three level system. A 980 nm photon excites the Er^{3+} ion to a upper level which rapidly decays to the upper laser state, as shown in fig. 2.19(a). A 1480 nm pump photon excites the Er^{3+} ion directly into the lasing state, and hence resembles a two level system. However, it can be modelled as a three level system since the energy band of the upper laser state is significantly broadened, and a relaxation occurs to the lower portion of the upper laser state, as shown in fig. 2.19(b). In the case of 1480nm pumping, it is not possible to achieve unity inversion since the ground state population can never be zero. This has implications for the quantum limit of noise figure when 1480 nm pumping is employed, as described below.

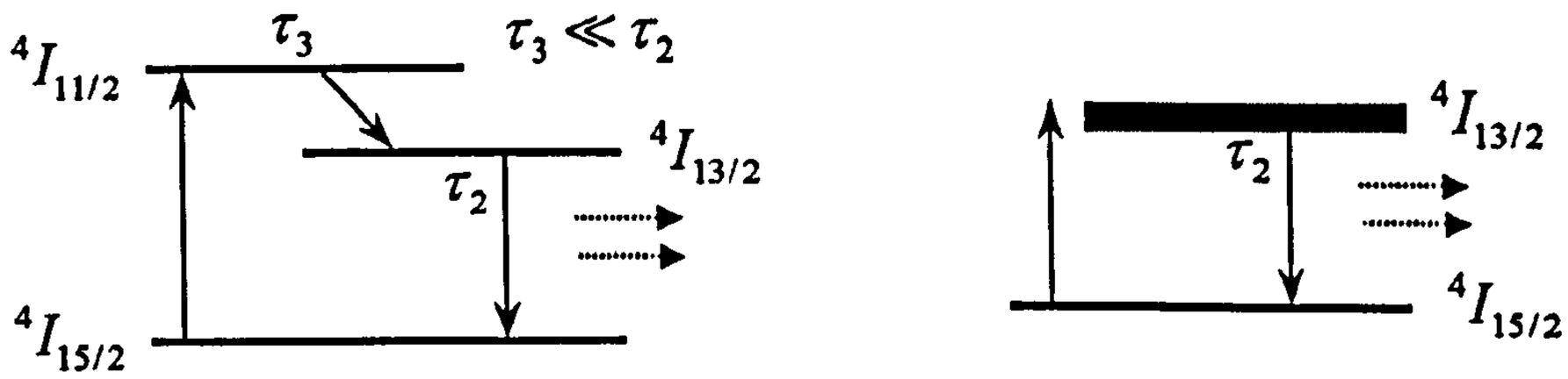

Figure 2.19: (a) 3-level and (b) quasi 2-level laser systems

2.13.2 Amplified spontaneous emission and the noise figure

Stimulated emission in the amplifier is also accompanied by spontaneous emission, due to the spontaneous relaxation of the excited ions from the upper laser state to the ground state, in the absence of a signal photon. In the EDFA this results in a broad fluorescence spectrum, extending from 1525nm to 1560 nm in a Silica host, which propagates with the signal, as illustrated in fig. 2.20.

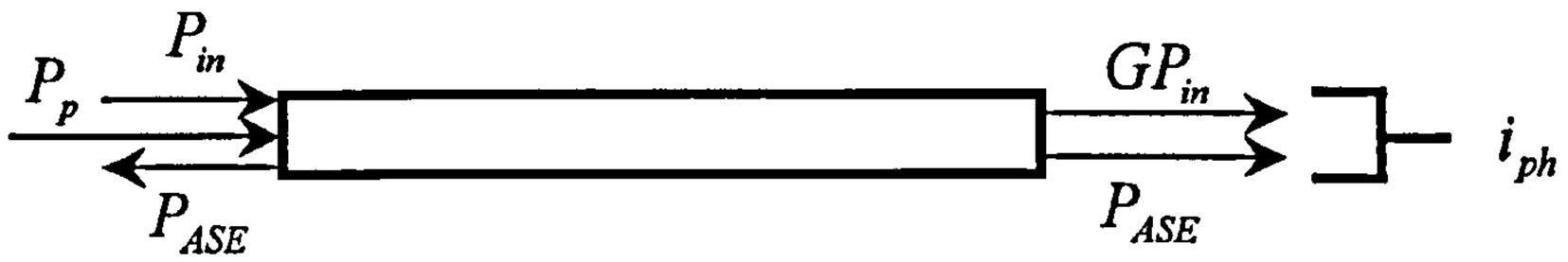

Figure 2.20: Principle of operation of the optical amplifier

For a single transverse mode amplifier with a gain, G, the amplified spontaneous emission power in one polarisation mode per unit bandwidth at the output of the amplifier, assuming the amplifier is unsaturated is [2.87],

$$P_{ASE} = n_{sp}(G-1)h\nu \tag{2.91}$$

where n_{sp} is the inversion parameter, h is Planck's constant, ν is the optical frequency and $\Delta\nu_{opt}$ is the optical bandwidth. Thus we can define the optical signal-to-noise ratio (OSNR) as,

$$OSNR = \frac{GP_{in}}{2P_{ASE}\Delta\nu_{opt}} = \frac{P_{in}}{4n_{sp}h\nu\Delta\nu_{opt}} \tag{2.92}$$

where P_{in} is the input power to the amplifier and we have assumed that $(G-1) \sim G$. The factor of two accounts for the presence of two polarisation modes in the EDFA. When the output of the EDFA is detected by a photodiode, the photocurrent generated is given by the square of the total optical field where,

$$E_{tot} = E_{sig} + E_{ASE} \tag{2.93}$$

Thus, from (2.36) the photodiode current is,

$$i_{pd} = r\left(E_{sig}^2 + E_{ASE}^2 + 2E_{sig}E_{ASE}\right) \tag{2.94}$$

where the first term is pure signal, the second term is pure ASE noise (referred to as spontaneous-spontaneous beat noise) and the third term results from the beating of the signal with the ASE (referred to as signal-spontaneous beat noise). r is the photodiode responsivity. The ASE signal also generates its own shot noise. The noise currents for each noise source are given by [2.88],

$$\overline{i_{s-sp}^2} = 4r^2 G P_{in} P_{ASE} \Delta f \tag{2.95}$$

$$\overline{i_{sp-sp}^2} = 4r^2 P_{ASE}^2 \Delta \nu_{opt} \Delta f \tag{2.96}$$

$$\overline{i_{sp-sh}^2} = 4re P_{ASE} \Delta \nu_{opt} \Delta f \tag{2.97}$$

$$\overline{i_{s-sh}^2} = 2e^2 \eta G P_{in} \Delta f / h\nu \tag{2.98}$$

where $\overline{i_{s-sp}^2}$ is the signal-spontaneous beat noise (s-sp), $\overline{i_{sp-sp}^2}$ is the spontaneous-spontaneous beat noise (sp-sp), $\overline{i_{sp-sh}^2}$ is the spontaneous-shot beat noise (sp-sh) and $\overline{i_{s-sh}^2}$ is the signal-shot noise. Note that $\overline{i_{s-sp}^2}$ is calculated using the ASE power in the same polarisation mode as the signal. The spectral shape of (2.95) and (2.96) has been investigated in [2.89]. Here it was shown that s-sp noise exhibits a flat spectral density and occupies a single-sided bandwidth between dc and the electrical bandwidth. However, sp-sp noise exhibits a triangular spectral shape with a maximum at dc which falls linearly to zero at a frequency of $\Delta \nu_{opt}$. When $\Delta f \ll \Delta \nu_{opt}$ sp-sp noise can be approximated by a white noise source, with a power density equal to $4r^2 P_{ASE}^2 \Delta \nu_{opt}$.

One can analyse the noise performance of the amplifier by determining the electrical signal-to-noise ratio produced by an ideal detector placed at the input and output of the amplifier; we ignore the detector thermal noise in this calculation. By inspection, it can be seen that $\overline{i_{s-sp}^2} \gg \overline{i_{s-sh}^2}$ and $\overline{i_{sp-sp}^2} \gg \overline{i_{sp-sh}^2}$ and the electrical signal-to-noise ratio (SNR) at the amplifier output is given by,

$$SNR_{out} = \frac{(rGP_{in})^2}{\overline{i_{s-sp}^2} + \overline{i_{sp-sp}^2}} \tag{2.99}$$

Thus, providing the condition $2GP_{in} > P_{ASE} \Delta \nu_{opt}$ is met by reducing $\Delta \nu_{opt}$ with an optical filter, then $\overline{i_{s-sp}^2} \gg \overline{i_{sp-sp}^2}$ such that,

$$SNR_{out} = \frac{P_{in}}{4 n_{sp} h\nu \Delta f} \tag{2.100}$$

and SNR_{out} is limited by s-sp noise only. For the case when the noise of the input signal is limited by shot noise,

$$SNR_{in} = \frac{(rP_{in})^2}{\overline{i_{sh}^2}} = \frac{rP_{in}}{2e\Delta f} \tag{2.101}$$

The noise figure of the amplifier is defined as,

$$F = \frac{SNR_{in}}{SNR_{out}} \tag{2.102}$$

and is calculated assuming an ideal detector with unity quantum efficiency using (2.101) and (2.100) such that,

$$F = 2n_{sp}\frac{(G-1)}{G} \simeq 2n_{sp}\chi \tag{2.103}$$

where we have added χ, an excess noise factor due to splice and component losses. This is the so called 'quantum limit' of the noise figure for a high gain amplifier. For the case when $\chi=1$ and $n_{sp}=1$ then $F=2$ (or 3 dB). It is not a true 'quantum limit' since a noise figure less than 2 can be achieved with a low gain amplifier; however these are generally not used in practice; it does however show that amplification will always be accompanied by the addition of noise in accordance with the Heisenberg Uncertainty principle. We can determine the input power required for a typical EDFA to ensure s-sp limited detection. The noise figure as a function of input power is shown in fig. 2.21, calculated using (2.99), (2.101) and (2.102) and plotted for values of n_{sp} from 1 to 32. Here we have assumed $\lambda=1550$ nm, $\Delta f=1$ Hz, $\Delta\nu_{opt}=100$ GHz, $\chi=1$ and $\eta=1$. In general, it is possible to achieve noise figures of ~2 with 980nm pumping and ~3 with 1480nm pumping.

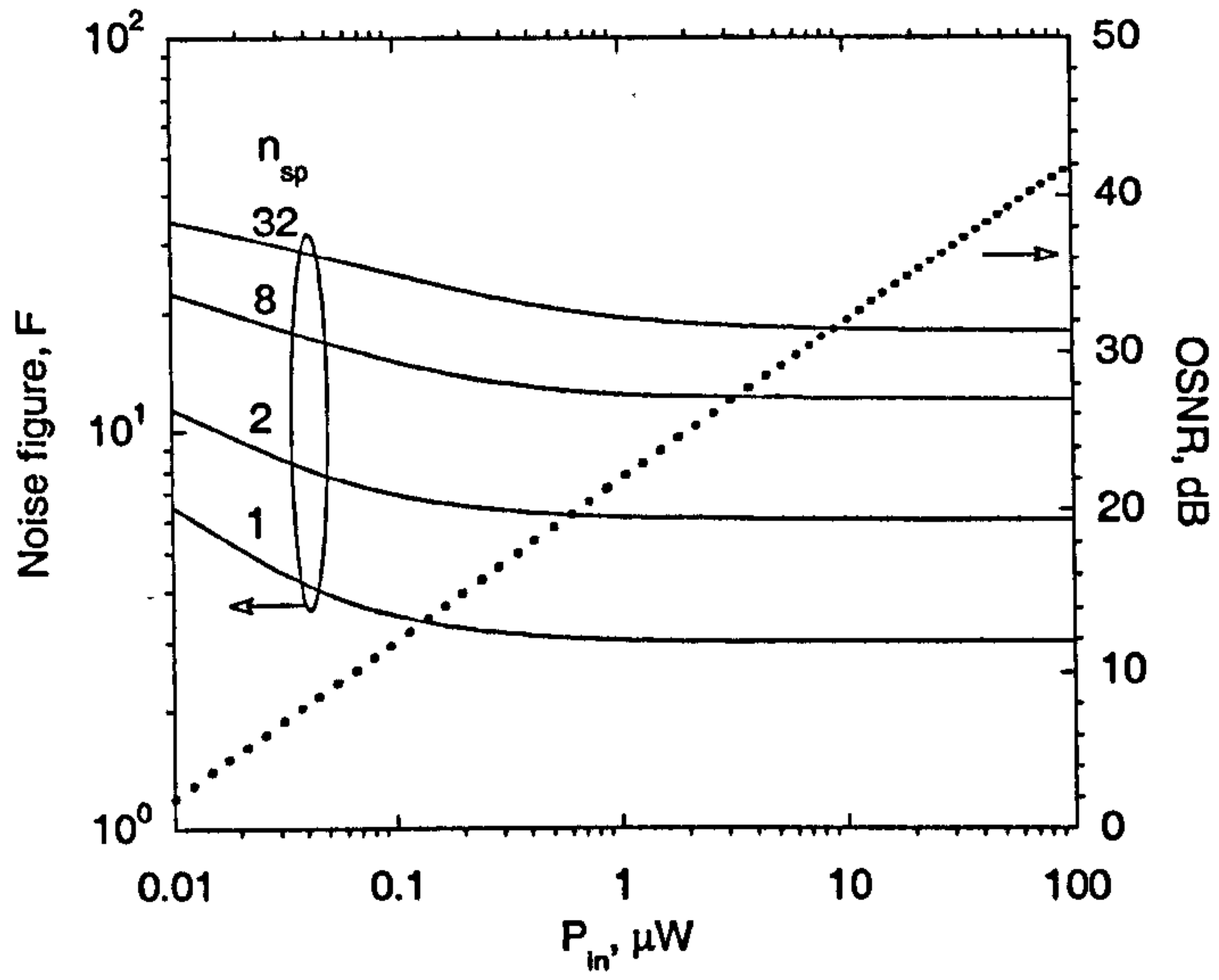

Figure 2.21: Noise figure and OSNR as a function of input power

Thus, the noise figure is 'quantum limited' for P_{in} greater than 0.5μW when n_{sp}~1. In an EDFA, n_{sp} and hence F are wavelength dependent (due to the wavelength dependence of the absorption and emission cross sections). However, if the signal wavelengths are chosen to occupy a flat region of the gain spectrum, then one can ignore this wavelength dependence. In this case, the small signal performance of the EDFA is fully characterised by G and F. We can also determine the OSNR as a function of input power and this also is shown in fig. 2.21, where we have assumed λ=1550 nm, n_{sp}=1 and $\Delta\nu_{opt}$ = 12.5 GHz (1 Å or 0.1 nm), which is a typical measurement bandwidth for optical spectrum measurements. The OSNR is close to unity when P_{in}~10 nW.

2.13.3 Noise in concatenated optical amplifiers

It is necessary in many system configurations to concatenate several amplifiers together, as shown schematically in fig. 2.22. Here G_i, F_i $(i=1,2,3...j)$ are the gain and noise figure of each amplifier and L_i is the amplifier spacing. We can thus define the transmission loss between each amplifier as $T_i = \exp(-\alpha L_i)$ where α is the fibre attenuation.

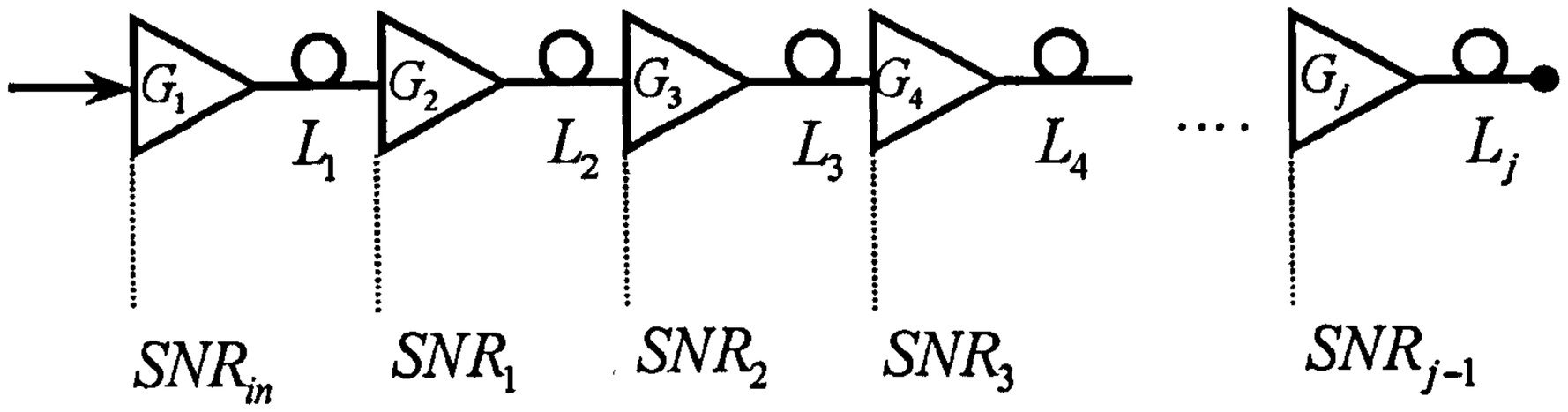

Figure 2.22: Concatenated amplifier chain

The total noise is now dependent on the cumulative ASE noise contributed by each amplifier and can be expressed by a total noise figure. Considering the case of two concatenated amplifiers the total ASE power is given by,

$$G_2 \mathrm{T}_2 P'_{ASE} + P''_{ASE} \tag{2.104}$$

where P'_{ASE}, P''_{ASE} are the ASE power generated by amplifiers 1 and 2 respectively. The SNR at the end of the two amplifier chain is thus,

$$SNR_2 = \frac{(rG_1\mathrm{T}_1G_2\mathrm{T}_2P_{in})^2}{2r^2G_1\mathrm{T}_1G_2\mathrm{T}_2P_{in}[\mathrm{T}_1G_2\mathrm{T}_2F_1(G_1-1)+F_2(G_2-1)]h\nu\Delta f} \tag{2.105}$$

From (2.102),

$$F_{tot} = \frac{SNR_{in}}{SNR_2} \tag{2.106}$$

Thus using (2.101), (2.105) and (2.106),

$$F_{tot} = F_1 + \frac{F_2}{G_1\mathrm{T}_1} \tag{2.107}$$

Extending this analysis to the case of fig. 2.22 yields the general form of (2.106),

$$F_{tot} = F_1 + \frac{F_2}{G_1\mathrm{T}_1} + \frac{F_3}{G_1\mathrm{T}_1G_2\mathrm{T}_2} + \ldots\ldots + \frac{F_j}{\prod_{i=1}^{j-1} G_i\mathrm{T}_i} \tag{2.108}$$

In the limit when $L_i \to 0$, the total noise figure is dominated by the noise figure of the first amplifier, as is the case for concatenated electrical amplifiers. If the transmission loss between amplifiers is set to equal the amplifier gain such that $T_i = (G_i)^{-1}$ and the noise figures of the amplifiers are equal to F, then (2.108) reduces to,

$$F_{tot} = jF \tag{2.109}$$

2.13.4 Power amplifiers

When the EDFA is used as a power booster, for optimum performance it must exhibit high output saturation power and this is generally achieved by optimising the pump to signal photon conversion efficiency. The large signal characteristics of the EDFA have been investigated in [2.90]. A figure of merit for the power amplifier is the quantum conversion efficiency (QCE), which is defined as the increase in the number of signal photons, due to the amplification, divided by the number of launched pump photons. By optimising the design of the waveguide, erbium confinement and erbium concentration, it is possible to achieve broadly similar QCE with either 980nm or 1480nm pumping. However, in a practical amplifier, the amplifier efficiency is usually characterised by the maximum output power as a function of the input pump power. In this case, higher efficiency is achieved with a pump wavelength close to the signal wavelength (i.e. 1480 nm pumping). It follows from the discussion given above that an amplifier with a high gain, high output saturation power and low noise figure is achieved with a two stage amplifier comprising a 980nm pumped section followed by a 1480nm pumped section.

When modulated signals are injected into the EDFA, the long lifetime of the Er^{3+} ion lasing state results in the amplifier gain being independent of the modulation rate when the modulation rate is greater than $\sim 1/\tau_2$ (125 Hz); thus, in general the amplifier responds to the average input power. The performance of the power amplifier is characterised by the large signal gain curve, as shown in figure 2.23. The saturation power can be defined as the input power for which 3 dB gain compression has occurred from the small signal gain level. It is also found that the noise figure increases slightly with high input power and is due mainly to the signal gain saturation with a high input signal power.

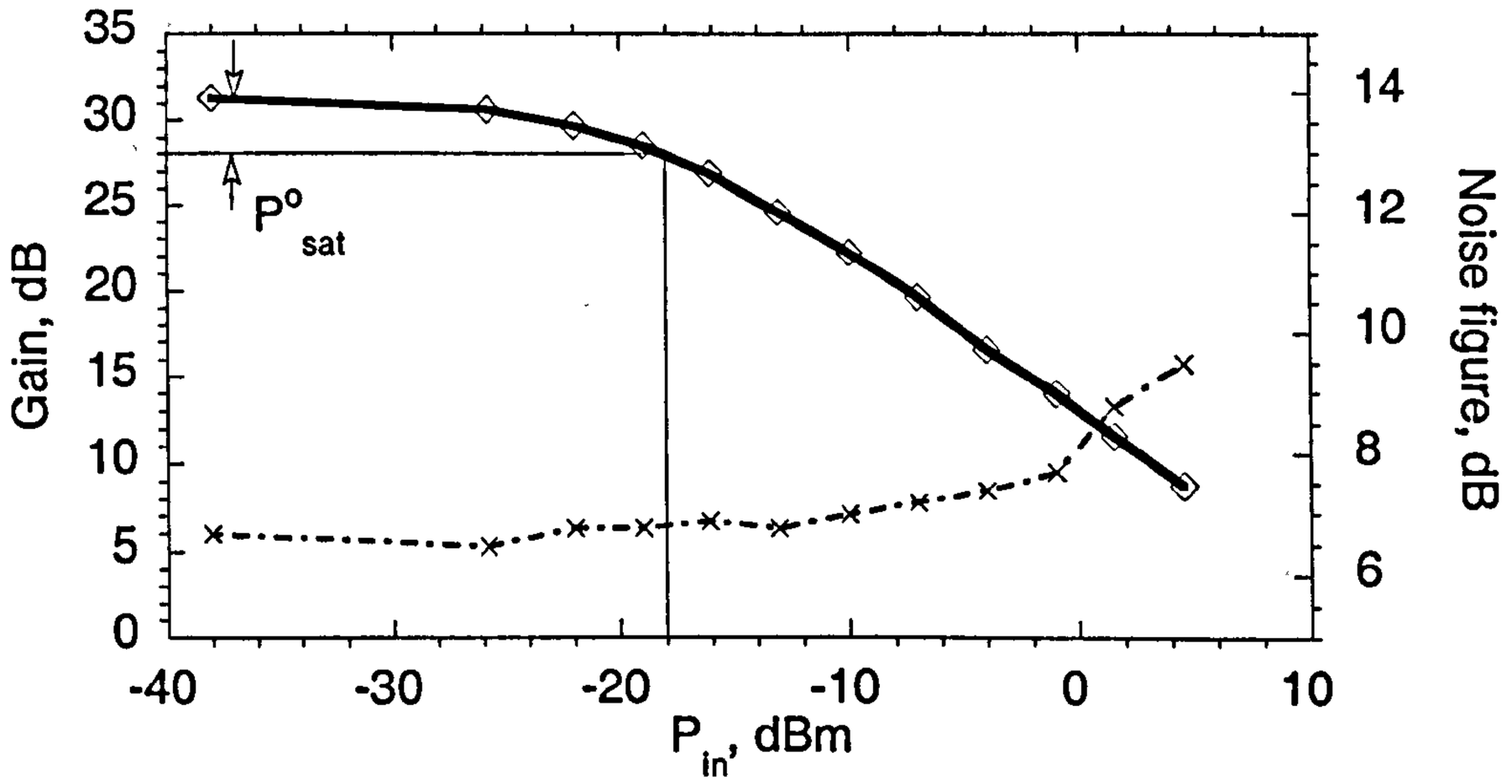

Figure 2.23: Large-signal gain and noise figure curve for the EDFA (MPB Model:EFA-P18)

2.13.5 Multi-channel amplifiers

The large gain bandwidth and long lifetime of the laser state of the Er^{3+} ion also permits low crosstalk multi-channel amplification, which makes it ideal for dense wavelength division multiplexed systems (DWDM). The gain per wavelength is determined by calculating the total input power and using the gain curve figure in fig. 2.23. For systems with multiple amplifiers, the dependence of the gain on wavelength must be considered. In a heavily pumped amplifier (i.e. fully inverted), the gain can be found to increase by up to 10 dB at wavelengths around 1530nm compared to the gain above 1540nm. In order to ensure that constant power per wavelength is maintained, gain equalisation should be used. One technique is to operate the amplifier in saturation such that the inversion towards the end of the doped fibre is reduced. This has the effect of generating absorption in the low wavelength region, and hence flattens the gain. The ASE spectrum as a function of pump power in mW (at 1480nm) is plotted in fig. 2.24, which shows that an approximately flat gain can be achieved with a pump power of around 16-18 mW.

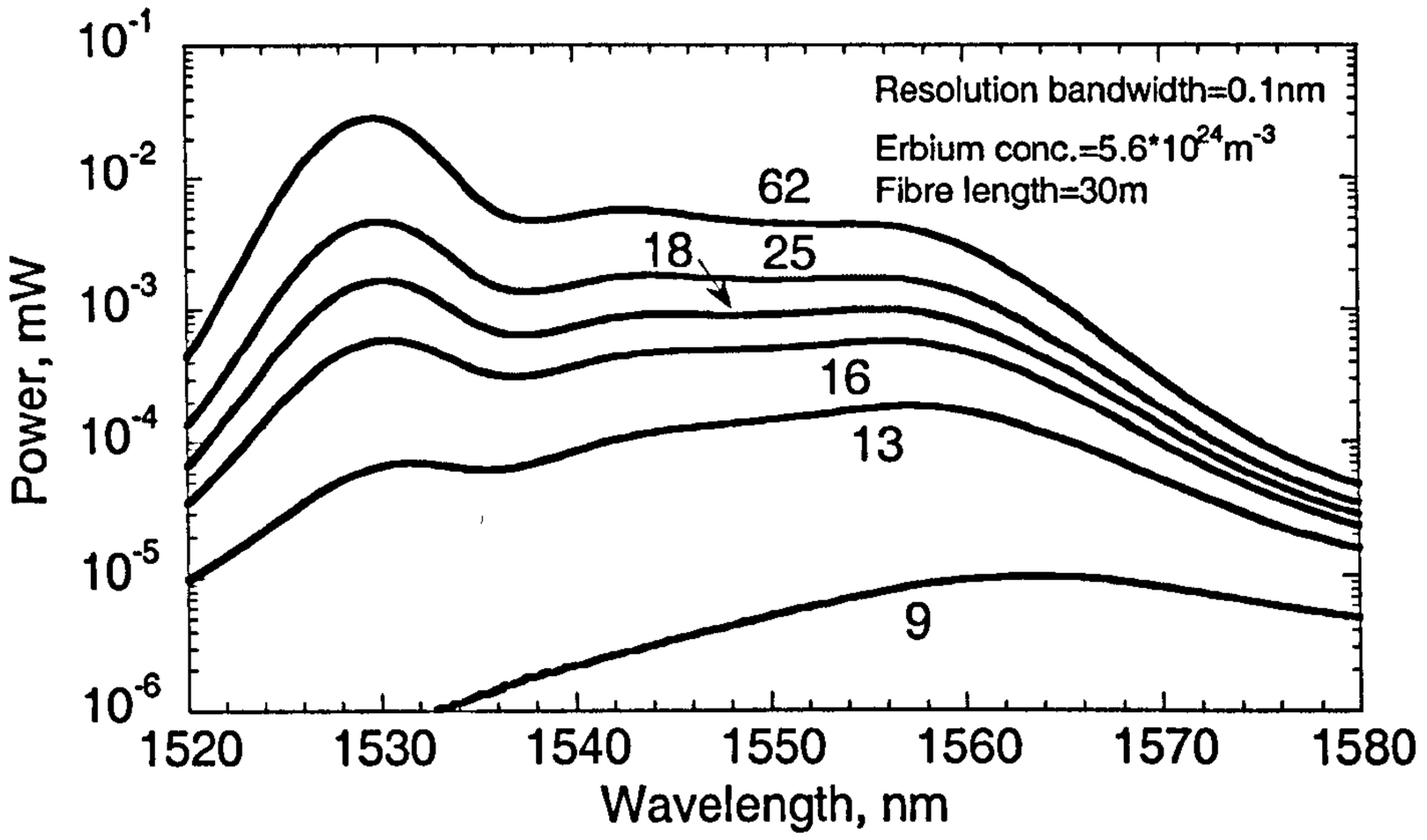

Figure 2.24: ASE power vs. wavelength and pump power

Gain flattening by operating the amplifier in saturation imposes further limitations on the input powers and can complicate system design, particularly when large numbers of amplifiers are involved. Other techniques involve use of a different host glass (such as fluoride or tellurite fibres); broadband gain clamping by reducing the doped fibre to cryogenic temperature such that the amplifying medium is primarily inhomogenously broadened; hybrid EDFA's comprising doped fibres with different host glasses; and by using a passive filter [2.85]. The latter technique is generally the most commonly used method of gain flattening at present and can achieve gain flatness within 1 dB over 30 nm. However, some degree of dependence of the gain flatness on the input powers still exists, and must be taken into account when designing a system.

2.14 The In-Fibre Bragg Grating

We now turn our attention to the in-fibre Bragg grating (IFBG) and discuss the basic principles and its use as a sensor.

An IFBG can be formed in germanium doped fibre by illuminating the core of the fibre with a sufficiently intense beam of light such that a localised change in refractive index is induced, due primarily to the photosensitivity of the germanium dopant. Light from a UV laser (typically ~240nm) is focused onto the side of the fibre and using either interferometric [2.92] or phase mask [2.93] techniques, a sinusoidal variation in the refractive index can be induced in the core forming a diffraction grating. When illuminated by a white light source, the grating will couple light into a counter propagating mode at a wavelength known as the Bragg resonance, λ_B, given by,

$$\lambda_B = 2n\Lambda \tag{2.110}$$

where n is the effective core refractive index and Λ is the grating pitch. Thus the effects of strain, temperature and pressure on either of these quantities provides a means of sensing by encoding this information on the wavelength. It follows from (2.110) and the analysis presented in section 2.6 that the fractional change in wavelength of the IFBG is given by,

$$\left.\frac{\Delta\lambda_B}{\lambda_B}\right|_T = \varepsilon_z - \frac{n^2}{2}\left[(p_{11}+p_{12})\varepsilon_r + p_{12}\varepsilon_z\right] \tag{2.111}$$

and,

$$\left.\frac{\Delta\lambda_B}{\lambda_B \Delta T}\right|_P = \left.\frac{1}{n}\frac{\partial n}{\partial T}\right|_\rho + \frac{1}{\Delta T}\left[\varepsilon_z^T - \frac{n^2}{2}\left[(p_{11}+p_{12})\varepsilon_r^T + p_{12}\varepsilon_z^T\right]\right] \tag{2.112}$$

where the subscripts T and P denote constant temperature or pressure and the other terms are as defined above. A large number of techniques exist for interrogation of IFBG's [2.94-2.96]; however, high resolution measurement of the wavelength shift can be achieved using an unbalanced interferometer as a frequency discriminator [2.97], where the sensitivity increases with the path imbalance. The maximum possible path imbalance in the interferometer is determined by the coherence length of the light returned from the grating that can be approximated by,

$$L_c = \frac{\lambda_B^{\,2}}{\Delta\lambda} \tag{2.113}$$

where $\Delta\lambda$ is the full-width half-maximum (FWHM) bandwidth of the IFBG. For an IFBG with λ_B=1550 nm, $\Delta\lambda$=0.05 nm then L_c=48 mm, which using the relation $|\Delta\phi| = \left(2\pi n L_c/\lambda_B^2\right)\Delta\lambda$ gives $\Delta\phi/\Delta\lambda$=184 rad.nm^{-1}. The responsivity of a bare grating to pressure has been measured in chapter 4 to be about -3.5×10^{-9}nm.Pa^{-1} which agrees well with the value of –4.4×10^{-9} nm.Pa^{-1} calculated using (2.111) and assuming hydrostatic boundary conditions. Assuming an interferometric phase resolution approaching 100 μrad.Hz$^{-1/2}$ at 1 kHz is achievable with PGC or heterodyne techniques, the minimum detectable pressure from a

Bragg grating sensor would be about 150 Pa, limited by the path imbalance in the decoding interferometer. This resolution is generally not high enough for acoustic measurements that typically require a pressure resolution less than 100 $\mu Pa.Hz^{-1/2}$. Reducing the linewidth of the IFBG allows a longer path imbalance to be incorporated into the interferometer; however, this also results in reduced optical power being returned from the IFBG. Typically, it is possible to make gratings around 10cm in length, which would exhibit a linewidth, $\Delta\lambda$ =0.016nm (assuming a weak grating). A potential solution is to replace the IFBG with an active grating such as an in-fibre laser (IFL). We shall see in chapter 7 that the linewidth of the spectral emission from these devices is of the order of 1 kHz, which allows a large imbalance to be incorporated into the interferometer.

An IFL sensor may consist of two closely spaced IFBG reflectors forming a Fabry-Pérot (FP) cavity or a distributed feedback structure (DFB), of the type described in chapter 7. If the fibre is doped with a rare earth element such as erbium then the device can be forced to lase if a sufficiently powerful optical pump is injected into the cavity. In the case of the Fabry-Pérot design, the laser can be forced to oscillate in a single longitudinal mode by making the cavity length sufficiently short (typically about 5 cm) such that the free spectral range of the cavity is much larger than the IFBG FWHM [2.98,2.99]. Single longitudinal mode lasing will occur if the Bragg resonances of the IFBGs are designed to overlap one of the cavity modes of the FP. Since the lasing wavelength is proportional to the cavity length, temperature, strain or pressure will modulate the lasing wavelength. In this case, the sensor self-noise is determined by the thermal noise generated in the laser cavity. The unbalanced interferometer merely acts to amplify the frequency noise-induced phase-shift in order to overcome the noise sources associated with the interferometer (such as laser intensity noise and detector thermal noise). An optimised sensor would be realised when the path imbalance is set such that the sensor self-noise is due to laser cavity thermal noise and the other noise sources (which are not dependent on the interferometer imbalance) are some way below this. Having measured the laser frequency noise, as 15 $Hz.Hz^{-1/2}$ at 1 kHz in chapter 7, for the DFB fibre laser (a similar or slightly lower noise level would be expected for the Fabry-Pérot type laser), and taking the responsivity to pressure in terms of frequency as, $\Delta\nu/\Delta P$ =536 $Hz.Pa^{-1}$, the thermal noise equivalent pressure is 37 $mPa.Hz^{-1/2}$. This is an improvement in pressure resolution of 4020 compared with the IFBG. Although these sensors are still at an early stage in their

development, they offer the possibility of an ultra-high resolution pressure/strain measurement from a very short gauge length device and distributed feedback IFLs have been demonstrated as multiplexed acoustic sensors [2.100].

References

[2.1] S.C.Rashleigh, 1980 "Acoustic sensing with a single coiled monomode fiber" *Optics Letters* 5 (9) 392-394

[2.2] S.C.Rashleigh, H.F.Taylor, 1981 "Beamforming fiber optic sensor" *Elec. Lett.* 17 (3) 138-139

[2.3] N.Lagakos, T.Litovitz, P.Macedo, R.Mohr and R.Meister, 1981 "Multimode optical fiber displacement sensor" *Applied Optics* 20 (2) 167-168

[2.4] S.K.Sheem, J.H.Cole, 1979 "Acoustic sensitivity of single-mode optical power dividers" *Optic Lett.* 4 (10) 322-324

[2.5] J.A.Bucaro, E.F.Carome, 1978 "Single fibre interferometric acoustic sensor" *Appl. Optics* 17 (3) 330-331

[2.6] J.A.Bucaro, N.Lagakos, J.Cole, T.Giallorenzi, 1982 "Fibre Optic Acoustic Transduction" *Physical Acoustics* XVI 385-457

[2.7] L.E.Kinsler, A.R.Frey, A.B.Copens, J.V.Sanders *Fundamentals of acoustics 3rd edn.* John Wiley and Sons 1982

[2.8] D.G.Tucker, B.K.Gazey, 1966 *Applied underwater acoustics 1st edn.* Oxford, New York, Pergamon, chapter 6

[2.9] G.M.Wenz, 1962 "Acoustic ambient noise in the ocean: spectra and sources" *J. Acoustical Soc. America* 34 (12) 1936-19

[2.10] Ref [2.8], chapter 5

[2.11] W.T.Thomson, 1993 *Theory of vibration with applications 4th edn.* Chapman and Hall

[2.12] Ed. by M.Berliner, J.F.Lindberg, 1995 *Acoustic particle velocity sensors: design, performance and applications*, AIP conference proceedings 368

[2.13] C.D.Butter, G.B.Hocker, 1978 "Fiber optic strain gauge" *Applied Optics* 17 (18) 2867-2869

[2.14] N.Lagakos, J.A.Bucaro, J.Jarzynski, 1981 "Temperature induced optical phase-shifts in fibres" *Applied Optics* 20 (13) 2305-2308

[2.15] E.Rønnekleiv, 1999 Fiber DFB lasers for sensor applications, PhD Thesis, chap. 3

[2.16] D.A.Brown, T.Hofler, S.L.Garrett, 1989 "High-sensitivity, fiber-optic, flexural disk hydrophone with reduced acceleration response" *Fiber and Integrated Optics* 8 169-191

[2.17] L.K.Cheng, D.De Bruijn, 1996 "Fieldtest of a Fibre Optic Hydrophone" *Proc. of the Optical Fibre Sensors Conf. 11* Advanced Sensing Photonics Japan Soc. of Appl. Phys. 2 vol. 712+17 184-187 vol. 1

[2.18] R.Sato, H.Ishii, K.Dobashi, H.Kamata, S.Saito, 1993 "Pressure balancing structure for fiber-optic flexural disk acoustic sensor" *Jpn. J. Appl. Phys.* 32 (1,5B) 2473-2476

[2.19] N.Lagakos, J.A.Bucaro, 1993 "Linearly configured embedded fiber-optic acoustic sensor" *J. Lightwave Tech.* 11 (4) 639-642

[2.20] P.J.Nash, J.Keen, 1990 "Design and construction of practical optical fibre hydrophones" *Proc. Inst of Acoustics* 12 (4) 201-212

[2.21] J.A.Bucaro, B.Houston, E.Williams, 1991 "Fibre-optic air backed hydrophone transduction mechanisms" *J. Acoust. Soc. Am.* 89 451-453

[2.22] S.Knudsen, A.B.Tveten, A.Dandridge, K.Bløtekjær, 1996 "Low frequency transduction mechanisms of fiber-optic air-backed mandrel hydrophones" *Proc. of the Optical Fiber Sensors Conf. 11* Advanced Sensing Photonics Japan Soc. of App. Phys. 208-211

[2.23] S.Knusden, G.B.Havsgård, Ø.Christensen, G.Wang, A.Tveten, A.Dandridge, 1997 "Bandwidth limitations due to mechanical resonances of fiber-optic air backed mandrel hydrophones" *Proc. of the Optical Fibre Sensors Conf. 12* Opt. Soc. America Washington DC, US OThC35-1 544-547

[2.24] C.C.Wang, A.Dandridge, A.B.Tveten, A.Yurek, 1994 "Very high responsivity fiber optic hydrophones for commercial applications" *Proc. of the Optical Fibre Sensors Conf. 10 SPIE* 2360

[2.25] L.Lagakos, P.Ehrenfeuchter, T.R.Hickman, A.Tveten, J.A.Bucaro, 1988 "Planar flexible fiber-optic interferometric acoustic sensors" *Optics Letters* 13 (9) 1298-1303

[2.26] D.A.Danielson, S.L.Garrett, 1989 "Fibre-optic ellipsoidal flextensional hydrophones" *IEEE J. Lightwave Tech.* 7 (12) 1995-2002

[2.27] S.Knudsen, 1996 Fiber-optic acoustic sensors based on the Michelson and Sagnac interferometers : responsivity and noise properties, PhD thesis, chapter 6

[2.28] O.H.Waagaard, G.B. Havsgård, G.Wang, 2001 "An investigation of pressure-to-acceleration responsivity of fiber-optic hydrophones" *J. Light. Tech.* 19 (7) 994-1003

[2.29] A.Tveten, A.Dandridge, C.M.Davis, T.G.Giallorenzi, 1980 "Fibre optic accelerometer" *Elec. Lett.* 16 (22) 854-855

[2.30] A.D.Kersey, D.A.Jackson, M.Corke, 1982 "High-sensitivity fibre-optic accelerometer" *Elec. Lett.* 18 (13) 559-561

[2.31] C.M.Davis, J.G.Eustace, C.J.Zarobila, 1986 "Fiber-optic seismometer" *Fiber Optic and Laser Sensors IV SPIE 718* 203-211

[2.32] D.L.Gardner, S.L.Garrett, 1987 "Fiber optic seismic sensor" *Fiber Optic and Laser Sensors V* SPIE 838 271-278

[2.33] D.A.Brown, S.L.Garrett, 1990 "An interferometric fiber optic accelerometer" *Fiber Optic and Laser Sensors VIII* SPIE 1367 282-288

[2.34] K.Krakenes, K.Bløtekjær 1989 "Sagnac interferometer for underwater sound detection: noise properties" *Optics Letters* 14 (20) 1152-1154

[2.35] S.Knudsen, 1996 Fiber-optic acoustic sensors based on the Michelson and Sagnac interferometers : responsivity and noise properties, Dr.ing. Thesis, Norwegian Univ. of Sci. and Tech., chap. 2

[2.36] E.Udd, 1983 "Fiber-optic acoustic sensor based on the Sagnac interferometer" *SPIE* 425 90-95

[2.37] B.J.Vakoc, M.J.F.Digonnet, G.S.Kino, 1999 "A novel fiber optic sensor array based on the Sagnac interferometer" *Fiber Optic Sensor Technology and Applications, SPIE* 3860 276-284

[2.38] D.A.Jackson, A.K.Kersey, M.Corke, J.D.C.Jones, 1982 "Pseudoheterodyne detection scheme for optical interferometers" *Elect. Lett.* 18 (25) 1081-1083

[2.39] A.D.Kersey, D.A.Jackson, M.Corke, 1982 "Demodulation scheme fibre interferometric sensors employing laser frequency switching" *Elec. Lett.* 19 (3) 102-103

[2.40] K.P.Koo, A.B.Tveten, A.Dandridge, 1982 "Passive stabilization scheme for fiber interferometers using (3*3) fiber directional couplers" *Appl. Phys. Lett.* 41 (7) 616-618

[2.41] J.H.Cole, B.A.Danver, J.A.Bucaro, 1982 "Synthetic-Heterodyne interferometric demodulation" *J. Lightwave Tech.* 18 (4) 694-697

[2.42] A.Dandridge, A.B.Tveten, T.G.Giallorenzi, 1982 "Homodyne demodulation scheme for fiber optic sensors using phase generated carrier" *IEEE J Quant Elec.* 18 (10) 1647-1653

[2.43] A.Dandridge, A.D.Kersey, 1987 "Signal processing for optical fiber sensors" *Fiber Optic Sensors II SPIE* 798 158-165

[2.44] A.Dandridge, A.D.Kersey, 1988 "Overview of Mach-Zehnder sensor technology and applications" *Fiber Optic and Laser Sensors VI SPIE* 985 34-52

[2.45] A.Dandridge, "Fiber-optic sensor based on the Mach-Zehnder and Michelson Interferometers", in Fiber Optic Sensors: an introduction for engineers and scientists, ed. E.Udd, Wiley Interscience, 1991

[2.46] D.A.Jackson, R.Priest, A.Dandridge, A.B.Tveten, 1980 "Elimination of drift in a single-mode optical fiber interferometer using a piezoelectrically streched coiled fiber" *Applied Optics* 19 (17)

[2.47] A.Dandridge, L.Goldberg, 1982 "Current-induced frequency modulation in diode lasers" *Elec. Lett.* 18 (7) 302-304

[2.48] F.G.Stremler, 1982 *Introduction to Communication Systems* 2nd edn. (Addison-Wesley Publishing) section 6.2

[2.49] A.Yariv, 1991 *Optical Electronics* 4th edn (Saunders College Publishing) 430-431

[2.50] C.C.Davis, 1996 *Lasers and Electro-Optics Fundamentals and Engineering* 1st edn (Cambridge University Press) 567-568

[2.51] K.H.Wanser, 1994 "Theory on thermal phase noise in Michelson and Sagnac Fiber interferometers" *Proc. of the Optical Fibre Sensors Conf. 10* SPIE 2360 584-587

[2.52] K.H.Wanser, A.D.Kersey, A.Dandridge, 1993 "Measurement of fundamental thermal phase fluctuations in optical fiber" *Proc. of the Optical Fibre Sensors Conf. 9* Florence Italy Associazione Elettrotecnica 255-258

[2.53] K.H.Wanser, 1992 "Fundamental phase noise limit in optical fibers due to temperature fluctuations" *Elec. Lett.*, 28 (1) 53-54

[2.54] M.Henning, 1985 "Improvements in reflectometric fiber optic hydrophones", Proc. 2nd Int. Symp. Opitcal and Electro Optical Science and Eng. (SPIE), Cannes

[2.55] A.D.Kersey, T.A.Berkoff, 1990 "Novel passive phase noise cancelling technique for interferometric fibre optic sensors" *Electronics Letters* 26 (10) 640-641

[2.56] Ref [2.48], p.313

[2.57] A.D.Kersey, 1990 "Multiplexed interferometric fiber sensors" *Proc. of the Optical Fibre Sensors 7* The Institution of Radio and Electronics Engineers 313-319

[2.58] A.D.Kersey, A.Dandridge, 1989 "Comparative analysis of multiplexing techniques for interferometic fiber sensing" *Fiber Optic and Laser Sensors SPIE* 1120 236-246

[2.59] A.Dandridge, A.B.Tveten, A.D.Kersey, A.M.Yurek, 1987 "Multiplexing of interferometric sensors using phase generated carrier techniques" *J. Lightwave Technology* 5 (7) 947-952

[2.60] J.L.Brooks, B.Moslehi, B.Y.Kim, H.J.Shaw, 1987 "Time domain addressing of remote fiber optic interferometric sensor arrays" *IEEE J. Lightwave Technology* 5 (7) 1014-1023

[2.61] J.P.Dakin, C.A.Wade, M.L.Henning, 1984 "Novel optical fibre hydrophone array using a single laser source and detector" *Electronic Letters* 20 (1) 53-54

[2.62] A.D.Kersey, K.L.Dorsey, A.Dandridge, 1989 "Cross talk in a fiber-optic Fabry-Pérot sensor array with ring reflectors" *Optics Letters* 14 (1) 93-95

[2.63] S.Vohra, A.Dandridge, 1996 "An hybrid WDM/TDM reflectometric array" *Proc. of the Optical Fiber Sensors Conf. 11* Advanced Sensing Photonics Japan Soc. Of Applied Phys Tokyo Japan 2 vol. 712+17 1 Th3-29

[2.64] A.D.Kersey, A.Dandridge, A.B.Tveten, 1987 "Time division multiplexing of interferometric fibre sensors using passive phase generated carrier interrogation" *Optics Letters* 12 (10) 775-777

[2.65] A.D.Kersey, A.Dandridge, 1989 "Ten-Element time-division multiplexed interferometric fiber sensor array" *Proc. of the Optical Fibre Sensors Conf. 6* Springer-Verlag Berlin West Germany xvi+576 486-490

[2.66] J.Sæther, K.Bløtekjær, 1996 "Optical amplifiers in multiplexed sensor systems – Theoretical prediction of noise performance" *Proc. of the Optical Fibre Sensors Conf. 11* Advanced Sensing Photonics Japan Soc Appl. Phys. Tokyo Japan 1 518-521

[2.67] J.Sæther, K.Bløtekjær, 1997 "Optical amplifiers in time domain multiplexed sensor systems" *Proc. of the Optical Fibre Sensors Conf. 12* OSA Tech. Digest Series 16 586-589

[2.68] J.L.Wagener, C.W.Hodgson, M.J.F.Digonnet, H.J.Shaw, 1997 "Novel fiber sensor arrays using Erbium-doped fiber amplifiers" *J. Lightwave Tech.*15 (9) 1681-1688

[2.69] C.W.Hodgson, M.J.F.Digonnet, H.J.Shaw, 1997 "Large-scale interferometric fiber sensor arrays with multiple optical amplifiers" *Optics Letters* 22 (21) 1651-1653

[2.70] I.P.Kaminow, 1981 "Polarisation in optical fibers" *IEEE J. Quant. Elec.* 17 (1) 15-22

[2.71] M.Martinelli, 1994 "Time-reversal of the polarization state in optical fiber circuits" *Proc. of the Optical Fibre Sensors Conf. 10 SPIE* 2360 312-318

[2.72] M.J.Marrone, A.D.Kersey, A.Dandridge, 1992 "Polarization independent array configuration based on Michelson interferometer networks" *Distributed and Multiplexed Fiber Optic Sensors II, SPIE* 1797 196-200

[2.73] A.D.Kersey, M.J.Marrone, A.Dandridge, 1988 "Optimization and stabilization of visibility in interferometric fiber-optic sensors using input-polarization control" *J. Lightwave Tech.* 6 (10) 1599-1609

[2.74] A.K.Kersey, A.Dandridge, M.J.Marrone, 1987 "Single-mode fiber pseudo-depolarizer" *Fiber Optics and Laser Sensors V SPIE* 838 360-364

[2.75] J.T.Ahn, B.Y.Kim, 1995 "Fiber-optic sensor array without polarization signal fading" *Optics Letters* 20, (4) 416-418

[2.76] A.Simon, R.Ulrich, 1977 "Evolution of polarisation along a single-mode fiber" *Applied Physics Lett.* 31 (8) 517-520

[2.77] N.J.Frigo, A.Dandridge, A.B.Tveten, 1984 "Technique for elimination of polarisation fading in fibre interferometers" *Elec. Lett.* 20 (8) 319-320

[2.78] K.H.Wanser, N.H.Safar, 1997 "Remote polarization control for fiber-optic interferometers" *Optics Letters* 12 (3) 217-219

[2.79] A.D.Kersey, M.J.Marrone, A.Dandridge, 1988 "Observation of input-polarisation-induced phase noise in interferometric fiber-optic sensors" *Optics Letters* 13 (10) 847-849

[2.80] M.J.Marrone, A.D.Kersey, C.A.Villarruel, C.K.Kirkendall, A.Dandridge, 1992 "Elimination of coherent Rayleigh backscatter induced noise in fibre Michelson interferometers" Elect. Lett. 28 (19) 1803-1804

[2.81] D.M.Dagenais, K.P.Koo, F.Bucholtz, 1993 "Fiber interferometry limitations due to parasitic optical cavities" *Lasers and Electro-Optics Society Annual Meeting* LEOS '93 Conference proceedings 141 -142

[2.82] T.A.Berkoff, A.D.Kersey, A.Dandridge, 1989 "Noise aliasing in interferometric sensors utilizing phase-generated carrier demodulation" *Fiber Optic and Laser Sensors VII* SPIE 1169 80-88

[2.83] C.K.Kirkendall, A.D.Kersey, A.Dandridge, M.J.Marrone, A.R.Davis, 1996 "Sensitivity limitations due to aliased high frequency phase noise in high channel-count TDM interferometric arrays" *Proc. 11th Int. Conf. on Optical Fiber Sensors* Advanced Sensing Photonics, Japan Society of Applied Physics 678-681

[2.84] R.J.Mears, L.Reekie, I.M.Jauncey, D.N.Payne, 1987 "Low-noise erbium-doped fibre amplifier operating at 1.54 μm" *Elec. Lett.* 23 (19) 1026-1027

[2.85] P.C.Becker, N.A.Olsson, J.R.Simpson, 1999 *Erbium doped fiber amplifiers: fundamentals and technology* Academic Press, Optics and Photonics Series

[2.86] Y.Yamamoto, T.Mukai, 1989 "Fundamentals of optical amplifiers" *Optical and Quantum Electronics* 21 S1-S14

[2.87] M.J.F.Digonnet, *Fiber laser sources and amplifiers* Short course presented at Photonics East, Boston, SPIE SC22

[2.88] R.C.Steele, G.R.Walker, N.G.Walker, 1991 "Sensitivity of optically preamplified receivers with optical filtering" *IEEE Phot. Tech. Lett.* 3 (6) 545-547

[2.89] N.A.Olsson, 1989 "Lightwave systems with optical amplifiers" *J. Light. Tech.* 7 (7) 1071-1082

[2.90] M.L.Dakss, B.Pedersen, G.R.Joyce, W.J.Miniscalco, 1991 "Signal output power and noise in erbium-doped fiber power amplifiers" *Fiber Laser Sources and Amplifers III SPIE 1581* 236-250

[2.91] P.J.Nash, A.B.Gallaher, D.J.W.Hardie, 1995 "Finite element modelling of optical fibre hydrophones" *Proc. Inst of Acoustics*17 (3) 164-172

[2.92] G.Meltz, W.W.Morey, W.H.Glen, 1989 "Formation of Bragg gratings in optical fibers by a transverse holographic method" *Optics Lett.* 14 (15) 823-825

[2.93] K.O.Hill, B.Malo, F.Bilodeau, D.C.Johnson, J.Albert, 1993 "Bragg gratings fabricated in monomode photosensitive optical fiber by UV enposure through a phase mask" *Appl. Phys. Lett.* 62 (10) 1035-1037

[2.94] A.D.Kersey, 1993 "Interrogation and multiplexing techniques for fiber Bragg grating strain-sensors" *SPIE 2071* 30-48

[2.95] A.D.Kersey, M.A.Davis, T.A.Berkoff, D.G.Bellemore, K.P.Koo, R.T.Jones, 1996 "Progress towards the development of practical fiber Bragg grating instrumentation systems" *SPIE 2839* 40-63

[2.96] W.W.Morey, G.A.Ball, H.Singh, 1996 "Applications of fiber grating sensors" *SPIE 2839* 2-7

[2.97] K.P. Koo, A.D.Kersey, 1995 "Bragg grating-based laser sensor systems with interferometric interrogation and wavelength division multiplexing" *J. Lightwave Technology* 13 (7) 1243-1249

[2.98] G.A.Ball, C.G.Hull-Allen, J.Livas, 1994 "Frequency noise of a Bragg grating fiber laser" *Electron. Lett.* 30 (15)

[2.99] G.A.Ball, G.Hull-Allen, C.Holton, W.W.Morey, 1993 "Low noise single frequency linear fibre laser" *Elec. Lett.* 29 (18) 1623-1625

[2.100] D.J.Hill, P.J.Nash, D.A.Jackson, D.J.Webb, S.F.O'Neil, I.Bennion, L.Zhang, 1999 "A fiber laser hydrophone array" *SPIE* 3860 Boston USA

[2.101] M.N.Inci, S.R,Kidd, J.S.Barton, J.D.C.Jones, 1992 "Fabrication of single-mode fibre optic Fabry-Pérot interferometers using fusion spliced titanium dioxide optical coatings" *Meas. Sci. Technol.* 3 678-684

[2.102] D.A.Mortimore, 1988 "Fiber loop reflectors" *J.Light. Tech.* 6 (7) 1217-1224

[2.103] S.J.Petuchowski, T.G.Giallorenzi, S.K.Sheem, 1981 "A sensitivie fiber-optic Fabry-Pérot interferometer" *IEEE J. Quant. Elec.* QE-17 (11) 2168-2170

[2.104] A.D.Kersey, D.A.Jackson, M.Corke, 1983 "A simple fibre Fabry-Pérot sensor" *Optics Comms* 45 (2) 71-74

[2.105] J.M.Vaughan, 1989 *The Fabry-Pérot interferometer: history, theory, practice and applications* IOP Publishing, chapter 3

[2.106] S.K.Sheem, T.G.Giallorenzi, K.P.Koo 1982 "Techniques to solve the signal fading problem in fiber interferometers" *Appl. Opt.* 21 (4) 689-693

[2.107] S.K.Sheem, 1981 "Optical fiber interferometers with 3×3 dierectional couplers -analysis *J.Appl.Phys.* 52 (6) 3865-3872

[2.108] G.A.Johnson, M.D.Todd, B.L.Althouse, C.C.Chang 2000 "Fiber Bragg grating interrogation and multiplexing with a 3×3 coupler and a scanning filter" *J.Light.Tech.* 18 (8)

[2.109] A.B.Lobo Ribeiro, R.F.Caleya, J.L.Santos, 1995 "Progressive ladder network topology combining interferometric and intensity fiber-optic-based sensors" *Applied Optics* 34 (28) 6481-6488

[2.110] E.Desirvire, J.R.Simpson, P.C.becker, 1987 "High-gain erbium-doped traveling-wave fiber amplifier" *Optics Letters* 12 (11) 888

Part II
Sensor Design

Chapter 3

HIGH RESPONSIVITY FIBRE-OPTIC FLEXURAL DISK ACCELEROMETERS†

Abstract- This chapter presents performance measurements of fibre-optic flexural disk accelerometers. The flexural disk acts as a mass-spring element to which the fibre is bonded, such that an acceleration causes a strain to be imposed on the fibre which is measured interferometrically. Simple analytical models have been written to calculate the responsivity and resonant frequency of disks under various boundary conditions and the results of the models have been shown to be in good agreement with the measured responsivity for the case of moderately thick disks. Six optical fibre accelerometers based on flexural disks of different thickness and supports have been demonstrated to exhibit a responsivity in the range of 28 to 39 dB re 1 rad.g^{-1} with a resonant frequency between 2.4 kHz to greater than 5 kHz respectively. Of the designs considered, the centrally supported disk is shown to give the highest combination of responsivity and bandwidth. A centrally supported disk has been demonstrated to exhibit a flat response up to 2 kHz and a responsivity of 37 dB re 1 rad.g^{-1}, which when combined with an interferometric phase resolution of 10 μrad.Hz$^{-1/2}$ would give a minimum detectable acceleration of 141 ng.Hz$^{-1/2}$. We have attempted to cover all aspects of the sensor design including responsivity, bandwidth, cross-responsivity, phase response and size and find that a complicated compromise between all of these design parameters is required to achieve the optimum performance.

3.1 Introduction

Detection of sound underwater has, conventionally, been achieved with pressure sensing hydrophones which exhibit an omni-directional response, where the wavelength of the acoustic signal is significantly greater than the maximum dimension of the hydrophone, as is

†This chapter is a transcript of the paper by G.A.Cranch and P.J.Nash, 2000 "High-Responsivity Fiber-Optic Flexural Disk Accelerometers" *J. of Lightwave Technology* 18 (9) 1233-1243

the case at low acoustic frequency. When such sensors are formed into an array, the outputs can be combined to form beams that can be steered, by applying time delays between the individual sensor signals before re-combination. This beam-forming technique allows the location of the source of acoustic emission; however, for many array designs there often remains an ambiguity in the precise location of the source due to the symmetry of the array [3.1]. It generally remains unknown as to whether the source is above or below, or to the left or right of the array. For this reason it is desirable for the sensor to exhibit a directional response over the entire frequency range, which will remove this location ambiguity and hence allow precise location of the source of acoustic emission. A sensor that responds to a vector component associated with the acoustic field, such as the acceleration, velocity or particle displacement, will exhibit this desired directional response and therefore can be used as an alternative to the scalar pressure measurement. The sensor is required to be of low mass and small size compared with the acoustic wavelength, and may be mounted such that it exhibits neutral buoyancy in the array structure.

Development of the fibre optic hydrophone array [3.2] has led to interest in a fibre optic 'vector sensor' that can be interrogated using the same techniques as for the hydrophone array, i.e. interferometry. Fibre optic based accelerometers provide all the advantages inherent with fibre optics sensors such as ease of multiplexing, immunity to EMI, an electrically passive sensor and the ability to include in the same network sensors designed to measure different parameters. Recent interest in fibre optic based accelerometers has led to a number of sensor designs being developed [3.3], optimised for particular combinations of bandwidth and responsivity, which we reviewed briefly in section 2.6.3. The basic design of the accelerometer uses inertial force to generate strain in the fibre, which is measured interferometrically by the effect on the phase of the optical signal propagating through the fibre. The relationship between the induced phase-shift and the acceleration is known as the responsivity, $\Delta\phi/\Delta A$, and is expressed in units of radians per g, where 1 g is approximately equal to 9.8 ms^{-2}. The responsivity is often expressed in decibels by calculating $20\log_{10}(\Delta\phi/\Delta A)$ re 1 $rad.g^{-1}$.

One design uses as a sensing element a mass-loaded compliant mandrel, around which the fibre is wound. The sensor demonstrated in [3.4] achieved a responsivity of 80.4 dB re 1 $rad.g^{-1}$ and a resonant frequency of 300 Hz with an inertial mass of 542 gramme. A similar type of sensor designed for high temperature applications achieved a responsivity of 52.6 dB re 1 $rad.g^{-1}$ and a

resonant frequency of 413 Hz with an inertial mass of 127.5 grammes [3.5]. These sensors, although achieving high responsivity, are less practical for the array applications described above due to their high mass and size, approximately 60mm in diameter by 70 mm for the device described in [3.4].

A design, potentially lighter and more compact is based on a flexural disk onto which the fibre is bonded. A design of this type comprising two edge-supported flexural disks demonstrated a responsivity of 34 dB re 1 rad.g^{-1} and a resonant frequency of 2450 Hz with a mass of 7.7 grammes [3.6]. A similar design based on a single edge-supported disk achieved a responsivity of 20 dB re 1 rad.g^{-1} and a resonant frequency of 17 kHz, and in a centre-supported disk configuration achieved 19 dB re 1 rad.g^{-1} and a resonant frequency of 12.5 kHz in a device of size 35mm diameter by 17mm [3.7,3.8]. More recently a design consisting of two flexural disks and a large seismic mass has demonstrated a responsivity of 69 dB re 1 rad.g^{-1} and a resonant frequency of 180 Hz [3.9]. The flexural disk design has, thus, been demonstrated to achieve a range of combinations of responsivity and bandwidth in a device of sufficiently small size and low mass for array applications.

This chapter describes work carried out to design flexural disk based accelerometers that are simple to manufacture, exhibit high responsivity and flat frequency response, low responsivity to orthogonal motion, i.e. cross-responsivity, moderately high bandwidth (up to 10kHz) and small size. The acceleration resolution obtained from the sensor will depend on the interferometric phase resolution. We shall assume a phase resolution of 10μrad.Hz$^{-1/2}$ and aim to achieve an acceleration resolution of less than 100ng.Hz$^{-1/2}$. Thus, the transducer responsivity must be greater than 100rad.g^{-1} (or 40 dB re 1 rad.g^{-1}). We shall also aim for a bandwidth of ~3 kHz with a maximum dimension of 70mm. Achieving this resolution must not compromise the other design requirements of the sensor. The requirement for high responsivity and high bandwidth has led us to develop detailed analytical models to identify the most efficient method of mounting the disk. The work carried out has identified this optimum mounting technique in a device of fixed size and fibre length and the sensors that have been constructed exhibit some of the highest combinations of responsivity and bandwidth reported in the literature to date.

A number of disk mountings are modelled using theory based on small static deflections of moderately thick circular plates and on the dynamic motion of thin circular plates; the models used to predict the responsivity of the disks are described in sec. 3.3. The prediction of the resonant frequency of the various disks is then described in sec. 3.4 along with an explanation of the treatment of the composite disk structure in sec. 3.5. A comparison between the performance achieved by the disks under the various boundary conditions considered is given in sec. 3.6. Sec. 3.7 and 3.8 then discuss the sensor construction and responsivity calibrations. The results and discussion are then given in sec. 3.9. Finally, sec. 3.10 describes system noise sources.

3.2 Principle Of Operation

The operating principle of the flexural disk sensor is illustrated in fig. 3.1. The sensor consists of a coil of fibre encapsulated into the surface of an epoxy disk which is either rigidly supported around the edge or through the centre by an aluminium support. An inertial force acting on the support will cause the disk to flex, shown by the dotted line, and this flexing motion induces strain in the fibre coil, which is detected interferometrically. The underlying assumption when modelling the sensor is that the central plane in the disk is the neutral surface and any point not lying within this plane will shift its origin, thus inducing a strain. The sensor will exhibit maximum responsivity to the inertial force acting through the axis normal to the disk surface and minimum responsivity when the force acts in the plane of the disk.

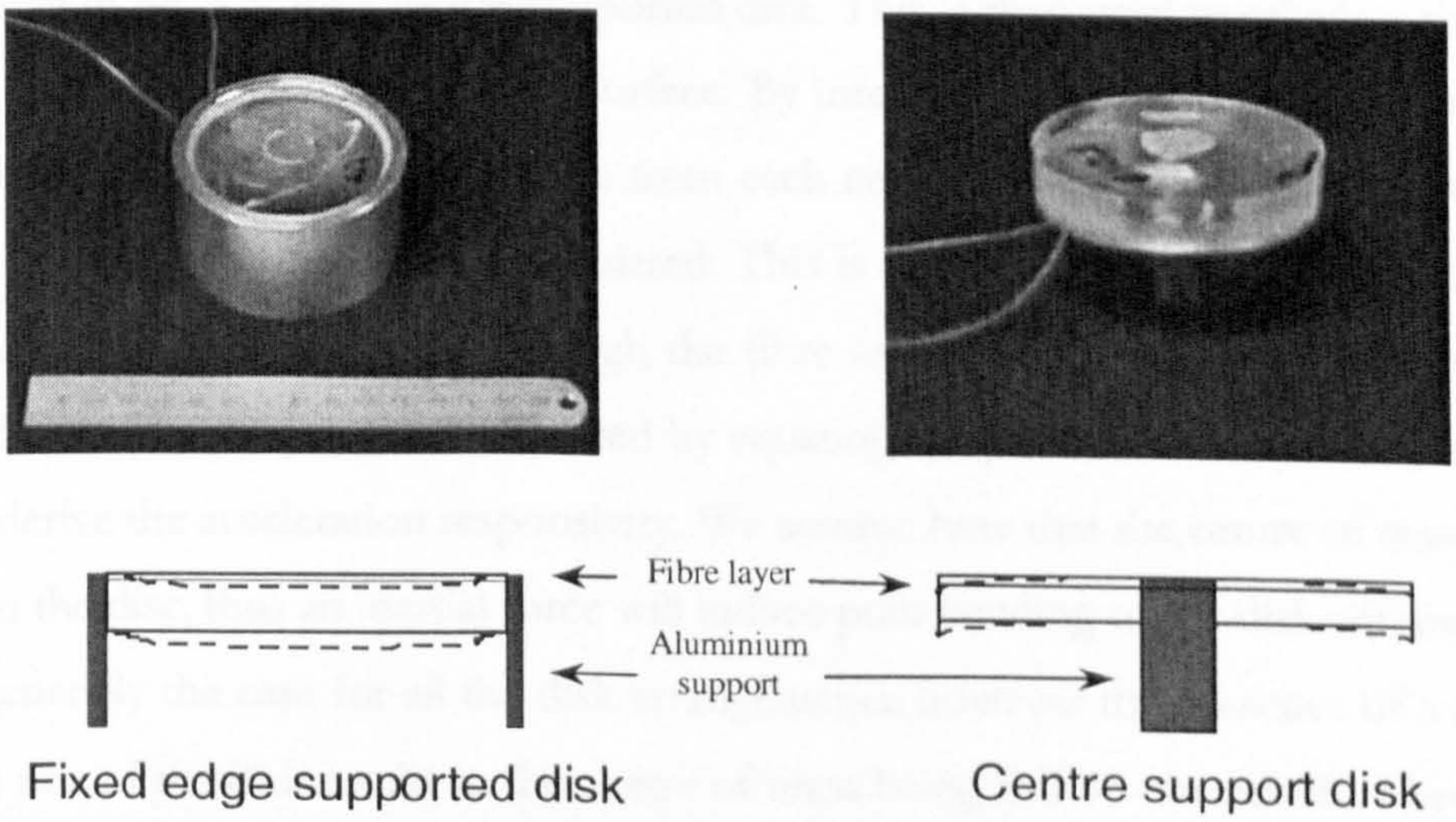

Figure 3.1: Principle of operation of the flexural disk sensor

3.3 Modelling The Sensor Responsivity To Acceleration

The responsivity of the sensor can be found by initially calculating the displacements of points in a disk as it flexes under acceleration and converting these displacements into strain in the fibre. The mounting conditions considered are illustrated in Fig. 3.2a,b,c and d and are referred to as (a) fixed-edge support; (b) simple-edge support; (c) fixed-centre support; and (d) simple-centre support, and these form the boundary conditions. The physical realisation of these boundary conditions is discussed later.

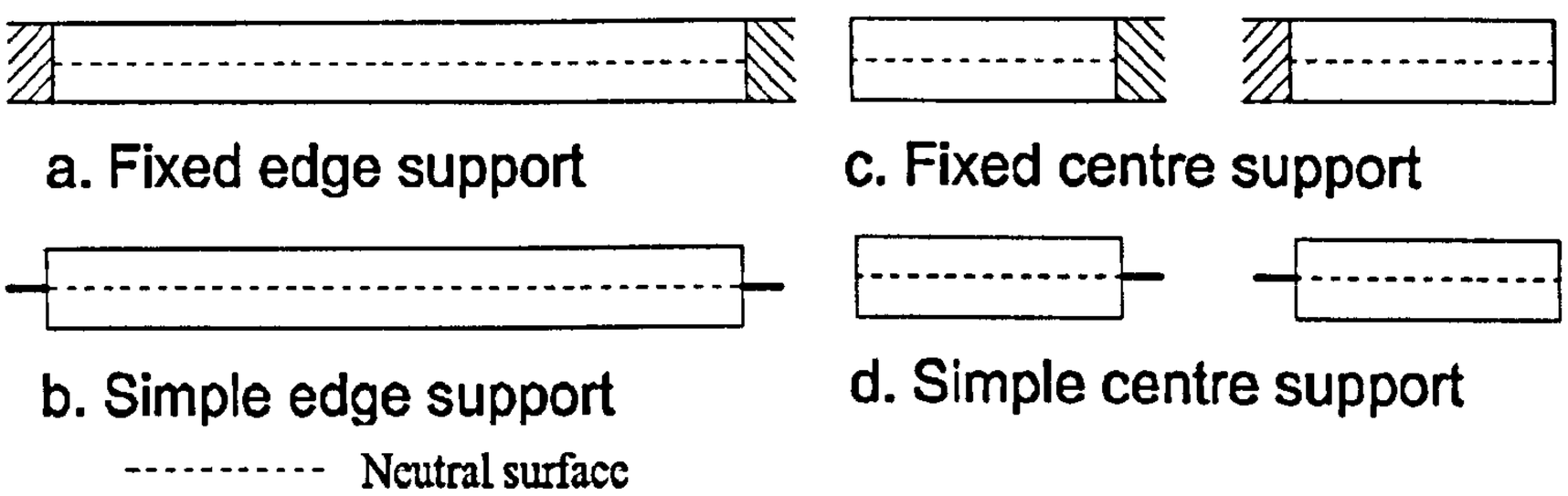

Figure 3.2: a,b,c,d. Mounting configurations for the flexural disks

The approach used is similar to that described in [3.10,3.11] and extends this analysis for different disk supports and multiple fibre coils. Each model initially calculates the angular displacement, $\theta(r)$, of the disk when exposed to a uniform pressure acting on the top surface as illustrated in fig. 3.3. for a centre supported disk. This is then used to calculate the strain in a coil at a distance, z, from the neutral surface. By integrating the strain over the surface of the fibre coil and then adding contributions from each coil, if there is more then one coil present, the total strain in the fibre layer is calculated. This is then used to calculate the induced phase change in a light beam travelling through the fibre as a function of the applied pressure. The acceleration responsivity is then calculated by equating the pressure-induced force to an inertial force to derive the acceleration responsivity. We assume here that the centre of mass is centrally located in the disc, thus an inertial force will induce pure bending of the disk without distortion. This is generally the case for all the disk arrangements; however the presence of a fibre coil on only one side of the disk results in the centre of mass being shifted towards the fibre coil, which may affect the cross-axis responsivity, discussed later.

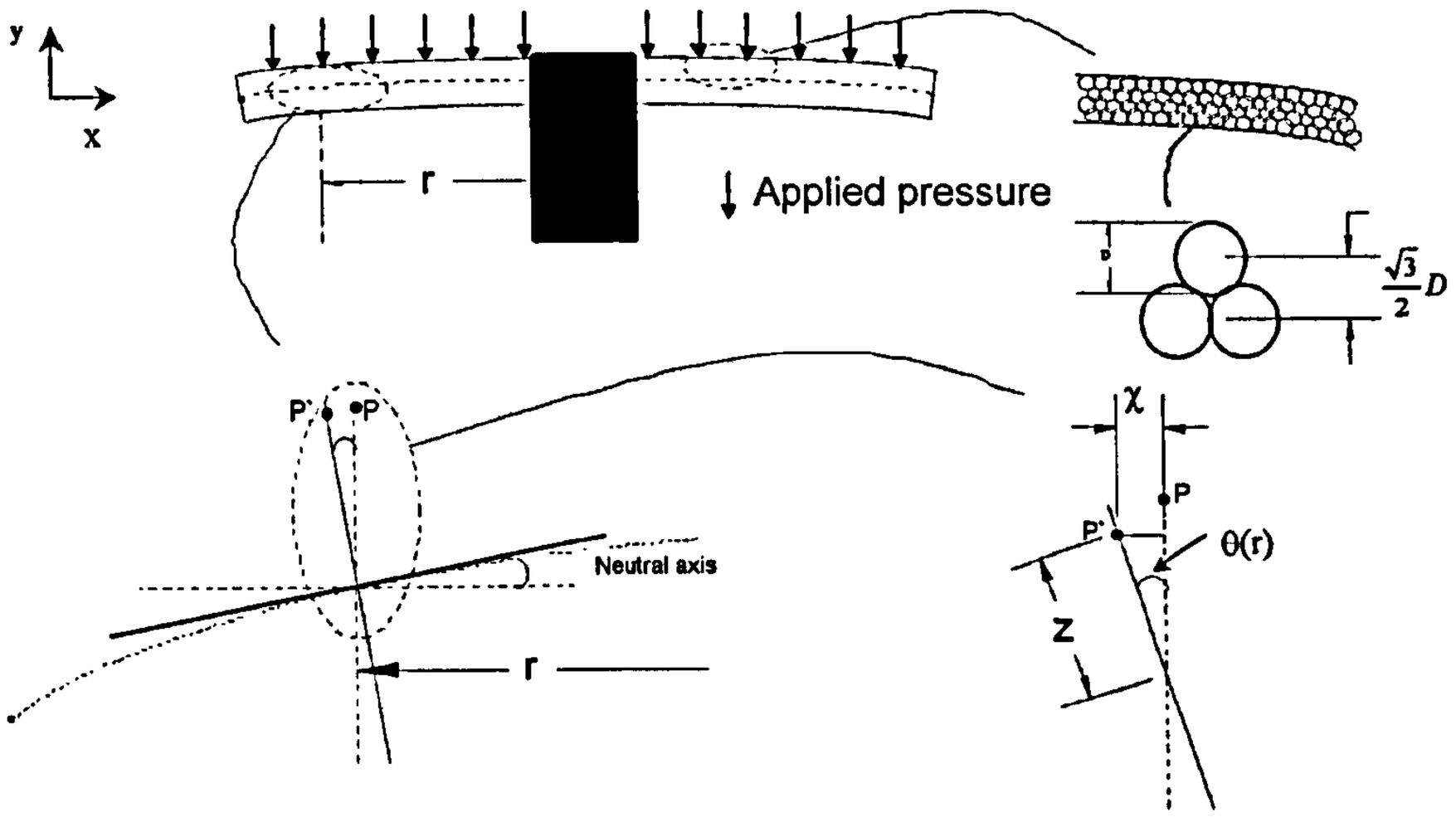

Figure 3.3: Illustration of the displacements in a flexing disk

This calculation is now described in detail for the case of a fixed-centre supported disk. The variables used in the analysis are shown in table 3.1.

Table 3.1: Definition of variables used in model[5]

Symbol	*Typical value*	*Description*
ε		axial strain
a	30 mm	disk radius
b	7.5mm	inner radius of fibre coil
c	28mm	outer radius of fibre coil
E		Average Young's modulus of disk material
ν	0.4	Poisson's ratio of disk material
ρ	1000kg.m^{-3}	Density of disk material
r		radial distance from plate centre
h		half the disk thickness
z		Distance along normal to neutral surface
L		total length of fibre in the sensor
D		fibre diameter
n	1.46	group refractive index of fibre core
λ	1310 nm	Wavelength of light
k	$2\pi/\lambda$	free space wavenumber of light

[5] The Poisson ratio, V, incorrectly appeared as σ in this table in the Journal paper. This has been corrected here.

Table 3.1(cont) : Definition of variables used in model

Symbol	*Typical value*	*Description*
p_{11}	0.121	Pockels coefficient of fibre
p_{12}	0.270	Pockels coefficient of fibre
ν_f	0.17	Poisson ratio of fibre
j		no. of fibre coils
g	9.8 ms^{-1}	Acceleration due to gravity
P		Pressure
A		Acceleration
F_L	$\frac{E(2h)^3}{12(1-\nu^2)}$	Flexural modulus
Q_b	$\frac{\Delta P(a^2-b^2)}{2b}$	Boundary condition - unit shear force
M_{rb}	$-\frac{\Delta P a^2}{C_8}\left[\frac{C_9}{2ab}(a^2-b^2)-L_{17}\right]$	Boundary condition- Unit radial bending moment
C_7	$\frac{1}{2}(1-\nu^2)\left(\frac{a}{b}-\frac{b}{a}\right)$	Plate constant
C_8	$\frac{1}{2}\left[1+\nu+(1-\nu)\left(\frac{b}{a}\right)^2\right]$	Plate constant
C_9	$\frac{b}{a}\left(\frac{1+\nu}{2}\ln\left(\frac{a}{b}\right)+\frac{1-\nu}{4}\left[1-\left(\frac{b}{a}\right)^2\right]\right)$	Plate constant
L_{17}	$\frac{1}{4}\left[1-\frac{1-\nu}{4}\left[1-\left(\frac{b}{a}\right)^4\right]-\left(\frac{b}{a}\right)^2\left[1+(1+\nu)\ln\left(\frac{a}{b}\right)\right]\right]$	Loading constant
$F_5(r)$	$\frac{1}{2}\left[1-\left(\frac{b}{r}\right)^2\right]$	Plate function
$F_6(r)$	$\frac{b}{4r}\left[\left(\frac{b}{r}\right)^2-1+2\ln\left(\frac{r}{b}\right)\right]$	Plate function
$G_{14}(r)$	$\frac{1}{16}\left[1-\left(\frac{b}{r}\right)^4-4\left(\frac{b}{r}\right)^2\ln\left(\frac{r}{b}\right)\right]$	Plate function

The equation for the angular displacement of a fixed-centre supported disk under a uniform force/pressure, ΔP, on its top surface is given by (3.1) [3.12].

$$\theta(r)=\frac{M_{rb}}{F_L}rF_5(r)+\frac{Q_b}{F_L}r^2F_6(r)-\frac{\Delta P}{F_L}r^3G_{14}(r) \qquad (3.1)$$

where the flexural modulus, F_L, unit shear force, Q_b, unit radial bending moment, M_{rb}, and the general plate functions and constants C_n, F_n, G_n and L_n are given in table 3.1 [3.13].

Referring to the illustration in fig. 3.3, if $\theta(r)$ is the angle subtended by the tangent, at a radial distance r from the disk centre, to the horizontal, then the horizontal displacement of a point at a distance z from the neutral surface is given by χ (P to P` in fig. 3.3). If the solid line is taken as the neutral surface then a point on the disk, at a distance z along the normal to the neutral surface, will undergo a displacement in the x direction of $\chi = z\theta(r)$ for $\theta << 1$, i.e. for small displacements. The strain in a fibre loop of radius, r, and distance, z, from the neutral surface is then calculated from the change in its circumference and is given by (3.2)

$$\varepsilon(z,r) = \frac{z\theta(r)}{r} \tag{3.2}$$

The length of a spiral of fibre of inner radius, b, outer radius, c and a pitch equal to the fibre diameter, D, is given by, $\int_b^c \frac{2\pi r}{D} dr$. This is then used to calculate the total change in length of a fibre coil subject to a strain, ε,

$$\Delta l(z) = \int_b^c \varepsilon(z,r) \frac{2\pi r}{D} dr \tag{3.3}$$

If there are multiple coils wound into the disk, they are assumed to be in a hexagonal close-packed structure as shown in fig. 3.3. and if there are j coils, the total length change, ΔL, is the sum of the length changes in each coil given by (3.4)

$$\Delta L = \sum_{i=1}^{j} \Delta l\left(h - (i-1)\frac{\sqrt{3}}{2}D\right) \tag{3.4}$$

This is obtained by calculating the sum of the change in length of each fibre coil, Δl, which is a function of the distance from the neutral surface, z. Referring to the inset of fig. 3.3, the distance of the i^{th} coil from the neutral surface is $h - (i-1)\frac{\sqrt{3}}{2}D$. If the fibre coils of total length, L, are incorporated into the arm of a Michelson interferometer, then the phase of the return light at the input is given by (3.5)

$$\phi = 2nkL \tag{3.5}$$

The fractional phase change is then given by differentiation of (3.5) to obtain (3.6) and consists of two significant contributions from the axial length change of the fibre and the change in refractive index due to the stress-optic effect (3.7). A third term that describes the physical change in diameter of the waveguide can be shown to be negligible [3.14]

$$\frac{\Delta\phi}{\phi}=\left(\frac{\Delta L}{L}+\frac{\Delta n}{n}\right) \tag{3.6}$$

The second term (the stress-optic effect) in (3.6) can be shown to be 21% of the first term and of opposite sign, using (3.7), if the fibre is assumed to be under axial strain only [3.14] and values of the Pockels coefficient and Poisson ratio of the fibre are taken from table 3.1.

$$\Delta n=-\frac{n^3}{2}\left(\varepsilon(1-\nu_f)p_{12}+\nu_f\varepsilon p_{11}\right) \tag{3.7}$$

The normalized responsivity to pressure is then given by (3.8) where the factor of 0.79 accounts for responsivity reduction due to the stress-optic effect.

$$\frac{\Delta\phi}{\phi\Delta P}=(0.79)\frac{\Delta L}{\Delta P.L} \tag{3.8}$$

Using the relationships that pressure is force per unit area, force is the product of mass and acceleration and mass is the product of volume and density, the normalized acceleration responsivity, $\Delta\phi/\phi\Delta A$, can be calculated from (3.8). This assumes that the mass is uniformly distributed throughout the disc and is a reasonable assumption to make if the volume of glass in the disc is significantly less than the total volume of the disc. The non-symmetrical distribution of mass will also effect the cross-axis responsivity which is discussed in sec. 3.9. A pressure responsivity is then converted to an acceleration responsivity using,

$$\Delta P=2h\rho\Delta A \tag{3.9}$$

which gives a normalised acceleration responsivity in units of g^{-1} of,

$$\frac{\Delta\phi}{\phi\Delta A}=(9.8)\cdot(0.79)\frac{2h\rho}{\Delta P}\frac{\Delta L}{L} \tag{3.10}$$

where ρ is the disk density and h is half the disk thickness. It is useful to determine the form of (3.10) for a simplified case to establish the basic design parameters for the transducer. If the fibre is wound from the disk centre, i.e $b=0$ to the disk edge $c=a$ then evaluating (3.1), (3.3) and (3.8) for the strain in a single coil wound on the surface of the disk ($z=h$) gives[6],

$$\Delta l = \frac{\pi h a^4 \Delta P}{32 D.F_L}\left(\frac{7+3\nu}{1+\nu}\right) \tag{3.11}$$

where ν is the Poisson's ratio of the disk. Thus, from (3.10) the acceleration responsivity in units of g^{-1} is given by,

$$\left.\frac{\Delta\phi}{\Delta A}\right|_{\substack{fixed-\\centre}} = (9.8)\cdot(0.79)\frac{3\rho\pi nka^4(1-\nu^2)}{16EhD}\left(\frac{7+3\nu}{1+\nu}\right) \tag{3.12}$$

The equivalent expressions can be obtained for the remaining three disk supports. The angular displacement in a simple centre supported disk under a uniform force/pressure is [3.15],

$$\theta(r) = \theta_b F_4 + Q_b\frac{r^2}{F_L}F_6 - \Delta P\frac{r^3}{F_L}G_{14} \tag{3.13}$$

with the boundary condition, $\theta_b = \frac{-\Delta P a^3}{F_L C_7}\left[\frac{C_9\left(a^2-b^2\right)}{2ab} - L_{17}\right]$. This yields an acceleration responsivity given by,

$$\left.\frac{\Delta\phi}{\Delta A}\right|_{\substack{simple-\\centre}} = (9.8)(0.79)\frac{3\rho\pi nka^4}{16EhD}(\nu-1)(3\nu+7) \tag{3.14}$$

For a simple-edge supported disk under uniform pressure, the induced strain in a coil a distance z from the neutral surface is given by [3.16],

[6] The term in the brackets in (3.11) and (3.12) appeared incorrectly in the Journal paper. This has been corrected here.

$$\varepsilon(z)=\frac{2\Delta P}{E}\left[\frac{\nu}{4}-\frac{3z}{80h}\left(2+9\nu+\nu^2\right)-\frac{z^3}{16h^3}\left(2+\nu-\nu^2\right)\right]-\ldots\ldots \\ \frac{2\Delta P}{E}\left[\frac{3(1-\nu)z}{32h^3}\left[\frac{(3+\nu)a^2}{2}-\frac{(1+\nu)}{4}\frac{\left(a^4-b^4\right)}{\left(a^2-b^2\right)}\right]\right] \tag{3.15}$$

which yields an acceleration responsivity given by,

$$\left.\frac{\Delta\phi}{\Delta A}\right|_{\substack{simple-\\edge}}=-(9.8)(0.79)\frac{\pi h\rho nka^2}{ED}\left[\frac{3(1-\nu)(5+\nu)a^2}{16h^2}-\frac{1}{5}\left(\nu^2+21\nu-2\right)\right] \tag{3.16}$$

Finally, for the fixed-edge supported disk under a uniform pressure, the induced strain in a coil a distance z from the neutral surface is given by [3.16],

$$\varepsilon(z)=-\frac{3\Delta Pz(1-\nu^2)}{Eh^3}\left[\frac{a^2}{32}-\frac{\left(a^4-b^4\right)}{64\left(a^2-b^2\right)}+\frac{(2-\nu)z^2}{24(1-\nu)}-\frac{h^2}{24(1-\nu)}\right] \tag{3.17}$$

which yields an acceleration responsivity of,

$$\left.\frac{\Delta\phi}{\Delta A}\right|_{\substack{fixed-\\edge}}=-(9.8)(0.79)\frac{3\pi h\rho nka^2}{2ED}\left(\frac{a^2}{8h^2}+\frac{1}{3}\right) \tag{3.18}$$

Thus, the acceleration responsivity for a both the central and edge supported disk is proportional to: (i) the fourth power of the disk radius, (ii) the inverse of the disk thickness, (iii) the inverse of the Young's modulus and (iv) the disk density. Note that the second term in brackets in (3.16) and (3.18) adds only a small correction to the total responsivity, thus points (i) and (ii) approximately apply.

The values predicted by (3.12), (3.14), (3.16) and (3.18) can also be used for validation of the model.

3.4 Calculation of the Sensor Bandwidth

The dynamic operation of the flexural disk based accelerometer is modelled by assuming that its motion is analogous to that of a mass-spring system, shown in fig. 3.4 [3.17]. For a simple mass-spring system under harmonic excitation, with a viscous damping coefficient, ζ, and a

fundamental resonance frequency of ω_n, the frequency response in terms of the ratio of the relative displacement between the mass and the case, Z, to that of the forcing displacement, Y, is given by,

$$\left|\frac{Z}{Y}\right| = \frac{\left(\frac{\omega}{\omega_n}\right)^2}{\sqrt{\left[1-\left(\frac{\omega}{\omega_n}\right)^2\right]^2 + \left(2\zeta\,\frac{\omega}{\omega_n}\right)^2}} \tag{3.19}$$

and the phase between the two is given by [3.18],

$$\phi = \tan^{-1}\left[\frac{2\zeta\,\frac{\omega}{\omega_n}}{1-\left(\frac{\omega}{\omega_n}\right)^2}\right] \tag{3.20}$$

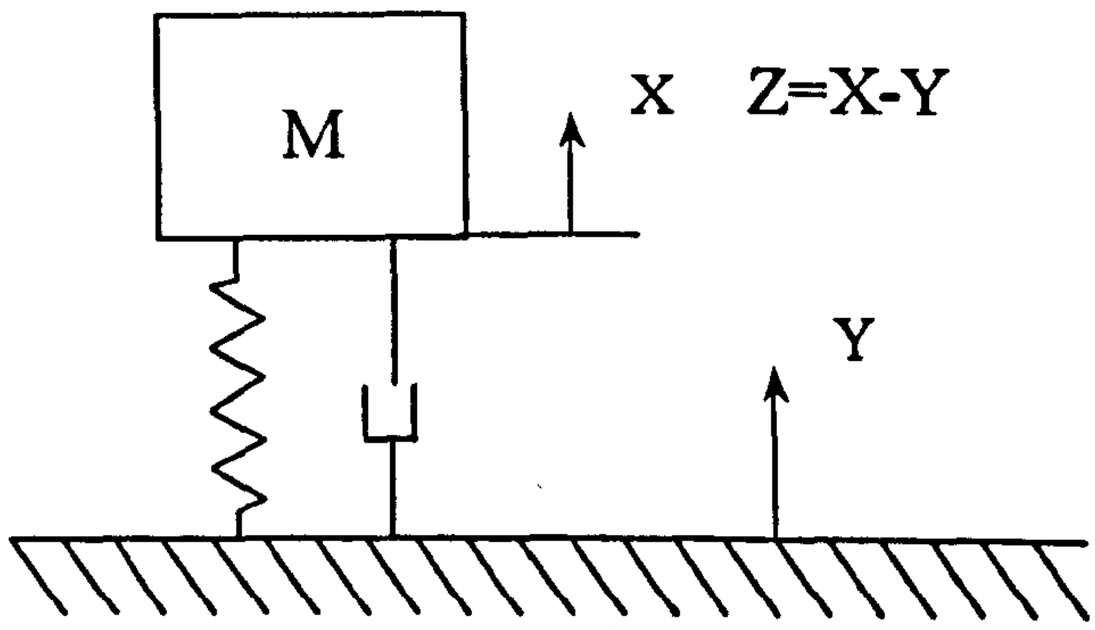

Figure 3.4: Simple Mass-Spring System

It can be shown using (3.19) that when $\omega << \omega_n$, the axial acceleration of the mass will be proportional to the forcing displacement and when $\omega >> \omega_n$, the displacement of the mass will be proportional to the forcing displacement. In the case of the flexural disk sensor, motion due to the inertia force of interest is transferred to the disk either through the edge or centre of the disk causing the disk to flex.

Equations (3.19) and (3.20) are plotted in fig. 3.5 as a function of normalised frequency, ω/ω_n, with various damping coefficients. For a sensor that exhibits this type of response, the bandwidth is limited, to a first approximation, by the resonance frequency.

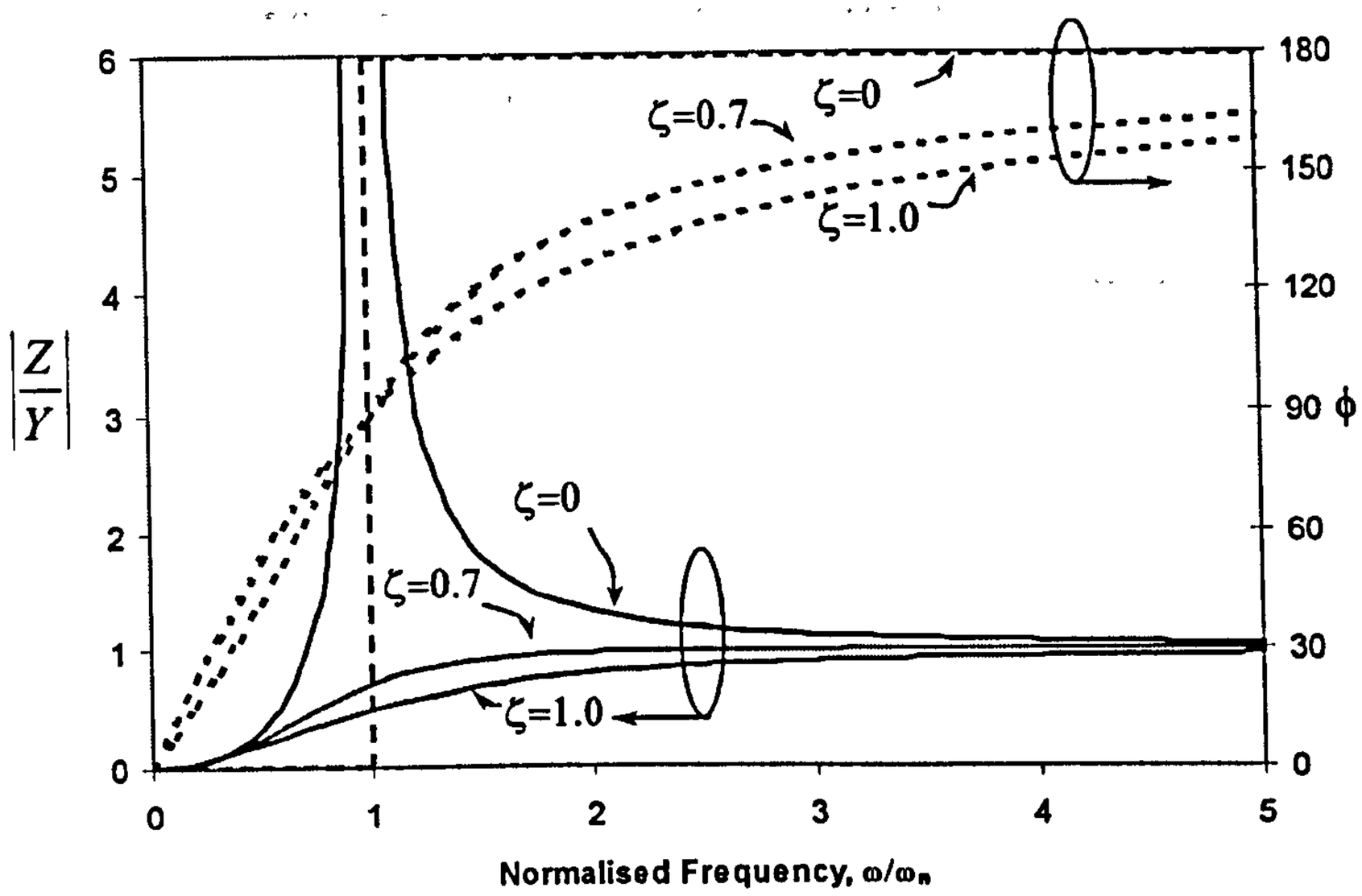

Figure 3.5: Mass-spring system frequency response.

It is desirable for the sensor to exhibit a linear phase response with frequency such that transient signals can be detected without significant distortion [3.19]. Referring to fig. 3.5, this is shown by the dashed line plots to occur when the viscous damping coefficient, ζ, is set to zero or 0.7, corresponding to critical damping. When ζ=0, the phase is zero for $\omega << \omega_n$ and π when $\omega >> \omega_n$ and when ζ=0.7, the phase is proportional to ω for $\omega << \omega_n$.

An approximate value for the fundamental resonance frequency of the disk sensor is given by (3.21) where Λ^2 is the resonance frequency parameter [3.20] and is tabulated in table 3.2 for the four disk boundary conditions under consideration.

$$\omega_n = \frac{\Lambda^2 (2.h)}{a^2} \sqrt{\frac{E}{12(1-\nu^2)\rho}} \qquad (3.21)$$

Table 3.2: Resonance frequency parameter

Boundary condition	Λ^2
Fixed edge support	10.216
Fixed centre support	5.76
Simply edge support	4.964
Simply centre support	3.24

It should be noted that the derivation of (3.21) neglects rotary inertia and shear forces [3.23] whose effect become more significant as the disk thickness increases in relation to the drive frequency [3.24]. For this reason (3.21) will predict a higher resonant frequency than that observed for the thick disks.

3.5 Treatment of the Composite Disk Structure

Calculation of the disk strains is complicated by the presence of the fibre coil, which makes the disk effectively composed of a composite material. The presence of this coil has the following effects: (i) changing the mechanical properties of the disk, i.e. Young's modulus, Poisson ratio and density; (ii) changing the position of the neutral surface if fibre is present on only one side of the disk; and (iii) affecting the assumption of the pressure-acceleration equivalence as described in sec. 3.3. In the models described here, the first issue is resolved by calculating a volume average of the mechanical properties using the rule of mixtures [3.21]. This has been carried out for the Young's modulus of the disk and adds a correction that becomes more significant as the length of fibre in the coil increases. For example, a disk of diameter 60 mm, thickness 5 mm and consisting of a single coil with 70m of optical fibre has a volume averaged Young's modulus of 1.6 times that of the encapsulant. This increases to 2.4 times that of the encapsulant with a 2mm thick disk and the same length of fibre. The rule of mixtures generally applies to uniform mixtures and in our case is a rather crude approximation since the stiffness of the fibre coil along the axis of the fibre is significantly higher than the stiffness normal (or transverse) to the fibre. Also, the fibre layer is not distributed evenly throughout the disk and is situated near one surface. However, the justification for its use here is to reduce the complexity of the proposed model. We have also neglected the effect of the fibre coil on the Poisson ratio and density of the disk in calculating the disk responsivities. This will not introduce significant error into the result, since we have already shown in (3.12), (3.14), (3.16) and (3.18) that the dependence of the responsivity on the Poisson ratio is weak. Also, the density of silica is ~2.3 times that of epoxy, thus the effect on the disk density due to the fibre coil is small. The second issue is taken into account by calculating the position of the neutral surface. As the thickness of

the fibre layer increases, the position of the neutral surface will move towards it. Without including this effect, the model described above will overestimate the responsivity of the disk since the coil strain is proportional to the distance from the neutral surface given by (3.2). The disk can be considered to be a two layer composite, where the top layer exhibits the properties of the fibre/epoxy composite calculated using the rule of mixtures and the bottom layer is epoxy. By using the technique of equivalent sections described in [3.22], the position of the neutral surface is found by locating the centre of area, i.e. centroid, of the equivalent section. This is then added as a correction to the distance of the fibre coil from the neutral surface in (3.4). For example, if the dimensions of the two layers are as shown in fig. 3.6a where the top and bottom layers have a Young's modulus of E_1 and E_2 respectively and $E_1 >> E_2$, the equivalent section can be drawn assuming it to made from a material of Young's modulus of E_2 as shown in fig. 3.6c.

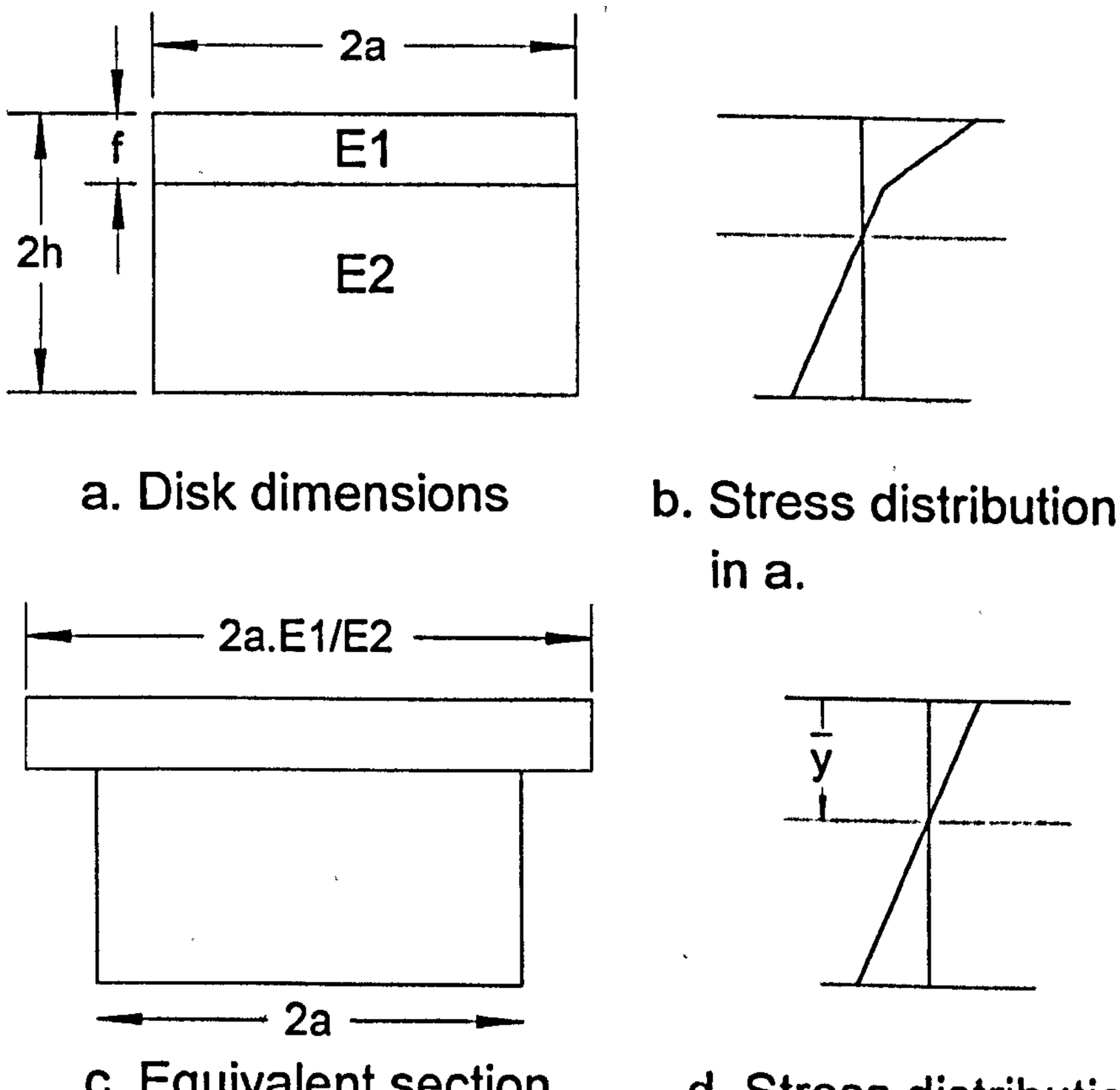

Figure 3.6: Equivalent section of composite disk.

The actual stress distribution obtained within the disk under bending is shown in fig. 3.6b and the neutral surface can be located as the point of zero stress. The stress distribution within the equivalent section is also shown in fig. 3.6d and although this does not represent the actual stress distribution in the disk, it can be used to locate the neutral surface. The centroid, $\bar{y}$, is then found by equating the product of the total area of the equivalent section and the distance to its centroid to the sum of the product of the areas of each layer of the disk and the distance to their centroid (3.22), where these distances are taken from a common reference point, i.e. the top of the disk,

$$\left(2a(2h-f)+\frac{E_1}{E_2}2af\right)\bar{y}=\left(\frac{E_1}{E_2}2af\right)\frac{f}{2}+2a(2h-f)\frac{(2h-f)}{2} \tag{3.22}$$

The distance to the neutral surface is therefore,

$$\bar{y}=\frac{E_1f^2+E_2(2h-f)^2}{2E_2(2h-f)+2E_1f} \tag{3.23}$$

3.6 Determination of Important Design Parameters of the Sensor

It is useful to make some preliminary observations on the responsivity and bandwidth that can be achieved with disks under different boundary conditions using the above analysis. A direct comparison will now be made between a fixed centre, a fixed edge and a simple edge supported disk configuration using the analysis given in section 3.3, by determining the highest responsivity obtainable from a disk under each boundary condition for a given resonant frequency. The equations for the strains in fixed edge and simple edge support can be found in [3.25].

In these calculations, the diameter of the disk and fibre length used are fixed and the disk thickness is varied such that the resonance frequency of each disk configuration is roughly equal. Table 3.3 shows this, together with the predicted responsivity of disks in each configuration. The simple edge support exhibits the highest responsivity followed by the fixed centre support. The responsivity of the disk in the fixed edge support is significantly lower than the other two since a significant proportion of the fibre is in the region of minimum strain in the disk, i.e. around the edge. In the simple edge and fixed centre supported disks, the majority of the fibre is in the region of highest strain. Highest responsivity is therefore obtained when

most of the fibre is in the region of largest displacement. Other combinations of the parameters used in table 3.3 arrive at the same conclusions as these.

*Table 3.3: Comparison between edge and centre supported disks**

Parameter	*Configuration*		
	Fixed-edge support	*Simple-edge support*	*Fixed-centre support*
Disk Thickness, mm	3.0	7.6	6.0
f_{res}, kHz	3.8	3.8	3.8
Responsivity, dB re 1 rad.g^{-1}	27.4	37.8	35.9

* Here E_{glass}=72 GPa, E_{epoxy}=3 GPa, D=135 μm, a=30mm, b=7.5mm, c=29mm, n=3, fibre length = 54.8m and other parameters are taken from Table 3.1.

3.7 Sensor Construction

The sensors were constructed by winding a thin coil of optical fibre between two closely-spaced plates and encapsulating the fibre layer in a disk of epoxy resin, type Ciba-Geigy HY1300 and CY 1301. The performance of the sensors is critically dependent on the boundary conditions and it is therefore important to ensure that the disk casing provides the required boundary conditions. For the prototype sensors, the edge-supported disks were bonded inside an aluminium can with adhesive. These were intended to be a fixed-edge support; however, the actual boundary condition was found to lie somewhere between fixed-edge and simple-support. Centrally-supported disks were constructed by encapsulating an aluminium support rod into the epoxy disk. Six sensors were constructed in total with different fibre lengths and disk thickness. Of the six sensors, four were edge-supported and two were centre-supported.

3.8 Acceleration Responsivity Calibration

The sensors were calibrated for acceleration using a vibration table, Brüel & Kjær 4809, and a reference B&K accelerometer model 8305 which exhibits a flat frequency response up to 25kHz. Each optical accelerometer was interrogated using a system configured in a pulsed reflectometric architecture [3.26] with heterodyne detection. The principle of operation of this system is shown in fig. 3.7.

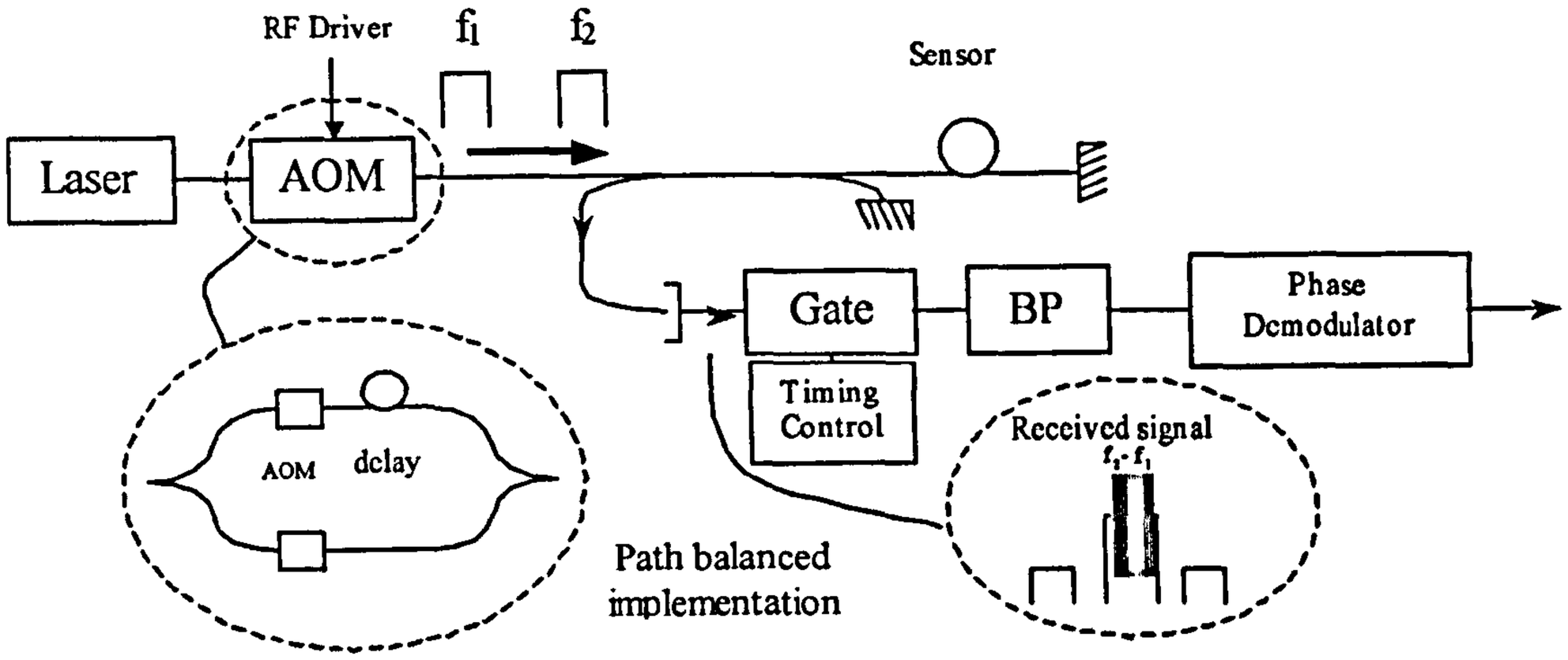

Figure 3.7: TDM interferometric interrogation system.

A directional coupler was spliced onto one lead of the sensor coil and mirrors were spliced onto the unused output port of the coupler and the other sensor lead, thus forming a Michelson interferometer. The sensor was then interrogated with two optical pulses, generated by an acousto-optic modulator (AOM) which also applies a frequency difference of 10 MHz ($\Delta f = f_1 - f_2 = 10\text{MHz}$) between them. The optical pulse is generated by driving each AOM by an RF pulse. The separation in time of the two pulses was set to twice the transit time in the interferometer which is achieved by choosing the fibre length in the delay coil within the path balance unit to be equal to twice the fibre length in the interferometer. The return optical signal from the sensor contains an overlap of the two pulses of different frequencies where one has reflected from the first mirror forming the reference and the other has travelled through the sensor. When detected, the overlapping pulses generate a heterodyne carrier signal that is phase modulated when a strain is applied to the sensor fibre. The heterodyne pulse is separated from the rest of the signal with a gate switch, the output of which is band pass filtered (BP) and phase demodulated.

In fig. 3.7, the optical pulses are shown to be generated by a single AOM; however, in this configuration the interferometer exhibits an effective path imbalance of twice the sensor fibre length. This may cause the phase resolution to be severely degraded by laser frequency noise (discussed later) but can be overcome with a path balanced implementation as shown in the inset in fig. 3.7. This generates the two pulses from the same time segment of light and can easily reduce the path imbalance to less than 1m.

The set-up used to calibrate the sensors is shown in fig. 3.8. The optical sensor was placed next to the reference accelerometer on the vibration table. To overcome polarisation fading in the interferometer, Faraday Rotation Mirrors (FRM) were used in place of the standard mirrors. This maintains a stable heterodyne carrier despite changes in the birefringence of the sensor fibre [3.27]. The laser source used was a diode pumped Nd:YAG Lightwave 120 laser.

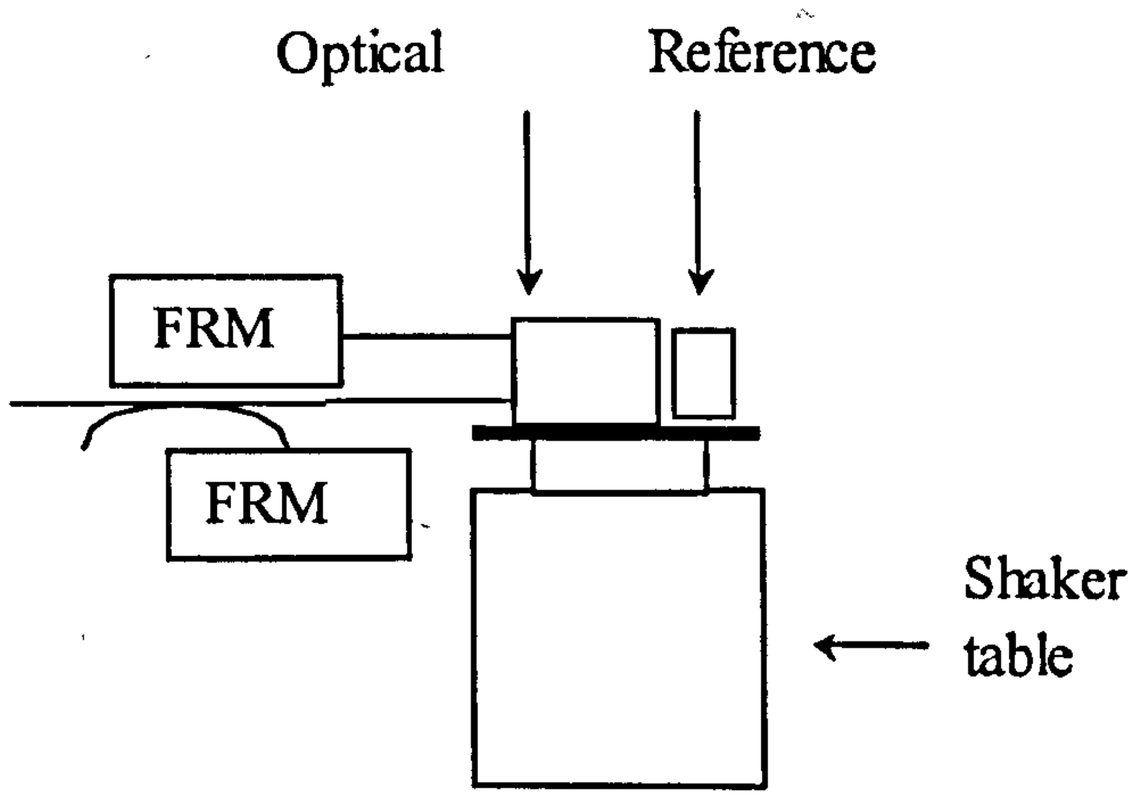

Figure 3.8: Experimental set-up

A frequency response was measured by applying a frequency sweep to the vibration table using a frequency analyser linked to a PC, to compare the demodulated output of the optical sensor to that of the reference accelerometer. In our measurements the frequency was swept from 100 Hz up to 5 kHz, limited at lower frequency by the phase demodulator low frequency cut-off and at the upper frequency by a resonance of the vibration table. The upper frequency exceeds the requirement for the bandwidth design aim (3 kHz). The sensors were placed close together such that they experience the same vibration field.

3.9 Results and Discussion

The calibrated acceleration responsivity of the six sensors is plotted in fig. 3.9 and 3.10, corresponding to edge and centre supported disks respectively as a function of frequency; the measured responsivities are tabulated in table 3.4 along with the predicted responsivities and resonant frequencies. The responsivity is expressed in units of optical phase-shift per unit acceleration and in the decibel unit referenced to 1 $rad.g^{-1}$.

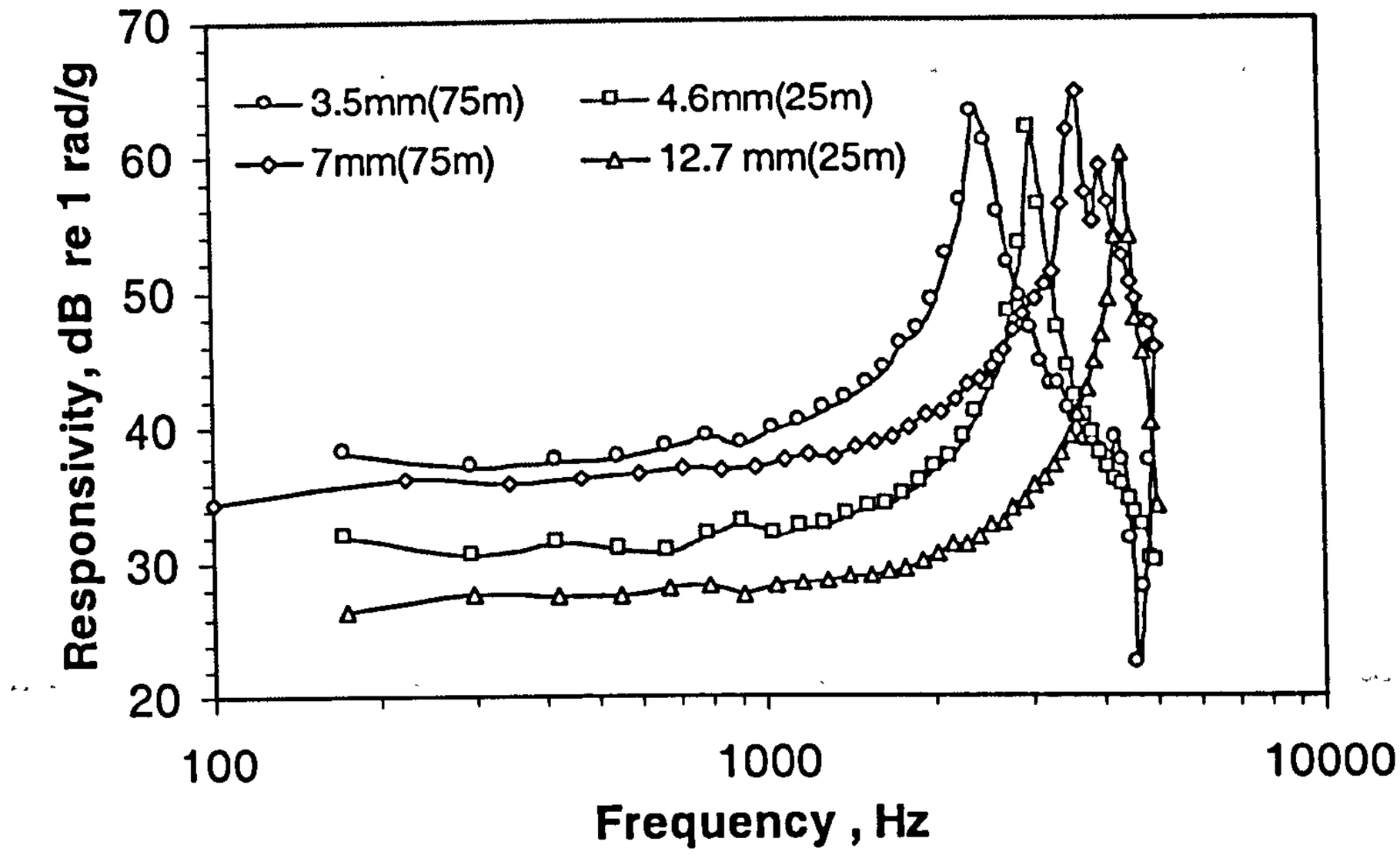

Figure 3.9: The responsivity of edge-supported flexural disk sensors for the disk thckness (and fibre length) shown.

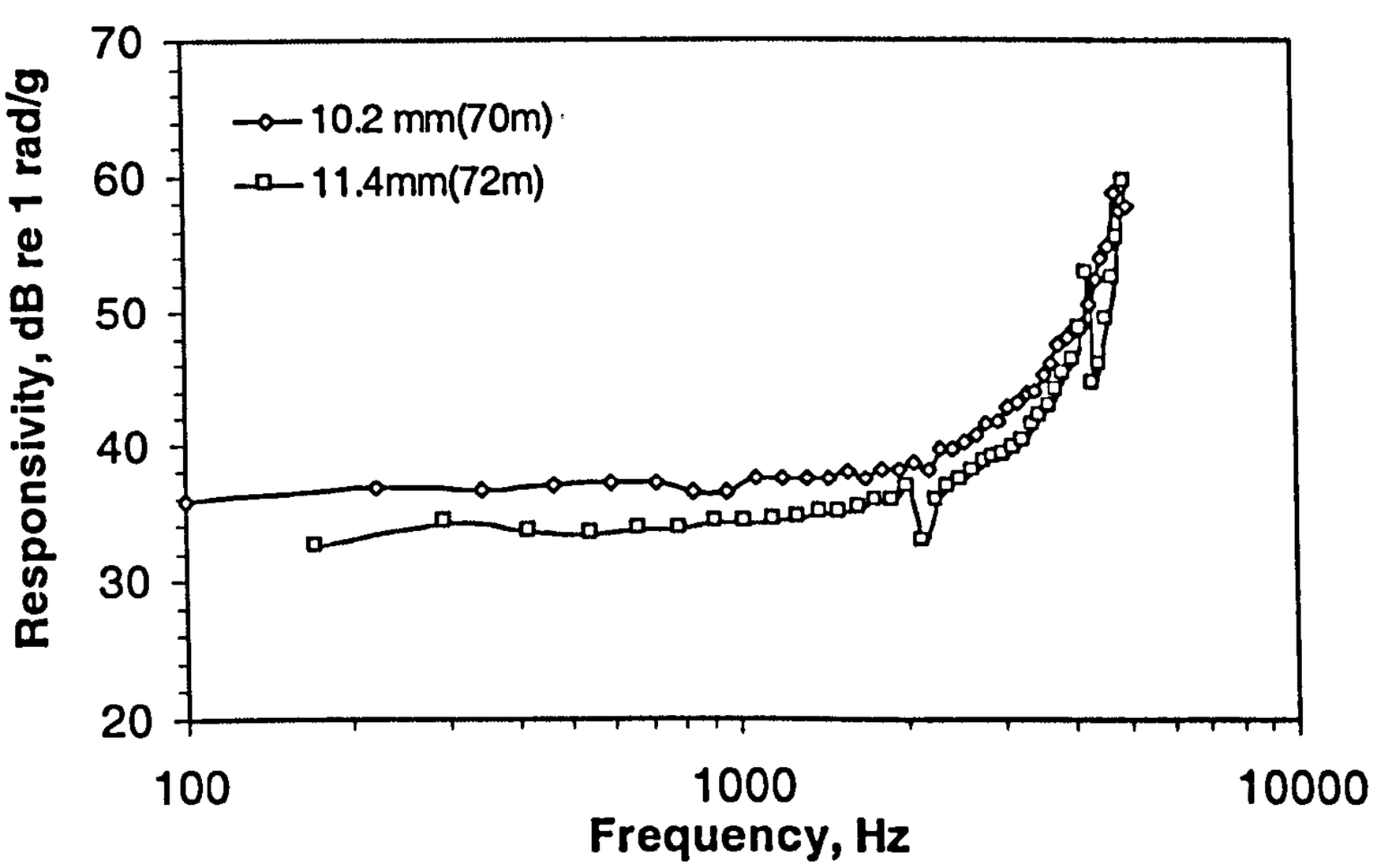

Figure 3.10: The responsivity of centre-supported flexural disk sensors for the disk thckness (and fibre length) shown.

*Table 3.4: Measured and calculated responsivities of optical accelerometers**

			Predicted Responsivity dB re 1 rad.g^{-1}			Predicted f_{ns} Hz		
Disk thickness/ mm	*Support*	*Measured responsivity*	*Simple*	*Fixed*	*Measured f_{ns}*	*Simple*	*Fixed*	*Fibre length /m*
3.5	Edge	39	38.8	26.9	2400	2250	4630	75*
4.6	Edge	32	32.4	24.5	3020	2400	4900	25+
7	Edge	37	38.6	26.9	3780	3930	8100	75*
12.7	Edge	28	28.6	20.1	4380	6200	12750	25+
10.2	Centre	37	44.7	35.4	>5000	3530	5880	70*
11.4	Centre	34	44.3	35.1	>5000	3900	6800	72*

* Here E_{glass}=72 GPa, E_{epoxy}=3 GPa, D*=135 μm, D+=165 μm and other parameters are taken from table 3.1.

The measured resonant frequency of the disks provides a good indication of the exact boundary condition imposed in practice. Referring to table 3.4, the measured resonant frequencies of the edge-supported disk are close to that predicted for a simply-supported disk, and the measured responsivity and that predicted for the simply supported disk confirm this. The disparity between the predicted and measured resonant frequency for the thickest edge-supported disk (12.7mm) is thought to be due to the reasons discussed in section 3.4. Hence, the resonant frequency (or bandwidth) cannot be increased without limit by increasing the disk thickness. We can see from the measured values of responsivity for the edge-supported disk the dependence of the responsivity on both the disk thickness and the fibre length. This illustrates the fact that the total phase change is proportional to the fibre length, but the fibre length also determines the maximum displacement of the disk (due to the increase in stiffness of the disk) for a given inertial force. Thus, increasing the fibre length will not necessarily lead to a proportional increase in the responsivity.

The resonant frequencies of the centre-supported disks cannot be observed directly due to the limited bandwidth of the measurement; however the measured responsivities are consistent with theoretical expectations for a fixed centre-support. The performance obtained from the centre-supported disk demonstrates that a higher overall combination of responsivity and bandwidth can be obtained with this type of disk than that from the edge supported disk.

The responsivity to other directions of acceleration (referred to as the cross-sensitivity) has been measured for the edge-supported disk by rotating the sensor by 90^0 such that the acceleration acts in a direction parallel to the disk. The calibration described above was then carried out and the result is shown in fig. 3.11.

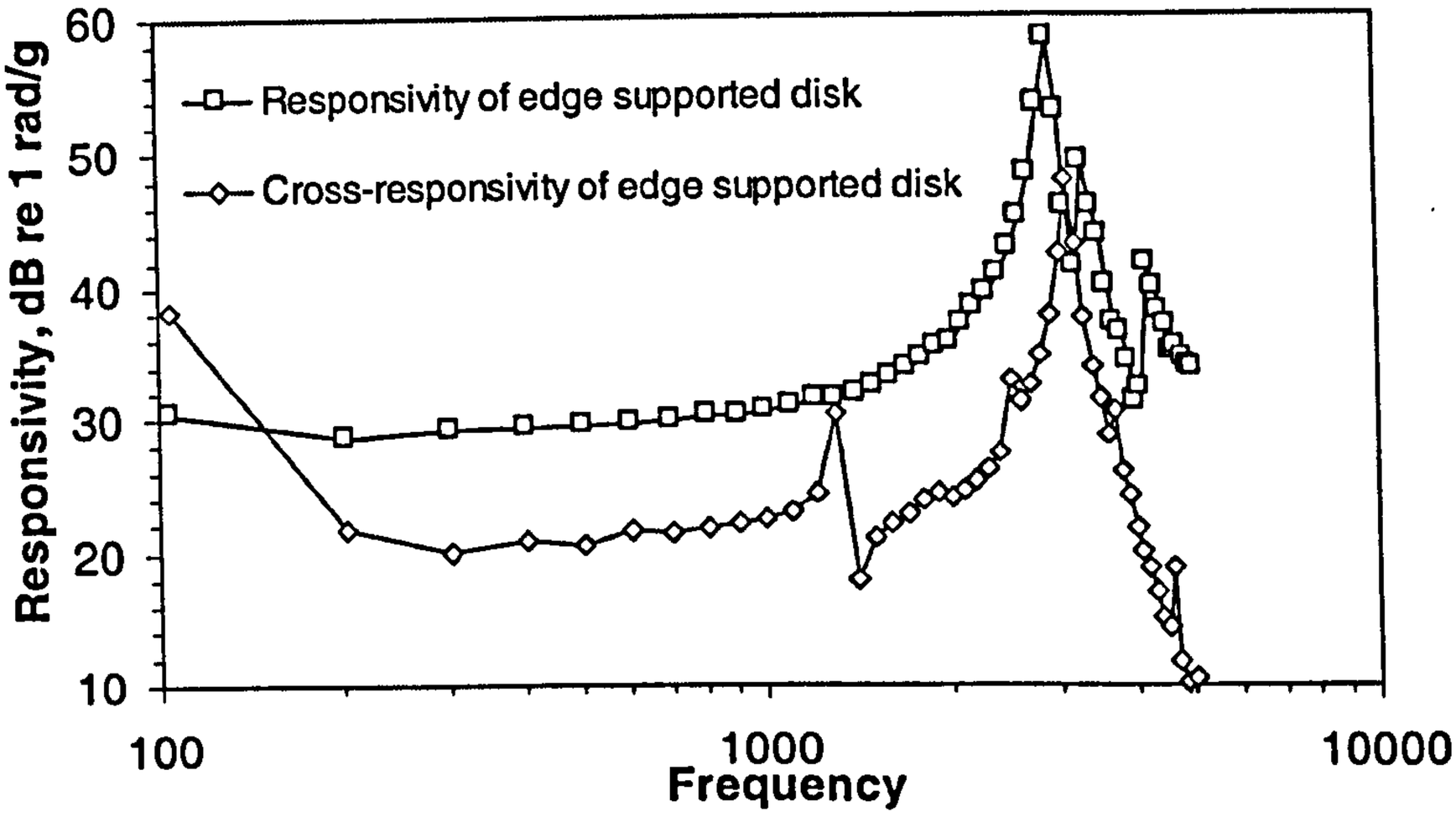

Figure 3.11: Edge Supported Disk Responsivity and Cross-Responsivity

The cross-responsivity was found to be typically 8 dB lower than the on-axis responsivity except for the presence of additional apparent resonances at 100 Hz and 1.3 kHz. The exact cause of the 1.3kHz resonance is unknown but the 100Hz resonance is thought to be due to the sensitivity of the connecting leads to the sensor and not a mechanical resonance of the sensor itself. Ideally, the sensor should exhibit zero cross-sensitivity; however, in-practice sensitivity to the measurand along this axis may arise for the following reasons; (i) the fibre coil may respond to the acoustic signal produced by the vibration table since there is no acoustic isolation; (ii) unwanted resonance of the case may enhance displacements of the disk; (iii) for a sensor with a single coil, the non-uniform distribution of the mass causes the centre of mass to be shifted towards the coil in the disk. An acceleration force acting parallel to the disk surface will, thus, induce rotational moments, causing the disk to bend; and (iv) deformation of the coil in the plane parallel to the surface of the disk may occur due to the anisotropic nature of the disk stiffness in the fibre layer. Cross-axis sensitivity caused by (i),(ii) and (iii) can be reduced by

appropriate design of the case and by incorporating a second coil on the opposite side of the disk, thus ensuring that the centre of mass is located in the central plane of the disk [2.28]. The effect described in (iv) is thought to impose a fundamental limit on the achievable cross-axis sensitivity and needs to be investigated further. A finite element analysis may provide a better insight into this effect.

3.10 Sources Of Noise In The Optical Sensor and Dynamic Range.

The primary focus of this work has centred on maximising the acceleration responsivity of the sensor, in order to achieve the highest acceleration resolution. The resolution is set by the sensor self-noise and in the case of optical fibre sensor systems, the dominant noise sources usually arise from the optical system architecture and components. The fundamental source of noise arises from the shot noise generated on detection of the signal which generates a shot current given by,

$$i_{shot} = \sqrt{2eR\bar{P}\Delta f} \qquad (3.24)$$

where e is the electron charge, R is the photodiode responsivity, Δf is the measurement bandwdith and $\bar{P}$ is the average optical power. The received optical power is set high enough such that the shot current dominates over the thermal noise generated in the detector pre-amplifier. However, in practice it is difficult to achieve the shot noise level due to other sources of noise such as RF oscillator noise (from the acousto-optic modulator drivers) or laser frequency noise, which is converted into phase noise by the interferometer. The latter noise source tends to dominate, particularly in multiplexed systems when a significant path imbalance is present in the interferometer. The diode pumped Nd:YAG laser, used in the calibrations exhibits a laser frequency-induced phase noise of less than 2 $\mu rad.Hz^{-1/2}$ for frequencies above 100 Hz and an interferometer path imbalance of 1m [3.29]; however, similar performance can be obtained from a significantly lower cost source based on a single longitudinal mode fibre DFB laser. These have been shown to exhibit a phase noise of less than 4 $\mu rad.Hz^{-1/2}$ for frequencies above 100 Hz and a 1m fibre path imbalance [3.30] and are investigated further in chapters 7 and 8.

In past systems, demodulation of the sensor signal has been carried out with analogue FM demodulators, based on frequency discriminators, that typically achieve a phase resolution of

less than 10 μrad.$Hz^{-1/2}$ and a dynamic range limited by the maximum frequency deviation over which the frequency discriminator can respond linearly (typically around 90 dB) [3.31]. However more recently, digital signal processing techniques have been applied to the demodulation process based on sampling of the modulated carrier signal, followed by applying a signal processing algorithm to extract the modulating signal phase. The dynamic range then becomes limited, ultimately, by the sampling rate. A single sensor based system has been developed for DERA by Sensor Dynamics[7] that achieved a phase resolution of 6 μrad.$Hz^{-1/2}$ and a dynamic range of greater than 120 dB, where we define the dynamic range as the ratio of the maximum recoverable narrowband signal with less than 1% total harmonic distortion to the noise floor normalised to a 1 Hz bandwidth [3.30]. DERA has also recently demonstrated a digital demodulator with the potential to demodulate simultaneously up to thirty channels with comparable performance to that of a single channel digital demodulator [3.32]. Similar performance using digital demodulation techniques has been demonstrated by other groups [3.33]. The incorporation of digital techniques provides enhancements in both the electronic phase resolution and dynamic range achievable from such sensors. In chapter 5, we present a detailed noise analysis of a multiplexed interferometric sensor array and indicate how phase resolutions approaching 10-20 μrad.$Hz^{-1/2}$ can be achieved.

3.11 Conclusion

In conclusion, six optical fibre accelerometers based on a flexural disk design have been demonstrated that exhibit responsivities in the range of 28 to 39 dB re 1 rad.g^{-1} with resonant frequencies between 2.4 kHz to greater than 5 kHz respectively. Simple analytical models have been written to calculate the responsivity and resonant frequency of each disk under various boundary conditions and the results of the model have been shown to be in good agreement with the measured responsivity for moderately thick disks. It has also been shown that the centrally supported disk sensor achieves a higher combination of responsivity and bandwidth than the equivalent edge supported disk. For a centrally supported disk with a flat frequency response up to 2 kHz and a responsivity of 37 dB re 1 rad.g^{-1}, an interferometric phase resolution of 10μrad.$Hz^{-1/2}$ at 1 kHz would give a minimum detectable acceleration of 141ng.$Hz^{-1/2}$. This could, in principle, be reduced by up to a factor of two by attaching a second coil to the opposite side of the disk and operating them in a push-pull configuration. Taking the

[7] SensorDynamics Ltd, 3 Abbas Business Centre, Itchen Abbas, Winchester, Hampshire, SO21 1BQ, UK

dynamic range as 120dB, the maximum narrowband signal recoverable would be about $0.14g.Hz^{-1/2}$ dependent on frequency. The cross-responsivity of the edge-supported disk has also been measured to be at least 8 dB lower than the on-axis responsivity and methods of improving this have been discussed in the text.

Thus, we have demonstrated a sensor that meets the requirements of size and bandwidth. We believe that by adding a second coil to the opposite side of the disk and operating them in a push-pull configuration as a Michelson interferometer will also reduce the cross-axis responsivity further due to both the common-mode rejection this configuration provides and the improvement in symmetry for the reasons described above.

References

[3.1] R.J. Urick, *Principles of Underwater Sound*, 3rd ed. McGraw-Hill, chap. 3, 1983.

[3.2] P.J. Nash, 1996 "Review of interferometric optical fibre hydrophone technology" *IEE Proc. Radar, Sonar Navig.* 143 (3) 204-209

[3.3] D.A. Brown, 1996 "Fiber optic accelerometers and seismometers" *Acoustic Particle Velocity Sensors: Design, Performance and Applications,* AIP Conf. Proc. 368, Mystic CT, 260-273

[3.4] D.L. Gardner and S.L. Garrett, 1987 "Fiber optic seismic sensor" *Fiber Optic and Laser Sensors V* SPIE vol. 838 271-278

[3.5] R.D. Pechstedt, D.A. Jackson, 1995 "Performance analysis of a fibre optic accelerometer based on a compliant cylinder design" *Rev. Sci. Instrum.* 66 (1) 207-214

[3.6] D.A. Brown, S.L. Garrett, 1990 "An interferometric fiber optic accelerometer" *Fiber Optic and Laser Sensor VIII* SPIE Vol. 1367 282-288

[3.7] S.T. Vohra, B. Danver, A. Tveten, A. Dandridge, 1996 "Fiber Optic Interferometric Accelerometers" *Acoustic Particle Velocity Sensors: Design, Performance and Applications,* AIP Conf. Proc. 368, Mystic, CT, 285-293

[3.8] S.T. Vohra, B. Danver, A.B. Tveten, A. Dandridge, 1996 "High Performance Fiber Optic Accelerometers", *Proc. 11th Conf. Optical Fibre Sensors,* Japan Society of Applied Physics, Th5-5, 654-657

[3.9] Y. Shindo, N. Tsuchida, K. Dobashi , H. Kamata, 1997 "Fiber-Optic Accelerometer", *Proc. 12th Conf. Optical Fibre Sensors,* OSA Technical Digest, Vol. 16, Washington DC, 202-205

[3.10] D.A. Brown, T. Hofler, S.L. Garrett, 1988 "Fiber optic flexural disk microphone" *Fiber Optic and Laser Sensors VI* SPIE vol. 985 172-182

[3.11] D.A Brown, T Hofler, S.L. Garrett, 1989 "High-Sensitivity, Fiber-Optic, Flexural Disk Hydrophone with Reduced Acceleration Response" *Fiber and Integrated optics* 8 169-191

[3.12] W.C. Young, *Roark's Formulas For Stress and Strain 6th ed.* McGraw-Hill, pp. 408, case 2l, 1989.

[3.13] Ref. [3.12], pp. 398.

[3.14] C.D. Butter and G.B. Hocker, 1978 "Fiber optic strain gauge" *Applied Optics* 17 (18) 2867-2869

[3.15] A.E.H.Love, *Mathermatical Theory of Elasticity* Cambridge University Press, 1934

[3.16] Ref. [3.12] case 2k

[3.17] W.T. Thomson, *Theory Of Vibration With Applications 4th ed*, Chapman and Hall, pp. 17, 1993.

[3.18] Ref. [3.15], pp. 66-67.

[3.19] Ref [3.15], pp. 83-84.

[3.20] Leissa A, "Vibration of plates", NASA Technical Document SP-160 N70-18461, chap. 2, 1969.

[3.21] S.W. Tsai, H.T. Hahm, *Introduction To Composite Materials*, Technomatic Publishing, pp. 388-394, 1980.

[3.22] P.P. Benham, R.J. Crawford, *Mechanics Of Engineering Materials*, Longman Scientific and Technical, pp. 129-132, 1980.

[3.23] Ref. [3.18], pp. 334.

[3.24] Skudrzyk E, *Simple and Complex Vibratory Systems*, The Pennsylvania State University Press, chap. 8, 1968.

[3.25] Ref [3.12], for fixed edge support, case 10b, p. 429, for simple edge support, case 10a, p.429, for simple centre support, case 2k, p. 408.

[3.26] J.P. Dakin, C.A. Wade, M. Henning, 1984 "Novel optical fiber hydrophone array using a single laser source and detector" *Electronics Letters* 20 (1) 53-54

[3.27] M. Martinelli, 1994 "Time-Reversal For The Polarization State In Optical Fibre Circuits", *Proc. 10th Conf. Optical Fibre Sensors*, 312-318

[3.28] S.T.Vohra, B.Danver, A.Tveten, A.Dandridge, 1997 "High performance fibre optic accelerometers" *Elec. Lett.* 33 (2) 155-157

[3.29] A.D. Kersey, K.J. Williams, A. Dandridge, 1993 "Characterisation of a diode laser pumped Nd:YAG ring laser for fibre sensor applications", *Proc. 9th Conf. Optical Fibre Sensors*, IROE-CNR, Firenze, Italy, 255-258

[3.30] G.A. Cranch, P.J. Nash, DERA internal report, June 1999.

[3.31] M.L. Henning, C. Lamb, 1988 "At-sea deployment of a multiplexed fiber optic hydrophone array", *Proc. Conf. Optical Fiber Sensors*, Opt. Soc. America, 1988 Tech. Digest Series, vol. 2, Washington D.C.,pp. p.1/84-91

[3.32] G.A. Cranch, DERA internal memorandum, August 1999.

[3.33] J. Bush, A. Cekorich, C. Kirkendall, 1997 "Multi-channel interferometric Demodulator", *Third Pacific Northwest Fiber Optic Sensor Workshop*, SPIE Vol. 3180, 19-29

Chapter 4

IN-FIBRE BRAGG GRATING PRESSURE SENSORS†

Abstract: In this chapter we investigate the enhancement obtained in the responsivity to pressure and temperature of an in-fibre Bragg grating (IFBG) when the fibre is coated with an elastic material. We demonstrate both theoretically and experimentally that amplification of the static pressure responsivity by a factor of 18.8±21% is possible with a compliant polyeurethane coating, approximately 40 times the diameter of the fibre. We also show theoretically that the responsivity to temperature is likely to be enhanced by a factor of between 10 and 20. Finally, a discussion is given on the various practical aspects of a coated pressure/temperature sensor such as sensor response time, linearity and long-term stability. We discuss how these techniques may also be applied to an in-fibre laser sensor configured as an acoustic sensor.

4.1 Introduction

Early work on interferometric fibre-optic sensors was aimed at developing acoustic sensors for hydrophone applications, and investigated the use of compliant coatings on fibres incorporated into the arm of a fibre interferometer to enhance the responsivity of the fibre to pressure. Typically an amplification factor of ~30 was obtained referenced to a bare fibre [4.1-3,4.5] using a compliant coating a few millimetres thick. Taking the bare fibre responsivity from section 2.6, the acoustic responsivity of a 1m coated fibre is -5×10^{-4} rad.Pa^{-1} (assuming λ =1550 nm and taking the data from table 4.1). Assuming an interferometric phase resolution of 10 μrad.Hz$^{-1/2}$, the pressure resolution would be 20 mPa.Hz$^{-1/2}$, which is generally inadequate from most sonar applications (c.f. chap. 1). The need for higher resolution and a sensor head smaller than the acoustic wavelength led to the development of the air-backed mandrel hydrophone, which can provide amplification factors of ~100. Taking the responsivity

†This chapter contains a transcript of the paper D.J.Hill and G.A.Cranch, 1999 "Gain in hydrostatic pressure sensitivity of coated fibre Bragg grating" published in Electronics Letters 35 (15) 1268-1269 and re-edited to include details of the modeling and experimental set-up.

of the mandrel hydrophone as 0.5 rad.Pa^{-1} (typical for 100m of fibre), this would achieve a pressure resolution of 20 μPa.Hz$^{-1/2}$ which is adequate for most sonar applications.

Further reduction in the size of the transducer without compromising sensor performance (such as resolution) is desirable for many sonar arrays. In particular the size and weight of a towed array can be reduced with smaller transducers. The in-fibre Bragg grating (IFBG) sensor may allow the transducer size to be reduced significantly. In an interferometric sensor, the reflective properties of the grating can be used as a replacement for the directional coupler to define the sensor region of a fibre, in a reflectometric architecture [4.6]. Alternatively, the IFBG can be used as a sensor due to the dependence of the Bragg resonance on temperature, pressure and strain. The IFBG is typically a few centimetres in length, which leads to the possibility of near point sensing of pressure and temperature [4.4]. Since the measurand is encoded on the wavelength (which is an absolute parameter), this may allow for accurate dc tracking of measurands; however stable (i.e. low drift) wavelength measurement instrumentation must be used to achieve high accuracy. We discussed the typical performance of the IFBG based acoustic sensor in section 2.14, when a decoding interferometer is used and this revealed that the resolution is limited to ~150 Pascals. We also showed in section 2.14, that a bare in-fibre laser (IFL) could be used as an acoustic sensor; however, further mechanical amplification is required to increase the pressure resolution to meet sonar requirements. The compliant coating provides a simple method of amplifying the responsivity of the IFBG and IFL sensors and is therefore worthy of investigation. Also, use of a low drift wavelength tracking interrogation scheme may also permit high-resolution measurement of temperature.

We first review, in section 4.2, the theory used to determine the amplification in quasi-static pressure sensitivity of a coated optical fibre and apply this to the IFBG. We then extend this model to include the effects of thermal expansion of the layers and determine the responsivity to temperature of the coated IFBG in section 4.3. Published experimental data is used to validate this model. We then describe the experimental arrangement used to calibrate the coated fibres for responsivity to pressure, in section 4.4; and finally in section 4.5 we present the results for two different coating materials.

4.2 Modelling of the Quasi-Static Pressure Sensitivity Enhancement in Coated Fibre Bragg Gratings

A coated fibre can be approximated as being a composite cylindrical structure comprising a homogenous glass core with one or more homogenous elastic coatings. It is thus required to determine the strains induced in the glass core when the composite structure is acted on by an external pressure, ΔP_o. This is shown in fig. 4.1 for a fibre with a single coating. The strains are then substituted into the responsivity equation for the IFBG.

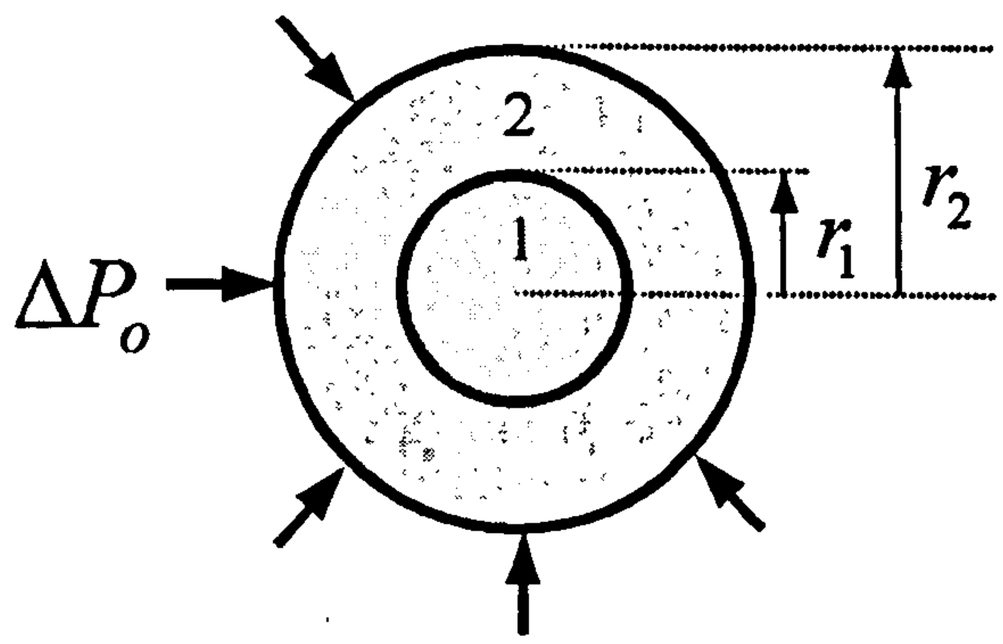

Figure 4.1: Cross-section of fibre with a single coating

To determine the strains in this composite structure we use the plain strain model described in [4.3] which is based on a linear elastic model and is valid in our case since the induced strains are small (typically a few 100 με). It is also assumed that the mechanical properties of the fibre and coating are isotropic and that each layer is homogenous. The fibre is actually made up of a separate core and a cladding material, such that the core has a slightly higher refractive index than the cladding. The presence of index raising impurities in the core, such as Germanium, will modify the mechanical properties slightly; however, for this analysis we assume that the core and cladding have the same mechanical properties. This assumption is considered to be valid since the mismatch in the mechanical properties of these two layers is small compared with the mismatch in mechanical properties of the coating materials and the fibre. The plain strain model is two dimensional and assumes circular symmetry about the fibre axis. It also assumes that the end effects are negligible; that is, the end effects do not affect the strain distribution a long way from the end. Saint Vernant's principle states that the strain distribution will not be modified at distances greater than the maximum linear dimension of the end. This is valid in our case since the length of the coated IFBG is much larger that its diameter. The plain strain

model has been shown to produce results that are within 1% of an exact 3D model, which included end effects [4.5].

The general stress components for an elastic multi-layered cylinder, in cylindrical coordinates, are given by,

$$\sigma_{ri} = \frac{\alpha_i}{r^2} + \beta_i(1+2\log r) + 2\gamma_i \tag{4.1}$$

$$\sigma_{\theta i} = -\frac{\alpha_i}{r^2} + \beta_i(3+2\log r) + 2\gamma_i \tag{4.2}$$

$$\sigma_{zi} = \delta_i \tag{4.3}$$

where i is the layer number and α_i, β_i, γ_i and δ_i are constants for each layer to be determined. The associated strain components in terms of the Young's modulus, E, and Poisson's ratio, ν, are then given by Hooke's law,

$$\varepsilon_{ri} = \frac{1}{E_i}\left(\sigma_{ri} - \nu_i(\sigma_{\theta i} + \sigma_{zi})\right) \tag{4.4}$$

$$\varepsilon_{\theta i} = \frac{1}{E_i}\left(\sigma_{\theta i} - \nu_i(\sigma_{ri} + \sigma_{zi})\right) \tag{4.5}$$

$$\varepsilon_{zi} = \frac{1}{E_i}\left(\sigma_{zi} - \nu_i(\sigma_{ri} + \sigma_{\theta i})\right) \tag{4.6}$$

The radial displacement is also given by,

$$s_{ri} = \int \varepsilon_{ri} dr \tag{4.7}$$

It can be shown that $\beta = 0$ to ensure single valued results and we set $\alpha_1 = 0$ to avoid the singularity at $r = 0$.

First consider an uncoated cylinder, in which case $\sigma_r = \sigma_\theta = 2\gamma$ and $\sigma_z = \delta$. We now define two different boundary conditions for the ends of the fibre:

(i) Hydrostatic boundary conditions or HBC (sometimes referred to as the fibre being axially free) where the applied pressure is isotropic. Therefore, $\sigma_r\big|_{r=r_1} = -\Delta P_o$ and hence $\sigma_r = \sigma_\theta = -\Delta P_o$. Balancing the force on the end of the cylinder yields, $\sigma_z = -\Delta P_o$. Thus using (4.4), (4.5) and (4.6), the strain components are

$$\varepsilon_r = \varepsilon_\theta = \varepsilon_z = -\frac{\Delta P_o}{E}(1-2\nu)$$

(ii) Radial boundary conditions or RBC (sometimes referred to as the fibre being axially constrained) where $\sigma_z = 0$ (i.e. zero end pressure) yields $\varepsilon_r = \varepsilon_\theta = -\frac{\Delta P_o}{E}(1-\nu)$ and $\varepsilon_z = \frac{2\nu\Delta P_o}{E}$.

For a multi-layer cylinder, the unknown constants are determined using the following boundary conditions:

1. The radial stress at the outermost boundary is equal to the pressure, $\sigma_{rm}\big|_{r=r_m} = -\Delta P_o$

2. Continuity of radial stress at each boundary, $\sigma_{ri}\big|_{r=r_i} = \sigma_{r(i+1)}\big|_{r=r_i}$ where $i = 1,2,....,(m-1)$

3. Continuity of radial displacement at each boundary, $s_{ri}\big|_{r=r_i} = s_{r(i+1)}\big|_{r=r_i}$ where $i = 1,2,....,(m-1)$

4. The axial strain in each layer must be equal

5. Balancing of forces on the ends of the fibre such that $\sum_{i=1}^{m} A_i\sigma_{zi} = -\Delta P_o$ for HBC and $\sum_{i=1}^{m} A_i\sigma_{zi} = 0$ for RBC where A_i is the cross sectional area of the layer.

For the case of a fibre with a single coating, as shown in fig. 4.1, the boundary conditions reduce to,

1. $\sigma_{r2}\big|_{r=r_2} = -\Delta P_o$

2. $\sigma_{r1}\big|_{r=r_1} = \sigma_{r2}\big|_{r=r_1}$

3. $s_{r1}\big|_{r=r_1} = s_{r2}\big|_{r=r_1}$

4. $\varepsilon_{z1} = \varepsilon_{z2}$

5. $\pi r_1^2 \sigma_{z1} + \pi\left(r_2^2 - r_1^2\right)\sigma_{z2} = -\pi r_2^2 \Delta P_o$

Combining (4.1), (4.2), (4.3), (4.4), (4.5), (4.6) and (4.7) with the above boundary conditions, a system of five linear equations are derived which are solved to determine the five unknowns γ_1, δ_1, α_2, γ_2 and δ_2 and hence the strains in the fibre layers. These are then substituted into the normalised responsivity equation (2.111) for an IFBG derived in section 2.14,

$$\frac{\Delta\lambda}{\lambda_B} = \varepsilon_z - \frac{n^2}{2}\left[\left(p_{11} + p_{12}\right)\varepsilon_r + p_{12}\varepsilon_z\right] \tag{4.8}$$

where p_{11} and p_{12} are the Pockel's coefficients of the fibre core and n is the effective refractive index of the fibre core. λ_B is the Bragg wavelength of the IFBG, given by $2n\Lambda$ where Λ is the grating pitch. Thus, for an uncoated fibre, the normalised responsivity of an IFBG under hydrostatic boundary conditions is[8],

$$\frac{\Delta\lambda}{\lambda_B} = -\frac{\Delta P_o(2\nu - 1)}{E}\left[1 - \frac{n^2}{2}\left(p_{11} + 2p_{12}\right)\right] \tag{4.9}$$

The precise values of the Pockel's coefficients for a photosensitised fibre are difficult to determine; however they are likely to be very similar to those of a standard fibre. Thus, using

[8] This is equivalent to (2.27).

the material parameters for a standard fibre, given in table 4.1, which were taken from [4.5] and substituting them into (4.9) yields $\Delta\lambda/(\Delta P_o \lambda_B) = -2.8\times10^{-12}$ Pa^{-1}. The corresponding value assuming radial boundary conditions is $\Delta\lambda/(\Delta P_o \lambda_B) = 8.1\times10^{-12}$ Pa^{-1}. Shown in fig. 4.2 is the amplification achieved (assuming HBC), relative to that of a bare grating, as a function of the ratio of the diameter of the coating to the fibre for two coating materials, (i) Scotch Cast 815 Resin and (ii) APT-Flex F17 polyurethane. The values of the Young's modulus and Poisson ratio of the coating materials were estimated using previously published data [4.7] and from discussions with the suppliers and are also given in table 4.1.

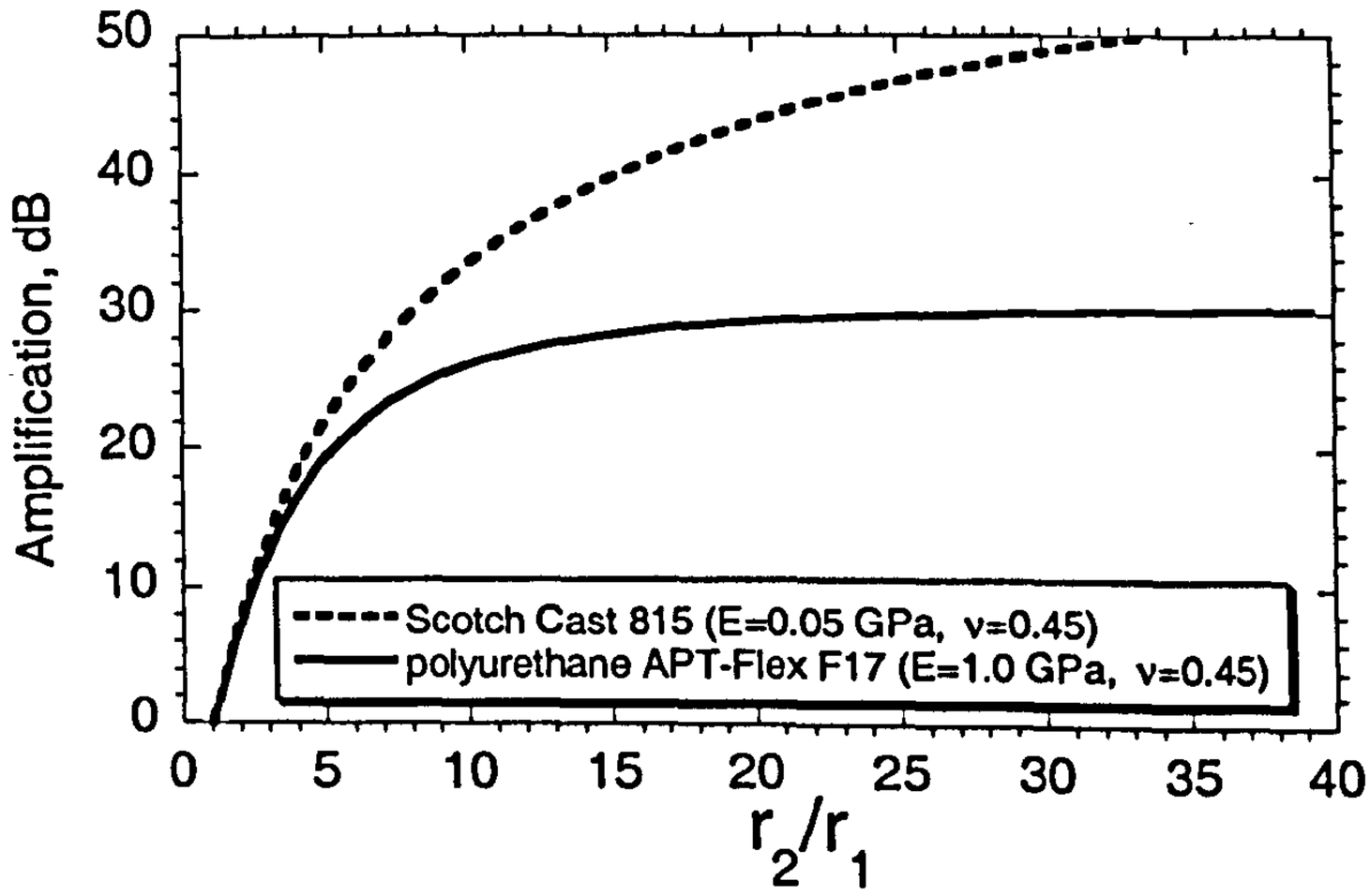

Figure 4.2: Amplification of the responsivity to static pressure change of an IFBG for two coating materials.

Table 4.1: Material parameters

Material	Parameter	Value	Unit
Fibre	n	1.456	
	r_1	62.5	μm
	p_{11}	0.121	
	p_{12}	0.27	
	E	72	GPa
	ν	0.17	
	α	10.2×10^{-7}	K^{-1}
	$\frac{1}{n}\frac{\partial n}{\partial T}\Big\vert_\rho$	0.68×10^{-5}	K^{-1}
Scotch Cast 815	E	0.05	GPa
	ν	0.45	
APT Flex F17	E	1	GPa
	ν	0.45	

Thus, between 33 dB and 55 dB[9] of amplification may be obtained by applying a single coating of these materials. It is also useful to observe the trend in the amplification obtained as a function of both Young's modulus and Poisson ratio. This is shown in fig. 4.3 for the case of HBC. The largest amplification can be achieved by using materials with a low Young's modulus and low Poisson ratio or equivalently materials with a low bulk modulus, (typically K <~3GPa) where $K = E\left(3(1-2\nu)\right)^{-1}$. Conversely, materials with $\nu \approx 0.5$, such as rubber, yield a low amplification since they are incompressible and hence generate low axial strain in the fibre. This is equivalent to saying that the material has a high K. For materials with ν <0.5; as the coating thickness increases, the amplification achieved will reach the "thick coating" limit beyond which the responsivity is no longer a function of the coating thickness and is only dependent on K. The coating thickness for which this limit is reached increases as the Young's modulus of the coating decreases.

9 To convert a linear pressure amplification factor to its equivalent dB unit, one must take $20\log_{10}$ of the amplification factor. This ensures consistency with the definition of acoustic responsivity in dB re **.Pa^{-1}, which is also calculated using $20\log_{10}$. The origin of this lies in the definition of sound pressure level discussed in section 2.4. Acoustic intensity (α pressure^2, see (2.9)) is therefore calculated using $10\log_{10}$. In general, when referring to a pressure sensor it is usually more familiar to use linear units; however, in the case of acoustic sensors, quantifying responsivity and amplification in dB's is more widely used. Since our main focus is on the acoustic application we shall use the decibel unit for expressing pressure responsivity and the linear unit for temperature responsivity.

Thus, a material with a low bulk modulus will provide a high amplification; however, a material with a very low Young's modulus will require a very thick coating to achieve the "thick coating" limit.

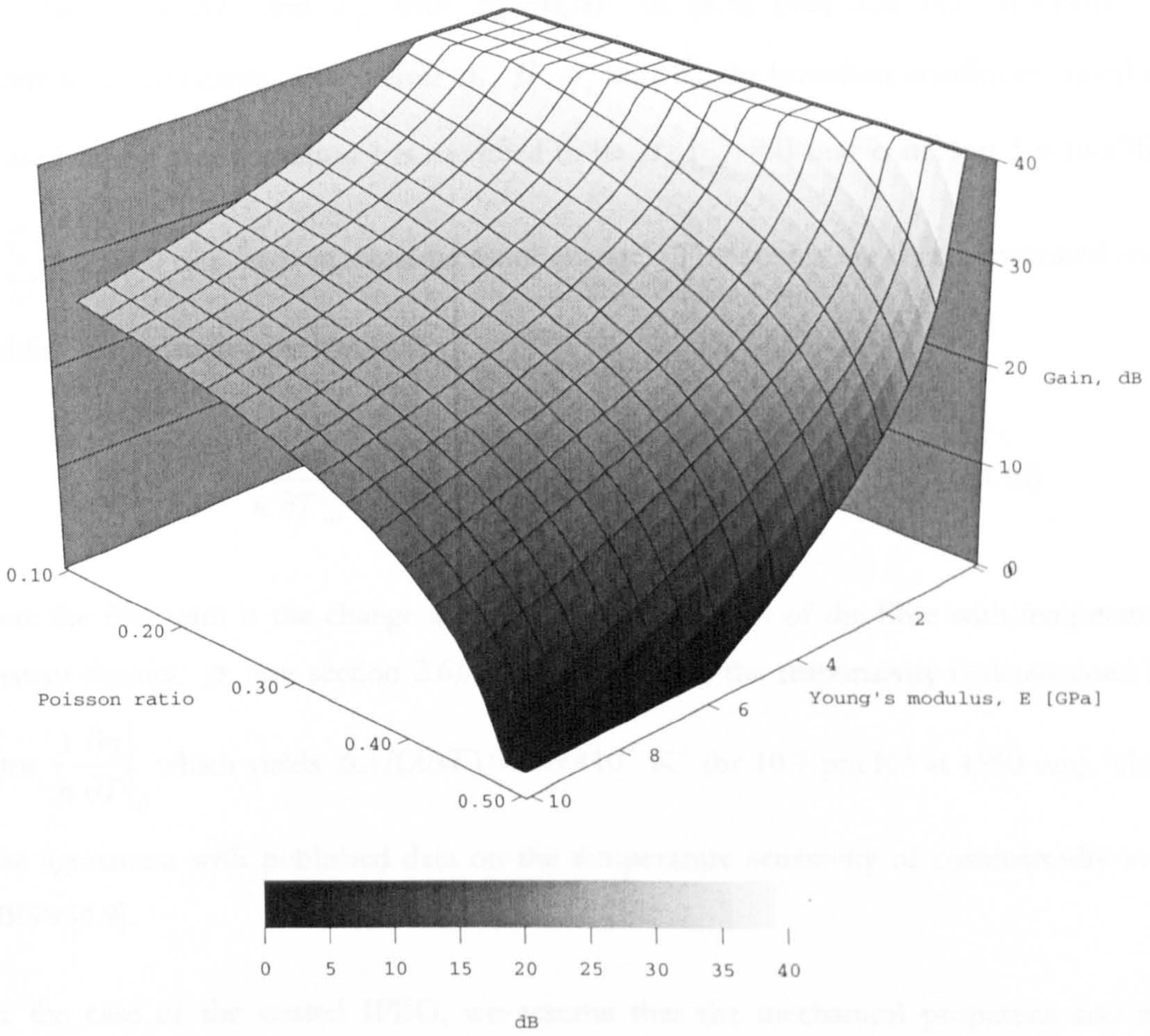

Figure 4.3: Amplification as a function of Young's modulus and Poisson ratio of the coating material

4.3 Modelling of the Quasi-Static Temperature Sensitivity Enhancement of Coated Fibre Bragg Gratings

Applying a compliant coating to the IFBG will also affect its responsivity to temperature due to the large mismatch in thermal expansion coefficient between the fibre and the coating. It is possible to modify the model presented above to include the effects of the thermal expansion of each layer. This approach was first presented in [4.8] where it was used to predict the change in responsivity to temperature of coated fibres. Firstly, we assume that the coating is much longer than the grating (we shall return to this assumption later when we consider the case

where the coating length is comparable to the IFBG length). By assuming the fibre is in thermal equilibrium with the coatings, then for a change in temperature of ΔT, the thermal expansion of the layers are included in the equations for the strains by substituting ε_{ri} with $\varepsilon_{ri}-\alpha_i\Delta T$, $\varepsilon_{\theta i}$ with $\varepsilon_{\theta i}-\alpha_i\Delta T$ and ε_{zi} with $\varepsilon_{zi}-\alpha_i\Delta T$ in (4.4), (4.5) and (4.6) respectively. To determine the constants of each layer α_i, β_i, γ_i and δ_i, the boundary conditions stated above are used except that condition 1 is modified to be $\sigma_{rm}\big|_{r=r_m}=0$ and condition 5 is modified to be $\sum_{i=1}^{m}A_i\sigma_{zi}=0$ (i.e. zero external pressure change). The strains are then substituted into the modified responsivity equation [4.8],

$$\frac{1}{\lambda_B}\frac{\Delta\lambda}{\Delta T}=\frac{1}{n}\frac{\partial n}{\partial T}\bigg|_{\rho}+\frac{1}{\Delta T}\left[\varepsilon_z-\frac{n^2}{2}\left[(p_{11}+p_{12})\varepsilon_r+p_{12}\varepsilon_z\right]\right] \qquad (4.10)$$

where the first term is the change in the index of refraction of the fibre with temperature for constant density, ρ (see section 2.6). For a bare fibre, the responsivity is determined by the factor $\frac{1}{n}\frac{\partial n}{\partial T}\Big|_{\rho}$ which yields $\Delta\lambda/(\lambda\Delta T)\approx 0.69\times10^{-5}$ K^{-1} (or 10.7 pm.K^{-1} at 1550 nm). This is in close agreement with published data on the temperature sensitivity of commercially available IFBG's [4.9].

For the case of the coated IFBG, we assume that the mechanical properties and thermal expansion coefficient of the core and cladding are equal. This is valid since the actual mismatch in thermal expansion coefficient of the core and cladding is very small compared with the mismatch between the fibre and coating. The increase in the responsivity to temperature for a fibre with a single coating is shown in fig. 4.4, plotted as a function of the ratio of the diameter of the coating to the fibre, for three values of E of the coating. Plotted in fig. 4.5 is the increase in responsivity as a function of the thermal expansion coefficient of the coating.

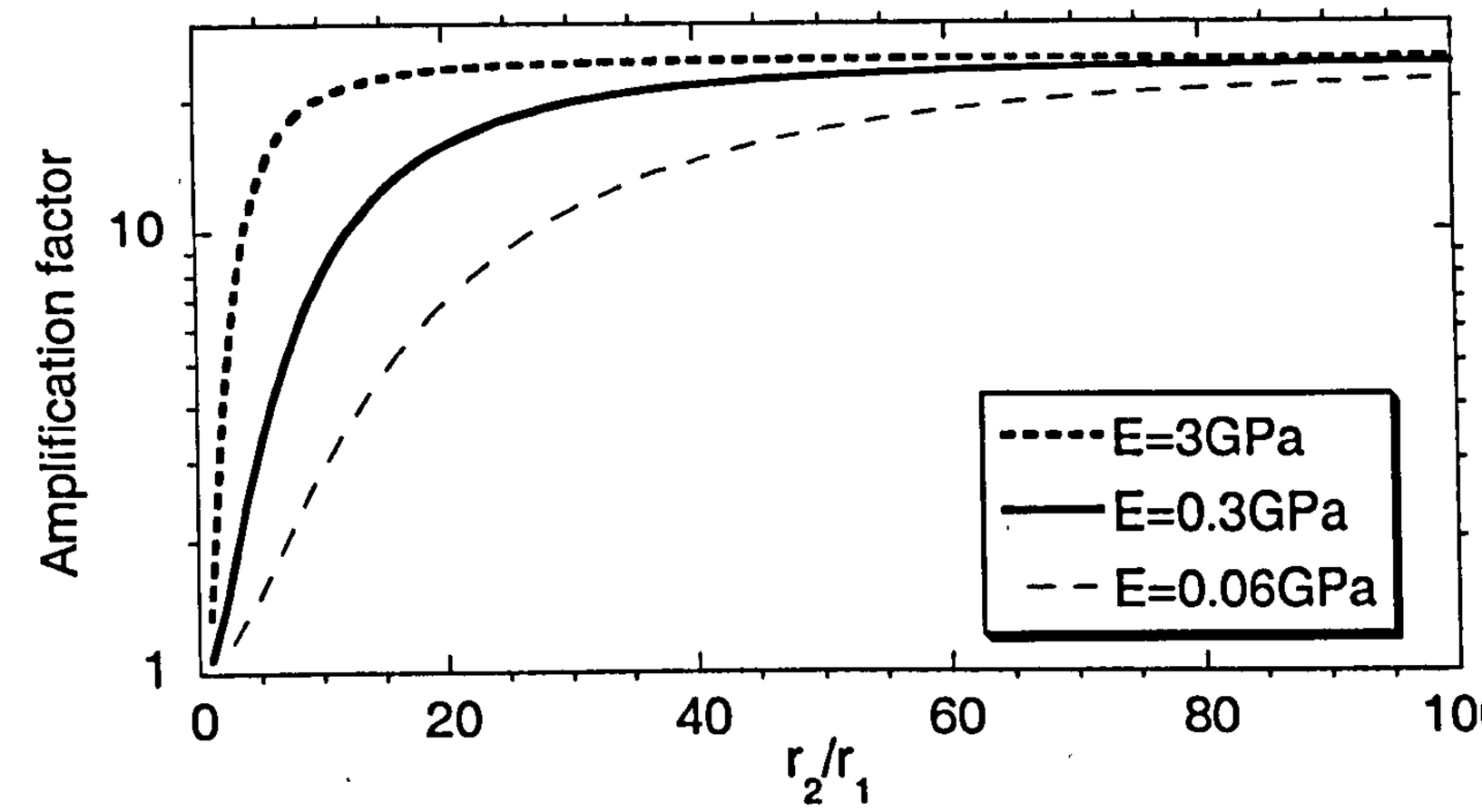

Figure 4.4: Increase in the responsivity to temperature of a coated IFBG as a function of the coating thickness

(Here we take $\alpha_2 = 2\times10^{-4}$ K^{-1}, typical for rubber/polymer)

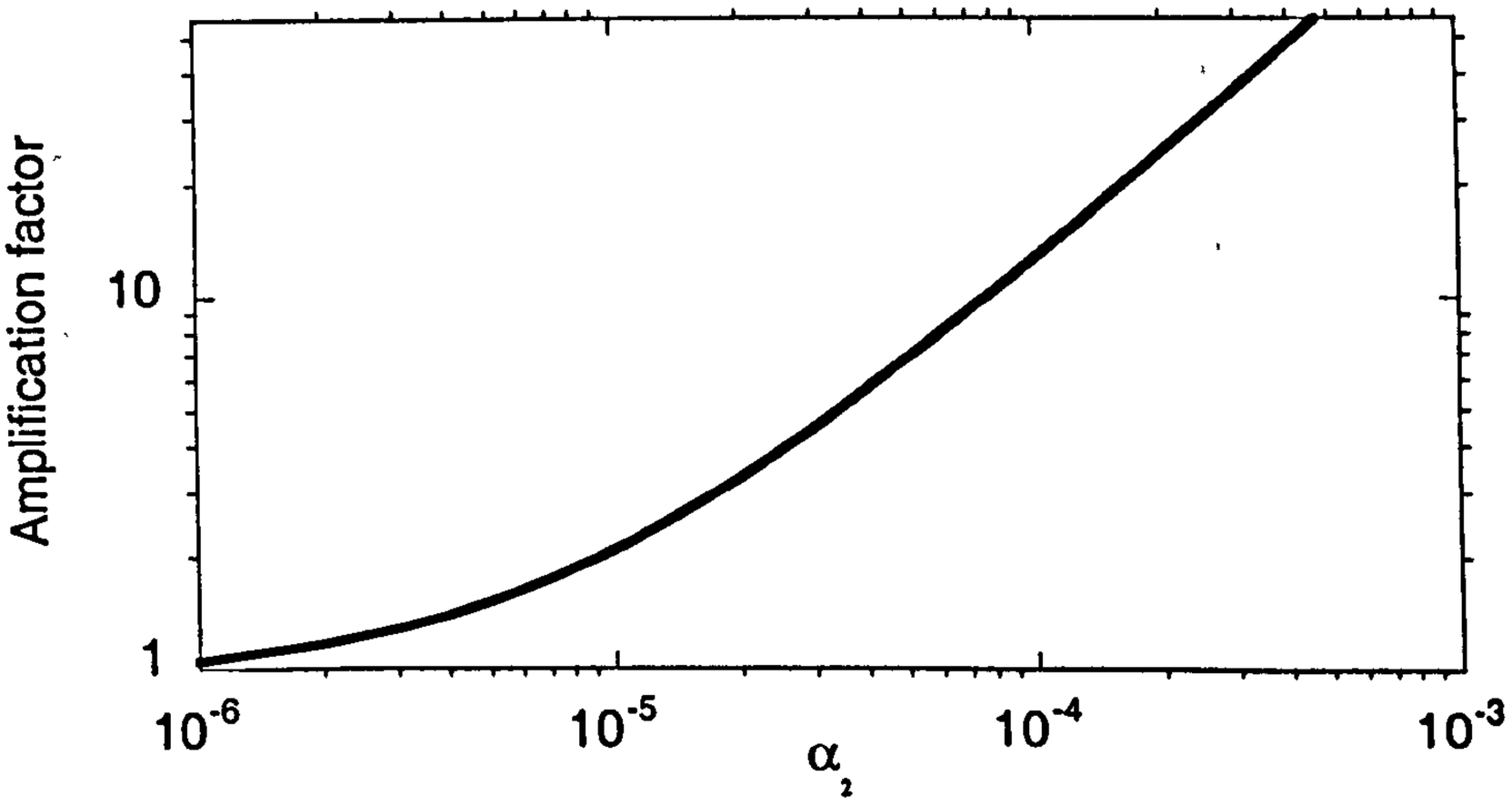

Figure 4.5: Increase in the responsivity to temperature of a coated IFBG as a function of the α of the coating (assumes thick coating limit)

In general, the amplification in responsivity increases as the coating thickness increases and as the mismatch in thermal expansion coefficient between the coating and the fibre increases. However, as the coating thickness increases, a "thick coating" limit is reached, analogous to the "thick coating" limit observed in the pressure amplification plots presented in sec. 4.2. The

coating thickness at which this limit is reached increases as the Young's modulus of the coating decreases, as shown in fig. 4.4. In a temperature sensor, it is desirable to minimise the coating thickness, in order to minimise the response time of the sensor. Thus, it follows from the discussion given above that a coating with a high thermal expansion coefficient and high Young's modulus is required to maximise the temperature responsivity whilst minimising the coating thickness and hence the response time of the sensor.

We return now to the assumption stated earlier that the coating length is much greater than the grating length and consider what happens to the temperature responsivity when the coating length approaches the length of the grating. This has been investigated recently where the temperature responsivity of an IFBG with a thick rubber coating was characterised for increasing coating length [4.10]. In this work, a shear-lag analysis was used to determine the strain transfer ratio between the coating and the fibre as a function of the axial position and the length of the coating. For the case where the coating is very long compared with the IFBG length, it is shown that the strain transfer is independent of axial position and is close to unity; however, as the coating length decreases, the strain transfer also decreases by an amount dependent on the coating thickness and stiffness. This paper also provides us with data that can validate the model presented above. A coated IFBG of thickness $r_2 = 100\, r_1$ and length 140 mm exhibited a value of $\Delta\lambda / \Delta T = 0.139$ nm.K^{-1} at 1550nm. Using the properties of the coating given in [4.10] ($E = 0.02$ GPa, $\nu = 0.5$ and $\alpha = 145 \times 10^{-6}$K^{-1}) the predicted responsivity to temperature is 0.144 nm.K^{-1}, in good agreement with the measured responsivity.

Response time

The response time of the sensor can be estimated by consideration of the rate of heat conduction through the coating. For an infinitely long cylinder, where we consider radial heat conduction only, the radial temperature distribution, $T(r)$, when the cylinder is not in thermal equilibrium with its surrounding is described by the Fourier equation [4.11],

$$\frac{\partial T}{\partial t} = \xi\left(\frac{\partial^2 T}{\partial r^2} + \frac{1}{r}\frac{\partial T}{\partial r}\right) \tag{4.11}$$

where r is the radial distance from the centre of the cylinder and ξ is the thermal diffusivity equal to $\kappa(c\rho)^{-1}$ where c, in this case, is the specific heat capacity, κ is the thermal conductivity and ρ is the density of the cylinder. (4.11) can be solved exactly yielding,

$$\frac{T_c - T_s}{T_0 - T_s} = 2\sum_{m=1}^{\infty} \frac{e^{-\xi z_m^2 t/R^2}}{z_m J_1(z_m)} \qquad (4.12)$$

where T_c, T_s are the temperature at the centre and surface of the cylinder respectively at time $t=t$, T_0 is the temperature of the cylinder at $t=0$, R is the radius of the cylinder, J_1 is the first order Bessel function and z_m is the *mth* root of the zeroth order Bessel function. Values of the right hand side (rhs) of (4.12) are tabulated in Appendix A of [4.11] in terms of $\xi t / R^2$.

In the case of a coated fibre we assume that the fibre diameter is small compared with the coating and hence ignore the difference in thermal conductivity and diffusivity of the fibre layer (also, glass generally has a higher thermal diffusivity than most rubbers). The response time of the sensor can be estimated by determining how long it takes for the centre of the coating to approach its surface temperature if the surface temperature is increased by an amount ΔT. So we calculate the time for the centre to increase in temperature by $0.9\Delta T$. In this case the left hand side (lhs) of (4.12) becomes equal to 0.9. Taking the values for the thermal conductivity, specific heat capacity and density for soft rubber, given in [4.11], as $\kappa=0.168$ J.s^{-1}.m^{-1}.K^{-1}, $c=1.88\times10^3$ J.kg^{-1}.K^{-1} and $\rho=1.1\times10^3$ kg.m^{-3} this yields a value of $\xi=8.1\times10^{-8}$m^2.s^{-1}. For the rhs of (4.12) to equal 0.9, the term $\xi t / R^2 \sim 0.085$, using Appendix A of [4.11]. Thus if R is $40\,r_1$ then $t=6.6$s. We can also determine the response time of a bare IFBG. Taking the diffusivity of glass as $\xi=5.1\times10^{-7}$m^2.s^{-1} [4.11], then $t=0.26$ ms for $R=40$ μm and $t=0.65$ ms for $R=62.5$ μm. Hence, the response time from a coating of this thickness tends to be relatively slow. It may, however, be possible to increase the response time by loading the polymer with high thermal diffusivity material. This will also modify the mechanical properties of the coating, which may slightly modify the temperature and pressure responsivity.

4.4 Experimental Set-Up

Commercially available gratings were tested (supplied by Kromafibre Inc) with a Bragg wavelength, λ_B, of 1543nm. These were supplied with a re-coat of acrylate over the grating, which was left in place on all but one of the coated sensors prior to over-moulding (to prevent damage to the IFBG). A 200mm length of fibre centred on the grating was coated to a diameter of 5mm, chosen to be 40 times the diameter of standard 125 μm optical fibre. The two materials used in these experiments were a 'soft' epoxy resin (Scotch Cast 815 Resin) and a 'hard' polyurethane (APT-Flex F17). The Young's modulus and Poisson's ratio of these materials were estimated to be E=0.05 GPa, ν=0.45 and E=1.0 GPa, ν=0.45 respectively. Once cured, the two coated and one bare IFBG were placed in a water-filled pressure vessel and the fibres were passed through a gland to the interrogation interferometer.

To interrogate the gratings, a drift-compensated interferometric detection scheme was used [4.12]. The experimental set-up is shown in fig. 4.6.

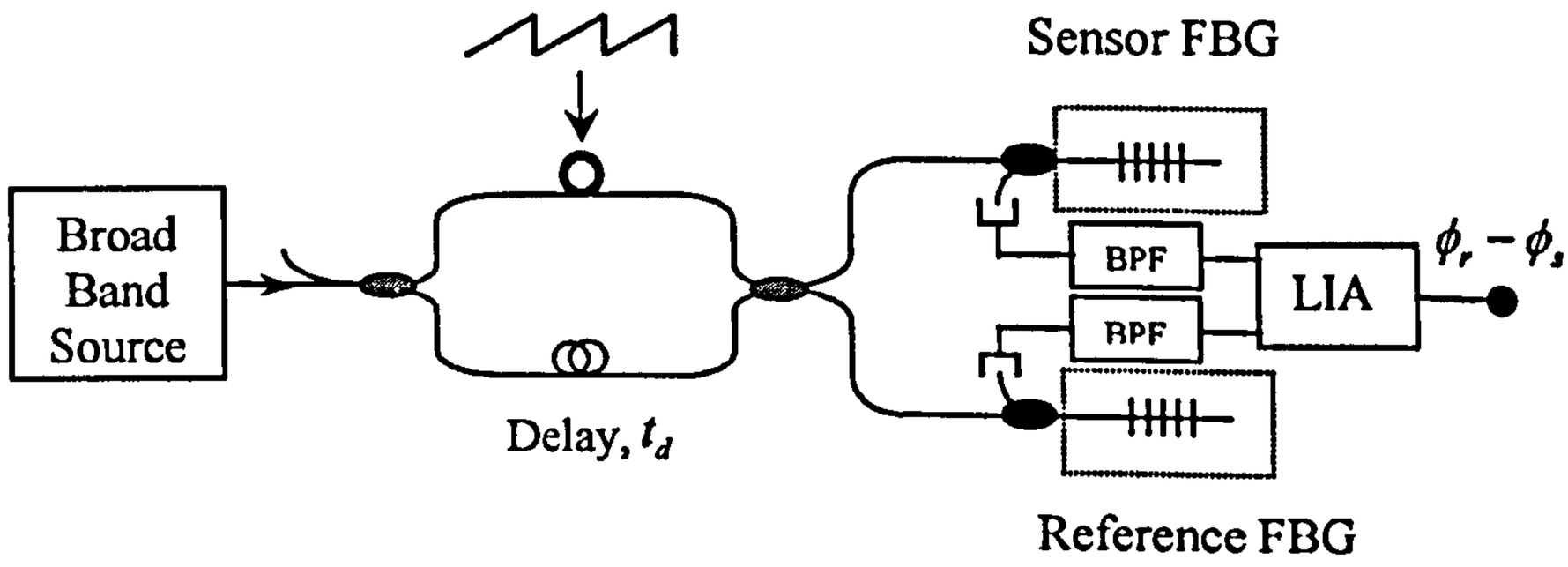

Figure 4.6: Experimental set-up

The set-up comprises a Mach-Zehnder interferometer (MZI) with a small path imbalance, d. A piezo-electric (PZT) fibre stretcher was incorporated into one arm to allow a carrier phase modulation to be applied. The sensor grating is spliced to one output port and the reference grating to the other port. Two directional couplers were also incorporated into the output ports to allow the reflected light from the IFBG's to be separated onto photodiodes. A 1550nm ASE

broadband source (BBS) provided 20mW of light to the input of the MZI. A 300Hz-serrodyne (rising ramp) modulation was then applied to a piezoelectric cylinder which had a number of turns of optical fibre from one arm of the MZI wrapped around its circumference. The amplitude of modulation on the PZT was adjusted to achieve a 2π phase excursion thus generating the carrier signals. These two carrier signals were then band pass filtered (BPF) at the modulation frequency and fed to a lock-in amplifier (LIA) which measures the phase difference between the two carriers. The lock-in amplifier was set with a 100ms integration time and gave an output of ±10V for a corresponding input signal deviation of $\pm\pi$ radians. The unbalanced MZI in this configuration had a path imbalance, d, measured to be 3.3mm giving an optical path difference ($OPD = nd$) of 4.8mm, which was less than the coherence length of the 0.1nm FWHM bandwidth IFBGs used in these tests. The scale factor between phase and wavelength shift is then given by,

$$\left|\frac{\Delta\phi}{\Delta\lambda_B}\right| = \frac{2\pi nd}{\lambda_B^2} \tag{4.13}$$

which yields a value of 13.1 rad.nm^{-1}. In this configuration, the difference in phase between the two carriers will depend only on changes in the reflected wavelength of each grating. Thus, phase-shifts induced by temperature changes of the interferometer will not give rise to an unwanted signal since they are common to both carrier signals. By maintaining the reference and sensor grating at a constant temperature, high resolution quasi-static strain measurements on the sensor grating can be made. In the experiment, the reference and sensor IFBG were placed with the interferometer in an isolated chamber.

The pressure within the vessel containing the coated and bare IFBGs was then cycled between zero and ~3.45x10^6 Pa (~500psi) over a 13 minute period using a hand pump. Attached to the pressure vessel was a strain-gauged pressure sensor (rated to 1000psi). The conditioned signal from this sensor was recorded on one channel of a PC-based ADC while a second channel was used to record the output from the LIA.

Once the measurements from all three IFBGs had been recorded, the results were scaled using the factor 41.6 V.nm^{-1}. These results were then plotted against the conditioned pressure sensor signal.

4.5 Results and Discussion

The results from the bare grating are shown in fig. 4.7 and the results for the 'soft' and 'hard' coating are shown in fig. 4.8 and 4.9 respectively. The measurements are summarised in table 4.2. (It should be noted that in the pressure response plots, the wavelength shift axis is reversed. In addition, the two plots have identical scales to make comparisons of the effect of gain on the IFBG pressure sensitivity easier to identify). A responsivity of -3.48×10^{-9}nm.Pa$^{-1}\pm23\%$ was obtained for the bare IFBG, which agrees well with the value of -4.4×10^{-9}nm.Pa^{-1} predicted by (2.111)[10]. Both the magnitude and sign of the observed wavelength shift are consistent with the assumption of hydrostatic boundary conditions. With the soft and hard coatings, responsivities of -3.19×10^{-8}nm.Pa$^{-1}\pm3\%$ and -6.52×10^{-8}nm.Pa$^{-1}\pm2\%$ respectively, were obtained. This corresponds to amplifications of 19.2 dB±1.7dB and 25.5 dB±1.7dB relative to the bare grating measurement for the 'soft' and 'hard' coating respectively.

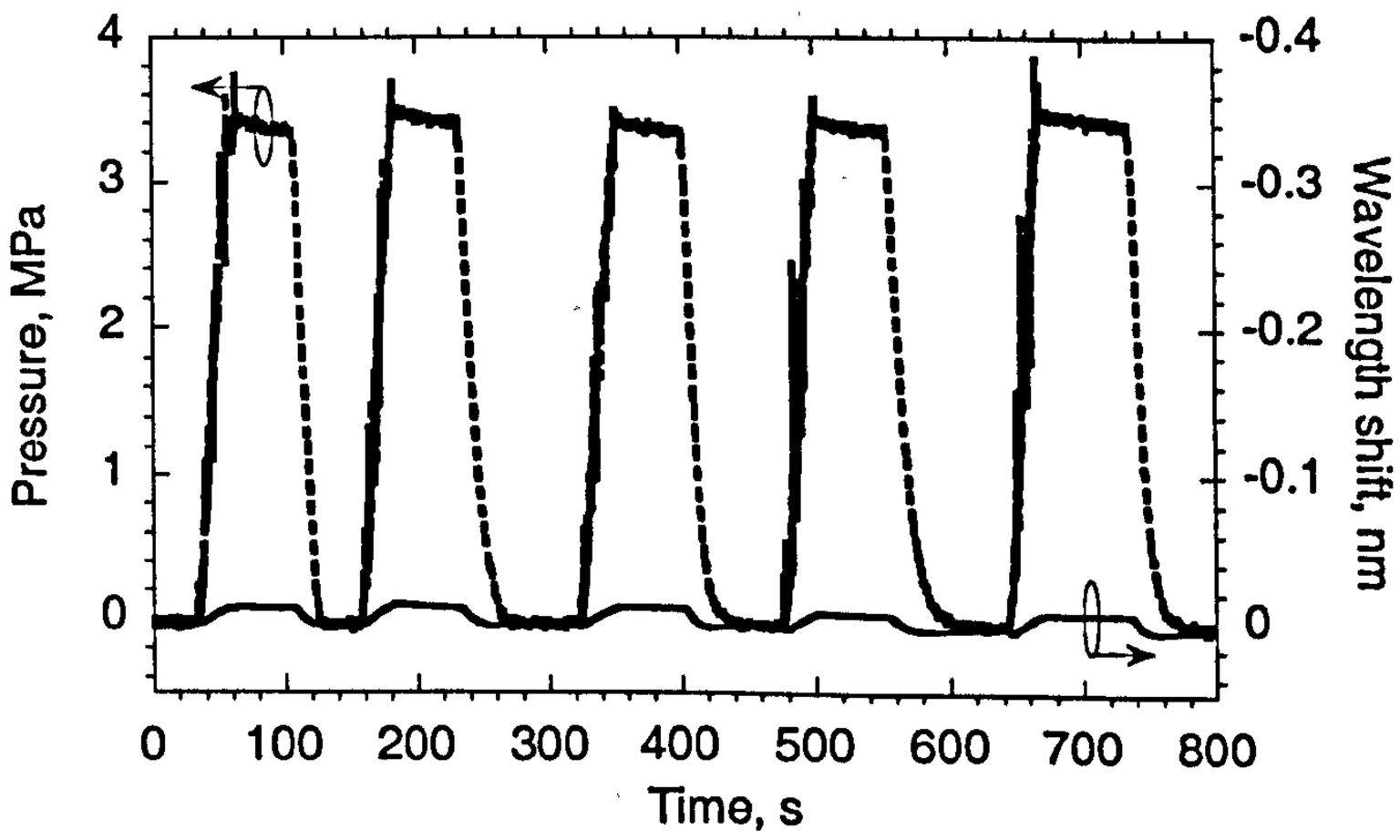

Figure 4.7: Responsivity of bare IFBG

[10] Taking a value of the Poisson ratio of the fibre core, $\nu = 0.23$, which is sometimes used in the literature, results in a predicted value of the responsivity of -3.6×10^{-9} nm.Pa^{-1}, which is somewhat closer to our measured value.

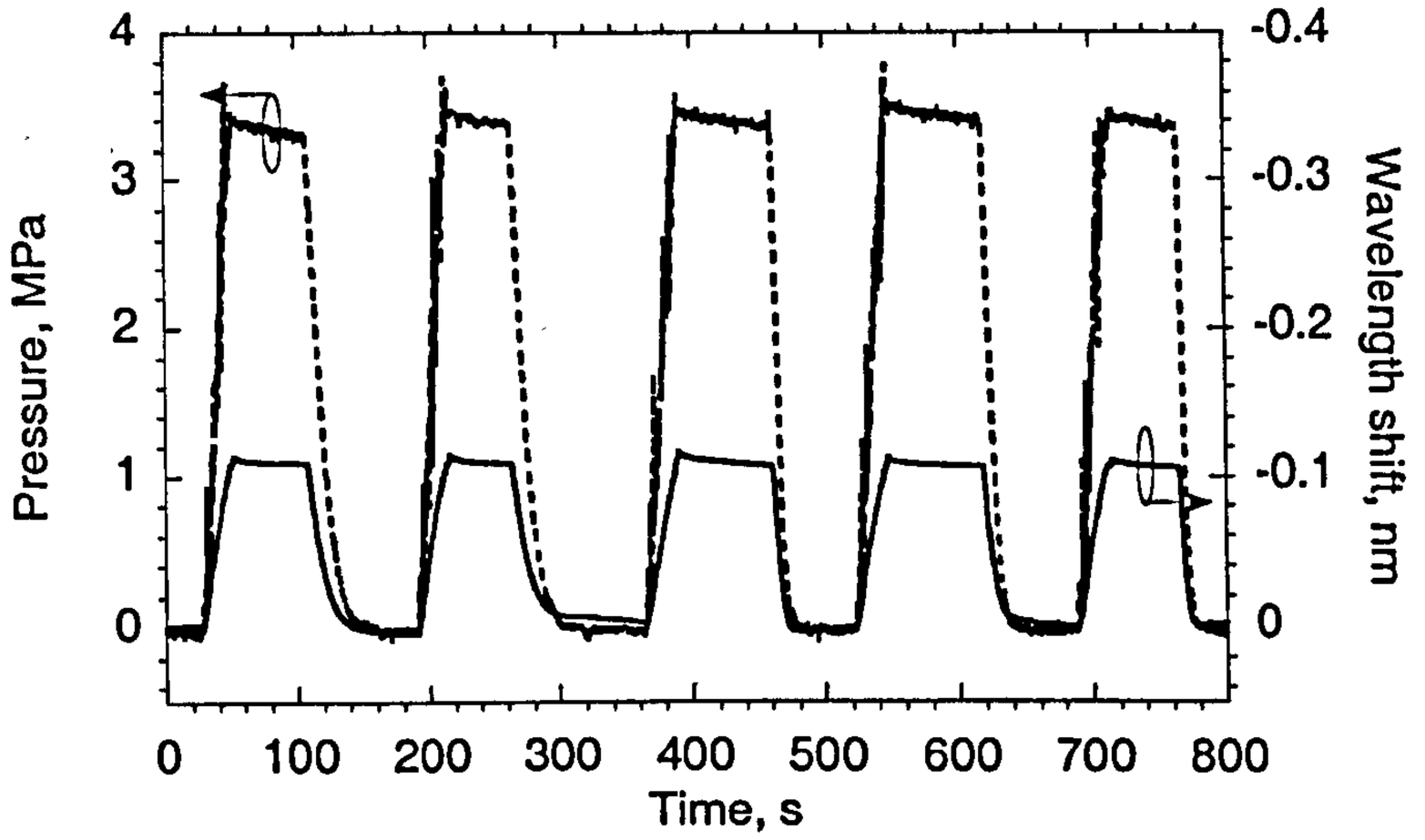

Figure 4.8: Responsivity of IFBG with a 'soft' coating

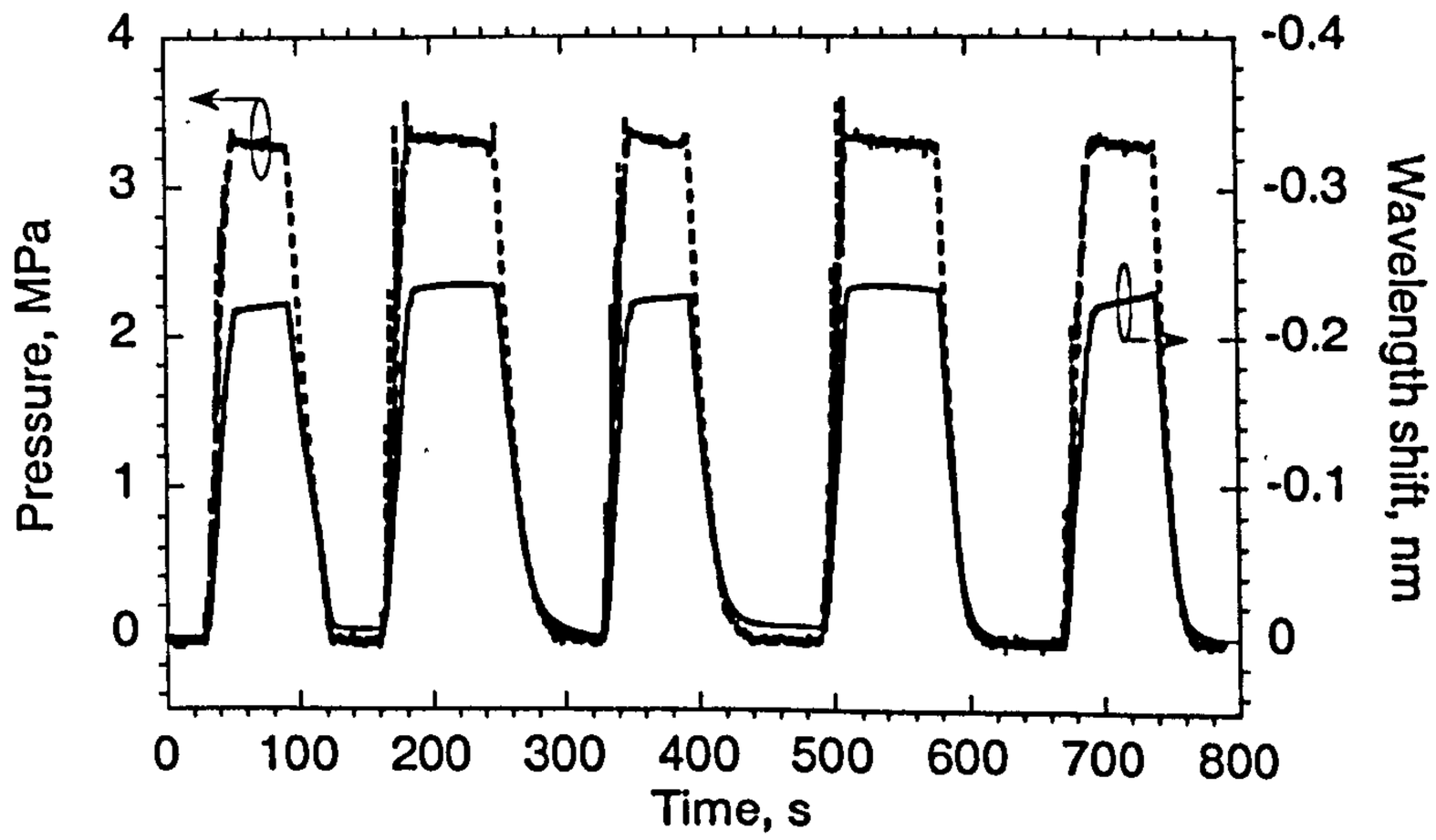

Figure 4.9: Responsivity of IFBG with a 'hard' coating

Table 4.2: Measurements of coated gratings

	Bare Grating	Soft Coating	Hard Coating
Pressure Difference (MPa)	3.45±1%	3.45±1%	3.45±1%
Wavelength Shift (nm)	-0.012±18%	-0.110±2%	-0.225±1%
Sensitivity ($nm.Pa^{-1}$)	-3.48×10^{-9}±23%	-3.19×10^{-8}±3%	-6.52×10^{-8}±2%
Amplification Factor	-	9.2±22%	18.8±21%
Gain (dB)	-	19.2±1.7dB	25.5±1.7dB
Predicted gain [dB]	--	55	30

The fact that the MZI output does not always return to zero after the pressure has been removed is attributed primarily to residual drift, caused by a small variation in temperature of the reference grating. The maximum drift observed on both coated and uncoated fibres over the duration of the measurements (800s) was ~0.01 nm, which corresponds to a change in temperature of the reference grating of ~0.9K. In the case of the coated fibres, this drift may also be partly attributed to creep between the fibre and coating. The measurement of the wavelength shift was carried out over the duration of a rising or falling edge of a single pressure cycle in fig. 4.7-9. The measurement error is thus due to the drift over this duration (20s), which was estimated to be $\delta\lambda_d = \pm 2.2\times10^{-3}$nm and due to the error in the reference sensor read-out (~±1%)[11]. The spurious 'spikes' seen in the reference sensor readout were due to electrical interference in the digital readout meter and where not caused by the pressure vessel.

Shown in table 4.2 is the amplification predicted by the theory presented in section 4.2. The predicted amplification for the 'hard' coating is ~4.5 dB greater than that measured. The difference here may be explained by the following factors: (i) the uncertainty in the mechanical properties of the coating materials. Taking the Young's modulus of the coating as 1.6GPa (instead of 1GPa) results in a predicted amplification of 25.5dB; and (ii) the bond between the fibre and the polyurethane coating may not give rise to complete transfer of strain between the coating and the fibre. Thus, strain in the coating will not be fully transferred to the fibre and the assumption that the strain in each layer is equal will no longer be valid. However, on inspection of the coated fibre after the tests were carried out, no significant debonding was visible.

The reason for the large discrepancy found between measurement and prediction for the soft coating is less certain. The presence of the primary acrylate coating on the IFBG may prevent a good bond between the fibre and the coating; however, this discrepancy is more likely to be due to an inaccurate estimation of the Poisson ratio of the 'soft' coating. On inspection, the 'soft' coating may be more rubbery with a Poisson ratio approaching 0.5. Setting the Poisson ratio of the coating, $\nu = 0.4987$ results in a predicted amplification of 19.2 dB, corresponding to the measured value.

---

[11] If two parameters x and y have errors δx and δy respectively, then the error, ε, in the ratio $(x+\delta x)/(y+\delta y) = x/y + \varepsilon$ is given by $\varepsilon \simeq \delta x/y - x\delta y/y^2$ providing $\delta x/x \ll 1$ and $\delta y/y \ll 1$. This equation is only approximate in our case since the small error approximation is not valid. Thus, the errors in table 4.2 have been calculated exactly.

To our knowledge, conventional coating materials have not yielded amplifications of greater than 30 dB. However, recent work based on microsphere loaded polymers has demonstrated up to 40 dB of gain from a coating a few mm thick [4.13]. The compressibility of the microsphere loaded coating generates high axial strain in the fibre; however, it has been shown that buckling of the microspheres under moderate hydrostatic pressures can cause the compliance of the coating to change [4.14]. With conventional coatings, it has also been found that shear can occur between the coating material and the fibre as pressure is being applied [4.15].

It is interesting to determine the resolution of a coated in-fibre laser (IFL) configured as an acoustic sensor. Assuming the resolution of an uncoated IFL is 37 $mPa.Hz^{-1/2}$ and an amplification factor of 18.8 is achieved, the resolution is increased to 2 $mPa.Hz^{-1/2}$. Thus, although the coated IFL acoustic sensor does not match the mandrel type interferometric acoustic sensor in terms of pressure resolution ($20\mu Pa.Hz^{-1/2}$), it may be adequate for some lower performance sonar applications where a small transducer is desirable. Other issues must also be investigated such as the effect of the coating on the grating properties, which may modify the behaviour of the laser.

In conclusion, we have demonstrated the increase in responsivity to pressure of a coated IFBG compared to a bare IFBG. Amplification factors of up to 25.5 dB±1.7dB were obtained with a 5mm diameter coating of polyurethane. A simple model to determine the strain in this composite fibre structure was presented to explain this result. We also presented a simple model to predict the increase in responsivity to temperature due to the higher thermal expansion coefficient of the coating compared with the fibre and obtained good agreement between this model and previously published experimental data. Finally, we considered the practicality of these types of sensor, in particular the response time of a coated IFBG configured as a temperature sensor and also how these techniques may be applied to an in-fibre laser acoustic sensor.

Coated IFBG's are attractive as discrete sensors due to their simplicity and small size and the increase in responsivity to temperature obtained from the coating may be useful if the grating is configured as a temperature sensor. Using a dual grating approach where each grating has different scale factors for temperature and pressure responsivity (i.e. one coated and one

uncoated IFBG) would allow both temperature and pressure to be extracted simultaneously [4.9]. However, further work is necessary to improve the bonding between the coating material and fibre and to investigate the effects of creep, in order to assess the long term accuracy as a quasi-static pressure/temperature sensor. Although the IFBG and IFL sensors may not replace the fibre-optic interferometric acoustic sensor, they may compliment them or replace them in some specialised applications. For example, high resolution depth information can be obtained from static pressure measurements from an IFBG which is useful for some array applications and an IFL acoustic sensor could be used for applications where a very small sensor head is required.

References

[4.1] G.B.Hocker, 1979 "Fiber–optic sensing of pressure and temperature" *Applied Optics* 18 (9) 1445-1448

[4.2] G.B.Hocker, 1979 "Fiber optic acoustic sensors with composite structure – an analysis" *Applied Optics* 18 (21) 3679-3683

[4.3] B.Budiansky, D.C.Drucker, G.S.Kino and J.R.Rice, 1979 "Pressure sensitivity of a clad optical fiber" *Applied Optics* 18 (24) 4085-4088

[4.4] W.W.Morey, G.Meltz, J.M.Weiss, 1991 "Evaluation of a fiber Bragg grating hydrostatic pressure sensor" *Proc. of the 8th Conf. on Optical Fibre Sensors* New York

[4.5] R.Hughes, J.Jarzynski, 1980 "Static pressure sensitivity amplification in interferometric fiber optic hydrophones" *Applied Optics* 19 (1) 98-106

[4.6] S.T.Vohra, A.Dandridge, 1996 "An hybrid WDM/TDM reflectometric array" *Proc. of the 11th Int. Conf. on Optical Fiber Sensors* Advanced Sensing Photonics Japan Soc. of Applied Physics Tokyo Japan 2 vol. 712+17 1 Th3-29

[4.7] N.Lagakos, J.Jarzynski, J.H.Cole, J.A.Bucaro, 1986 "Frequency and temperature dependence of elastic moduli of polymers" *J. Appl. Phys. Lett.* 59 (12) 4017-4031

[4.8] N.Lagakos, J.A.Bucaro, J.Jarzynski, 1981 "Temperature-induced optical phase-shifts in fibers" *Applied Optics* 20 (13) 2305-2308

[4.9] Y.J.Rao, 1997, "In-fibre Bragg grating sensors", *Meas. Sci. Technol.*, 8 355-375

[4.10] S.T.Vohra, C.C.Chang, 2000 "High Sensitivity Fiber Bragg Grating Temperature Sensors Utilizing Polymer Coatings" *Proc. of the 14th Int. Conf. on Optical Fiber Sensors*, SPIE vol. 4185, Venice, Italy , 584-587

[4.11] L.R.Ingersoll, O.J.Zobel, A.C.Ingersoll, 1954 *Heat Conduction with Engineering, Geological and Other Applications,* The University of Wisconsin Press, Chapter 9

[4.12] A.D.Kersey, T.A.Berkoff, W.W.Morey, 1993 "Fiber-optic Bragg grating strain sensor with drift-compensated high-resolution interferometric wavelength-shift detection" *Optics Letters* 18 (1) 72-74

[4.13] S.T.Vohra, A.Dandridge, C.C.Chang, G.A.Johnson, A.B.Tveten, G.M.Nau 1999, "High sensitivity pressure sensors utilizing advanced polymer coatings" *Proc. of the 13th Int. Conf. on Optical Fibre Sensors*, Korea, 557-560

[4.14] Private communication with the DERA Materials Science Sector, Farnborough

[4.15] W.L.Schulz, E. Udd, J.M.Seim, H.M.Laylor, 2000 "Static and dynamic testing of bridges and highways using long-gage fiber Bragg grating based strain sensors", Presented at Photonics East, Industrial Sensing Systems, Boston, Paper 4202-19

Part III
Sensor Multiplexing

Chapter 5

LARGE-SCALE MULTIPLEXING OF FIBRE-OPTIC INTERFEROMETRIC SENSORS USING TDM AND DWDM†

Abstract—Multiplexing schemes for interferometric fibre sensors based on TDM and DWDM using optical add/drop multiplexers are described. The results of an experimental arrangement which is based on one of the architectures is also presented. Topics include a discussion of the noise sources in the system, dynamic range and a characterisation of the DFB fibre laser source noise. We show the crosstalk levels in the experimental arrangement to be between -47 dB and –76 dB depending on the mechanism involved. The multiplexing schemes demonstrate the potential to address at least 192 interferometric sensors through two fibres based on a system with 6 wavelengths with a phase resolution less than 20 μrad.$Hz^{-1/2}$. For application to sonar arrays, our analysis has shown that hydrophones multiplexed in this type of architecture would achieve ambient acoustic noise limited pressure resolution with an in-water dynamic range up to 135 dB at frequencies up to 10 kHz. In general, these architectures would find application in systems requiring very large numbers of sensors with a minimum of telemetry cabling required.

5.1 Introduction

Interferometric fibre optic sensors have been an area of active research for the last two decades. Of particular interest is their application to military sonar arrays where they provide an alternative to the conventional electro-ceramic based hydrophone, and it is this application that has been the main driver behind the development of optical fibre sensor based hydrophone arrays. The optical hydrophone array offers advantages since they are electrically passive, immune to electro-magnetic interference and may provide a reduced through-life cost. The technology has reached a level of maturity such that at-sea deployments of prototype

†This chapter is a transcript of the paper by G.A.Cranch and P.J.Nash, 2001 "Large-scale multiplexing of interferometric fiber-optic sensors using TDM and DWDM" *J. Light. Tech.* 19 (5) 687-699

optical hydrophone arrays have been reported by various groups [5.1,5.2]. The largest array reported to date consisted of sixty-four hydrophones in a time and wavelength division multiplexed (TDM, WDM) architecture [5.2] and demonstrated the potential to address up to 128 hydrophones through three separate fibres. In the TDM scheme, the sensors are sequentially addressed using a pulsed input signal such that time of flight of optical pulses in the multiplexed array allows individual sensor signals to be distinguished. Wavelength division multiplexing allows many TDM signals at different wavelengths to be combined on a single fibre. Since full size sonar arrays may contain in excess of 1000 sensors, techniques that allow multiplexing of many sensors through one or two fibres are of particular interest.

When designing a multiplexing scheme, the following design aims must be considered: (i) maximise the number of sensors addressable through one or two fibres; (ii) maximise the optical efficiency of the array (i.e. ensure that optical power is efficiently distributed between sensors with low excess loss); (iii) minimise the sensor to sensor crosstalk; (iv) maintain comparable performance from a multiplexed sensor to that of a single sensor; and (v) maintain an electrically passive array. Once these design aims are met, comparison between one architecture and another can be made in terms of the crosstalk between sensors. In this paper the sensor to sensor crosstalk is determined by applying a narrowband tone to one sensor and measuring the crosstalk signal amplitude on adjacent sensors. In general the crosstalk signal will vary with time since it consists of the interference of unwanted signals generated by different mechanisms that have random phase relationships. Measurement of the crosstalk is usually carried out by taking an arithmetic mean of multiple time records of the sensor signal output.

Many multiplexing schemes have been proposed based on techniques including time, frequency, coherence and wavelength division multiplexing and are reviewed in detail in [5.3]. However, to date, only those based on time, frequency and wavelength [5.4-5.6] have been demonstrated to multiplex greater than ten sensors with crosstalk levels less than -40 dB onto two fibres or less and achieve an interferometric phase resolution approaching 10 $\mu rad.Hz^{-1/2}$, where this figure is considered to be a typical aim for most sonar applications. The TDM scheme has been shown to be the most successful technique for achieving the design aims stated above. Many sensor networks based on TDM have been proposed, which generally differ in terms of the way in which optical pulses are delivered(returned) to(from) the sensor. However, in general the launched and received signal for these various networks are very

similar. The choice of TDM network is usually determined by constraints on crosstalk levels, number of components and cost.

Recent work has investigated the use of remotely pumped erbium doped fibre amplifiers (EDFA) in TDM based ladder architectures to increase the number of sensors addressable through two fibres [5.7-5.9]. A system was demonstrated which consisted of a ten rung ladder structure using multiple low gain amplifiers to overcome the branching loss in each ladder rung and achieved a phase resolution approaching 1 $\mu rad.Hz^{-1/2}$ [5.10]. In these schemes, however, the increase in number of sensors addressable is accompanied by a proportional reduction in the optical duty cycle or interrogation rate of each sensor, which reduces the available bandwidth and hence dynamic range.

The use of wavelength multiplexing combined with time division multiplexing has been previously reported [5.11]. This paper extends this principle to novel multiplexing schemes based on time and dense wavelength division multiplexing (TDM, DWDM). Recent developments in dense wavelength division multiplexing technology, mainly for the telecommunications applications, have made possible practical realisations of large, highly multiplexed systems that meet the design aims laid out above. This paper presents a theoretical and experimental investigation into these new architectures and discusses the performance implications of these architectures for practical large systems.

The architectures we present combine DWDM with the TDM architecture reported in [5.12]. This TDM architecture has demonstrated high performance from sensors in an optically efficient arrangement with low component numbers. The performance of this TDM architecture has been significantly improved since it was initially proposed. In sec. 5.2, we discuss how the crosstalk has been reduced by use of asymmetric directional coupler-based reflectors, and how the power returned from each sensor is equalised by tailoring the coupler ratios. Sec. 5.3 then describes the proposed DWDM/TDM architectures and the component requirements and characteristics. Sec. 5.4 describes the experimental implementation and a description of the fibre lasers used for interrogation of the sensors. Sec. 5.5 presents the results of the architecture characterisation. Sec. 5.6 presents a theoretical analysis to determine the signal resolution and dynamic range of a sensor in an array and discusses the extent by which the array architecture can be scaled up. Finally, conclusions are summarised in sec. 5.7.

5.2 The Pulsed Reflectometric Architecture

The pulsed reflectometric architecture (PRA) with heterodyne detection reported in [5.12] provides a technique to multiplex a practical maximum of ten interferometric sensors onto a single fibre. A typical multiplexed sensor arrangement is shown in fig. 5.1.

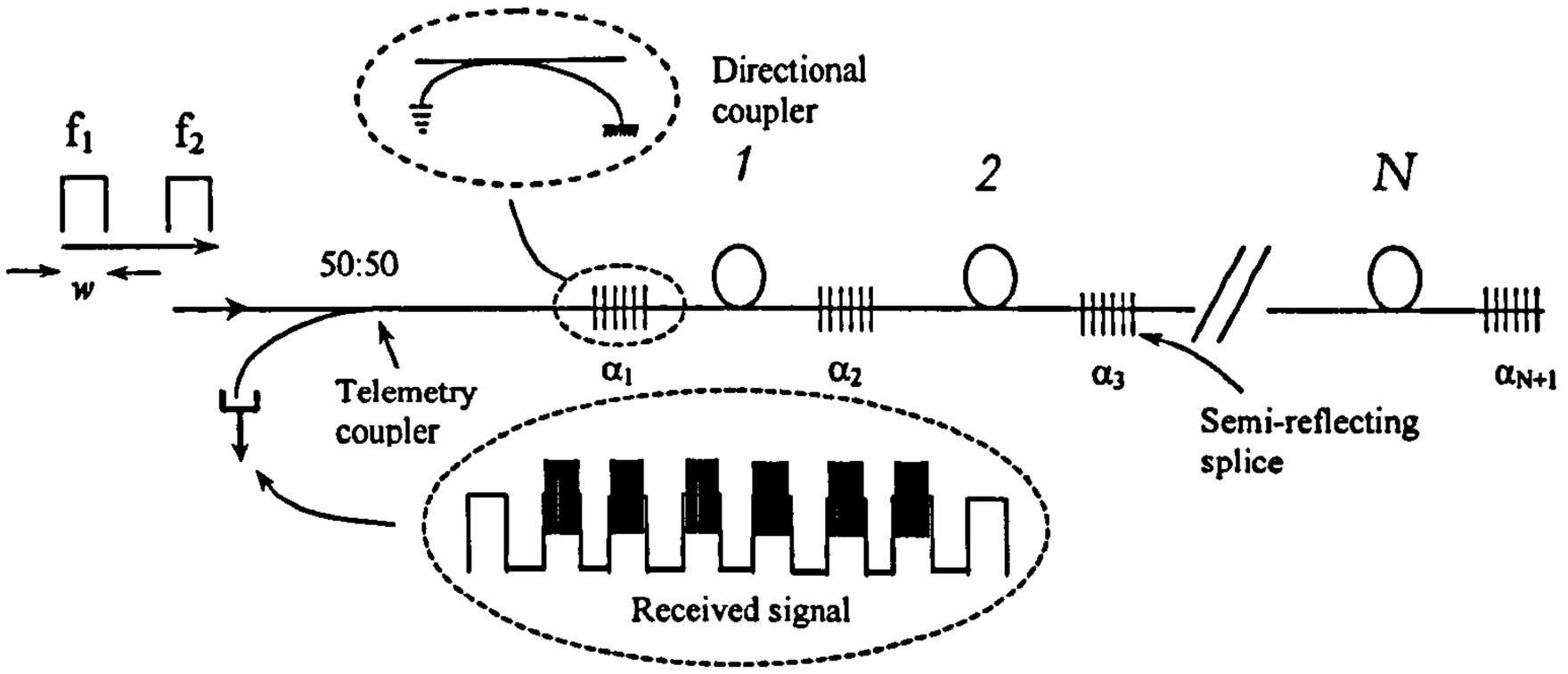

Figure 5.1: Pulsed reflectometric architecture using TDM after [5.12]

The array comprises a number of sensor coils, labelled 1 to N, spliced in series and separated by either a semi-reflecting splice or a directional coupler arranged to operate as an asymmetric mirror. This latter configuration is achieved by applying a silvered mirror coating to the output port of the coupler and index-matching the unused input port. Thus, each sensor coil forms one arm of an unbalanced Michelson interferometer. If two pulses separated in time by 2τ, where τ is equal to the one-way optical transit time in the sensor fibre, are launched into the array then a reflection of each pulse will be produced by each mirror. If a frequency shift of f_c is applied between the two launched pulses, i.e. $f_c = f_1 - f_2$ where f_1 and f_2 are the optical frequencies of the two pulses, then the overlap of these two pulses will, on detection, generate a beat frequency designated as the heterodyne frequency or intermediate frequency (IF). The launched pulses are generated using a path balancing optics arrangement, discussed in Sec. 5.6. This ensures that the returned pulses from the array overlap in time. The received signal from the array thus consists of a series of heterodyne pulses corresponding to each sensor, as shown by the inset in fig. 5.1. The signal from an individual sensor is extracted by electronic time gating of this pulse train. Applying a dynamic strain to the sensor fibre imposes a phase

modulation, $\phi(t)$, on the heterodyne signal which can be extracted by frequency discrimination or phase locked loop techniques. The photodiode current for a single heterodyne pulse can be represented by,

$$i(t) = RP_1 + RP_2 + 2RV\sqrt{P_1P_2}\cos(2\pi f_c t + \phi(t)) \qquad (5.1)$$

where R is the photodiode responsivity, P_1 and P_2 are the powers returned from consecutive reflectors to the photodiode and V is a fringe visibility term.

In a practical system, the power split ratios of the couplers are chosen such that equal power is returned from each reflector and are a function of the splice and coupler excess losses and the number of sensors, N. The coupler ratios required to ensure equal power is received from each sensor has been investigated in [5.13] and we can apply this analysis to our case. For an array of N sensors, the required power transmission ratio of the *nth* coupler is given by,

$$\alpha_n = \frac{\left[\sum_{j=n}^{N-1}\beta^{(N-1)-j}\right]+1}{\left[\sum_{j=n}^{N}\beta^{(N-j)}\right]+1} \qquad \text{for} \quad n = 1,2,3..(N-1) \qquad (5.2)$$

where β is the lumped loss per sensor and includes the sensor fibre loss, coupler excess loss and two splices, $\alpha_N = 1/2$, $\alpha_{N+1} = 0$ and we assume a 100% mirror reflectance. In this case $P_1 = P_2 = P$ and (5.1) reduces to,

$$i(t) = 2RP(1 + V\cos(2\pi f_c t + \phi(t))) \qquad (5.3)$$

The insertion loss (IL) of the TDM array shown in fig. 5.1 (referred to later as an array module) is defined as the ratio of the peak pulse power returned from a reflector, P, to the peak pulse power launched, P_0,

$$IL_{am} = \frac{P}{P_0} = \frac{(1-\alpha_1)^2}{4} \qquad (5.4)$$

where the factor of 4 accounts for the loss due to the telemetry coupler required to separate launch and return pulses (this loss could be avoided if a circulator is used in place of the coupler).

The number of sensors that can be multiplexed in series onto a single fibre is limited by the required interrogation rate for each sensor and the optical power. The maximum interrogation rate, f_{rep}, can be deduced from the transit time of the optical pulse through the array and for the array in fig. 5.1 can be maximised to be $1/(2\tau(N+1))$ Hz. Assuming the pulse width, w, is set to 2τ, the optical duty cycle, D, is $1/(N+1)$. The maximum interrogation rate can also be expressed in terms of the sensor coil fibre length, l, and the fibre effective refractive index, n_{eff},

$$f_{rep} = \frac{c}{2n_{eff}l(N+1)} \tag{5.5}$$

where c is the speed of light in a vacuum.

Using the basic architecture shown in fig. 5.1, up to 32 sensors have been multiplexed onto two fibres by interleaving the pulse returns from four sections consisting of eight sensors each [5.14], as shown in fig. 5.2. By setting the launch pulse width, w, to half the optical transit time in the sensor coil, $\tau/2$, and setting the length of the delay coils such that $L_3 = 3L_1$, $L_2 = 2L_1$ and $L_1 = l/4$, the received pulse train consists of 32 individual heterodyne pulses. Similar multiplexing schemes can be implemented using alternative interrogation methods, such as phase-generated carrier [5.4].

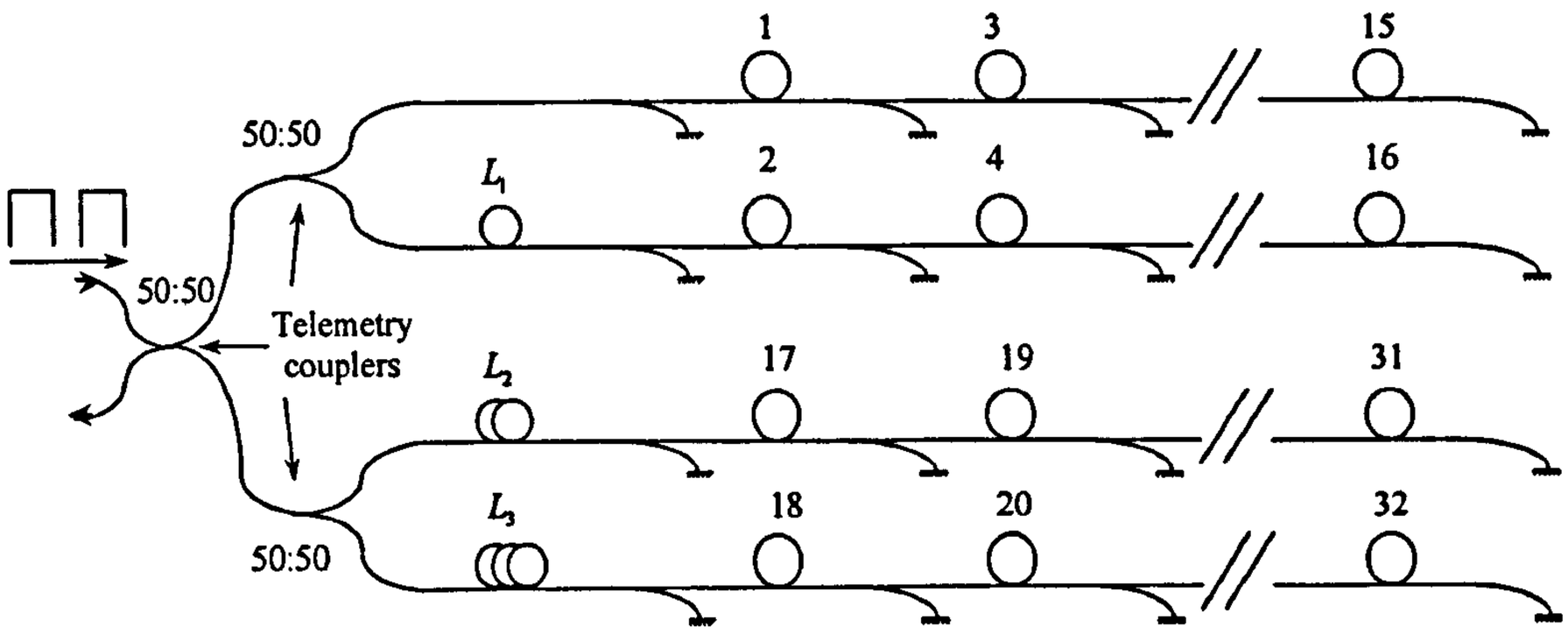

Figure 5.2: Thirty-two element TDM PRA based array

5.3 DWDM/TDM Architecture Designs

The principle of the large-scale architectures proposed here is based on a common telemetry fibre that carries the interrogation pulses for m wavelengths, λ_1 to λ_m. Optical add/drop multiplexers (OADM) are spliced in series into the telemetry fibre at appropriate positions, which allow a single wavelength to be coupled into a corresponding separate fibre. This wavelength is then launched into a TDM array module and the return signals from this array module are then either re-combined with the telemetry fibre or combined onto a second telemetry fibre that carries the return signals. In the following discussion we refer to the wavelength that is separated from the telemetry fibre as the "dropped" wavelength and the wavelength that is recombined as the "added" wavelength. Three architectures based on this principle are shown in fig. 5.3a,b,c and are referred to as architectures (a), (b) and (c) respectively.

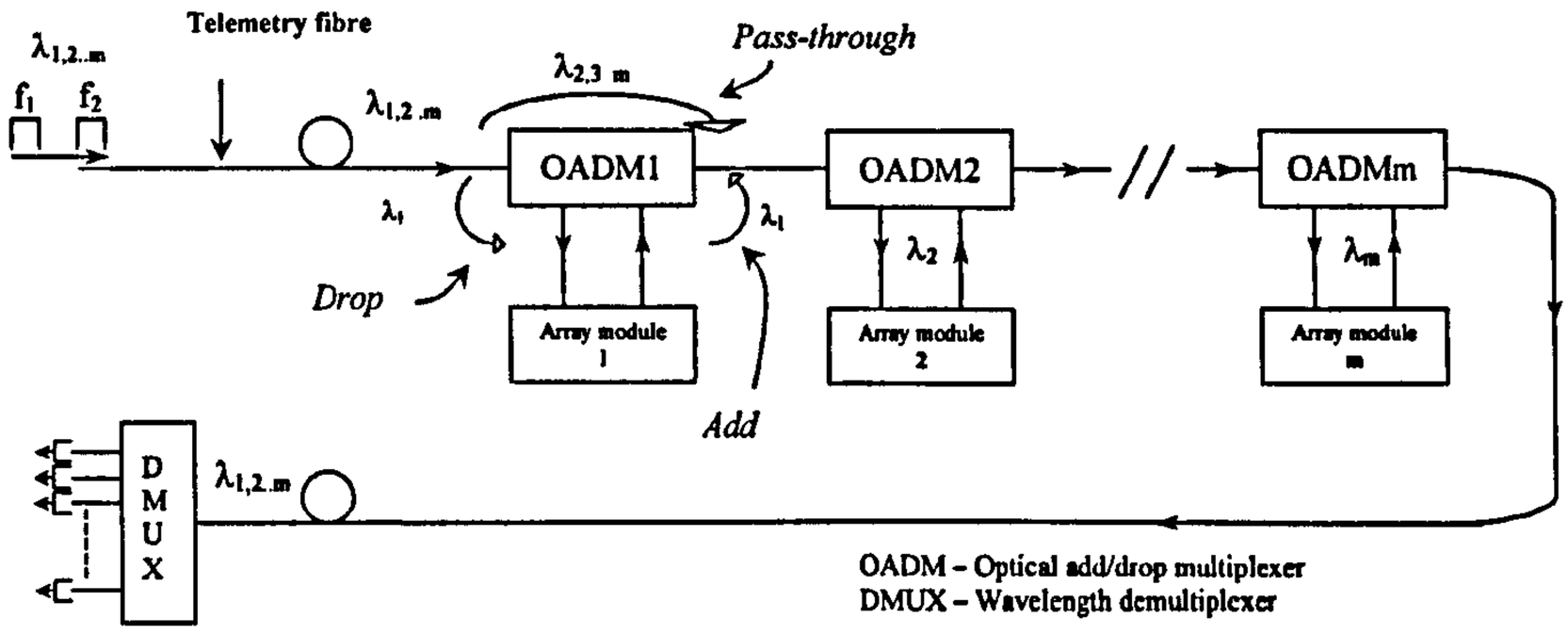

DWDM/TDM Architecture (a)

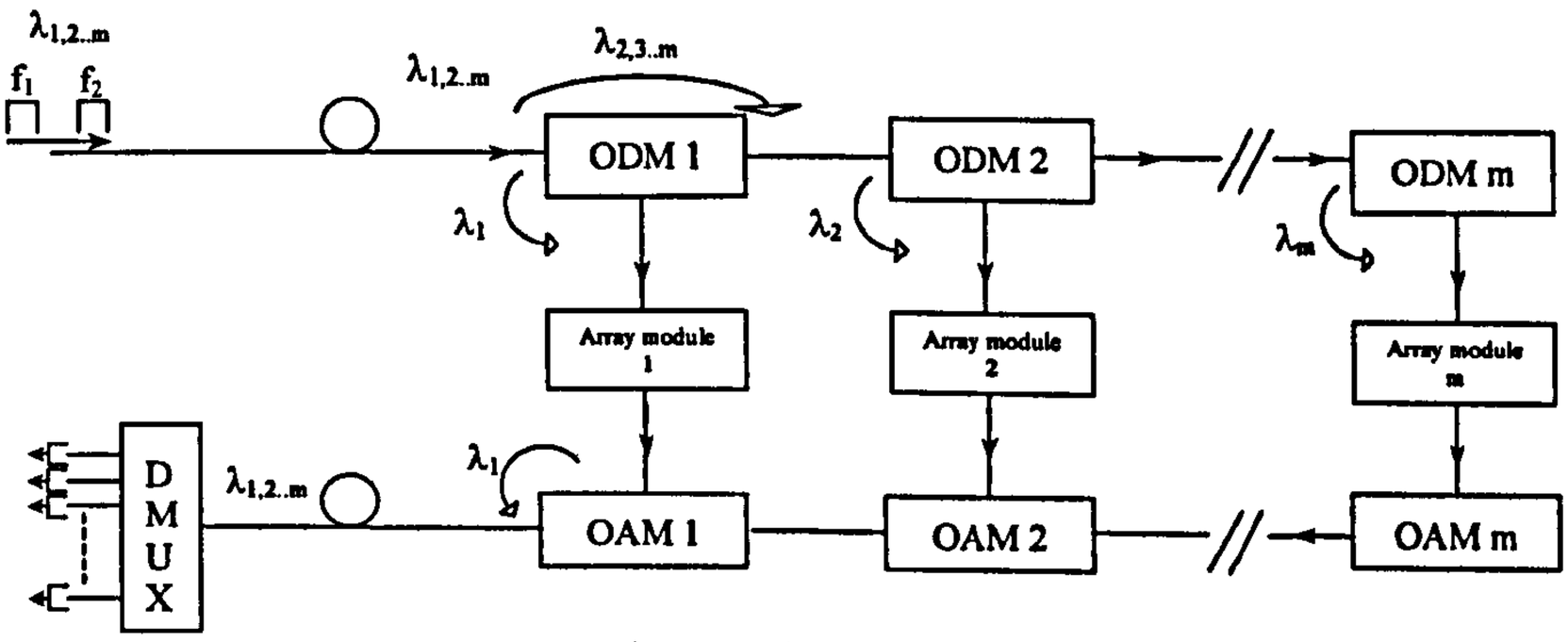

DWDM/TDM Architecture (b)

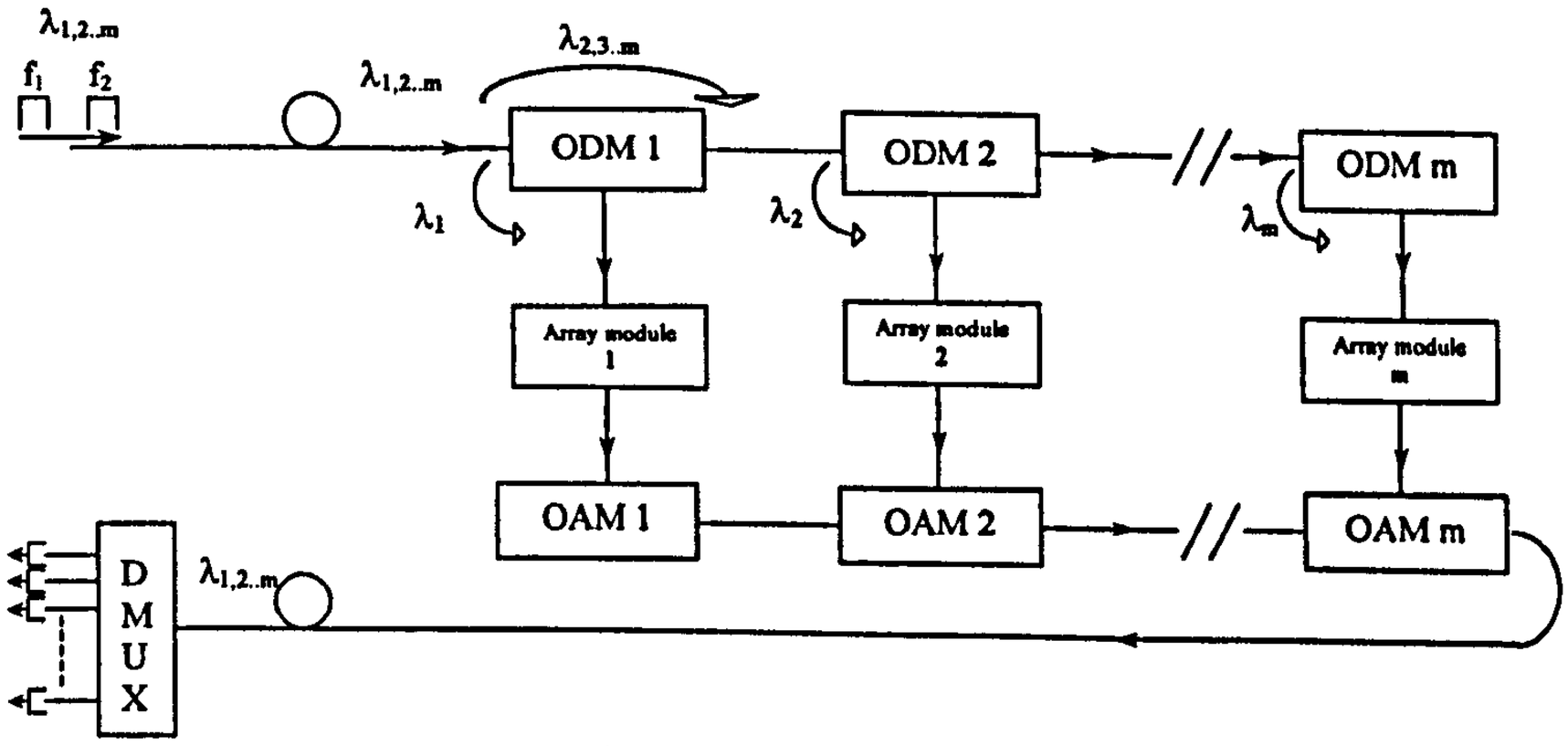

DWDM/TDM Architecture (c)

Figure 5.3: DWDM/TDM Architecture Designs

In architecture (a), the OADMs are arranged in series along the telemetry fibre, such that each wavelength is coupled from the telemetry fibre and launched into an array module. The return signal from the array module is re-combined onto the telemetry fibre and passes through all the remaining OADMs. Architecture (b) requires the "add" and "drop" functions to be performed by separate devices since the return signals from an array module are combined onto a separate telemetry fibre. This architecture has the advantage that if the telemetry fibre is severed then only the signals from the array modules corresponding to OADMs positioned after the break are lost. However, in this configuration the optical signals from each array module do not pass through a common path and therefore do not experience the same optical loss. The optical power levels received for signals from array module 1, for example, will be significantly higher than those from array module m and some form of equalisation will be needed to balance the powers. This could be achieved by either incorporating excess loss into the optical add (or drop) port of the OAM (or ODM) or by pre-emphasis of the launched signals. Architecture (c) is similar to architecture (b); however, the optical signals from all array modules now take a similar path and hence experience approximately the same optical loss.

The insertion loss of each array architecture can be estimated by tracing the path of a single wavelength passing through the array. If there are m array modules and the insertion loss of an "add", "drop" or "pass-through" in the OADM is γ, then the array insertion loss for architectures (a) and (c) is $\gamma^{(m+1)} \cdot IL_{am}$ where we have neglected the extra splice losses in the telemetry fibres. For architecture (b), the insertion loss is estimated for the wavelength that takes the path of highest loss (i.e. λ_m in fig. 5.3b). In this case the array insertion loss is $\gamma^{2m} \cdot IL_{am}$. The insertion loss of this architecture is therefore a factor of γ^{m-1} higher than that of architectures (a) and (c).

5.4 Experimental Arrangement and Component Characterisation

5.4.1 Experimental arrangement

To demonstrate the architectures described in Sec. 5.3, the experimental arrangement shown in fig. 5.4 was set up. This comprises an array interrogated by three wavelengths in an arrangement corresponding to architecture (a). Two OADMs were used, one based on a multi-layer interference filter [5.15] and one based on an interferometric arrangement with in-fibre Bragg gratings [5.16].

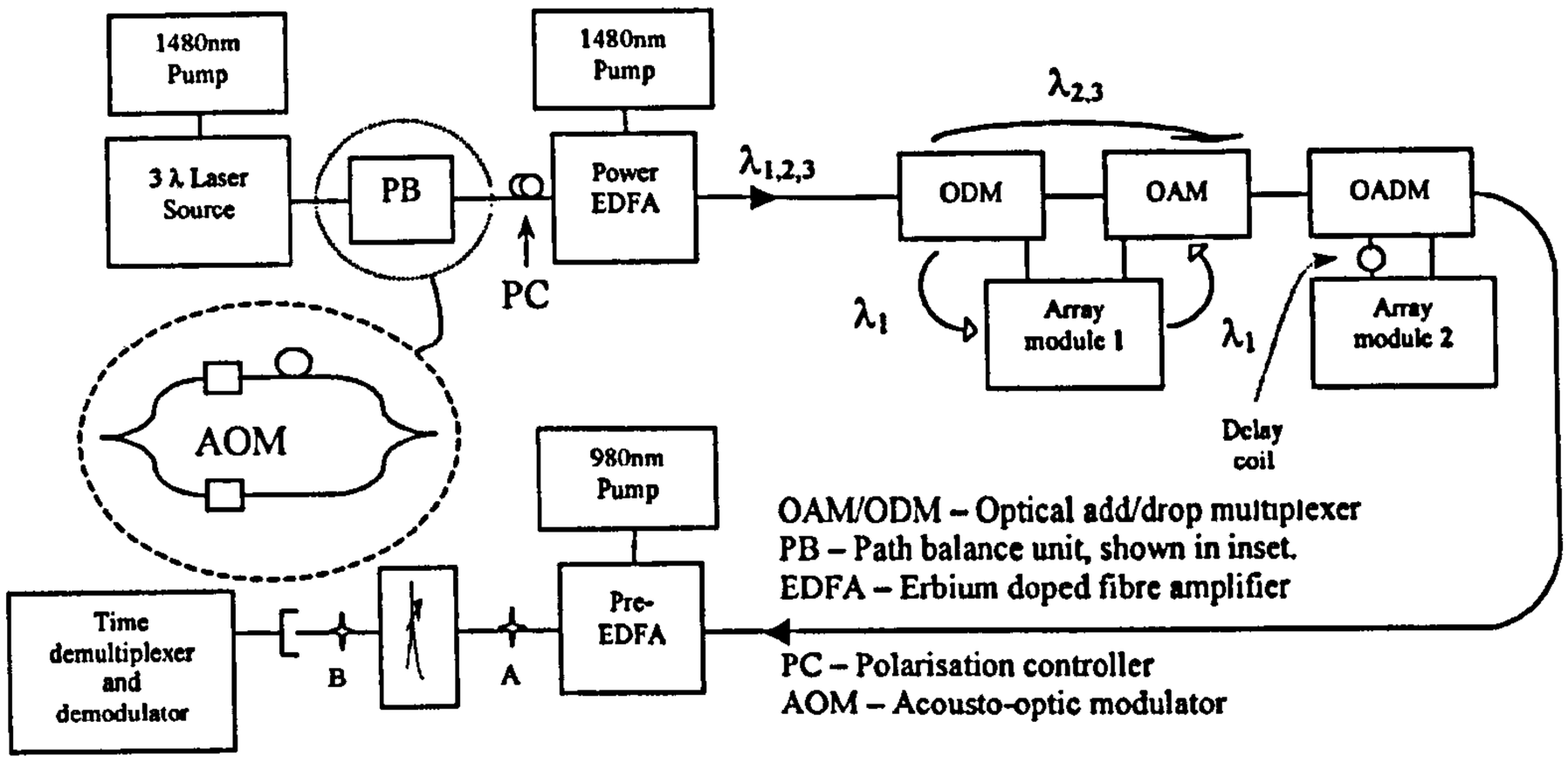

Figure 5.4: Experimental Arrangement

The experimental arrangement comprises two coupler based (with mirror reflectivities ~80-90%) TDM pulsed reflectometric array modules combined onto a pair of fibres. The primary aim of the experiment is to characterise crosstalk between sensors. This was achieved by applying dynamic strains to the fibres in individual sensors and was implemented by winding approximately 1m of the sensor fibre onto individual piezo-electric fibre stretchers made from lead-zirconate titanate (PZT) rings. This allows large test signals, representative of an acoustic signal, to be injected in a quantifiable way into individual sensors and also ensures that there is no non-optical cross-coupling of the test signal between sensors (this was verified by injecting a signal onto a PZT ring that wasn't connected to the other sensors). A hydrophone coil with 100m of fibre [5.17] was also inserted into each sensor coil, such that the total fibre length in each sensor was approximately 101m.

Array module 1 consisted of eight hydrophone coils and array module 2 consisted of four hydrophone coils. The PZT stretchers were shielded from the hydrophone coils to prevent non-optical crosstalk due to acoustics or vibrations. The output of the laser source is launched into the path balance unit. This splits the light into two separate fibres and launches it into separate fibre coupled acousto-optic modulators (AOM) which produce the frequency shifted optical pulses when driven by a pulsed RF signal (in our experiment f_c =10.7MHz). One of the pulses is delayed relative to the other by passing it through a delay coil (202m in length) and re-combined with the other pulse onto a single fibre. These re-combined pulses are then amplified in a power amplifier and launched into the array.

A single wavelength is coupled from the telemetry fibre by the OADM and launched into an array module, and the return signal is then recombined with the telemetry fibre. The fibre used in the array modules has a high numerical aperture (NA=0.21) to reduce bend losses. To overcome the splice losses between the standard telecom fibre (NA=0.11) of the OADMs and this high NA fibre, a mode-matching technique was used, based on splice fattening [5.18], to maintain splice losses typically less than 0.2 dB (low loss splices between the two fibres were supplied by Feasa Enterprises, Ireland). The return signals from the array were amplified in an EDFA configured as a pre-amplifier. This amplifier was pumped by a 980 nm laser diode that supplied 70 mW of optical power and could provide 30 dB of small-signal gain with a noise figure of 3.5 dB. The tuneable optical filter was used to discriminate between the wavelengths. This exhibited an insertion loss of 5 dB and a 3dB bandwidth of 0.42nm. The output of the filter was then detected on a photodiode and the TDM signal was electronically time gated and demodulated to extract the acoustic signals using frequency discriminators.

5.4.2 WDM component specification

The performance of the OADM influences the crosstalk levels observed in an array. Two mechanisms that can give rise to crosstalk are known as: (i) inter-channel crosstalk and (ii) intra-channel crosstalk. Inter-channel crosstalk refers to the power level of adjacent wavelengths that are coupled into the "drop" port of the OADM from the through port or into the through port from the "add" port. This results in a small amount of power at all other wavelengths passing through an array module. Intra-channel crosstalk refers to the amount of light at the "drop" wavelength that passes through the device into the through port rather than being coupled into the "drop" port. This light will interfere with signals coupled back into the telemetry fibre. Intra-channel crosstalk only needs to be considered for architecture (a) and can be ignored in architectures (b) and (c).

The specifications of two OADMs used in the experiment are shown in table 5.1.

Table 5.1: Characteristics of OADMs Used in the Experiment

Device[1]	Insertion Loss	Inter-channel crosstalk	Intra-channel crosstalk	Return Loss
Interference filter based add or drop device[2]	< 0.71 dB	25.9 dB	20.7 dB	> 45 dB
Interferometric, in-fibre Bragg grating device[3]	< 0.5 dB	> 31 dB	28 dB	> 16 dB

[1] Here the channel spacing for each device is 200 GHz. [2] Supplied by JDS-Fitel, US
[3] Supplied by Tecos, Germany

Using the data in table 5.1, we can now consider the implication of the OADM specifications on the cross-talk. The inter-channel crosstalk causes unwanted light from adjacent channels to be coupled into each array; however, since adjacent channels undergo a minimum optical suppression of 51.8 dB (2 × 25.9 dB) for an "add" and "drop" process (for the interference filter based device), crosstalk by this mechanism is negligible. The intra-channel crosstalk causes the two input pulses to each array module to be transmitted directly to the output port of the OADM. These pulses will overlap in time with the return pulses from the array module, obscuring the heterodyne signals; however, by inserting a delay coil of suitable length in the fibre link to the array module, these pulses can be separated in time from the array module return signals.

The performance of the wavelength demultiplexer (WDMUX) may determine the crosstalk levels between sensors in adjacent array modules. Incomplete suppression of adjacent channels by the WDMUX will produce unwanted signals from adjacent array modules on the photodiode. Typically, the adjacent channel suppression for a wavelength demultiplexer is greater than 30 dB [5.19], equivalent to 60 dB in the electrical domain, which is adequate for most applications.

5.4.3 Laser characterisation

The laser sources used in the experiment were based on the Er^{3+} doped distributed feedback fibre laser (DFB FL)[12]. The source consisted of three separate laser cavities spliced in series and pumped by a single 100 mW 1480nm semiconductor pump diode, as shown in fig. 5.5.

[12] The DFB fibre lasers where supplied by Ionas, Blokken 84, DK-3460, Birkerød, Denmark

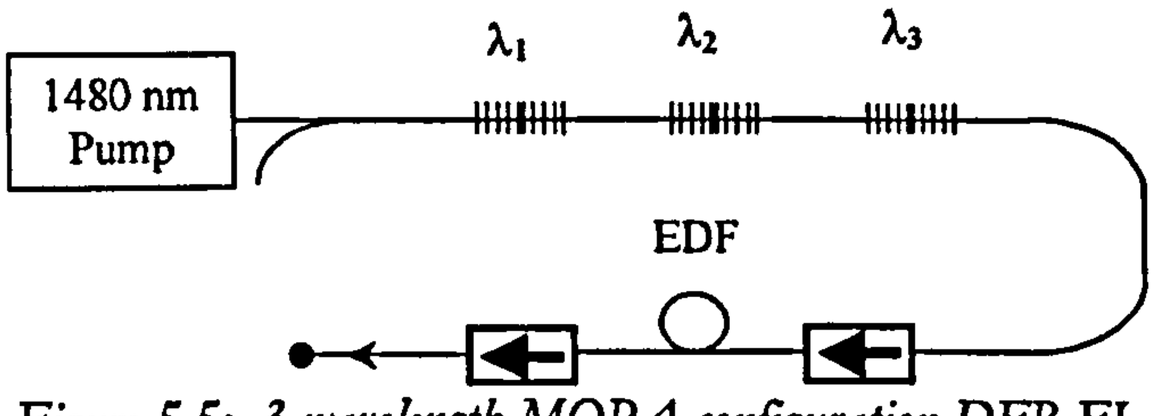

Figure 5.5: 3-wavelength MOPA configuration DFB FL.

The three wavelengths were launched into a length of Er^{3+} doped fibre which was pumped by the residual 1480nm power to form a master-oscillator/power-amplifier (MOPA) configuration [5.20] and produced approximately 2 mW of optical power per wavelength. Each fibre laser produced a single longitudinal mode output and was forced to lase in a single polarisation mode by applying a birefringent phase-shift to the grating [5.21]. The lasers, designed for telecommunications applications, produced optical radiation at wavelengths, compatible with the International Telecommunications Union (ITU) grid, of 1551.68nm, 1553.36nm and 1554.93nm. The optical spectrum is shown in fig. 5.6.

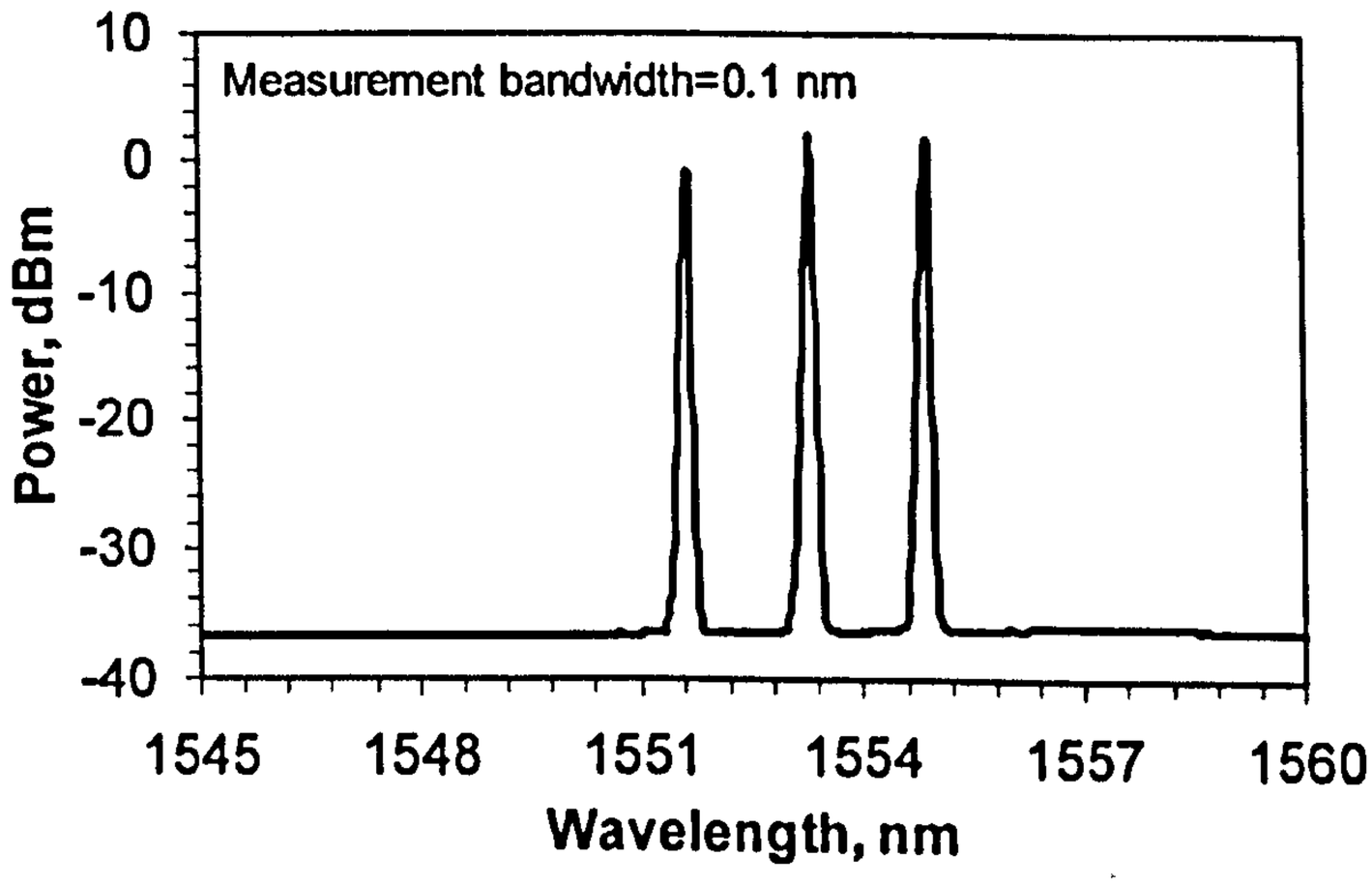

Figure 5.6: Optical spectrum of MOPA output

In an interferometric fibre sensor, the phase resolution can be degraded by both laser relative intensity noise (RIN) and frequency noise. The frequency noise is converted to phase noise by the interferometer and is proportional to the path imbalance in the interferometer. For a Mach-Zehnder interferometer, the phase difference between the two output arms of the interferometer is given by,

$$\Delta\phi = n_{eff} kd \tag{5.6}$$

where k is the free-space wavenumber ($k = 2\pi/\lambda = 2\pi\nu/c$) and d is the fibre path-imbalance. Differentiation of (5.6) with respect to optical frequency, ν, yields,

$$\delta\phi = \frac{2\pi n_{eff} d}{c}\delta\nu \tag{5.7}$$

where $\delta\phi$ and $\delta\nu$ are the phase and frequency noise spectral density respectively. The path imbalance, d, in the experimental arrangement is minimised by the path balancing unit; however, in practice, a non-zero path imbalance will exist. The frequency noise of the laser was measured using a 100m imbalanced interferometer with heterodyne detection [5.22]. The result is plotted in fig. 5.7 for the 1551.68nm laser, in terms of the phase noise amplitude from a Mach-Zehnder interferometer normalised to a 1 m fibre path imbalance as a function of frequency.

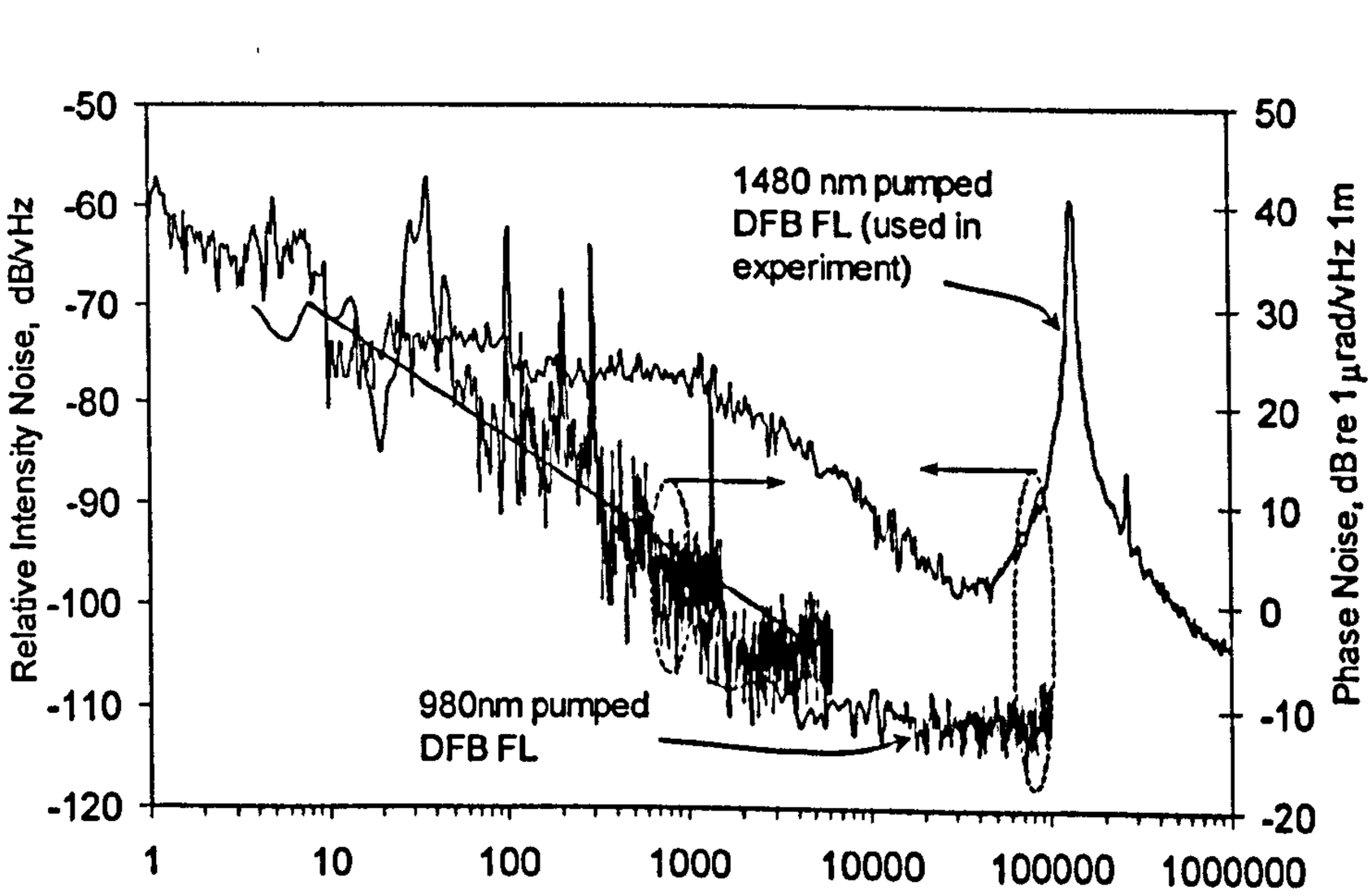

Figure 5.7: Frequency induced phase noise and relative intensity noise of the Er^{3+} DFB fibre laser (λ =1551.68nm) used in the experiment.

The frequency noise of the DFB fibre laser was found to exhibit an $f^{-\gamma}$ relationship where γ=0.6 for frequencies up to 1 kHz. Between 1 kHz and 6 kHz the phase noise spectrum was

flat at 0.6 μrads.$Hz^{-1/2}$ ±58% for a 1m fibre path imbalance. Significant structure was observed at 30 Hz, 40 Hz and 200 Hz where the phase noise was above 100 μrads.$Hz^{-1/2}$ and is believed to be caused by ambient acoustics even though the laser was packaged in an acoustically shielded box.

The RIN of the laser is defined as,

$$RIN\ \left[dB.Hz^{-1}\right] = 10\log\left(\frac{S_{\delta P}(f)}{\overline{P}^2}\right) \qquad (5.8)$$

where $S_{\delta P}(f)$ is the spectral density of the laser power fluctuation and $\overline{P}$ is the mean laser power. The measured RIN of the λ =1551.68nm DFB FL is also shown in fig. 5.7. The RIN was measured to be –77 dB.Hz^{-1} ±2 dB at 1 kHz for a pump power of 100 mW. This level of RIN is unusually high for this type of laser and was found to be due to excess low frequency noise from the current source. Measurements carried out on a single DFB FL of the same design, pumped at 980 nm with a power of 140 mW and a low noise current source have demonstrated RIN levels less than –110 dB.Hz^{-1} ±2 dB at 1 kHz, as shown in fig. 5.7. This laser arrangement also exhibited similar frequency induced phase noise levels to the 1480 nm-pumped DFB FL. This indicates that sufficiently low RIN can be obtained from the DFB FL with these choices of pump power and wavelength. The relaxation oscillation is present at 137kHz and is dependent on the pump power and grating strength [5.23]. Suppression of this peak would be achieved using active feedback to the pump diode [5.24], as described in sec. 7.5. Similar results were obtained for the other two DFB FL's used in the experiment. We return to the subject of noise suppression in DFB fibre lasers in chapter 7.

5.4.4 Power budget considerations

The power budget determines the peak pulse power received from a single reflector in the array and is calculated by considering the insertion loss (IL) or gain of each component in the system. The power budget for the arrangement in fig. 5.4 is given in table 5.2.

Table 5.2: Power Budget

Component	*Loss / Gain*	*Unit*
Laser source	2	dBm
PB unit loss	-14	dB
Post-EDFA gain	22	dB
ODM IL	-0.8	dB
Array module IL	-37	dB
OAM IL	-0.8	dB
Splice loss × 8(0.4 dB per splice)	-3.2	dB
Pre-EDFA gain	14	dB
Tunable filter IL	-5	dB
Margin	-3	dB
Received single pulse power	**-25.8**	**dBm**

Each fibre laser supplies around 2 dBm of optical power, which is reduced by a factor of 14 dB due to the AOM IL and coupler loss in the path balancing unit. The power amplifier is able to supply a considerable amount of gain to the input signals, since despite the relatively high input pulse power, the pulsed nature of the input signals significantly reduces the average input power to the amplifier (the duty cycle was 8.3 dB). The power amplifier supplies 22 dB of gain and thus launches 10 dBm peak power per wavelength into the array. The array module IL is calculated from (5.2) and (5.4) for the case when N =8 and β =0.5 dB and the OAM/ODM IL are taken from table 5.1. The input power to the pre-amplifier for the two wavelengths carrying sensor signals was ~–31.8 dBm per wavelength; however, the power of the third wavelength that did not interrogate an array was ~–3 dBm. The total input power to the pre-EDFA was thus ~–3 dBm which reduced the gain to 14 dB per wavelength.

The received heterodyne signals from each array module are shown in fig. 5.8(a) and (b) corresponding to array module 1 and 2 respectively. The length of the delay coil in array module 2 was set such that the heterodyne signals from this module arrived back at the photodetector in the same time slot as the last four heterodyne pulses from array module 1. Fig. 5.8(c) shows the received signals from array module 2 with the extra pulses due to the intra-channel crosstalk clearly visible, which have been separated from the heterodyne pulses by the delay coil.

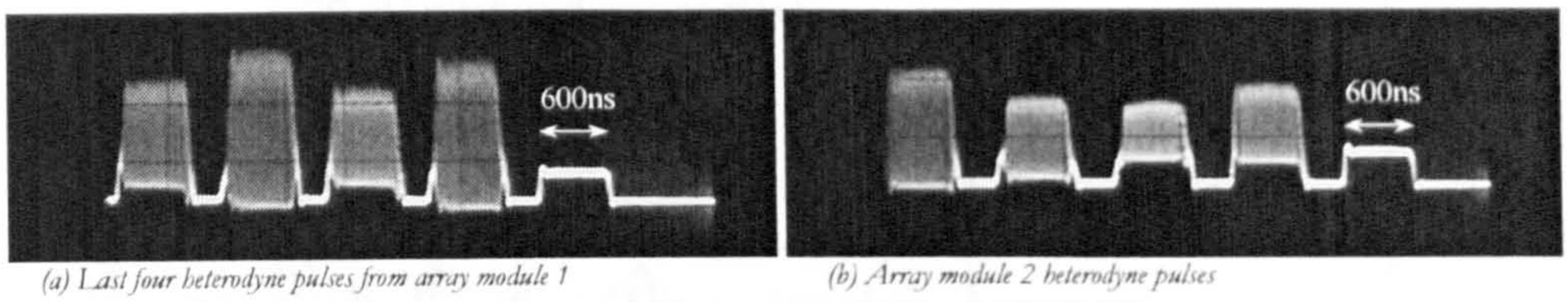

(a) Last four heterodyne pulses from array module 1

(b) Array module 2 heterodyne pulses

(c) Array module 2 TDM signal with intra-channel crosstalk

Figure 5.8: Received heterodyne signals

5.5 Experimental Results

The system was characterised in terms of crosstalk. The sensor-to-sensor crosstalk was measured on array module 2 by applying a narrowband tone at 1 kHz to sensor 2. The signal on an adjacent channel was then measured as shown in fig. 5.9a.

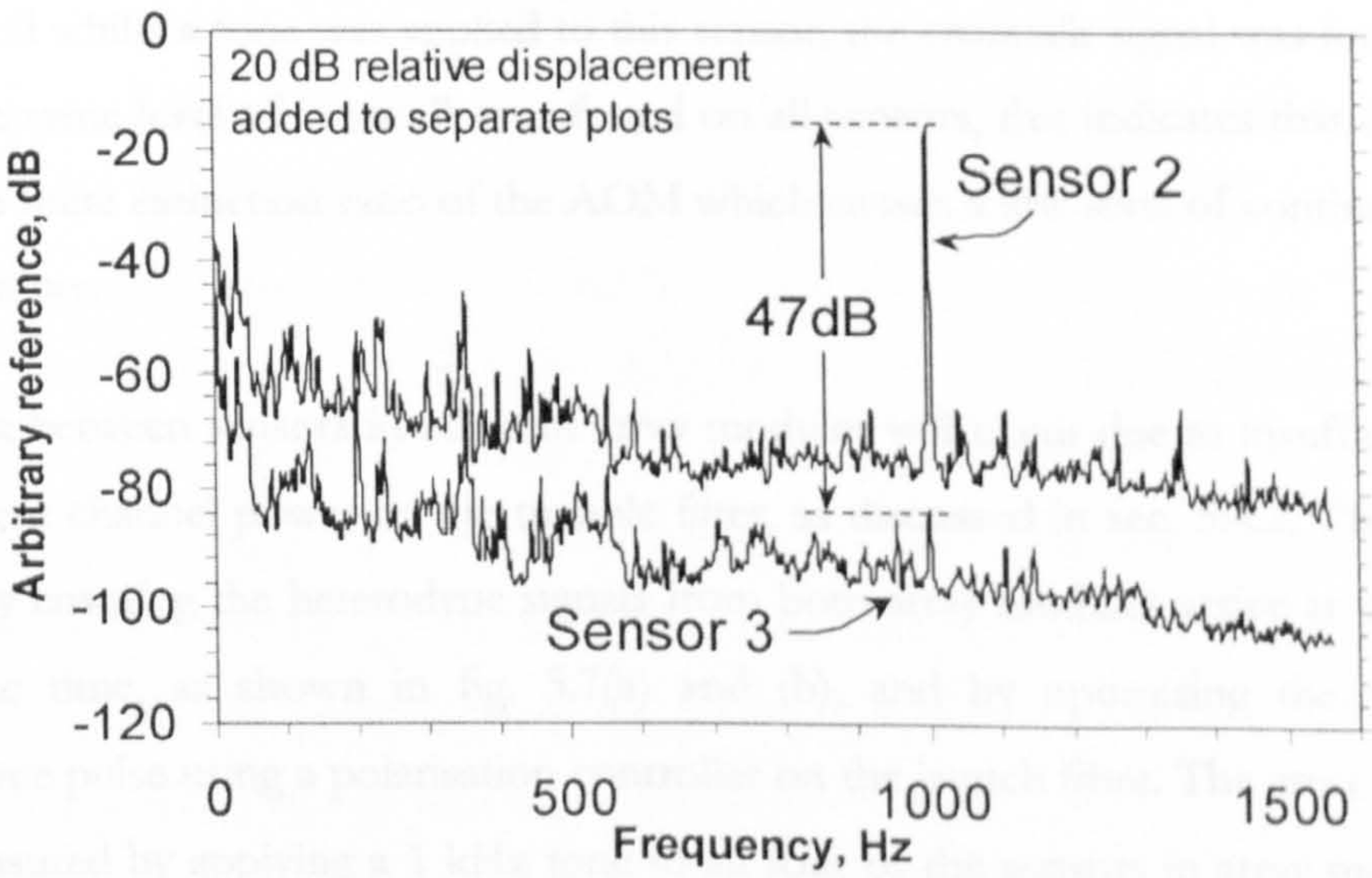

Figure 5.9: (a) Sensor-sensor crosstalk

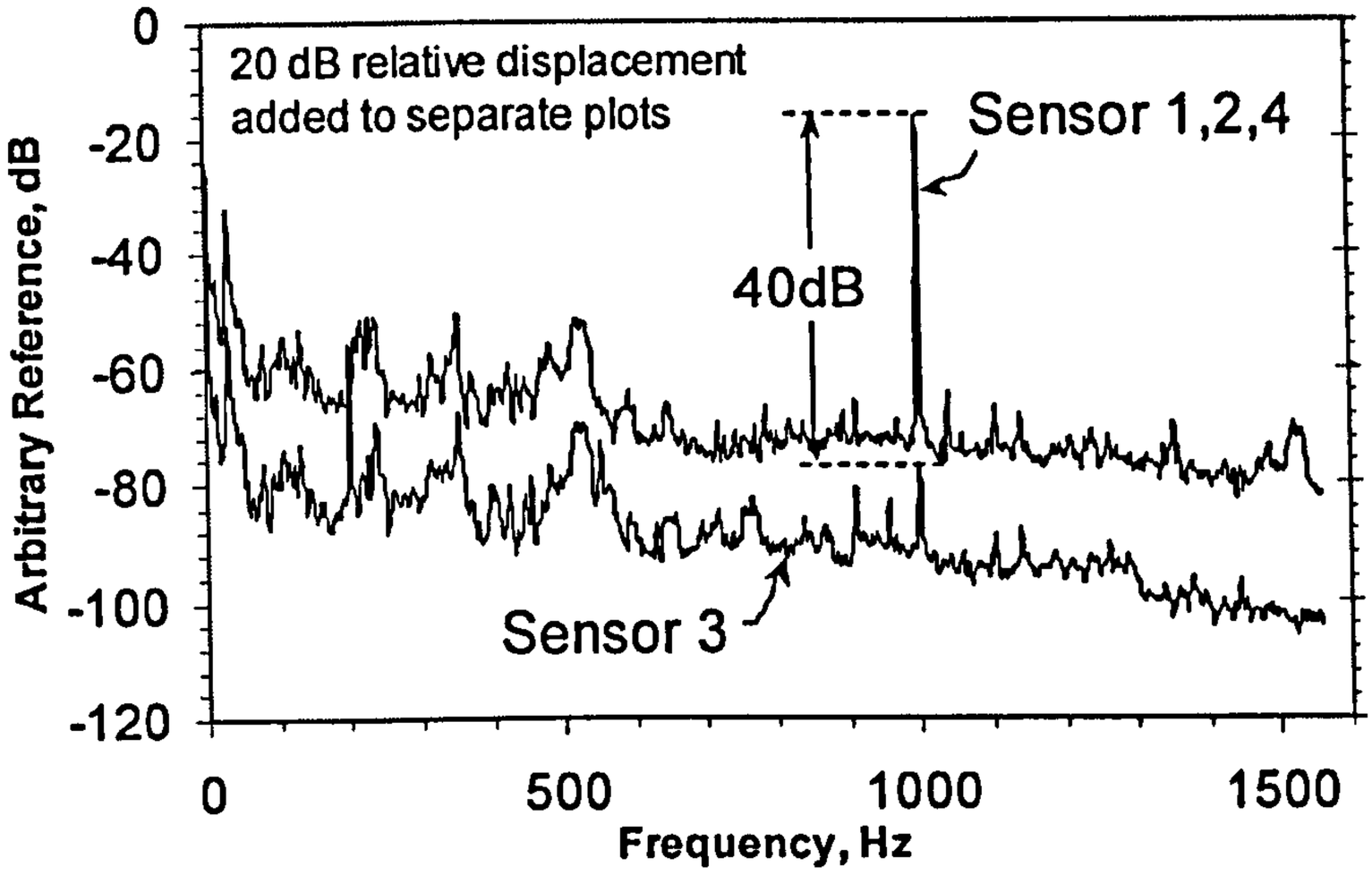

Figure 5.9(con't): (b) Array-sensor crosstalk

The crosstalk level observed after thirty averages was found to be –47 dB and the same level of crosstalk signal was also found on sensors 1 and 4. When tones were simultaneously applied to sensors 1, 2 and 4, the observed level of crosstalk increased to –40 dB as shown in fig. 5.9b. Similar results were found with different combinations of the above measurement. This crosstalk was confirmed to be optical or electronic in origin since, by disconnecting the last sensor coil whilst a tone was applied to this sensor, the crosstalk signal was found to disappear. Since the same level of crosstalk was found on all sensors, this indicates that the cause is likely to be the finite extinction ratio of the AOM which causes a low level of continuous light to leak into the array.

Crosstalk between sensors in adjacent array modules will occur due to insufficient suppression of adjacent channel power by the tunable filter, as discussed in sec. 5.4.2. The worst case was set-up by ensuring the heterodyne signals from both array modules arrive at the photodiode at the same time, as shown in fig. 5.7(a) and (b), and by optimising the visibility of each heterodyne pulse using a polarisation controller on the launch fibre. The array to array crosstalk was measured by applying a 1 kHz tone to all four of the sensors in array module 2, to give a modulation depth of 1 rad, and observing the outputs of the corresponding four sensors in array module 1. The signal applied to one of the array module 2 sensors is shown in fig. 5.10, along with the measured outputs of the array module 1 sensors. The measurement bandwidth was 2.97 Hz. There is a signal visible on the output of sensor 3 which sets the crosstalk level to be -76 dB, taking into account the measurement bandwidth. By slightly detuning the tuneable

filter such that the suppression of the adjacent wavelength is reduced, the crosstalk signal at 1 kHz was found to increase, confirming that the array to array crosstalk includes this mechanism.

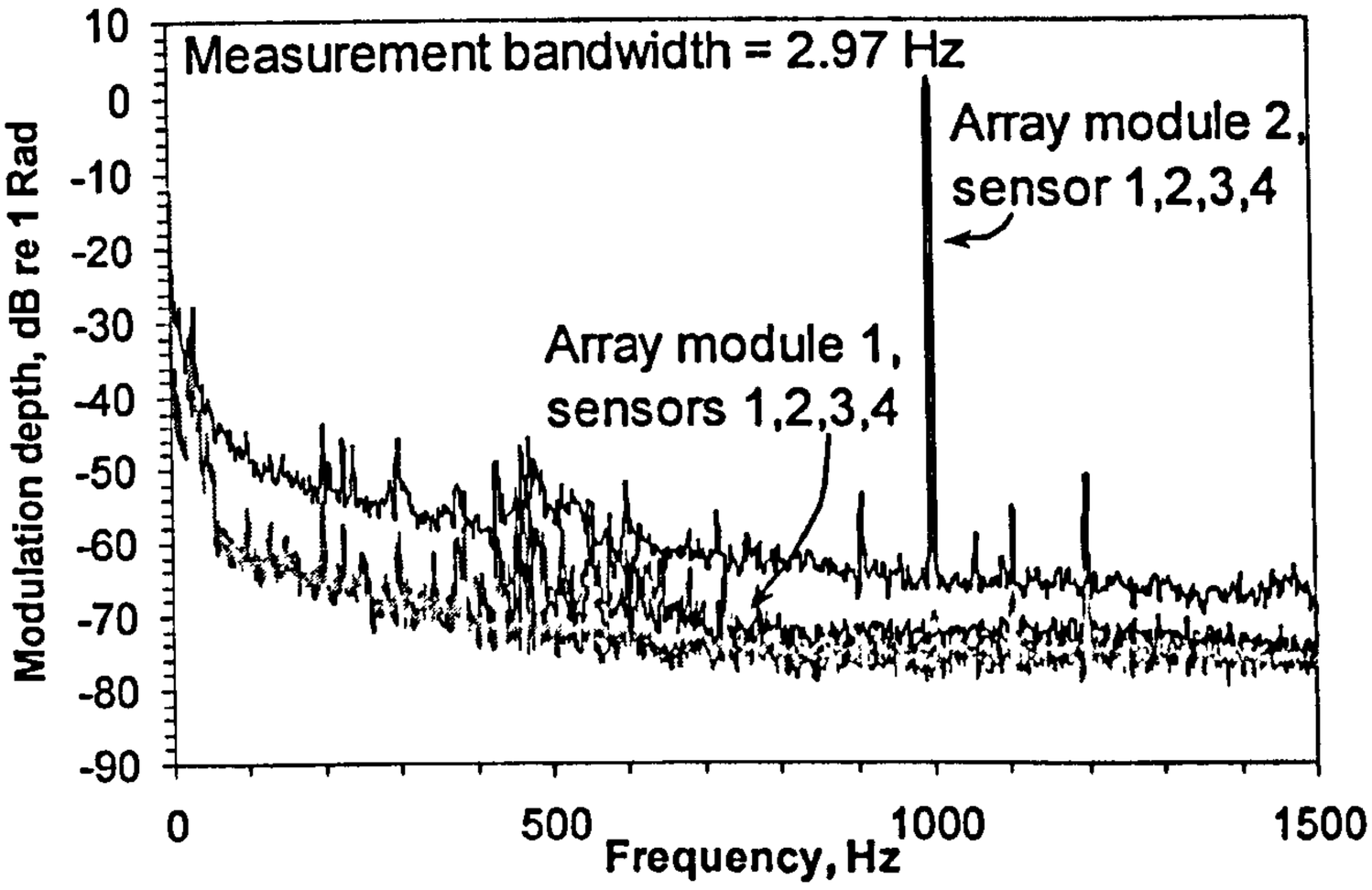

Figure 5.10: Array-array crosstalk

It is straightforward to show that the array-array crosstalk is determined by the adjacent channel suppression of the WDMUX, by measuring the optical spectrum of the signal before and after the tuneable filter (points marked A and B in fig. 5.4). This is shown in fig. 5.11. The received signal consists of three wavelengths, two of which carry TDM signals (1551.68nm and 1553.36nm) and one at 1554.93nm, on a background of laser and amplifier amplified spontaneous emission (ASE) (upper plot in fig. 5.11). When the pass-band of the tuneable filter is centred on the wavelength at 1553.36nm, the adjacent TDM channel at 1551.68 nm is suppressed by 37 dB (lower plot in fig. 5.11). This corresponds to 74 dB in the electrical domain, which agrees closely with the observed level of crosstalk.

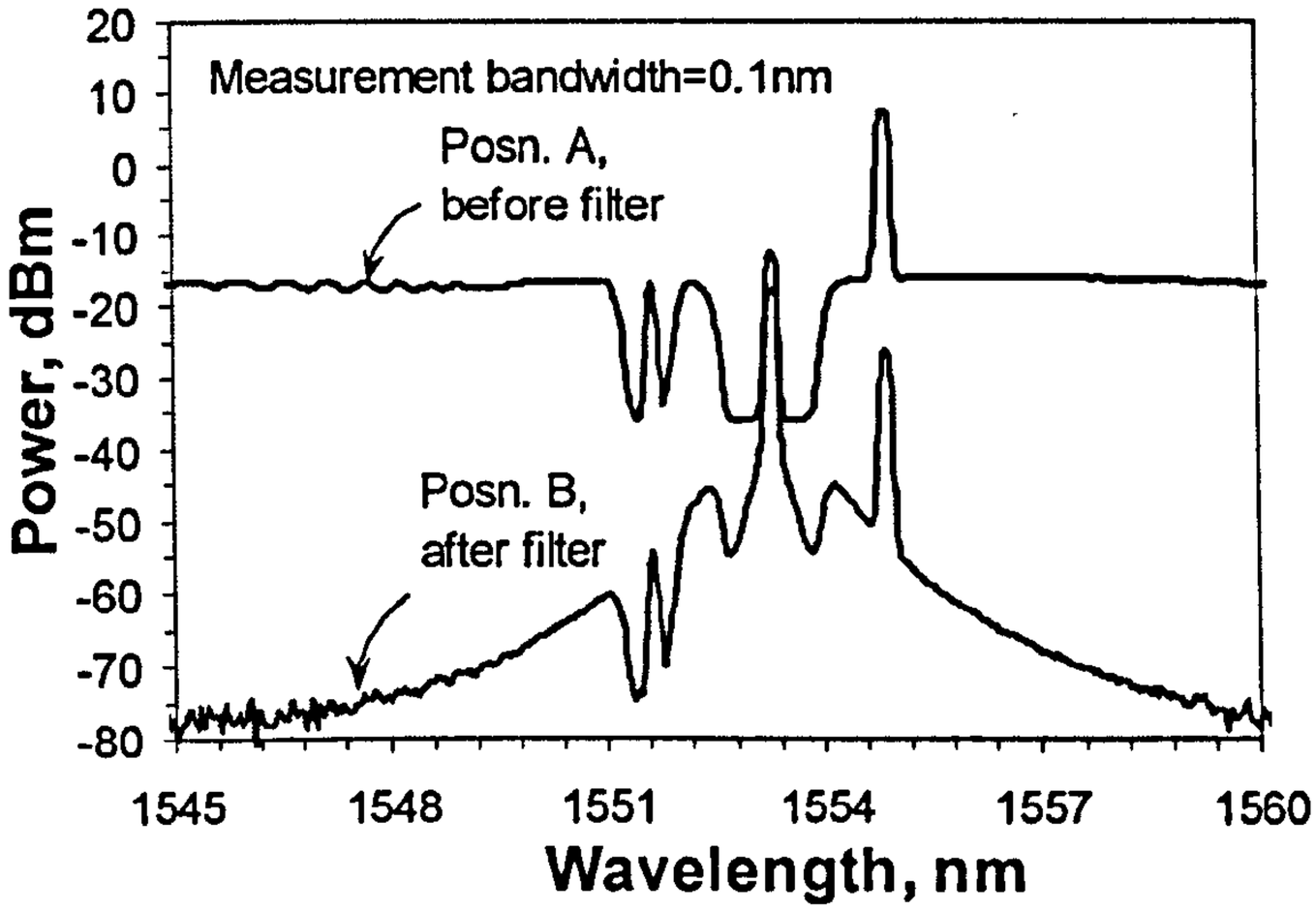

Figure 5.11: Optical spectrum at input and output of the tuneable filter

Referring to fig. 5.10, a difference of 9 dB was observed in the noise floors from sensors in array modules 1 and 2. An independent calibration of the hydrophone responsivities showed a difference of 9 dB between the sensors used in each array module. This would imply that the phase resolution in this experiment was limited by ambient acoustic noise in the laboratory.

5.6 System Model: Signal Resolution and Dynamic Range

We now consider the pressure resolution and dynamic range of a hydrophone incorporated into the architecture described above. By considering the sources of noise in the system, the phase resolution of the interferometer and hence the pressure resolution of the hydrophone can be determined. By also considering the maximum signal that can be faithfully measured and demodulated, the dynamic range can be determined. The relationship between the sensor phase resolution as a function of the number of sensors in an array is shown and the theoretical performance of a hydrophone incorporated into this type of array is determined.

5.6.1 Maximum signal

The maximum measurable signal is determined by the available bandwidth that the phase modulation sidebands have to occupy and this is dependent on the degree of time multiplexing. To determine the maximum signal, we use the same approach as that taken in [5.25]. In the TDM scheme, the received signal from a single sensor consists of a burst of modulated IF of frequency f_c and pulse width, w, which is repeated at a frequency, f_{rep}. For the case where $f_c >> f_{rep}$, the spectrum of this signal is as shown in fig. 5.12. The bandwidth available, ΔB, for the phase modulated signal to occupy is also shown to be equal to f_{rep}.

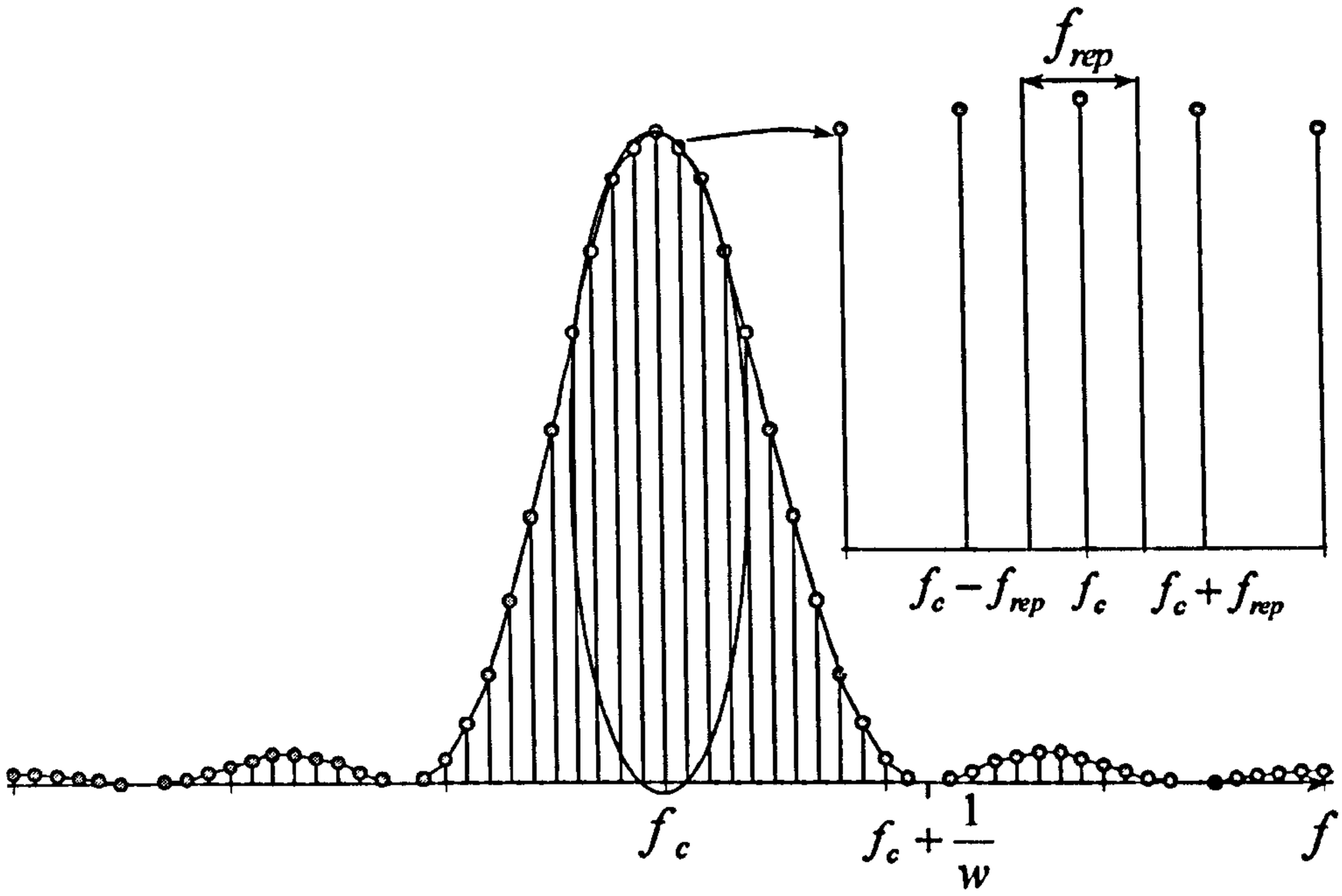

Figure 5.12: Power spectrum of gated heterodyne pulse (DC offset removed)

Carson's rule states that for sinusoidal angular modulation, the bandwidth occupied by the signal is equal to twice the sum of the peak frequency deviation, f_{pk}, and the modulation frequency, f_{mod}, [5.26]

$$\Delta B = 2(f_{pk} + f_{mod}) \tag{5.9}$$

For a sinusoidal modulating function, $\phi(t)$ equal to $\phi_o \cos(2\pi f_{mod} t)$, the peak frequency deviation, f_{pk}, is given by, $\frac{1}{2\pi}\left|\frac{d\phi(t)}{dt}\right|$ such that,

$$\left|f_{pk}\right| = \phi_o f_{mod} \tag{5.10}$$

Therefore, the maximum modulation depth, ϕ_{max}, that can be accommodated by the available bandwidth, f_{rep}, is given by equating (5.9) and (5.10) and using (5.5) such that,

$$\phi_{max} = \left(\frac{c}{4n_{eff} l (N+1) f_{mod}} - 1\right) \tag{5.11}$$

From this, the maximum bandwidth limited signal can be determined. For example, if N =8, l =80m, n_{eff} =1.465 and f_{mod} =1 kHz then ϕ_{max} ~68 rad which occupies a bandwidth of ΔB ~139 kHz. In practice, the maximum signal may be limited by the performance of the demodulation electronics; for example, the dynamic range and linearity of the frequency discriminator. It is thus necessary to design the demodulator such that the bandwidth limited dynamic range is achieved. By applying digital techniques to the demultiplexing and demodulation process, it is possible to improve both the electronic phase resolution and dynamic range over that achieved by analogue devices. It is straightforward to implement a fringe counter in the demodulation algorithm that allows unambiguous phase measurement greater than 2π [5.27]. The simplicity of the digital demodulator also significantly reduces the cost of the demodulation electronics for large multiplexed arrays.

5.6.2 Interferometric phase resolution

The interferometric phase resolution for the system can be determined by calculating the IF power to noise power ratio or carrier-to-noise ratio (CNR) after the heterodyne pulse has been gated and band-pass-filtered. This is then equated to the phase resolution, $\delta\phi_{min}$ by assuming the noise level is a small-signal phase modulation and deducing the ratio of the carrier power to the power in the first modulation sideband. The carrier power is given by the mean-square of the ac component of (5.3) multiplied by the duty cycle, D, and the pre-amplifier gain, G_{pre}, such that the CNR is,

$$CNR = \frac{2(RVP_r DG_{pre})^2}{\overline{i_n^2}} \approx \left(\frac{\sqrt{2}}{\delta\phi_{min}}\right)^2 \qquad (5.12)$$

where P_r is the power returned from a single reflector at the input to the pre-EDFA and $\overline{i_n^2}$ is the noise power.

The value of $\overline{i_n^2}$ contains contributions from the following: (i) laser relative intensity noise; (ii) laser frequency noise; (iii) RF oscillator phase noise; (iv) detector thermal noise; (v) signal shot noise; (vi) signal-spontaneous beat noise; (vii) spontaneous-spontaneous beat noise; and (viii) spontaneous-shot beat noise; where the last three noise terms are due to the amplifier

spontaneous emission (ASE) generated by the pre-EDFA. We assume that the ASE added by the power-EDFA is negligible.

To allow comparison of the magnitude of each noise source it is useful to convert each one, using (5.12), into an equivalent phase noise. By assuming each noise source is statistically uncorrelated, the sum of the square of each noise source is then calculated to determine $\delta\phi_{min}$.

Intensity noise from the laser induces amplitude modulation of the optical signal, causing the RIN spectrum to appear as amplitude modulation sidebands around the carrier. The equivalent phase noise contribution due to RIN is thus,

$$\delta\phi_{laser-RIN} = \sqrt{RIN(f)} \qquad (5.13)$$

Laser frequency noise is quantified by assuming that the interferometer path imbalance is 1 m and plotting a best-fit line through the phase noise spectrum of the laser, shown in fig. 5.6. The phase noise amplitude, in rad.$Hz^{-1/2}$, due to the laser frequency noise can then be expressed as,

$$\delta\phi_{laser-freq} = 112\times10^{-6} f^{-0.61} \qquad (5.14)$$

over the frequency range of 10 Hz to 1 kHz. A 1m fibre path imbalance is representative of the accuracy to which the sensor fibre lengths can be matched in practice.

The RF signal that drives the AOM will impose sideband noise on the optical signal. Oven controlled clock oscillators can achieve a CNR of 105 dB.$Hz^{-1/2}$ at 10Hz and 110 dB.$Hz^{-1/2}$ at 1 kHz [5.29]. We take the oscillator noise $\delta\phi_{osc}$ to be 8 μrad.$Hz^{-1/2}$.

The detector thermal noise current is determined by the value of the load resistance, R_L, and is given by,

$$\overline{i_{th}^2} = \frac{4kT_e\Delta f}{R_L} \qquad (5.15)$$

where k is the Boltzman constant and T_e is the effective noise temperature of the amplifier. The value of R_L is chosen to be high enough to give sufficient gain to the photocurrent but

low enough to allow sufficient dynamic range to be available for the carrier signal to occupy without distortion. (5.15) can be expressed in terms of an equivalent phase noise, thus,

$$\delta\phi_{th} = \frac{1}{RVDP_r G_{pre}} \sqrt{\frac{4kT_e \Delta f}{R_L}} \tag{5.16}$$

Photon shot noise generated on detection is given by,

$$\overline{i_{sh}^2} = 2ei(t)\Delta f = 4eRDP_r G_{pre} \Delta f \tag{5.17}$$

where e is the electron charge, Δf is the measurement bandwidth and the average photocurrent, $\overline{i(t)}$, is taken from (5.3). The signal-spontaneous, spontaneous-spontaneous and spontaneous-shot noise currents (assumed to be white in spectral shape) are given by (5.18), (5.19) and (5.20) respectively [5.28],

$$\overline{i_{s-sp}^2} = \frac{4(e\eta G_{pre})^2 FDP_r \Delta f}{h\nu_m} \tag{5.18}$$

$$\overline{i_{sp-sp}^2} = (e\eta G_{pre} F)^2 \Delta\nu_{opt} \Delta f \tag{5.19}$$

$$\overline{i_{sp-sh}^2} = 2e^2 \eta G_{pre} F \Delta\nu_{opt} \Delta f \tag{5.20}$$

where η is the detector quantum efficiency, F is the pre-amplifier noise figure, h is the Planck constant, ν_m is the optical frequency, $R = e\eta / h\nu_m$ and $\Delta\nu_{opt}$ is the optical bandwidth. By inspection of (5.17), (5.18), (5.19) and (5.20) it can be seen that $i_{sp-sp}^2 >> i_{sp-sh}^2$ by a factor of $0.5\eta G_{pre} F$ and $\overline{i_{s-sp}^2} >> \overline{i_{sh}^2}$ by a factor of $\eta G_{pre} F$, thus $\overline{i_{sp-sh}^2}$ and $\overline{i_{sh}^2}$ can be neglected. $\overline{i_{sp-sp}^2}$ and $\overline{i_{s-sp}^2}$ can be re-expressed in terms of an equivalent phase noise such that,

$$\delta\phi_{sp-sp} = \frac{h\nu F}{VP_r D} \sqrt{\Delta\nu_{opt} \Delta f} \tag{5.21}$$

$$\delta\phi_{s-sp} = \sqrt{\frac{4Fh\nu\Delta f}{V^2 P_r D}} \tag{5.22}$$

When a hydrophone is placed in the ocean, the background acoustic noise will contribute to the total noise. This has been empirically determined for the quietest sea state referred to as deep sea state zero (DSS0) [5.30], such that the root-mean-square amplitude of pressure fluctuations, in $Pa.Hz^{-1/2}$, can be approximated by,

$$\delta P_{DSS0} = 3.1\times10^{-2} f^{-0.83} \tag{5.23}$$

where f is the acoustic frequency. The phase noise generated due to sea state, $\delta\phi_{DSS0}$ is thus determined by the hydrophone responsivity, r, measured in $rad.Pa^{-1}$.

The acoustic pressure resolution of the hydrophone can thus be calculated for the two cases limited by: (i) the sensor self noise and (ii) self-noise and ambient acoustic noise in the ocean using (5.24) and (5.25) respectively,

$$\delta\phi_{self} = (\delta\phi^2_{laser-RIN} + \delta\phi^2_{laser-freq} + \delta\phi^2_{osc} + \delta\phi^2_{th} + \delta\phi^2_{sp-sp} + \delta\phi^2_{s-sp})^{-1/2} \tag{5.24}$$

$$\delta\phi_{ambient} = (\delta\phi^2_{laser-RIN} + \delta\phi^2_{laser-freq} + \delta\phi^2_{osc} + \delta\phi^2_{th} + \delta\phi^2_{sp-sp} + \delta\phi^2_{s-sp} + \delta\phi^2_{DSS0})^{-1/2} \tag{5.25}$$

5.6.3 Sensor pressure resolution and dynamic range

It is now necessary to determine the received optical power, P_r, at the input to the pre-EDFA, since this will determine the sensor phase resolution. P_r will be a function of the number of hydrophones in the array and the launched power, P_l. P_l will be determined by the large signal gain characteristics of the power-EDFA. The pre-amplifier used in the above experiment has been characterised for large signal gain and the result will be used for the following analysis. Fig. 5.13 shows the variation in gain with input power for this amplifier. The EDFA will respond to the average total input power: thus to calculate the launched power, the total average input

power is calculated and fig. 5.13 is used to determined the gain provided. The average launched power is then converted to peak power launched per wavelength.

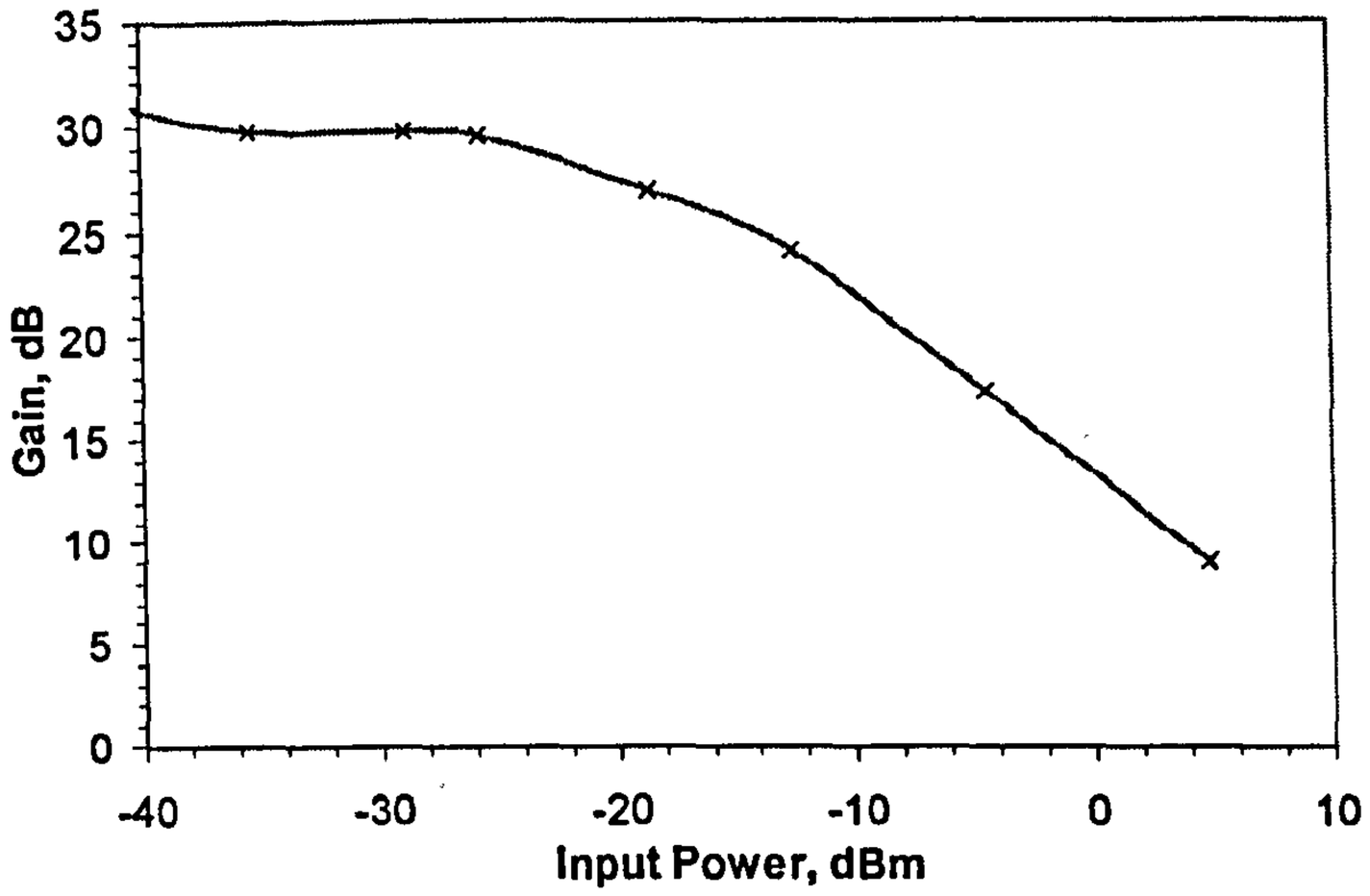

Figure 5.13: Input power versus gain for the power amplifier used in the analysis

We will assume the TDM architecture is that shown in fig. 5.2 and hence the IL of this array module is,

$$IL_{am} = \frac{(1-\alpha_1)^2}{16} \tag{5.26}$$

where α_1 is given by (5.2) and the factor of 16 arises due to the three telemetry couplers shown in fig. 5.2. The insertion loss of an array for architecture 1 or 3 can thus be expressed as,

$$IL_a = \gamma^{(m+1)} IL_{am} \tag{5.27}$$

and the input power to the pre-EFDA, P_r, is then given by $IL_a P_l$. The number of sensors in an array is given by $4Nm$. Fig. 5.14 shows the variation of phase resolution (due to sensor self noise) with the number of sensors in the array and the variation in received power with number of sensors. Here we have taken V=0.5, F=2.5, R=1A.W^{-1}, λ=1550nm, D=1/36, N=8, $\Delta\nu_{opt}$=98GHz , Δf=1Hz, β=0.5dB, γ=1.5dB, $R_L = 1.28\times10^5\Omega$, n_{eff}=1.465 and

T_e=600K which are considered representative values for a practical system. The peak input power to the power-EDFA is taken to be 2mW per wavelength.

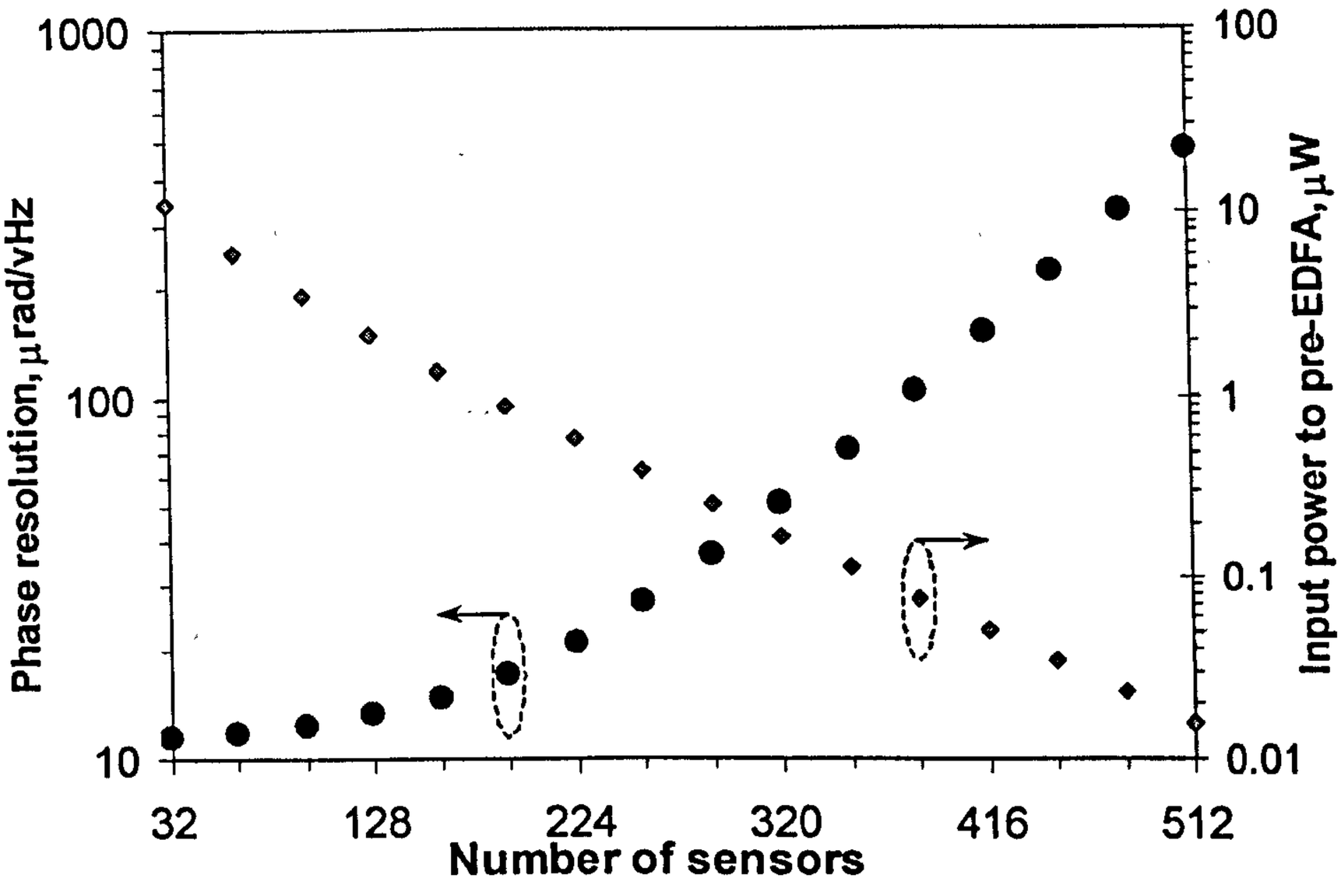

Figure 5.14: Variation of phase resolution with number of sensors

Each consecutive point on the graph corresponds to an increase in the number of sensors by 32 and hence an addition of one extra wavelength. Thus, 512 sensors require 16 wavelengths; at a spacing of 1.6nm these can easily be accommodated within the Er^{3+} gain window.

It is now possible to determine the pressure resolution and maximum bandwidth limited signal of a hydrophone incorporated into this architecture. This is shown in fig. 5.15 for an array with m=6, l=80m and r=0.31 rad.Pa^{-1} and hence 192 hydrophones, for the cases of the sensor limited by self-noise and ambient acoustic noise. With this value of hydrophone responsivity, the in-water hydrophone is limited by self-noise above 2 kHz and ambient acoustic noise below 2 kHz. The dynamic range is given in fig. 5.16 for both cases.

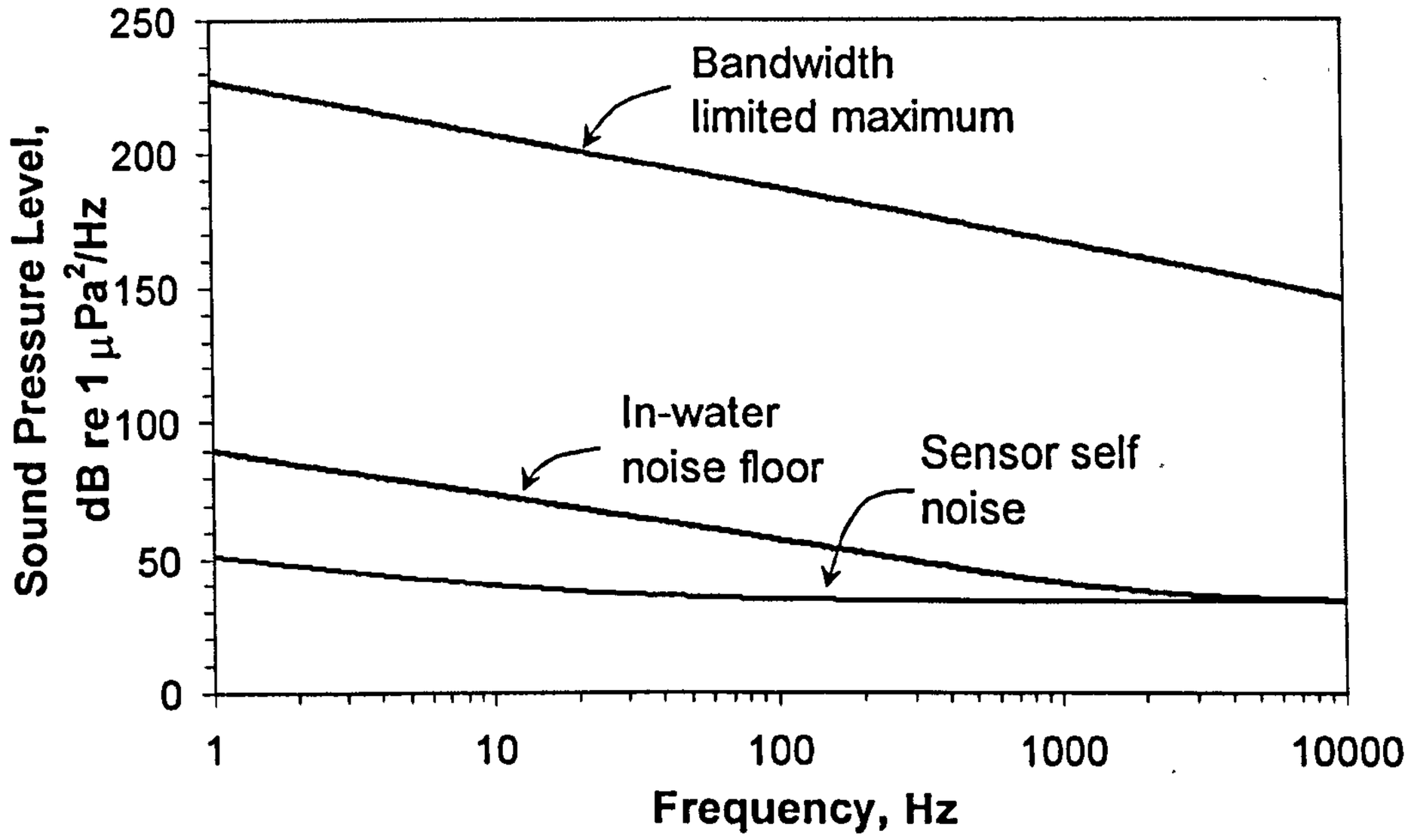

Figure 5.15: Minimum and maximum detectable pressures

In a practical system, the hydrophone responsivity is chosen to be low enough such that the reduction in low frequency dynamic range, due to the ambient acoustic noise, is minimised. However, it must be high enough such that the required pressure resolution at higher frequencies is achieved. If the hydrophone is self-noise limited, it exhibits a dynamic range between 110 dB and 176 dB up to 10 kHz. This is reduced to between 110 dB and 130 dB when the hydrophone pressure resolution is limited by ambient acoustics.

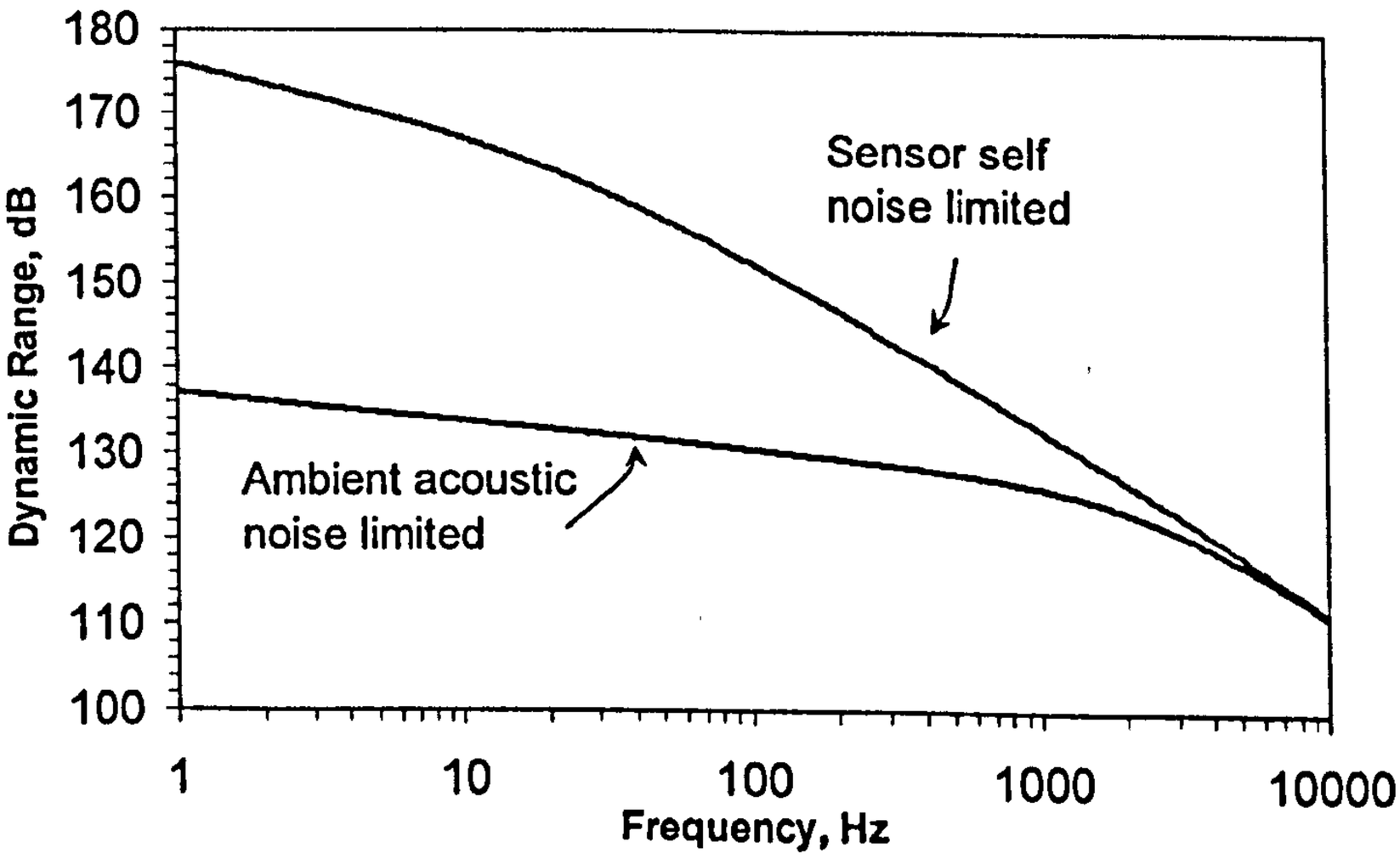

Figure 5.16: Sensor dynamic range

We now consider the relative magnitudes of each noise source to determine the most significant. The magnitude of each noise source is given in table 5.3, calculated using the design parameters stated above for arrays with 192 and 384 sensors at a frequency of 500Hz.

Table 5.3: Magnitude of each noise source for an array with 192 and 384 sensors at a frequency of 500 Hz

Noise contribution	192	384
	$\mu rad.Hz^{-1/2}$	
$\delta\phi_{th}$	0.4	3.5
$\delta\phi_{sp-sp}$	7.2	72
$\delta\phi_{s-sp}$	14	43
$\delta\phi_{laser-freq}$	2.5	2.5
$\delta\phi_{laser-RIN}$	4	4
$\delta\phi_{osc}$	8	8
$\delta\phi_{DSS0}$	56	56
$\delta\phi_{self}$	15	79

It is shown in table 5.3 that for a 192 sensor array (self-noise only), the sensor resolution will be limited by signal-spontaneous beat noise from the pre-EDFA. If the array size is increased to 384 sensors, the spontaneous-spontaneous beat noise dominates. This is due to the signal power dependence of the signal-spontaneous beat noise in (5.18). When the hydrophone is placed in the ocean, the pressure resolution will be limited in both cases by ambient acoustics. It is worth noting that in the above analysis it is assumed that non-linear effects due to the high launch peak powers (>1W) are negligible. This is valid for the case where the array link fibres are short (<<1 km) however these effects must be considered for longer link lengths. We shall investigate the effects of high launch powers and long link lengths in the next chapter.

In the experimental arrangement, the phase resolution of the sensors in array module 1 was found to be ~100 $\mu rad.Hz^{-1/2}$ ±25% at 1.5 kHz using the data in fig. 5.10. The contribution from laser RIN in these experiments would limit the resolution to approximately this value using the data given in fig. 5.7. However, as stated above, the difference in noise floors obtained from the different hydrophone sensors indicates that the phase resolution was limited by ambient acoustics. The contributions from other noise sources would be significantly lower

than this. Optimisation of the laser performance would allow the sensor noise performance described above to be achieved.

5.7 Conclusion

In this paper we have demonstrated multiplexing of interferometric fibre-optic sensors using TDM and DWDM. An array consists of m TDM array modules each interrogated by a single wavelength. We have presented various architectures and demonstrated a practical implementation of one of the architectures. The demonstration used single-mode DFB fibre lasers as sources and discussed the typical performance obtainable from this type of laser. We have shown that these architectures can theoretically be extended to interrogate at least 192 sensors through two fibres whilst achieving low frequency pressure resolution limited by optical amplifier noise with a bandwidth-limited dynamic range up to 177 dB. If the sensors are designed as underwater hydrophones in a sonar array, the low frequency pressure resolution in-water becomes limited by the ambient acoustics and the maximum effective dynamic range is between 110 dB and 135 dB dependent on frequency.

These types of architecture can be adapted for any applications requiring large arrays or networks of sensor elements to be efficiently multiplexed. In particular, for seismic surveying arrays such as ocean bottom-cables, these multiplexing architectures may provide a considerable reduction in the weight, volume and cost of the cable.

References

[5.1] P.J. Nash, G.A. Cranch, 1999 "Multi-channel optical hydrophone array with time and wavelength division multiplexing", *Proc. 13th Conf. Optical Fibre Sensors*, SPIE vol. 3746, pp. 304-307, Kyongju, Korea

[5.2] A.R. Davis, C.K. Kirkendall, A. Dandridge, A.D. Kersey, 1997 "64 channel all optical deployable acoustic array", *Proc. 12th Conf. Optical Fibre Sensors*, Technical Digest, Post conference Edition. Opt. Soc. America, Washington, DC, USA, pp. 616-619

[5.3] A.D. Kersey, A. Dandridge, 1989 "Comparative analysis of multiplexing techniques for interferometic fiber sensing ", *Fiber Optic and Laser Sensors*, SPIE 1120 236-246

[5.4] A.D. Kersey, A. Dandridge, A.B. Tveten, 1987 "Time division multiplexing of interferometric fibre sensors using passive phase generated carrier interrogation" *Optics Letters* 12 (10) 775-777

[5.5] A. Dandridge, A.B. Tveten, A.D. Kersey, A.M. Yurek, 1987 "Multiplexing of interferometric sensors using phase generated carrier techniques" *J. Light. Tech.* LT-5 (7) 947-952

[5.6] S. Vohra, A. Dandridge, 1996 "A hybrid WDM/TDM reflectometric array ", *Proc. 11th Optical Fibre Sensors*, Advanced Sensing Photonics. Japan Soc. Appl. Phys, Tokyo, Japan; 2 vol. 712+17, vol. 1, pp..534-7

[5.7] J. Sæther, K. Bløtekjær, 1996 "Optical amplifiers in multiplexed sensor systems – Theoretical prediction of noise performance ", *Proc. 11th Opt. Fibre Sensors Conf.*, Advanced Sensing Photonics. Japan Soc. Appl. Phys, Tokyo, Japan, vol. 1, pp. 518-521

[5.8] J. Sæther, K. Bløtekjær, 1997 "Optical amplifiers in time domain multiplexed sensor systems", *Proc. 12th Opt. Fibre Sensors Conf.*, OSA Tech. Digest Series, vol. 16, pp. 586-589

[5.9] J.L. Wagener, C.W. Hodgson, M J F Digonnet, H J Shaw, 1997 "Novel fiber sensor arrays using Erbium-doped fiber amplifiers" *J. Light. Tech.*, 15 (9) 1681-1688

[5.10] C.W. Hodgson, M.J.F. Digonnet, H.J. Shaw, 1997 "Large-scale interferometric fiber sensor arrays with multiple optical amplifiers" *Optics Letters* 22 (21) 1651-1653

[5.11] A.D.Kersey, 1991 "Demonstration of a hybrid time/wavelength division multiplexed interferometric fibre sensor array" *Elec. Lett.* 27 (7) 554-555

[5.12] J. Dakin, C.A. Wade, M.L. Henning, 1984 "Novel optical fibre hydrophone array using a single laser source and detector" *Elec. Lett.* 20 53-54

[5.13] J.L. Santos, F. Farahi, T. Newson, A.P. Leite, D.A. Jackson, 1992 "Frequency multiplexing of remote all-fiber Michelson interferometers with lead insensitivity" *J. Light. Tech.* 10 (6) 853-863

[5.14] P.J. Nash, G.A. Cranch, L. Cheng, D. de Bruijn, I. Crowe, 1998 "32 element TDM optical hydrophone array", *Proc. European Workshop on Optical Fibre Sensors*, SPIE vol. 3483, pp. 238-242

[5.15] G.P. Agrawal, *Fiber-Optic Communication Systems.* New York: Wiley 2nd edn., 1997, sec. 7.2.2.

[5.16] See for example I. Baumann, J. Seifert, W. Nowak, M. Sauer, 1995 "Compact all-fiber add-drop-multiplexer using fibre Bragg gratings" *IEEE Phot. Tech. Lett.* 8 (10) 1331-1333

[5.17] P.J. Nash, J. Keen, 1990 "Design and construction of practical optical fibre hydrophones" *Proc. Inst of Acoustics* 12 (4) 201-212

[5.18] E.M. O'Brien and C.D. Hussey, 1999 "Low-loss fattened fusion splices between different fibres" *Elect. Lett.* 35 (2) 168-169

[5.19] Photonetics MICS-16 wavelength demultiplexer specification sheet, Feb. 1998.

[5.20] M. Sejka, P. Varming, J. Hübner, M. Kristensen, 1995 "Distributed feedback Er^{3+}-doped fibre laser" *Elec. Lett.* 31 (17) 1445-1446

[5.21] J.L. Philipsen, M.O. Berendt, P. Varming, V.C. Lauridsen, J.H. Povlsen, J. Hübner, M. Kristensen and B. Pálsdóttir, 1998 "Polarisation control of DFB fiber laser using UV-induced birefringent phase-shift" *Elec. Lett.* 34 (7) 678-679

[5.22] See for example T. Okoshi, K. Kikuchi K and A Nakayama, 1980 "Novel method for high resolution measurement of laser output spectrum" *Elec. Lett.* 16 (16) 630-631

[5.23] Y. Qian, P. Varming, J.H. Povlsen and V.C. Lauridsen, 1999 "Dynamic noise responses of DFB fibre lasers in presence of pump power fluctuations" *Elec. Lett.* 35 (4) 299-300

[5.24] G.A. Ball, G. Hull-Allen, C. Holton, W.W. Morey, 1993 "Low noise single frequency linear fibre laser" *Elec. Lett.* 29 (18) 1623-1625

[5.25] P.L. Chu, T.W. Whitbread and P.M. Allen, 1990 "Trade-off between sensitivity and dynamic range of reflectometric pulsed interferometric fibre sensors", *Proc. 7th Conf. Optical Fiber Sensors*, The Inst. of Radio and Elec. Engineers, Australia, pp. 229-232

[5.26] R.F.W Coates, *Modern Communication Systems 2nd edn.* The Macmillan Press 1982, pp. 135-137.

[5.27] G.A. Cranch, Internal DERA memorandum, October 1999.

[5.28] Ref. 5.15, pp. 404-406.

[5.29] Ultra Precision Ovened Oscillators from Total Frequency Control Ltd, West Sussex, U.K.

[5.30] G.M. Wenz, 1962 "Acoustic ambient noise in the ocean: spectra and sources" *J. Acoustical. Soc. America* 34 (12) 1936-1956

Chapter 6

EXTENDING THE FIBRE LINK LENGTH IN MULTIPLEXED ARRAYS USING REMOTELY PUMPED AMPLIFIERS AND SENSOR PERFORMANCE DEGRADATION FROM NONLINEAR EFFECTS

Abstract: In this chapter we identify the significant nonlinear effects that will cause degradation of the phase resolution of sensors multiplexed in a DWDM/TDM architecture, of the type described in chapter 5, when a long link fibre is added. These are found to be stimulated Brillouin scattering (SBS), stimulated Raman scattering (SRS), cross phase modulation (XPM) and four wave mixing (FWM). It is shown that stimulated Brillouin scattering generally sets the lower limit on launch powers; however, in some configurations with more than 10 wavelengths, the launch power becomes limited by stimulated Raman scattering. A technique involving staggering of the launch pulses is suggested to significantly increase the thresholds set by SRS, XPM and FWM. This allows us to determine the maximum permitted launch powers of the interrogation signals. We then present simple models to analyse array configurations incorporating inline optical amplifiers and remotely pumped optical amplifiers in the link fibre. It is shown that adding inline optical amplifiers may permit link fibre lengths around 1000 km. It is also shown that the link length scales inversely with the number of sensors when a remotely pumped amplifer is incorporated.

6.1 Introduction

One potential application of fibre-optic interferometric sensor arrays in sonar is the remotely interrogated array, as described in chapter 1. In these systems, the array may consist of several hundred sensors that may be located several tens of kilometers from the interrogation electronics. Increasing the number of sensors in an array requires increasing the

total launched optical power, due to the increase in number of wavelengths required. In arrays with short link fibres, increasing the peak launched power to greater than several hundred milliwatts is unlikely to result in any significant degradation of the sensor performance due to the nonlinear response of the transmission medium. However, as the link fibre increases to greater than a few kilometers, nonlinear effects become increasingly important and may result in significant degradation of the sensor performance.

In this chapter we shall investigate the detrimental effects on the interferometric phase resolution caused by nonlinear effects in the fibre link when both the launched power and link lengths are increased. In the interferometric sensor array, effects that may reduce the transmitted optical power or degrade the coherence or frequency noise of the interrogating optical signals are of interest. Firstly, in section 6.2 we shall consider each non-linear effect individually and determine its impact (if any) on these properties of the interrogating signals. We then apply this to the multiplexing configuration presented in chapter 5, where the launch and return pulses from the sensor array are carried through separate fibres. Thus, any nonlinear effects will occur only in the launch fibre and will affect only the launched interrogating pulses. In section 6.3, we determine the maximum launch powers permitted in these architectures. In section 6.4, we then determine the phase resolution vs. the number of sensors and link length for the basic DWDM/TDM architecture and show how the link length can be increased by incorporating inline optical amplifiers and remotely pumped optical amplifiers. Finally, in section 6.5, we summarise our conclusions.

6.2 Nonlinear Effects

In the following section we review the origin and consequence of five nonlinear effects observed in silica based optical fibres which are considered to be the most significant for the interferometric sensor application. Reviews of this type have been published for DWDM based communications systems [6.1-6.3] and we draw on the information provided here and from [6.4] and apply this to the case of the interferometric sensor application.

Any dielectric medium will exhibit a nonlinear response when subjected to sufficiently high electric field strength. Fundamentally, nonlinear response arises from the anharmonic motion of bound electrons in the presence of a strong electric field, $\underline{E}$. The induced polarisation, $\underline{P}$, from the electric dipole can be expressed as,

$$\underline{P} = \varepsilon_0 \left(\chi^{(1)} \underline{\mathrm{E}} + \chi^{(2)} \underline{\mathrm{EE}} + \chi^{(3)} \underline{\mathrm{EEE}} + ... \right) \tag{6.1}$$

where ε_0 is the vacuum permittivity and $\chi^{(i)}$ is the i^{th} order susceptibility ($i = 1,2,3..$). For low field strengths, $\underline{P}$ is related to $\underline{\mathrm{E}}$ through the linear susceptibility, $\chi^{(1)}$. The linear refractive index, n_0, and absorption, α, can be related to the real and imaginary parts of $\chi^{(1)}$. For higher field strengths, higher order terms in (6.1) become significant. The inversion symmetry of the SiO_2 molecule reduces $\chi^{(2)}$ to zero leaving the third-order susceptibility, $\chi^{(3)}$, which is responsible for nonlinear refraction, four wave mixing and second harmonic generation. $\chi^{(3)}$ in (6.1) gives rise to an intensity dependence of the refractive index such that,

$$n = n_o + n_2^I I \tag{6.2}$$

where n_o is the linear refractive index, I is the intensity ($I = \frac{1}{2}\varepsilon_0 c n_o |\mathrm{E}|^2$) and n_2^I is the nonlinear refractive index in units of $m^2.W^{-1}$. The linear and nonlinear refractive indices are related to their respective susceptibilities by,

$$n_o = 1 + \mathrm{Re}\left[\chi^{(1)}\right] \tag{6.3}$$

$$n_2^I = 2n_2 / \varepsilon_0 c n_o \tag{6.4}$$

$$n_2 = \frac{3}{8n_o} \mathrm{Re}\left[\chi^{(3)}_{xxxx}\right] \tag{6.5}$$

The optical field in (6.2) is assumed to be linearly polarised such that only one component of the fourth rank susceptibility tensor, $\chi^{(3)}_{xxxx}$, contributes to the refractive index.

Processes such as nonlinear refraction and four wave mixing (discussed below) are elastic in the sense that no energy is exchanged between the incident field and the medium. The medium merely acts in a passive role in that it mediates the processes through a nonlinear response of its bound electrons, which gives rise to a modulation of a physical property of the medium; in the case of nonlinear refraction, this property is the refractive index. These processes are generally

referred to as parametric processes. Processes that involve exchange of energy between the incident field and the medium are inelastic processes. Two of the most significant are Raman and Brillouin scattering which both lead to an effective power loss during transmission. We shall consider the impact on signal transmission of these two first.

It is useful to define some parameters to characterise the nonlinear processes in optical fibre. The strength of the nonlinear process is dependent on the interaction length. In a waveguiding structure where the interaction length is very large, the attenuation of the signal must be accounted for. Thus, the effective interaction length, L_e, for a fibre of length, L, and attenuation constant, α, for the nonlinear process can be defined as $\int_0^L e^{-\alpha l} dl$ such that,

$$L_e = \frac{1 - e^{-\alpha L}}{\alpha} \tag{6.6}$$

This simplifies to $L_e \simeq L$ for $\alpha L \ll 1$ and $L_e \simeq \alpha^{-1}$ for $\alpha L \gg 1$. The effective area of the overlapping waves, A_e, in a nonlinear interaction is given by calculating the average modal overlap; however, if the wavelengths of the interacting waves are similar, A_e can be approximated to the area of the fibre core, πa^2 where a is the core radius [6.6]. A summary of the fibre parameters used in the following calculations are given in table 6.1.

Table 6.1: Parameters used in calculations

Parameter	*Value*	*Unit*	*Description*
α_s (1550nm)	0.25	dB km^{-1}	Fibre attenuation
α_p (1480nm)	0.35	dB km^{-1}	Fibre attenuation
a	4	μm	Core radius
A_e	5×10^{-11}	m^2	Effective overlap area
g_R †	7×10^{-14}	m.W^{-1}	Raman gain constant
g_B †	4×10^{-11}	m.W^{-1}	Brillouin gain constant
p	2		Polarisation factor for SBS and SRS
n_o	1.465		Core refractive index
n_2 †	3×10^{-20}	m^2.W^{-1}	Nonlinear refractive index
$\chi^{(3)}_{1111}$	6×10^{-14}	m^3.J^{-1}	Third-order electronic susceptibility
D_c	16	ps.(km.nm)$^{-1}$	GVD in SMF28 at 1550nm
D_c	1	ps.(km.nm)$^{-1}$	GVD dispersion in DSF at 1550nm
$\frac{dD_c(\lambda_k)}{d\lambda}$ ††	0.075	ps.km^{-1}.nm^{-2}	GVD dispersion slope at zero dispersion point in SMF28

† These values correspond to a wavelength of 1550 nm and are taken from [6.3].
†† Measured at the zero dispersion wavelength in DSF [6.4]

6.2.2 Stimulated Raman scattering

Stimulated Raman scattering (SRS) is an interaction between the incident optical beam and the molecular vibrations of the medium. A signal photon is annihilated to generate an optical phonon and a second photon downshifted in frequency by an amount equal to the frequency of the optical phonon. The incident optical signal is usually referred to as the pump signal. Thus, the result of this effect is to couple optical power from the pump to a lower frequency signal. Due to the amorphous nature of silica glasses, the molecular vibrations are spread out into bands, which overlap to form a continuum. The frequency shift is therefore not discrete, but occupies a bandwidth of approximately 20 THz. In the absence of other signals, the Raman component will build up most rapidly in the region where the Raman gain is the highest. In

fused silica this corresponds to a downshift from the pump frequency of about 13.2 THz and is generally known as the Raman or Stokes shift. It can be shown that if the pump signal is increased above a certain threshold, this Stokes wave builds up almost exponentially. By assuming that the pump signal is not attenuated by the nonlinear effect, then the critical power required before the onset of the nonlinear process can be calculated analytically. However, if other signals occupy this bandwidth (such as is the case in DWDM systems) then these signals will experience gain due to the coupling of power from the pump signal. Assuming that the Raman gain spectrum exhibits a Lorentzian profile, then for the case of a single wavelength launched into an optical fibre, the critical power level before 50% of the pump signal is converted to a Stokes wave at the output of the fibre is given by [6.2],

$$P_{cR} \simeq 16\frac{pA_e}{L_e g_R} \tag{6.7}$$

where g_R is the peak Raman gain and p is a factor that takes into account the polariation of the pump and Stokes waves. In conventional single mode fibre, the polarisation changes unpredictably along the length of the fibre and it can be shown that in this case p =2 [6.12]. (6.7) also applies to the case of a few wavelengths occupying a bandwidth less than 13.2 THz launched into a fibre. In this case P_{cR} refers to the total launched power.

Thus, in DWDM systems SRS has the effect of causing growth in the power of the longer wavelength signals, at the expense of the shorter wavelength signals. As the number of wavelengths increases, the interaction between the zeroth wavelength and the other wavelengths must be considered. The critical power requirements in this case have been calculated by approximating the Raman gain profile by a triangular function [6.5]. For a system with m wavelengths at a frequency spacing, $\Delta\nu_\lambda$, then the critical launch power required before the power in the zeroth wavelength is depleted by a factor, δ, is given by,

$$P'_{cR} = \frac{3\times10^{13} A_e p\delta}{g_R L_e \Delta\nu_\lambda m(m-1)} \text{ for the case when } (m-1)\Delta\nu_\lambda < 15 \text{ THz} \tag{6.8}$$

$$P''_{cR} = \frac{2A_e p\delta\Delta\nu_\lambda}{1.5\times10^{13} L_e g_R} \text{ for the case when } (m-1)\Delta\nu_\lambda > 15 \text{ THz} \tag{6.9}$$

where (6.8) applies when all the wavelengths fall within the Raman gain bandwidth and (6.9) applies when the total optical bandwidth occupied by the signals is greater than the Raman bandwidth. In this case, for a given fibre length the critical power becomes independent of the number of wavelengths and only dependent on the channel spacing.

The SRS process involves amplification through stimulated emission and therefore no detrimental effects on the linewidth or frequency noise of these signals would be expected. However, some additional noise would be added to these signals due to spontaneous Raman scattering and double Rayleigh backscattering. It is useful to recall that SRS arises from a third order nonlinear susceptibility, which has a time constant in the femptosecond range (due to the short lifetime of the optical phonon). SRS is essentially an instantaneous effect compared with the pulse repetition rates and is thus the same for both pulsed and CW systems. It also generally dominates in the forward direction (i.e. co-propagating with the pump).

6.2.3 Stimulated Brillouin scattering

Stimulated Brillouin scattering involves an interaction between an optical pump wave, the Stokes wave and an acoustic wave. The pump wave generates acoustic waves through the process of electrostriction, which itself causes a modulation of the refractive index. Pump light is then scattered by Bragg diffraction and downshifted in frequency due to the Doppler shift generated by the travelling acoustic wave. From a quantum mechanical viewpoint, a photon at the pump wavelength is annihilated to produce an acoustic phonon and a second photon, which is downshifted by a frequency equal to the frequency of the phonon. Unlike SRS, SBS dominates in the reverse direction, and covers a bandwidth of approximately 20 MHz in silica (although the exact bandwidth depends on fibre geometry and composition). The gain coefficient for SBS is also around two orders of magnitude larger than for SRS, hence it is generally a more significant effect. The critical power before significant Brillouin scattering occurs can be derived in a similar way to that for Raman scattering. In DWDM systems, the wavelength spacing will be much greater than the Brillouin bandwidth, and as a result the critical power is independent of the number of wavelengths. It was shown in [6.2] that the critical launched power required before significant power is coupled into a Stokes wave is given by,

$$P_{cB} \simeq \frac{21pA_e}{g_B L_e} \tag{6.10}$$

The narrow bandwidth of Brillouin gain is due to the longer lifetime of the acoustic phonon (compared with the optical phonon associated with Raman scattering). This also results in the critical power being strongly dependent on both the modulation format and linewidth of the source [6.2]; thus, (6.10) only applies for cw signals. In the interferometric sensor array, the source linewidth may be less than 10 kHz and is unlikely to affect the Brillouin gain efficiency. However, the pulsed nature of the interrogating signals, will increase P_{cB} by a factor of $(2D)^{-1}$, where D is the duty cycle (where the factor of two applies to two launch pulses).

6.2.4 Self-phase modulation and cross-phase modulation

The intensity dependence of the refractive index gives rise to two nonlinear effects; self-phase modulation (SPM) and cross phase modulation (XPM). Fluctuations in the intensity of the optical signals will thus give rise to fluctuations in the optical phase of the signals, which using (6.2), can be expressed as,

$$\phi = n_o kL + n_2^! kIL_e \tag{6.11}$$

where $k = 2\pi\lambda^{-1}$ and I is the optical intensity which can be approximated to PA_e^{-1} [6.6]. It can be shown that for multiple wavelengths, the phase-shift for the i^{th} channel is given by [6.4],

$$\phi_i^{NL} = \frac{n_2^! kL_e}{A_e}\left(P_i + 2\sum_{n\neq i}^{m} P_n\right) \tag{6.12}$$

The first term in (6.12) is responsible for SPM and the second for XPM. It is interesting to note the factor of two in the second term which indicates that the affect of XPM is twice that of SPM for a given power level. In interferometric fibre optic sensors, the result of SPM and XPM is to convert intensity noise from the source into phase noise. We assume that the intensity

noise of each source is equal and uncorrelated and power is divided equally between the wavelengths. We consider the case of two rectangular optical pulses launched into the fiber and assume the intensity noise to be uncorrelated on time scales equal to the pulse separation; this thus represents the worst case. Then, if the variance of the intensity fluctuations is $\langle \delta P^2 \rangle$ ($\langle\ \rangle$ denotes time average), where the power spectral density of the intensity fluctuations is related to the RIN by, $S_{\delta P}(f) = P^2 \cdot RIN(f)$ (as defined by (7.7)) then the nonlinear induced phase noise is,

$$\delta\phi_{SPM}^{NL}(f) = \frac{5}{6}\frac{kn_2^I L_e P}{A_e}\sqrt{RIN(f)} \tag{6.13}$$

for SPM and,

$$\delta\phi_{XPM}^{NL}(f) = \frac{5}{6}\frac{2kn_2^I L_e P}{A_e}\sqrt{RIN(f)}\sqrt{m} \tag{6.14}$$

for XPM. The factor of 5/6 in each equation accounts for the randomly changing polarisation in standard fibre [6.6], which is different for the cases of Raman and Brillouin scattering. In polarisation preserving fibre this factor should be neglected.

6.2.5 Four wave mixing

Four wave mixing (FWM), as its name implies, involves the mixing of three waves to produce a fourth. It arises due to the same nonlinearly that produces SPM, XPM and SRS; the third order susceptibility. FWM has been studied extensively for its impact on optical communication systems [6.8-6.9]. In the case of DWDM systems where the wavelength spacing is constant, it results in the generation of new waves where some correspond to existing frequencies. This has been shown to lead to significant crosstalk [6.10]. We can gain a qualitative understanding of the process of FWM by considering the case of three primary waves of frequencies, f_i, f_j and f_k where $i \neq j \neq k$. FWM will produce secondary waves at frequencies given by

$f_{ijk} = f_i + f_j - f_k$ as illustrated in figure 6.1. Some of the secondary waves will have the same frequency (i.e. $f_{123} = f_{213} = f_{112}$) which results in three times as much power being generated at this frequency.

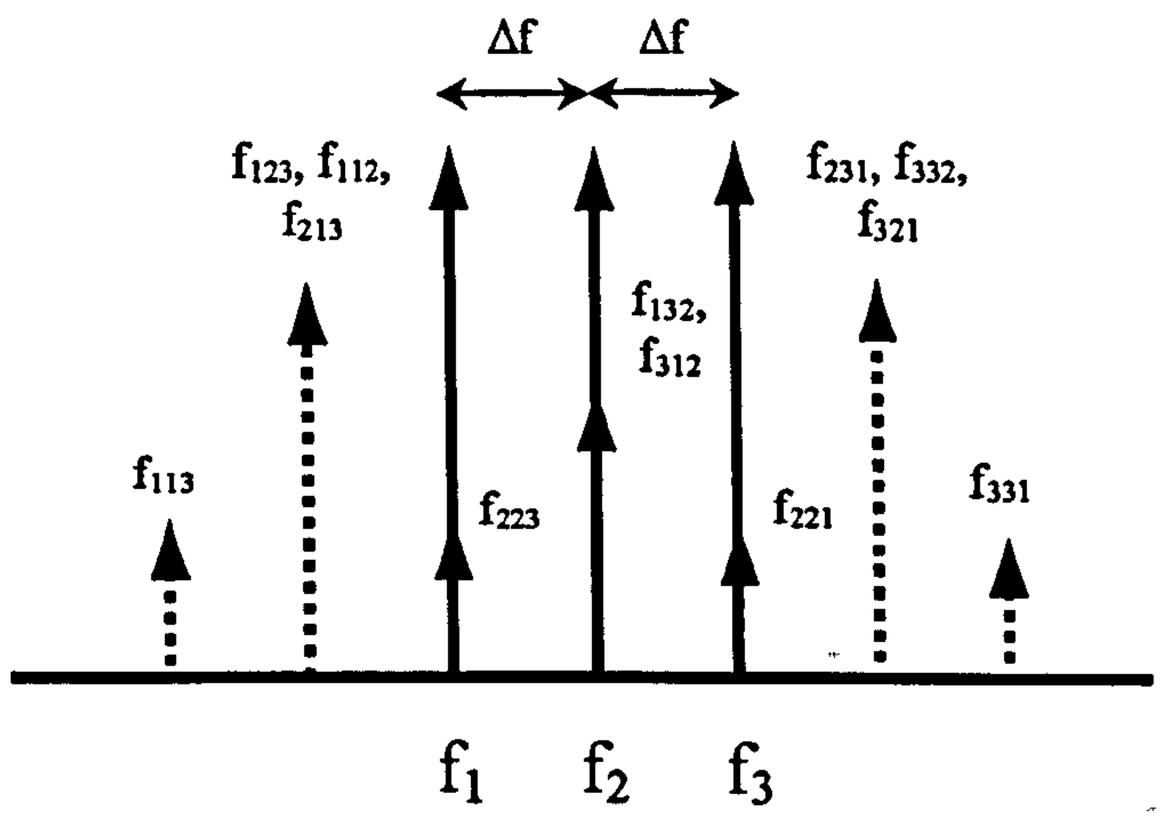

Figure 6.1: Frequency mixing products of FWM

The power in an individual secondary wave can be expressed by [6.8],

$$P_{ijk} = \eta \frac{1024\pi^6}{n_o^4 \lambda_k^2 c^2} \left(6\chi^{(3)}_{1111}\right)^2 \left(\frac{L_e}{A_e}\right)^2 P_i P_j P_k \, e^{-\alpha_s L} \qquad (6.15)$$

where $\chi^{(3)}_{1111}$ is the third-order electronic susceptibility, $P_{i,j,k}$ are the powers in the incident waves and η is the efficiency of the nonlinear process (the factor of 6 in (6.15) should be replaced with 3 if only two primary waves are present). For maximum efficiency, the primary waves must remain phase matched to the secondary waves; however, in dispersive media, the secondary waves will gradually become out of phase with the primary waves, resulting in energy being coupled back into the primary waves. An expression for η has been derived in [6.11],

$$\eta = \frac{P_{ijk}(L, \Delta\beta)}{P_{ijk}(L, \Delta\beta = 0)} = \left[\frac{\alpha_s^2}{\alpha_s^2 + \Delta\beta^2}\right]\left[1 + \frac{4e^{-\alpha_s L}\sin^2(\Delta\beta L/2)}{\left(1 - e^{-\alpha_s L}\right)^2}\right] \qquad (6.16)$$

where $\Delta\beta$ is the propagation constant difference between the waves and is given by,

$$\Delta\beta = \left(\frac{2\pi\lambda_k^2}{c}\right)\Delta\nu_{ik}\Delta\nu_{jk}\left[D_c + \frac{\lambda_k^2}{2c}\left(\Delta\nu_{ik} + \Delta\nu_{jk}\right)\frac{dD_c(\lambda_k)}{d\lambda}\right] \qquad (6.17)$$

where D_c is the group velocity dispersion (GVD) at λ_k and $\Delta\nu_{..}$ is the primary wave's wavelength spacing. Away from the zero dispersion point, the second term in (6.17) is negligible. It is useful to determine the efficiency of FWM in both SMF28 (D_c ~16ps.(km.nm)$^{-1}$) and dispersion shifted fibre (DSF) (D_c ~1 ps.(km.nm)$^{-1}$) at λ_k =1550nm and this is shown in fig. 6.2, computed from (6.16) and (6.17).

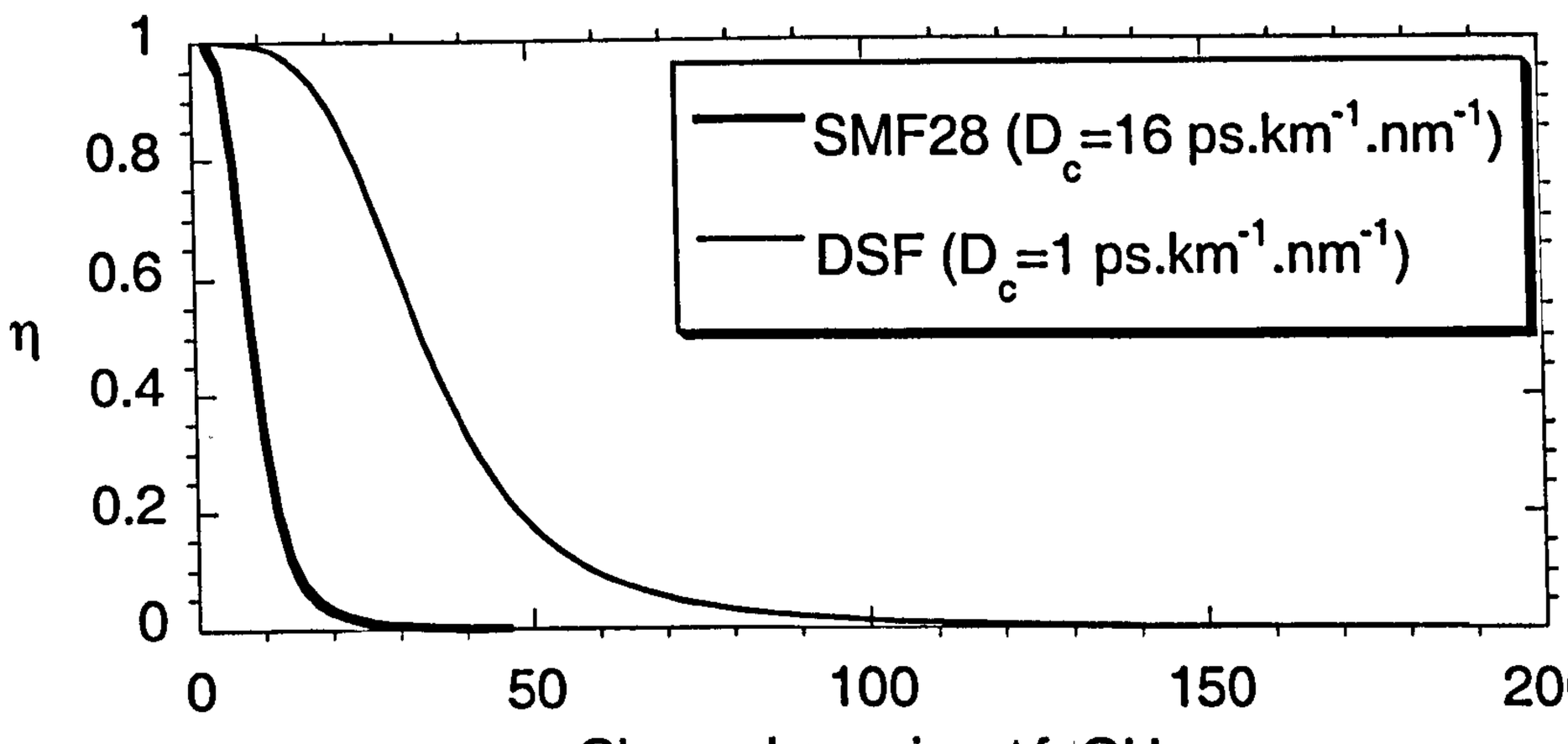

Figure 6.2: Efficiency of FWM process as a function of wavelength separation (assumes $L_e \approx \alpha^{-1}$)

Thus for a wavelength spacing of 100 GHz, the efficiency of FWM is 1% for DSF and less than 10^{-2}% for SMF28. In general for large wavelength spacing, FWM is only significant between a wave and its two nearest neighbours (due to the phase matching requirement). Thus, a reasonable estimate of the impact on primary wave depletion by FWM would be given by determining the critical power for which a primary wave is depleted by an amount, δ, using (6.15).

6.3 Nonlinear Effects in Interferometric Sensor Systems

We can now determine the restrictions imposed on the launch powers due to the nonlinear effects described above for a typical interferometric sensor array. In a communications system, nonlinearities will result in a degradation of the bit-error-rate (BER) and this can be quantified in terms of a power penalty (i.e. the reduction in power required to give the same increase in

BER). In a sensor array, optical nonlinearities will result in a reduction in the phase resolution of the sensor. In the case of SPM and XPM, (6.13) and (6.14) can be used to determine the critical power, above which a set level of phase noise will be added to the signals. For calculations here we take this level to be 10 μrad.$Hz^{-1/2}$. However, SBS, SRS and FWM will only cause a reduction in phase resolution if the sensor phase resolution is limited by optical power level (which is not always the case). Otherwise, they will merely cause power to be lost to nonlinearity on transmission through the link fibre. SBS causes significant depletion of the pump wave above a threshold given by (6.10). For SRS and FWM we shall determine the critical power required before 0.5 dB is lost to nonlinearity. The pulsed nature of the interrogation signals need only to be taken into account for SBS where we include the factor of D^{-1} in the right hand side of (6.10) where D is the optical duty cycle (corresponding to a single launch power).

Shown in fig. 6.3(a) is the critical power level for each nonlinearity for the case of an array link fibre greater than 50 km and a channel separation of 100 GHz. It can be seen that only SRS and XPM are dependent on the number of channels. XPM is plotted for the cases of a laser source RIN equal to –120 dB Hz^{-1} and –140 dB Hz^{-1}. In the latter case, SBS limits the launch power to around 100 mW for m <10 and SRS limits it for m >10. The same plot for a channel spacing of 200 GHz, is shown in fig. 6.3(b). The thresholds for XPM and SBS remain unchanged, however the threshold for SRS decreases and for FWM increases. In the case of SRS, increasing the channel spacing moves adjacent channels nearer the peak gain of the Raman spectrum (~13.2 THz) thus the amount of SRS for the same optical power increases. The threshold for FWM increases as the channel spacing increases due to the reduction in the efficiency associated with increased channel spacing (due to (6.16)). The threshold of SRS follows a m^{-1} slope for low m (due to (6.7)) and an m^{-2} slope for higher m (due to (6.8)). The XPM threshold falls with a $m^{-1/2}$ slope (due to (6.14)).

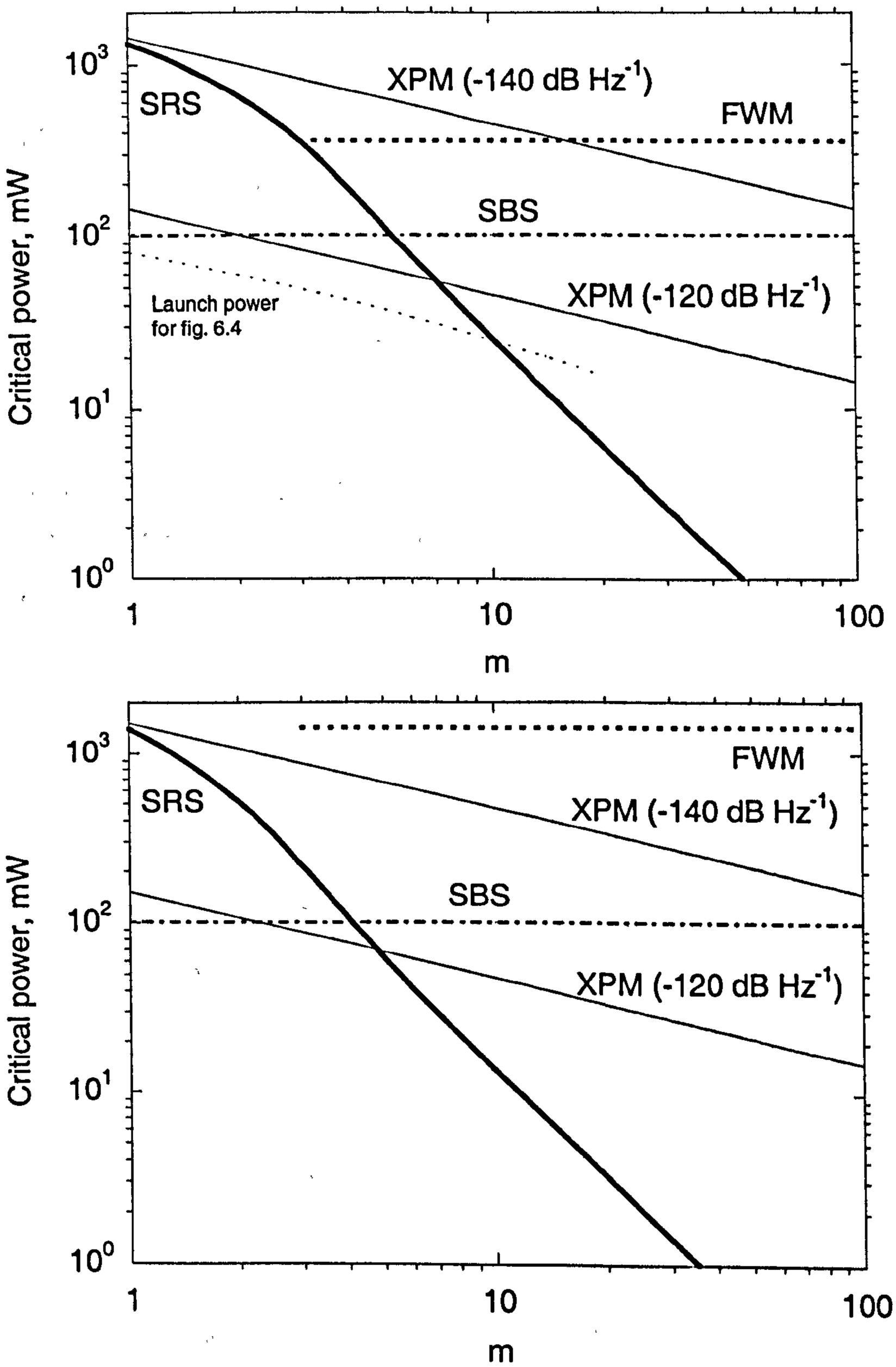

Figure 6.3: Critical power level for each nonlinear effect, (a) $\Delta\nu_\lambda$ =100 GHz and (b) $\Delta\nu_\lambda$ =200 GHz

Here we take λ =1550nm, D =1/36, L >50km, δ =0.5dB, α_s =0.25 dB.km^{-1}. XPM threshold corresponds to 10 μrad.Hz$^{-1/2}$

Another effect that will generally cause an increase in the threshold of some of the nonlinear effects described above is that due to group velocity dispersion. To determine the threshold powers for SRS, XPM and FWM it is assumed that the pulses arrive back at the same time. In practice GVD will cause the pulses to "walk-off" one another as they propagate through the fibre. For SMF28 fibre, the GVD parameter is ~16 ps.(km.nm)$^{-1}$ which will cause two pulses spaced by 26 nm (corresponding to 16 wavelengths spaced by 200 GHz each) to "walk-off" by ~33 ns over a fibre length of 80 km. Typically, pulse widths are between 100 and 500 ns in length and thus this effect will generally be relatively small.

6.4 Determining the Maximum Fibre Link Length for Interferometric Sensor Arrays With a DWDM/TDM Multiplexing Architecture

Having determined the maximum launch powers, the relationship between the number of sensors, phase resolution and link fibre length can be determined. We shall first consider the architecture presented in the example in section 5.6 and a schematic of this array is shown in fig. 6.4. The array is characterised by its insertion loss, $IL_a(m)$, which is a function of the number of wavelengths, m. This architecture contains a single power amplifier to boost the launch powers and a single preamplifier, after which wavelengths are separated using an optical filter. Optical amplifiers will provide gain to compensate for the loss due to an extended link fibre or an increased array size. However, each optical amplifier will also add noise to the signal, in the form of amplified spontaneous emission (ASE). As a result, the improvement in phase resolution due to the optical amplifiers does not scale with the cumulative gain of the amplifiers, but is dependent on both the cumulative gain and ASE power in the received signals. Indeed, the phase resolution in most systems with multiple optical amplifiers or a preamplifier is usually limited by ASE noise. A measure of the relative amount of ASE power to the signal power is given by the optical signal-to-noise ratio (OSNR). We shall later introduce the concept of total noise figure of a system, which allows us to quantify the ASE power generated in a system of multiple optical amplifiers.

However, we can simplify the analysis for the configuration shown in fig. 6.4, by noting that the OSNR at the output of the power amplifier will generally be very high compared with the OSNR at the output of the preamplifier. Thus, we neglect the ASE added in the power amplifier and assume that the input signal to the preamplifier is limited by shot noise; therefore, the ASE noise generated in the detector is due only to the preamplifier noise (we also made this

assumption in the analysis of sec. 5.6). We can increase the launch powers to just below the limits set by nonlinearity (assuming a link length of 50 km), as shown by the dotted line in fig. 6.3(a).

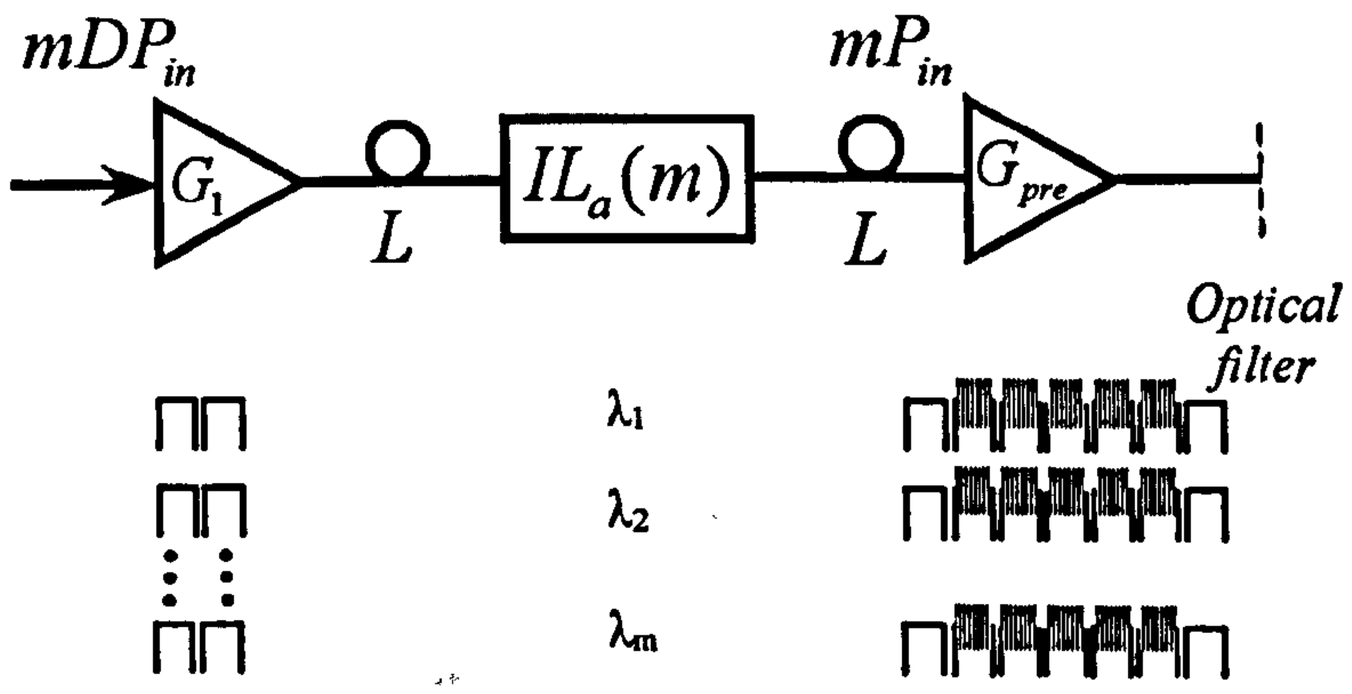

Figure 6.4: Remote array configuration with link fibre (case 1)

By including the extra attenuation from transmission in the link fibre, the phase resolution versus the number of sensors for link lengths, L, of 1, 10, 20 and 40 km is shown in fig. 6.5. Thus, a link length of 40 km will only allow around 32 sensors to be interrogated and achieve a phase resolution of less than 100 $\mu rad.Hz^{-1/2}$. Reducing the link length to 20 km increases this to around 160 sensors. The limits imposed by nonlinearity shown in fig. 6.3 correspond to $L>50$ km. When $L<<50$ km, the threshold powers will generally increase, thus the launch powers can be increased correspondingly. This would improve the phase resolution shown in fig. 6.5, when the number of sensors is greater than 32 and $L<<50$ km.

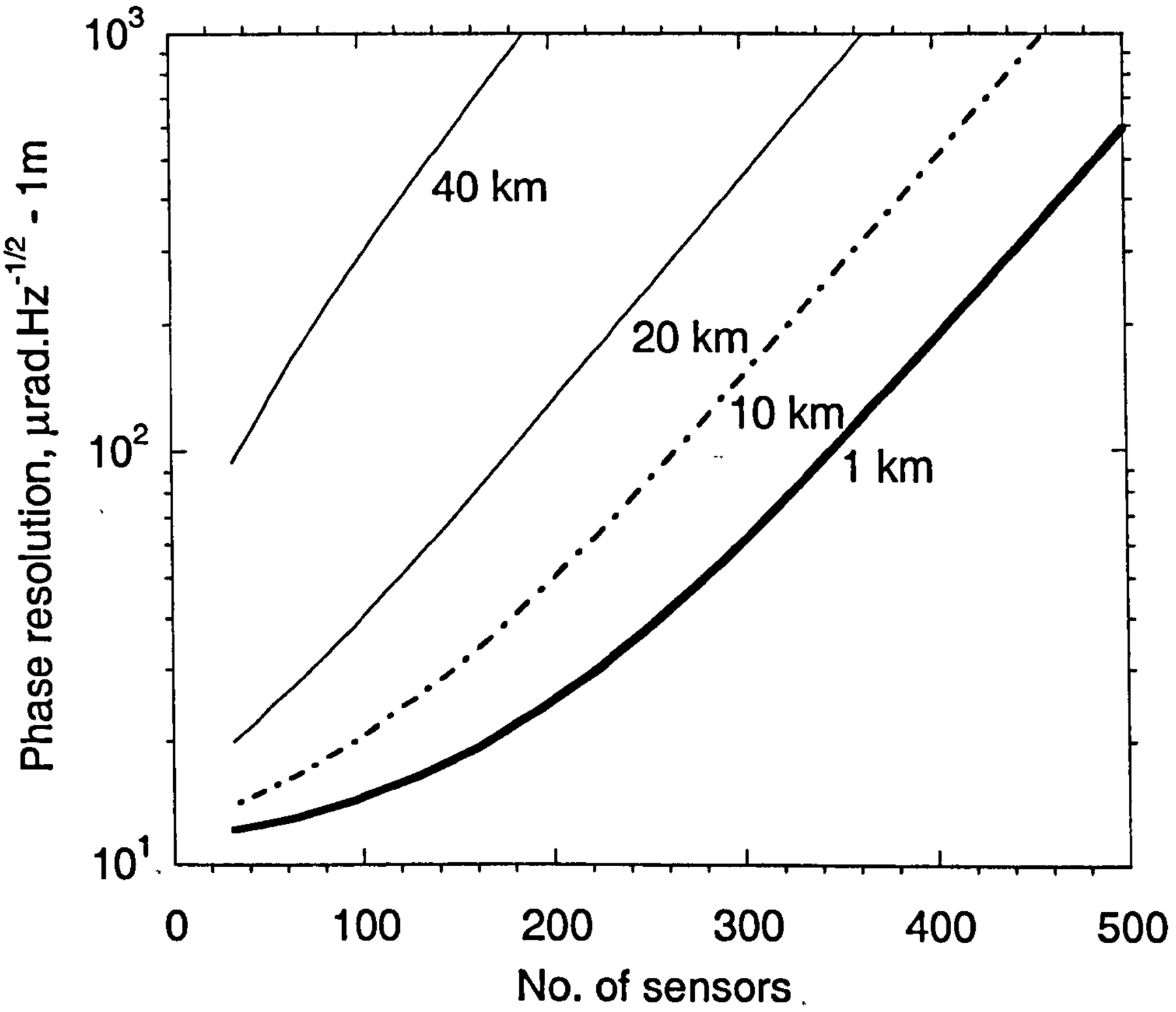

Figure 6.5: Phase resolution vs. number of sensors (case 1)

A technique to increase the nonlinear threshold is to stagger the launch pulses, as illustrated in fig. 6.6. Using this technique, the instantaneous total power can be reduced by up to a factor of m. This can be achieved in practice by using a combination of a wavelength demultiplexer, a series of delay coils and a wavelength combiner. In our example the total peak power is twice the peak power in a single wavelength; however, by increasing the delays further this could be reduced to the peak power in a single wavelength. The thresholds of the nonlinear effects are now as shown in fig. 6.7. In this case, when the laser RIN is –140 dB.Hz^{-1}, the nonlinear threshold is set by SBS at ~100 mW and is independent of the number of wavelengths when m >2. The parameters used in these calculations are the same as that used to derive fig. 5.14.

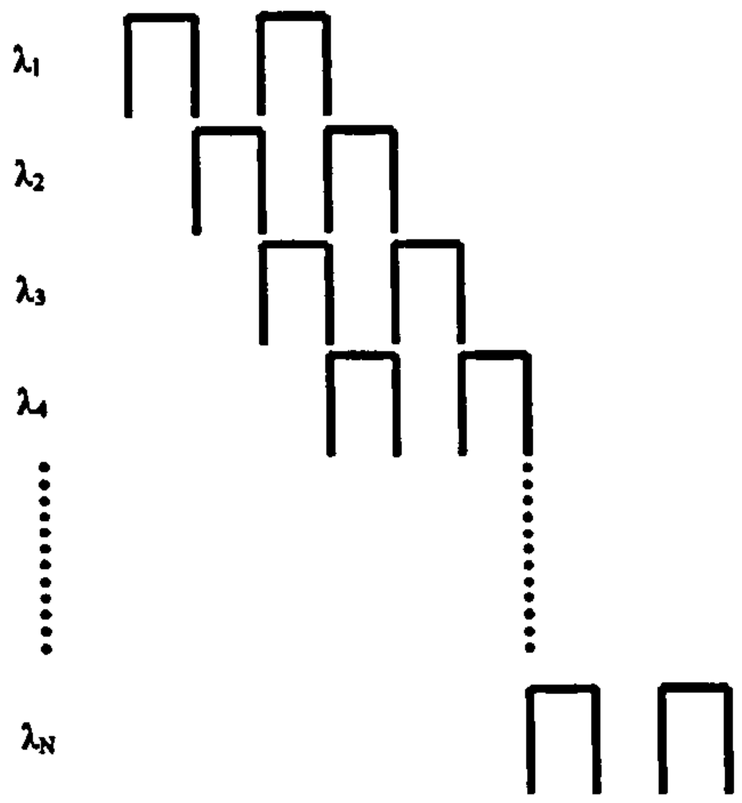

Figure 6.6: Staggered launch pulses (case 2)

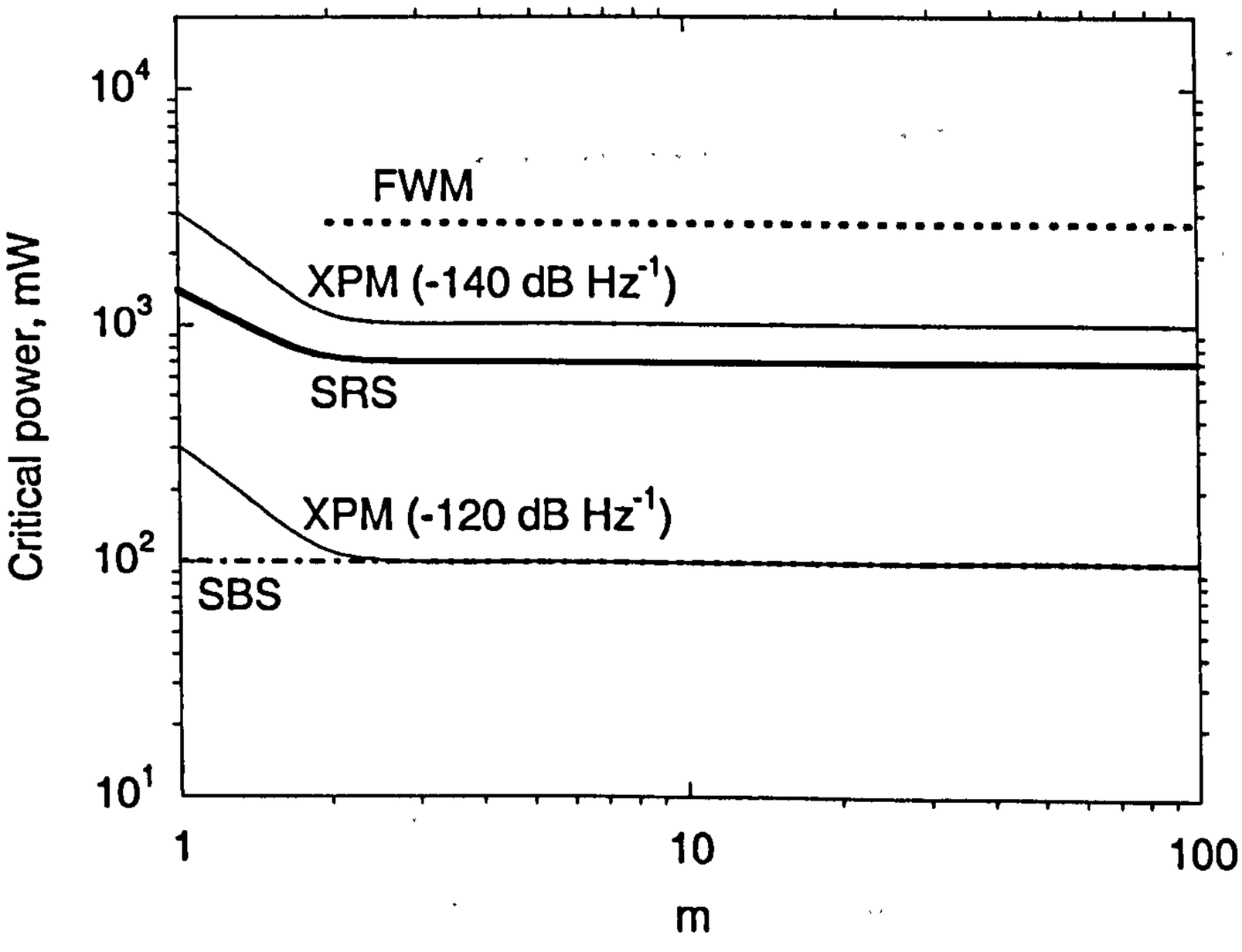

Figure 6.7: Nonlinear threshold levels with staggered launch pulses

The increase in the threshold level for $m > 2$ due to the staggered pulse scheme allows higher optical powers to be launched per wavelength. Thus, increasing the launch powers of each wavelength to the SBS limit yields the corresponding graph to fig. 6.5, which is shown in fig. 6.8. To generate this graph, the launch powers were calculated using (6.10) to determine the SBS power limit as a function of the link length.

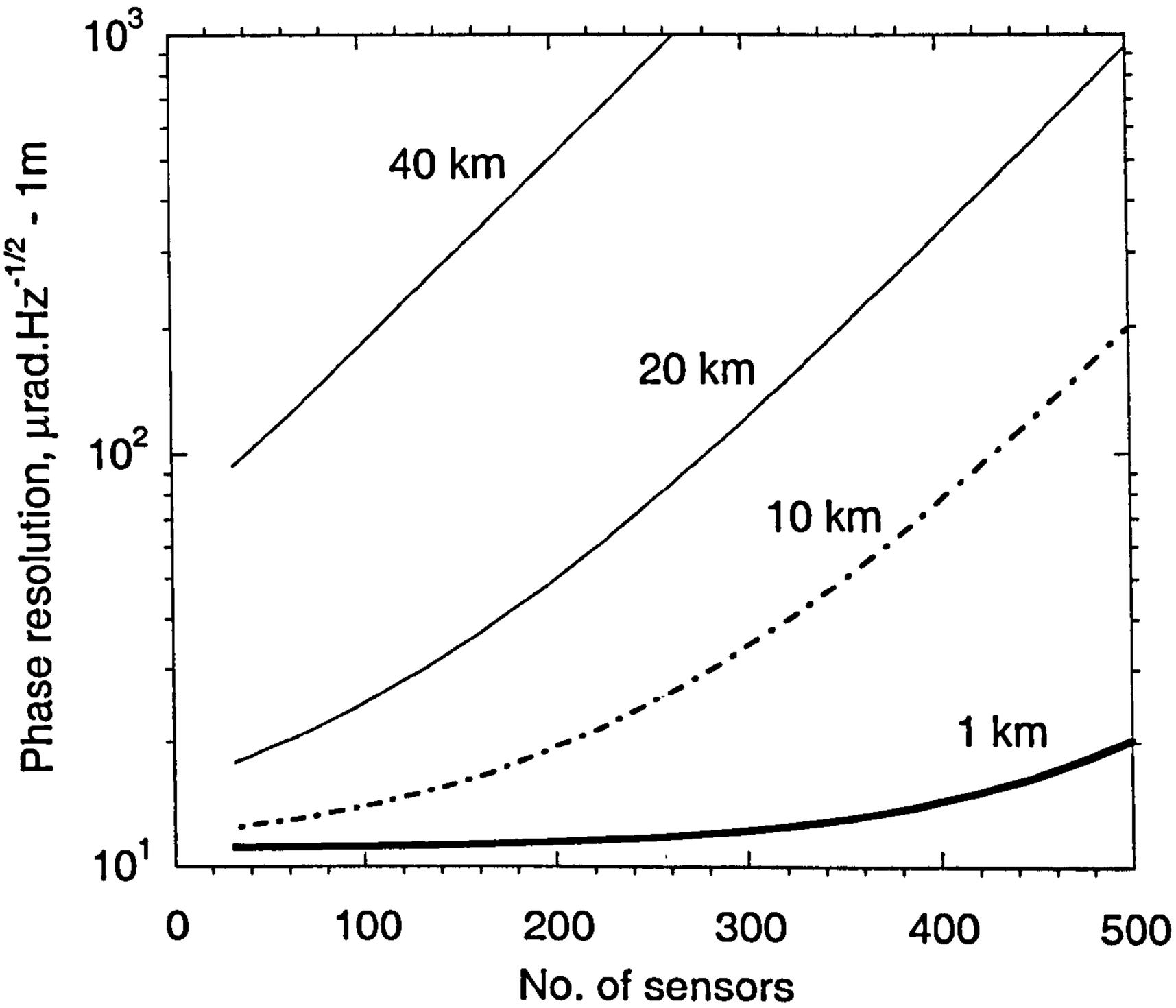

Figure 6.8: Phase resolution vs. number of sensors with staggered launch pulses (case 2)

The scheme still only allows around ~32 sensors to be interrogated over a 40 km link while achieving a phase resolution of 100 μrad.Hz$^{-1/2}$, however reducing the link length to 20 km increases this to ~288 sensors.

In this configuration, the array size and link length are limited by the SBS power threshold (if the laser RIN is assumed to be –140 dB Hz^{-1}). A common technique used in optical communication links to increase the SBS threshold is to broaden the launch signal linewidth [6.19]. When the signal source is singlemode, the efficiency of SBS is proportional to the ratio of the SBS linewidth and the signal linewidth, i.e. $\Delta\nu_{SBS} / \Delta\nu_s$, when $\Delta\nu_s > \Delta\nu_{SBS}$ [6.1]. In the interferometric sensor application, the linewidth of the laser source is generally much less than $\Delta\nu_{SBS}$ although a pulsed source effectively broadens the launch signal linewidth. A multimode source with a mode spacing greater than $\Delta\nu_{SBS}$ would also reduce the SBS threshold by an amount proportional to the number of modes. A technique based on high frequency phase modulation of the launch signal demonstrated a significant increase in the SBS threshold [6.13].

The launch signal thus consists of a series of modulation sidebands spaced by a frequency equal to the modulation frequency and with an amplitude dependent on the modulation depth. In terms of signal spectrum, it thus resembles that obtained from a multimode laser. It was found that for a cw signal launched into a fibre with an effective length of 9.1 km, the SBS threshold (with no modulation) was found to be 5.5mW (this agrees remarkably well with a P_{cB}=5.8mW predicted by (6.10)). With modulation applied, the threshold was increased to well above 20 mW. It was also found that the intensity noise of the signal in transmission increased significantly when the SBS threshold was exceeded, although no explanation was given to explain this effect. Interrogation of fibre interferometers with multimode laser sources limits the available interrogation techniques and is generally not compatible with multiplexed systems.

6.4.2 Adding inline optical amplifiers to the link fibre

In the example given in section 5.6, we calculated the phase resolution achieved by sensors in an array with a short link fibre, a power amplifier and a preamplifier. In this case, the sensor resolution was primarily limited by signal-spontaneous (s-sp) beat noise for received peak powers of greater than ~1 μW and by spontaneous-spontaneous (sp-sp) beat noise for received peak powers less than ~1 μW, generated in the optical preamplifier (see table 5.3). For the analysis we assumed that the input optical signal-to-noise ratio (OSNR) to the preamplifier was limited by shot noise and the phase resolution of a sensor was optimised by increasing the launch powers to just below the limit imposed by nonlinearities in the transmission fibre. We now consider the increase in link fibre length provided by in-line repeater type optical amplifiers, which are placed periodically along its length. A typical system configuration is shown in fig. 6.9.

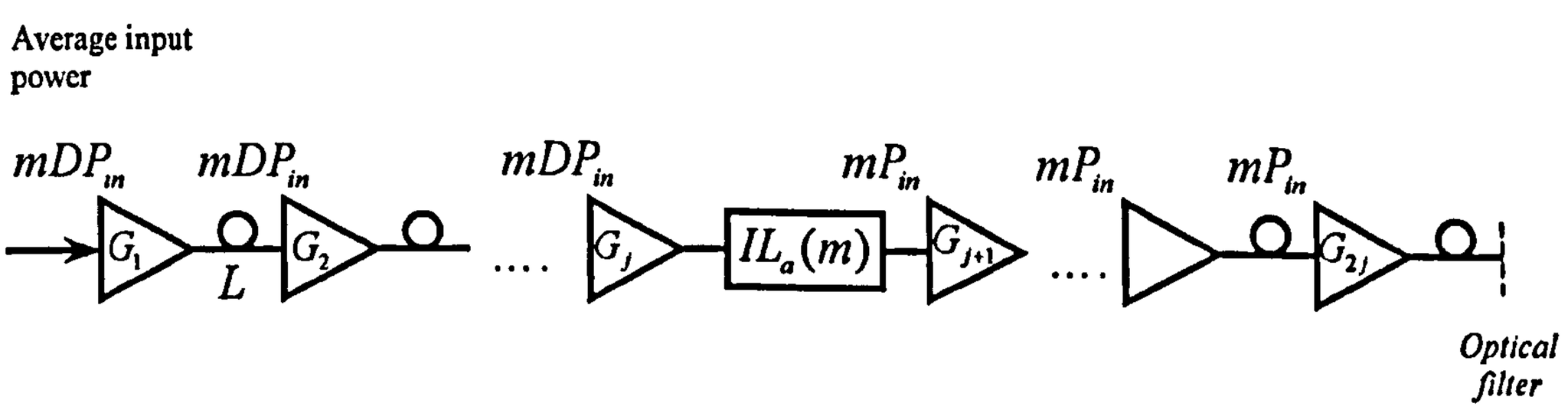

Figure 6.9: Array configuration with inline optical amplifiers incorporated periodically along the link fibre (case 3)

The system consists of $2j$ optical amplifiers spaced a distance L apart, each with a gain, G_i, and noise figure, F_i, where $i = 1,2,3...2j$. The array is situated after the j^{th} amplifier and is characterised by an insertion loss, $IL_a(m)$, which is a function of the number of wavelengths, m. The aim is to determine the optimum spacing of the amplifiers and the interferometric phase resolution. Analysis of this type of configuration for a multi-wavelength coherent communications link has been presented in [6.14]. This work showed that providing the total input powers to the link were within a certain range, with a lower limit set by the required BER and an upper limit set by the output saturation power of the amplifiers, then a virtually transparent optical link could be realised, with a noise figure set only be the cumulative ASE power from each amplifier. We can use the simple design rules presented in [6.14] and in sec.2.13 to analyse the interferometric sensor array configuration shown in fig. 6.9.

Firstly, we make a set of simplifying assumptions: (i) the input OSNR to the first amplifier is limited by shot noise; (ii) the gain of each amplifier is equal to the transmission loss of the fibre length following it, such that $G = \mathrm{T}^{-1}$, where $\mathrm{T} = \exp(-\alpha_s L)$, and the input power to each optical amplifier is the same; (iii) the power levels are sufficiently high, such that s-sp beat noise dominates the electrical CNR; (iv) the optical amplifiers operate in their small-signal regime, thus the gain of the amplifiers is not depleted significantly by the buildup of ASE; and (v) the power levels thoughout the system are sufficiently low such that nonlinear effects are negligable.

Although the large bandwidth (~35 nm) available in standard EDFA's make them ideal for multichannel amplification, certain properties of the erbium gain medium complicate the design of a multi-amplifier system, as discussed in sec. 2.13.5. The characteristic emission spectrum of erbium at full inversion results in a wavelength dependent gain [6.15]. Thus, in multi-amplifier systems, some channels are amplified more than others and the difference in power per channel increases with the number of amplifiers. Operating the amplifier in saturation, either by increasing the total input power or reducing the pump power, results in a reduced inversion towards the end of the doped fibre and this has the effect of flattening the gain spectrum, due to the increased absorption at the short wavelength part of the spectrum. However, this imposes strict limits on input power and may result in increased noise figure if the input powers

are too high. An alternative method is to incorporate gain flattening filters [6.15], which gives rise to a flat gain profile in the small-signal regime of the amplifier.

For the following analysis, we shall assume that the amplifiers are gain flattened in their small-signal regime, so that the dependence of G on the wavelength is minimised. Since the insertion loss of the array is dependent on the number of wavelengths and will exceed the transmission loss of a fibre span between amplifiers, the gain of amplifier j shall be increased to compensate. We show by example that this suggestion is practical. For the array configuration example given in section 5.6, $IL_a(m)$ is plotted against m in fig. 6.10. If the small-signal gain of each amplifier except amplifier j is 20 dB, then the amplifier spacing, L, ($L = -\alpha_s^{-1} \ln G$) must be 80 km. The insertion loss of the array defines the transmission loss of a single pulse launched into and returned from an array. However, the return signals from the array are quasi-cw signals in the form of fully populated TDM pulse trains. Thus, the peak power returned from the array now defines the average input power to the optical amplifiers. This is taken into account by defining the insertion loss between amplifiers j and $j+1$ to be $IL_a(m)D^{-1}$. The required gain of the amplifier preceding the array is shown on the right hand axis of fig. 6.10. Thus, with 16 wavelengths an amplifier gain of 44 dB is required to compensate for the array insertion loss. This gain can be provided by a dual stage amplifier, such as the one demonstrated in [6.16] which achieved 54 dB of gain with a noise figure of 3.1 dB.

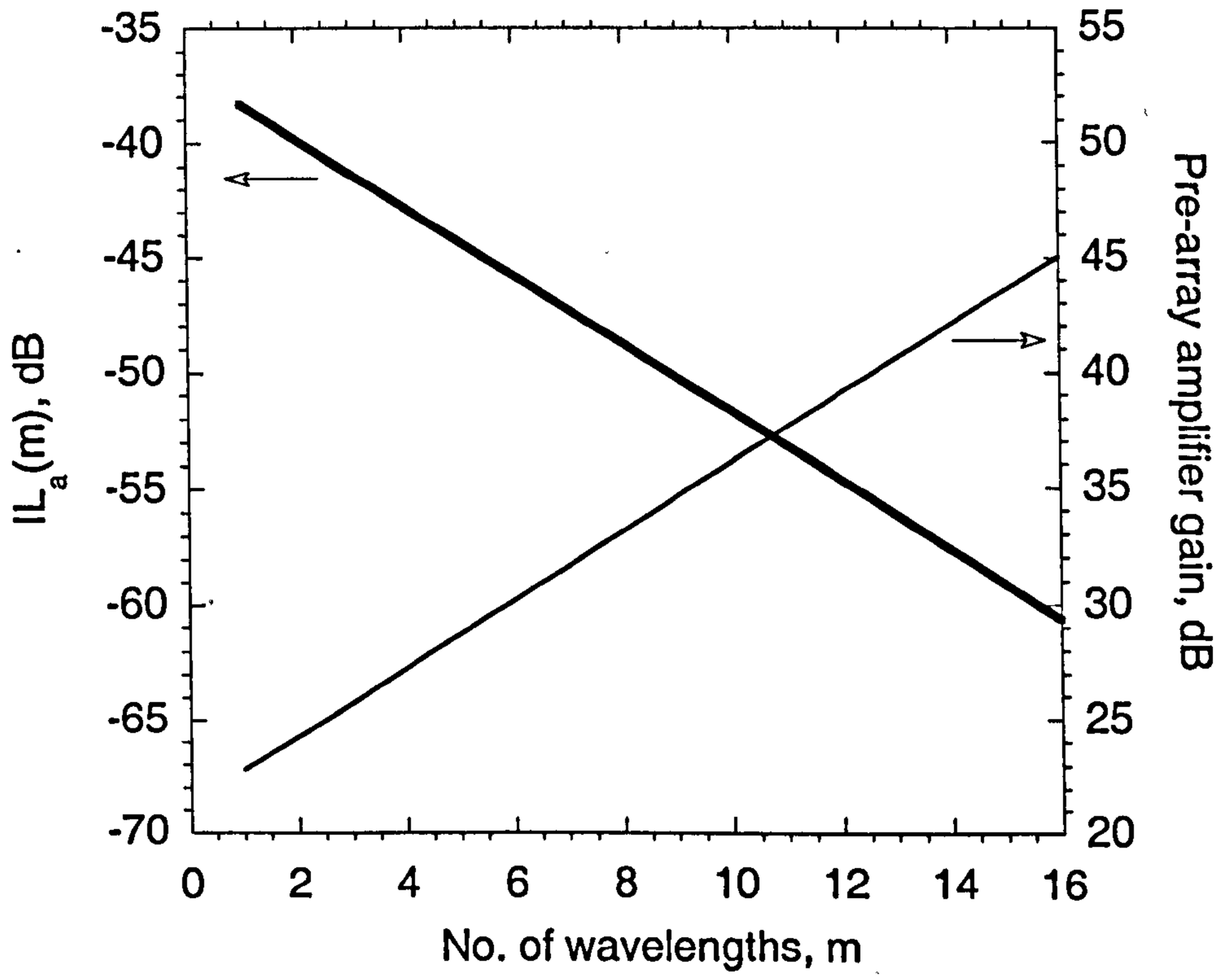

Figure 6.10: Array insertion loss versus the number of wavelengths

The input signal to the array comprises two optical pulses on a background of cw ASE power. The output of the array comprises the pulses corresponsing to each sensor and the ASE. However, the architecture of the array will cause the ASE power falling within a return sensor pulse time slot to be multiplied by the total number of return paths. In the case of the reflectometric architecture, this is equal to the number of mirrors. To account for this effect, we can calculate the total ASE power generated in the configuration shown in fig. 6.9. Assuming the gain of amplifier j is increased to compensate for the difference between the array insertion loss and inter-amplifier span loss, then the total ASE power per unit bandwidth at the input to the array is,

$$(j-1)P_{ASE}\mathrm{T}G + P_{ASE}^{j} \qquad (6.18)$$

where $\mathrm{T}=\exp(-\alpha_s L)$ and P_{ASE}^{j} is the ASE power generated by amplifier j. The total ASE power per unit bandwidth at the input to the optical filter is therefore,

$$P_{ASE}^{tot} = \left[(j-1) P_{ASE} \mathrm{T} G + P_{ASE}^{j} \right] IL_a(m) 4(N+1) + j \mathrm{T} P_{ASE} \qquad (6.19)$$

and we use (2.95) and (2.70) to determine the s-sp beat noise induced phase noise. The phase noise due to s-sp beat noise from the concatenated amplifiers is plotted as a function of link length in fig. 6.11 taking the noise figure of each amplifier, F, to be 5. This scheme essentially maintains a constant average power at the input to each amplifier and the ASE level gradually increases, as more amplifiers are included. Thus, from fig. 6.11, providing the average input power per wavelength to the amplifiers is maintained at 10 μW throughout the system, then the phase noise due to s-sp noise will be less than ~30 μrad.$Hz^{-1/2}$ for link lengths up to 1000 km. The dotted lines in fig. 6.11 show the phase resolution obtained if the multiple ASE paths in the array are not accounted for.

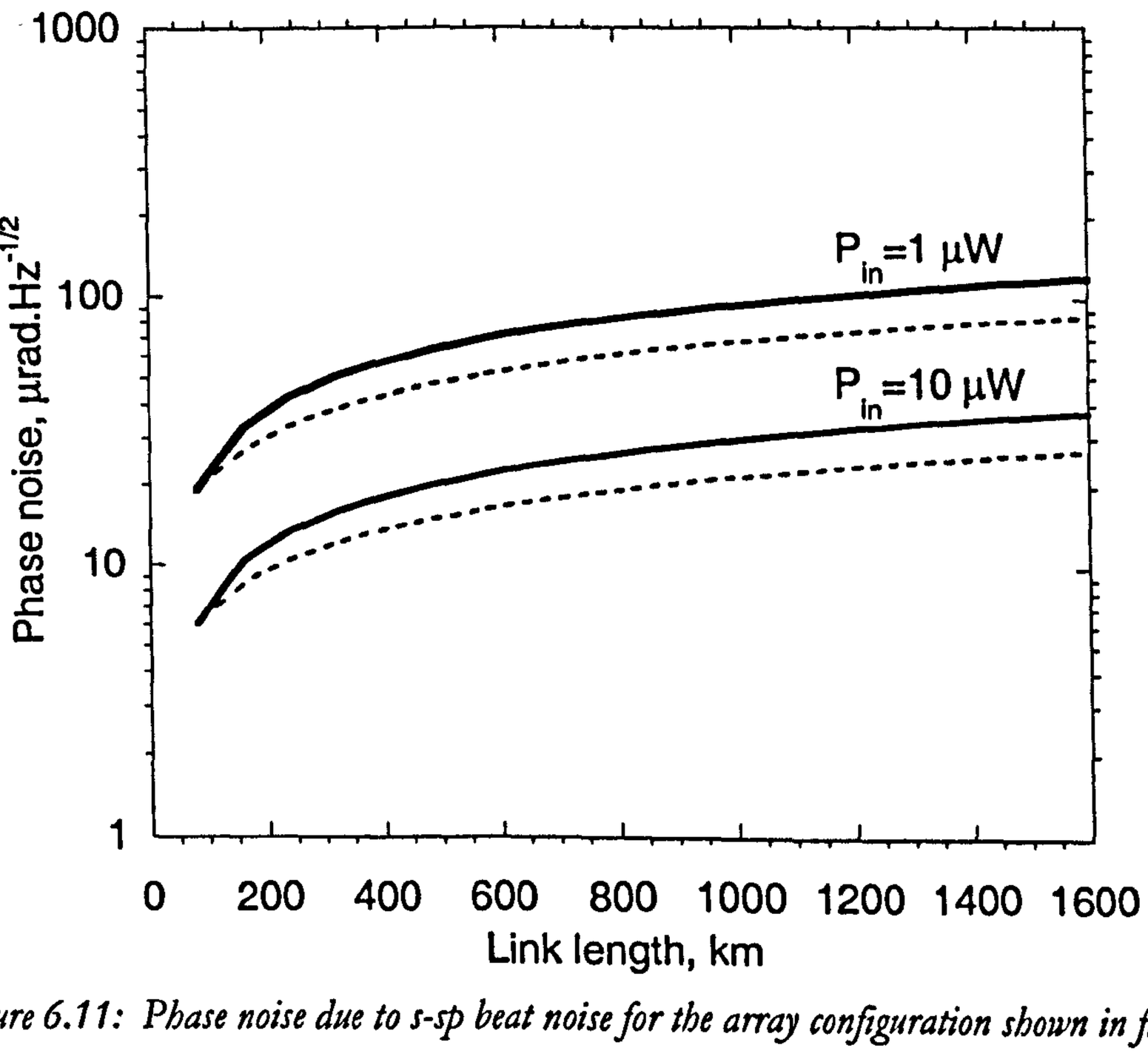

Figure 6.11: Phase noise due to s-sp beat noise for the array configuration shown in fig. 6.9

In practice, the build up of ASE will deplete the gain at the expense of the signal powers and can be compensated for by reducing the amplifier spacing [6.17]. In systems where the utilised bandwidth is well below the amplifier bandwidth (i.e. $m\Delta\nu_\lambda$ <35nm), optical filters can be placed between amplifiers to reject out-of-band ASE. The cumulative ASE power at the input

to the $2j^{th}$ amplifier must be less than the saturation power of the amplifier (i.e. $P_{ASE} \ll P_{sat}$) and from (6.19) the ASE power is $\left(P_{ASE}^{tot} - \mathrm{T}P_{ASE}\right)\Delta\nu_{opt}$, where $\Delta\nu_{opt}$ is the amplifier optical bandwidth. For the case of m =16, F =5, $\Delta\nu_{\lambda}$ =200 GHz, $\Delta\nu_{opt} = m\Delta\nu_{\lambda}$, j =10 and L =80 km then P_{ASE} ~38 μW and the amplifier must be designed to achieve an output saturation power ~ $P_{ASE} + mP_{in}$.

In this configuration, it is not necessary to stagger the launch pulses since the optical power levels are well below the nonlinear threshold levels.

6.4.3 Adding remotely pumped optical amplifiers

Including inline optical amplifiers in the link fibre would require electrical power to be supplied to the pump lasers. However, in order to maintain an electrically passive array, the pump light could be supplied from a remote laser that may be collocated with the interrogation electronics. In this configuration the amplifiers are referred to as remotely pumped amplifiers. Remotely pumped erbium doped fibre amplifiers (RPEDFA) have been used to boost transmission distances in optical communication links, without the need for inline repeaters and their associated electronics [6.18-6.21]. In these systems, the aim is to optimise the location of the RPEDFA's depending on available pump power, fibre attenuation and signal launch powers. The RPEDFA can either be configured as a postamplifier or as a preamplifier. In the former configuration, the amplifier would be situated near the launch end; the input power would generally be high and thus the amplifier would be configured with high output saturation power. In practice, these amplifiers provide only a few dB of gain due to the limited pump power and high input powers. In the latter configuration, the amplifier is situated near the receive end and can be considered as an extended receiver. This is generally the most efficient configuration since the input signal power is low and high gain can be achieved with low pump power. We shall investigate the benefit of this type of amplifier in the sensor array application and determine the increase in link length achievable. Our aim here is to derive a simple model to predict the increase in link length achievable by incorporating a RPEDFA as a preamplifier. A typical architecture is shown in fig. 6.12 in which we have placed the RPEDFA immediately after the array. A separate fibre is used to deliver the pump power.

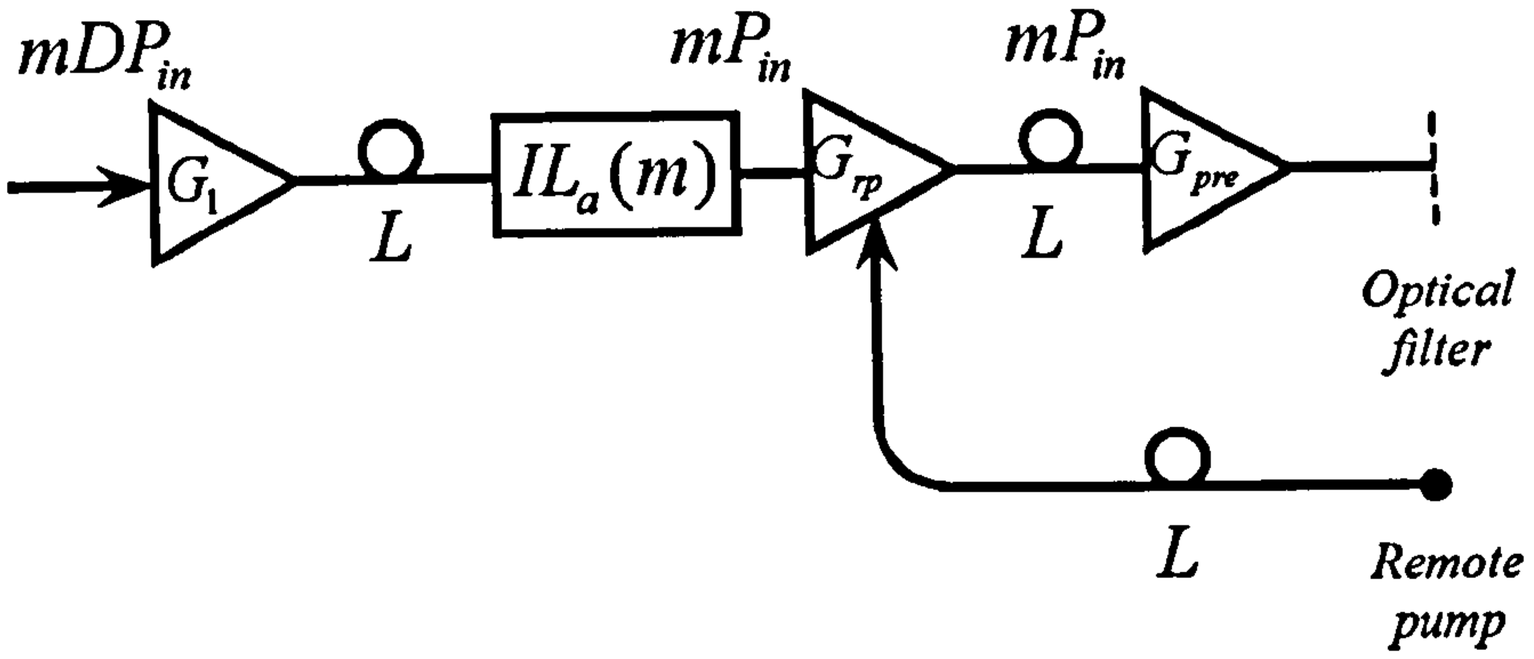

Figure 6.12: Array configuration with remotely pumped preamplifier (case 4)

To analyse this configuration, we shall make some simplifying assumptions: (i) we assume that the RPEDFA and preamplifier operate in their small-signal regime, i.e. such that the gain is not saturated and (ii) the accumulated ASE does not deplete the gain of remaining amplifiers. Thus, we can fix the gain and noise figure of the RPEDFA and preamplifier to be independent of the input powers and we assume that sufficient pump power is available to achieve the specified RPEDFA performance. We shall later verify these assumptions by determining the input powers to each amplifier and the RPEDFA pump power requirements for the system configurations of interest.

In the previous configuration (case 3), the aim was to maintain constant input power to each amplifier such that the total noise figure of the system was equal to the sum of the noise figures of each amplifier. In this configuration, the aim is to maximise the fibre lengths between each amplifier. In this case, the noise figure of the system is given by (2.102), i.e. the general case for concatenated amplifiers. The total noise figure for the configuration shown in fig. 6.12 is thus,

$$F_{tot} = F_1 + \frac{F_{rp}}{G_1 \mathrm{T}\left(IL_a(m)/D\right)} + \frac{F_{pre}}{G_1 \mathrm{T}\left(IL_a(m)/D\right) G_{rp} \mathrm{T}} \qquad (6.20)$$

where G_1, F_1, G_{rp}, F_{rp}, F_{pre} are the gain and noise figure of the power, remote and preamplifier respectively and $\mathrm{T} = \exp(-\alpha_s L)$. Again, we have used the effective insertion loss of the array, $IL_a(m)/D$ and assumed fully populated TDM pulse trains. Shown in fig. 6.13 is the total noise figure as a function of the link length. Also plotted are the magnitudes of the individual

contributions to F_{tot}. Here we have taken G_1=1000, G_{rp}=100, F_1=4, F_{rp}=4, F_{pre}=4, D=1/36 and calculated for 8 wavelengths (i.e. m=8). The range of link length has been chosen such that the total input power for both the RPEDFA and preamplifier are between 1 μW and P_{sat}=100 μW. In this regime, the noise figure of either amplifier is not increased by gain saturation.

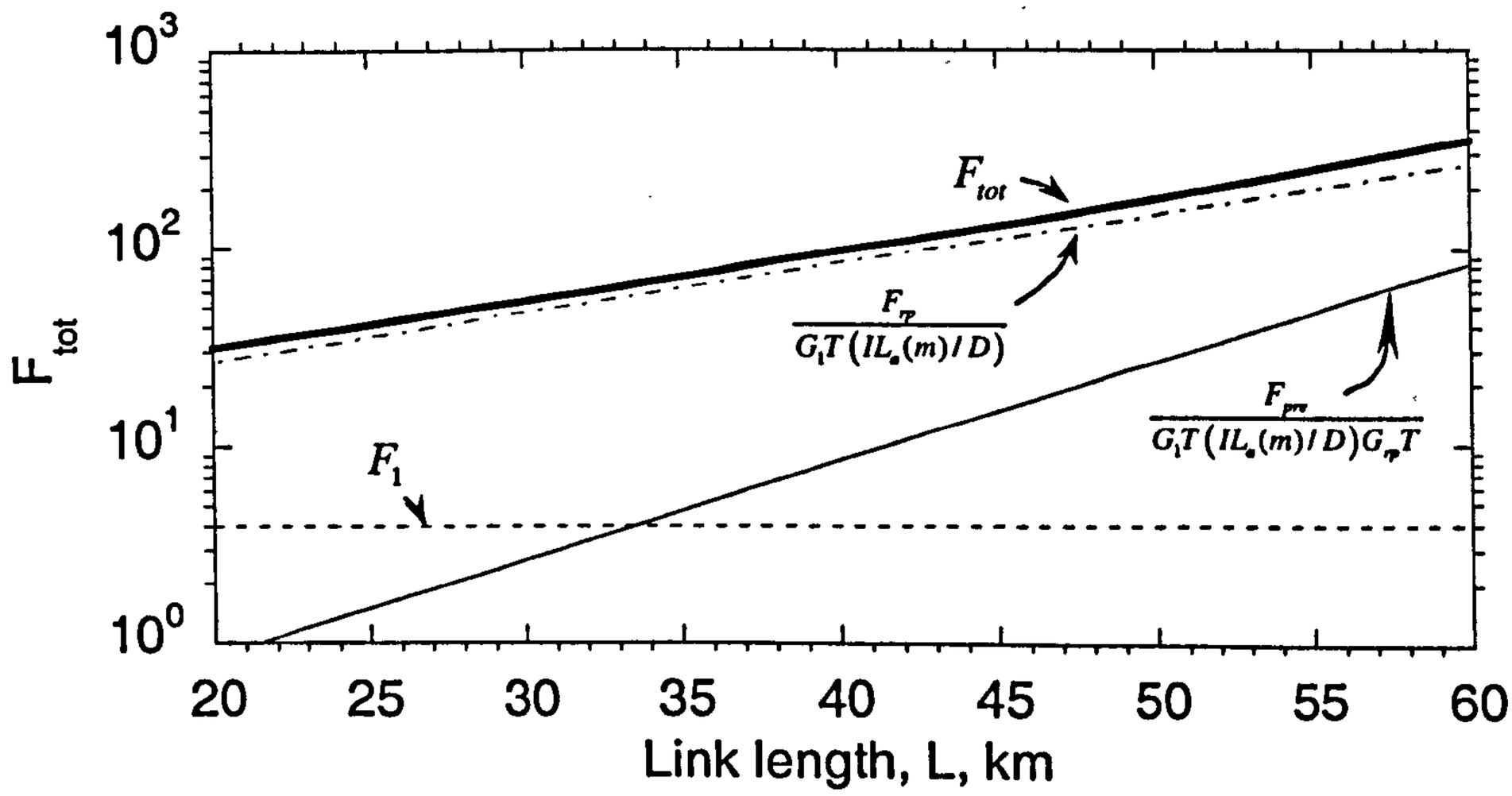

Figure 6.13: F_{tot} for the configuration shown in fig. 6.12

Thus, in this configuration, the second term of (6.20) dominates the noise figure of the system; reducing F_{rp} will minimise F_{tot}. We now use this total noise figure to determine the phase resolution. This is calculated using the model presented in section 5.6 and we substitute F_{tot} into (5.21) and (5.22). This is shown in fig. 6.14 where the launch power is determined by P_{cB}.

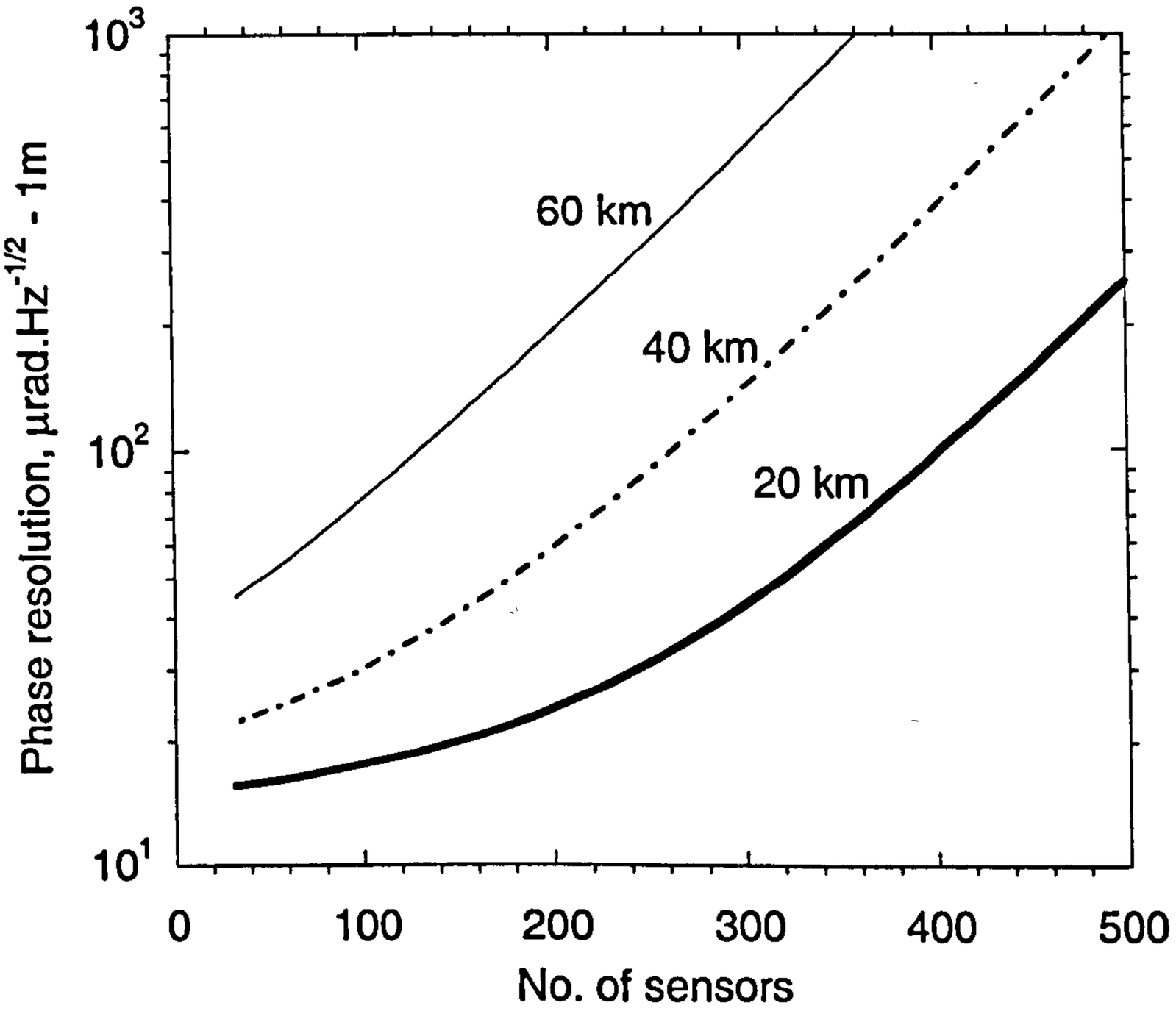

Figure 6.14: Phase resolution vs. number of sensors with staggered launch pulses (case 4)

With the RPEDFA, around 270 sensors can be interrogated over a 40 km link and achieve a phase resolution of 100 μrad.Hz$^{-1/2}$. Reducing the link length to 20 km allows around 400 sensors to be interrogated. Despite the simplicity of this model, it clearly shows that the increase in link fibre length is not simply related to the gain provided by the RPEDFA, but is also dependent on the noise generated by the RPEDFA, given by the second term of (6.20). As the link length increases, the input power to the RPEDFA falls, which reduces the OSNR at the output of the RPEDFA. The low input power to the RPEDFA is the main factor that increases the noise figure of the system. When the total noise figure is large enough such that,

$$F_{tot} > \frac{2DP_{in}}{h\nu}\Delta\nu_{opt} \tag{6.21}$$

where P_{in} is the total input power to the pre-EDFA, then sp-sp beat noise dominates the detection. Plotted in fig. 6.15 is the phase resolution vs. the number of sensors and link length, which shows that there is a direct trade-off between these two parameters. By doubling the link length, the number of sensors must be approximately halved in order to maintain the same phase resolution. Finally, in fig. 6.16 we show the relationship between the number of sensors in the array and the link length with a decreasing phase resolution.

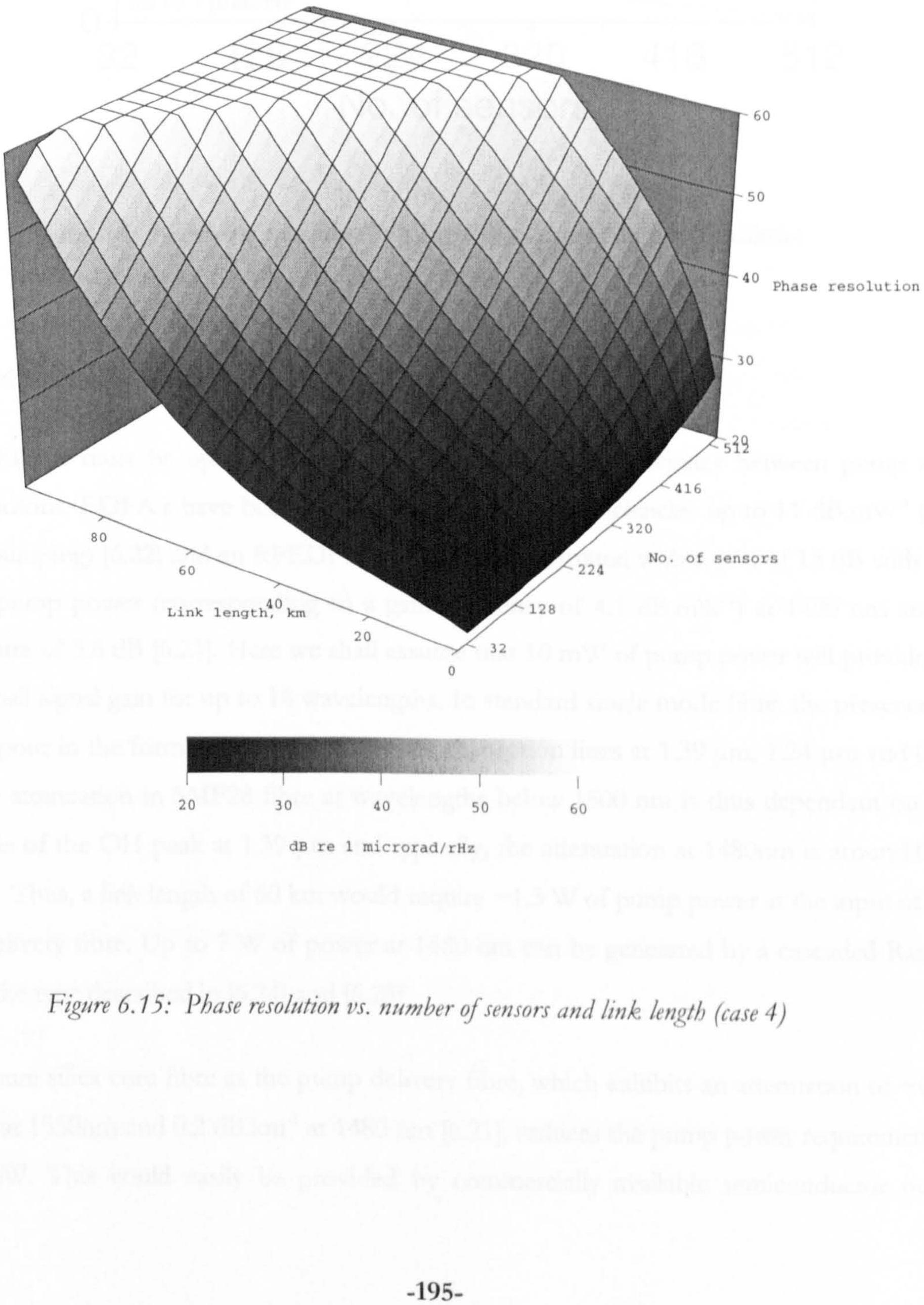

Figure 6.15: Phase resolution vs. number of sensors and link length (case 4)

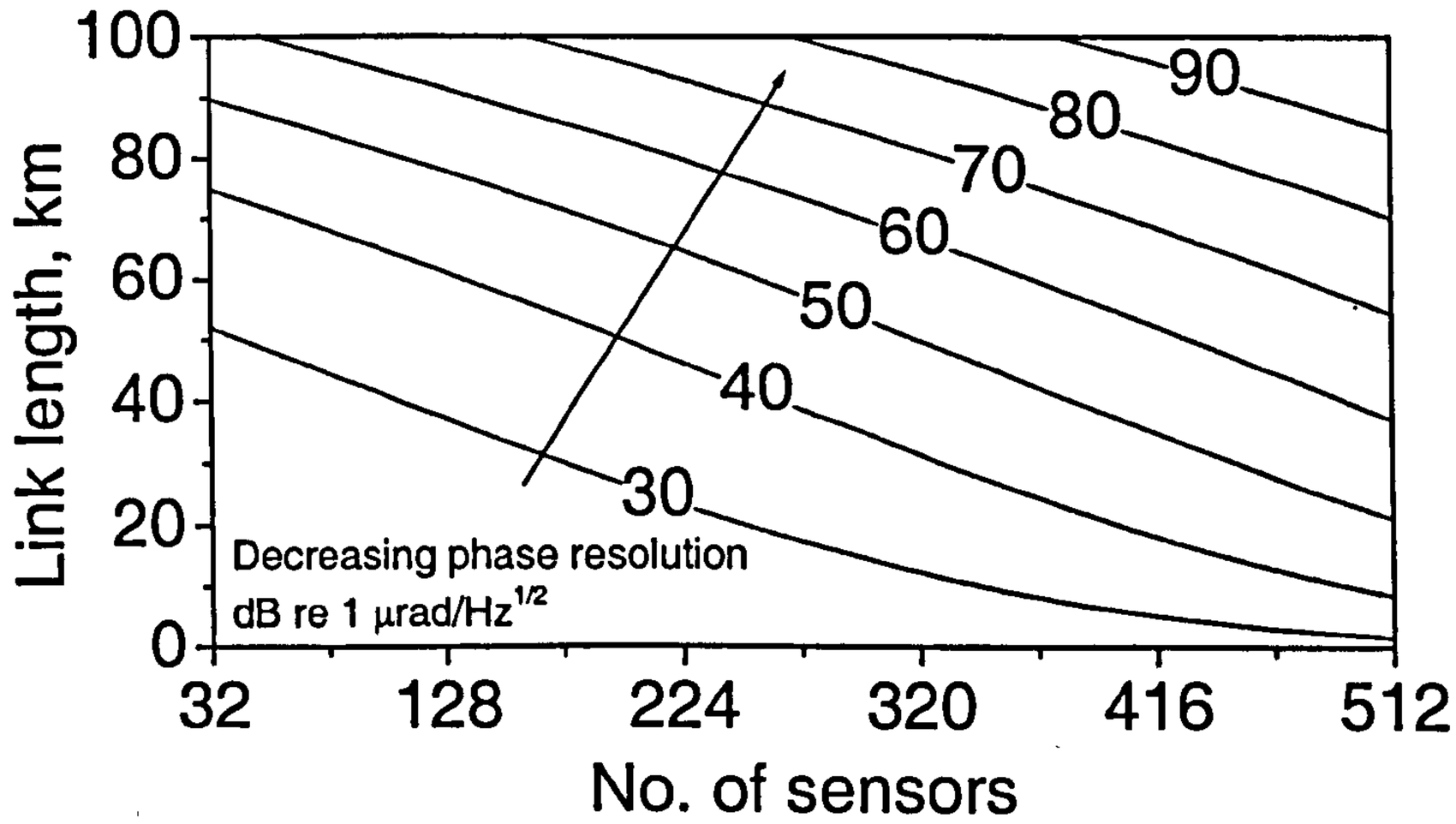

Figure 6.16: Number of sensors vs. link length with a decreasing phase resolution.

RPEDFA pump requirements

The RPEDFA must be optimised to give a high conversion efficiency between pump and signal photons. EDFA's have been demonstrated with gain efficiencies up to 11 dB.mW^{-1} (for 980nm pumping) [6.22] and an RPEDFA has been demonstrated with a gain of 15 dB with 3.8 mW of pump power (corresponding to a gain efficiency of 4.1 dB.mW^{-1}) at 1480 nm and a noise figure of 5.6 dB [6.23]. Here we shall assume that 10 mW of pump power will provide 20 dB of small signal gain for up to 16 wavelengths. In standard single mode fibre, the presence of water vapour in the form of OH ions generates absorption lines at 1.39 μm, 1.24 μm and 0.95 μm. The attenuation in SMF28 fibre at wavelengths below 1500 nm is thus dependent on the amplitude of the OH peak at 1.39 μm and typically, the attenuation at 1480nm is around 0.35 dB.km^{-1}. Thus, a link length of 60 km would require ~1.3 W of pump power at the input of the pump delivery fibre. Up to 7 W of power at 1480 nm can be generated by a cascaded Raman laser of the type described in [6.24] and [6.25].

Use of pure silica core fibre as the pump delivery fibre, which exhibits an attenuation of ~0.17 dB.km^{-1} at 1550nm and 0.2 dB.km^{-1} at 1480 nm [6.21], reduces the pump power requirement to ~160 mW. This could easily be provided by commercially available semiconductor pump

diodes. Use of this fibre as the array launch and return fibres would also permit a small increase in link length.

6.5 Conclusion

In this chapter we have identified the significant nonlinear effects that will cause degradation of the phase resolution of sensors multiplexed in a DWDM/TDM architecture of the type described in chapter 5. These are stimulated Brillouin scattering, stimulated Raman scattering, cross phase modulation and four wave mixing. It was shown that stimulated Brillouin scattering generally sets the lower limit on launch powers; however, in some configurations with more than ten wavelengths, the launch power becomes limited by stimulated Raman scattering. A technique involving staggering of the launch pulses was shown to significantly increase the thresholds set by SRS, XPM and FWM. This allowed us to determine the maximum permitted launch powers of the interrogation signals. We then presented simple models to analyse array configurations incorporating repeater type optical amplifiers and remotely pumped optical amplifiers in the link fibre. It was shown that adding repeater type optical amplifiers may permit link fibre lengths around 1000 km. It was also shown that there is a direct trade-off between link length and array size in order to achieve a predetermined sensor phase resolution.

It should be noted that a small increase (~10 km) in the link length may also be achieved with a post-amplifier to boost the signals at the input to the array. The extra amplification required on the return fibre could be achieved with either a second remotely pumped amplifier or using Raman amplification.

References

[6.1] R.H.Stolen, 1980 "Nonlinearity in fiber transmission" *Proc. of the IEEE* 68 (10) 1232-1236

[6.2] R.G.Smith, 1972 "Optical power handling capacity of low loss optical fibers as determined by stimulated Raman and Brillouin scattering" *Applied Optics* 11 (11) 2489-2494

[6.3] A.R.Chraplyvy, 1990 "Limitations on lightwave communications imposed by optical-fiber nonlinearities" *J. Light. Tech.* 8 (10) 1548-1557

[6.4] G.P.Agrawal, 1995 *Nonlinear fiber optics 2nd edn.* Academic Press, chapters 7-10

[6.5] A.R.Chraplyvy, 1984 "Optical power limits in multi-channel wavelength-division-multiplexed systems due to stimulated Raman scattering" *Elec. Lett.* 20 (2) 58-59

[6.6] R.H.Stolen, C.Lin, 1978 "Self-phase-modulation in silica optical fibers" *Physical Review A* 17 (4) 1448-1453

[6.7] G.P.Agrawal, 1997 *Fiber-optic communication systems 2nd edn.* Wiley-Interscience, section 2.3.3

[6.8] K.O.Hill, D.C.Johnson, B.S.Kawasaki, R.I.MacDonald, 1978 "CW three-wave mixing in single-mode optical fibers" *J. Appl. Phys.* 49 (10) 5098-5106

[6.9] R.H.Stolen, J.E.Bjorkholm, 1982 "Parametric amplification and frequency conversion in optical fibers" *IEEE J. Quant. Elec.* QE-18 (7) 1062-1072

[6.10] N.Shibata, R.P.Braun, R.G.Waarts, 1986 "Crosstalk due to three-wave mixing process in a coherent single-mode transmission line" *Elec. Lett.* 22 (12) 675-677

[6.11] N.Shibata, R.P.Braun, R.G.Waarts, 1987 "Phase-mismatch dependence of efficiency of wave generation through four-wave mixing in a single-mode optical fiber" *IEEE J. Quant. Elec.* QE-23 (7) 1205-1210

[6.12] R.H.Stolen, 1979 "Polarisation effects in fiber Raman and Brillouin lasers" *J. Quant. Elec.* QE-15 1157-1160

[6.13] M.A.Davis, A.D.Kersey, 1993, "Scheme for negating the SBS power limit in remotely interrogated interferometric fibre sensor arrays" *Fibre Optic and Lasers Sensor* SPIE vol. 2071 112-119

[6.14] G.R.Walker, N.G.Walker, R.C.Steele, M.J.Creaner, M.C.Brain, 1991 "Erbium-doped fiber amplifer cascade for multichannel coherent optical transmission" *J. Light. Tech.* 9 (2) 182-193

[6.15] P.C.Becker, N.A.Olsson, J.R.Simpson, 1999 *Erbium-doped fiber amplifiers: Fundamentals and Technology* Academic Press

[6.16] R.I.Lambing, M.N.Zervas, D.N.Payne, 1992 *IEEE Phot. Tech. Lett.* 4 1345-1347

[6.17] C.R.Giles, E.Desurvire, 1991 "Propagation of signal and noise in concatenated erbium-doped fiber optical amplifiers" *J. Light. Tech.* 9 (2) 147-154

[6.18] P.B.Hansen, L.Eskildsen, 1997 "Remote amplification in repeaterless transmission systems" *Optical Fiber Tech.* 3 221-237

[6.19] P.B.Hansen, L.Eskildsen, S.G.Grubb, A.M.Vengsarkar, S.K.Korotky, T.A.Strasser, J.E.J.Alphonsus, J.J.Veselka, D.J.DiGiovanni, D.W.Peckham, D.Truxal 1996 "442 km repeaterless transmission in a 10 Gbit/s system experiment " *Elec. Lett.* 32 (11) 1018-1019

[6.20] C.Cremer, U.Gaubatz, P.Krummrick, 1996 "4*10Gbit/s WDM transmission with remote post and preamplifiers" *Elec. Lett.* 32 (12) 1116-1118

[6.21] L.Eskildsen, P.B.Hansen, S.G.Grubb, A.M.Vengsarkar, T.A.Strasser, J.E.J.Alphonsus, D.J.Digiovanni, D.W.Peckham, D.Truxal, W.Y.Cheung 1996 "465-km repeaterless transmission using a 2.488 Gb/s directly modulated DFB laser" *IEEE Phot. Tech. Lett.* 8 (5) 724-726

[6.22] M.Shimizu, M.Yamada, M.Horiguchi, T.Takeshita, M.Okayasu, 1990 "Erbium-doped fibre amplifiers with an extremely high gain coefficent of 11.0 dB/mW" *Elec. Lett.* 26 (20) 1641-1643

[6.23] V.L.da Silva, D.L.Wilson, G.Nykolak, J.R.Simpson, P.F.Wysocki, P.B.Hansen, D.J.DiGiovanni, P.C.Becker, S.G.Kosinski, 1995 "Remotely pumped erbium-doped fiber amplifiers for repeaterless submarine systems" *IEEE Phot. Tech. Lett.* 7 (9) 1081-1083

[6.24] S.G.Grubb, T.Strasser, W.Y.Cheung, W.A.Reed, V.Mizrahi, T.Erdogan, P.J.Lamaire, A.M.Vengsarkar, D.J.Digiovanni, B.H.Rockney, 1995 "High power 1.48 μm cascaded

Raman laser in germanosilicate fibers" *Optical Amplifiers and their Applications,* OSA Tech. Digest Series, vol. 18, 197-199

[6.25] IRE-POLUS Group 2000, Fibre Raman Laser PYL-R spec. sheet

Part IV
Laser Sources for Sensor Arrays

Chapter 7

THE ERBIUM DOPED DISTRIBUTED FEEDBACK FIBRE LASER AS A SOURCE FOR INTERFEROMETRIC SENSOR ARRAYS†

Abstract - In this chapter we characterise the performance (slope efficiency, frequency and intensity noise) of the Er^{3+} doped DFB fibre laser and discuss the origins of the observed frequency and intensity noise. We show that, with appropriate packaging, the frequency noise can be reduced to the level determined by thermal effects in the laser cavity. We describe the detailed design of an electro-optic feedback circuit which reduced the intensity noise at the relaxation oscillation by 30 dB to –116 dB.Hz^{-1}±2dB. We investigate techniques to modulate the emission frequency of the laser. We also show how these techniques can be used to reduce the frequency noise of the laser by up to 18 dB below the limit thought to be set by cavity thermal noise, by locking the laser emission to an interferometer. This is equivalent to a frequency noise of 1.5Hz.$Hz^{-1/2}$±25% at 1 kHz. By optimising and combining these techniques, this laser would be ideally suited as a high performance source for interrogation of interferometric sensors.

7.1 Introduction and Brief Historical Review

The phase resolution obtained in an interferometric measurement is often limited by the stability of the frequency and intensity of the interrogating laser source. In principle, any noise source (frequency or intensity) generated by the source can be compensated for by a direct continuous measurement of the laser emission. The noise would then be appropriately subtracted from the sensor output. In the interferometric sensor, excess noise is generated

†This chapter contains a re-edited transcript of the paper "Frequency noise reduction in erbium doped fiber DFB lasers using electronic feedback" submitted for publication in Optics Letters.

either directly from the intensity noise of the source or indirectly from the frequency noise which is converted into intensity noise by an unbalanced interferometer. However, in large systems with significant signal processing, the added complexity involved and the need to ensure high coherence between the noise to be subtracted and the sensor self-noise (i.e. by adding time delays to compensate for the signal processing delay), renders this technique less practical. Techniques have been demonstrated for rejection of intensity noise using balanced detection [7.1] and frequency noise using common mode rejection at the demodulation stage in a single interferometric sensor [7.2]; however the technique demonstrated in [7.1] is generally ineffective for multiplexed systems and the technique described in [7.2] becomes less effective with large multiplexed systems, for the reasons described above. Thus, it is generally desirable to reduce these noise sources at their origin.

Early demonstrations of interferometric fibre-optic sensors used either semiconductor lasers [7.3] or bulk HeNe lasers [7.4]. The semiconductor laser generally exhibits low intensity noise (<120 dB.Hz^{-1} at 1 kHz); however, the linewidth of the output emission is typically ~1 MHz. Thus, either accurate path balancing is necessary in the interferometer or phase noise reduction is required on the laser [7.5]. The HeNe source generally exhibits low intensity noise (<-90 dB.Hz^{-1}) and a narrow linewidth (<5 kHz); however, its bulk optic design, large size and wavelength of operation only at 543 nm, 633 nm, 1150 nm and 3390 nm, which are all some way from the low loss region of silica fibre, make it less practical.

More recently, high performance lasers such as the diode-pumped Nd:YAG ring laser [7.6], the solid state Er^{3+}:Yb^{3+} laser [7.7] and the Er^{3+} ring laser [7.8] have become commercially available. The diode pumped ring laser operates in the 1310nm spectral region and with noise control can exhibit very low intensity noise (<-140 dB.Hz^{-1}) and a narrow linewidth (<5 kHz). The Er^{3+}:Yb^{3+} bulk glass laser and Er^{3+} fibre ring laser operate in the 1550nm spectral region and have been demonstrated to exhibit low intensity noise and a narrow linewidth. However, these lasers are, at present, high cost due to their complex design. The short cavity length erbium fibre laser (EFL) is a potential alternative to these lasers and in some configurations may be low cost, with the required performance for the interferometric sensor application. This laser also operates in the 1550nm spectral region, which makes it compatible with wavelength division multiplexing technology.

Invention of the fibre-laser is usually attributed to Snitzer and Koester [7.9-10] in 1963, who published work on multicomponent glass fibre lasers while at American Optical. Although research continued on various laser configurations, the are enjoyed a considerable resurgence shortly after the development of the erbium doped fibre amplifier [7.12, 7.63] at Southampton University, UK and Bell Labs, US in 1987. An excellent review of rare earth doped fibre laser devices can be found in [7.11]. The short cavity length EFL was one of a number of fibre laser devices demonstrated; however, its simplicity makes it particularly attractive and the remarkable progress made over the last decade in photosensitive doped fibre and in-fibre Bragg gratings (IFBG) have made it a practical device. Indeed, by ensuring single longitudinal mode operation, the linewidth of the laser emission may, in principle, approach the limit set by the spontaneous emission (known as the Schawlow-Townes limit named after the early laser pioneers C.H.Towns and S.L.Schawlow who derived a formula for this limit). It will be shown that, in fact, spontaneous emission limited linewidth is not achievable; however, these devices can still exhibit spectral linewidths comparable to and in some cases significantly lower than many of the laser types discussed above. We first review the techniques used to achieve single longitudinal mode operation from an erbium fibre laser.

In a linear fibre laser with no wavelength selective elements, where the effective cavity length is relatively long, the number of modes that will oscillate will depend on the free spectral range (FSR) of the cavity and the bandwidth of the gain medium. The relatively small mode spacing therefore, will require a high degree of wavelength selectivity to be incorporated into the cavity. Techniques used to demonstrate this are: an interferometric resonator [7.13]; a travelling wave structure [7.14]; by injection locking [7.15]; and by using an intra-core fibre grating [7.16]. The interferometric resonator relies on the wavelength discrimination property of the interferometer to ensure that a high round-trip cavity loss is experienced by all but one of the possible modes. The travelling wave structure uses the property of the homogenously broadened gain medium, whereby the mode with the highest roundtrip gain reaches threshold first and saturates the gain. Provided that there is no spectral hole burning, there will not be sufficient gain available for the other modes to reach threshold. The travelling wave configuration prevents spectral hole burning in the cavity, and thus ensures single longitudinal mode operation. The injection locking technique is based on ensuring that only one longitudinal mode has sufficient round-

trip gain to reach threshold. This requires seeding the fibre laser with an external narrow-band source at a frequency corresponding to one of the longitudinal modes of the fibre laser.

The mode spacing of the linear fibre laser is determined by the free spectral range of the cavity and can be increased by reducing the cavity length, as indicated in fig. 2.9(ii). Single-longitudinal mode operation can be achieved by reducing the cavity length to a few centimetres and using the wavelength selective properties of the intra-core Bragg grating as the feedback element. Provided that only one mode falls within the grating reflection bandwidth, then only this mode will experience a high enough round trip cavity gain required to achieve threshold. This configuration is often referred to as the distributed Bragg reflector (DBR) design. This technique was first demonstrated in [7.16] using a Nd^{3+} doped fibre. However, the first demonstration of a short cavity length erbium fibre laser (EFL) was reported in [7.17] which used two separate intra-core Bragg gratings to provide feedback to the gain region and longitudinal mode discrimination. The design of these devices was analysed in [7.18] where it was shown that robust single-mode operation was achievable by appropriate design of the IFBG profile and reflectance. These sources may provide an alternative to the semiconductor laser diode for high bandwidth communications, due to their narrow linewidths, small size, simplicity in design, low sensitivity to temperature and intrinsic compatibility with the transmission medium. We now review the progress on the development of this laser configuration over the last decade.

The frequency and intensity noise performance was first experimentally investigated for these lasers in [7.20-21], which showed that they can exhibit a linewidth less than 20 kHz and using active electronic feedback to the pump diode reduces their relative intensity noise (RIN) to less than –110 dB Hz^{-1}. Due to the short cavity length of these lasers and the constraints set on the erbium doping concentration, these lasers are limited to emitting only a few hundred microwatts of power. However, a master-oscillator power-amplifier (MOPA) configuration (where a length of erbium doped fibre is placed after the laser resonator to provide extra gain to the laser emission) demonstrated up to 60 mW of output power using two semiconductor pump diodes [7.21]. Although the performance of these lasers was adequate for many applications, some potential problems remained concerning the sensitivity of the laser wavelength to the relative separation of the Bragg gratings and stability of the laser in the presence of environmental perturbations. A more stable resonator was demonstrated using a

distributed feedback fibre laser (DFB) design. The DFB EFL consists of a single grating, as shown in fig. 7.1 which confines the laser cavity to within the region of the grating (it is worth noting here that the number of modulation cycles in a 50mm grating is ~10000). Typical values of Δn are between 10^{-5} and 10^{-3}.

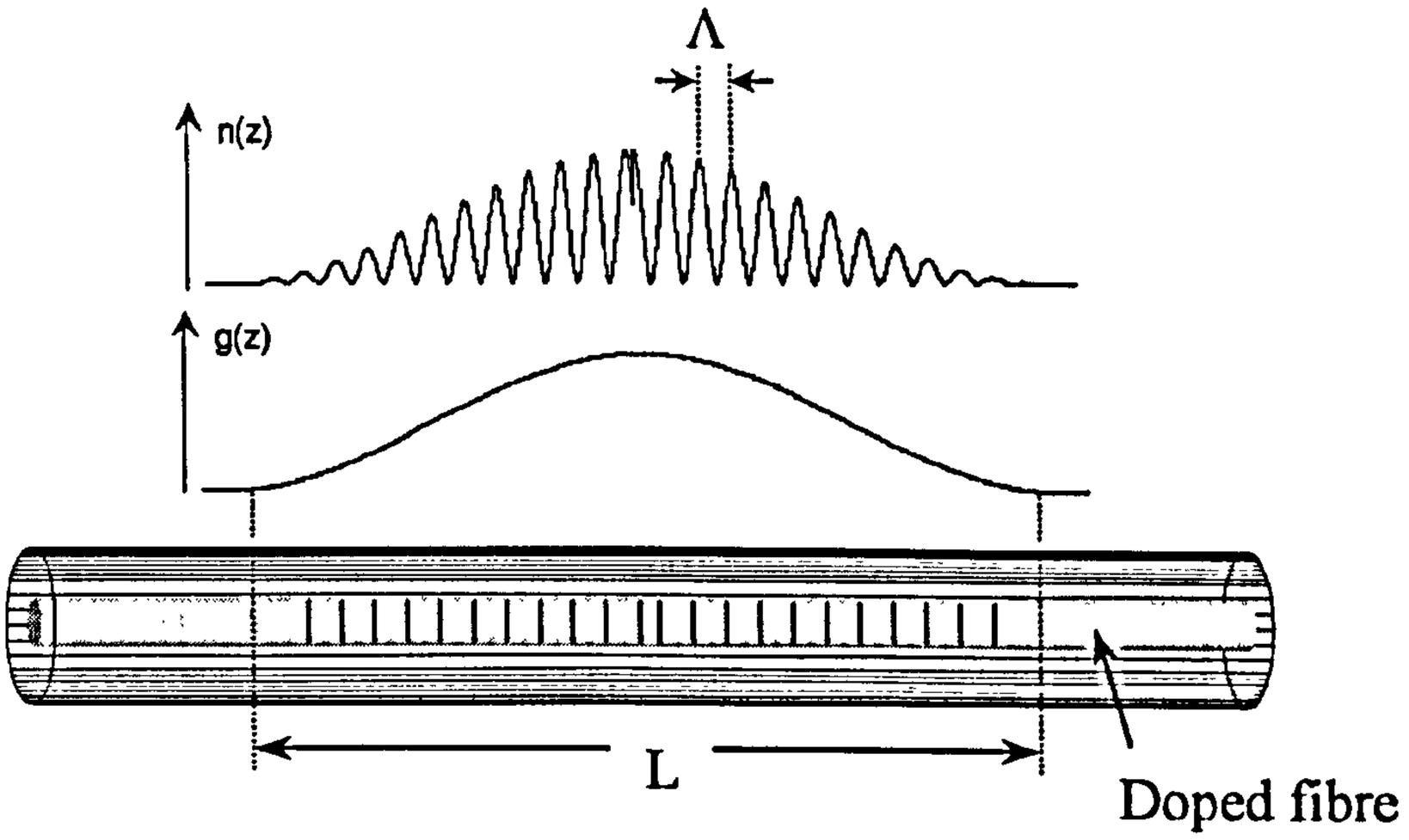

Figure 7.1: DFB fibre laser configuration incorporating central discrete $\pi/2$ phase-shift, a raised cosine apodisation profile, $g(z)$ and index modulation, $n(z)$

While a uniform grating will support lasing, the presence of more than one mode with equal lasing threshold, results in gain competition between the modes and unstable operation. However, incorporating a phase-shift within the IFBG confines the fundamental mode to the locality of the phase-shift, and generally favours single-mode operation. The reflection spectrum for a $\pi/2$ (single pass) phase-shift in the centre is shown in fig. 7.2.

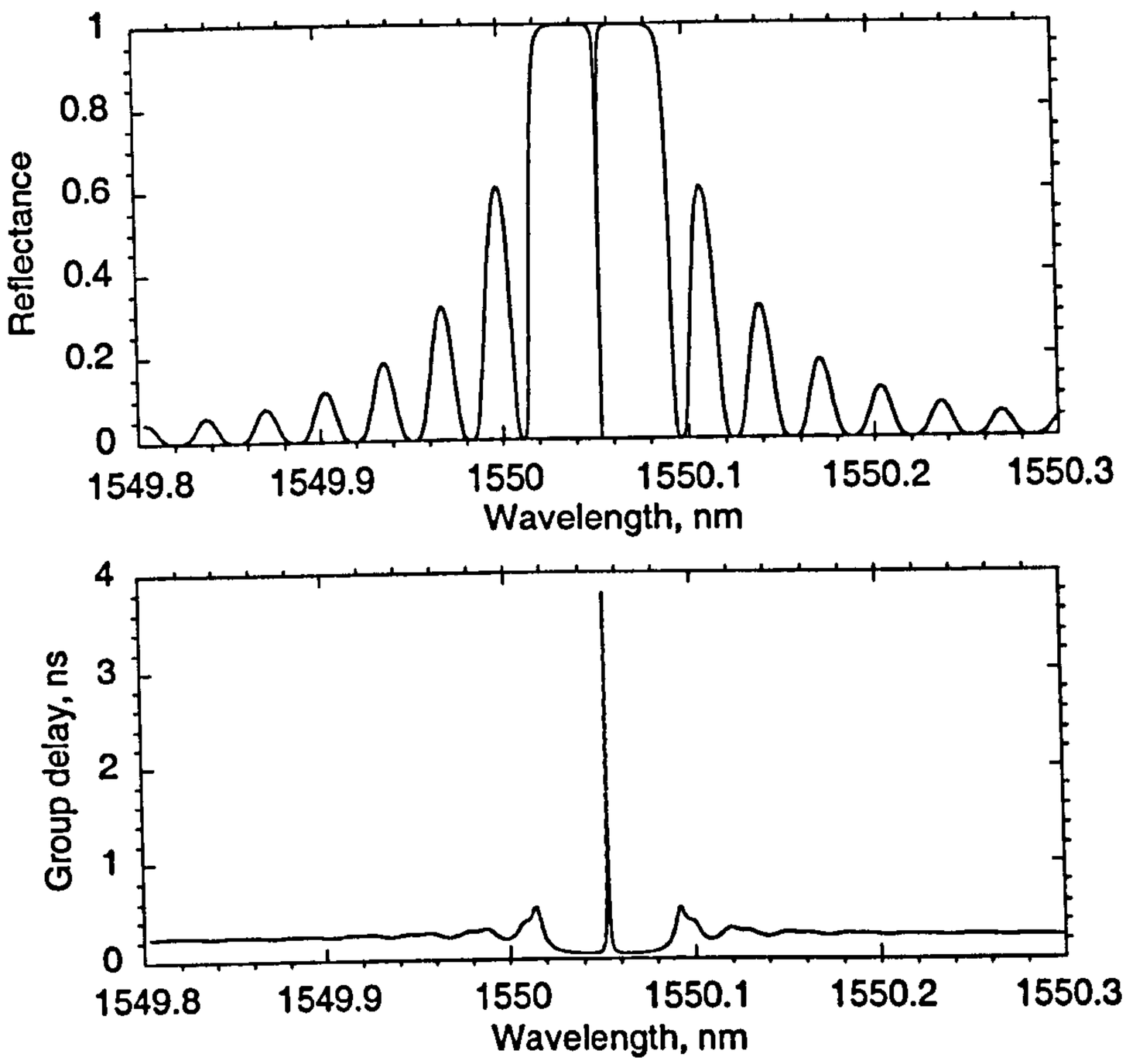

Figure 7.2: Reflection and group delay spectrum of $\pi/2$ (single pass), 50 mm, unapodised, $\kappa L = 5.1$, phase-shifted IFBG. (These plots were calculated using the transfer matrix method)[13]

The presence of the phase-shift causes a sharp dip to appear in the centre of the grating reflection spectrum, which corresponds to the wavelength of the fundamental mode of the resonator. The resonator properties of this structure are better visualised from the group delay, also shown in fig. 7.2. The resonance's of the DFB structure can be seen to correspond to the side-lobes of the IFBG profile and about the phase-shift. The mode corresponding to the central phase-shift is referred to as the fundamental and higher order modes correspond to the side-lobe nulls. Robust single-mode operation is usually obtained since the thresholds of the higher-order modes are generally much higher than the fundamental mode, providing the grating strength is not made too high. Apodisation of the grating profile, as shown in fig. 7.1, allows the higher-order mode thresholds to be increased further [7.27].

---

13 To calculate the reflectance and group delay of the phase-shifted IFBG, we have used the popular transfer matrix approach, described in [7.36,38]. In this technique the IFBG is divided into a number of segments such that each segment can be approximated to a uniform grating. In this case a single matrix describes the coupling between forward and reverse propagating beams in the grating segment. By applying appropriate weighting factors to the coupling coefficent (defined later) and including phase-shift matracies as necessary, the response of an arbitrary grating profile with phase discontinuities can be determined by simply multiplying the matrix for each segment from one end of the grating to the other.

Although the concept of the DFB structure is well known and has been used in semiconductor lasers since the early 1970's, its use in fibre lasers is more recent since the development of the IFBG. The first reported DFB fibre laser used a Bragg grating written into a hydrogen loaded Er^{3+}:Yb^{3+} codoped fibre [7.22]. Two lasers were demonstrated; one used a single grating formed in a hydrogen loaded Er^{3+}:Yb^{3+} fibre as one feedback element and a reflective fibre end to form the second feedback element and a DFB structure was formed by inducing a phase-shift in the centre of the grating using a heated wire. The use of codoped fibre resulted in a pump absorption around two orders of magnitude higher than that obtained in Er^{3+} doped fibre and hence an output power of a few mW. Following this, DFB erbium fibre lasers were demonstrated which incorporated the required phase-shift during the grating writing process either by translation of the fibre by the appropriate amount during the fibre-scanning beam technique [7.23] or by UV post-processing of the grating to induce the phase-shift [7.24]. It was then demonstrated that by application of a birefringent phase-shift by UV post-processing, the lasers could be forced to lase in a single-polarisation mode [7.25-26]. In this configuration, the two orthogonal polarisation modes experience a different phase-shift, hence by adjusting the magnitude of the birefringence, the lasing threshold of one mode can be increased relative to the other. Alternatively, writing a strongly polarisation dependent IFBG (resulting in strong polarisation dependent loss for one polarisation mode) would also ensure single-polarisation mode operation.

Although the codoped fibre laser promises high output power without the need for a separate power amplifier stage, these lasers tend to exhibit broader linewidths and poorer frequency stability than the EFL's [7.28], possibly due to the elevated temperature in the cavity due to non-radiative transitions. For this reason we concentrate here on the noise properties of the EFL and investigate its use as a source for interrogation of fibre-optic interferometric sensors. The chapter is set out as follows: in section 7.2 and 7.3 we define the terms to be used to characterise the grating properties and laser output spectrum, pertinent to the interferometric sensor application. Then a brief outline of the laser characteristics necessary for most interferometric sensor applications is given in section 7.4. In section 7.5, the basic set-up of the fibre lasers under test is presented and a discussion is given on issues such as choice of pump and laser packaging. This is followed by a discussion on the performance of the free-running laser. In sections 7.6 and 7.8, we present techniques based on active electronic feedback to

suppress the relaxation oscillation induced intensity noise. In section 7.7 we investigate frequency modulation of the laser though pump power modulation and cavity strain and provide a discussion on the mechanisms giving rise to correlation between pump modulation and EFL frequency modulation. In section 7.8 we present a DFB fibre laser in a MOPA configuration with relative intensity noise reduction and frequency noise reduction. Finally, in section 7.9 we summarise our conclusions.

7.2 Grating Parameters

It is useful, at this stage, to define the relevant grating parameters. Referring to the grating profile, shown in fig. 7.1, we define the coupling coefficient, $\kappa(z)$, which is related to the index modulation, $\Delta n(z)$, by [7.36],

$$\kappa(z) = \frac{\pi}{\lambda} g(z) \Gamma \Delta n(z) \tag{7.1}$$

where λ is the wavelength, $g(z)$ is the apodisation profile and Γ is the overlap integral between the mode and the transverse grating profile. For a non-chirped grating, the refractive index in the region of the grating can be expressed as,

$$n(z) = n_0 + \Delta n \sin\left(\frac{2\pi}{\Lambda} z\right) \tag{7.2}$$

where n_0 is the uniform index change, Λ is the grating pitch. It thus follows that the grating strength is defined by κL, where L is the grating length. For a uniform grating, the peak reflectance is given by,

$$R_{pk} = \tanh^2(\kappa L) \tag{7.3}$$

We can now determine the effective mirror transmittance by noting that for a uniform, strong (i.e. high κ) grating with a discrete $\pi/2$ phase-shift, (7.3) leads to,

$$M \simeq 4\exp(-2\kappa L) \tag{7.4}$$

It can also be shown that on entering the grating, the amplitude of the optical field falls as $\exp(-2\kappa z)$ [7.37] and therefore we can define a penetration depth as the $1/e$ evanescent decay depth, $l_{1/e} = 1/2\kappa$. It follows that for the discrete $\pi/2$ phase-shifted grating based laser, the effective cavity length can be approximated by, $l_e \simeq 1/\kappa$. If the phase-shift is distributed, a distance approximately equal to the length of the phase-shift should be added to this value.

7.3 Characterisation of the Laser Source: Definition of Terms

The laser output field can be expressed by,

$$V(t) = \mathrm{Re}\left[E(t)e^{i(2\pi\nu(t)\cdot t)}\right] \tag{7.5}$$

where $E(t)$ and $\nu(t)$ indicate that the amplitude and frequency of the optical signal are time dependent. For the following analysis, they are assumed to vary only slightly with time. We define $E(t) = E_0 + \Delta E(t)$ and $\nu(t) = \nu_0 + \Delta\nu(t)$ where $\Delta\nu(t)$ is the instantaneous time dependent frequency fluctuation and is related to the instantaneous phase fluctuation by $\Delta\nu(t) = (2\pi)^{-1} d\phi(t)/dt$. In general, $\Delta\nu(t)$ will be a random variable with zero mean, so we define the root-mean-square (rms) frequency excursion as $\nu_{rms}^2 = \left\langle |\Delta\nu(t)| \right\rangle^2$ and correspondingly the rms phase excursion as $\phi_{rms}^2 = \left\langle |\phi(t)| \right\rangle^2$ (where $\langle\ \rangle$ indicates an average over time). The term in the square brackets in (7.5) is sometimes referred to as the "analytical signal".

7.3.1 Amplitude/intensity noise

The laser power can be expressed as $P(t) = E(t)^2 = P_0 + \delta P(t)$ where P_0 is the unperturbed or average output power and $\delta P(t)$ is the time-dependent fluctuation and exhibits zero mean (i.e. $\langle \delta P(t) \rangle = 0$). So we define the variance of the power fluctuation,

$$\left\langle \delta P(t)^2 \right\rangle = \left\langle \left(P(t) - P_0\right)^2 \right\rangle = \int_0^{\infty} S_{\delta P}(f)\,df \tag{7.6}$$

where $S_{\delta P}(f)$ is the spectral density function of the power fluctuation. The relative intensity noise (RIN) of the laser output is then defined as,

$$RIN(f) \equiv \frac{S_{\delta P}(f)}{P_0^2} \tag{7.7}$$

The RIN is usually normalised to a 1 Hz bandwidth and expressed in logarithmic units using,

$$RIN\left[dB\,Hz^{-1}\right] = 10\log_{10}\left[RIN(f)\right] \tag{7.8}$$

where the reference to Hz^{-1} simply states that the noise measurement is normalised to a 1 Hz bandwidth. Measurement of the RIN of a given source can be carried out by measurement of the noise current generated in a photodiode, δi_{pd}. This is then related to the laser power fluctuations by,

$$\delta i_{pd}(t) = \frac{e\eta}{h\nu}\delta P(t)\Delta f \tag{7.9}$$

where Δf is the receiver bandwidth, the factor $e\eta/h\nu$ is the photodiode responsivity, e is the electron charge, η is the photodiode quantum efficiency and h is Plancks constant. Fourier transformation of the auto-correlation of (7.9) will then yield the power spectral density of the photodiode current and division by the square of the average power yields $RIN(f)$.

7.3.2 The laser field spectrum and linewidth

The laser linewidth indicates the spread of energy of the optical field about the centre frequency, ν_0 (i.e. how much the laser deviates from purely monochromatic). By assuming that the laser noise spectrum is broadened only by fluctuations of the optical phase (i.e. fluctuations in the intensity have a negligible effect on the laser spectrum) and that the phase fluctuations obey Gaussian statistics, Yariv [7.30] showed that the auto-correlation function of the laser field spectrum is given by,

$$C_E(\tau) = \frac{1}{2}E_0^{\,2}\cos(2\pi\nu_0\tau)e^{-\frac{\tau}{\tau_c}} \tag{7.10}$$

where τ_c is the laser coherence time and from (7.10) can be seen to indicate the value of τ for which the auto-correlation function of the laser has fallen to e^{-1} of its peak value. Using the Wiener-Khintchine theorem, which relates the spectral density of the optical field to its auto-correlation function,

$$S_E(\nu) = \frac{1}{\pi}\int_{-\infty}^{\infty} C_E(\tau) e^{-i2\pi\nu\tau} d\tau \qquad (7.11)$$

the field spectrum was determined to be,

$$S_E(\nu) = \frac{E_0^2}{4\pi} \frac{\frac{1}{\tau_c}}{\frac{1}{\tau_c^2} + 4\pi^2(\nu - \nu_0)^2} \qquad (7.12)$$

which is a Lorenzian shaped function centred on ν_0 with a full width at half-maximum defined as the laser linewidth, $\Delta\nu_{laser} = (2\pi\tau_c)^{-1}$.

For narrow linewidth lasers, direct measurement of the laser spectrum using techniques, such as *Fourier transform spectroscopy,* to determine directly the field auto-correlation function given in (7.10) tend to be problematic due to the large variable delay times necessary (i.e. a laser linewidth of 10 kHz, typical for fibre lasers, would require a delay time varied from 0 to greater than 3×10^{-5}s or 9km of free space). A simpler technique is known as the delayed self-heterodyne which involves delaying the optical field by a time, t_d, relative to itself using a similar interferometric set-up to that shown in fig. 2.11 and incorporating an acousto-optic modulator in position A or B [7.30]. We consider here only the special case where $t_d \gg \tau_c$. Maintaining the assumption that the laser field spectrum is due only to fluctuations in the phase and that these fluctuations obey Gaussian statistics, the spectral density of the photodiode current can be shown to be given by [7.29],

$$S_{i_{pd}}(\Upsilon) = \frac{2R^2E_0^4}{\pi}\left[\frac{\frac{4}{\tau_c}}{\left(\frac{2}{\tau_c}\right)^2 + \Upsilon^2} + 2\delta(\Upsilon)\right] \tag{7.13}$$

where Υ is the frequency offset and $\delta(\Upsilon)$ is the Dirac delta function. Thus, the spectral density of the current contains a Lorenzian distribution centred on zero frequency with a full width at half-maximum equal to twice the laser linewidth, $2\Delta\nu_{laser}$. The delayed self-heterodyne technique provides a quick method of obtaining the coherence time of the laser. However, we have assumed throughout that the noise mechanisms obey Gaussian statistics and exhibit a flat spectral density (i.e. a white noise source). Deviations from a flat spectrum must be negligible for equation (7.8) and (7.9) to apply. The presence of f^{-1} noise causes the lineshape to deviate from Lorenzian and more closely resemble a Gaussian [7.31]. In the case of the fibre lasers it will be shown that the frequency noise spectrum deviates from white noise due to contributions from other noise sources. Thus, the use of linewidth to accurately characterise the frequency noise of a fibre laser source should be treated with caution. In the case of the interferometric fibre optic sensor, it is more useful to characterise the spectral density of the frequency fluctuations of the laser and hence determine $\Delta\nu(f)$ directly.

7.3.3 Frequency/phase noise

Frequency noise of the optical spectrum can be measured using the frequency discrimination property of an imbalanced interferometer. A typical interferometric set-up using balanced detection to reject intensity noise, is shown in fig. 2.10. It is usually sufficient for the EFL to set t_d=0.5 μsec corresponding to a 100m imbalance to ensure that the contribution to the photocurrent from laser RIN and receiver noise are negligible compared to the contribution from $\delta\phi(t)$. The laser frequency noise is then related to the phase noise through the relation, $\delta\phi(t) = 2\pi t_d \Delta\nu(t)$. Note that this definition of phase noise should not be confused with the definition of phase fluctuations of the laser optical field defined earlier in the section.

7.4 Laser Source Requirements

An unbalanced fibre-interferometer interrogated by a laser source with a frequency noise of $\Delta\nu$ will generate a noise current on detection equivalent to a phase noise of $(2\pi nd/c)\Delta\nu$ where d is the imbalance in the interferometer. Thus, to achieve 1 μrad.Hz$^{-1/2}$ phase resolution in an interferometer with a fibre imbalance of 1 m, a frequency stability of less than 32Hz.Hz$^{-1/2}$ is required. Also, the power stability must be better than 1 in 10^6 measured in a 1 Hz bandwidth (corresponding to RIN=-120 dB Hz^{-1}). By assuming a received optical power of 10 μW (typical), taking V =0.5, r =1A.W^{-1} and using (2.38) and (5.17) the shot noise limited phase resolution, $\delta\phi_{sh}$ =0.36μrad.Hz$^{-1/2}$ and is generally lower than the noise due to laser frequency and intensity noise fluctuations. Typically, an output power of a few mW is adequate since optical amplification can be used to further boost the power level. However, in order to minimise the ASE power content of the received signal, a high output power (>10 mW) with a high optical signal-to-noise ratio (> 50dB) is desirable. The laser performance should not degrade significantly with age or increased environmental noise.

7.5 EFL Characterisation

7.5.1 Fibre laser set-up

The set-up used for characterisation of the fibre lasers is shown in fig. 7.3. The pump power from a Nortel LC92F grating stabilised diode is combined onto Corning SMF28™ fibre through a 980/1550nm WDM. This fibre is spliced to the 80 micron laser fibre. The other output of the laser is spliced onto a 1550nm dual stage isolator (>50 dB isolation) and erbium doped fibre section, which is followed by a second dual stage isolator. A bypass route for the pump power around the first isolator using two 980/1550nm WDM's is also necessary due to the high insertion loss of the isolator at 980nm. This does not negate the effect of the isolator since the rejection of 1550nm signal through the 980nm port of the WDM coupler is greater than 30dB, giving a total rejection of 60dB into the laser output[14].

[14] It is well known that back reflection into a laser cavity, with a randomly varying phase, leads to laser instability. The back reflection may arise from a connector, splice or in-line component. The tolerable level of back reflection for the DFB EFL has been investigated in [7.60]. The effect was characterised by injecting a controlled level of back reflection with random phase into the laser cavity while monitoring the rms intensity and frequency noise of the laser. Any observed increase above a certain threshold indicated a disturbance to the cw operation of the laser. It was found that the permitted level of back reflection depended on the grating strength, in the same way that the tolerable level of back reflection into a semiconductor laser increases with increasing mirror reflectivity. For a discrete mirror placed close to the laser output, the tolerable back

This configuration provides two signal outputs. One output contains the signal after being amplified through 4m of erbium doped fibre (characterised to provide 3.8 $dB.m^{-1}$ of gain) which boosted it to a few mW with 100 mW of pump power. The other output provides a few hundred μW of power.

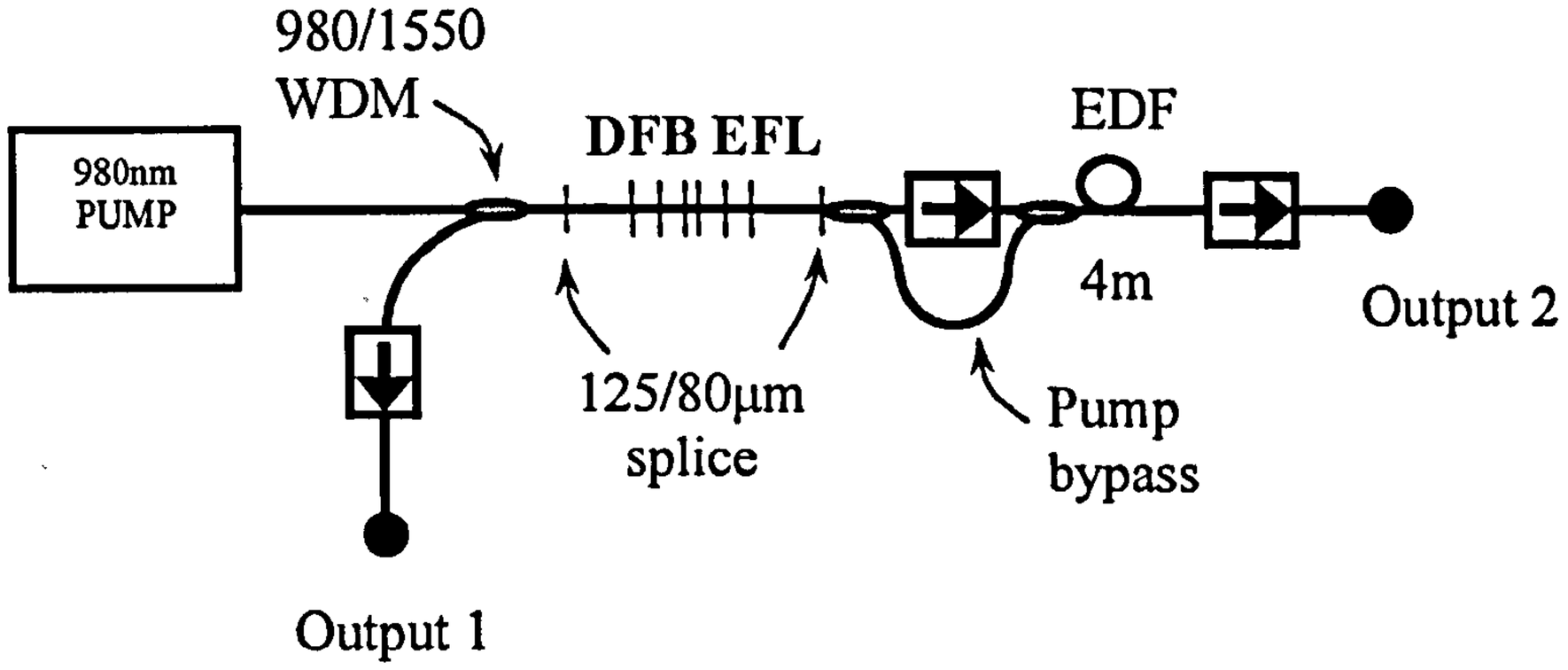

Figure 7.3: Fibre laser set-up

7.5.2 Pump source

The EFL can be pumped at any of the absorption bands characteristic of the Er^{3+} gain medium (514.5nm, 600nm, 790-840nm, 980nm, 1480nm); however, the 980nm and 1480nm pumping bands are generally used since they are free from significant excited state absorption (ESA) for Er^{3+} in a silica host glass. It is also convenient to use commercially available 980 nm or 1480 nm pump diodes developed for the erbium doped fibre amplifier. For the lasers characterised here, we have used a 980nm pump diode stabilised with an in-fibre Bragg grating that delivered approximately 100mW of power to the EFL. To obtain low noise performance from the fibre laser, a number of factors related to the pump need to be considered. Firstly, it has been shown that pump power fluctuations at high frequencies can drive the relaxation oscillation in the EFL and generate excess noise [7.32] and at low frequencies can directly modulate the EFL intensity generating excess noise [7.33]. This is often caused by noise from the current source. For example, to ensure a fibre laser RIN of less than 10^{-12} Hz^{-1}, the pump laser must also exhibit a

reflection level was found to be ~-16dB and ~-35dB for lasers with KL=8.5 and 15 respectively. Thus, we conclude that a -50dB isolator will be adequate to suppress excess noise from back reflection.

RIN of less than 10^{-12} Hz^{-1}. If the pump diode is drawing 200 mA, the current noise density must be less than 0.2 $\mu A.Hz^{-1/2}$. Secondly, non-stabilised pump diodes (980nm and 1480nm) are multi-mode (mode spacing typically a few hundred GHz) and random exchange of energy between the modes can lead to fluctuations in the EFL cavity gain due to the frequency dependent absorption of the Er^{3+} ion. This will also lead to fluctuations in the output power. This effect is stronger in the 980nm pump region due to the narrow absorption peak at 980nm compared to 1480nm. Incorporating a low reflectance in-fibre Bragg grating into the output fibre at a distance longer than the coherence length of the laser forces it to lase in a coherence collapse regime. A large number of modes are now present in the laser emission (due to the extended cavity length) which all fall within the bandwidth of the grating. Exchange of energy between modes now occurs very rapidly and is confined to a narrow bandwidth, which results in a stable output emission power [7.34].

Thirdly, fluctuations in the pump polarisation may also lead to excess intensity noise due to polarisation dependence of the grating reflectance and pump absorption. In the lasers tested, changes in the pump polarisation induced by a polarisation controller on the pump fibre, caused the EFL output power to vary less than ±1%.

Finally, another factor that may affect the laser intensity is the cut-off wavelength of the fibre laser pigtails. The EFL's tested consisted of a grating, formed in a section of (active) erbium doped fibre (typically a few cm's long), which is spliced to a (passive) fibre with a numerical aperture of 0.16 and a cut-off wavelength of 1270nm. The passive fibre is therefore multi-mode at 980nm. Hence coupling of pump power between modes in the delivery fibre may cause fluctuation in the output power of the EFL, due to the difference in the value of the overlap integral for each mode in the laser cavity. Providing the pump diode is stabilised with an external grating and is packaged with the laser in a stable environment, the impact of these noise sources will be minimised.

7.5.3 Fibre laser packaging issues

The emission frequency of the EFL is sensitive to changes in ambient pressure (i.e. acoustics) and temperature, which both contribute to changes in the cavity length and refractive index. For an uncoated fibre in air, it has been shown that the acoustically induced temperature change, caused by the adiabatic process of expansion and contraction of air, increases the EFL

sensitivity to acoustics by between 2 to 3 orders of magnitude, compared with assuming a constant temperature across the laser. When the temperature of the air surrounding the fibre is altered due to an acoustic wave, the temperature gradient set up between the surrounding air and the fibre causes heat to be transferred by forced convection to the fibre surface and by conduction though the cladding to the fibre core. Generally, the forced convection is accompanied by free convection due to temperature gradients at the air-glass interface (which may arise from heat generation by non-radiative transitions in the fibre core). It was argued in [7.35] that the magnitude of the temperature induced index change for a harmonically varying temperature field is determined primarily by pure diffusion and hence the thermal diffusion time through the cladding. Any contribution due to the convection between the surrounding air and glass was generally small, since the harmonic variation of the temperature change reduced the temperature gradients. The responsivity of a bare fibre laser in air to an acoustic signal, $|\Delta\nu/\Delta P|$, where ΔP is the pressure (125 μm outer diameter fibre) was measured to be ~600kHz.Pa^{-1} at 100 Hz and ~8kHz.Pa^{-1} at greater than 1 kHz [7.35] which is in reasonable agreement with a value of the DC responsivity of 1.6MHz.Pa^{-1} predicted by (2.32). (Compare this with values of $(\Delta\nu/\Delta P)|_T$ =536 Hz.Pa^{-1} for a hydrostatic boundary condition and –1580 Hz.Pa^{-1} for radial boundary conditions, where the subscript T denotes constant temperature, calculated using the analysis in chapter 4). The reduction in sensitivity at higher frequency is due to the low thermal diffusivity of the glass cladding (i.e. the rate at which the heat travels through the glass). We determined in chapter 4 that the diffusion time, τ_d, from the core to the cladding surface was 0.65ms for a 62.5μm cladding radius fibre and 0.26ms for a 40 μm cladding radius fibre. Thus, we would expect that the temperature contribution to the acoustic responsivity to be significantly reduced at frequencies greater than $1/\tau_d$ or ~1.5 kHz for 67.5μm fibre and ~3.8kHz for 40μm fibre. It thus follows that to reduce the temperature induced acoustic responsivity of the EFL, a layer of low thermal diffusivity material should be applied to the fibre (which effectively acts as a low-pass filter to heat flux). For the measurements described below, the lasers were supplied with a single acrylate coating. In the frequency noise reduction experiments described later, the lasers were coated with a layer of low thermal diffusivity epoxy resin.

7.5.4 Characteristics of the free-running laser

Six lasers were tested for slope efficiency, relative intensity noise, frequency noise and modulation characteristics. These lasers were supplied by Ionas, Denmark and the measured characteristics of the lasers are summarised in table 7.1. The precise characteristics of the grating and doped fibre type are not known, although all the lasers tested are based on a similar grating design, fibre type and fabrication technique.

Slope efficiency

The laser slope efficiency can be defined by, $k_{slope} = \Delta P_{FL} / \Delta P_P \big|_{f \to 0}$, where the subscripts FL and P refer to the fibre laser and pump respectively. This was measured with the set-up shown in fig. 7.3 and using a power meter to measure the power at output 1 as a function of the pump current. The pump power vs. pump current was previously characterised and appropriate correction was made for the WDM coupler excess loss and splice loss. The slope efficiency of IFL1221 is shown in fig. 7.4(i); the slope efficiency given in table 7.1 is calculated from points in the linear region of the laser power/pump power slope in fig. 7.4(i). The lasers tested exhibited a slope efficiency of between 1 and 3 $\mu W.mW^{-1}$ and produced between 100 μW and 300 μW of power when pumped with 100 mW at 980nm. When incorporated into a master-oscillator power-amplifier configuration the slope efficiency was increased up to 170 $\mu W.mW^{-1}$, measured at output 2 in fig. 7.1.

Table 7.1: Erbium doped fibre laser characteristics

Laser serial no.	Wavelength nm	Slope efficiency $\mu W.mW^{-1}$	Pump power mW	f_{RO} kHz ±1%	RIN peak dB Hz^{-1} ±2dB
IFL01WiEB-AD(MOPA)	1550.08	170	70	152	-65
IFL1220	1540.51	1.45	--	--	--
IFL1221	1541.17	1.80	105	314	-83
IFL1221 (MOPA)	1541.17	47.5	105	314	-83
IFL1222	1543.73	--	105	285	-76
IFL1223	1545.23	1.93	100	300	-78
IFL1224	1550.08	2.26	100	264	-71

Relative intensity noise (RIN)

When a laser has reached steady-state operation, it will exhibit periodic fluctuations in its output power due to the exchange of energy between the upper lasing level and the signal photon flux. This is then followed by a corresponding exchange from the pump photon flux that repopulates the upper lasing level. The frequency at which this occurs is known as the relaxation oscillation frequency, f_{RO}. The frequency of the relaxation oscillation in the DFB EFL will depend on the coupling coefficient of the grating, the Er^{3+} concentration and the pump power [cf. chapter 8]. The spectral shape of the intensity fluctuations is that of an underdamped harmonic oscillator. We can gain a basic qualitative understanding of the dependence of f_{RO} on these parameters by considering the physical mechanisms involved. We assume that the pump depletion is small, which is generally the case in the EFL. As the coupling coefficient increases, the photon lifetime increases (since $l_c \simeq 1/\kappa$) and hence the gain depletion increases resulting in a decrease in the relaxation frequency. As the erbium ion concentration increases, the available gain increases and the gain depletion is reduced and hence f_{RO} increases. Finally, as the pump power increases, the rate at which the upper laser level is repopulated increases and hence f_{RO} increases.

The relative intensity noise (RIN) spectrum for laser IFL1221 is shown in fig. 7.4(ii) and the dependence of f_{RO} on the pump power is shown in fig. 7.4(i). The intensity noise spectrum was measured by taking the Fourier Transform of the current from a photodiode placed at output 1 in fig. 7.3 using an HP89410A spectrum analyser. The mean power is also measured and (7.7) is used to calculate the RIN. The plots, shown in fig. 7.4(i) and (ii), are representative for all the lasers measured. The relaxation oscillation frequency and relative amplitude were measured for all the lasers at the specified pump power and are given in table 7.1. The variation in f_{RO} and k_{slope} for the lasers tested is thought to be due to differences in the coupling coefficient of the grating and differences in the delivered pump power due to splice losses between the active and passive fibre. We shall return to the underlying mechanisms giving rise to the observed levels of intensity noise in chapter 8.

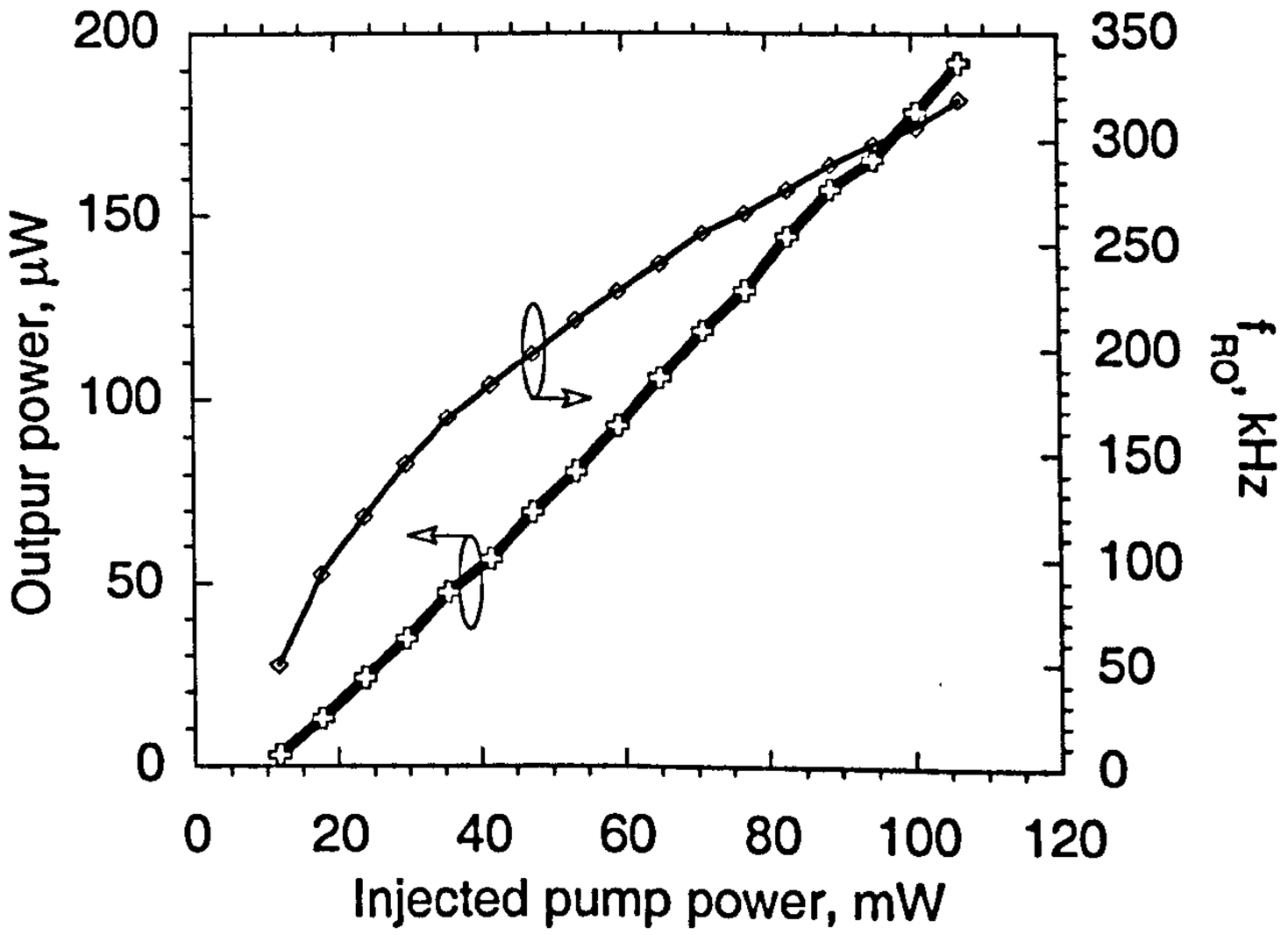

Figure 7.4: (i) Dependence of output power and relaxation oscillation frequency on injected pump power

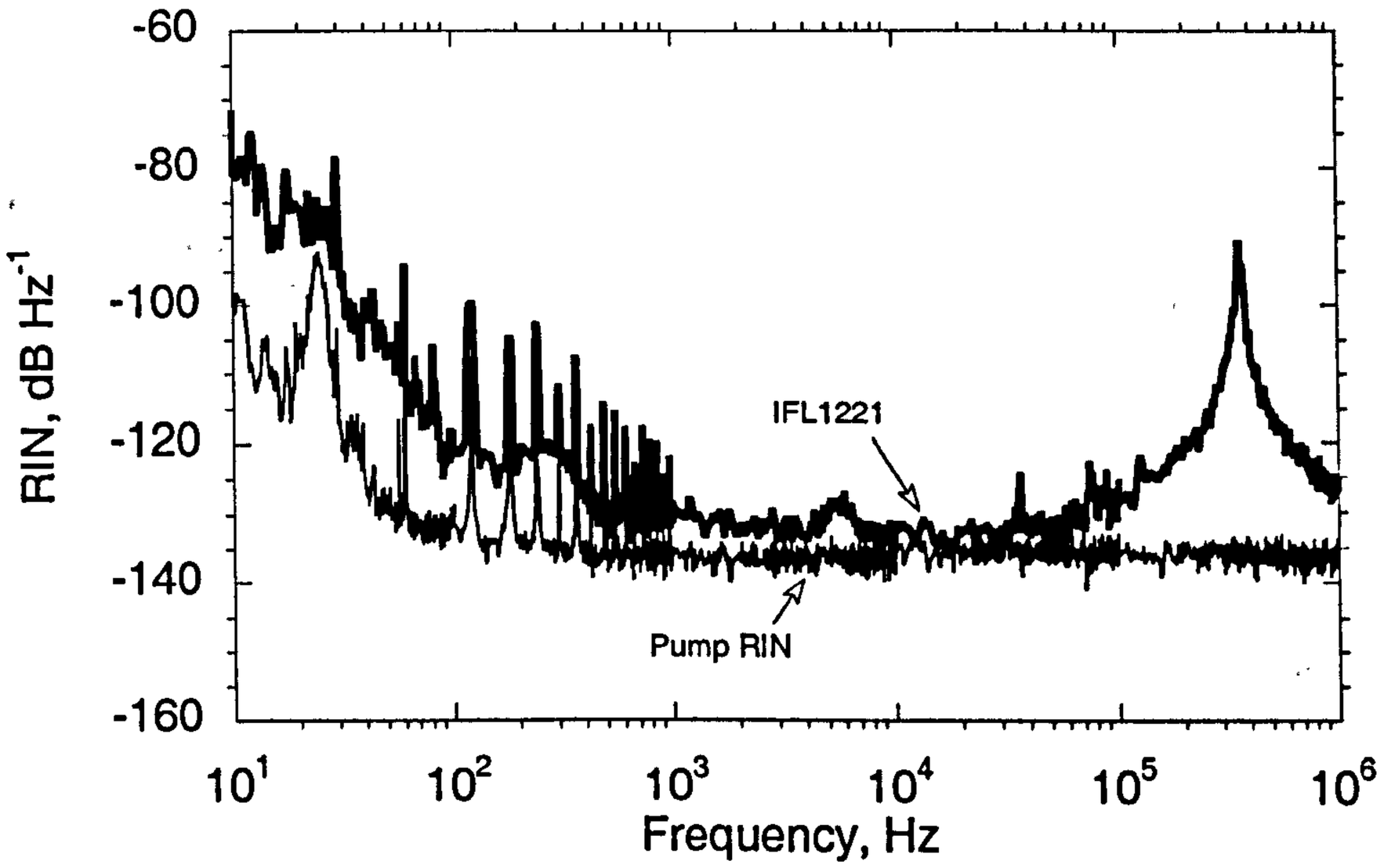

Figure 7.4: (ii) Low-frequency RIN spectrum of EFL

Frequency/phase noise

The frequency noise of the EFL was measured using a Mach-Zehnder interferometer with a 100m fibre imbalance. A high gain-bandwidth feedback loop (described in section 2.9.1) was used to stabilise the interferometer for measurements of frequency noise between 1 Hz and 10 kHz and a low gain-bandwidth configuration was used to measure between 10 kHz and 1 MHz. The frequency noise of IFL1221 is shown in fig. 7.5. The data has been corrected for variations in the frequency response of the feedback loop and detector. Also included for comparison, in fig. 7.5, are the frequency noise spectra for two other lasers commonly used as sources: (i) the semiconductor DFB laser (with and without phase noise reduction (PNR)) [7.5] and (ii) the diode pumped Nd:YAG laser [7.6].

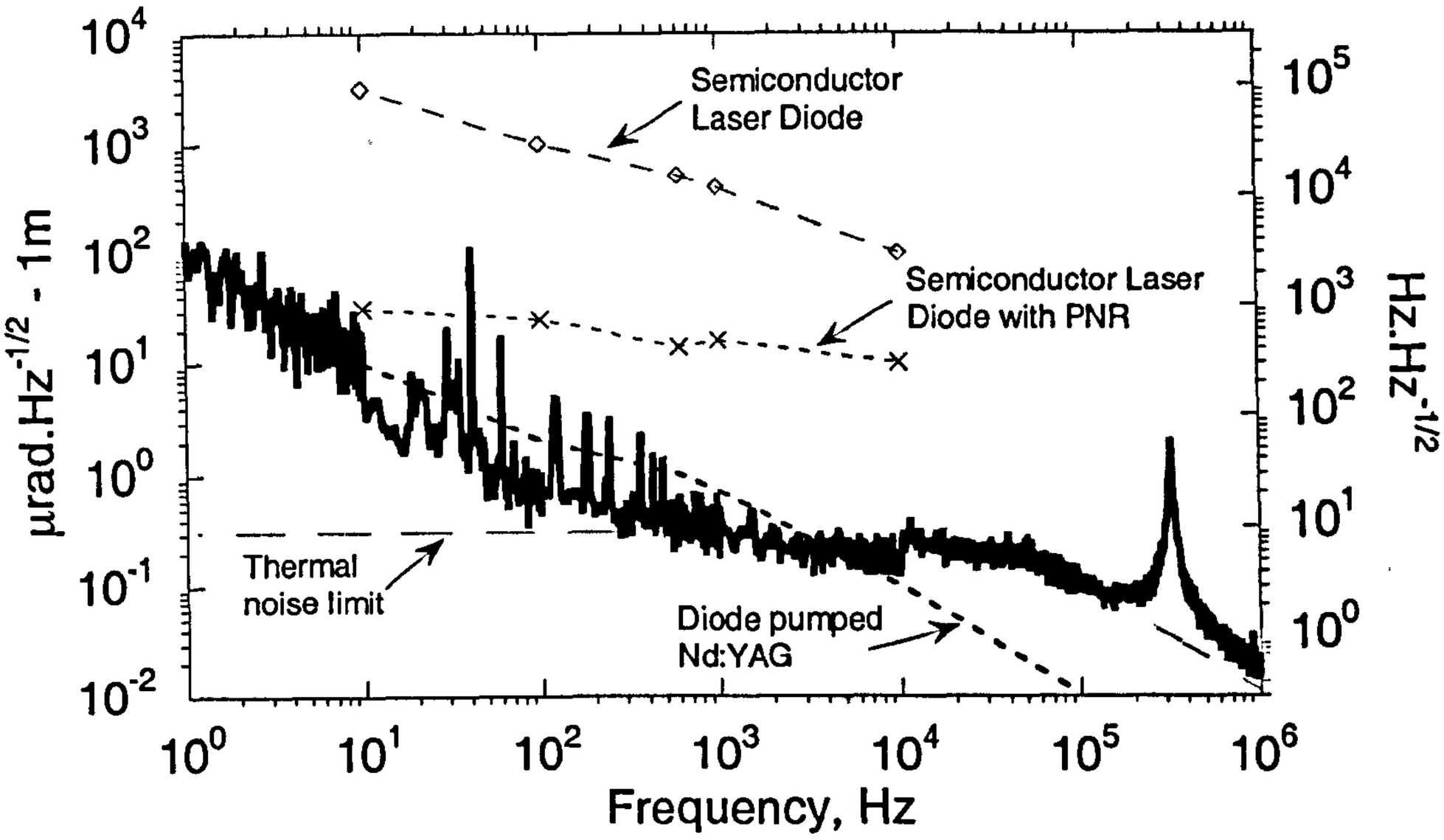

Figure 7.5: Phase/frequency noise of the EFL

The left hand axis is the phase noise, in units of $\mu rad.Hz^{-1/2}$, generated in an interferometer with a 1m fibre path imbalance and the right hand axis is the frequency noise in units of $Hz.Hz^{-1/2}$. During the measurements, the lasers and measurement interferometer were placed in an acoustically isolated box; however, some acoustic pick-up was still observed around 30 Hz (likely to be due to noise from cooling fans). For the high frequency measurement, a balanced detector was not used; as a result some of the contribution to the frequency noise around the relaxation oscillation is due directly to intensity noise. The frequency noise spectrum of this laser comprises contributions from four different mechanisms:

(i) At frequencies up to 1 kHz, the frequency noise exhibits an f^{-n} type spectrum, with a slope that falls off at ~20dB/decade. The origin of this noise is not well understood, however a similar shaped noise spectrum is found in diode pumped Nd:YAG lasers [7.39].

(ii) Between 1 kHz and f_{RO}, the frequency noise is likely to be caused by fluctuations in the refractive index of the cavity due to instantaneous changes in the temperature and density of the medium. Other groups have arrived at the same conclusion [7.33, 7.61]. This noise source was first investigated in [7.40] for bulk materials where it was shown that the instantaneous temperature and density of a body in thermal equilibrium with its surrounding will undergo statistical fluctuations which will modulate the refractive index of the medium. This will

manifest itself as a phase noise imposed on an optical signal propagating through the medium. In general, it was shown that for frequencies up to ~1 MHz the dominant contribution to the refractive index modulation was due to thermally induced refractive index fluctuations. For frequencies greater than 1 MHz, the density fluctuation induced refractive index fluctuation contribution (or equivalently the direct acoustic phonon interaction) was dominant and exhibited a spectral density that increased by approximately 20 dB/decade up to a frequency of ~1 GHz. Expressions for the spectral density of the phase fluctuations were derived for an unbounded bulk medium. The case of a bounded medium with insulating boundary conditions and including the effect of the mode-field profile was investigated in [7.42]. This yielded an expression for the spectral density of phase fluctuations (considering only the contribution from thermally induced index fluctuations and thermally induced strain fluctuations), which can be applied to the fibre laser and expressed in terms of frequency fluctuations,

$$\nu_{rms}^2(f) = \left(\frac{1}{n} \frac{\partial n}{\partial T}\bigg|_{\rho} + \alpha \right)^2 \nu_0^2 \Delta T^2(f) \tag{7.14}$$

where α is the thermal expansion coefficient of the fibre, $\nu_0 = c/\lambda_0$, and the temperature fluctuation term is given by,[15]

$$\Delta T^2(f) = \frac{k_B T^2}{2\pi l_c \kappa_c} \ln \left[\frac{\left(\left(\frac{2}{w} \right)^2 + \left(\frac{2\pi f}{c/n} \right)^2 \right)^2 + \left(\frac{2\pi f}{\xi} \right)^2}{\left(\left(\frac{2.405}{r_1} \right)^2 + \left(\frac{2\pi f}{c/n} \right)^2 \right)^2 + \left(\frac{2\pi f}{\xi} \right)^2} \right] \tag{7.15}$$

where k_B is Boltzmann's constant, T is the absolute temperature, l_c is the effective cavity length, κ_c is the fibre thermal conductivity, ξ is the fibre thermal diffusivity, w is the mode

[15] We note here that the derivation of (7.15) has not been published and its accuracy has only been verified experimentally in [7.42].

field radius, c is the velocity of light in a vacuum, n is the effective refractive index of the fibre, and r_1 is the radius of the cladding. For our calculations we use T =300K, l_c=12mm, κ_c=1.37W.(m.K)$^{-1}$, ξ=0.82×10^{-6}m^{2}s^{-1}, w=2.3μm, r_1=40μm, n=1.465, λ_0=1550nm and the thermo-optic coefficient, $\left(\frac{1}{n}\frac{\partial n}{\partial T}\bigg|_\rho + \alpha\right)$=5.2×10^{-6}K^{-1} where we have taken the values of the thermal conductivity and diffusivity from [7.40] and the thermo-optic coefficient from [7.33]. (7.14) has been experimentally verified, using measurements from an unbalanced fibre interferometer, for frequencies between 1 kHz and 100 kHz [7.42]. This yielded noise spectrums that were the same spectral shape and ~1-3dB higher than that predicted by the theory presented in [7.41]. The predicted thermal noise spectrum is shown in fig. 7.5. It can be seen that good agreement is obtained between the measured and predicted frequency noise over the frequency range 1 kHz to 100 kHz, if we assume the above values to be accurate. This result would imply that the laser frequency stability is limited by thermally induced refractive index fluctuations over this frequency range. It is interesting to note the $l_c^{-1/2}$ dependence of the thermally induced frequency noise. It thus follows that a longer cavity length yields a lower frequency noise. This implies a potential advantage for the DBR laser where the cavity length is typically 50mm compared with 5 to 20mm for the DFB design. We would therefore expect the DBR laser to exhibit a thermal noise limited frequency noise of up to a factor of ~3 lower than the DFB laser.

(iii) Around f_{RO}, strong coupling between the intensity fluctuations and the frequency noise occurs, which causes a large increase in the frequency noise. This is thought to be due to the gain modulation induced refractive index fluctuations [7.33] through the Kramers-Krönig relation. This contribution is removed when relaxation oscillation suppression is implemented, as described in section 7.5.

(iv) Above f_{RO} the frequency noise may approach the Schawlow-Townes limit (i.e. the spontaneous emission frequency noise limit). The Schawlow-Townes noise limited linewidth, $\Delta\nu_{S-T}$, can be estimated from [7.64],

$$\Delta\nu_{S-T} = \frac{hc}{\lambda}\frac{M^2}{2\pi\tau_n^2 P} \tag{7.16}$$

where we assume a unity inversion, h is Planck's constant, c is the light velocity in a vacuum, λ is the wavelength (1542.17 nm), M is the effective mirror transmittance (4×10^{-4}), $\tau_n = nL/c$ is the cavity photon round-trip time, L is the effective cavity length (12 mm) and P is the output power (200 μW). Using the estimated values shown in brackets yields $\Delta\nu_{S-T}$ =5 mHz, which corresponds to a frequency noise spectral density of ~0.13 Hz.Hz$^{-1/2}$. Although these parameters are estimated, increasing T by a factor of 10 yields a frequency noise spectral density of ~0.94 Hz.Hz$^{-1/2}$, which is still below our observed noise floor. As mentioned above, noise contributions from direct interaction with acoustic phonons may prevent this limit from being reached. Currently, no experimental evidence is available to show this.

It is instructive to compare the fundamental linewidth of the semiconductor DFB and fibre DFB lasers. It has been shown that the linewidth of the semiconductor DFB is limited by fluctuations in the refractive index of the laser cavity, arising from instantaneous variations in the electron density across the active region of the junction due to spontaneous emission; an effect first explained by Henry [7.43]. This led to a linewidth enhancement factor (known as the Henry factor), which broadens the linewidth (over that predicted by spontaneous emission only) to ~1 MHz. In the EFL this effect is small; however, the linewidth is now broadened by fluctuations in the refractive index due to thermal effects. Despite this, the linewidth of most EFL's is of the order of a few kHz.

We have shown that frequency noise of the EFL over the frequency range of interest for the interferometric sensor application is dependent on the f^{-n} contribution below ~1 kHz and a contribution due to the thermal diffusion of heat across the mode field in the core at frequencies greater than 1 kHz and less than f_{RO}. Although the boundary conditions at the fibre cladding-air interface affect the shape of the thermal noise spectrum, this noise is intrinsic to the fibre and cannot be significantly reduced by design of the EFL. The noise spectrum shown in fig. 7.5 is thus thought to represent the fundamental noise limit in the EFL. However, since the noise sources are not quantum mechanical in origin, we shall show in sec. 7.8 how the

frequency noise can be reduced to below the thermal noise limit by locking the laser emission to an interferometer using cavity strain to impose the feedback signal.

7.6 Suppression of the Intensity Noise Using Electronic Feedback to the Pump Diode Current

7.6.1 Intensity noise suppression techniques

The DFB fibre laser exhibits a relaxation oscillation peak typically around a few hundred kiloHertz, which must be suppressed if the laser is used to interrogate high performance fibre interferometers. Two techniques exist for the suppression of intensity noise, those based on injection locking of the laser and those based on use of an electro-optic feedback loop. These can be implemented separately or simultaneously [7.49,7.51]. The injection locking technique is a well-understood method, which involves injecting the light from a low power master laser, with the required spectral characteristics, into the cavity of the slave laser. The spectral properties of the master laser emission will take on many of the properties of the slave laser, including to some degree linewidth and intensity characteristics [7.44-7.47]. The electro-optic feedback loop involves detecting a small portion of the laser field, applying appropriate gain and phase-shift and using the resulting signal to modulate the intensity of the pump. This technique has been demonstrated with several lasers, for example: the diode pumped non-planar ring laser [7.48-7.50], the solid state Er^{3+}:Yb^{3+} glass laser [7.51-52,7.7], the Er^{3+} doped DBR laser [7.19] and the Er^{3+} doped DFB laser [7.33]. The intensity modulation response of the Nd:YAG ring laser and the Er^{3+} doped lasers are very similar and resemble that of an underdamped harmonic oscillator. The feedback circuit design for both of these lasers is therefore very similar. In the case of the Er^{3+}:Yb^{3+} laser, the presence of the codopant introduces a single pole roll-off in the modulation response at around 1 kHz, due to the energy exchange process between the Yb^{3+} and the Er^{3+} ions. The response of the feedback loop must therefore be modified to account for this.

In this section we discuss the design of the electronic feedback technique for the Er^{3+} doped DFB laser. We choose this technique over the injection locking technique due to its simplicity and compatibility with the frequency modulation techniques discussed later on. The principle of this technique involves detecting a portion of the laser emission field, shifting its phase by 180^0 and using this signal to modulate the pump intensity. The design of the feedback loop is complicated by the fact that the phase response of the laser power modulation undergoes a

180^0 phase-shift at the relaxation oscillation. The design aim is therefore to ensure that the phase lag between the unity gain points of the open loop transfer function does not exceed 360^0, in order to ensure loop stability. We test this criterion by the use of Bode and Nyquist plots, as described in [7.54]. The basic component of the feedback loop is a proportional-integral-derivative (PID) controller, which has been used in previous reported examples [7.47, 7.19, 7.33]. It will be shown that the main challenge is in optimising the modulation response of the pump diode. Many commercially available low noise current sources incorporating modulation inputs do not provide the required bandwidth for this type of feedback loop. For this reason, we used a conventional power supply and injected the modulation signal at the output of the power supply. However, this requires incorporating series inductance in order to increase the input impedance of the low impedance power supply which itself affects the modulation response of the pump diode and must be compensated for.

We shall show in chapter 8, that the primary mechanisms giving rise to intensity noise are pump power fluctuations driving the relaxation oscillation and cavity loss modulation. However, the stochastic variation in the photon flux of the laser emission gives rise to shot noise when the laser emission is detected. The quantum nature of this noise results in a fundamental limit on the suppression achievable in an electro-optic feedback loop system. It can be shown that the maximum level of suppression achievable, in the absence of saturable absorber losses, is 3 dB above the quantum noise generated in the feedback loop photodiode [7.44]. Our primary aim here is to achieve suppression of the RIN to around –120 $dB.Hz^{-1}$, which is typically required for high performance interferometric sensors.

7.6.2 Experimental set-up and circuit design

The experimental set-up for the RIN suppression circuit is shown in fig. 7.6. The laser is pumped with a 980 nm grating stabilised laser diode, which delivers approximately 100 mW of power to the fibre laser. The pump power exiting the fibre laser then pumps an Er^{3+} amplifying section, which amplifies the laser power to a few mW. The output of the power amplifier is split with a directional coupler. 10% is delivered to the feedback photodiode and the remainder is detected on the out-of-loop detector used to make the RIN measurements. The detector in the feedback loop is a TTI (Model TIA-500) InGaAs photodiode with an integrated transimpedance amplifier ($R_L = 14 \times 10^3 \Omega$).

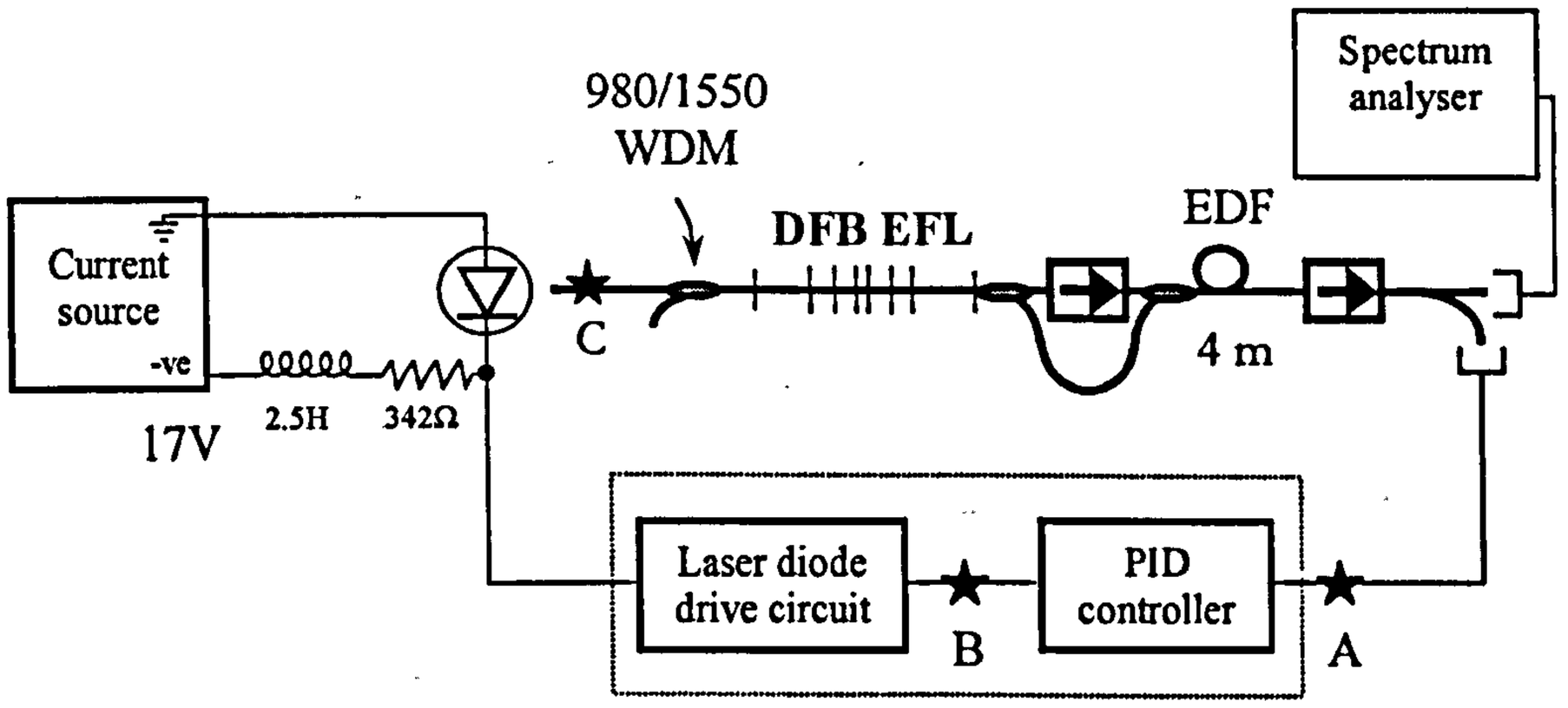

Appendix 2

Figure 7.6: Experimental set-up for RIN reduction

A linear system block diagram of the feedback loop is shown in fig. 7.7. We can separate each component of the feedback loop and characterise their amplitude and phase response using the complex transfer functions, $\widetilde{H}(f)$ and $\widetilde{G}(f)$. Thus, if $\widetilde{H}(f)$ represents the linear product of the complex transfer functions of the current source modulation, pump laser, EFL and photodiode such that $\widetilde{H}(f)=\widetilde{H}1(f)\cdot\widetilde{H}2_p(f)\cdot\widetilde{H}3_p(f)\cdot\widetilde{H}4(f)$ and $\widetilde{G}(f)$ is the complex transfer function of the PID controller, then $\widetilde{H}(f)\cdot\widetilde{G}(f)$ is the open loop transfer function. The subscript P denotes that the transfer function is in terms of optical power. The feedback circuit must therefore be designed such that to ensure stability [7.53],

$$\widetilde{H}(f)\cdot\widetilde{G}(f)<-1 \tag{7.17}$$

It thus follows that the quantity $180-\angle\widetilde{H}(f)\cdot\widetilde{G}(f)$ is the phase margin.

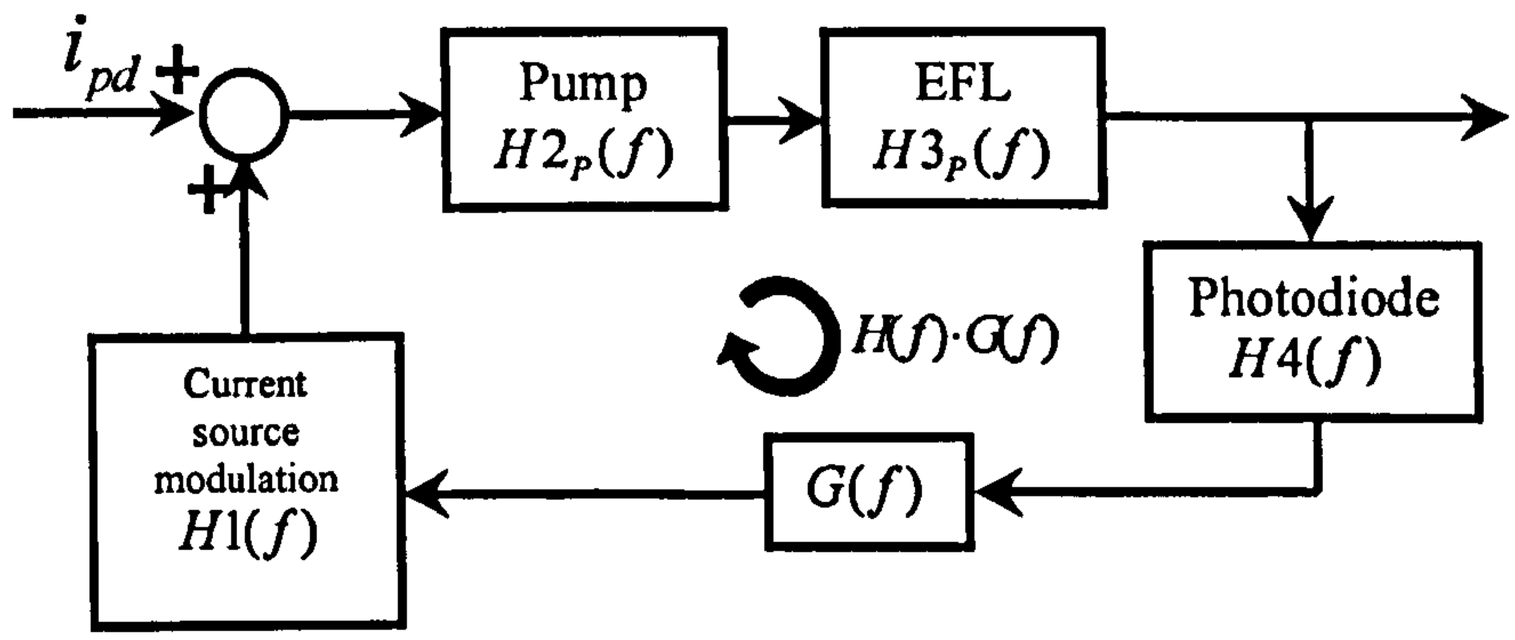

Figure 7.7: Linear system block diagram for EFL RIN reduction

The control electronics is based on the Analog Electronics AD8047 voltage feedback amplifier, chosen for its high bandwidth, and is shown in Appendix 2. The PID controller comprises separate proportional, integral and derivative amplifiers, which are summed together to form the controller signal. This is then followed by three amplifier stages, which are used to add some control to the phase response of the modulation signal applied to the laser diode. Without this control, shunt capacitance associated with the power supply connection caused a significant lag in the phase of the modulation response of the laser diode at frequencies above 100 kHz. Finally, a coupling capacitor (22 μF) is added to AC couple the modulation. This ensures that the dc laser power is not affected by the feedback loop. We can determine the shot noise limited RIN from,

$$RIN_{sh} = \left(\frac{2h\nu\Delta f}{P}\right)^2 \tag{7.18}$$

The power detected on the feedback photodiode was 600 μW, thus the quantum limited RIN is about –149 dB.Hz^{-1}. The modulation response, $\widetilde{H}3_p(f)$, of the EFL is shown in fig. 7.8.

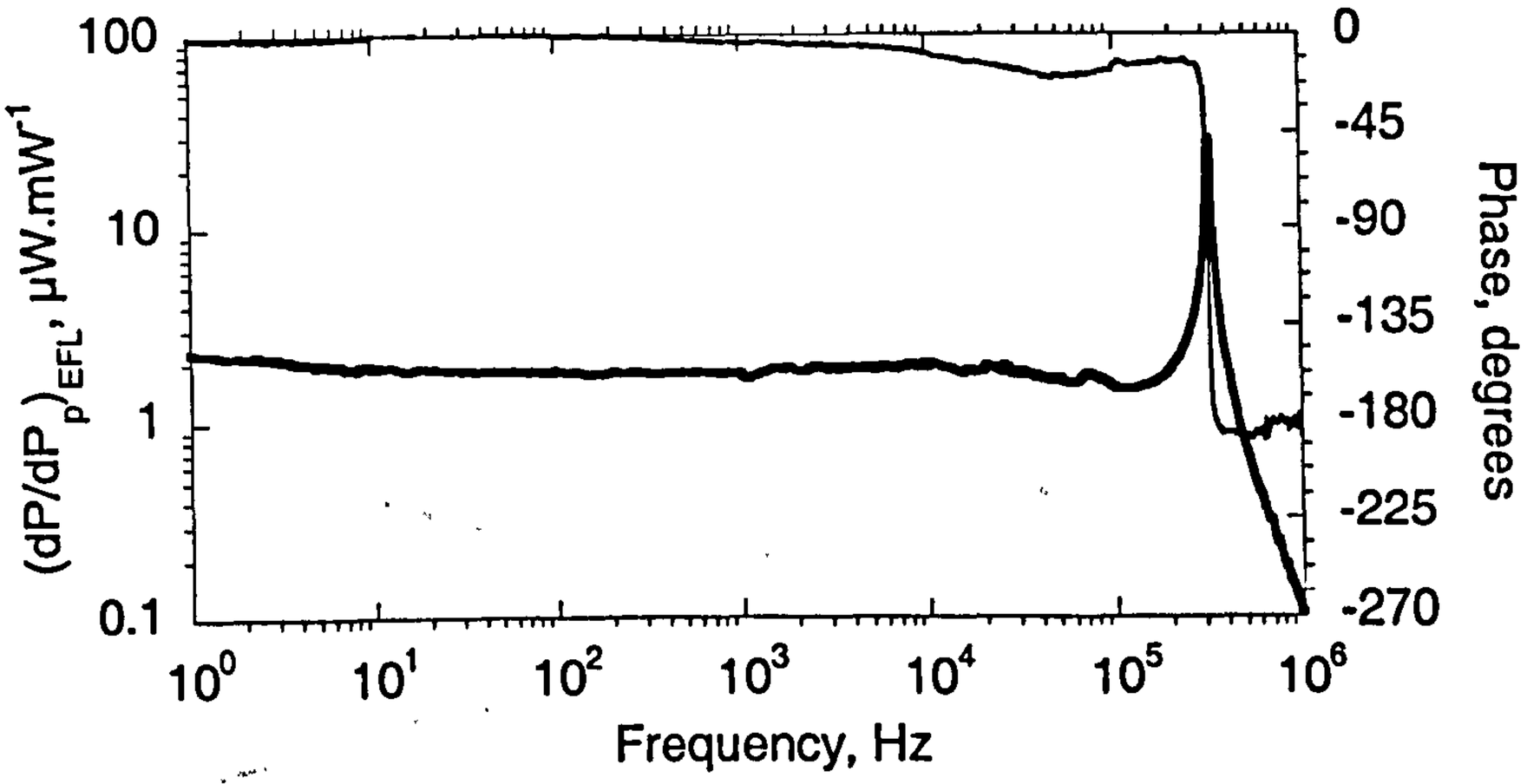

Figure 7.8: Intensity modulation response, $\widetilde{H}3_p(f)$, of the EFL

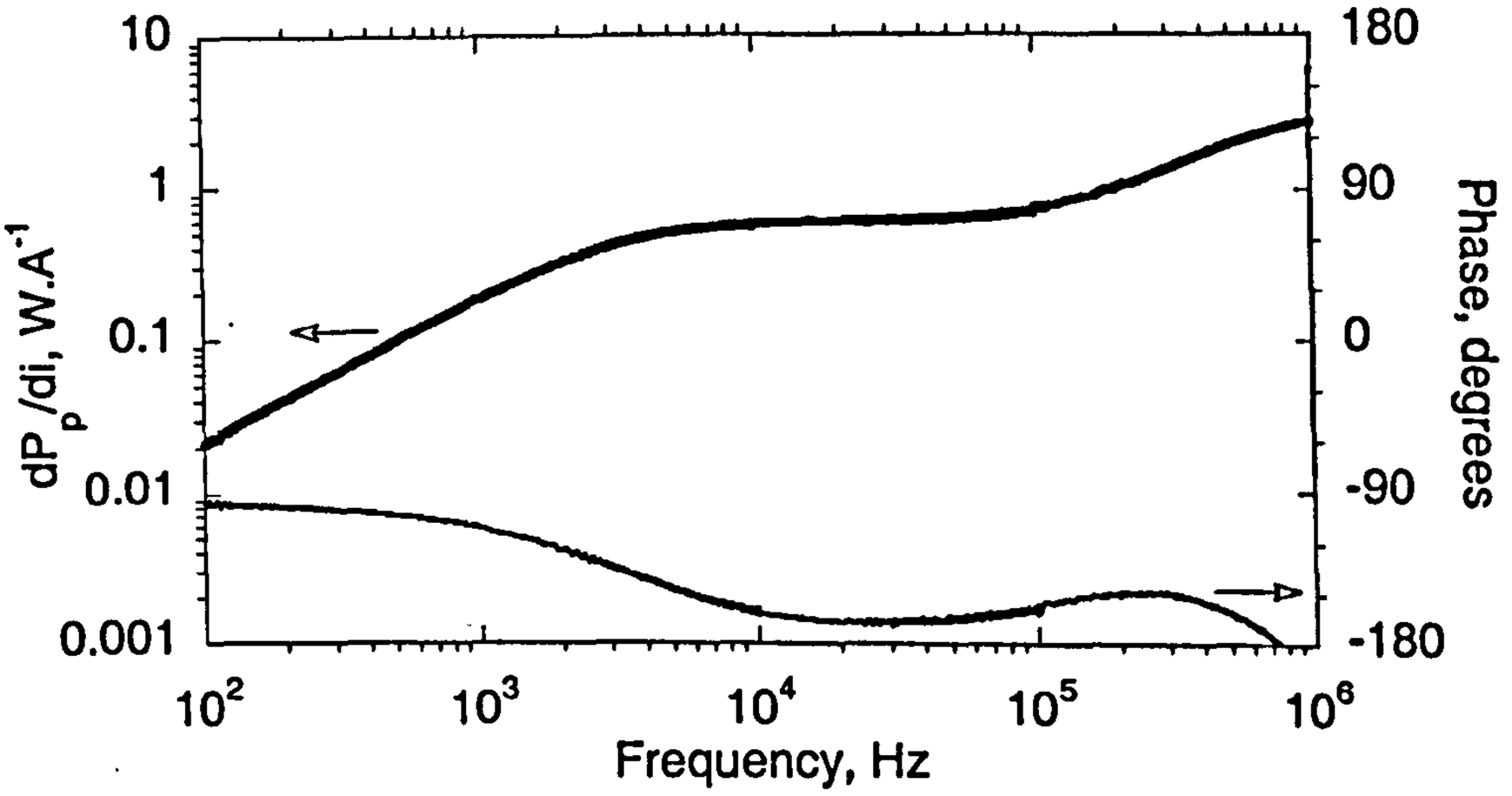

Figure 7.9: Pump modulation response, $\widetilde{H}1(f)\cdot\widetilde{H}2_p(f)$

The relaxation oscillation occurs at 310 kHz, at which point a 180^0 shift is observed in the phase response, as expected. The corresponding modulation response of the laser diode and drive electronics, $\widetilde{H}1(f)\cdot\widetilde{H}2_p(f)$, measured from point B round to C in fig. 7.6, is shown in fig. 7.9. A lag in the phase of the modulation is observed at frequencies above 100 kHz. This has been partially compensated for by incorporation of a differentiating stage in the drive electronics to provide some phase advance. As a result, the amplitude of the modulation is seen to increase above this frequency. The loop was then closed and the gain and phase were adjusted until maximum suppression of the relaxation oscillation was achieved. The Bode plot

of the open loop transfer function, measured from point A back to point A, is shown in fig. 7.10.

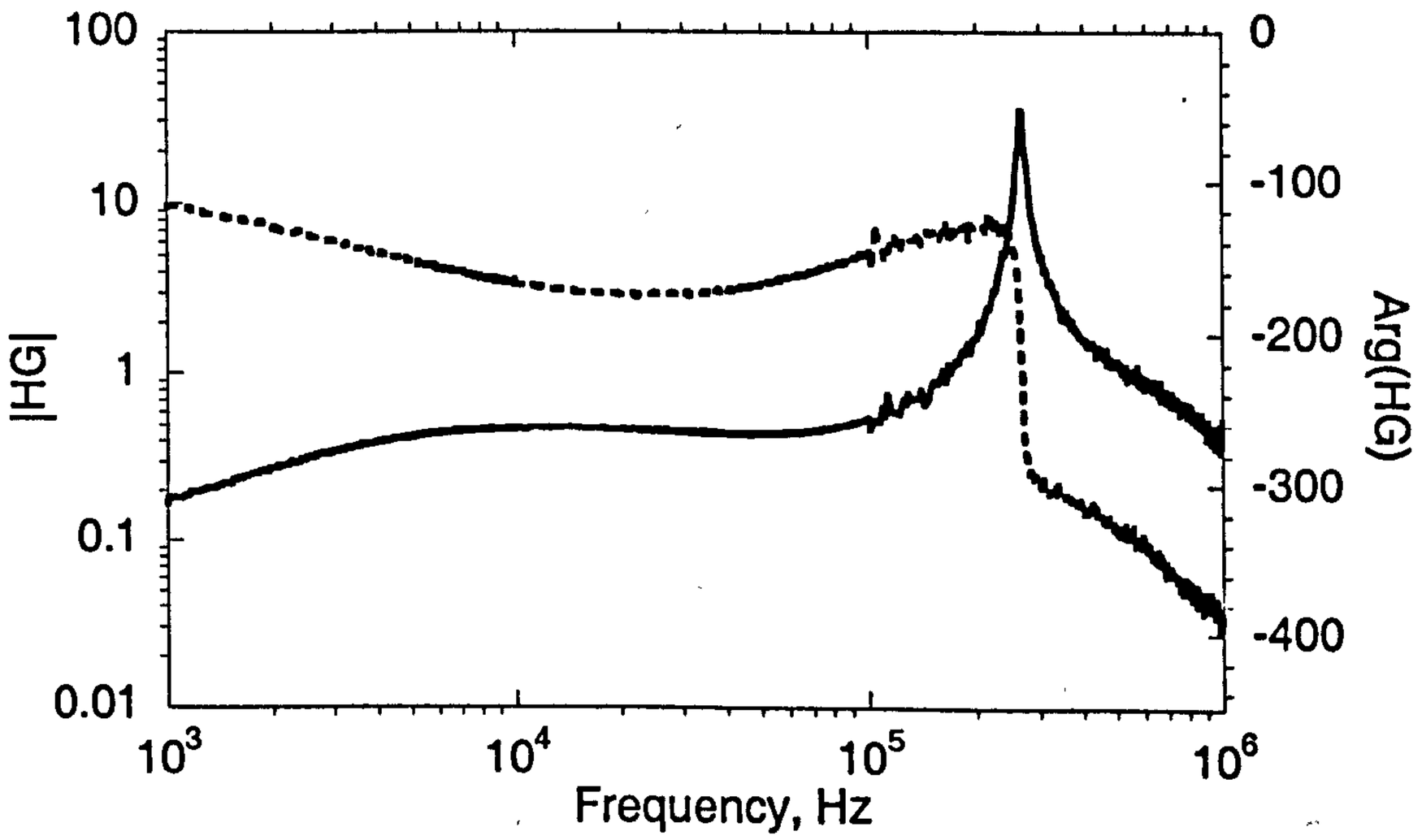

Figure 7.10: Bode plot of loop transfer function

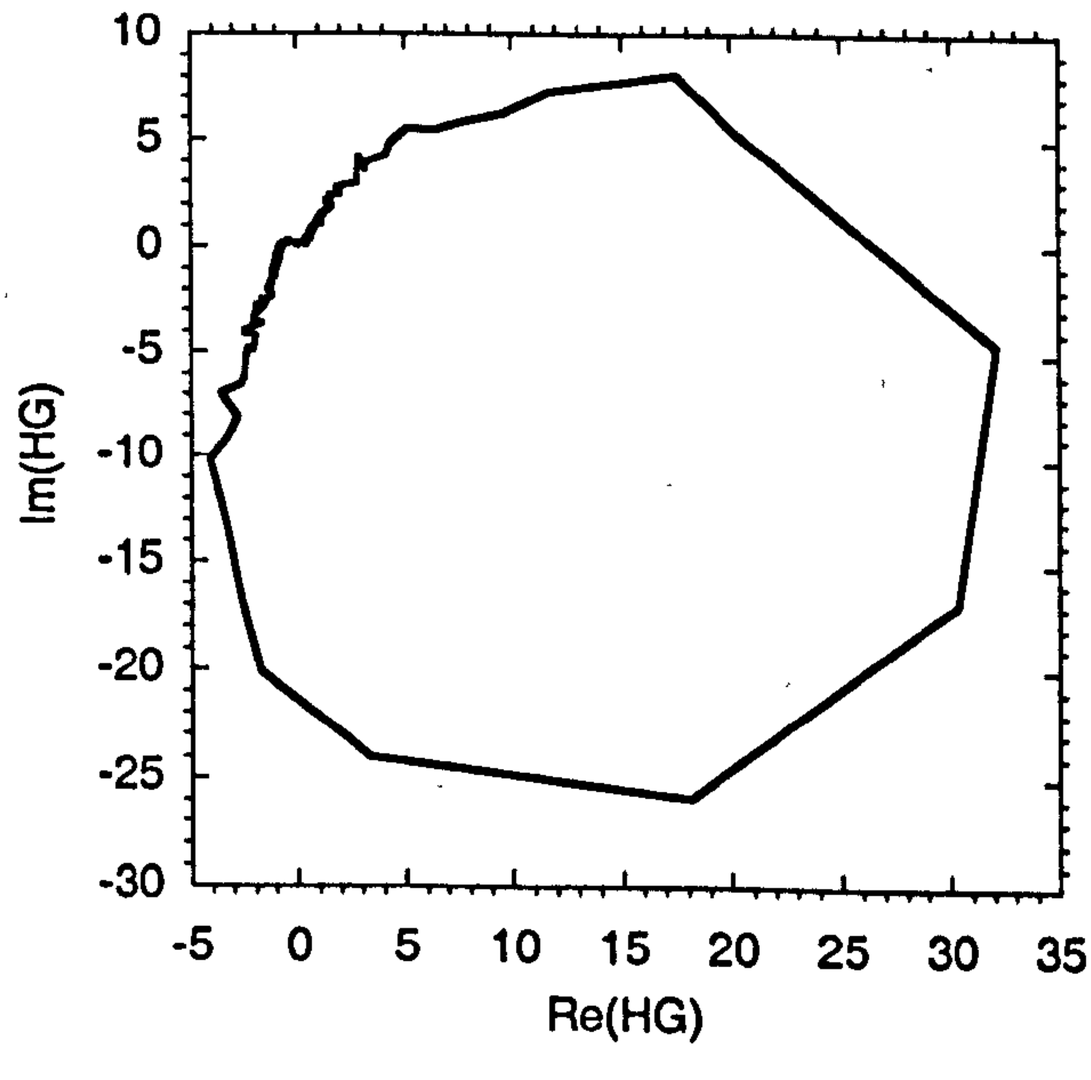

Figure 7.11: (a) Nyquist plot of loop transfer function

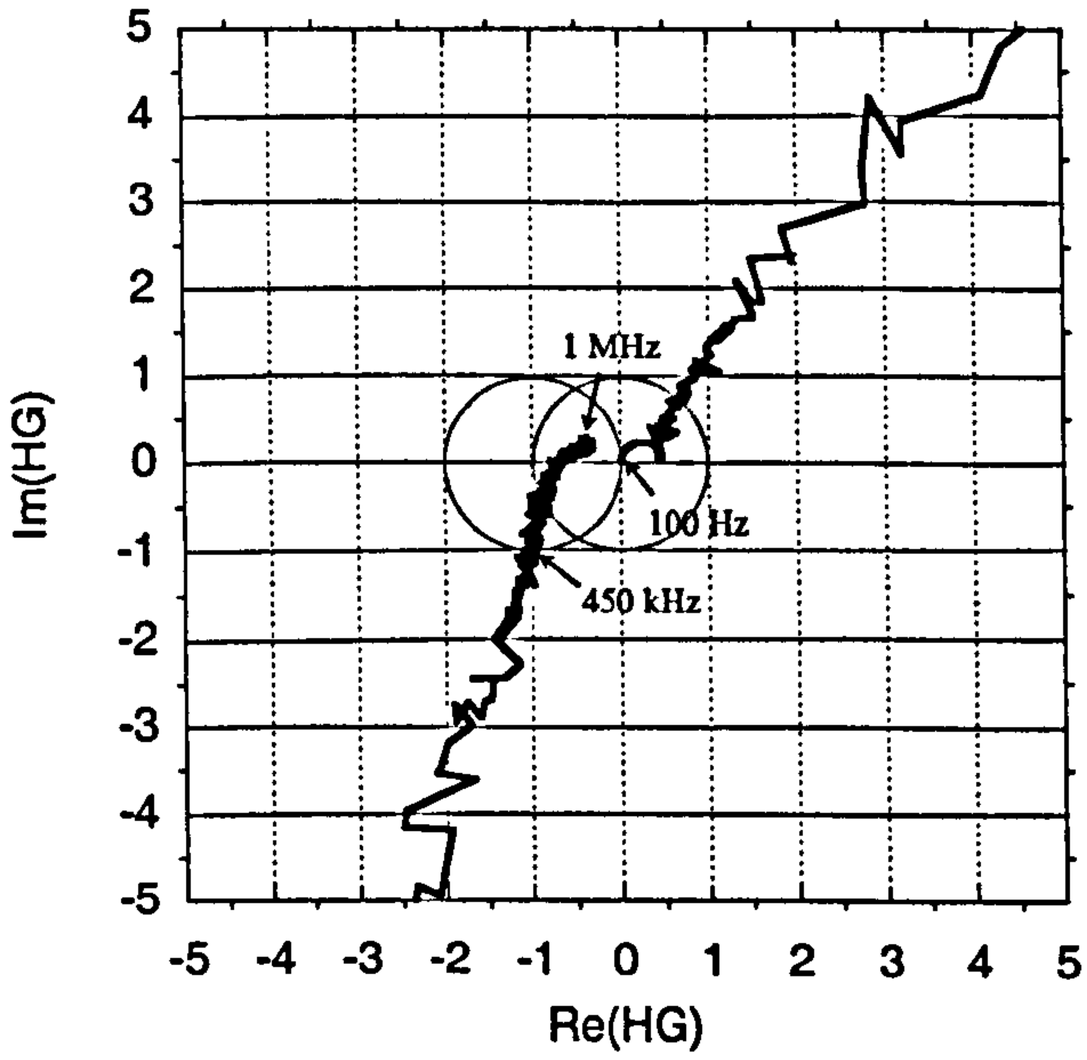

Figure 7.11(cont): (b) Nyquist plot of loop transfer function showing instability point (-1,0)

At the relaxation oscillation, the loop gain is approximately 32 dB and the unity gain points occur at 150 kHz and 550 kHz. The stability of the feedback loop is best visualised using a Nyquist plot, which shows the real vs. the imaginary parts of the complex open loop transfer function. This is shown in fig. 7.11(a) where we have followed the convention of adding a 180^0 phase-shift to $\widetilde{H}(f)\cdot\widetilde{G}(f)$, such that the instability point is at (-1,0). Stability is ensured if the instability point is not encompassed by the plot. The radial distance between the origin and a point on the plot is the open loop gain at that frequency. Thus, the extreme point of the plot from the origin corresponds to the relaxation oscillation frequency. Fig. 7.11(b) is an enlargement of the Nyquist plot clearly showing the instability point. The instability point falls outside the plot, thus inferring stability. Any point falling inside the unit radius circle centred on the instability point will experience an increase in noise at that frequency. Also, any point falling inside the unit radius circle centred on the origin corresponds to less than unity gain at that frequency. The level of suppression is calculated from the open loop transfer function using [7.54],

$$S(f)=\frac{1}{1+\widetilde{H}(f)\widetilde{G}(f)} \tag{7.19}$$

This is plotted for our feedback loop in fig. 7.12 and the measured RIN of the EFL with and without the loop closed is shown in fig. 7.13.

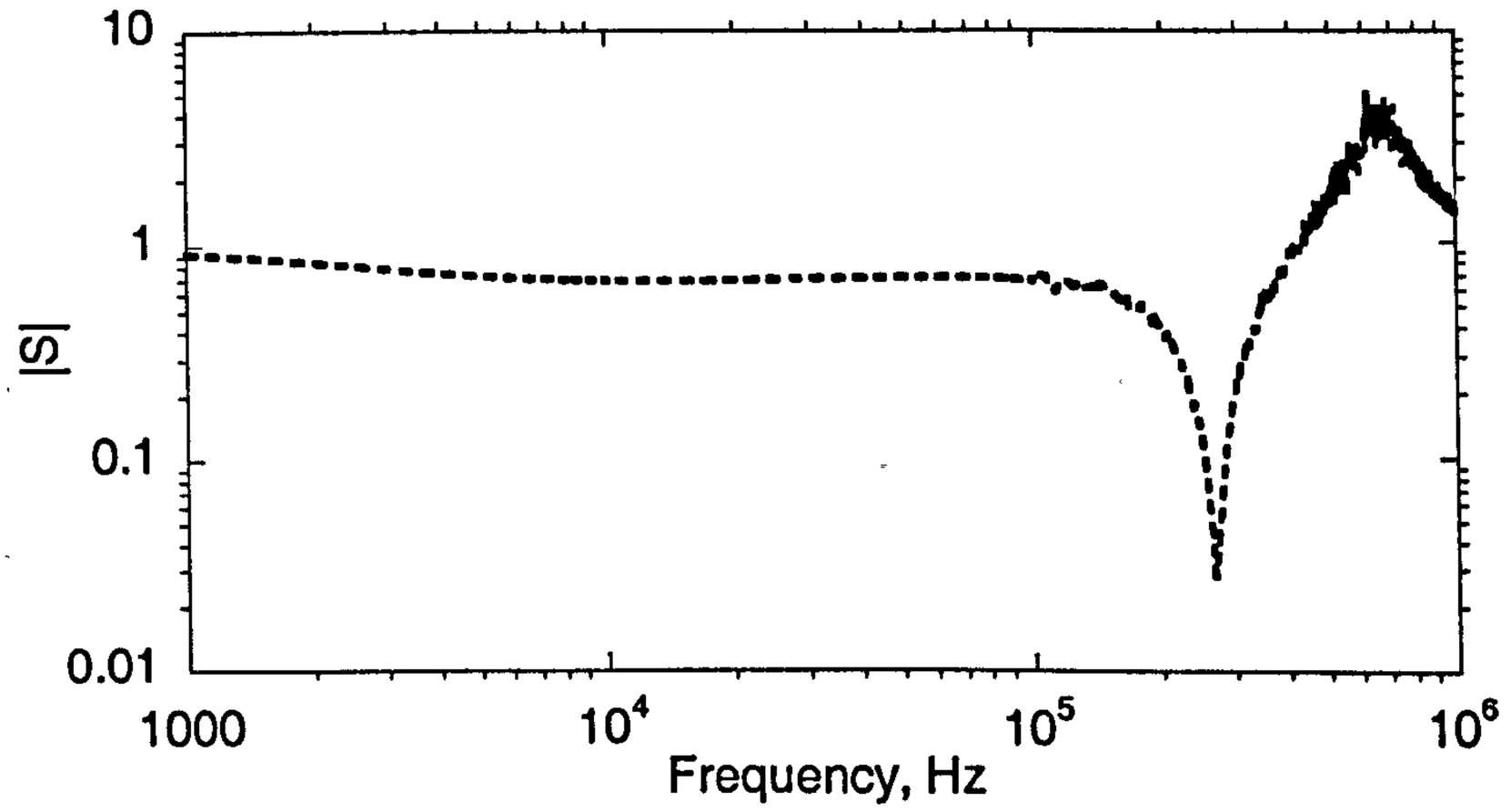

Figure 7.12: Suppression factor

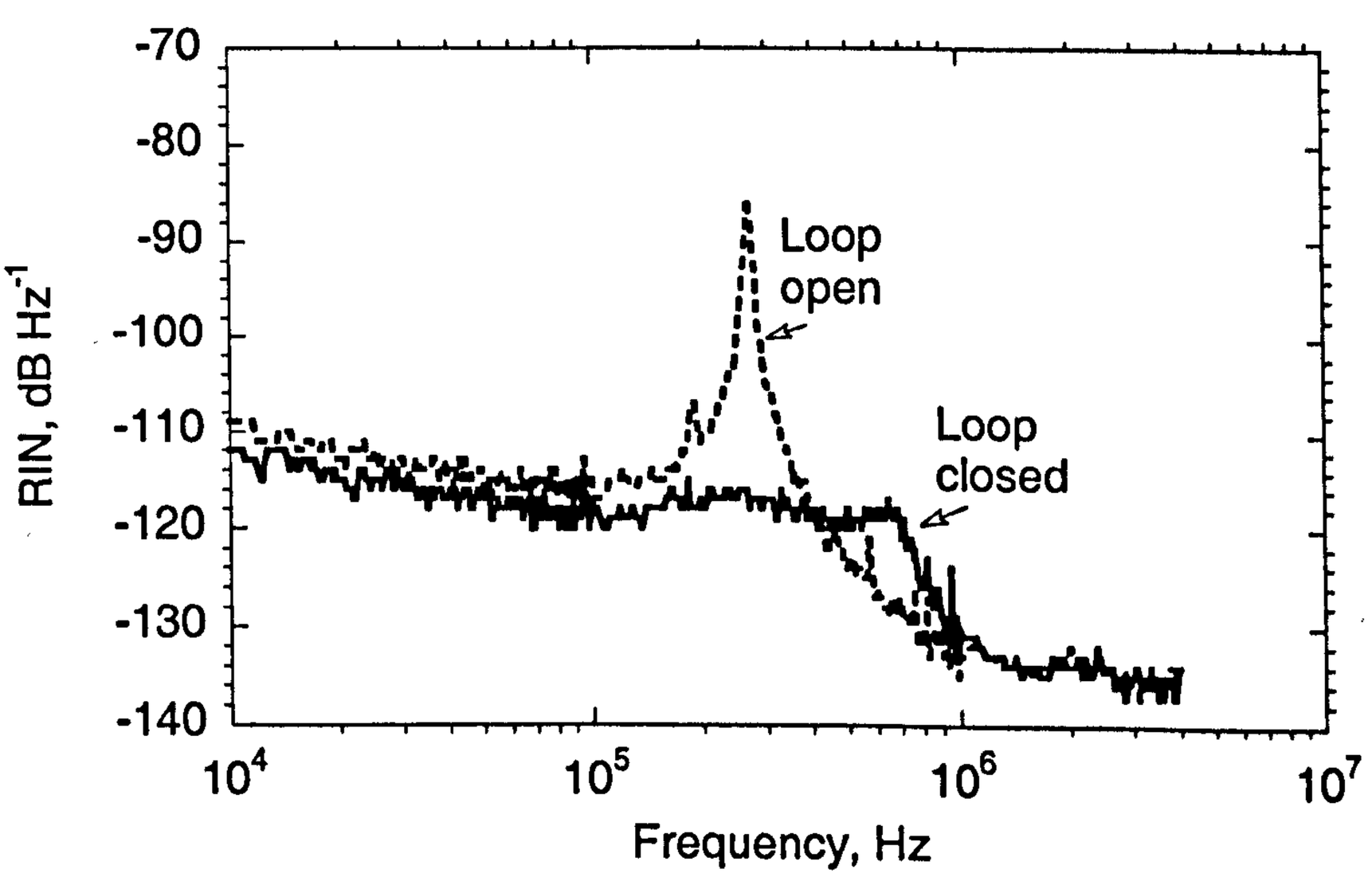

Figure 7.13: RIN with loop open and closed

The maximum suppression is observed at the relaxation oscillation frequency and an increase in noise is observed at frequencies between 450 kHz and 1 MHz. The absolute level of RIN at the relaxation oscillation is –86 dB.Hz^{-1}±2dB when the loop is open and –116 dB.Hz^{-1}±2dB when the loop is closed corresponding to a suppression of 30 dB, which agrees with that predicted by (7.19). Increasing the gain of the feedback loop would also increase suppression; however, this was not possible with our set-up, since the loop would become unstable due to the increasing phase lag of the pump modulation response with increasing frequency (see fig. 7.9). Incorporation of extra phase advance in the form of a differentiator would not solve the problem in this case, since the upper unity gain point would be correspondingly increased. Thus, reduction of the shunt capacitance causing this phase lag, rather than compensation for it, would allow the loop gain to be increased. The increase in RIN at frequencies below 100 kHz was attributed to excess noise originating from the power supply. Increasing the loop gain (and hence the suppression at low frequencies) would also reduce this noise. The phase lag above ~450 kHz causes an increase in RIN above this frequency.

7.7 Laser Emission Frequency Modulation

Frequency modulation of the laser source is useful for implementation of passive interrogation techniques for fibre interferometers such as 'phase-generated-carrier' (PGC), as discussed in chapter 2. In the PGC scheme, the frequency excursion required is dependent on the interferometer path imbalance. For example, for a fibre imbalance of 1m and using $\phi_{pgc} = 2\pi nd\Delta\nu / c$ from section 2.9.2, yields a required peak frequency excursion, $\Delta\nu$=82.8MHz to achieve ϕ_{pgc}=2.6. Reducing the imbalance to 1cm increases the required frequency excursion to 8.28GHz. Typically, the modulation frequency is set to less than 100kHz dependent on bandwidth requirements. The frequency of the laser emission in the EFL is dependent on both the cavity length and refractive index. Modulation of the cavity length and refractive index can be achieved by either changing the temperature of the cavity or applying strain.

Here we investigate the frequency modulation characteristics of the DFB EFL by: (i) modulation of the pump power and (ii) modulation of the cavity length by applying a strain from a piezo-electric element. We compare the characteristics of the EFL with those of the semiconductor laser-diode (LD). Frequency modulation of the semiconductor laser diode is

achieved by modulation of the injected current [7.55]; this also causes modulation of the output power. A figure of merit can thus be derived which expresses the ratio of the frequency excursion to the relative intensity modulation, $((P.d\nu)/dP)$. The characteristics of the semiconductor laser are taken as $(d\nu/di)_{SLD}$=5 GHz.mA^{-1} and $(dP/di)_{SLD}$=0.12 mW.mA^{-1} which yields $((P.d\nu)/dP)_{LD}$=1042 GHz where P is the maximum operating power of the LD (taken to be 25 mW) [7.55].

7.7.1 Frequency modulation by pump power modulation

It is found experimentally that the emission frequency of the EFL is modulated by a pump power modulation. This direct modulation is potentially useful, and was investigated for laser IFL1221. The parameter $(d\nu/dP_p)_{EFL}$ was characterised using the interferometric technique described in chapter 2 to measure the frequency excursion as a function of the pump power modulation. The emission from the EFL was launched into a Mach-Zehnder interferometer with a 100m fibre path imbalance. Balanced detection was used to isolate the frequency excursion signal from any intensity modulation signal and a high gain-bandwidth feedback loop was used to maintain the interferometer at quadrature. The source from an HP 89410A Vector Signal Analyser generated a modulation signal to add to the pump diode current. A frequency response measurement was then made between the modulation signal and the EFL emission frequency modulation. The result after removing the effects of the responses of the current source, pump diode and receiver is shown in fig. 7.14.

Thus we find for this laser, $(d\nu/dP_p)_{EFL}$=5MHz.mW^{-1} ±10% at 1 Hz and $(d\nu/dP_p)_{EFL}$=0.4MHz.mW^{-1} ±10% at 10 kHz. The maximum output power was 20 mW and the slope efficiency is taken from table 7.1 which yields a value of $((P.d\nu)/dP)_{EFL}$=2.1GHz±10% at 1 Hz and 0.17GHz±10% at 10 kHz. Thus, the normalised frequency excursion in the EFL is between two and three orders of magnitude lower than that observed in the LD (1024GHz) when pump power modulation is used.

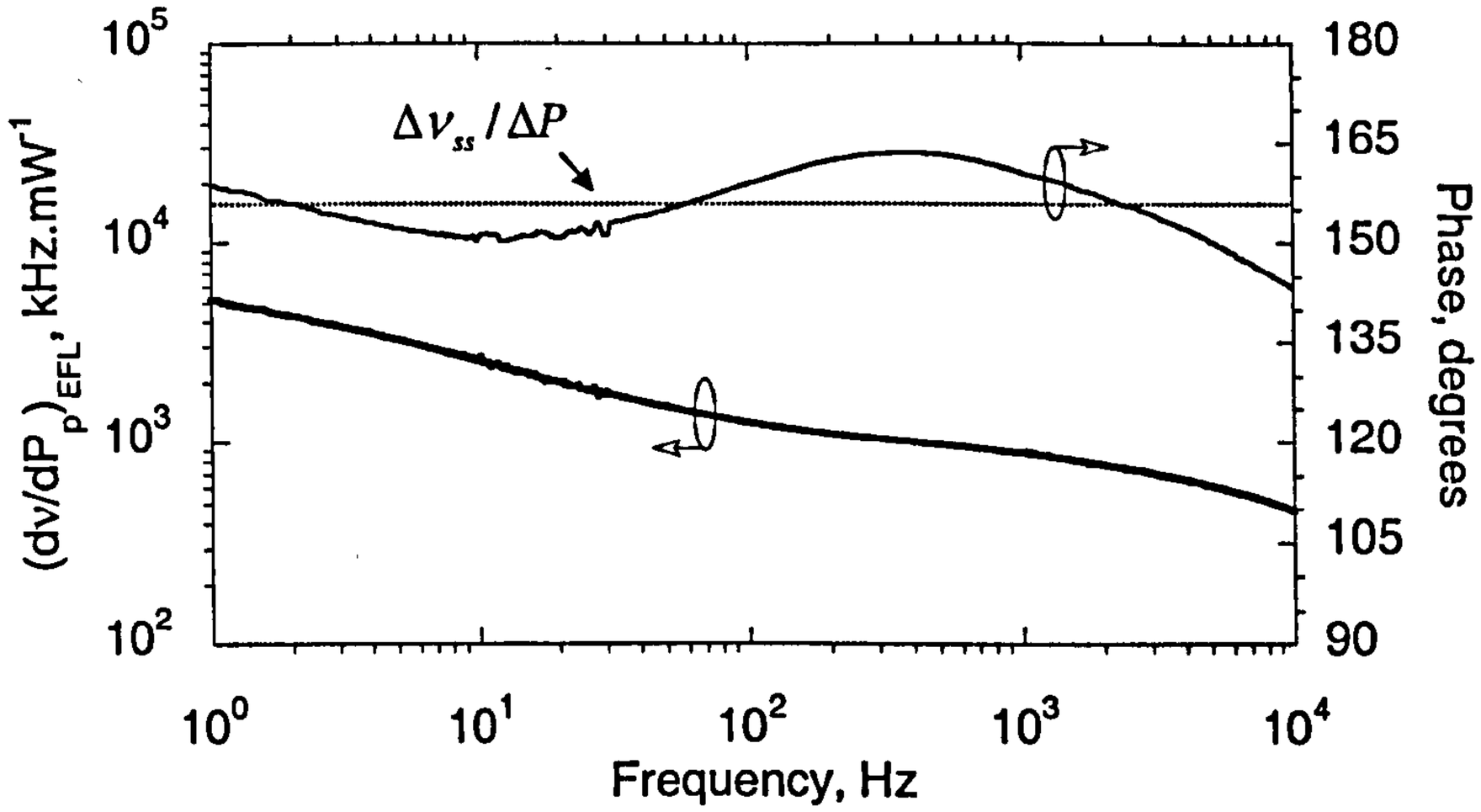

Figure 7.14: Frequency modulation vs pump power modulation

There are two possible mechanisms that may give rise to this effect. Gain or loss modulation through pump power modulation, gives rise to a refractive index induced nonlinear phase-shift via the Kramers-Krönig causality principle. The change in the ground state population is linked to a change in refractive index, via this principle, due to the contribution the ground state ions make to the refractive index. This effect is quantified by the ratio of the real and imaginary parts of the refractive index,

$$\alpha = \frac{\Delta n'}{\Delta n''} \tag{7.20}$$

where $\Delta\tilde{n} = \Delta n' + i\Delta n''$. It has been found that α =3-7 in semiconductor lasers [7.52] and is generally a significant effect, giving rise to the linewidth broadening factor. In the fibre DFB laser, the round trip gain is much lower and the magnitude of this effect is thought to be quite small, particularly at frequencies much lower than the relaxation oscillation frequency. A second, and more likely mechanism particularly at lower frequencies, arises through the self-heating of the fibre core due to non-radiative relaxations. When pumping at 980nm, the fast non-radiative transition $^4I_{11/2} \rightarrow {}^4I_{13/2}$ will give rise to self-heating. Other potential mechanisms giving rise to heating are pump excited state absorption, UV induced lifetime quenching and ion-ion upconversion, particularly in heavily clustered fibres. Self-heating in the fibre core will cause heat to diffuse through the cladding, and the induced temperature change

will depend on a number of factors, such as the heat capacity of the glass, the diffusion time (or thermal diffusivity) of the glass, the heat transfer coefficient and boundary conditions at the cladding surface. The temperature induced frequency shift can be approximated at quasi-dc frequencies by solving the heat conduction equation at steady-state. In this case it is the Fourier equation, (4.11), with a heat source added, referred to as the general heat conduction equation,

$$\frac{\partial T(r,t)}{\partial t}-\xi\left(\frac{\partial^2 T(r,t)}{\partial r^2}+\frac{1}{r}\frac{\partial T(r,t)}{\partial r}\right)=\frac{\eta P_{abs}}{\rho c\pi w^2 L} \qquad (7.21)$$

where ξ is the thermal diffusivity, ρ is the density, c is the specific heat capacity of silica, w is the mode field radius of the pump, P_{abs} is the absorbed pump power, L is the length of doped fibre, and η is the fraction of absorbed power turned into heat. Note that in order to arrive at (7.21), we have neglected axial heat flow. The fibre dimensions imply that axial heat flow would contribute negligibly to the overall heat flow compared with radial heat flow. We assume that the fibre is unjacketed and later consider the effect of adding a jacket. We also assume that the heat generated is proportional to the injected pump power (which we know is valid from the linearity of the laser signal power with pump power). We shall ignore the axial dependence of the pump power since the doped fibre is short and the pump absorption is generally low, thus the axial temperature profile is assumed constant. This is possibly a crude approximation since it has been found that in DFB Er^{3+}:Yb^{3+} fibre lasers, the number of absorbed pump photons is spatially related to the mode intensity [7.62]. Hence, the axial temperature profile is related to the longitudinal mode profile. The magnitude of this effect in the Er^{3+} fibre laser is not known, but since the pump absorption is generally low, we shall use this approximation. The steady-state temperature profile can be found by setting $\partial/\partial t=0$ in (7.21) and solving using the boundary conditions requiring continuity of temperature at the core-cladding interface and energy conservation at the fibre surface. A simple expression has been derived in [7.59] for the steady-state temperature profile in the cladding for $r \geq r_1$,

$$\Delta T_{ss}(r)=\frac{\eta P_{abs}a^2}{2hr_1 L\pi w^2}\left(1-\frac{hr_1}{\kappa_g}\ln\left(\frac{r}{r_1}\right)\right) \qquad (7.22)$$

where a is the core radius, h is the heat transfer coefficient between the core and surrounding air, r_1 is the cladding radius and κ_g is the thermal conductivity of glass and we have used the relation, $\xi = \kappa_g / \rho c$. The heat transfer coefficient was determined in [7.59] for the case of an infinitely long rod, cooling in air at 20^{0}C. For small temperature changes it was shown that h can be approximated by,

$$h(\Delta T \to 0) = 0.20\kappa_a / r_2 \tag{7.23}$$

where κ_a is the thermal conductivity of air. To calculate the induced temperature change in the core, (7.22) can be evaluated at the core-cladding boundary. We find that the second term in (7.22) is typically 2% of the first and thus using (7.23) the steady-state temperature in the core is approximated by,

$$\Delta T_{ss-core} \simeq \frac{\eta P_{abs} a^2}{0.4\kappa_a \pi w^2 L} \tag{7.24}$$

and is thus independent of the fibre diameter. Finally, we must determine the fraction of absorbed power turned into heat. Considering only the fast $^4I_{11/2} \to {}^4I_{13/2}$ transition as a possible heat generation mechanism, thus results in $\eta = (1-980/1550) = 37\%$. It follows therefore, that for an ideal laser (i.e. one pump photon generates one signal photon), we should find that the total laser power, $P_s = (980/1550)P_{abs} = 0.63P_{abs}$. In fact, we find for our laser that $P_s \approx 400\mu W$ for $P_p = 100mW$ and $P_{abs} \approx 0.05P_p$ for $L = 100mm$. This corresponds to ~92% of the energy being lost to other mechanisms. Some of this energy will be turned into amplified spontaneous emission and the green fluorescence emitted from these lasers. For our calculations we shall take $\eta = 0.5$ as a worst case. The temperature induced frequency shift is thus given,

$$\frac{\Delta \nu_{ss}}{\Delta T_{ss-core}} = \nu\left(\frac{1}{n}\frac{\partial n}{\partial T}\bigg|_\rho + \alpha_L\right) \tag{7.25}$$

Taking values of $\left(\frac{1}{n}\frac{\partial n}{\partial T}\bigg|_{\rho}+\alpha_L\right)$=5.2×10^{-6}K^{-1}, λ_s=1550nm ($\nu_s=c/\lambda_s$), a=3.5μm, w=2.5μm, κ_a=2.54×10^{-2}W.(m.K)$^{-1}$ at 293K, κ_g=1.38W.(m.K)$^{-1}$, η=0.5 and assuming a pump modulation of 1 mW, 5% absorbed power in 100mm long doped fibre, yields from (7.24) and (7.25) $\Delta\nu_{ss}/\Delta P_p$=16MHz.mW^{-1}, corresponding to $\Delta T_{ss}/\Delta P_p$=15mK.mW^{-1}. Thus, this effect can account for the observed levels of pump induced frequency modulation.

So far we have considered only a bare fibre. Applying a jacket or coating to the fibre is likely to result in a longer time required for the fibre to reach steady-state temperature due to the fact that κ_c for most polymers is between 0.12 and 0.23W.(m.K)$^{-1}$ compared with silica glass which is 1.38W.(m.K)$^{-1}$. The presence of the jacket will not significantly change the steady-state temperature reached, according to (7.22), since this is controlled by the heat transfer coefficient. It will only modify the temperature profile across the fibre. Thus, the overestimate of the frequency excursion by (7.25) compared with our measurement at 1 Hz (5MHz.mW^{-1}) may be due partly to the fact that steady-state temperature is not reached at this frequency as well as errors in the assumed fibre parameters and η.

For implementation of a passive interrogation scheme for an interferometric sensor, it is necessary to achieve several MHz frequency excursion at several tens of kHz. Thus a more efficient frequency modulation mechanism is required.

7.7.2 Frequency modulation by cavity strain

Applying a strain to the laser cavity will modulate the frequency of the laser emission. This has been implemented by bonding the laser cavity along the length of a lead-zirconate titanate tube (PZT5h), as shown in fig. 7.15. A thin layer of epoxy resin was used to bond the fibre to the tube (40mm×10mm×1mm), which ensured high strain transfer. The strain responsivity of the EFL is expected to be similar to that of an in-fibre Bragg grating [7.56], such that,

$$\frac{1}{\nu}\frac{d\nu}{d\varepsilon_z}=0.78 \tag{7.26}$$

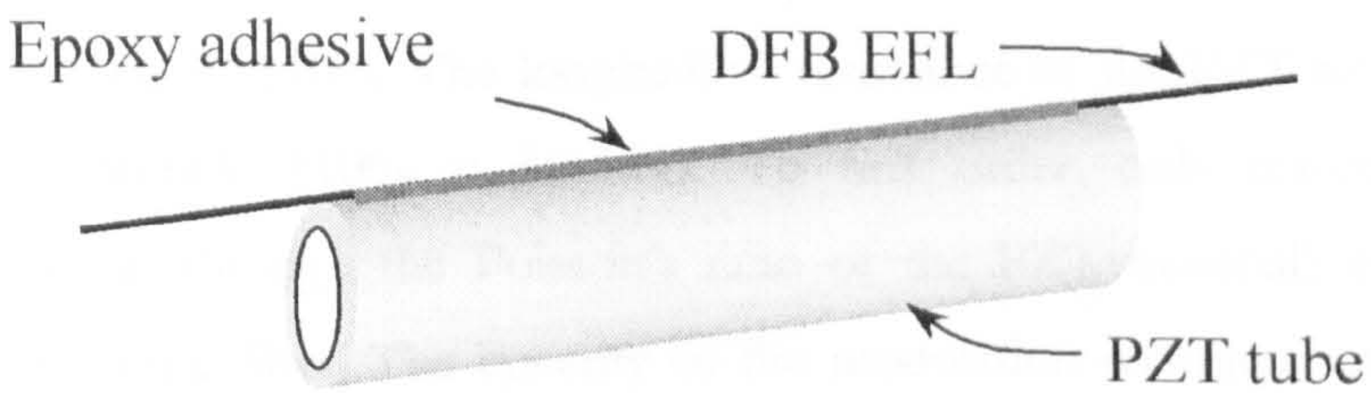

Figure 7.15: EFL bonded to piezo-electric tube

The frequency modulation response was characterised using an interferometric technique. The laser emission was launched into an interferometer with a path imbalance of 100m and a sinusoidal modulation was applied to the laser PZT. By observing the resulting fringe pattern on a spectrum analyser, the voltage required to achieve a phase excursion of 2.6 rads (i.e. such that the amplitude of the first and second order Bessel function components of the photocurrent are equal, $J_1(\phi) = J_2(\phi)$, as described in section 2.9.2) could be found. From this, the frequency excursion scale factor, $d\nu / dV$, was calculated. The strain induced frequency modulation response at frequencies up to 65 kHz is shown in fig. 7.16.

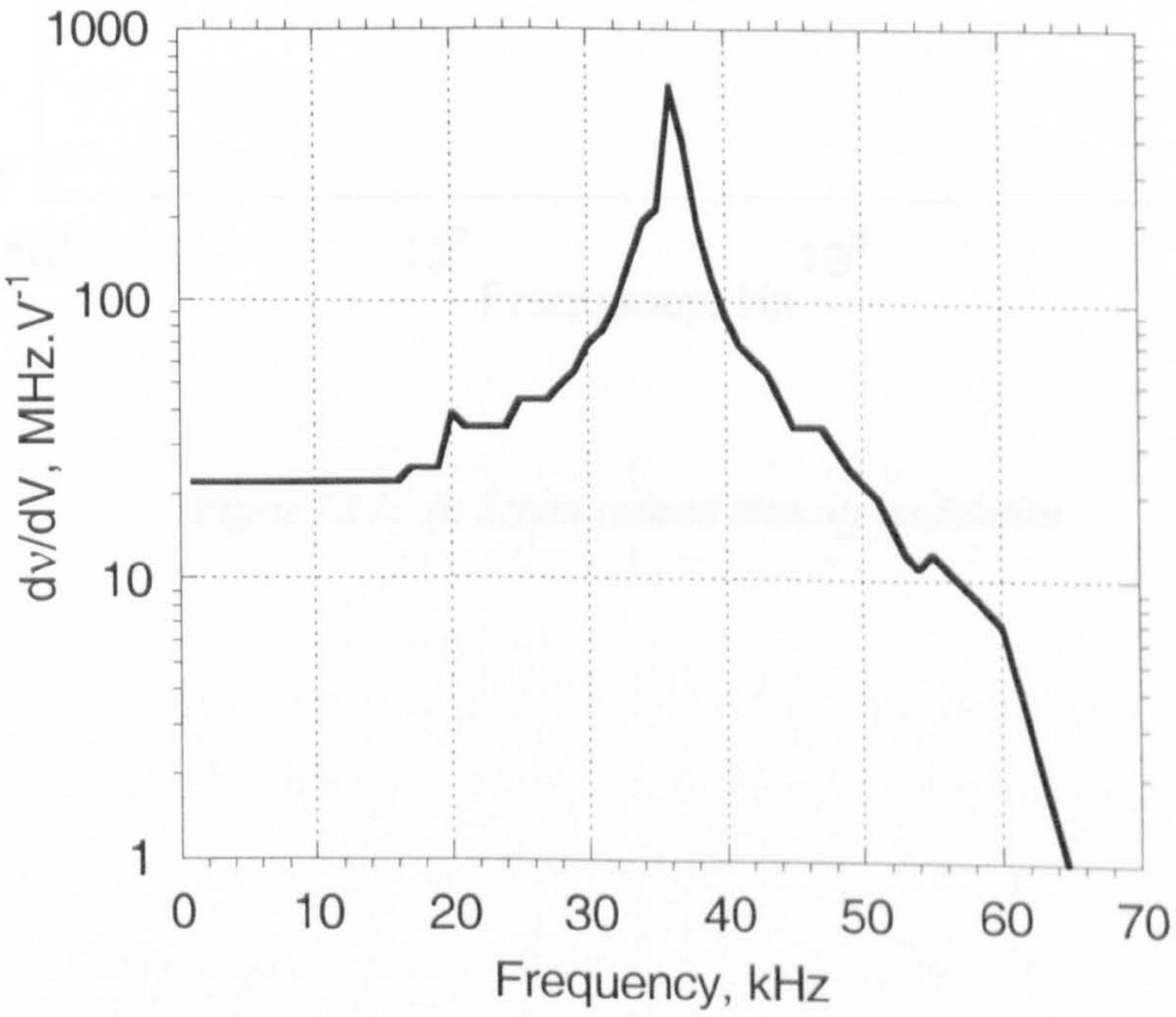

Figure 7.16: Strain induced frequency modulation response of EFL

Up to 15 kHz, the frequency modulation response exhibits a constant off-resonance scale factor of ~22 $MHz.V^{-1}\pm10\%$. The longitudinal resonance of the PZT tube increases the scale factor to 623 $MHz.V^{-1}\pm10\%$ at 36 kHz. To first order, only resonance's that generate longitudinal strain (through the Poisson's ratio of the PZT material) in the PZT tube will generate strain in the fibre. The linearity of the modulation technique exceeded the dynamic range of the interferometric measurement (~90 dB). It was found, however, that strain applied in this way caused a modulation of the intensity of the laser output. This was characterised by directly detecting the laser output on a photodiode, and carrying out a frequency response measurement between the photocurrent and the modulation signal applied to the laser PZT. The result is shown in fig. 7.17 expressed in terms of the scale factor between the relative intensity modulation and applied voltage, $dP/(P.dV)$.

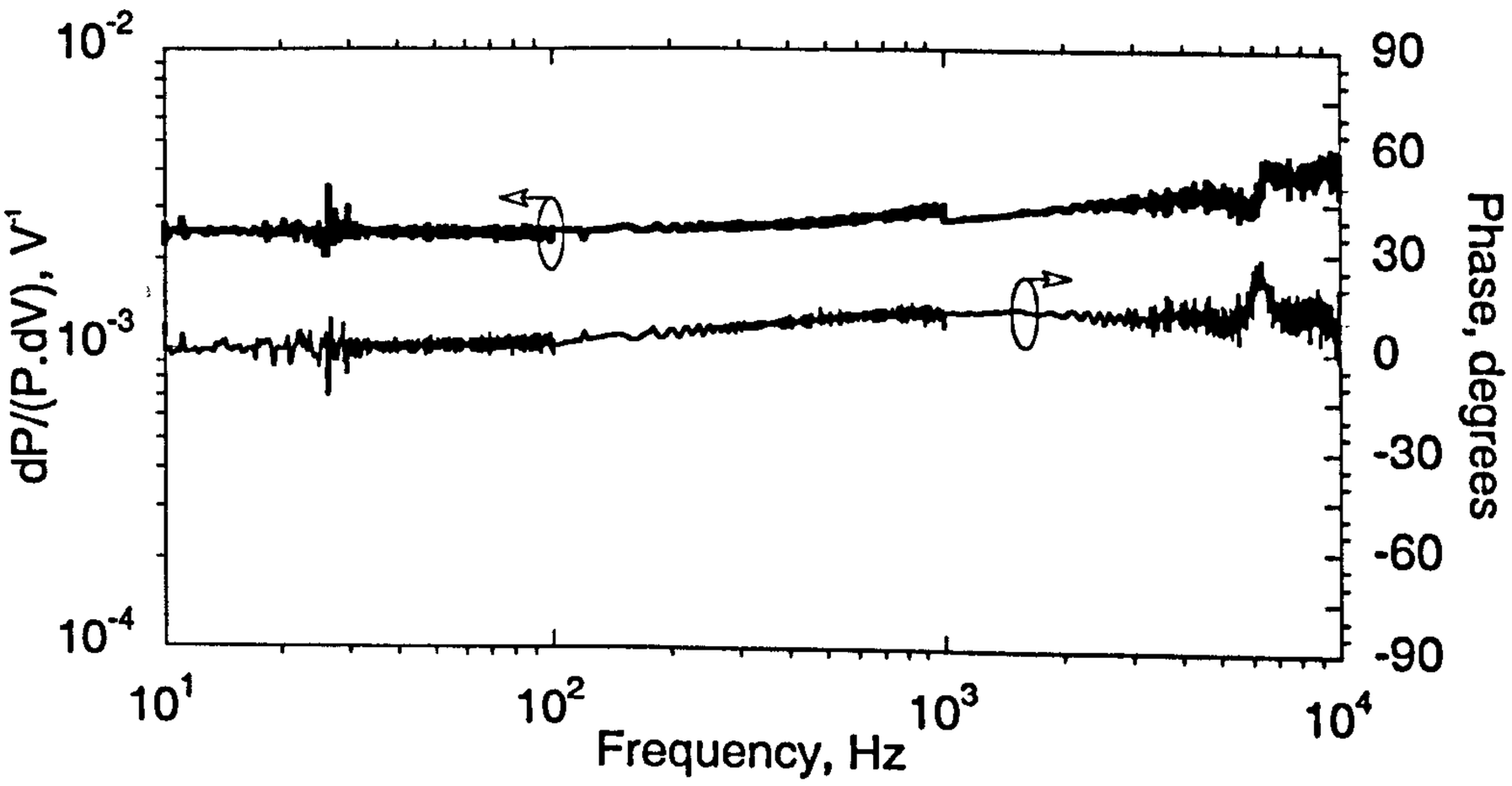

Figure 7.17: (i) Strain induced intensity modulation

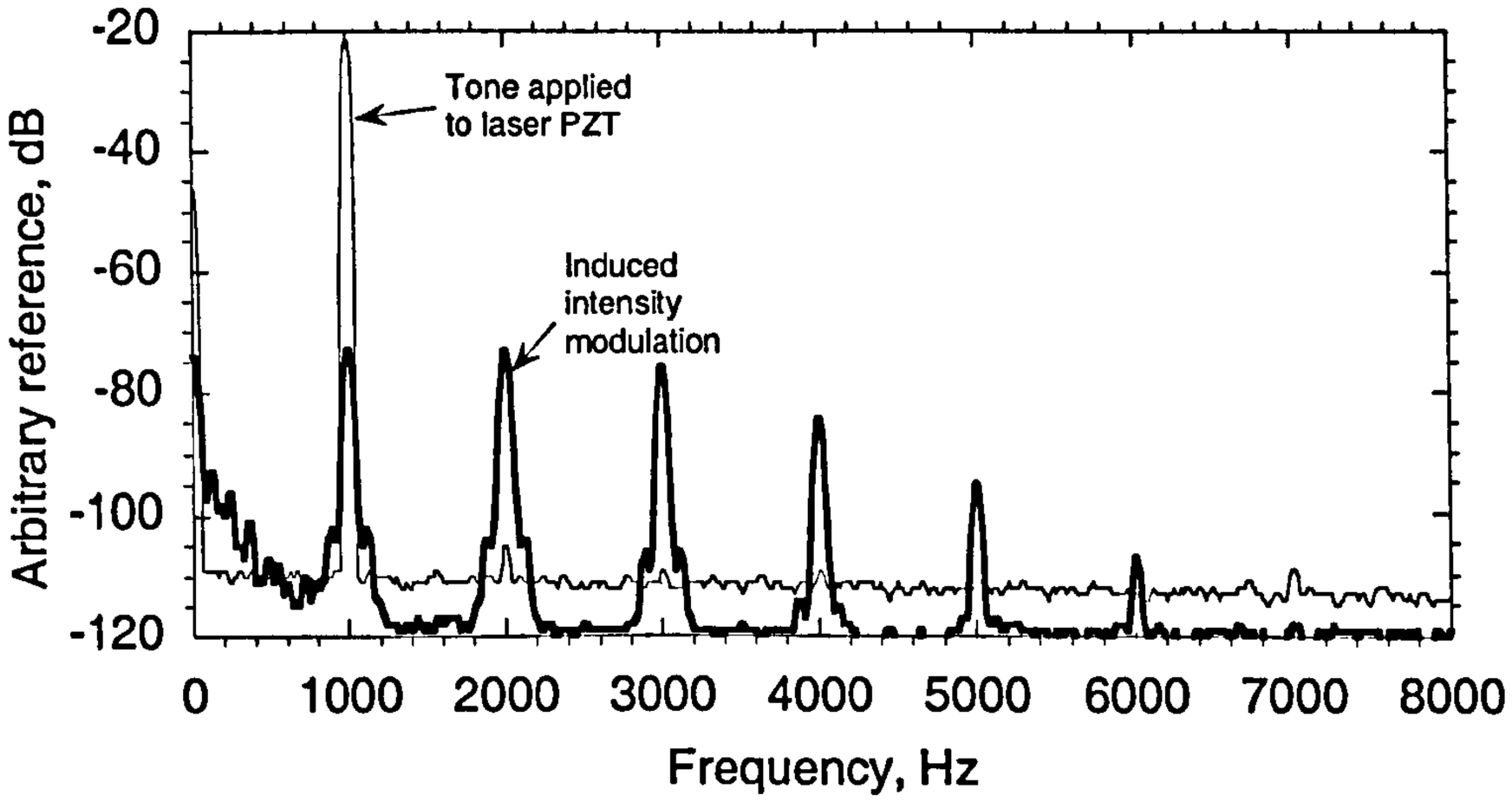

Figure 7.17 (cont): (ii) Relative intensity modulation induced by tone applied to laser PZT

Upon measurement of $dP/(P.dV)$ it was found that the intensity modulation induced by cavity strain was highly non-linear and the induced relative intensity modulations exhibited temporal variations. The intensity modulation induced from a single tone (corresponding to a $\Delta\nu$=3.1MHz) applied to the laser cavity is shown in fig. 7.17(ii). The amplitudes of the harmonics were found to fluctuate unpredictably with time. To obtain the plot shown in fig. 7.17(i), the intensity modulation resulting from excitation of the cavity strain by a chirp signal was measured for each decade. A peak-hold measurement was carried out to obtain fig. 7.17(i) and therefore represents a worst case for this laser.

We can derive the figure of merit from the intensity modulation scale factor, $dP/(P.dV)=2.1\times10^{-3}V^{-1}$ and $d\nu/dV=22MHz.V^{-1}$ yielding, $(P.d\nu)/dP=10GHz$. This is approximately two orders of magnitude lower than that observed in the LD (1024GHz).

The primary cause of this effect can be linked to the frequency dependence of the effective mirror reflectance which leads to cavity loss dispersion, for a non-ideal fibre laser (i.e. a DFB fibre laser with a phase-shift not equal to exactly $\pi/2$). This effect can be understood by considering the cavity loss due to the mirror transmittance, M, and roundtrip phase, ϕ_n, for a DFB fibre laser with a $\pi/2$ phase-shift in the centre.

In fig. 7.18(i) we plot the cavity loss due to the mirror transmittance, M, as a function of the detuning, $\Delta\nu$, for a grating with κL=9.1. The detuning is defined as the frequency deviation from the frequency corresponding to the minimum cavity loss. The roundtrip phase, ϕ_n, is shown in fig. 7.18(ii).

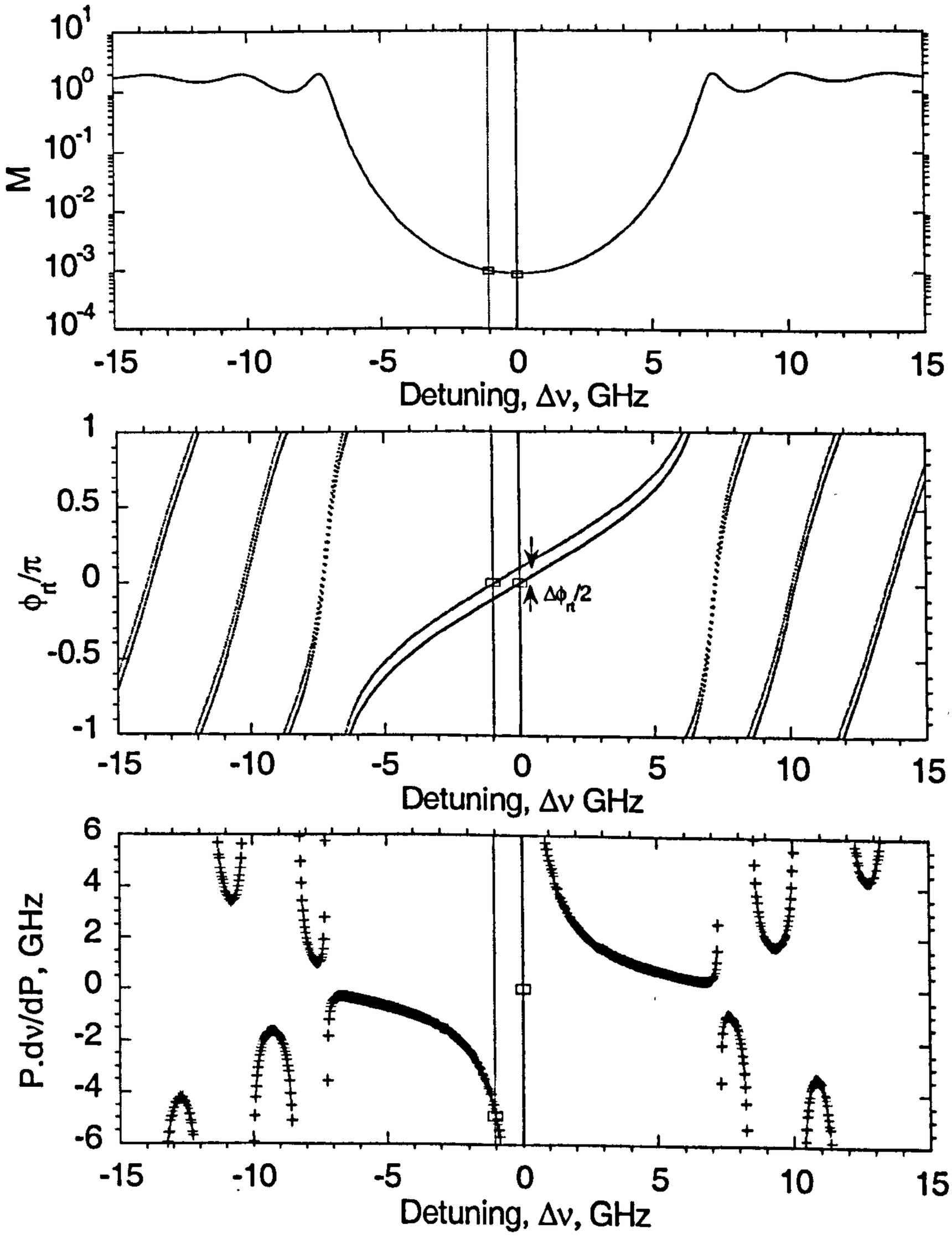

Figure 7.18: (i) Cavity loss, (ii) cavity roundtrip phase and (iii) loss dispersion induced relative intensity fluctuation for an ideal 50mm, $\pi/2$ discrete phase-shifted EFL (κL=9.1)

Lasing will occur at the wavelength corresponding to zero roundtrip phase-shift (i.e. $\phi_n=0$). Therefore, for an ideal $\pi/2$ phase-shifted grating, the loss dispersion is zero, to first order. However, when the phase-shift is $\pi/2+\Delta\phi_n/2$, the lasing wavelength is shifted to a lower frequency. This is shown in fig. 7.18(i) and (ii), for the case of $\Delta\phi_n=0.2\pi$, corresponding to a detuning, $\Delta\nu\approx$-1GHz. The loss now becomes frequency dependent. The quantity $P.d\nu/dP$ is given by calculating $M.d\nu/dM$ and is shown in fig. 7.18(iii). This illustrates that a phase-shift error of, $\Delta\phi_n/2=0.1\pi$ will lead to $P.d\nu/dP\approx$ 5GHz.

We do not know the exact grating strength for IFL1221; however, if it is assumed to be equal to the grating strength used in our example then only a $\Delta\phi_n<<0.1\pi$ is required to account for the observed effect. If a temperature profile exists across the length of the EFL (as suggested in the previous section), then low frequency fluctuations in pump power may locally modulate the refractive index by an amount related to the temperature profile. This may lead to localised modulation of the magnitude of the phase-shift, which would modulate the centre wavelength of the laser and hence give rise to the observed temporal variations in induced intensity modulation. Finally, as the modulation frequency approaches the relaxation oscillation, the magnitude of the intensity modulation will be further amplified; ultimately leading to laser instability. A RIN suppression circuit of the type described in sec. 7.6, will counter this effect to some degree.

In summary, we find that the most effective method of frequency modulating the EFL is through cavity strain; however, as with the pump power modulation method, this gives rise to intensity modulation due to the presence of cavity loss dispersion. The magnitude of this effect may be reduced by ensuring that the grating phase-shift is very close to $\pi/2$. For the case of a grating strength, $\kappa L=9.1$, the phase-shift must be within $\pi/2\pm0.004\pi/2$ (equivalent to a detuning of less than ±0.04GHz) in order to achieve a $|Pd\nu/dP|\approx$1000 GHz (equivalent to the semiconductor DFB laser).

The modulation parameters are summarised in table 7.2.

Table 7.2: Summary of laser frequency modulation parameters

Laser	$\left\|\frac{Pd\nu}{dP}\right\|$	Scale factor
Semiconductor DFB	1024 GHz	$\frac{d\nu}{di}$ =5 GHz.mA^{-1}
EFL (Pump modulation)	0.17-2.1 GHz	$\frac{d\nu}{dP_p}$ =0.4-5 MHz.mW^{-1}
EFL (Strain induced)	10 GHz	$\frac{d\nu}{dV}$ =22 MHz.V^{-1}

7.8 A Distributed Feedback Fibre Laser in a MOPA Configuration with Frequency Noise Reduction[16]

We now describe a technique to suppress the frequency noise by locking the EFL emission to a fibre interferometer. A feedback signal is applied to the laser cavity through a piezo-electric element onto which the fibre laser is bonded. The frequency noise is thus reduced by applying a compensating strain to the laser cavity. To demonstrate both low frequency and intensity noise, we have also incorporated a low frequency RIN suppression circuit.

A DFB EFL (supplied by Koheras ,Denmark) with an emission wavelength of 1542.17 nm was used as the master-oscillator. It exhibited single-polarisation mode output through the application of a birefringent phase-shift to the grating during manufacture[7]. The EFL was incorporated into a MOPA configuration as shown in fig. 7.19. It was pumped with a grating stabilized, 979.7nm pump source (Nortel LC92F) which delivered ~100 mW of power to the EFL. The pump current was generated by an ultra-low noise current source (ILX Lightwave, LDX-3620), which also allowed a modulation signal to be added to the pump current for the intensity noise suppression. The EFL produced 127 μW to the amplifier input (measured after the first isolator) and 200 μW from the other output. The difference here was due to differences in splice and component losses and a slightly off-center phase-shift in the grating, causing an asymmetry in the output power. The two WDM's after the laser allowed the residual pump power to bypass the 1550 nm dual-stage isolator (ISO), which exhibits high insertion loss at 980 nm, and be delivered with negligible loss to the amplifying section. The power-amplifier

[16] This section is a transcript of the paper "Frequency noise reduction in erbium doped fiber DFB lasers using electronic feedback" submitted for publication in Optics Letters.

consisted of 4 m of erbium doped fibre (EDF) and was characterized to provide a gain of 3.8dB.m^{-1}. This amplified the EDFL emission to 5.8 mW, measured after the second dual-stage isolator. An OSNR of 39 dB was achieved, measured in a 0.07 nm bandwidth, as shown in fig. 7.20. Two directional couplers were spliced to the MOPA output to allow light to be tapped off for each feedback and measurement component. To demonstrate both low frequency noise and intensity noise from this laser, a pump feedback circuit was also incorporated to reduce the low frequency relative intensity noise (RIN). This used one MOPA output to generate an error signal, which modulated the pump current out of phase with the intensity noise. Another tap was used to conduct out-of-loop intensity noise measurements and light from the remaining tap was launched into the locking interferometer described below. The RIN suppression circuit was based on a proportional-integral (PI) feedback controller of a similar type to that previously described. The time constant of the integrator was set to 0.1 ms and the error signal was delivered through the modulation input of the current source. Finally, light from the spare output of the EFL was launched into the measurement interferometer. This was used to conduct independent frequency noise measurements.

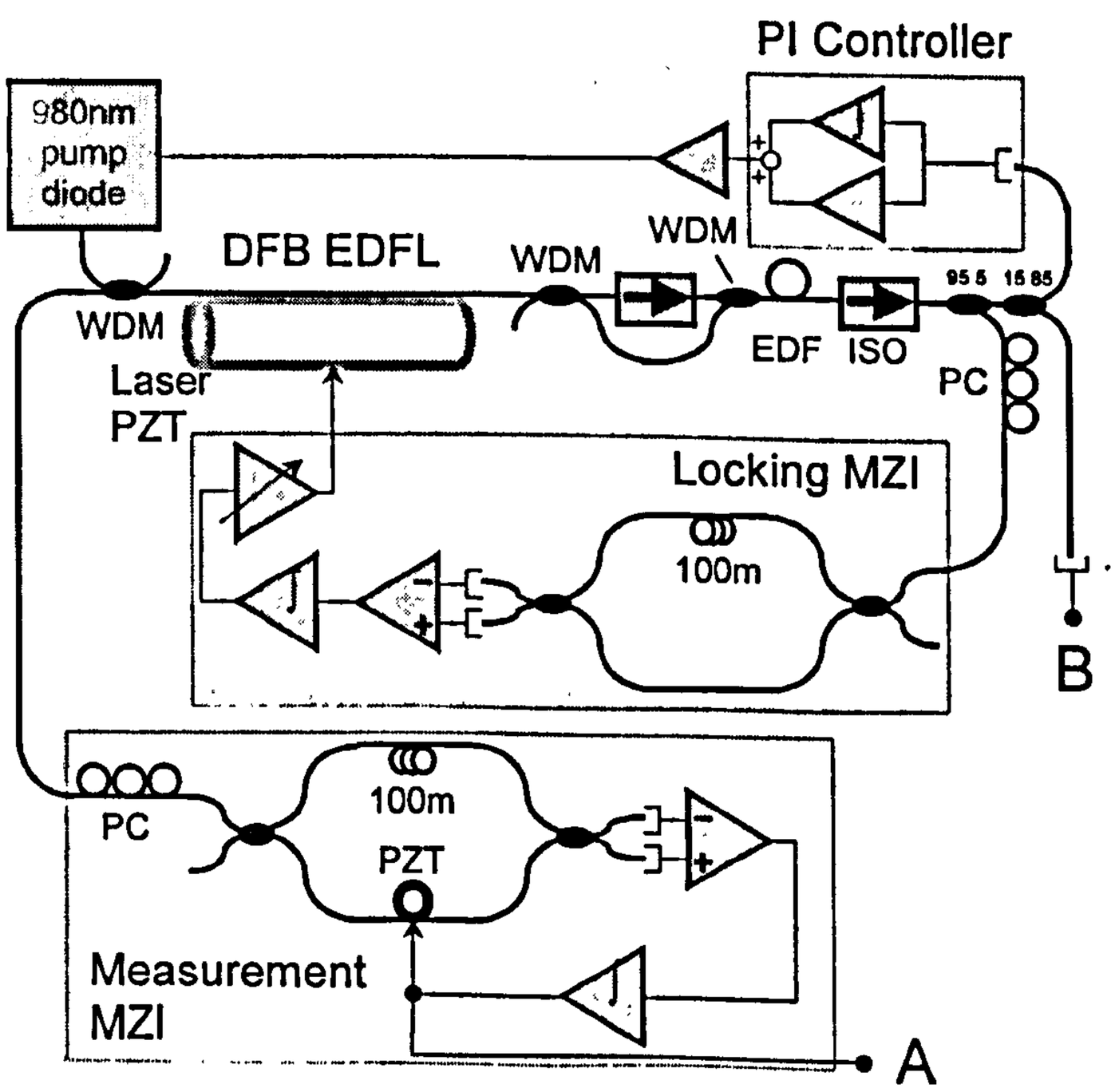

Figure 7.19: EFL configuration with noise reduction

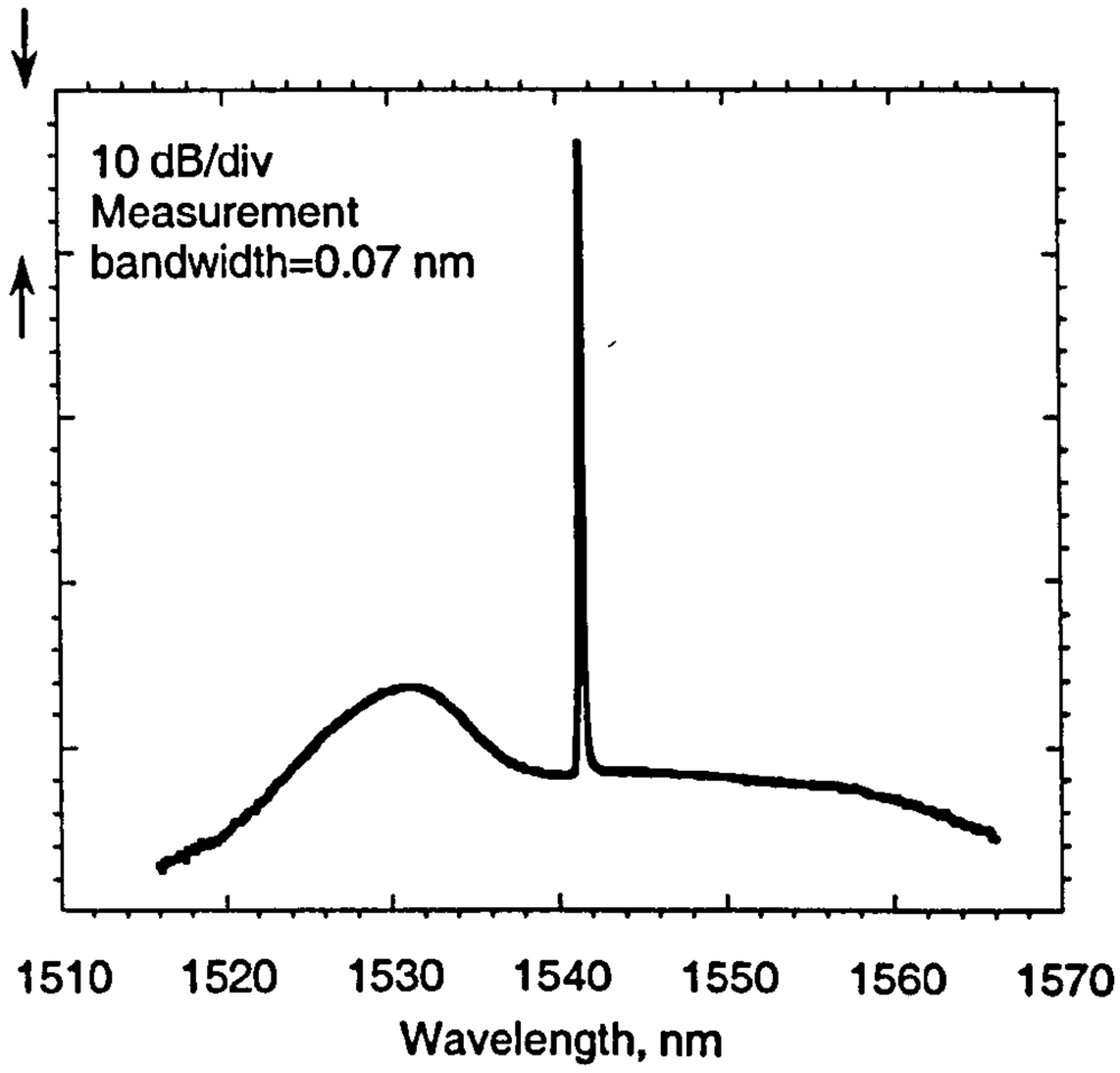

Figure 7.20: Optical spectrum of MOPA output

The laser cavity was bonded along the length of a piezo-electric (PZT) tube of dimensions 40mm×10mm×1mm with a thin layer of rapid cure epoxy resin, as shown in fig. 7.15. The locking interferometer consisted of a fibre Mach-Zehnder interferometer (MZI) with a 100m fiber path imbalance. A high gain-bandwidth active homodyne feedback technique (shown in Appendix 7.1) was used to maintain the MZI output at quadrature and the feedback voltage generated by the homodyne electronics was applied to the laser PZT. This type of locking technique was favoured over other techniques due to the reduced sensitivity of the loop gain to variations in input power and polarisation. The combination of the integrator (time constant=1.95ms) and variable gain voltage amplifier allowed the loop unity gain point to be set to ~10 kHz. A polarisation controller (PC) was also placed before the MZI to optimize the input polarisation. The MOPA laser and feedback MZI were placed together in an acoustically isolated test enclosure. A second MZI used the spare EFL output to make independent frequency noise measurements (referred to as the measurement MZI). This was placed in a separate acoustically isolated enclosure some distance away from the laser.

7.8.2 Results and conclusion

The RIN spectrum of the EFL is shown in fig. 7.21 (measured at point B) with and without the loop closed. Note that 10dB has been added to the open loop RIN measurement to separate

plots. With the loop closed, the RIN is reduced to a minimum of –139 dB.Hz^{-1}±2dB at 1 kHz (corresponding to 10dB±2dB suppression). The suppression is limited by photodiode amplifier noise (also shown in fig. 7.21) below 1 kHz and loop gain between 1 kHz to 10 kHz. In our experiment the optical power on the photodiode was 700 μW±5% which yields a shot noise limited RIN of –154 dB.Hz^{-1}, thus increasing the detected power would allow higher suppression to be achieved if necessary.

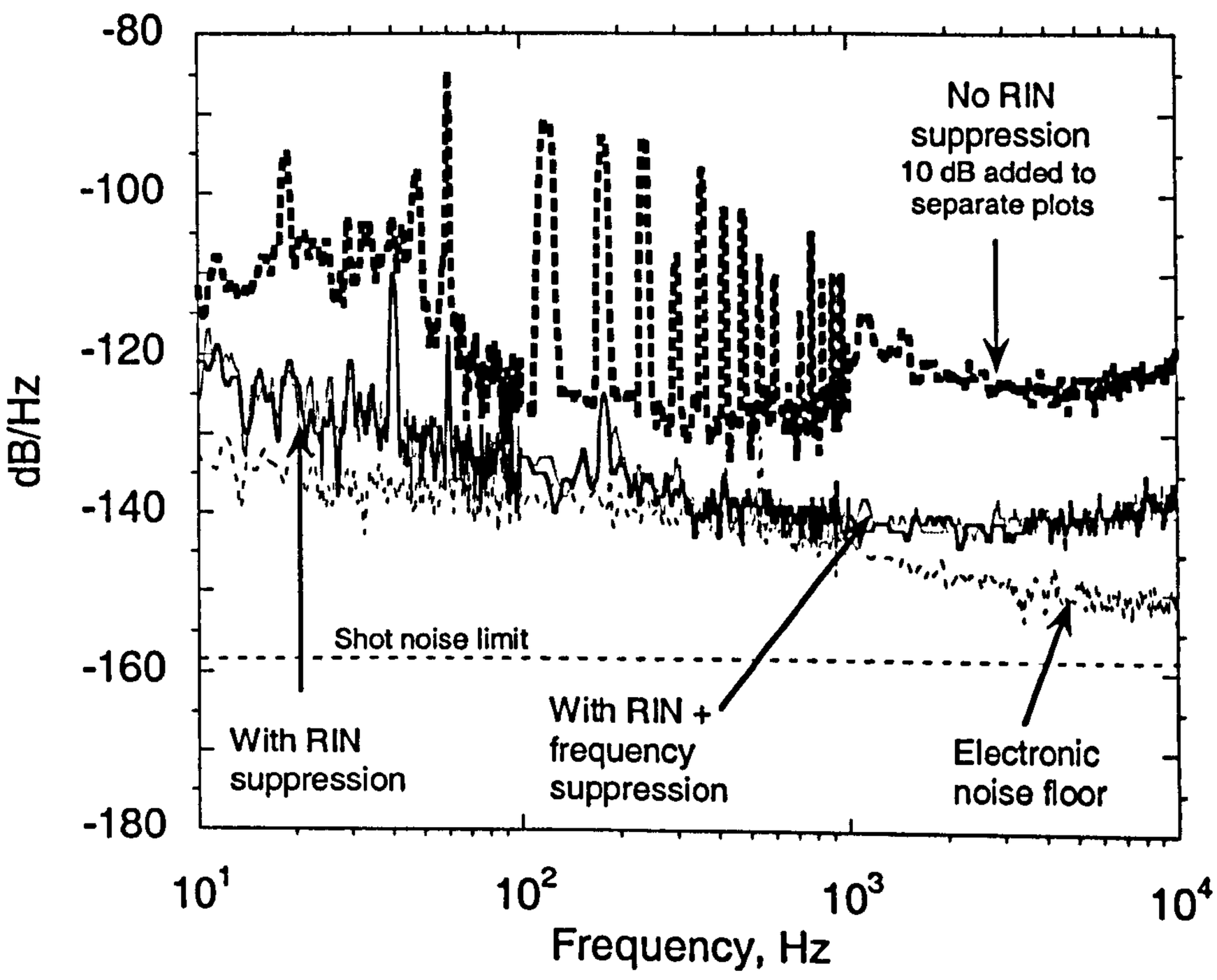

Figure 7.21: Intensity noise spectra

The frequency noise of the laser with the loop open and closed is shown in fig. 7.22 (measured at point A). The left axis shows the phase noise spectral density produced in a MZI normalized to a 1 m fiber path imbalance [μrad.Hz$^{-1/2}$] and the right axis shows the frequency noise spectral density [Hz.Hz$^{-1/2}$].

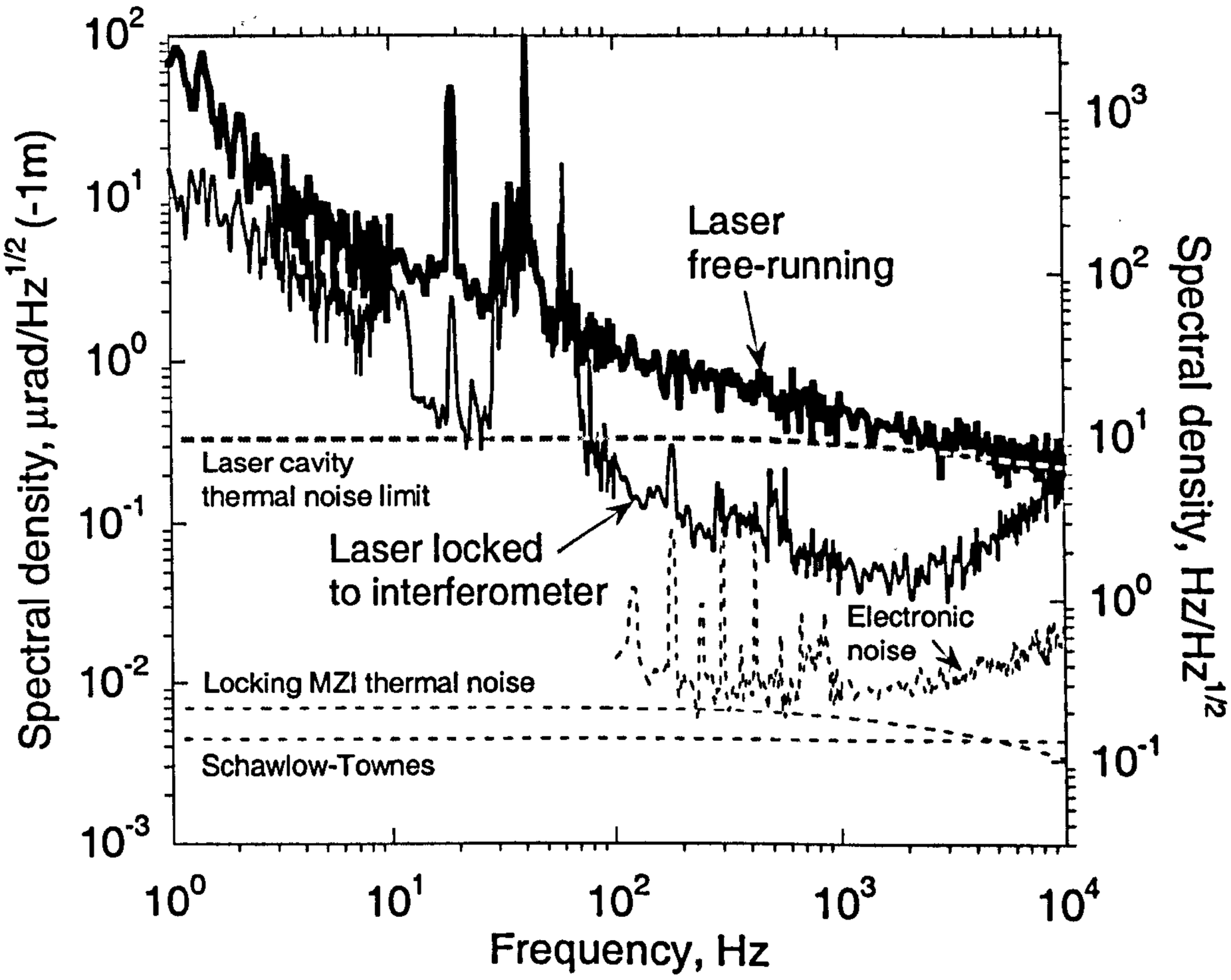

Figure 7.22: Frequency noise spectra and noise sources

With the loop open, the free-running frequency(phase) noise of the EFL is 15Hz.Hz$^{-1/2}$±25% (0.5 μrad.Hz$^{-1/2}$±25%) at 1 kHz and exhibits a "1/f" type spectrum below ~100 Hz and a noise spectrum believed to be due to the thermal noise in the laser cavity above 100 Hz. When the loop is closed, the frequency noise was reduced to 1.5Hz.Hz$^{-1/2}$±25% (0.05 μrad.Hz$^{-1/2}$±25%) at 1 kHz (i.e. a 20 dB noise reduction at 1 kHz). Increasing the gain of the voltage amplifier driving the laser PZT effectively increases the loop bandwidth. However, this tended to increase noise at higher frequencies since the bandwidth of the feedback loop must be significantly lower than any mechanical resonance of the PZT tube to avoid excess noise being added to the frequency noise spectrum due to excitation of these resonances. In the experimental set-up, the PZT tube exhibited a longitudinal resonance at 36 kHz (as observed in fig. 7.16), so adjustment of the locking MZI feedback loop bandwidth was included to ensure that no excess noise was added. Since the longitudinal resonance of the PZT tube approximately scales inversely with the length, an increase in the suppression bandwidth can be achieved by reducing the length of the PZT tube. This is made possible since the effective

cavity length in the DFB EFL is typically 10 to 20 mm. The EFL frequency was also found to be significantly less sensitive to mechanical perturbations, and was limited by the residual acoustic sensitivity of the locking MZI. The excess noise at 20Hz and between 30-70 Hz is likely to be generated from test equipment fans used in the measurements. The reduction in frequency noise suppression at low frequency (<100Hz) is most likely to be due to the acoustic sensitivity of the locking interferometer, even though the laser and MZI were contained in an acoustically isolated chamber. The spectral shape of the frequency noise when the laser is locked to the MZI is determined by the increasing phase margin of the feedback loop above 1 kHz and by the residual acoustic sensitivity of the MZI at frequencies below 1kHz. The frequency noise of the EFL above 1 kHz is most likely to be limited by thermally induced refractive index fluctuations across the mode field in the fiber core given by (7.14). This noise level is plotted in fig. 7.22, assuming an effective laser cavity length of 12 mm and fiber parameters given in section 7.5.4. This result would indicate that we have achieved suppression of the frequency noise to ~18 dB below the thermal noise limit. The thermal noise from the locking MZI is also shown in fig. 7.22.

A known limitation of the active homodyne feedback technique is the need to reset the integrator for large frequency excursions, caused by changes in ambient temperature of the MZI or laser cavity, when the laser PZT voltage approaches the output rails of the integrator. For example, the dc scale factor of the laser PZT was measured to be ~22 $MHz.V^{-1}$±20% and the maximum output voltage of the integrator was ±10V. Therefore, the feedback loop was able to track frequency excursions of up to ±220 MHz before a reset was required. Taking the temperature responsivity of the EDFL as $1.0GHz.K^{-1}$, this corresponds to a maximum temperature fluctuation of the EDFL of ±0.22K, relative to the MZI. The isolation to temperature changes provided by the test enclosures resulted in no resets being required throughout the duration of the tests (a few days). It is also straightforward to include an automatic reset in the electronic circuit and to incorporate the MZI and laser into an environmentally controlled chamber.

To summarise, we have demonstrated, for the first time, frequency noise reduction in an erbium doped DFB fiber laser in a MOPA configuration by phase locking the laser output emission to a fiber interferometer. We have shown that the frequency noise reduction technique has no effect on the intensity noise, when the intensity noise is greater than

-120dB.Hz^{-1} and achieves noise reduction to below what is thought to be the intrinsic thermal noise level of the laser cavity. The relative intensity noise spectral density of the laser was reduced to below –120 dB.Hz^{-1} over the frequency range 10 Hz to 10 kHz and the frequency noise of the laser was reduced from 15Hz.Hz$^{-1/2}$ to 1.5Hz.Hz$^{-1/2}$ at 1 kHz. This is believed to be the lowest frequency noise reported from an erbium-doped fibre Bragg grating laser to date and requires only low speed electronics to implement.

7.9 Conclusions

In conclusion, we have characterised the free-running performance (slope efficiency, frequency and intensity noise) of the Er^{3+} doped DFB fibre laser and discussed the origins of the observed frequency and intensity noise. We have shown that with appropriate packaging, the frequency noise can be reduced to the level thought to be determined by thermal effects in the laser cavity. We have described the detailed design of an electro-optic feedback circuit which reduced the intensity noise at the relaxation oscillation by 30 dB to –116 dB.Hz^{-1}±2dB. We demonstrated a technique that would allow the frequency of the laser emission to be modulated. We also showed how this technique can be used to reduce the frequency noise of the laser by up to 18 dB below the limit set by cavity thermal noise, by locking the laser emission to an interferometer. By optimising and combining these techniques, this laser would be ideally suited as a high performance source for interrogation of interferometric sensors. We can compare lasers using the frequency noise data at 1 kHz from fig. 7.5 and 7.22. The frequency noise of the semiconductor DFB laser with(without) phase noise suppression is ~500Hz.Hz$^{-1/2}$ (10 kHz.Hz$^{-1/2}$), for the diode pumped Nd:YAG laser is 20Hz.Hz$^{-1/2}$ and for the fibre laser is 1.5Hz.Hz$^{-1/2}$ (7 Hz.Hz$^{-1/2}$) at 1 kHz. Thus, for an interferometric phase measurement limited by frequency noise, we would expect a frequency dependent improvement in resolution of between 1 to 4 orders of magnitude with the fibre laser source.

APPENDIX 7.1: Homodyne feedback circuit

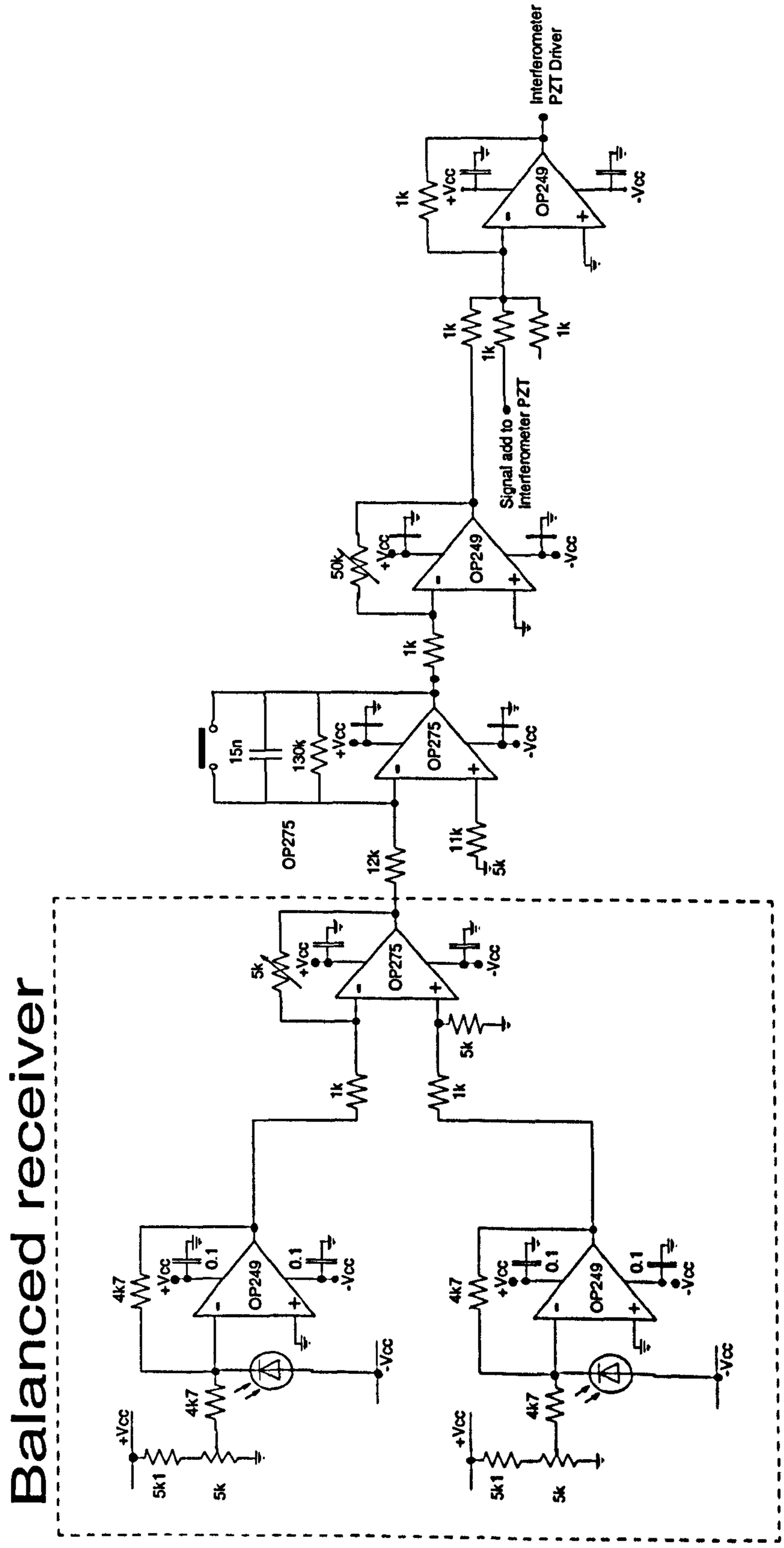

APPENDIX 7.2: RIN suppression circuit

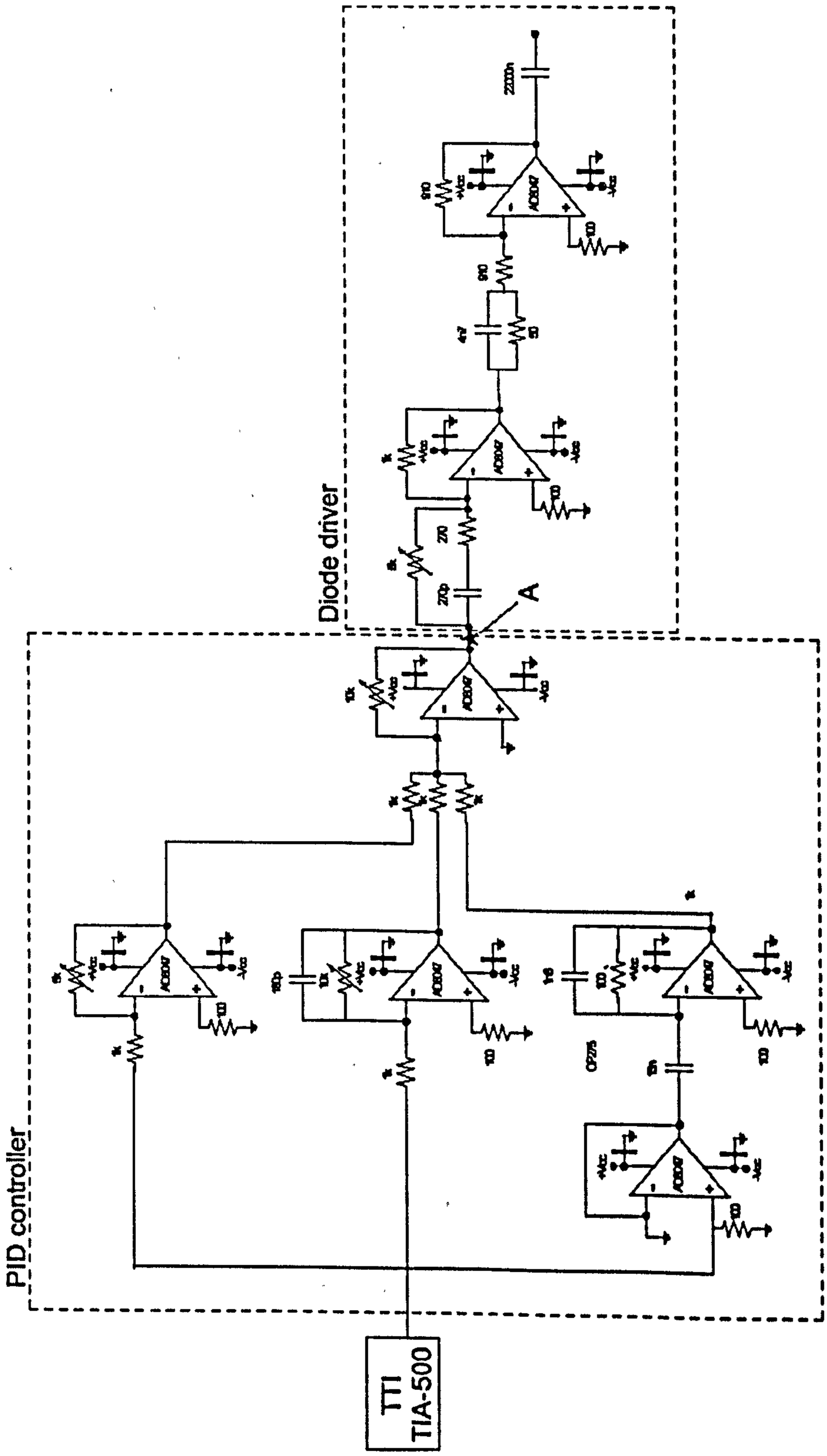

References

[7.1] A.D.Kersey, T.A.Berkoff, 1990 "Novel passive phase noise cancelling technique for interferometric fibre optic sensors" *Elec. Lett.* 26 (10) 640-641

[7.2] A.Dandridge, A.B.Tveten, 1981 "Noise reduction in fiber-optic interferometer systems" *Applied Optics* (20) 14 2337-2339

[7.3] A.Dandridge, A.B.Tveten, R.O.Miles, T.G.Giallorenzi, 1980 "Laser noise in fiber-optic interferometer systems" *Appl. Phys. Lett.* 37 (6) 526-528

[7.4] J.P.Dakin, C.A.Wade, M.L.Henning, 1984 "Novel optical fibre hydrophone array using a single laser source and detector" *Elec. Lett.* 20 (1) 53-54

[7.5] A.Dandridge, A.B.Tveten, 1981, "Electronic phase-noise suppression in diode lasers" *Elec. Lett.* 17 (25) 937-938

[7.6] A.D.Kersey, K.J.Williams, A.Dandridge, J.F.Weller 19989 "Characterisation of a diode laser-pumped Nd:YAG ring laser for fibre sensor applications" *Proc. of the 6th Int. Conf. on Optical Fiber Sensors* Springer-Verlag Berlin West Germany 172-178

[7.7] T.L.Boyd, D.Klemer, P.A.Leilabady, J.Noriega, M.Pessot, 1999 "A 1.55-μm solid-state laser source for DWDM applications" *J. Light. Tech.* 17 (10) 1904-1908

[7.8] R.S.Weis, A.D.Kersey, I.N.Duling, 1991 "Interferometric measurements of linewidth and phase noise of an Er-doped ring laser", Proc. of the 8th Int. Conf. on *Optical Fiber Sensors*, New York, 1991

[7.9] E.Snitzer, 1963 "Neodymium glass laser" *Proc. 3rd Int. Conf. on Solid State Lasers* 999-1019

[7.10] C.J.Koester, E.Snitzer, 1964 "Amplification in a fiber laser" *Appl. Optics* 3 (10) 1182-1186

[7.11] P.Urquart, 1988 "Review of rare earth doped fibre lasers and amplifiers" *IEE Proc.* vol. 135 Pt. J no. 6

[7.12] R.J.Mears, L. Reekie, I.M.Jauncey, D.N.Payne, 1987 "Low-noise erbium-doped fibre amplifier operating at 1.54 μm", *Elec. Lett.* 23 (19) 1026-1028

[7.13] P.Barnsley, P.Urquhart, C.Millar, M.Millar, M.Brierly, 1988 "Fiber Fox-Smith resonators: Application to single longitudinal-mode operation of fiber lasers" *J. Opt. Soc. Am. A*, 5 (8) 1339-1346

[7.14] P.R.Morkel, G.J.Cowle, D.N.Payne, 1990 "Travelling wave erbium fibre ring laser with 60 kHz linewidth" *Elec. Lett.* 26 (10) 632-634

[7.15] J.D.C.Jones, P.Urquhart, 1990 "An injection-locked erbium fibre laser", *Opt. Comm.*, 76 (1) 42-46

[7.16] I.M.Jauncey, L.Reekie, J.E.Towsend, D.N.Payne, C.J.Rowe, 1988 "Single-longitudinal-mode operation of a Nd^{3+} -doped fibre laser" *Elec. Lett.* 24 (1) 24-26

[7.17] G.A.Ball, W.W.Morey, W.H.Glenn, 1991 "Standing-wave monomode erbium fiber laser" *IEEE Phot. Tech. Lett.* 3 (7) 613-615

[7.18] G.A.Ball, W.H.Glenn, 1992 "Design of a single-mode linear-cavity erbium fiber laser utilizing Bragg reflectors" *J.Light. Tech.* 10 (10) 1338-1343

[7.19] G.A.Ball, G.Hull-Allen, C.Holton, W.W.Morey, 1993 "Low noise single frequency linear fibre laser" *Elec. Lett.* 29 (18) 1623-1625

[7.20] G.A.Ball, C.G.Hull-Allen, J.Livas, 1994 "Frequency noise of a Bragg grating fibre laser" *Elec. Lett.* 30 (15) 1229-1230

[7.21] G.A.Ball, C.E.Holton, G.Hull-Allen, W.W.Morey, 1994 "60 mW 1.5 micron single-frequency low-noise fiber laser MOPA" *IEEE Phot. Tech. Lett.* 6 (2) 192-194

[7.22] J.T.Kringlebotn, J.L.Archambault, L.Reekie, D.N.Payne, 1994 "Er^{3+}:Yb^{3+} -codoped fiber distributed-feedback laser" *Optics Letters* 19 (24) 2101-2103

[7.23] W.H.Loh, R.I.Laming, 1995 "1.55micron phase-shifted distributed feedback fibre laser" *Elec. Lett.* (31) 17 1440-1442

[7.24] M.Sejka, P.Varming, J.Hübner, M.Kristensen, 1995 "Distributed feedback Er3+-doped fibre laser" *Elec. Lett.* 31 (17) 1445-1446

[7.25] H.Storøy, B.Sahlgren, R.Stubbe, 1997 Single polarisation fibre DFB laser *Elec. Lett.* 33 (1) 56-58

[7.26] J.L.Philipsen, M.O.Berendt, P.Varming, V.C.Lauridsen, J.H.Povlsen, J.Hübner, M.Kristensen and B.Pálsdóttir, 1998 "Polarisation control of DFB fiber laser using UV-induced birefringent phase-shift" *Elec. Lett.* 34 (7) 678-679

[7.27] D.Yu Stepanov, J.Canning, L.Poladian, R.Wyatt, G.Maxwell, R.Smith, R.Kashyap, 1999 "Apodized distributed feedback fiber laser" *Optical Fiber Tech.* 5 209-214

[7.28] W.S.Man, Y.Z.Xu, H.Y.Tam, M.S.Demokan, 1999 "Frequency instability in Er/Yb fiber grating lasers due to heating by non-radiative transitions" *IEEE Phot. Tech. Lett.* 11 (11) 1390-1392

[7.29] T.Okoshi, K.Kikuchi, A.Nakayama, 1980 "Novel method for high resolution measurement of laser output spectrum" *Elec. Lett.* 16 (16) 630-631

[7.30] A.Yariv 1991 *Optical Electronics* 4th edn (Saunders College Publishing) sec. 10.7-10.8

[7.31] L.B.Mercer, 1991 "1/f frequency noise effects on self-heterodyne linewidth measurements", *J. Light. Tech.* 9 (4) 485-493

[7.32] Y.Qian, P.Varming, J.H.Povlsen and V.C.Lauridsen, 1999 "Dynamic noise responses of DFB fibre lasers in presence of pump power fluctuations" *Elec. Lett.* 35 (4) 299-300

[7.33] E.Rønnekleiv, 2001 "Frequency and intensity noise of single frequency fiber Bragg grating lasers" *Optical Fiber Techn.* 7 206-235

[7.34] B.F.Ventrudo, G.A.Rogers, G.S.Lick, D.Hargreaves, T.N.Demayo, 1994, "Wavelength and intensity stabilisation of 980nm diode lasers coupled to fibre Bragg gratings" *Elec. Lett.* 30 (25) 2147-2149 and ref [7.56] pp.50-51

[7.35] S.W.Løvseth, J.T.Kringlebotn, E.Rønnekleiv and K.Bløtekjær, 1999 "Fiber distributed-feedback lasers as acoustic sensors in air" *Applied Optics* 38 (22) 4821-4830

[7.36] A.Othonos, K.Kalli, 1999 *Fiber Bragg Gratings: Fundamentals and Applications in Telecommunications and Sensing* Artech House sec. 5.2.1

[7.37] J.L.Archambault, 1994 *Photorefractive gratings in optical fibre* PhD thesis, Univ. Southampton, sec. 2.5.4

[7.38] M.Yamada, K.Sakuda, 1987 "Analysis of almost-periodic distributed feedback slab waveguides via a fundamental matrix approach" *Applied Optics* 26 (16) 3474-3478

[7.39] P.Fritchhel, A.Jefferies, T.J.Kane, 1989 "Frequency fluctuations of a diode-pumped Nd:YAG ring laser" *Opt. Lett.* 14 (18) 993-995 and K.J.Williams, A.Dandridge, A.D.Kersey, J.F.Weller, A.M.Yurek, A.B.Tveten, "Interferometric measurement of low-frequency phase noise characteristics of diode laser-pumped Nd:YAG ring laser" *Elec. Lett.* 25(12) 774-775

[7.40] W.H.Glenn, 1989 "Noise in interferometric optical systems: an optical Nyquist theorm" *IEEE J. Quant. Elec.* 25 (6) 1218-1224

[7.41] K.H.Wanser, 1992 "Fundamental phase noise limit in optical fibers due to temperature fluctuations" *Elec. Lett.*, 28 (1) 53-54

[7.42] K.H.Wanser, A.D.Kersey, A.Dandridge, 1993, "Measurement of fundamental thermal phase fluctuations in optical fibre" *Proc. 9th Int. Conf. on Optical Fiber Sensors*, IROE-CNR Firenze Italy 255-258

[7.43] C.H.Henry, 1982 "Theory of the linewidth of semiconductor lasers" *IEEE J. Quant. Elec.* QE-18 (2) 259-264

[7.44] T.C.Ralph, E.H.Huntington, C.C.Harb, B.C.Buchler, P.K.Lam, D.E.Mcclelland, H.A.Bachor, 1999 "Understanding and controlling laser intensity noise" *Optical and Quantum Electronics* 31 583-598

[7.45] I.Freitag, H.Welling, 1994 "Investigation on amplitude and frequency noise of injection locked diode pumped Nd-YAG lasers" *App. Phys.* B 58 (6) 537-543

[7.46] C.C.Harb, T.C.Ralph, I. Freitag, E.H.Huntington, H.A.Bachor, 1996 "Intensity noise properties of injection locked lasers" *Physical Review A* 54 (5) 4370-4382

[7.47] C.C.Harb, M.B.Gray, H.A.Bachor, R.Schilling, P.Rottengatter, I.Freitag, H.Welling, 1994 "Suppression of the intensity noise in diode-pumped neodymium:YAG nonplanar ring laser" *IEEE J. Quant. Elec.* 30 (12) 2907-2913

[7.48] B.C.Buchler, E.H.Huntington, C.C.Harb, T.C.Ralph, 1998 "Feedback control of laser intensity noise" 57 (2) 1286-1294

[7.49] Y.Yamamoto, S.Machida, 1992, "Shot noise limited low frequency intensity noise of Nd:YAG laser" *Jpn. J.Appl. Phys.* 31 1241

[7.50] H.M.Wiseman, G.J.Milburn, 1994 "All-optical versus electro-optic quantum-limited feedback" *Phys. Rev. A* 49 (5) 4110-4125

[7.51] S.Taccheo, P.Laporta. O.Svelto, G.De Geronimo, 1998 "Theoretical and experimental analysis of intensity noise in a codoped erbium-ytterbium glass laser" *Appl. Phys. B* 66 19-26

[7.52] M.Marano, S.Longhi, P.Laporta, 1999 "Optoelectronic feedback loop for intensity noise suppression in a high bit rate FM operated Er:Yb laser" *Elec. Lett.* 35 (21) 1877-1878

[7.53] A.C.McDonald, H.Lowe, 1981, *Feedback and Control Systems* Reston Publishing Company, Prentice Hall, Chapter 8

[7.54] D.L.R.Jacobs, *Intorduction to control theory 2nd edn.* Oxford Science Publication

[7.55] A.Dandridge, L.Goldberg, 1982 "Current-induced frequency modulation in diode lasers" *Elec. Lett.*, 18 (7)

[7.56] J. Dakin and B Culshaw (Edt), 1996 *Optical Fibre Sensors: Components and Subsystems (v3)* Artech House, Boston

[7.57] K.Petermann, 1991, *Laser diode modulation and noise* Kluwer Academic Publishers, sec. 2.3.4

[7.58] H.Simonsen, J.Henningsen, S.Søgaard, "DFB fiber lasers as optical wavelength standards in the 1.5-μm region" *IEEE Trans. on Instr. and Meas* 50 (2) 482-485

[7.59] M.K.Davis, M.J.Fdigonnet, R.H.Pantell, 1998 "Thermal effects in doped fibers" *J.Light.Tech.* 16 (6) 1013-1023

[7.60] E.Rønnekleiv, S.Løvseth, 1999 "Stability of distributed fiber lasers with optical feedback" *Proc. 13th Int. Conf. on Optical Fiber Sensors* SPIE 3746 466-469

[7.61] K.P.Koo, A.D.Kersey, A.Dandridge, G.Ball, 1995 "Measurement of the thermal-noise-limited frequency stability of a fiber-optic Bragg grating laser" *OFC* , Thursday afternoon, OSA Tech. Dig. vii+438 297-8

[7.62] O.Hadeler, M.N.Zervas, 2000 "Application of a DFB fibre laser temperature sensor for characterizing pump induced temperature distributions along another DFB fibre laser" *Proc. 14th Int. Conf. Optical Fiber Sensors* SPIE 4185 Venice, Italy, *142-145*

[7.63] E.Desirvire, J.R.Simpson, P.C.becker, 1987 "High-gain erbium-doped traveling-wave fiber amplifier" *Optics Letters* 12 (11) 888

[7.64] Ref [7.30] sec. 10.6

Chapter 8

INTENSITY NOISE CHARACTERISTICS OF ERBIUM DOPED FIBRE BRAGG GRATING LASERS†

Abstract- In this chapter we investigate the intensity noise characteristics of erbium-doped DFB fibre lasers. We present an analytical model for the dynamics of the intensity noise in a linear fibre laser. We then describe the fabrication and characterisation of seven DFB fibre lasers and discuss their intensity noise characteristics with reference to our analytical model. Overall we find good agreement between the intensity noise characteristics of the lasers and that predicted by our model. In particular we find the intensity noise at frequencies close to the relaxation oscillation peak to be dominated by cavity loss modulation and we discuss possible origins of this mechanism.

8.1 Introduction

In the previous chapter we developed a technique based on active electronic feedback to suppress the relaxation oscillation peak induced intensity noise, which is necessary to achieve high-resolution interferometric measurements when the fibre laser is used as the interrogating source. In this chapter we shall investigate the underlying mechanisms that give rise to the relaxation oscillation and experimentally investigate the dynamics of the DFB fibre laser; in particular the dependence of the relaxation oscillation frequency, the relaxation oscillation quality factor, Q (i.e. relative bandwidth of the relaxation oscillation peak) and the relative amplitude of the relaxation oscillation peak on the grating and doped fibre parameters. An improved understanding of the mechanisms giving rise to intensity noise may allow us to optimise the design of the EFL in order to minimise intensity noise.

The intensity noise of any laser is dominated by the relaxation oscillation frequency. In the DFB erbium fibre laser (EFL), this usually occurs at around a few hundred kHz. The relaxation

†A re-edited version of this chapter will be submitted for publication in the IEEE J. Quantum Electronics.

oscillation frequency arises from the dynamic energy exchange process between the injected pump field and the laser signal field, the spectrum of which usually resembles an underdamped harmonic oscillator. Pump perturbations drive the relaxation oscillation and increase the intensity noise; however, in the absence of pump perturbations such as when the pump is operated in a sub-quantum regime (referred to as a *squeezed state*), the relaxation oscillation still occurs due to vacuum fluctuations. We shall find that in the DFB EFL other mechanisms are present, other than pump power perturbations, which generally result in an increase in the observed levels of relative intensity noise (RIN).

A number of groups have investigated the dynamic properties of fibre lasers. Much of the early work involved understanding the underlying mechanisms giving rise to self-pulsation, which we shall discuss further in section 7.2. Other groups have developed models to predict the spectral shape of the relative intensity noise [8.1-6]. However, only the models presented in [8.3,4,6] include the effect of cavity loss modulation, which we shall find makes a very significant contribution to the observed RIN spectrum. Only limited experimental data for the DFB EFL has been presented in [8.3]. The data presented in [8.4] was for an Er:Yb glass laser.

The chapter is set out as follows. In section 8.2 we describe our analytical model for the linear cavity fibre laser. In section 8.3 we describe the experimental characterisation of seven DFB fibre lasers. In section 8.4 we present the results from our characterisation experiments and use our analytical model to explain the observed levels of RIN. Finally, in section 8.5 we summarise our conclusions.

8.2 Theory of Intensity Noise

In order to accurately model the dynamic properties of the DFB EFL, it is necessary to numerically solve the laser rate equations combined with coupled mode theory, in order to take into account the spatial dependence of the photon density and excited state population.

We described above how, in an ideal laser, the RIN is determined by the pump perturbations driving the relaxation oscillation. However, in the DFB EFL a number of other effects must be included in order to develop a comprehensive model. We shall assume that the laser is operating in its fundamental mode. Operation of the laser with higher-order modes present results in high RIN levels due to the short photon lifetime and high sensitivity to back

reflection and should generally be avoided. We shall also assume that pump depletion is small and discuss the effects that have been found to influence the dynamic behaviour of the DFB EFL:

(i) *Spatial hole burning (SHB), local and global: Global* spatial hole burning occurs due to the spatial dependence of the photon density centrally located about the phase-shift. In the case of the fundamental mode, the peak intensity occurs at the phase-shift and the intensity falls off exponentially on either side of the phase-shift [8.7]. As a result, the excited state population becomes depleted in the region of highest photon density. *Local* spatial hole burning occurs due to the standing wave pattern formed by the signal field within the periodic structure, since the phase is locked to the grating. Depletion of the excited ion population occurs in the regions corresponding to antinodes of the signal standing wave pattern, and a gain-grating is formed. The formation of a gain-grating is generally a weaker effect than that observed in semiconductor lasers due to carrier diffusion. These two effects cause a reduction of the round trip gain and a corresponding increase in the saturation power[17]. The presence of strong SHB will also result in a reduction in the relaxation oscillation frequency, f_{RO}.

(ii) *Amplified spontaneous emission (ASE):* ASE seeds the lasing process and gives rise to the fundamental limit to the laser linewidth (the Schawlow-Towns limit). It's primary effect is to reduce the excited state population, n_2 and is characterised by its associated lifetime, τ_2. It may also contribute to the loss modulation mechanism we discuss later.

(iii) *Unbleachable loss:* This refers to any loss mechanism that is not dependent on the pump or signal intensity over typical practical parameter ranges. Examples are coupling losses such as splice losses which give rise to loss of pump and signal photons and fibre attenuation which can cause significant reduction in the signal photon density. The intrinsic attenuation of photosensitive fibres is generally higher than that of standard telecom fibre, such as SMF-28, particularly when the fibre has been hydrogen or deuterium loaded to increase its photosensitivity [8.8]. Erbium clusters (groups of Er^{3+}

17 Recall that saturation power is defined as the pump power required to achieve equal population of ground and excited states.

ions participating in inhomogeneous ion-ion upconversion) have also been suggested as an unbleachable loss mechanism and give rise to a reduction in slope efficiency.

(iv) *Bleachable losses*: These are loss mechanisms that exhibit a dependence on pump intensity and act as saturable absorbers. Proposed mechanisms giving rise to saturable absorber states are UV induced excited state lifetime quenching [8.9] and homogenous co-operative upconversion due to ion-pairs in high ion concentration fibres [8.12]. An excited state lifetime quenching effect has been observed in deuterium loaded Er^{3+}:Yb^{3+} fibre after UV exposure [8.9]. Although the mechanism giving rise to this effect is not well understood, its presence causes a loss of an excited ion that would have otherwise contributed to the population inversion and hence an increase in the laser threshold. Many early fibre lasers were found to exhibit self-pulsations [8.10], an effect linked to the presence of ion-pairs in highly doped fibres [8.11-13], which were shown to act as saturable absorbers [8.14]. In highly doped fibres, the spacing between adjacent Er^{3+} ions becomes sufficiently small such that they interact, in a process know as co-operative ion-ion upconversion. This process can be explained with reference to the energy level diagram in fig. 8.1. When two closely spaced ions are excited to the ${}^4I_{13/2}$ level, transfer of energy from one ion to the other is likely to occur, resulting in one excited ion (the acceptor) being raised (or upconverted) to the ${}^4I_{9/2}$ level and the other ion (the donor) returning to the ground state. The upconverted ion then rapidly decays non-radiatively back to the ${}^4I_{13/2}$ level. The result is an effective loss of one excited ion that would have contributed to the population inversion. This process occurs more rapidly than the time taken for the population inversion to recover resulting in spiking or self-pulsation of the laser. A number of techniques to suppress self-pulsations were demonstrated such as resonant pumping [8.15-16], auxiliary pumping [8.17], phase-conjugated optical feedback [8.18] and Yb^{3+} codoping [8.19-20]. However, the reduction in ion clustering by Al co-doping of the erbium-doped fibre became an effective and simple technique to reduce self-pulsations [8.21].

(v) *Grating imperfections*: It has been shown in [8.22] that grating imperfections can cause an increase in the threshold of the fundamental mode and a reduction in threshold of higher order modes. Grating imperfections will give rise to a reduction in signal photon

density and also cause a reduction in slope efficiency. According to [8.22], grating imperfections such as linear, quadratic chirp and discrete phase errors will all cause an increase in the fundamental mode threshold and a decrease in the higher-order mode threshold. However, possibly the most significant is due to random fluctuations in the fibre diameter, which was shown to cause a significant decrease in higher-order mode threshold and increase in the fundamental mode threshold.

(vi) *Dual-polarisation modes:* The small amount of birefringence that exists in standard telecom optical fibre results in the possible existence of two orthogonal polarisation modes within the DFB cavity. They are typically spaced around a few GHz apart in frequency and may exhibit different thresholds and hence different relaxation oscillation frequencies. Suppression of one polarisation mode is possible by writing a polarisation dependent grating or a polarisation dependent phase-shift by post-processing [8.23] or by twisting the fibre [8.24].

(vii) *Back-reflection:* Randomly phased back-reflection into the laser cavity may give rise to laser instability and hence an increase in the RIN. The effects of back-reflection into the EFL have been investigated in [8.25]; however, we shall assume here that sufficient isolation is present to suppress back-reflection.

(viii) *Non-linear refractive index*: The peak intensity in a DFB fibre laser occurs around the centre phase-shift and in some cases can be sufficiently high to induce nonlinearity in the refractive index. Generally, in the EFL, the peak intensity is not high enough for this effect to be significant and we include it here only for completeness; however, in an Er^{3+}:Yb^{3+} fibre laser, the peak intensity is generally an order of magnitude higher. It was suggested in [8.26] that this effect would lead to self-pulsation and deterministic chaos for sufficiently high nonlinear refractive index.

To model the dynamic properties of the DFB EFL we choose an analytical model based on the laser rate equations, which allows us to determine analytical expressions for the important laser parameters. This approach prevents us from incorporating a number of effects peculiar to the DFB EFL such as spatial hole burning and grating imperfections. However, what we loose in accuracy we gain in physical insight, since we are able to determine closed form expressions and

hence derive the dependencies on the various laser parameters. The approach we have chosen has also been applied to Er^{3+}:Yb^{3+} glass lasers and demonstrated good accuracy [8.4].

Our primary aim is to determine the most significant effects giving rise to the observed levels of RIN and for this reason we include only the effects of pump perturbations driving the relaxation oscillation, spontaneous emission and a cavity loss modulation mechanism in our model. For now, we shall assume a cavity loss modulation mechanism is present and not concern ourselves with its cause. In the results section we shall discuss possible causes of this effect and also discuss the effects of neglecting SHB and bleachable losses.

The rate equation approach will break down when the laser intensity noise levels are very low and approach the quantum limit. However, for most practical lasers this is not the case and noise levels are generally much higher than the quantum limit, thus this approach should provide an accurate description. We assume that the laser active medium is homogenously broadened and that the erbium medium can be modelled as a quasi 2-level system, which has been shown to be a good approximation for erbium pumped at 980nm or 1480nm [8.27], although we shall restrict our discussion here to 980nm pumping. The rate equations can be derived from the energy level diagram shown in fig. 8.1. The parameters we shall use in our model are summarised in table 8.1.

Table 8.1: Definition of terms

Symbol	*Unit*	*Value*	*Description*
W	s^{-1}		Absorption/emission rate
τ_3	s	10 μs	$^4I_{11/2}$ lifetime
τ_2	s	10.5 ms	$^4I_{13/2}$ lifetime
n_1			Steady-state fractional ground-state ion density
n_2			Steady-state fractional excited ion density
q_0	m^{-3}		Steady-state cavity signal photon density
W_p	s^{-1}		Steady-state pump rate
γ_0			Cold-cavity loss (i.e. cavity loss neglecting loss due to active medium.)
$\delta n_2(t)$	m^{-3}		Excited ion density perturbation
$\delta q(t)$	m^{-3}		Cavity signal photon density perturbation
$\delta W_p(t)$	m^{-3}		Pump rate perturbation
$\delta\gamma(t)$			Cavity loss perturbation

Table 8.1 (cont): Definition of terms

Symbol	*Unit*	*Value*	*Description*
c	$m.s^{-1}$	3×10^{8}	Light velocity in a vacuum
n		1.465	Fibre core effective refractive index
w	m		Mode-field radius
$\Gamma_{p/s}$			Pump/signal overlap factor
N_0	m^{-3}	6.9×10^{24}	Total ion density
σ_1	m^2		Pump absorption cross-section
σ_2	m^2		Signal emission/absorption cross-section
τ_c	s		Cavity photon lifetime
ω_{RO}	rad.Hz		Relaxation oscillation angular frequency
P_p	mW	100	Pump power
P_{s-out}	mW		Signal output power
M			Effective mirror transmittance
$A_{p/s}$	m^2	πw^2	Pump/signal mode effective area
L_e	m	$1/\kappa$	Effective cavity length
κ	m^{-1}	151	Grating coupling coefficient
L	m	50	Grating length
h	J.s	6.63×10^{-34}	Planck's constant
$\nu_{p/s}$	Hz		Pump/signal frequency
λ_p	nm	980	Pump wavelength
g_0			Small-signal gain

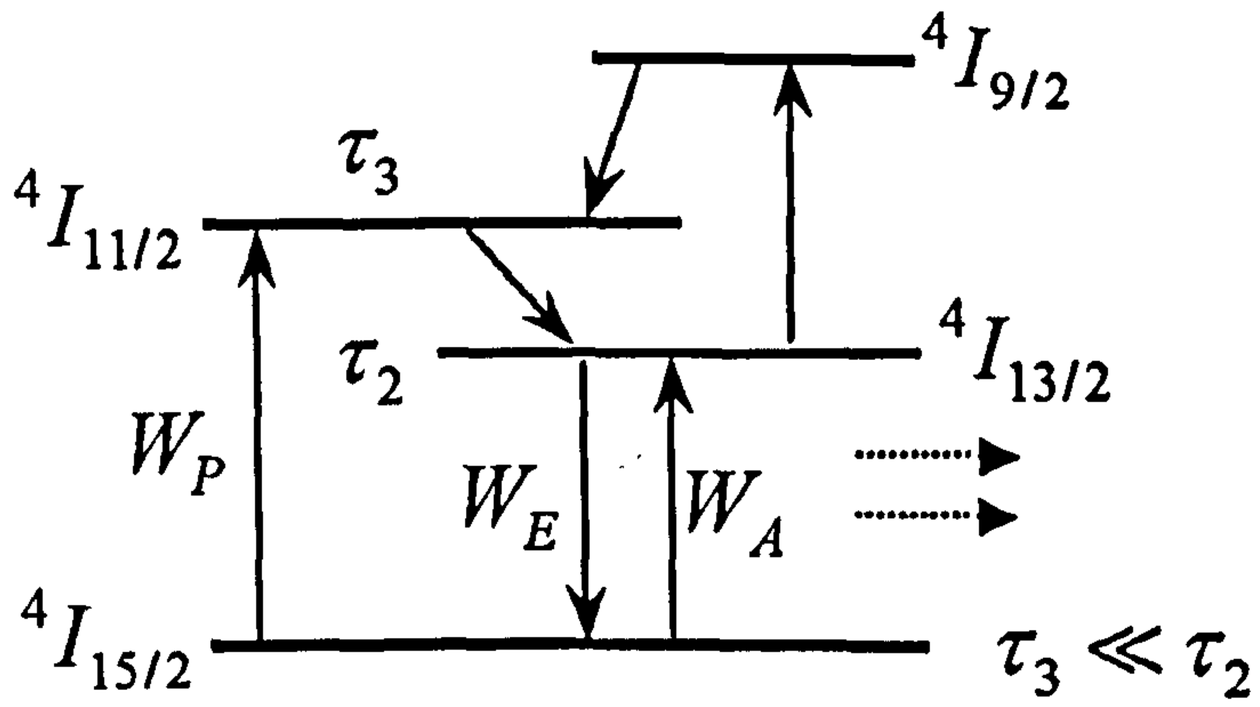

Figure 8.1: Energy level diagram for Er^{3+} including upconversion transition

Referring to fig. 8.1, an incident 980nm pump photon causes a transition from the ground state, $^4I_{15/2}$ to the $^4I_{11/2}$ level. This is followed by a rapid, non-radiative relaxation to the metastable

$^4I_{13/2}$ level and either a stimulated or spontaneous radiative relaxation back to the ground state. The rates of these three transitions are denoted W_p, W_E and $1/\tau_2$ respectively, where τ_2 is the metastable level lifetime. For a pump wavelength of 980nm (or 1480nm), and for a silica host glass, pump excited state absorption is generally negligible. However due to the large absorption cross-section at the signal wavelength, a direct transition from the ground state to the metastable state through the absorption of a signal photon is likely. The rate of this transition is denoted, W_A. Thus, the rate equations in terms of the fractional excited ion density, n_2, and cavity signal photon density, q, are given by [8.28],

$$\frac{dn_2}{dt} = (1-n_2)(W_p + W_A) - n_2(W_E + 1/\tau_2) \tag{8.1}$$

$$\frac{dq}{dt} = W_E N_0 n_2 - (1-n_2) W_A N_0 - \frac{q}{\tau_c} \tag{8.2}$$

where the terms on the right-hand-side (r.h.s.) in (8.1) correspond to the increase in excited ion density due to pump absorption, the increase in excited ion density due to ground state signal absorption and the decrease in excited ion density due to stimulated and spontaneous emission at the signal wavelength, respectively. The terms on the r.h.s. in (8.2) correspond to the increase in photon density due to stimulated emission, decrease in photon density due to ground state absorption at the signal wavelength, and decrease in photon density due to cavity loss (τ_c is the cavity photon lifetime). To simplify the analysis, we shall assume that the signal absorption and emission rates are equal ($W_A = W_E$), thus (8.1) and (8.2) become,

$$\frac{dn_2}{dt} = W_p(1-n_2) - qr_q(2n_2 - 1) - \frac{n_2}{\tau_2} \tag{8.3}$$

$$\frac{dq}{dt} = qN_0 r_q(2n_2 - 1) - \frac{q}{\tau_c} \tag{8.4}$$

where we have substituted $W_A = W_E = r_q q$ and the pump rate, $W_p = \Gamma_p P_p \sigma_1 / h\nu_p A_p$. N_0 is the total ion concentration, σ_1 and σ_2 are the pump absorption and signal

absorption/emission cross-sections respectively, A_p is the effective area of the pump mode, c is the light velocity in a vacuum, n is the effective core refractive index, Γ is a mode overlap factor and $r_q = c\sigma_2 / n$.

The steady-state solutions of the rate equations can be derived by setting $d/dt = 0$ in (8.3) and (8.4) and solving for n_2 and q such that,

$$n_2 = \frac{1}{2}\left(1+\frac{1}{N_0 r_q \tau_c}\right) \tag{8.5}$$

$$q = \frac{N_0\tau_c}{2}\left(W_p\left(1-\frac{1}{N_0 r_q \tau_c}\right)-\frac{1}{\tau_2}\left(1+\frac{1}{N_0 r_q \tau_c}\right)\right) \tag{8.6}$$

The cavity photon lifetime is defined as [8.29],

$$\tau_c = nL_e / c\gamma_0 \tag{8.7}$$

where γ_0 is the logarithmic cavity loss. By defining an effective mirror transmittance, M, and assuming that cavity loss is due to mirror transmittance losses only, then $\gamma_0 = -\log_e(1-M)$ and $\gamma_0 \approx M$ for $M \ll 1$. The output power is therefore,

$$P_{s-out} = q\Gamma_s A_s \gamma_0 h\nu_s c / n \tag{8.8}$$

and the threshold pump power is given by,

$$P_{p-th} = \frac{h\nu_p A_p}{\Gamma_p \sigma_1 \tau_2}\frac{\left(1+1/N_0 r_q \tau_c\right)}{\left(1-1/N_0 r_q \tau_c\right)} \tag{8.9}$$

We note here that $P_{p-th} = 0$ if we neglect spontaneous emission. Finally, the slope efficiency,

$$k_{slope} = \frac{dP_{s-out}}{dP_p} = \Gamma_s\Gamma_p \frac{A_s}{A_p}\frac{N_0 L_e \sigma_1}{2}\frac{\nu_s}{\nu_p}\left(1-\frac{1}{N_0 r_q \tau_c}\right) \tag{8.10}$$

Thus the slope efficiency is proportional to the total ion concentration, N_0, effective cavity length, L_e, pump cross-section, σ_1 and ratio of the laser signal and pump frequencies, ν_s/ν_p.

To determine the dynamic behaviour of n_2 and q in the presence of small perturbations of the pump rate and cavity loss such that,

$$W_p(t) = W_p + \delta W_p(t) \qquad |\delta W_p(t)| \ll W_p \qquad (8.11)$$

$$n_2(t) = n_2 + \delta n_2(t) \qquad |\delta n_2(t)| \ll n_2 \qquad (8.12)$$

$$q(t) = q_0 + \delta q(t) \qquad |\delta q(t)| \ll q_0 \qquad (8.13)$$

$$\gamma(t) = \gamma_0 + \delta\gamma(t) \qquad |\delta\gamma(t)| \ll \gamma_0 \qquad (8.14)$$

we substitute (8.11)-(8.14) into (8.3) and (8.4), and remove the steady-state terms [8.30]. Taking only first-order terms, the expression for the signal photon perturbations due to pump power and cavity loss perturbations is,

$$\frac{d^3\delta q}{dt^3} + A_1\frac{d^2\delta q}{dt^2} + A_4A_3\frac{d\delta q}{dt} = A_2A_4\frac{d\delta W_p}{dt} - A_1A_5\frac{d\delta\gamma}{dt} - A_5\frac{d^2\delta\gamma}{dt^2} \qquad (8.15)$$

The affect on the signal photon density due to pump perturbations and cavity loss are independent from each other and therefore (8.15) can be separated into two equations; one relating the signal photon density, δq_{W_p}, to the pump fluctuations and one relating the signal photon density, δq_γ, to the cavity loss such that,

$$\frac{d^3\delta q_{W_p}}{dt^3} + A_1\frac{d^2\delta q_{W_p}}{dt^2} + A_4A_3\frac{d\delta q_{W_p}}{dt} = A_2A_4\frac{d\delta W_p}{dt} \qquad (8.16)$$

$$\frac{d^3\delta q_\gamma}{dt^3} + A_1\frac{d^2\delta q_\gamma}{dt^2} + A_4A_3\frac{d\delta q_\gamma}{dt} = -A_1A_5\frac{d\delta\gamma}{dt} - A_5\frac{d^2\delta\gamma}{dt^2} \qquad (8.17)$$

For clarity we have introduced five constants, A_1 to A_5 which are dependent on the laser parameters and are defined in Appendix 8.1. Taking the Laplace Transform of (8.16) and (8.17) we can determine the closed loop transfer functions for the photon density fluctuations assuming harmonic perturbations. Thus, by using the fact that $d^n/dt^n = s^n$ where $s = i2\pi f$, (8.16) and (8.17) can be expressed as,

$$H_p(f) = \frac{\delta q_{W_p}/q_0}{\delta W_p/W_p} = \frac{A_2' A_4}{s^2 + A_1 s + A_4 A_3} \tag{8.18}$$

$$H_l(f) = \frac{\delta q_\gamma/q_0}{\delta\gamma/\gamma_0} = \frac{A_5'(A_1 + s)}{s^2 + A_1 s + A_4 A_3} \tag{8.19}$$

where $H_p(f)$ and $H_l(f)$ correspond to transfer functions for the pump perturbations and loss modulation respectively. Note here that the parameters q_0 and γ_0 have been absorbed into two new parameters A_2' and A_5'. Also, we note here that (8.16) is, of course, the equation describing a damped, forced harmonic oscillator[18]. It can be shown that the natural frequency is the relaxation oscillation frequency given by,

$$\omega_{RO} = A_1^{1/2} = \left[W_p\left(N_0 r_q - \frac{1}{\tau_c}\right) - \frac{1}{\tau_2}\left(N_0 r_q + \frac{1}{\tau_c}\right)\right]^{1/2} \tag{8.20}$$

In the case of the DFB fibre laser, with a centrally located phase-shift in a uniform grating, the effective mirror transmittance, $M \simeq 4\exp(-\kappa L)$ when $\kappa L \gg 1$, where L is the grating length, and effective cavity length, $L_e \simeq 1/\kappa$ (cf. sec. 7.2). The small-signal gain, g_0, assuming unity inversion, is given by $\Gamma_s N_0 \sigma_2 L_e$ and if we assume the cavity loss to be due only to loss through the mirrors, a further simplification for ω_{RO} can be made since $g_0/\gamma_0 \gg 1$ when $\kappa L > 6$ and assuming the strong pump regime. In this case (8.20) becomes,

$$\omega_{RO} = \left(W_p N_0 r_q\right)^{1/2} \tag{8.21}$$

---

[18] This is the same form of the equation as that used to describe the motion of the flexural disk accelerometer in chapter 3.

Thus, the relaxation oscillation frequency is proportional to $(W_p)^{1/2}$ which agrees with our measurement on IFL1221, shown in fig. 7.4(i). The RIN is therefore given by,

$$RIN(f) = \left|H_p(f)\right|^2 \frac{S_{\delta W_p}}{W_p^2} + \left|H_l(f)\right|^2 \frac{S_{\delta\gamma}}{\gamma_0^2} \qquad (8.22)$$

where $S_{\delta W_p}$ and $S_{\delta\gamma}$ are the power spectral density of pump and loss perturbations respectively. The magnitude and phase of $H_p(f)$ and $H_l(f)$ are plotted in fig. 8.2. Both contribute to the total RIN via (8.22). The values of the parameters used to generate fig. 8.2 are given in table 8.1.

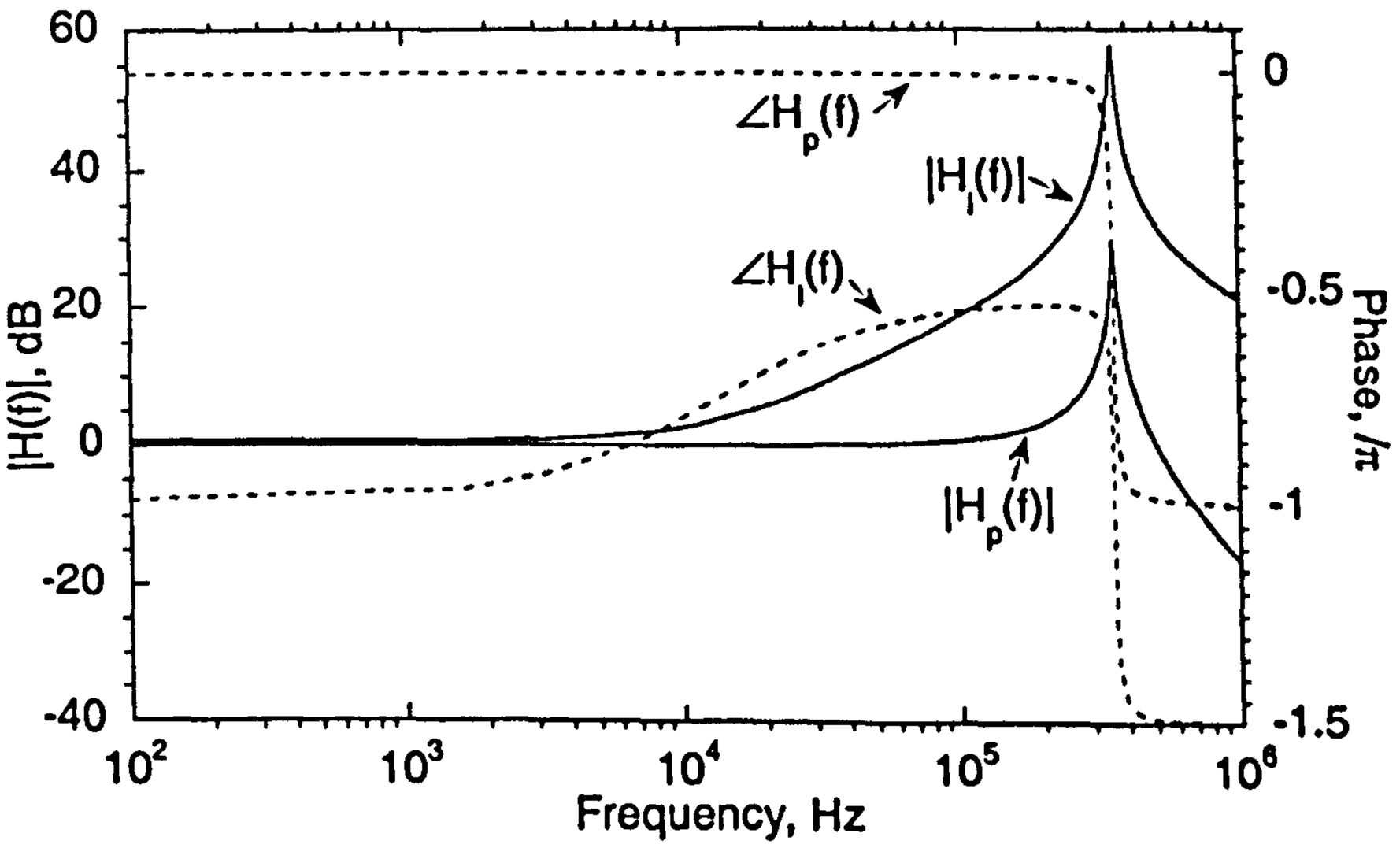

Figure 8.2: Pump perturbation and loss modulation transfer functions. In addition to the parameter values stated in table 8.1 we have also used $\Lambda_{s/p} = 33\mu m^2$

Thus, the presence of loss modulation is to significantly increase the RIN at frequencies around the relaxation oscillation and broaden the RIN peak.

8.3 Experimental Details

8.3.1 Laser fabrication

The lasers were written into three fibres with different dopant concentrations and slightly different core compositions and the measured fibre characteristics are presented in table 8.2[19]. The lasers were written using two techniques: (i) lasers 1,2,3 and 7 were written using a Sagnac ring interferometer [8.31], which produced emission wavelengths of around 1534nm and (ii) lasers 4,5 and 6 were written with a holographic phase mask, which produced emission wavelengths around 1555nm. It should be noted that gratings written interferometrically are likely to exhibit increased phase errors due to mechanical instabilities during the writing process, compared with the same grating written using a holographic phase mask. This is expected to lead to reduced threshold levels for higher order modes [8.22] resulting in a reduced mechanical stability of the laser resonator[20]. (By stability we refer to the tendency of a laser to exhibit multi-longitudinal mode output, instead of single-longitudinal mode output, and the resulting fluctuations in output power due to gain competition between modes). The lasers were constructed by removing the coating from a section of doped fibre approximately 5mm longer than the grating length (60-115mm) and splicing lengths of Corning SMF28™ (normal dispersion matched cladding) fibre onto each end of the doped fibre. An unapodised grating with a centrally located $\pi/2$ phase-shift was then formed in the uncoated region of doped fibre. Applying no apodisation to the grating profile is likely to result in reduced modal stability of the laser for increasing κL value of the grating (since the higher order mode thresholds generally reduce with increasing κL value). Apodisation or gain-tuning has been demonstrated to suppress higher-order modes [8.32-33].

---

[19] The lasers were manufactured at the University of Sydney by M. Englund and formed part of a TTCP collaboration between DERA and DSTO, Australia. The exact composition of the doped fibres is not known although the compositions of EDF1 and 2 are believed to be similar. Therefore, we have characterised the spectral absorption properties of these two fibres and we use this data in our analysis.

[20] In the $\pi/2$-phase-shifted DFB fibre laser, the mode spatially located around the center phase-shift has the lowest threshold power and is referred to as the fundamental mode. Modes corresponding to resonances on the side-lobes of the grating (cf. fig. 7.2) are referred to as higher-order and generally have threshold levels higher than the fundamental (cf. sec. 7.1).

Table 8.2: Doped fibre properties

Fibre type	NA	Mode field diameter @ 1550 (980) nm	Core diameter[21] (estimated)	Absorption at 980 nm ±0.05dB	Absorption at 1535 nm ±0.05dB	Estimated dopant conc. ±15%†	Pump cross-section, σ_2, at 980nm ±15%
		μm	μm	$dB.m^{-1}$	$dB.m^{-1}$	m^{-3}	m^2
EDF1	0.18	8.4 (4.7)	10.2	12	17	8.5×10^{24}	3.2×10^{-25}
EDF2	0.20	6.5 (4.3)	7.7	9	14	6.9×10^{24}	2.9×10^{-25}
EDF3	--	--	--	--	3	--	--
SMF-28	0.11	10.5	9.0	--	--	--	--

† Parameters used in the calculation were λ_c=1535nm, τ_2=10.5ms

8.3.2 Spectroscopy of the doped fibre and grating strength

Accurate determination of the absorption and emission cross-sections of the doped fibre is generally a complex process, and several techniques are described in [8.34]. We have used a technique to obtain approximate values for the cross-sections and dopant concentrations for EDF1 and 2, based on a measurement of the small-signal absorption and estimating two key parameters. Due to the similarity in the core composition of the two fibres characterised, we believe that this technique will provide sufficient relative accuracy; however, the absolute accuracy of the technique is dependent on the accuracy of the estimated parameters. Accurate measurement of the absorption of the doped fibres is easily achieved due to the high dopant concentration, thus requiring only a short length (~0.5m) of fibre to carry out the measurement and such that background loss can be neglected. The absorption is measured by injecting the output from a tuneable laser into the doped fibre and measuring the spectral dependence of the absorbed power. The small-signal gain can then be estimated using the McCumber relationship [8.34][22],

---

[21] Core diameter calculated from the mode field diameter and NA assuming a Myslinski Gaussian mode shape approximation where the mode field diameter, $w=2a\left(0.761+1.237V^{-3/2}+1.429V^{-6}\right)$ and $V=2\pi aNA/\lambda$ and a is the core radius [8.41].

[22] In an ideal, two-level laser system with discrete degenerate energy levels, the absorption and emission cross-sections are equal. However, in many practical cases, the level degeneracy is lifted due to the presence of an external electric field (originating from the host material). Each level now consists of a series of sublevels, forming a multiplet. In this case, the absorption and emission cross-sections will differ depending on the degeneracy of each level. The Ladenburg-Fuchtbauer relationship can be used to relate the absorption and emission cross-sections in this case [8.35]; however, its derivation relies on the key assumption that the sublevels are equally populated. In the case of erbium-doped silica glass, the levels are Stark split and the energy band occupied by each multiplet (300-400 cm^{-1}) greatly exceeds the mean thermal energy, kT (200 cm^{-1}). Thus, the levels are no longer equally populated. In this case the McCumber theory applies, since its derivation relies only on the

$$g(\nu)=\alpha(\nu)\exp\left((\varepsilon_c-h\nu)/kT\right) \tag{8.23}$$

where $\varepsilon_c\,(=hc/\lambda_c)$ is the free energy (corresponding to the wavelength at which $g(\nu)=\alpha(\nu)$), T is the temperature, k is Boltzmann's constant and the small-signal gain, $g(\nu)$, and absorption, $\alpha(\nu)$, coefficients are related to the cross-sections by $g(\nu)=\Gamma N_0\sigma_e(\nu)$ and $\alpha(\nu)=\Gamma N_0\sigma_a(\nu)$ respectively. N_0 is the total ion concentration and Γ is the overlap integral between the signal mode and the ion concentration profile, and is approximated by $\Gamma(\lambda)=1-\exp\left(-2b^2/w^2a^2\right)$ where we assume a uniform transverse ion concentration, a is the fibre core radius, b is the Er^{3+} radius and w is the mode field radius. This yields values of $\Gamma_p=1$ and $\Gamma_s=0.95$ for EDF1 and $\Gamma_p=1$ and $\Gamma_s=0.94$ for EDF2. We shall assume the free energy wavelength, λ_c is equal to 1535nm, which is typical for silica based erbium-doped fibre. The ion concentration can then be obtained from the relationship [8.35],

$$\frac{1}{\tau_2}=\frac{8\pi n^2}{c^2}\int\nu^2\frac{g(\nu)}{\Gamma N_0}d\nu \tag{8.24}$$

where τ_2 is the excited state (or metastable) lifetime, n is the core effective refractive index and c is the light velocity in a vacuum. The $^4I_{13/2}$-$^4I_{15/2}$ transition in a glass host is nearly 100% radiative (assuming no clustering is present), therefore the metastable lifetime can be obtained by observing the fluorescence decay from a length of uniformly, fully inverted doped fibre, when the pump is switched off. Generally τ_2 is between 9 and 12 ms [8.36] and we shall assume $\tau_2=10.5$ms for our calculations.

The measured and calculated absorption and emission cross-sections for EDF1 and 2 are shown in fig. 8.3(i) and (ii) respectively. Taking into account the typical host dependent variation in τ_2 and λ_c, the calculated values of the cross-sections can be shown to be accurate to within ±15%. The ion concentrations were calculated to be 8.5×10^{24} m^{-3} ±15% and

assumption that thermal equilibrium is reached within a multiplet in a time short compared with the overall lifetime of the multiplet. This is generally satisfied in the Er^{3+} $^4I_{13/2}\rightarrow{}^4I_{13/2}$ transition.

$6.9\times10^{24}m^{-3}$ ±15% for EDF1 and 2 respectively. These values can be considered to be an effective ion density, and corresponds only to ions contributing to gain and not clustered ions.

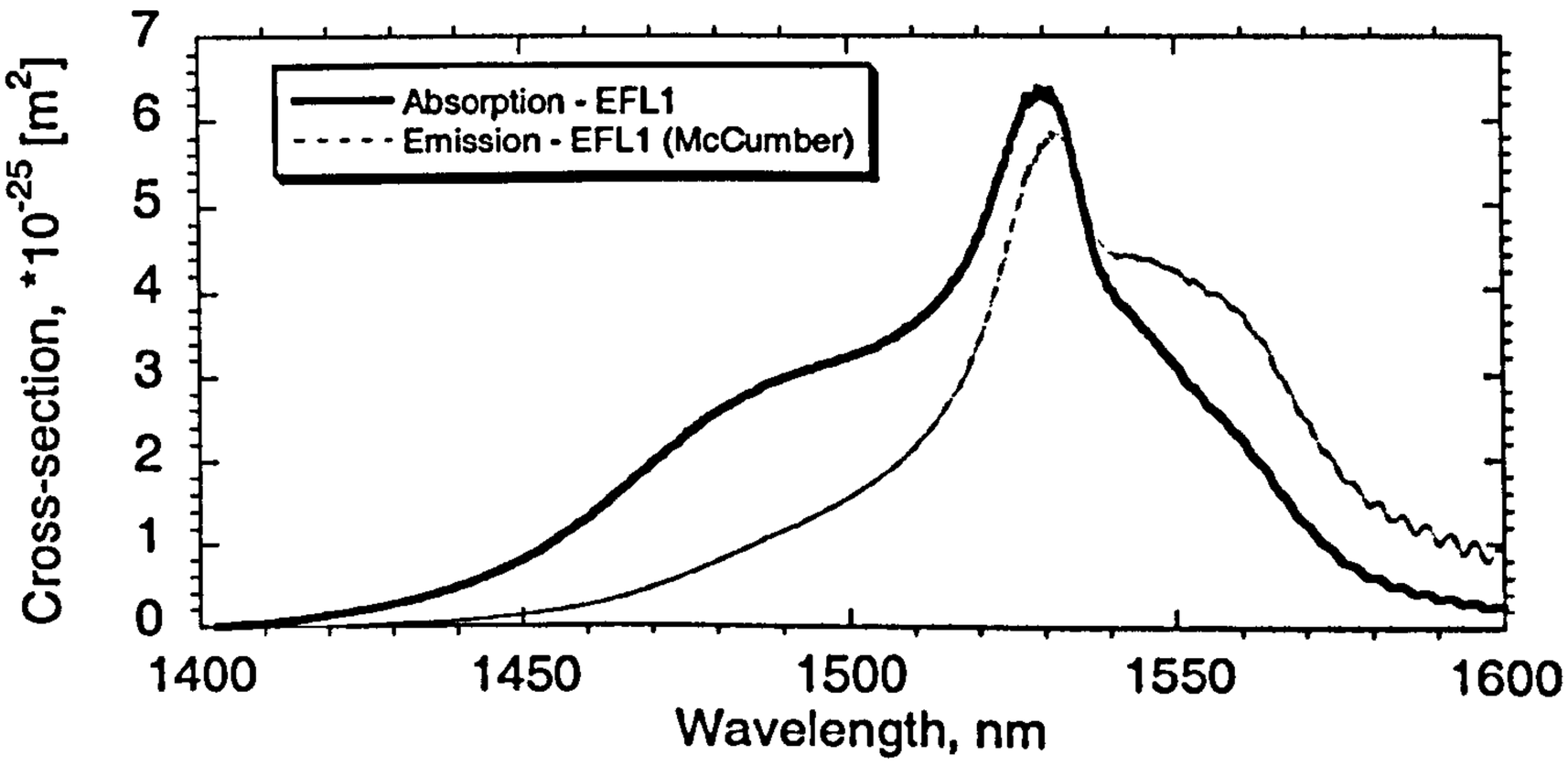

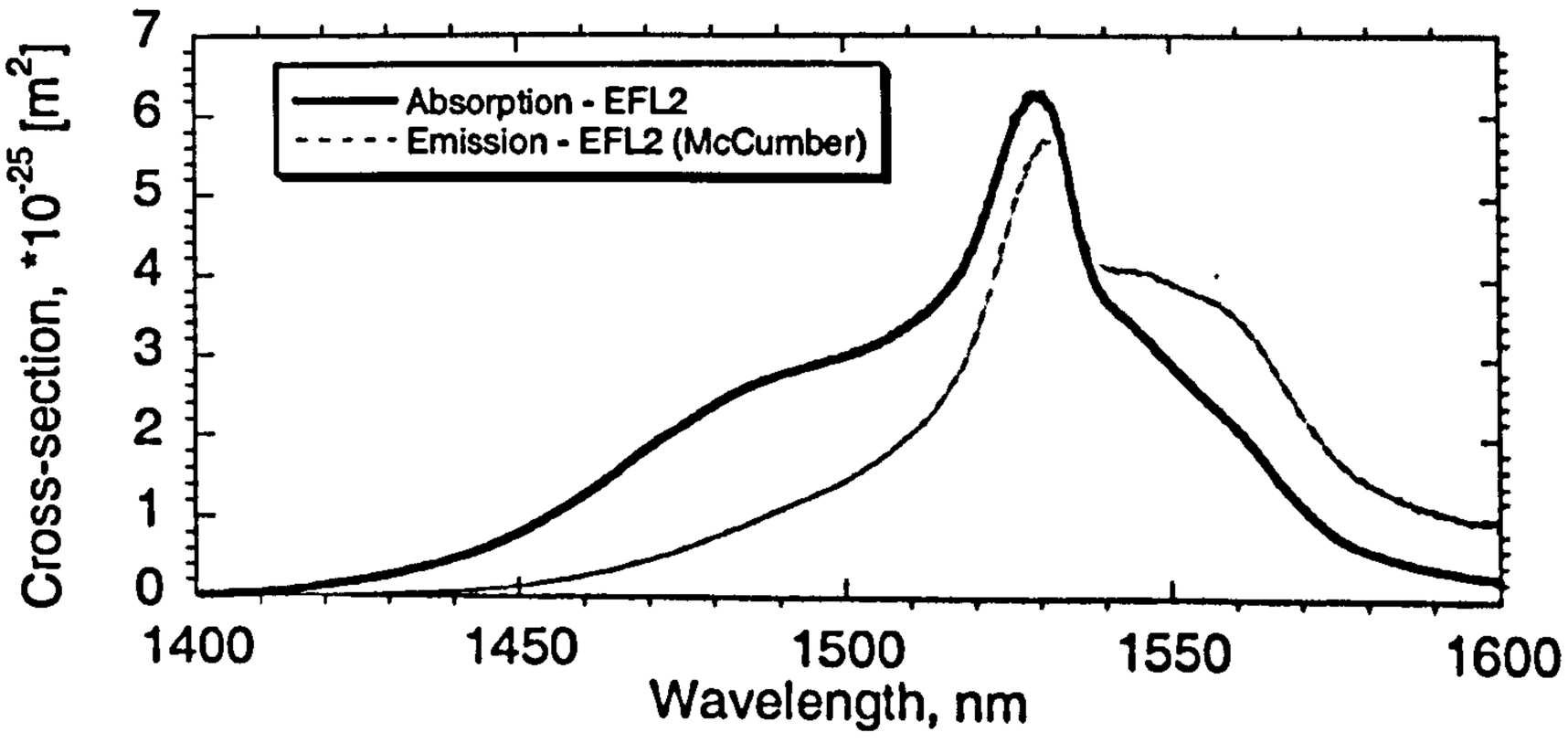

Figure 8.3: Absorption cross-sections for fibres (i) EDF1and (ii) EDF2 (assumes $\lambda_c = 1535nm$ and $\tau_2 = 10.5ms$)

Characterisation of the coupling coefficient, κ in the DFB fibre laser by measurement of the transmission or reflection spectrum is complicated by the presence of the gain medium and uncertainty in the internal loss within the region of the grating. For this reason other techniques have been developed based on heat perturbation [8.37,8.7], side-scatter [8.38] and green fluorescence profiling [8.39]. However, due to the added complexity of these techniques, we

choose a technique based on measurement of the minimum transmission of an unpumped fibre laser to yield an approximate value of the grating strength. By taking into account the maximum absorption due to the presence of the gain medium, a range of possible κ values is obtained for each laser. The measurement is carried out as follows: the output from a tuneable laser (the probe wavelength) is launched into an unpumped fibre laser and the transmitted signal is passed through a narrowband filter (to remove amplified spontaneous emission due to excitation of the gain medium by the probe wavelength) and monitored on an optical spectrum analyser. The probe wavelength is tuned until the minimum transmission wavelength is found (corresponding to the peaks either side of the phase-shift in fig. 7.2), and the transmission at this wavelength is recorded. The absorption due to the gain medium is taken into account using the product of the doped fibre length and small-signal absorption[23]. We also take into account the splice loss on either side of the doped fibre due to the mismatch in numerical aperture (NA) between the doped fibre and SMF28™, which gives rise to an excess loss of ~1 dB per pass. Having determined the minimum transmission, this is then related to the κ value using the numerical methods described in section 7.1 to determine the κ value from the minimum transmission for a uniform $\pi/2$-shifted grating. The accuracy of this method will depend on the magnitude of the internal loss within the grating, which we haven't account for. However, an internal grating loss of 1 dB would give rise to a reduction in the predicted κL of 0.06, therefore this error is likely to be small (the internal loss is likely to be much less than 1 dB). The results are tabulated in table 8.3. It can be seen that the effect of the gain medium absorption generates a small potential error in the grating strength measurement, and is unlikely to affect our overall conclusions. The κL values for the lasers range from 4.65 to 7.60.

8.3.3 Intensity noise and slope efficiency measurement

The intensity noise was measured using the set-up described in section 7.4, and is shown in fig. 7.3. The bare fibre laser was placed on a metal substrate and coated with an index matching gel in order to provide mechanical stability and reduce the sensitivity of the fibre laser to ambient acoustics. This was then placed in an acoustically isolated chamber. The laser emission from output 1 was detected on a photodiode and the spectrum of the intensity fluctuations was

---

[23] One could argue that the absorption due to the gain medium is only significant when the probe wavelength is small-signal. Therefore, we should calculate an effective penetration depth at which the probe wavelength reaches small-signal level. In our case, for the range of κ values to be measured, the penetration depth is less than ~12mm. Therefore, for our calculation we take the worst case corresponding to the total length of the doped fibre.

measured using a HP84910A spectrum analyser. The mean optical power was measured and the relative intensity noise calculated using (7.7). Similarly, the laser slope efficiencies were measured in the way described in sec. 7.4.4.

Table 8.3: DFB fibre laser properties

Serial	Doped fibre type	Wave-length	Grating length, L ±1mm
		nm	mm
1	EDF1	1534.2	60
2	EDF1	1534.9	60
3	EDF2	1533.0	115
4	EDF2	1555.4	80
5	EDF2	1555.5	95
6	EDF2	1553.0	80
7	EDF3	1534.6	60

Serial	Coupling coefficient, κ	κL	L_e	f_{RO} †	RIN @ f_{RO} † ±2dB	P_{out} @ P_p =100 mW ±5%
	m^{-1}		mm	kHz	$dB.Hz^{-1}$	μW
1	--	--	--	316	-80	77
2	125-127	7.48-7.60	8	312	-80	27
3	40-42	4.65-4.88	24	231	-90	133
4	71-73	5.72-5.82	14	197	-98	82
5	--	--	--	199	-98	102
6	56	4.47	18	78	-60	76
7	118	7.08	8	64	-58	4

† Measured at P_p =100mW

8.4 Results and Discussion

The output power characteristics and relative intensity noise for the lasers tested are shown in fig. 8.4 and 8.5 respectively and the results are summarised in table 8.2. We have also plotted the RIN of the pump diode in fig. 8.5.

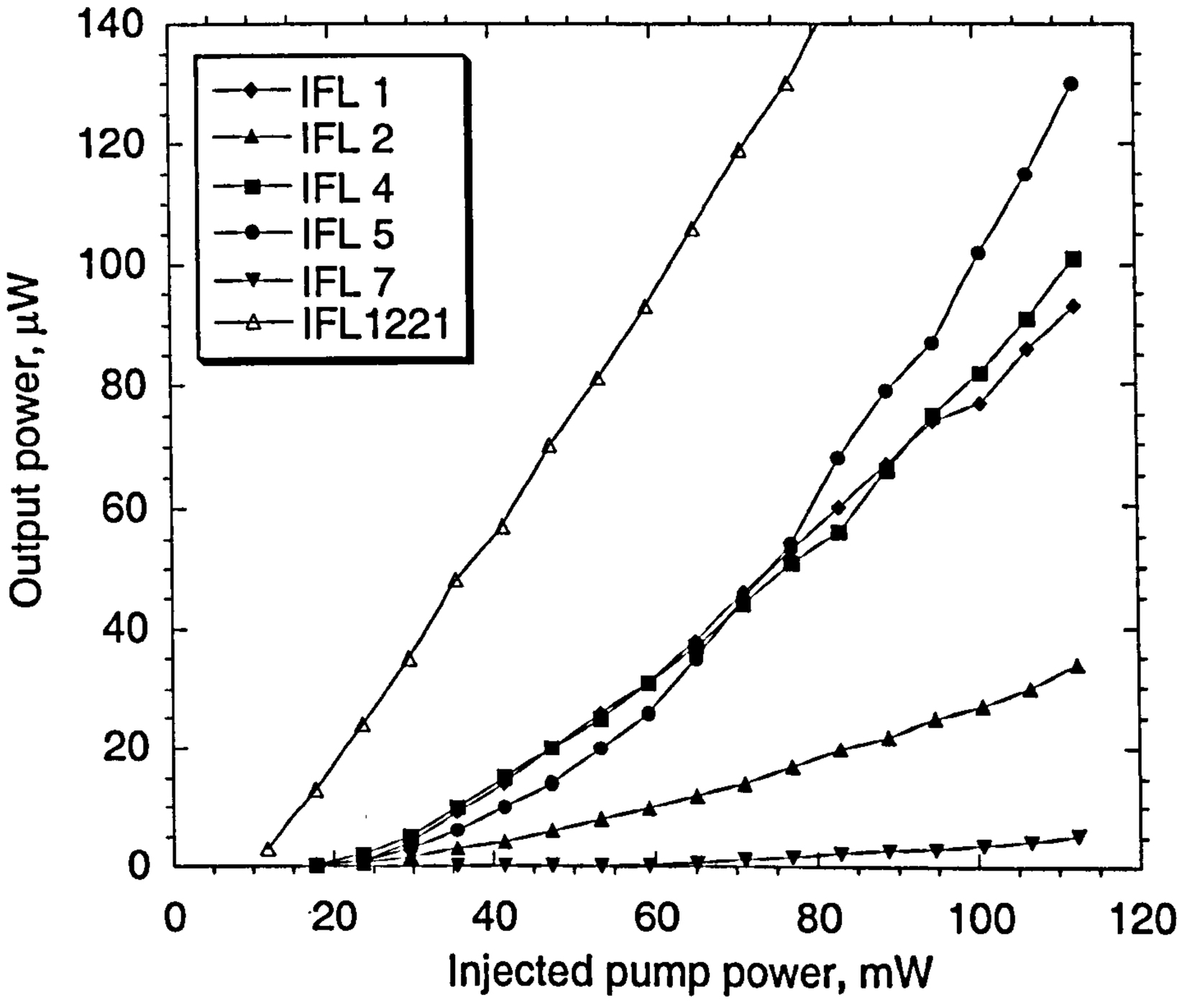

Figure 8.4: Output power characteristics of fibre lasers

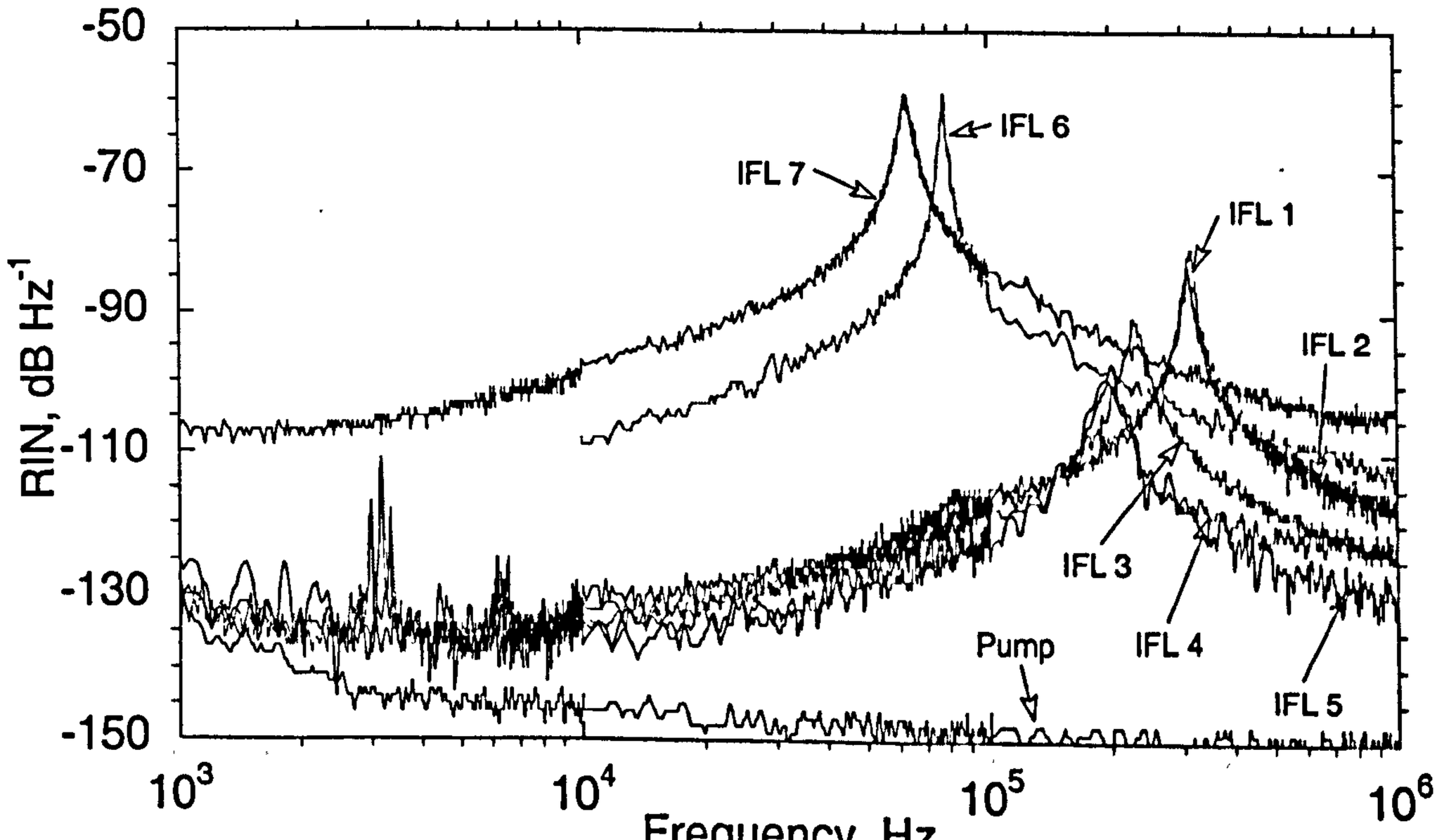

Figure 8.5: Intensity noise of fibre lasers

Referring to the output power characteristics shown in fig. 8.4, which are summarised in table 8.3, we find that in general, the highest output powers are obtained from lasers with the longer effective cavity length (IFL 3,4 and 5), in agreement with the conclusions of [8.40] and (8.10). The lowest output power was obtained from IFL7, due to its high κ value (and hence low L_e) and the low dopant concentration of EDF3. The pump power dependent slope efficiency observed for low pump powers is evidence of the presence of saturable absorbers. For low pump power, the saturable absorber acts as a loss mechanism and hence reduces the slope efficiency. As the saturable absorber is bleached, the slope efficiency increases and reaches a constant value. The pump power for which the saturable absorber is bleached, P_{p-sb}, can be deduced from the 'knee' in the slope efficiency curves. For IFL1,2,4 and 5, P_{p-sb} ~65mW. No observable evidence of a saturable absorber is present in the ouput power characteristics of IFL7. The threshold pump powers, P_{p-th}, for IFL1,2,4 and 5 were found to be ~15-25mW and for IFL7 P_{p-th} ~55mW. The absence of significant saturable absorption in EDF3 follows from the low ion concentration in this fibre and hence low erbium clustering. The high threshold pump power for IFL7, follows from the low ion concentration of EDF3.

For comparison, we have plotted the output power characteristics of IFL1221, tested in chap. 7. It is evident that no effects are observable due to saturable absorbers resulting in a nearly linear dependence of output power vs. pump power over the full range of pump power tested. As a result, the threshold of IFL1221 is also lower at P_{p-th} ~10mW.

Turning our attention to the intensity noise spectra shown in fig. 8.5 (each measured at a pump power of 100 mW), the relaxation oscillation frequency for IFL1 to 7 ranges from 64 kHz to 316 kHz and the relative peak of the relaxation oscillation ranges from -58dB.Hz^{-1} to -98dB.Hz^{-1}. IFL7 exhibited the highest intensity noise peaks due, as expected, to the low dopant concentration (and hence low absorption) of EDF3 compared to EDF1 and 2. IFL6 also exhibited high intensity noise and a low f_{RO} =78 kHz; however, during the measurements, it was noticed that higher-order modes were present from the observation of a green fluorescence from the extents of the grating. The RIN of higher-order modes is generally higher and they exhibit lower relaxation oscillation frequencies due to the short photon lifetime.

The relaxation oscillation frequency, f_{RO}, of IFL3 is higher than IFL4. This is explained by noting that the κ value for IFL3 is lower than IFL4; however, the operating wavelength of IFL3 is 1533.0nm and thus the signal cross-section, σ_2, for this laser will be approximately double that of IFL4, which lases at 1555.0nm (cf. fig.8.3). The net result is a higher f_{RO} for IFL3 than 4. We would expect a higher RIN peak for IFL4 and 5 than IFL3 due to the lower relaxation oscillation frequency; however, this is not observed.

So far we have mainly limited our discussion to lasers fabricated in the same doped fibre type. We can now compare the properties of the lasers fabricated in different doped fibres. As mentioned above, the lowest dopant concentration yields the highest intensity noise, which was found for IFL7. The increase in f_{RO} in IFL1 and 2 compared with IFL4 and 5 can be accounted for by noting the higher dopant concentration, N_0, of EDF1 and the increase in signal cross-section, σ_2, in IFL1 and 2 which both give rise to a higher f_{RO} for IFL1 and 2. However, IFL1 and 2 generally exhibit higher peak intensity noise than that of IFL3, 4 and 5. This is not expected, since the dopant concentration for EDF1 is higher than that of EDF2 and therefore lasers fabricated in EDF1 would be expected to exhibit a lower RIN peak amplitude (and higher f_{RO}) compared with an identical laser formed in EDF2. The increased overlap between the pump and signal modes in EDF2 compared with EDF1 will counter these effects slightly, but this effect is not sufficient to account for the observed differences. We conclude that another mechanism is causing an effective damping of the RIN peaks in IFL3,4, and 5.

It should be noted that the spurious noise peaks seen in fig. 8.5 around 3 kHz were found to originate from the current source driving the pump diode. This noise was removed before measurement of the pump RIN. Thus, we conclude that the EFL RIN was limited by pump noise at frequencies below ~1 kHz.

We now compare the characteristics of the lasers described above with that predicted by the model described in sec. 8.2. For each laser we have taken the measured parameters given in tables 8.2 and 8.3 and used these to calculate a RIN spectrum. The effect of neglecting SHB is to over predict the relaxation oscillation frequency. Thus, to compensate we reduce the dopant

concentration, N_0, such that the predicted f_{RO} matched our measured value. Finally, the predicted RIN spectra were then fitted to our measurements by selecting an appropriate value of $S_{\delta\gamma}$. The values of $S_{\delta\gamma}$ and N_0' used in the calculations are given in table 8.4. We have assumed that the loss modulation noise is white and hence has a constant power spectral density with frequency. The results are shown in fig. 8.6(i),(ii) and (iii) for IFL 2,3 and 4 respectively (note that sufficient data were not available for IFL 1,5,6 and 7).

Table 8.4: Loss modulation parameter and modified dopant concentration

IFL	$S_{\delta\gamma}$	N_0
2	1.5×10^{-15}	8.50×10^{24}
3	1.0×10^{-16}	5.30×10^{24}
4	5.0×10^{-17}	5.05×10^{24}

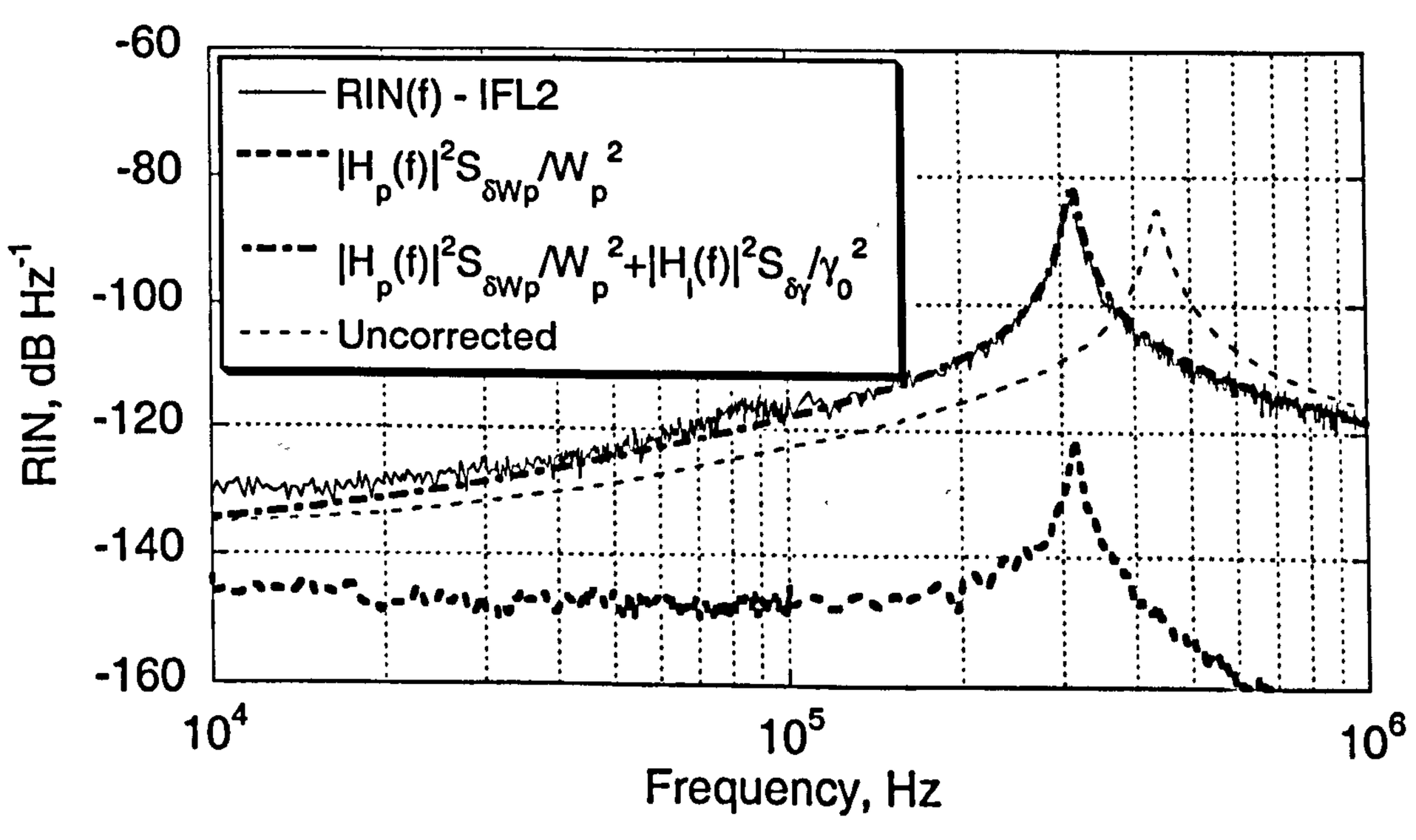

Figure 8.6: Comparison of measured intensity noise spectra with theory (i) ILF2

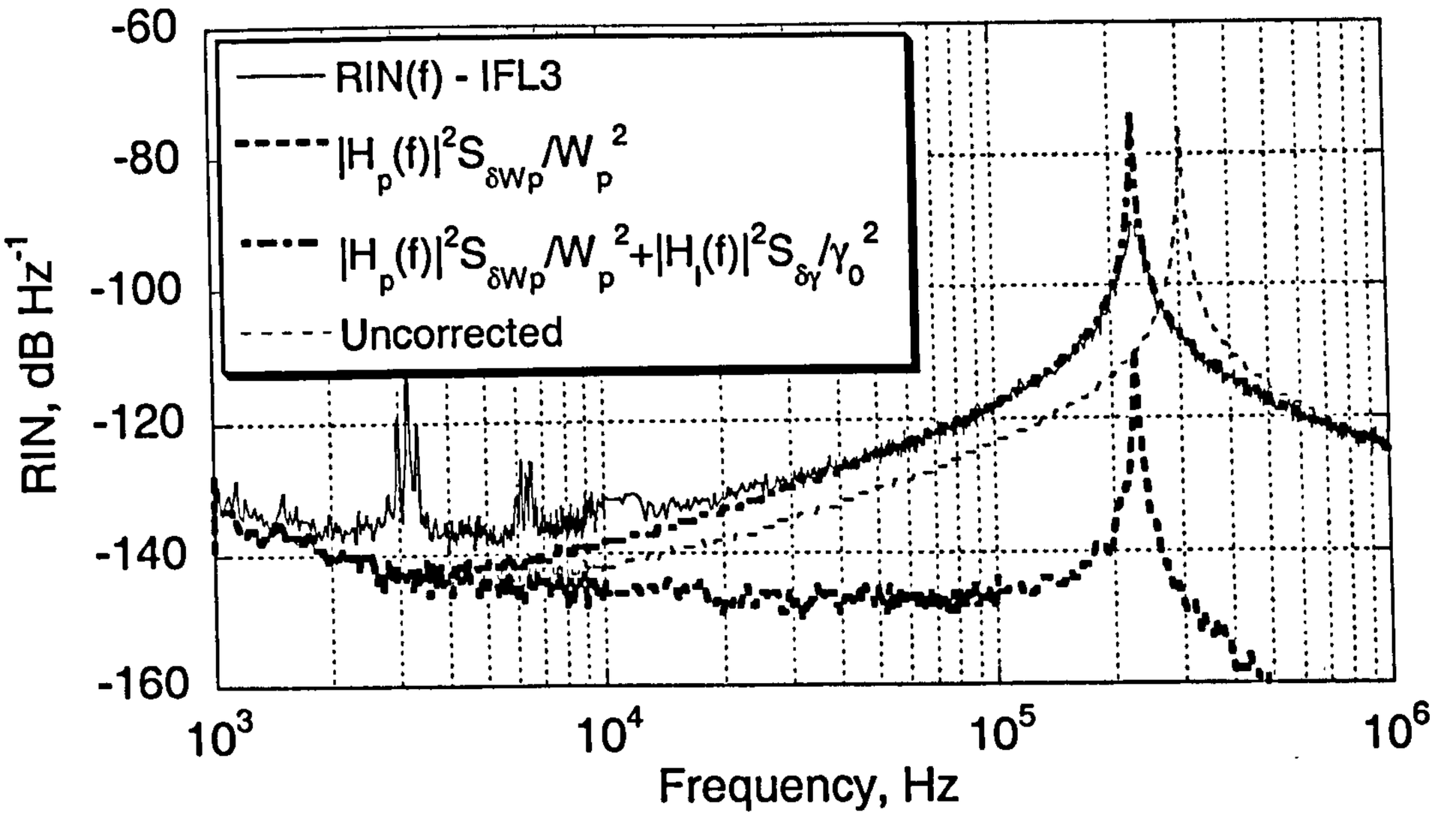

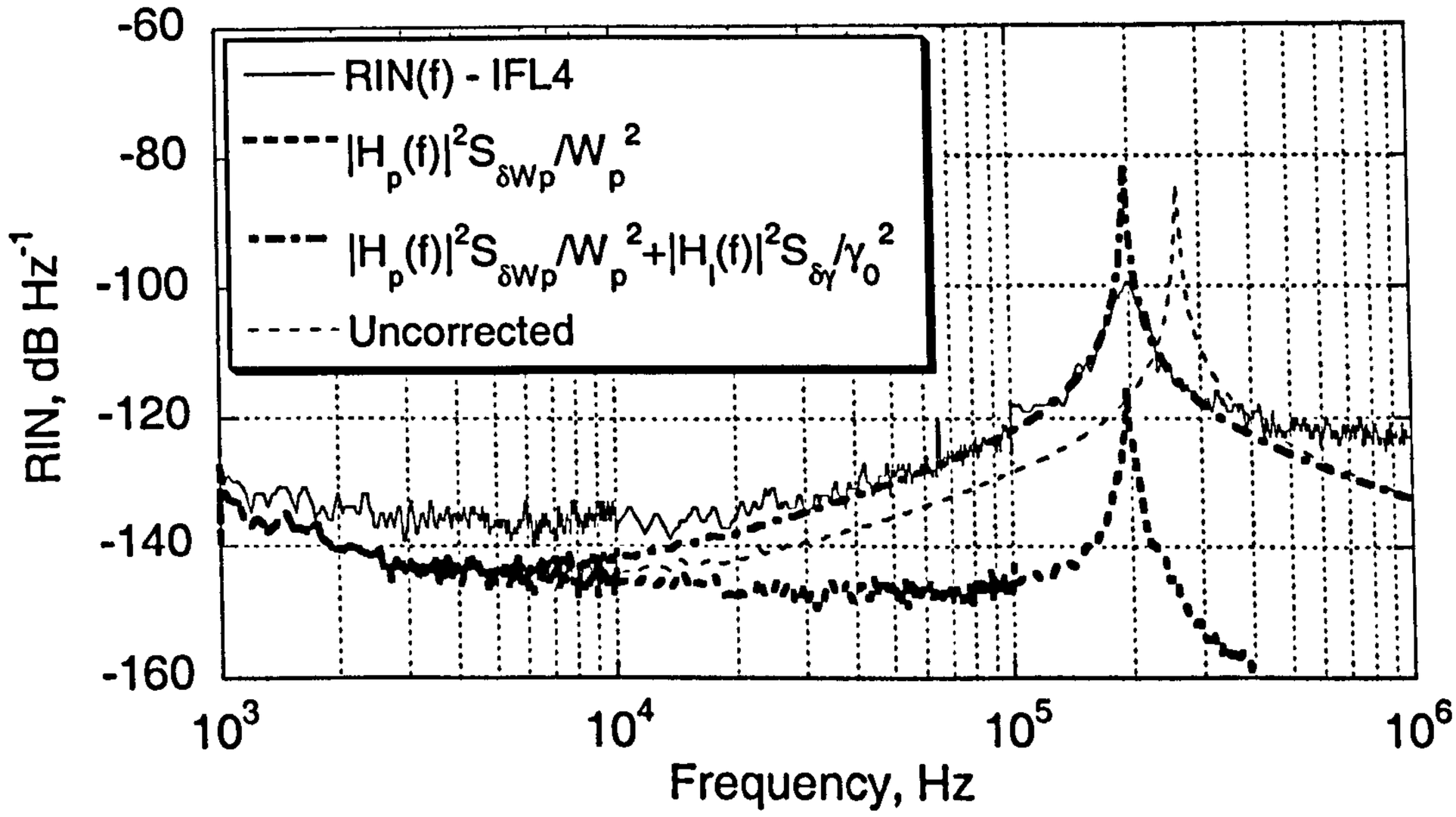

Figure 8.6 (cont): Comparison of measured intensity noise spectra with theory, (ii) IFL3, (iii) IFL4.

Both the total RIN due to pump power perturbations and loss modulations, $\left|H_p(f)\right|^2 S_{\delta W_p}/W_p^2 + \left|H_l(f)\right| S_{\delta\gamma}/\gamma_0^2$, and for pump perturbations only, $\left|H_p(f)\right|^2 S_{\delta W_p}/W_p^2$, are shown for each laser. Also, we have plotted the total RIN calculated using the measured

(and uncorrected) value of the dopant concentration. We note here that $S_{\delta\gamma}$ and N_0 are the only fitted parameters. All the other parameters used were obtained from measurements on the lasers. It can be seen that the measured intensity noise level cannot be accounted for by pump perturbations driving the relaxation oscillation frequency alone. The loss modulation mechanism gives rise to a significant increase in the intensity noise for frequencies above ~10kHz for all three lasers. When the loss modulation mechanism is included, we find good agreement between the measured RIN spectrum and that predicted by our model. A small deviation is observed around 5 kHz, which is thought to be due to excess noise originating from the pump current source. This noise was subsequently eliminated before the pump RIN was measured. The deviation of the predicted relaxation oscillation frequency (before correcting for N_0) and that measured correlates with the coupling coefficient, and hence the degree of SHB. The largest difference between measured and predicted f_{RO} is observed for the laser with the highest κ (IFL2), corresponding to the laser with the strongest SHB. The reason for deviation between the measured and calculated RIN spectrum for IFL4, above 300kHz is less certain. However, it was noted that this apparent flattening of the measured RIN spectrum observed for IFL4 above 400kHz was not observed for the similar laser, IFL5, and thus may have arisen from the measurement. The other deviation observed between the measured RIN spectra and our model is the peak RIN amplitudes. The peak RIN amplitude predicted by our model is generally higher than the measured values. The deviation is 2dB for IFL2 and 18dB for IFL3 and 4. This would imply that there is an extra mechanism not included in our model that effectively provides a small degree of negative feedback to the photon density at frequencies very close to the relaxation oscillation. Since this feedback is only observed very close to the relaxation oscillation, this would also imply that the mechanism is related to the magnitude of the photon fluctuation, which is highest at the relaxation oscillation. A possible explanation is linked to the presence of saturable absorber states (due to the presence of ion-pairs giving rise to co-operative upconversion). Fluctuations in the signal photon density, due to the relaxation oscillation are accompanied by corresponding fluctuations in the excited ion population, roughly in anti-phase with the signal photon density fluctuations, when the laser has reached steady-state operation. With a saturable absorber present, a decrease in the excited ion population causes an increase in the absorption due to the saturable absorber. This results in a further decrease in the excited ion population and hence a reduction in the signal photon

density. The saturable absorber thus acts as a negative feedback to the photon density, resulting in an effective damping of the relaxation oscillation peak. This explanation would also imply that the saturable absorber strength is stronger in EDF2 since the RIN peaks of the lasers fabricated in EDF2 are damped more than the lasers fabricated in EDF1.

Another investigation into the effects of erbium clusters on the intensity noise was reported in [8.6,20]. It was reasoned that the precise effects of clustering will depend on the distribution of clustered ions, since it may be possible to have uniformly distributed ion-pair clusters (the homogenous case) [8.12] or uniformly distributed multi-ion clusters, but where the local concentration can far exceed the uniformly distributed, isolated ion concentration (the inhomogeneous case) [8.6], as described in sec. 8.2. It was suggested that the multi-ion cluster model more accurately described the real case due to the tendency of the Er^{3+} ions to cluster closely in a silica host. A model was then presented which allowed an arbitrary number of ions per cluster to be assumed and was based on five coupled rate equations for the clustered and isolated ions and the signal field intensity. By carrying out the same small perturbation analysis as that described in sec. 8.2, it was found that the RIN consists of two contributions: one from the relaxation oscillation modulation due to pump perturbations and one due to cavity loss fluctuations. A similar RIN spectrum was found to that predicted by our model; however, a larger increase in the intensity noise below f_{RO} was observed due to pump perturbations driving the relaxation oscillation. The shape of the predicted RIN spectrum also deviated somewhat from our measured spectra. However, it was also found the RIN peak amplitude was reduced slightly with increased clustering, similar to the effect we have observed, although no explanation for this was given. Another possible mechanism suggested in [8.3], is that spontaneous emission may also partly contribute to the loss modulation term in (8.22). An accurate measurement of the spontaneous emission power may clarify this.

A better understanding of the nature of the saturable absorbers present in out fibre lasers is necessary to confirm these results; however, the link between the observed effects and ion-cluster based absorbers is quite strong.

8.5 Conclusion

In summary we have theoretically and experimentally investigated the intensity noise characteristics of fibre erbium-doped fibre Bragg grating lasers. We have discussed the

mechanisms other than pump perturbations giving rise to intensity noise in these lasers and we have characterised seven DFB fibre lasers with different doped fibre types and grating strength. To explain our observations, we developed an analytical model to predict the intensity noise spectra. We find that the intensity noise is significantly enhanced by the presence of a cavity loss modulation mechanism, over that predicted by pump perturbations alone and we discussed possible mechanisms giving rise to this effect.

Appendix 8.1: Constants used in model

The constants used in (8.15) to (8.19) are defined as follows:

$$A_1 = W_p + 2q_0 r_q + 1/\tau_2 \tag{8.25}$$

$$A_2 = (1 - n_2) \tag{8.26}$$

$$A_3 = (2n_2 - 1) r_q \tag{8.27}$$

$$A_4 = 2N_0 r_q q_0 \tag{8.28}$$

$$A_5 = q_0 c / nL_e \tag{8.29}$$

$$A_2' = (1 - n_2) W_p / q_0 \tag{8.30}$$

$$A_5' = \gamma_0 c / nL_e \tag{8.31}$$

$$r_q = c\sigma_2 / n \tag{8.32}$$

References

[8.1] M.Ding, P.K.Cheo, 1996 "Analysis of Er-doped fiber laser stability by suppressing relaxation oscillation" *IEEE Phot. Tech. Lett.* 8 (9) 1151-1153

[8.2] Y.Qian, P.Varming, J.H.Povlsen and V.C.Lauridsen, 1999 "Dynamic noise responses of DFB fibre lasers in presence of pump power fluctuations" *Elec. Lett.* 35 (4) 299-300

[8.3] E.Rønnekleiv, 2001 "Frequency and intensity noise of single frequency fiber Bragg grating lasers" *Optical Fiber Techn.* 7 206-235

[8.4] S.Taccheo, P.Laporta, O.Svelto, G.De Geronimo, 1998 "Theoretical and experimental analysis of intensity noise in a codoped erbium-ytterbium glass laser" *Appl. Phys. B* 66 16-26

[8.5] S.W.Løvseth, "Dynamic analysis of multiple wavelength DFB fiber lasers" submitted to the *IEEE J.Quant. Elec.*

[8.6] H.L.An, E.Y.B.Pun, X.Z.Lin, H.D.Liu, 1999 "Effects of ion-clusters on the intensity noise of heavily erbium-doped fiber lasers" *IEEE Phot. Tech. Lett.* 11 (7) 803-805

[8.7] E.Rønnekleiv, M.Ibsen, M.N.Zervas, R.I.Lambing, 1999 "Characterisation of fiber distributed-feedback lasers with an index perturbation method" *Applied Optics* 38 (21) 4558-65

[8.8] G.Meltz, W.W.Morey, 1991 "Bragg grating formation and germanosilicate fiber photosensitivity" *Photoinduced Self-Organised Effects in Optical Fiber* ed. F.Oullette SPIE 1516 pp.1815-199

[8.9] E.Rønnekleiv, O.Hadeler, G.Vienne, 1999 "Stability of an Er-Yb-doped fiber distributed-feedback laser with external reflections" *Opt. Lett.* 24 (9) 617-619

[8.10] J.L.Zyskind, V.Mizrahi, D.J.Digiovanni, J.W.Sulhoff, 1992 "Short single frequency erbium-doped fibre laser" *Elec. Lett.* 28 1385-1387

[8.11] P.Le.Boudec, M.Le.Flohic, P.L.Francois, F.Sanchez, G.Stephan, 1993 "Self-pulsing in Er^{3+}-doped fibre laser" *Opt. and Quant. Opt.* 25 359-367

[8.12] P.Le.Boudec, P.L.Francois, E.Delevaque, J.F.Bayon, F.Sanchez, G.M.Stephan, 1993 "Influence of ion pairs on the dynamical behaviour of Er^{3+} -doped fibre lasers" *Opt. and Quant. Elec.* 25 501-50

[8.13] H.L.An, E.Y.B.Pun, H.D.Liu, X.Z.Lin, 1998 "Effects of ion clusters on the performance of a heavily doped erbium-doped fiber laser" *Optics Lett.* 23 (15) 1197-1199

[8.14] D.Marcuse, 1993 "Pulsing of three-level laser with saturable absorber" *IEEE J. Quant. Elec.* 29 (8) 2390-2396

[8.15] W.H.Loh, 1996 "Suppression of self-pulsing behaviour in erbium-doped fiber lasers with resonant pumping" *Optics Lett.* 21 (10) 734-736

[8.16] W.H.Loh, J.P.de Sandro, 1996 "Suppression of self-pulsing behaviour in erbium-doped fiber lasers with resonant pumping: experimental results" *Optics Lett.* 21 (18) 1475-1477

[8.17] L. Luo, P.L.Chu 1997, "Suppression of self-pulsing in an erbium-doped fiber laser" *Optics Lett.* 22 (15) 1174-1176

[8.18] M.A.Englund, D.Y.Stepanov, E.C.Mägi, Z.M.Brodzeli, 2000 "Stabilisation of a DFB fibre laser using a tunable loop mirror" *Proc. of the 14th Int. Conf. on Optical Fibre sensors*, Venice, Italy, P1-04, 50-5

[8.19] M.Ding, P.K.Cheo, 1997 "Effects of Yb codoping on suppressing self-pulsation in Er-doped fiber lasers" *IEEE Phot. Tech. Lett.* 9 (3) 324-326

[8.20] H.L.An, X.Z.Lin, H.D.Liu, 2000 "Intensity noise suppression by ytterbium codoping in heavily erbium-doped fiber lasers with partly clustered erbium ions" *Optics Lett.* 25 (24) 1747-1749

[8.21] J.L.Wagener, M.J.F.Digonnet, P.F.Wysocki, H.J.Shaw, 1994, "Effects of Er^{3+} pairs on the gain and noise figure of EDFA's" *SPIE* 2073 86-91

[8.22] S.W.Løvseth, E.Rønnekleiv, 2001 "Effects of grating errors in distributed feedback fiber lasers" submitted to the *J. Light. Tech.*

[8.23] J.L.Philipsen, M.O.Berendt, P.Varming, V.C.Lauridsen, J.H.Povlsen, J.Hübner, M.Kristensen and B.Pálsdóttir, 1998 "Polarisation control of DFB fiber laser using UV-induced birefringent phase-shift" *Elec. Lett.* 34 (7) 678-679

[8.24] Z.E.Harutjunian, W.H.Loh, R.I.Lambing, D.N.Payne, 1996, "Single polarization twisted distributed feedback fibre laser" *Elec. Lett.* 3 346

[8.25] E.Rønnekleiv, S.W.Løvseth, 1999 "Stability of distributed feedback fiber lasers with optical feedback" *Proc. 13th Int. Conf. on Optical Fiber Sensors* SPIE 3746 466-469

[8.26] Y.H.Liao, H.G.Winful, 1996 "Dynamics of distributed-feedback fiber lasers: effect of nonlinear refraction" *Opt. Lett.* 21 (7) 471-473

[8.27] C.R.Giles, E.Desurvire, 1991 "Modelling erbium-doped fiber amplifiers" *J.Light.Tech.* 9 271-283

[8.28] O.Svelto, 1998 *Principles of Lasers 4th edn.* Plenum Press, section 7.2.2

[8.29] Ref. [8.28], sec. 5.3

[8.30] Ref. [8.28], sec.8.2

[8.31] G.W.Yoffe, J.W.Arkwright, B.C.Smith, 1993, "Flexible and stable interferometer for fabricating fiber Bragg gratings" *OSA Tech. Dig.* vol. 22, Bragg Gratings, Photosensitivity, and Poling in Glass Waveguides, Stuart, Florida, 93-95

[8.32] D.Yu.Stepanov, J.Canning, L.Poladian, R.Wyatt, G.Maxwell, R.Kashyap, 1999 "Apodized distributed-feedback fiber laser", *Opt. Fib. Tech.* 5 209-214

[8.33] M.A.Englund, S.W.Løvseth, D.Yu.Stepanov, E.C.Mägi, 2001 "Selective gain tuning in erbium doped fibres" OECC/ACOFT, Sydney, Australia, Post-deadline session

[8.34] W.J.Miniscalco, R.S.Quimby, 1991 "General procedure for the analysis of Er^{3+} cross sections" *Optics Lett.* 16 (4) 258-260

[8.35] E.Desurvire, 1994 *Erbium-doped fiber amplifiers: Principles and Applications* John Wiley & Sons, section 4.5

[8.36] W.J.Miniscalco, 1991 "Erbium-doped glasses for fiber amplifiers at 1500nm" *J. Light. Tech.* 9 (2) 234-250

[8.37] E.Brinkmeyer, G.Stolze, D.Johlen, 1997 "Optical space domain reflectometry (OSDR) for determination of strength and chirp distribution along optical fibre gratings" *Photosensitivity in* Glasses vol. 17 of OSA Technical Digest Series (OSA, Washington D.C.)

[8.38] P.A.Krug, R.Stolte, R.Ulrich, 1995 "Measurement of index modulation along an optical fiber Bragg grating" *Optics Lett.* 20 (17) 1767-9

[8.39] W.H.Loh, B.N.Samson, J.P. de Sandro, 1996 "Intensity profile in a distributed feedback fiber laser characterized by a green fluorescence scanning technique" *Applied Physics Letters* 69 (25) 3773-5

[8.40] V.C.Lauridsen, J.H.Poulsen, P.Varming, 1999 "Optimising erbium-doped DFB fibre laser length with respect to maximum output power" *Elec. Lett.* 35 (4) 300-302

[8.41] P.Myslinski, J.Chrostowski, 1998 "Gaussian-mode radius polynomials for modeling doped fiber amplifiers and lasers" *Microwave and Optical Tech.* 11 (2) 61-64

Chapter 9

CONCLUSION

In this thesis we have demonstrated, for the first time, a number of advances in interferometric sensor array multiplexing technology. Our original aims were to increase multiplexing capability by incorporating dense wavelength division multiplexing (DWDM) with time division multiplexing (TDM) and improve sensor performance using fibre laser sources. Here is what we found.

In chapter 5 we demonstrated novel multiplexing architectures using time division multiplexing and dense wavelength division multiplexing that permitted a significant increase in the number of interferometric sensors that can be interrogated through two fibres. We showed that the crosstalk between sensors multiplexed on adjacent wavelengths was less than –76 dB (for a wavelength spacing of 1.6nm) and identified the most likely mechanism causing crosstalk, to be the adjacent channel crosstalk of the wavelength demultiplexer. To interrogate our experimental array, we used novel erbium doped DFB fibre laser (EFL) sources. We then developed a model to predict the phase resolution and dynamic range of sensors multiplexed in these architectures.

Using these multiplexing architectures, the number of interferometric sensors that can be multiplexed onto two fibres is ultimately limited by the launch powers. Thus, increasing the launch powers would permit more sensors to be multiplexed. However, in chapter 6, we discussed the detrimental effects on the phase resolution of the nonlinear transmission properties in the fibre medium in the presence of high optical powers. Using previously developed theory on nonlinear phenomena in fibre waveguides we were able to identify the significant nonlinear interactions and determine the degradation on the phase resolution of a

multiplexed sensor. The nonlinear interaction occurs where the optical powers are highest, which for an interferometric sensor array is in the delivery fibre. By ensuring that the launched optical powers fell just below the critical power levels required before significant degradation due to nonlinearity occurred, it was possible to theoretically determine the relationship between the link length (distance between electronics unit and array) and number of multiplexed sensors in order to achieve a pre-determined phase resolution (typically 100 $\mu rad.Hz^{-1/2}$). We then determined the increase in link length achievable when periodic discrete erbium doped fibre amplifiers (EDFA) where placed along the link fibre and when a remotely pumped EDFA was used. For the configuration presented, which incorporated a single remotely pumped pre-EDFA, with a link length of 55 km a maximum of 32 sensors can be multiplexed onto two fibres plus one pump delivery fibre and achieve a phase resolution of less than 100 $\mu rad.Hz^{-1/2}$. Reducing the link length to 38 km, increases the number of sensors to 160. Reducing the link length to less than 10 km allows in excess of 500 sensors to be multiplexed and in this case the remotely pumped EDFA can be omitted without loss of performance. This work therefore demonstrates the theoretical limits on the performance of the multiplexed interferometric sensor technology using DWDM and TDM in a fully electrically passive array..

The current state-of-the-art multiplexed interferometric sensor arrays use TDM, frequency division multiplexing (FDM) or some degree of WDM with TDM. Practical laser sources are diode pumped Nd:YAG lasers (1310nm) or semiconductor DFB lasers (1550nm) to interrogate the arrays. High sensor resolution is achieved with a diode pumped Nd:YAG laser (due to its narrow linewidth); however, the array size is limited to ~8 sensors using FDM [9.1] or 64 sensors using TDM [9.2] (note that WDM cannot be used in the 1300nm spectral region). Semiconductor DFB lasers operating at 1550nm permit the use of DWDM with TDM; however, these lasers must be carefully stabilised to ensure a stable emission frequency and sensor resolution is generally limited to around 0.1-1$mrad.Hz^{-1/2}$ due to source phase noise [9.3]. The DFB fibre laser allows use of the DWDM/TDM architecture and a high sensor resolution (<10 $\mu rad.Hz^{-1/2}$) would be achievable due to the potentially low frequency noise of this laser source. In principle, high phase resolution could be maintained even in very large-scale arrays. We note also that the DWDM/TDM architecture significantly reduces the complexity of the fibre telemetry compared with the FDM approach.

In the experiment described in chapter 5, we used a multiplexed fibre laser source to interrogate the interferometric sensors, which prevented the predicted phase resolution from being achieved due to excess frequency and intensity noise, in our fibre laser configuration. Therefore, in chapter 7, we presented novel techniques based on electronic feedback to simultaneously suppress the frequency noise and relaxation oscillation induced intensity noise. We showed that the free-running frequency noise of the DFB fibre laser was likely to be fundamentally limited by cavity thermal noise; however, by locking the laser emission to an interferometer and using cavity strain induced feedback, we could overcome this limit and reduce the frequency noise by a further 18 dB. Using a fibre laser with the performance demonstrated would permit the predicted phase resolution of the sensors described in chapter 5, to be achieved. Further to this, a sizeable path imbalance could be present in each interferometric sensor, without loss of sensor resolution due to frequency induced phase noise. This is due to the considerably lower frequency noise of the EFL compared with the semiconductor laserdiode and thus relaxes the requirements on path balancing of interferometric sensors. We also demonstrated a feedback technique to reduce intensity noise around the relaxation oscillation peak as well as a novel technique to allow frequency modulation of the EFL.

In chapter 8, we investigated the fundamental mechanisms giving rise to intensity noise in the EFL. By characterising seven fibre lasers of various designs, and developing a rate equation based model, we were able to provide a quantitative explanation for the observed levels of intensity noise. In particular we found that the intensity noise of the EFL around the relaxation oscillation was some way higher than that due to pump power perturbations and suggested that this is likely to be due to the effect of cavity loss modulation.

Away from the main theme of sensor multiplexing and interrogation, in chapter 3 we presented a detailed model of fibre-optic flexural disk accelerometers. We compared the results from the model with the measured performance of prototype accelerometers and obtained excellent agreement. These accelerometers exhibited some of the highest combinations of responsivity and bandwidth reported in the literature to date. Of particular interest to the sonar community is the development of vector sensor based acoustic arrays. Accelerometers of the type described in this chapter multiplexed in the DWDM/TDM architectures described above may provide a

low cost solution to the vector sensor based acoustic array, particularly when very large arrays (greater than 1000 sensors) are required.

Finally, in chapter 4 we presented a technique to increase the responsivity to pressure of an in-fibre Bragg grating (IFBG) using compliant coatings. An amplification factor of up to 18.8±21% (measured relative to a bare IFBG) was demonstrated using a 5 mm thick coating of polyurethane. We also showed how this may be used to increase the acoustic responsivity of an in-fibre laser sensor, with the potential to achieve an acoustic resolution of ~2 mPa.$Hz^{-1/2}$ at 1 kHz.

Future work

The work presented here can be extended in a number of areas. Further development of the fibre laser source is required to combine all the techniques presented in chapter 7 (i.e. RIN suppression, frequency noise suppression and frequency modulation) in a single laser. Longer-term tests are then required to ensure that this performance is maintained with age. Also, significant scope exists in modifying the laser design. For example, by co-doping the laser cavity with ytterbium significantly increases the pump absorption and high power can be obtained directly from the laser cavity without the need for an amplifying section [9.4]. However, the effects on the frequency noise exhibited by this type of laser would need to be explored further. Also, fabrication of the DFB fibre laser in polarisation maintaining fibre would ensure that a well-defined state of polarisation is obtained that is compatible with external modulators. Increasing the accuracy by which the central $\pi/2$ phase-shift is obtained, as discussed in chapter 8, may also reduce the effect of loss dispersion, which degraded the performance of a frequency modulated laser.

In chapter 6, we determined theoretically the detrimental effects of nonlinearity in the transmission fibre. The results obtained can now be verified with some basic experiments, using a noise reduced DFB EFL source.

In chapter 3, we found that the cross-responsivity of the flexural disk accelerometer was 8 dB lower than the on-axis responsivity and reasons for this were discussed. Further work is required to reduce this cross-responsivity and develop a water-proof housing. For use as an acoustic vector sensor, characterisation of the sensor beam pattern and responsivity to pressure

is required. Also, external damping may be required to reduce the Q of the fundamental resonance (in order to reduce ringing effects in the presence of pulsed acoustic signals).

In chapter 4, we found that applying a compliant coating to an in-fibre laser sensor would increase its acoustic responsivity by a factor of 18.8±21%. However, the coating material must be chosen carefully. Materials that exhibit large expansion/contraction during the curing process may induce nonuniform stress in the fibre, which may significantly alter the Bragg grating profile. In the worst case, this may prevent the laser from lasing. However, low expansion materials exist which may make this technique practical.

On a more general note, applications of fibre lasers extend further than optical sources. As mentioned briefly in chap. 2 and 4, their use as the sensor itself is particularly attractive due to the very short cavity length and potentially high sensitivity. Novel waveguide structures in which to form the lasers, such as photonic crystal fibre and holey fibre [9.5], may make possible novel laser devices due to the control these structures provide over the mode field shape and size. One would expect a fibre, filled primarily with air, to exhibit a responsivity to pressure somewhat higher than that observed in conventional optical fibre due to its higher compliance. Certainly, we can expect to see some interesting developments in the area of fibre Bragg grating lasers in the near future.

Publications

This thesis has produced five peer-reviewed journal papers (two pending peer-review), one book chapter, ten conference papers and presentations and one patent pending. These are listed below:

Peer-reviewed journal papers and book chapters

G.A.Cranch and P.J.Nash, 2002 "Optical fibre hydrophones" in *Lasers and their Applications*, IOP Publishing, section D2.5

G.A.Cranch and P.J.Nash 2001 "Large-scale multiplexing of interferometric fibre-optic sensors using TDM and DWDM" *J. Light. Tech.* 19 (5) 687-699

G.A.Cranch, 2001 "Frequency noise reduction in erbium doped fiber DFB lasers using electronic feedback" submitted for publication in Optics Letters.

G.A.Cranch, M.A.Englund, 2001 "Intensity noise properties of erbium doped fiber Bragg grating lasers" to be submitted to the IEEE J.Quantum Electronics.

G.A.Cranch and P.J.Nash, 2000 "High-responsivity fiber-optic flexural disk accelerometers" *J. Light. Tech.* 18 (9) 1233-1243

D.J.Hill and G.A.Cranch, 1999 "Gain in hydrostatic pressure sensitivity of coated fibre Bragg grating" *Elec. Lett.* 35 (15) 1268-1269

Conference papers and presentations

G.A.Cranch, 2002 "Frequency noise reduction in erbium doped fibre Bragg grating lasers using active electronic feedback" to be presented at the 15th Int. Conf. on Optical Fiber Sensors, Portland, OR, USA

G.A.Cranch, 2002 "Frequency modulation properties of erbium doped DFB fiber lasers using cavity strain" to be presented at the 15th Int. Conf. on Optical Fiber Sensors, Portland, OR, USA

G.A.Cranch, 2001 "Erbium doped fiber Bragg grating lasers: applications as sources and sensors" seminar at Heriot-Watt University, Edinburgh, UK

G.A.Cranch (INVITED) 2001 "Realisation of remote arrays of fibre-optic interferometric sensors" OSA Tech. Meeting, Long Beach, CA

P.J.Nash, G.A.Cranch, D.J.Hill, 2000 "Large-scale multiplexed fibre-optic arrays for geophysical applications" *SPIE 4202* Photonics East 2001, Boston, US

G.A.Cranch, 2000 "Large-scale multiplexed fibre-optic arrays for geophysical applications" presented at Schlumberger-Doll Research Centre, Connecticut, USA, Nov. 2000

G.A.Cranch, P.J.Nash, 2000, "Large-scale arrays of interferometric fibre-optic sensors for applications in military surveillance and seismic surveying" Proc. 14th Int. Conf. on Optical Fiber Sensors, SPIE 4185, Venice, Italy 260-263

P.J.Nash, G.A.Cranch, 1999 "Multi-channel optical hydrophone array with time and wavelength division multiplexing" *Proc. of the 13th Int. Conf. on Optical Fiber Sensors* SPIE 3746 304-307

G.A.Cranch, P.J.Nash, 1999 "High multiplexing gain using TDM and WDM in interferometric sensor arrays" *SPIE 3860* Photonics East Boston USA 531-7.

G.A.Cranch, 1999 "Fibre-optic sensors for underwater applications" seminar at Heriot-Watt University, Dept. of Physics, Edinburgh

P.J.Nash, G.A.Cranch, 1998 *Fibre optic sensor research at DERA* DSTO, Adelaide, Australia.

Other

P.J.Nash, G.A.Cranch, D.J.Hill, R.Crickmore, 1998 Optical fibre sensors for ASW applications *DERA Journal of Defence Science*

Patents

"Fibre optic sensor array", G.A.Cranch, filed April 2000

References

[9.1] A.Dandridge, A.B.Tveten, A.D.Kersey, A.M.Yurek, 1987 "Multiplexing of interferometric sensors using phase generated carrier techniques" *J. Light. Tech.* 5 (7) 947-952

[9.2] A.D.Kersey, A.Dandridge, A.B.Tveten, 1987 "Time division multiplexing of interferometric fibre sensors using passive phase generated carrier interrogation" *Optics Letters* 12 (10) 775-777

[9.3] A.D.Kersey, A.Dandridge, A.R.Davis, C.K.Kirkendall, M.J.Marrone, D.G.Gross, 1996 "64-element time-division multiplexed interferometric sensor array with EDFA

telemetry" *Optical Fiber Communications* Tech. Digest Series (IEEE Cat. No. 96CH35901) Optical Co. Amer. Washington DC USA ix+326 ThP5 270-271

[9.4] W.H.Loh, B.N.Samson, L.Dong, G.J.Cowle, K.Hsu, 1998 "High performance single frequency fiber grating-based erbium/ytterbium-codoped fiber lasers" *J.Light.Tech.* 16 (1) 114 –118

[9.5] T.Søndergaard, 2000 "Photonic crystal distributed feedback fiber lasers with Bragg gratings" *J. Light.Tech.* 18 (4) 589-597